# Journal of Turbomachinery

Published Quarterly by ASME

VOLUME 131 • NUMBER 1 • JANUARY 2009

Editor, **DAVID C. WISLER (2008)**
Assistant to the Editor: **ELIZABETH WISLER**
Associate Editors
Gas Turbine (Review Chair)
**KLAUS BRUN (2008)**
Aeromechanics
**M. MONTGOMERY (2008)**
**A. SINHA (2008)**
Boundary Layers and Turbulence
**G. WALKER (2008)**
Compressor Aero
**ZOLTAN S. SPAKOVSZKY (2011)**
Computational Fluid Dynamics
**J. ADAMCZYK (2008)**
**M. CASEY (2008)**
Experimental Methods
**W.-F. NG (2008)**
Heat Transfer
**R. BUNKER (2009)**
**J.-C. HAN (2008)**
Radial Turbomachinery
**R. VAN DEN BRAEMBUSSCHE (2008)**
Turbomachinery Aero
**S. GALLIMORE (2008)**
**D. PRASAD (2008)**
**A. R. WADIA (2009)**

**PUBLICATIONS COMMITTEE**
Chair, **BAHRAM RAVANI**

**OFFICERS OF THE ASME**
President, **THOMAS M. BARLOW**
Executive Director, **THOMAS G. LOUGHLIN**
Treasurer, **T. PESTORIUS**

**PUBLISHING STAFF**
Managing Director, Publishing
**PHILIP DI VIETRO**
Manager, Journals
**COLIN MCATEER**
Production Coordinator
**JUDITH SIERANT**

**Transactions of the ASME, Journal of Turbomachinery** (ISSN 0889-504X) is published quarterly (Jan., Apr., July, Oct.) by The American Society of Mechanical Engineers, Three Park Avenue, New York, NY 10016. Periodicals postage paid at New York, NY and additional mailing offices. POSTMASTER: Send address changes to Transactions of the ASME, Journal of Turbomachinery, c/o THE AMERICAN SOCIETY OF MECHANICAL ENGINEERS, 22 Law Drive, Box 2300, Fairfield, NJ 07007-2300. **CHANGES OF ADDRESS** must be received at Society headquarters seven weeks before they are to be effective. Please send old label and new address.

**STATEMENT from By-Laws.** The Society shall not be responsible for statements or opinions advanced in papers or ... printed in its publications (B7.1, Par. 3). **COPYRIGHT © 2009** by the American Society of Mechanical Engineers. For authorization to photocopy material for internal or personal use under those circumstances not falling within the fair use provisions of the Copyright Act, contact the Copyright Clearance Center (CCC), 222 Rosewood Drive, Danvers, MA 01923, tel: 978-750-8400, www.copyright.com. Request for special permission or bulk copying should be addressed to Reprints/Permission Department.

Canadian Goods & Services Tax Registration #126148048

## RESEARCH PAPERS

(Contents continued on inside back cover)

This journal is printed on acid-free paper, which exceeds the ANSI Z39.48-1992 specification for permanence of paper and library materials. ∞™
♲ 85% recycled content, including 10% post-consumer fibers.

Downloaded 28 May 2010 to 128.113.26.88. Redistribution subject to ASME license or copyright; see http://www.asme.org/terms/Terms_Use.cfm

(**Contents continued**)

**Journal of Turbomachinery** **Volume 131, Number 1** **JANUARY 2009**

The ASME Journal of Turbomachinery is abstracted and indexed in the following:

*Aluminum Industry Abstracts, Aquatic Science and Fisheries Abstracts, Ceramics Abstracts, Chemical Abstracts, Civil Engineering Abstracts, Compendex (The electronic equivalent of Engineering Index), Corrosion Abstracts, Current Contents, Ei EncompassLit, Electronics & Communications Abstracts, Energy Information Abstracts, Engineered Materials Abstracts, Engineering Index, Environmental Science and Pollution Management, Excerpta Medica, Fluidex, Fuel and Energy Abstracts, INSPEC, Index to Scientific Reviews, Materials Science Citation Index, Mechanical & Transportation Engineering Abstracts, Mechanical Engineering Abstracts, METADEX (The electronic equivalent of Metals Abstracts and Alloys Index), Metals Abstracts, Oceanic Abstracts, Pollution Abstracts, Referativnyi Zhurnal, Shock & Vibration Digest, Steels Alert*

**Xingen Lu**
e-mail: xingenlu@hotmail.com

**Wuli Chu**

School of Power and Energy,
Northwestern Polytechnical University,
Xi'an, 710072, P.R.C.

**Junqiang Zhu**
Institute of Engineering Thermophysics,
Chinese Academy of Sciences,
Beijing 10080, P.R.C.

**Yangfeng Zhang**
School of Power and Energy,
Northwestern Polytechnical University,
Xi'an, 710072, P.R.C.

# Numerical Investigations of the Coupled Flow Through a Subsonic Compressor Rotor and Axial Skewed Slot

*In order to advance the understanding of the fundamental mechanisms of axial skewed slot casing treatment and their effects on the subsonic axial-flow compressor flow field, the coupled unsteady flow through a subsonic compressor rotor and the axial skewed slot was simulated with a state-of-the-art multiblock flow solver. The computational results were first compared with available measured data, that showed the numerical procedure calculates the overall effect of the axial skewed slot correctly. Then, the numerically obtained flow fields were interrogated to identify the physical mechanism responsible for improvement in stall margin of a modern subsonic axial-flow compressor rotor due to the discrete skewed slots. It was found that the axial skewed slot casing treatment can increase the stall margin of subsonic compressor by repositioning of the tip clearance flow trajectory further toward the trailing of the blade passage and retarding the movement of the incoming/tip clearance flow interface toward the rotor leading edge plane.*
[DOI: 10.1115/1.2948959]

*Keywords: compressor instability, casing treatment, tip clearance flow*

## Introduction

The continuing trend toward increased thrust-to-weight ratio engines has led to highly loaded compressor and with greatly reduced loaded compressor with greatly reduced blade and stage count. With increased aerodynamic blade loading, it is critical to maintain a suitable operating range. The safe operating range of a gas turbine compressor is limited at low mass flow rates by the onset of flow instabilities. Typically, the peak pressure rise and peak efficiency of a compressor are located close to the stability boundary. Although an operational point close to the stability limit is desirable, the disturbances that emerge from the flow instabilities have several unwanted effects. Besides a lowered pressure rise and efficiency, they introduce thermal and mechanical loads onto the blades as well as induce oscillations that could cause severe damage. Alternatively, throughout the aeropropulsion history, much work has been done to control the stall phenomenon in compressors and broaden the compressor operating range.

Under many conditions, it is in the end-wall flow regions of a compressor that unstable flow conditions are initiated [1,2]. If aerodynamic stall in the end-wall region can be delayed, the stable working range of the compressor could be increased. Since the late 1950s, casing treatment was known as a powerful method to enhance the flow stability in compressors and many experimental investigations have been conducted to reveal the impact of a variety of casing treatments on the compressors [3–8]. However, most of these studies were just aimed at quantifying the influence on the compressor's performance; the exact mechanism of the stall suppression imposed by casing treatments have still not been fully understood. So far, much of the knowledge regarding casing treatments and their effectiveness is empirical. A clear understanding of the interaction between the rotor tip flow and axial skewed slot is significant for in-depth understanding of the fluid dynamic processes responsible for the influence brought about by the axial skewed slot casing treatment, which results in the enhancement of the stable operating range. This will help in designing better treatment geometries for various applications with little or no loss in overall compressor efficiency.

It is difficult to clarify the detailed flow structures around and within the casing treatment configurations in only experimental technique because they occur in the very small region near the tip in the rotor passage. Therefore, with the advance of computational techniques and increasing availability of low cost computing, considerable amount of numerical and modeling activity has been devoted in recent years to investigate the coupled flow through blade passage and casing treatment by the solution of Navier–Stokes equations. Significant results have been obtained with steady approaches applying circumferential averages of the fluid dynamic flow features [8–11]. However, many modern casing treatments are nonaxisymmetric in nature, due to the relative motion between rotating blade passage and casing treatment; the flow in these tip treatments is fundamentally three dimensional and unsteady. It remains possible to construct simplified steady models of these casing treatments, in which circumferential average properties are exchanged between the casing treatment and blade passage. However, these models fail to capture the fundamental unsteadiness induced by the interaction between the casing treatment and the blade passage, which may affect the rotor performance remarkably [9]. For this case, a time-accurate coupling procedure would be extremely necessary for simulating the interaction between the casing treatment and the blade passage.

Regarding the direct simulations on the unsteady interaction between the casing treatment and rotor passage in the literature, to the knowledge of the author, the coupled flow through the axial skewed slot and rotor blade passage under transonic conditions has been extensively studied and is believed to be well understood [12–15]. However, investigations on the coupled flow through the rotor blade passage and axial skewed slot under subsonic conditions are relatively few and the relevant physical mechanisms are not as well understood in subsonic compressors as it is in the transonic compressors. The axial skewed slot casing treatment for a subsonic compressor has different unsteady effects than tran-

---

Contributed by the Turbomachinery Division for publication in the JOURNAL OF TURBOMACHINER. Manuscript received June 14, 2005; final manuscript received November 16, 2006; published online September 25, 2008. Review conducted by Roger L. Davis.

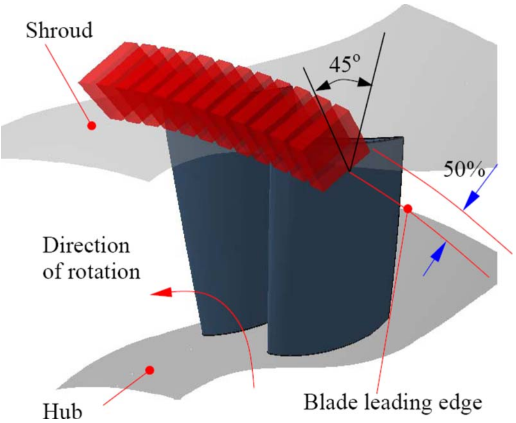

**Fig. 1 Tested axial skewed slots casing treatment configuration**

sonic compressor, which have large shock effects. In addition, most of the past numerical work has not been anchored with experimental data to show that the simulations are valid, nor have the simulations been advanced enough to describe the details of the flows in the casing area and the rotor tips.

This paper presents a numerical investigation of the unsteady flow through a subsonic compressor rotor coupled with axial skewed slot casing treatment with the help of NUMECA software. The main objectives of the current study is to advance our understanding of the flow field near the casing of a subsonic compressor rotor with axial skewed slot and determine the changes in the flow field by which casing treatments improve compressor stability.

## Test Compressor Rotor and Axial Skewed Slot Casing Treatment

The test compressor used for the current study is the isolated rotor of a subsonic single stage axial-flow compressor test rig at the Northwestern Polytechnical University. The rotor design total pressure ratio is 1.249 at a mass flow of 5.6 kg/s. At a wheel speed of 15,200 rpm, the relative Mach number is 0.78 at the tip, which yields a nominal tip speed of 237 m/s. The rotor has 30 blades, with an aspect ratio of 1.94, a hub-to-tip ratio of 0.61, and a tip solidity of 0.96. For all sets of simulations, the same nominal running tip clearance of 0.3 mm (about 0.5% of the rotor span) is maintained. More details about the rotor's aerodynamic design can be found in Refs. [10,16,17].

The end-wall treatment employed in this numerical study consists of a series of discrete square-edged axial skewed slot located over the rotor tip, as illustrated in Fig. 1, which is geometrically identical to the configuration used in Ref. [16]. Only its axial position is shifted upstream so that approximately 50% of the blade chord is covered by the treated slots. A total of 183 treatment slots were utilized for the 30 rotor passages and had an open area of 67% in the circumferential direction. The slots were parallel to the rotation axis of the rotor and were inclined by 45 deg against a meridian plane in the direction of blade rotation; the depth of the treatment slot was about 11 mm.

## Numerical Method

Computation was done for three-dimensional flow using the Navier–Stokes solver EURANUS [18]. The Favre–Reynolds-averaged Navier–Stokes equations are discretized using a cell-centered explicit finite volume scheme according to Jameson in a relative coordinate system rotating with the reference frame. The steady-state flow solution is achieved at the convergence of a four-stage explicit Runge–Kutta integration scheme. The time-marching algorithm is stabilized using scalar eigenvalue-based second- and fourth-order difference smoothing operators. In order to speed up convergence to steady state, local time stepping, residual smoothing, and multigrid techniques were applied. The algebraic Baldwin–Lomax turbulence model was applied for turbulence closure. Time-dependent calculations were implemented in the implicit dual time-stepping scheme, which allows for the solution of a steady-state problem at each physical time step. This methodology allows keeping the main advantages of the explicit time integration scheme already implemented for resolving steady-state problems, as well as retaining local time stepping and implicit residual smoothing. For the time-dependent simulation, 40 physical time steps per blade passage and 20 pseudotime iterations with a CFL number of 2–3 within each physical time step were performed.

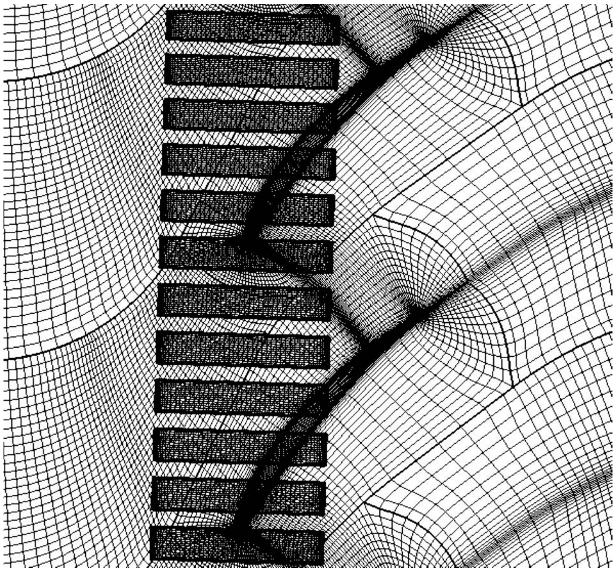

**Fig. 2 Blade-to-blade view of grids on the rotor-casing treatment sliding interface**

In order to carry out unsteady CFD simulations with an acceptable computational effort, the domain scaling method was applied. It was necessary to satisfy the condition of equal circumferential extent on both sides of the rotor-casing treatment sliding interface, such that spatial periodicity may be applied across both the casing treatment and blade passage mesh segments. The number of treatment slots was reduced from 183 to 180, and the ratio of treatment slots to rotor blade count was set to 6:1. This ratio permits the reduction of the problem to a single blade passage representation in conjunction with six end-wall treatment slots. For the prediction of coupled flow through the axial skewed slot and compressor rotor blade passage, block-structured grids are generated independently for the blade passage, tip gap, and the axial skewed slot. Precise geometric modeling of both blade tip gap and treatment slots were thought to be necessary in order to resolve variations in the flow structure due to the different geometrical configurations. Figure 2 presents a blade-to-blade view of the grids at the zonal interface where treated slots are visible. A block-structured topology consisting of I-blocks for the inlet and outlet and a main O-block (surrounding the rotor blade) was used to model the rotor blade passage. An H-grid embedded into an O-grid is applied to the tip gap while the simple H-type grid topology is used for each casing treatment segment. The nonrotating grids of the treatment slots are "mounted" on a very thin circumferentially closed base (10% of the tip clearance) and linked to the moving rotor passage by an unsteady rotor-stator interface using a sliding plane directly at the casing. Flow data were transferred from the blade passage to the discrete skewed slots using a time-space interpolation procedure, which was equivalent to an interblade row interface in a rotor/stator aerodynamic interaction analysis for multistage turbomachinery. The whole computational grids for the rotor with casing treatment consist of approximately 1,032,320 grid points.

To evaluate properly the viscous fluxes at the walls using the chosen boundary conditions (no-slip, adiabatic wall condition without a wall function method), the distance away from the wall of the first node had to be judiciously determined. This became an important grid parameter. In this work, the grids were designed such that the maximum distance between the wall and the first node was set such that $y^+$ was equal or smaller than 2. The meshing used proved to produce grid independent results in steady-state simulations. So far, no detail grid refinement studies have been carried out for the unsteady case due to the massive computing time requirements. However, the authors believe that this meshing is suitable for unsteady simulations as well.

No-slip and no-heat transfer conditions were imposed at solid boundaries. At the inflow boundary of the rotor, flow angle, total pressure and total temperature were prescribed according to the experimental data. At the subsonic outlet, static pressure was prescribed at the hub and its radial variation calculated based on the radial equilibrium equation.

## Results and Discussion

In order to save CPU time, the time-dependent solutions were initialized with either a steady solution or an unsteady solution from a different operating condition. Then the solutions were advanced in time until a time periodic solution was observed; this was assessed by placing a probe in a representative treatment slot. Flow properties at that point could then be checked for periodicity using a correlation function, which compares the similarity of point probe traces from consecutive periods. Figure 3 showed the unsteady pressure signal in a representative slot; it can be found from above-mentioned figure that after about eight rotor passing periods, a periodically repeated pattern was established, which implies that the calculation has converged. The unsteady pressure signal is processed in the second part of the figure with a fast Fourier transformation. In the frequency spectrum, the different periodic influences can clearly be separated from each other. It can be seen from the frequency spectrum of a representative slot that the highest amplitude appears at 5466.6 Hz, which is the product of the rotor speed and the number of rotor blade, and corresponds to the rotor blade passing frequency (BPF). Meanwhile the high frequency components up to the six BPF can also be observed with small amplitudes. The higher harmonics of the BPF, observed in the frequency spectrum, mainly appear due to the potential effects of several rotor blades on the representative slot. Other discrete frequency components that are not related to the rotor blade passing frequency do not appear.

To show the validity of the numerical tool in this paper, Fig. 4 shows the predicted rotor performance at the 71% design rotating speed with and without the axial skewed slot casing treatment compared to experimentally obtained data. Overall performance measurements are reported in terms of total-to-static pressure ratio, which is defined as the area-averaged rotor exit static pressure divided by mass-averaged rotor inlet stagnation pressure. Due to their physical nature, these averages were thus used to reduce the three-dimensional pressure ratio of the passage into a one-dimensional pressure ratio characteristic required to infer stall inception type. In order to accurately capture the near stall point, the increase of the compressor back pressure is reduced to the lowest level. The predicted "near stall point" was judged to be the last stable condition prior to incurring a numerical stall. Here, the same criteria (a divergent solution behavior or a continual dropping in mass flow rate with an increasing iteration count) were applied to determine numerical stall in the computation with solid casing or treated casing. It can be seen from Fig. 4 that the calculated compressor rotor characteristic and flow range agree fairly well with the experimental data and the simulations are able to predict the position of the stall limit within an accuracy of less than 1%. Therefore, it can be concluded that the numerical model used be able to reveal the important flow mechanisms, which are essential for understanding the influence of axial skewed slot casing treatment. In addition, the negative slope of the pressure ratio characteristic at the equilibrium solution limit (Fig. 4(*a*)) thus associated this case with spike stall inception. Figure 4 also reveals the overall impact of the axial skewed casing treatment on the compressor performance and stall margin. It can be observed from the figure that axial skewed slot casing treatment resulted in a decrease of mass flow at stall by 12.15%; this gain in flow stability correlates with a slight decrease in isentropic efficiency at the design point compared to untreated smooth wall case. The maximum efficiency reduced by 0.35%. However, the application of this kind of casing configuration is beneficial to the isentropic efficiency at the off design. In contrast to the axial skewed slot casing treatment used in Ref. [16], the upstream shifted axial skewed slot casing treatment can enhance the compressor's flow stability without significantly decreasing the efficiency.

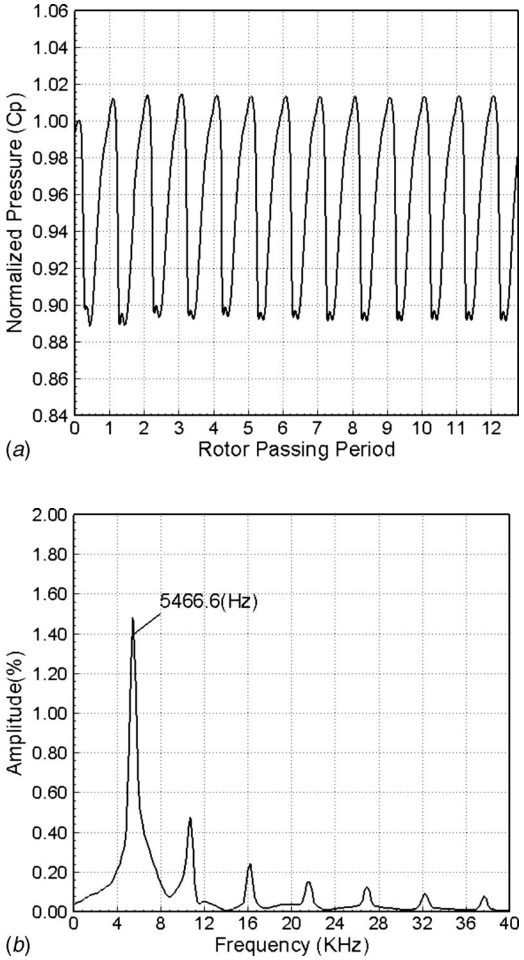

**Fig. 3 Unsteady pressure signal in a representative slot and its Fourier transformation**

A comparison of predicted and experimental radial distribution of isentropic efficiency is compared in Fig. 5 for both the base line (without casing treatment) and end-wall treated rotors near the base line rotor stall point. It is interesting to note that the isentropic efficiency distribution is fairly well predicted across the entire span for both the base line and treated rotor geometries. Also, one can find from Fig. 5 that the presence of the casing treatment causes a slight decrease of the isentropic efficiency near the tip but also a slight increase at 60–80% span so that the overall efficiency is only slightly decreased as compared to the case with the untreated smooth wall.

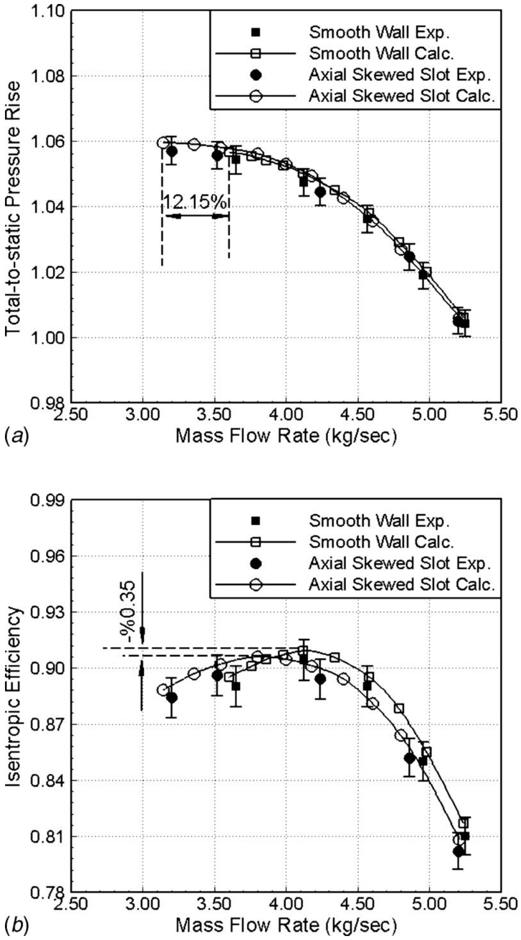

**Fig. 4 Computed and measured compressor map for 71% design speed: (*a*) total-to-static pressure ratio; (*b*) isentropic efficiency**

The coupled flow through the blade passage and the treated slots was solved using the unsteady-state simulation and then its time-mean calculated results were used to expose the interaction mechanism between axial skewed slot casing treatment and rotor blade passage. In order to understand the physics that underpin the performance variations shown in Fig. 4, the results should be compared under the same reference state. This is achieved by comparing the final predicted flow field at smooth wall stalling mass flow rate, through which a deep insight into the interaction mechanism between casing treatment and the rotor flow expected to be realized.

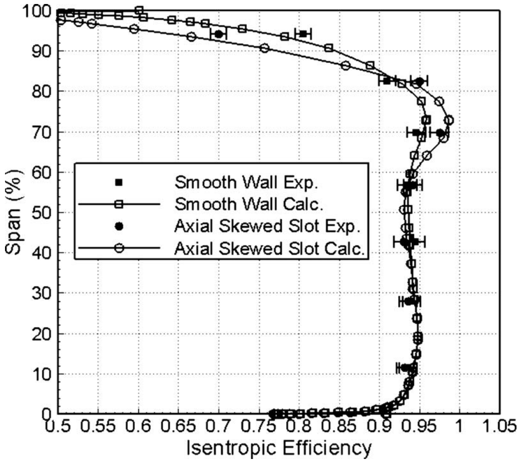

**Fig. 5 Comparison of predicted and experimental radial isentropic efficiency for the rotor with and without axial skewed slot casing treatment**

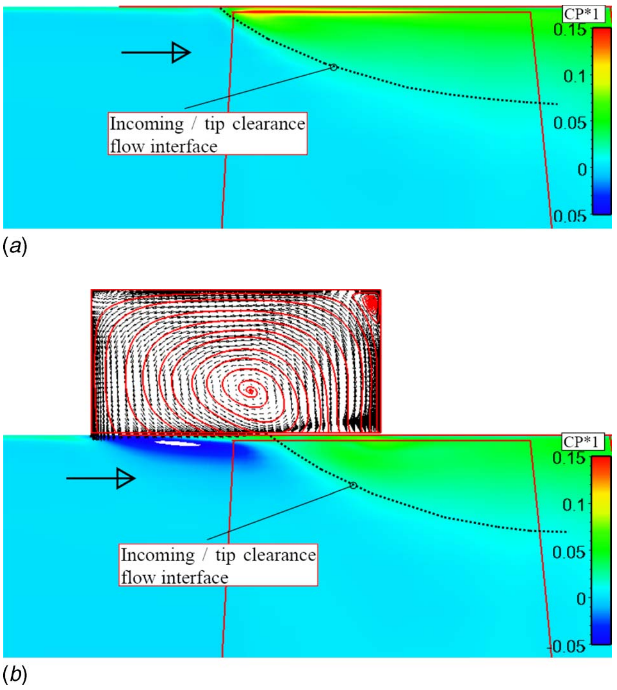

**Fig. 6 The distribution of circumferentially averaged total pressure loss coefficient at smooth wall stall mass flow: (*a*) smooth wall; (*b*) axial skewed slot**

To understand the mechanisms of axial skewed slot casing treatment in regard to the stall margin extension, it is useful at first to understand mechanism of stall for the compressor rotor with untreated smooth wall. Lu et al. [16] showed that this compressor exhibits spike-type stall inception; the fluid dynamic processes responsible for stall inception are the formation and forward movement of the tip leakage vortex. It is generally believed that tip leakage flow and it is resulting vortex are the major ingredients in spike-type rotating stall inceptions. Therefore, particular attention was given to examine the different tip leakage flow topologies with and without casing treatment.

Evidence supporting the predicted stall margin improvements are provided in Figs. 6 and 7, which shows the contours of relative Mach number at 99% blade span and circumferentially averaged total pressure loss near blade tip for both the untreated smooth casing and treatment casing at smooth wall stall mass flow rate. The high Mach number and total pressure loss gradient correspond to the incoming/clearance flow interface. With untreated smooth wall, a significant shift of the tip leakage vortex in the upstream direction is observed and the trajectory of the clearance vortex across the blade passage becomes more tangential as the rotor is throttled toward stall. At the near stall condition, the trajectory of the incoming/tip clearance flow interface lines up with the rotor leading edge plane at the rotor blade tip. However, when the axial skewed slot casing treatment was employed, the flow in the casing area and the rotor tips are rather drastically altered. With the inclusion of axial skewed slot casing treatment, a characteristic vortex in a counterclockwise orientation can be identified in the slot. This vortex, driven by the pressure gradient between the upstream and downstream treated slots, draws reversed tip clearance flow out of downstream of the treated slots and feeds it back into the main flow at the leading edge of blade passage (Fig. 7(*b*)). Through this removal/injection process, the axial

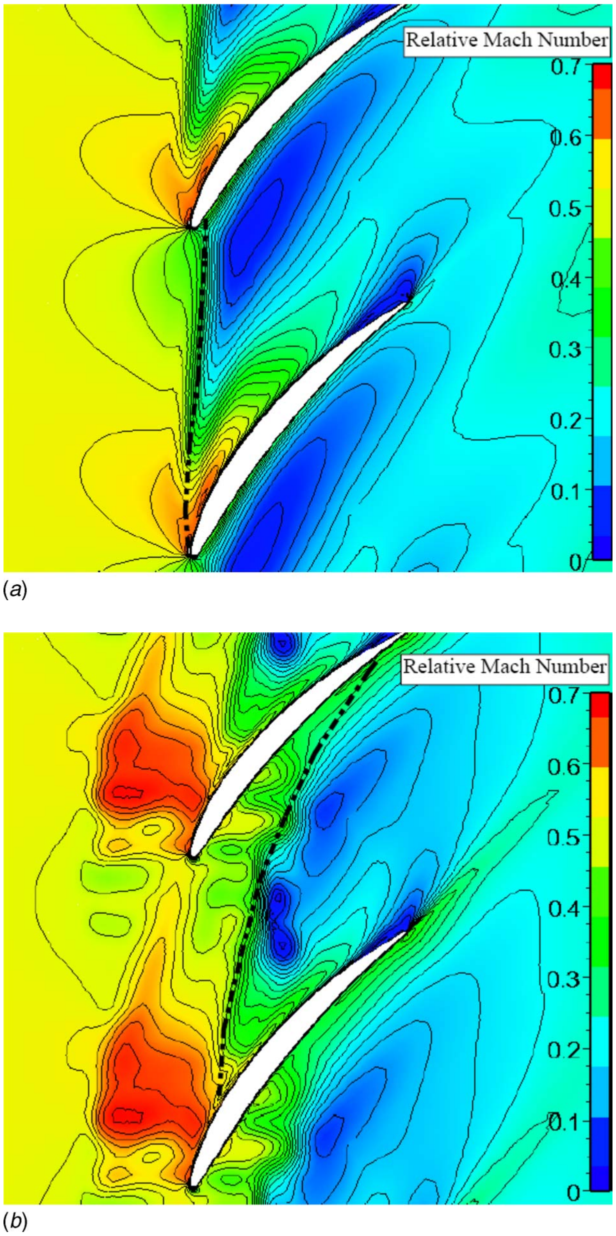

**Fig. 7 Comparison of relative Mach number at 99% blade span at smooth wall stall mass flow: (*a*) smooth wall; (*b*) axial skewed slot**

skewed slot casing treatment can delay the movement of incoming/tip clearance flow interface to the leading edge plane (Figs. 6(*b*) and 7(*b*)), therefore contributes to the stall margin enhancement process. Besides, most of the blockage (high loss region) associated with the clearance flow in the forward part of the blade passage is eliminated.

Time-averaged distributions of normalized vorticity ($\xi^*$) at several selected planes nearly normal to the rotor tip chord direction and three-dimensional traces of the tip clearance vortex, both with and without axial skewed slot casing treatment, are compared in Fig. 8. The tip vortex traces are formed by releasing particles from the region about 1% chord downstream of the leading edge and 50% normalized tip clearance above the blade tip. With the untreated smooth casing, the tip leakage vortex is detected as the region with the concentrated normalized vorticity. With the axial skewed slot casing treatment, strong changes can be observed in the structure of the tip leakage vortex and the vortex core corresponds to lower values of vorticity. This implies the reduction of tip leakage vortex intensity due to the effects of the casing treatment. The impact of casing treatment on the intensity of tip leakage vortex is illustrated in the comparison of the near blade tip loading interpreted from the blade surface static pressure distribution for the untreated smooth wall and the time-averaged static pressure for the casing treatment shown in Fig. 9. The incidence change caused by the flow removal at the front part of the passage

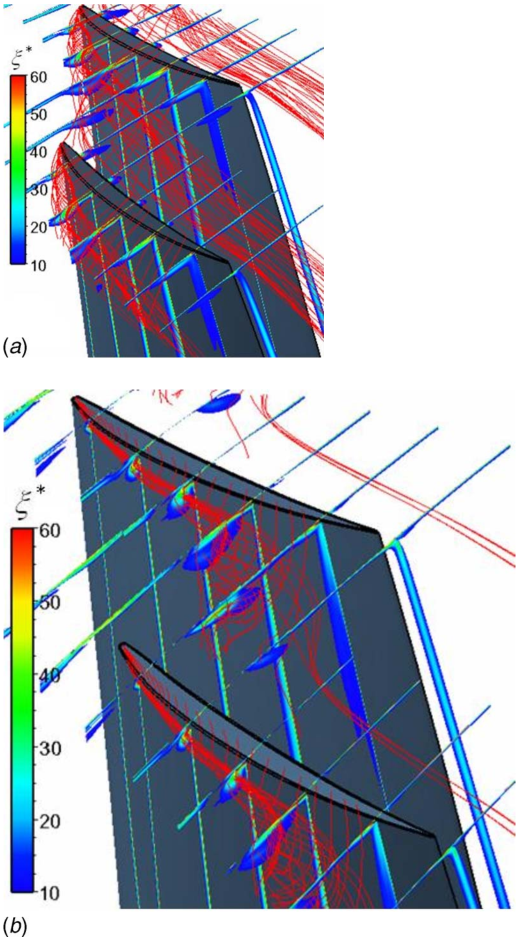

**Fig. 8 Computed tip clearance vortex particle traces at smooth wall stall mass flow rate: (*a*) smooth wall; (*b*) axial skewed slot**

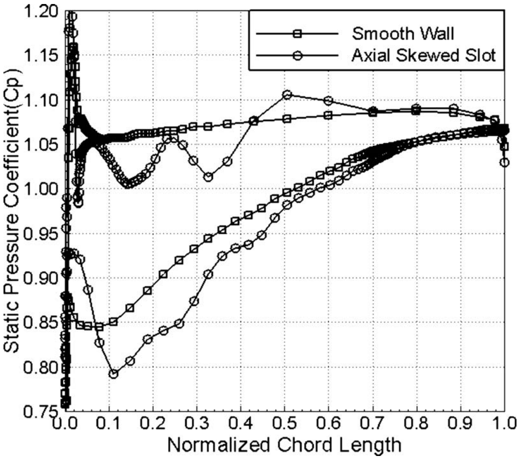

**Fig. 9 Comparison of predicted near rotor tip blade loading**

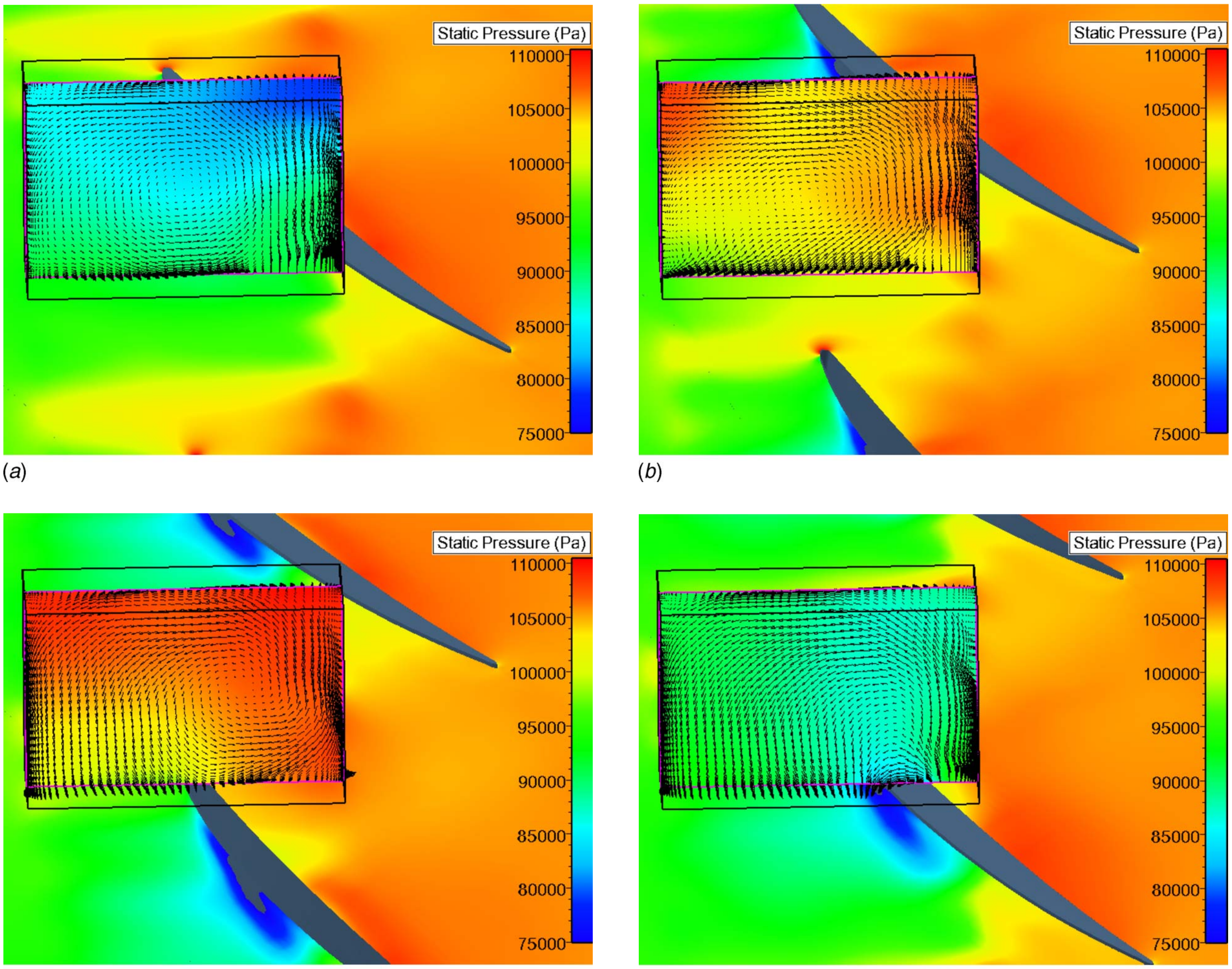

(*a*) (*b*) (*c*) (*d*)

**Fig. 10 Predicted treatment slot velocity vector patterns for different instants during one blade passing period: (*a*) $t = T/4$, (*b*) $t = 2T/4$, (*c*) $t = 3T/4$, and (*d*) $t = 4T/4$**

serves to reduce the loading of the pressure side where the blade is directly under a slot. It can be also seen from Fig. 8 that the location of the tip clearance vortex trajectory with casing treatment is shifted further downstream. The overall effect of the axial skewed slot casing treatment appears to be that of repositioning the tip clearance trajectory farther aft than that occurs in the untreated smooth casing. Therefore, as the stall inception is usually accompanied by the tip clearance vortex moving forward, the effect of casing treatment in delaying this phenomenon could be anticipated. In addition, the tip leakage vortex is deflected toward the suction surface and takes a more streamwise orientation.

Figure 10 shows the instantaneous midpitch treatment slot velocity vector patterns at different time instants during one blade passing period $T$ in order to provide some qualitative insight into aerodynamic interaction between casing treatment and the rotor flow from an unsteady point of view. The contour plots show the distribution of static pressure in the blade passage near the blade tip and inside a representative slot. The blade passage flow is from left to right in this figure. The figure shows how the fluid is transported in and out of the treatment slots. The flow through the casing treatment segment is complicated due to the fact that the pressure gradient between upstream and downstream of the axial skewed slot casing treatment varies during one rotor passing period. Flow removal from the blade passage occurs mainly over the rearward 30% of the slot opening and flow injection into the blade passage occurs mainly over the forward 40% of the treatment slot opening. Both flow injection and flow removal were found to be much intermittent and demonstrated a clear dependence on blade position. During the time after the rotor suction surface has passed the treatment slot opening (Fig. 10(*a*)) and before the rotor blade tip approaches the slot opening (Fig. 10(*b*)), the pressure gradient between upstream and downstream of axial skewed slot casing treatment strengthens the removal process from the blade passage to the slot but retards the flow injection process from the slot, this means the accumulation of fluid in the treatment slots due to the removal process being out of sync with injection process. However, if the blade has progressed to the point where the blade suction surface is exposed to the slot opening (Figs. 10(*c*) and 10(*d*)), a large and rapid decrease in the pressure caused by tip leakage flow occurs; at this time, a strong flow injection is initiated and the cycle is renewed with the advancement of the next rotor blade. Corner vortices are evident in all of the predicted velocity vector patterns, which suggest that the treatment passage need not be designed as rectangular slots. The skewing of the slot essentially acts to turn the flow passing through the treatment cavity, much like a vane. Depending on the relative position between rotor blade passage and treatment slots, on the one hand, the axial skewed slots can bleed reversed tip clearance flow into it. On the other hand, the axial skewed slot can produce high-energy injection flow and this injection flow is directed to the vicinity of the blade leading edge, energizing the low energy tip leakage flow. The effect of the flow removal/injection process was related to that tip clearance flow manipulation and delaying the upstream movement of incoming/tip clearance flow interface, which can efficiently enhance the flow stability of the subsonic compressor rotor.

## Links to Stall Margin Improvement Phenomenon

In the previous sections, the interaction mechanisms between the axial skewed slot and the rotor flow were examined. In addition, detailed analyses of the flow visualization at the tip have exposed the different tip flow topologies between the cases with axial skewed slot and with untreated smooth wall. To understand the mechanisms of the axial skewed slot in regard to the stall margin extension, the criteria defining stall and the sequence of process involved must established first. Previous studies [16,17] indicate that the test compressor rotor used for the current study obeys the stall criteria and associated mechanism proposed by Vo et al. [19], namely, the alignment of the incoming/tip clearance flow interface with the rotor leading edge plane and the presence of reversed tip clearance flow at the trailing edge plane. Khalid et al. [20] showed that the trajectory of the incoming/tip clearance flow interface results from a balance between the momentum of the incoming and that of tip clearance flow. As the incoming mass flow reduces, the axial momentum of incoming flow reduces, while the momentum of the flow through the tip clearance increases due to the increased blade loading. The result is the movement of the interface toward the rotor leading edge plane. On the one hand, with the inclusion of axial skewed slot, the axial momentum of incoming flow at the blade tip increases significantly due to the injected flow in front of the rotor leading edge. On the other hand, the momentum of flow through the tip clearance decreases due to the loading of the pressure side where the blade under the slots is reduced. This means the axial skewed slot casing treatment could help sweeping the tip clearance flow trajectory farther aft and delaying the movement of incoming/tip clearance flow interface to the leading edge plane.

The role of axial skewed slot casing treatment on stall suppression is linked to repositioning of the incoming/tip clearance flow interface further toward the trailing edge of the blade passage. So the tip leakage vortex trajectory is more aligned with the main flow and therefore represents less end-wall blockage in the tip region of the rotor passage. In fact, as proposed by Vo et al. [19], for any compressor exhibiting short length-scale (or spike) type of stall inception, any strategy that delays one of the two proposed criteria for spike formation should be effective in extending the operating range.

## Conclusion and Outlook

A computational study is carried out to understand the physical mechanism responsible for the improvement in the stall margin of an axial-flow compressor rotor due to the axial skewed slots casing treatment. The following conclusions can be drawn from this investigation.

1. The unsteady time-averaged results show reasonable agreement with available experimental data, and application of a concept similar to “domain scaling” treatment often used in multistage turbomachinery flow fields to the interface between the rotor blade passage and end-wall treatments is able to capture the unsteadiness induced by the interaction between the casing treatment and the blade passage quite successfully.
2. Detailed analyses of flow interactions between the casing treatment and the rotor tip flow under subsonic conditions have shown that the axial skewed slot casing treatment herein can directly impact the specific flow mechanisms, which are responsible for compressor stall. For the case of the untreated smooth wall, the tip clearance vortex trajectory moves upstream as the mass flow rate decreases and the incoming/tip clearance flow interface lines p with the rotor leading edge plane at the blade tip as the near stall state was approached. With the axial skewed slot casing treatment, the end-wall and tip clearance flows are rather drastically altered. The effect of the axial skewed slot casing treatment appears to be that of repositioning of the tip clearance vortex trajectory further toward the trailing edge of the blade passage and delaying the movement of incoming/tip clearance flow interface to the leading edge plane.
3. A time-dependent analysis of the subsonic compressor rotor with axial skewed slot casing treatment clearly illustrated the intermittent, time-dependent nature of the recirculating flow pattern for discrete skewed slots. The effect of the removal/injection process was related to that of a “booster stage” with the resultant effect of providing additional energy input for the high loss, high blockage clearance vortex, which retards the forward movement of incoming/tip clearance flow interface.

Encouraged by the results reported herein, the identification of a new design philosophy or a new flow alteration methodology, which are particularly advantageous to delay either of the stall criteria and extend the mass flow operating range successfully, will be the focus of future work.

## Acknowledgment

Financial support for the work presented is provided by National Natural Science Foundation of China (Project No: 50736007), China Postdoctoral Science Foundation (Project No: 20070420068) and K. C. Wong Education Foundation, this support is greatly appreciated.

## Nomenclature

$y^+$ = nondimensional wall distance, $\Delta y\sqrt{\rho\tau_w}/\mu$
$\Delta y$ = distance from the wall
$\mu$ = dynamic viscosity
$\boldsymbol{\xi}$ = vorticity vector $(\xi_x, \xi_y, \xi_z)$
$\xi^*$ = normalized vorticity, $\xi^*=|\boldsymbol{\xi}|/4\omega$
$\rho$ = density
$\tau_w$ = wall shear stress
$\omega$ = blade rotational speed (rad/s)
$Cp$ = normalized pressure, $Ps/Pt_{\text{in}}$
$Ps$ = static pressure
$Pt_{\text{in}}$ = mass averaged relative total pressure at inlet
$CP^*1$ = total pressure loss coefficient, $Pt_{\text{in}}-Pt/Pt_{\text{in}}$
$x, y, z$ = Cartesian coordinates

## References

[1] Adamczyk, J. J., Celestina, M. L., and Greitzer, E. M., 1993, “The Role of Tip Clearance in High-Speed Fan Stall,” ASME J. Turbomach., **115**, pp. 28–38.
[2] Hoying, D. A., Tan, C. S., Vo, H. D., and Greitzer, E. M., 1999, “Role of Blade Passage Flow Structures in Axial Compressor Rotating Stall Inception,” ASME J. Turbomach., **121**, pp. 735–742.
[3] Takata, H., and Tsukuda, Y., 1977, “Stall Margin Improvement by Casing Treatment—Its Mechanism and Effectiveness,” ASME J. Eng. Power, **99**, pp. 121–133.
[4] Greitzer, E. M., Nikkanen, J. P., and Haddad, D. E., Mazzawy, R. S., and Joslyn, H. D., 1979, “A Fundamental Criterion for the Application of Rotor Casing Treatment,” ASME J. Fluids Eng., **101**, pp. 237–243.
[5] Smith, G. D. J., and Cumpsty, N. A., 1984, “Flow Phenomena in Compressor Casing Treatment,” ASME J. Eng. Gas Turbines Power, **106**, pp. 532–541.
[6] Thompson, D. W., King, P. I., and Robe, D. C., 1998, “Experimental Investigation of Stepped Tip Gap Effects on the Performance of a Transonic Axial-Flow Compressor Rotor,” ASME J. Turbomach., **120**, pp. 477–486.
[7] Qing, Y., Qiushi, L., and Ling, L., 2002, “The Experimental Researches on Improving Operating Stability of a Transonic Fan,” ASME Paper No. 2002-GT-30640.
[8] Rabe, D. C., and Hah, C., 2002, “Application of Casing Circumferential Grooves for Improved Stall Margin in a Transonic Axial Compressor,” ASME Paper No. 2002-GT-30641.
[9] Wilke, I., and Kau, H.-P., 2002, “A Numerical Investigation of the Influence of Casing Treatments on the Tip Leakage Flow in a HPC Front Stage,” ASME Paper No. 2002-GT-30642.

[10] Lu, X., Zhu, J., and Chu, W., 2005, "Numerical and Experimental Investigation of Stepped Tip Gap Effects on a Subsonic Axial-Flow Compressor Rotor," Proc. Inst. Mech. Eng., Part A, **219**, pp. 605–615.
[11] Shabbir, A., and Adamczyk, J. J., 2004, "Flow Mechanism for Stall Margin Improvement Due To Circumferential Casing Grooves On Axial Compressors," ASME Paper No. 2004-GT-53903.
[12] Wilke, I., and Kau, H.-P., 2004, "A Numerical Investigation of the Flow Mechanisms in a HPC Front Stage with Axial Slots," ASME J. Turbomach., **126**, pp. 339–349.
[13] Hall, E. J., Crook, A. J., and Delaney, R. A., 1994, "Aerodynamic Analysis of Compressor Casing Treatment With a 3-D Navier–Stokes Solver," AIAA Paper No. 94-2796.
[14] Yang, H., Nuernberger, D., Nicke, E., and Weber, A., 2003, "A. Numerical Investigation of Casing Treatment Mechanisms With a Conservative Mixed-Cell Approach," ASME Paper No. 2003-GT-38483.
[15] Lu, X., Chu, W., and Zhang, Y., 2006, "A Numerical Investigation of the Interaction Between the Casing Treatment and Tip Leakage Flow in a Transonic Compressor Rotor," Journal of Xi'an Jiaotong University, **40**(11), pp. 1357–1360.
[16] Lu, X., Chu, W., Zhu, J., and Wu, Y., "Mechanism of the Interaction Between Casing Treatment and Tip Leakage Flow in a Subsonic Axial Compressor," ASME Paper No. 2006-GT-90077.
[17] Lu, X., Chu, W., and Zhu, J., 2006, "Application of Steady Micro Tip Injection for Improved Stall Margin in a Subsonic Axial Compressor," Int. J. Rotating Mach., pp. 1–11.
[18] NUMECA Int, 2003, "NUMECA's Flow Integrated Environment for Turbomachinery and Internal Flows," User manual version 6.1-1, NUMECA International, 5 Avenue Franklin Roosevelt, 1050 Brussels, Belgium.
[19] Vo, H. D., Tan, C. S., and Greitzer, E. M., 2005, "Criteria for Spike Initiated Rotating Stall," ASME Paper No. 2005-GT-68374.
[20] Khalid, S. A., Khalsa, A. S., Waitz, I. A., Tan, C. S., Greitzer, E. M., Cumpsty, N. A., Adamczyk, J. A., and Marble, F. E., 1998, "Endwall Blockage in Axial Compressors," ASME Paper No. 1998-GT-188.

**L. Porreca**[1]
e-mail: luca.porreca@ch.manturbo.com

**A. I. Kalfas**

**R. S. Abhari**

Turbomachinery Laboratory,
Swiss Federal Institute of Technology ETH Zürich,
Zurich 8005, Switzerland

**Y. I. Yun**

**S. J. Song**

School of Mechanical and Aerospace Engineering,
Seoul National University,
Republic of Korea

# Interstage Flow Interactions and Loss Generation in a Two-Stage Shrouded Axial Turbine

*The aerodynamics and kinematics of flow structures, including the loss generation mechanisms, in the interstage region of a two-stage partially shrouded axial turbine are examined. The nonaxisymmetric partial shroud introduces highly three-dimensional unsteady interactions, the details of which must be understood in order to optimize the design of the blade/shroud. Detailed measurements of the steady and unsteady pressure and velocity fields are obtained using a two-sensor fast response aerodynamic probe and stereoscopic particle image velocimetry. These intrusive and nonintrusive measurement techniques yield a unique data set that describes the details of the flow in the interstage region. The measurements show that a highly three-dimensional interaction occurs between the passage vortex and a vortex caused by the recessed shroud platform design. Flow coming from the blade passage suddenly expands and migrates radially upward in the cavity region, causing a localized relative total pressure drop. Interactions of vortex and wake structures with the second stator row are analyzed by means of the combination of the measured relative total pressure and nondeterministic pressure unsteadiness. The analysis of the data gives insight on unsteady loss mechanisms. This study provides improved flow understanding and suggests that the design of the blade/shroud and second stator leading edge may be further improved to reduce unsteady loss contribution.*

[DOI: 10.1115/1.2948961]

## Introduction

The flow within a multistage axial turbomachine is inherently unsteady and turbulent due to the interaction of wakes and secondary flow structures, shed by upstream blades, with the downstream blades. Furthermore, the incoming wakes are chopped by the rotor blades, and then diffuse and deform as they pass through the nonuniform pressure field in the rotor passage. These unsteady phenomena affect the performance of the airfoils and generate noise and structural vibration. An improved understanding of the unsteady flow physics is still a critical issue in rotating turbomachinery design and is thus a key requirement in achieving further improvements in performance.

Previous experimental studies that examined flow interactions have used miniaturized fast response aerodynamic probe (FRAP) devices (Schlienger et al. [1], Miller et al. [2], Pfau et al. [3], Gaetani et al. [4]) to measure unsteady pressures and derive as well other flow field parameters. Recently, optical techniques such as particle image velocimetry (PIV) have also been applied to rotating machinery. However this measurement technique is still a challenge in such an environment because of the difficult optical access and the need to use a uniquely defined calibration procedure to take into account the image distortion due to the cylindrical shape of the window. Moreover, since PIV measures the velocity field of tracers that are added to the flow, achieving a uniform seeding with an optimum concentration is crucial. In large scale rotating turbomachinery research facilities, these issues are very critical.

For these reasons, there are not many publications regarding the successful application of PIV to turbomachinery. Wernet [5], Balzani et al. [6], Sanders et al. [7], Uzol et al. [8], Ibaraki et al. [9], and Estevadeordal et al. [10] studied the 2D steady and transient flow fields in axial and centrifugal compressors. Liu et al. [11] and Göttlich et al. [12] made stereoscopic PIV measurements focusing on the wake-wake interaction at midspan in an axial transonic turbine and in the tip region of an axial compressor, respectively.

In the present work, extensive measurements using FRAP and stereoscopic PIV are made in a two-stage shrouded axial turbine. The investigation is focused on the flows within the interstage region. Partial shrouds are currently in use in some stationary industrial applications (Dorris et al. [13], Tomita [14], and Nirmalan and Bailey [15]), and they are receiving more attention due to the aerodynamic advantage of shrouded configuration as well as reducing thermal load and mechanical stress on the blade root (Harvey and Ramsden [16]; Willer et al. [17]). However, the optimal compromise between mechanical issues and aerodynamic performances is still an open issue due to the resulting highly three-dimensional unsteady flow field, difficulty in achieving an optimal cooling and severe heat load on the shroud sealing fins. The coupling between flow kinematics and loss generation is therefore investigated in order to gain a better understanding of the flow physics and to suggest ways to improve aerodynamic design of the blade/shroud components.

## Experimental method

**Research Facility.** The experimental investigation has been performed in the research turbine “Lisa” at the Turbomachinery Laboratory of the ETH Zurich. The facility can accommodate a maximum of two stages of an axial turbine. The air loop is quasiclosed type (open to the atmospheric conditions) and thus includes a radial compressor, a two-stage water to air heat exchanger, and a calibrated Venturi nozzle for accurate mass flow measurements. A dc generator absorbs the turbine power and controls the rotational speed of the turbine shaft. The first and second rotors are mechanically decoupled by use of a twin spool shaft design. A pair of independent torque meters allow the torque of each rotors to be separately measured. To achieve the same rotational speeds, the shafts are coupled again before the DC genera-

---

[1] Present address: MAN Turbo AG Schweiz, Zurich, Switzerland.

Contributed by the International Gas Turbine Institute of ASME for publication in the JOURNAL OF TURBOMACHINERY. Manuscript received August 8, 2006; final manuscript received September 27, 2007; published online September 25, 2008. Review conducted by Matthew Montgomery. Paper presented at the ASME Turbo Expo 2006: Land, Sea and Air (GT2006), Barcelona, Spain, May 8–11, 2006.

**Table 1 Main parameters of Lisa two-stage axial turbine research facility**

| | |
|---|---|
| Rotor speed (rpm) | 2625 |
| Overall pressure ratio | 1.38 |
| Mass flow (kg/s) | 10.65 |
| Blade count (stator/rotor) | 42/42 |
| Aspect ratio | 1.8 |
| Mach number (stator/rotor) | 0.35/0.1 |
| Reynolds number (rotor) based on $C_{ax}$ | $2\times10^5$ |
| $R_{hub}/R_{tip}$ | 0.77 |

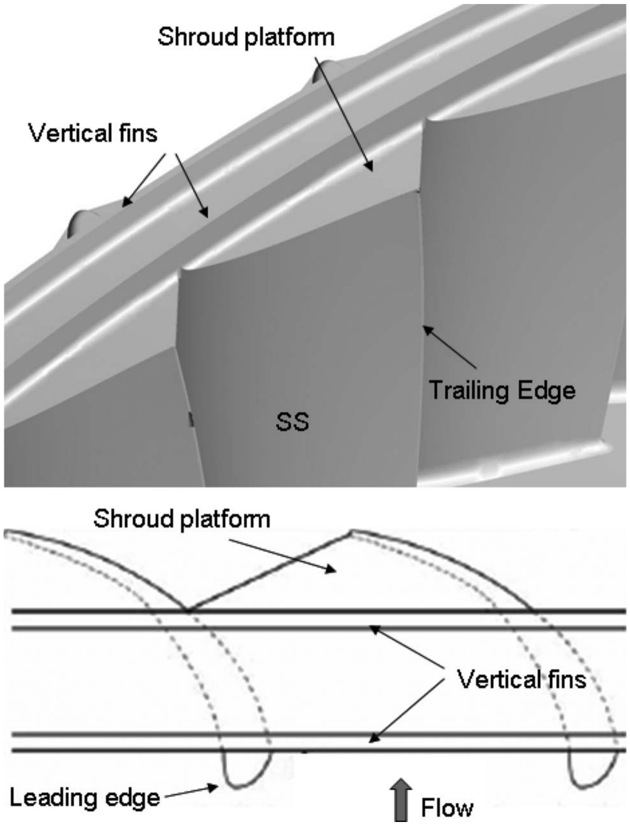

Fig. 1 Schematic of the rotor partial shroud geometry

tor. More details can be found in Porreca et al. [18].

The turbine's design allows quick and precise assembly and easy access to the measurement planes. The facility is equipped with a four-axis numerically controlled positioning system with high precision (±0.05 mm in the radial direction and ±0.002 deg in the yaw and circumferential angles). The turbine is normally operated at constant pressure difference across the stages. The turbine entry temperature is controlled to an accuracy of 0.3% and the shaft speed is kept constant by the dc generator within the range of ±0.02% (±0.5 rpm). The main operational parameters of the facility are listed in Table 1. The test case under investigation is representative of a partially shrouded axial turbine for power generation applications and is sketched in Fig. 1. The partial shroud has two vertical fins and a shroud platform with cutbacks at the leading and trailing edges. The tip clearance in both rotors is 1% of the blade span.

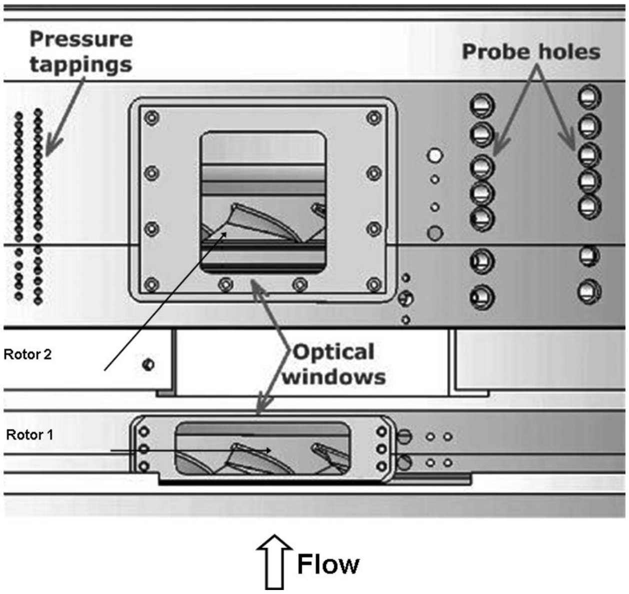

Fig. 2 Optical windows and probe holes in the test turbine

### Measurement Techniques

*Stereoscopic PIV*. The two-stage axial research turbine rig Lisa has been equipped with a 3D-PIV optical measurement system. The stereoscopic PIV method is used to compensate for perspective errors (Prasad [19]) as well as to observe the highly three-dimensional flows. Two optical windows made of acrylic polymethyl methacrylate (PMMA) are installed in the test turbine, as shown in Fig. 2. The window surfaces have been carefully polished to achieve good transparency. The first window is located between the first rotor and the second stator, and the second window is downstream of the second rotor. The windows are designed to reproduce the exact shape of the double curvature contour in the casing of the inner wall. The flow was seeded with fine oil dioctylsebacat $C_{26}H_{50}O_4$ (DEHS) particles generated by a Laskin nozzle (Kähler et al. [20]). To obtain a uniform concentration an injection device was designed to seed the entire air mass flow. The injection location was selected at the outlet of the radial compressor and upstream the heat exchanger to guarantee a sufficient mixing between the flow and the seeding particles. Deposits of seeding material on the casing windows were not significant during the operation of the turbine. The nominal particle diameter was around 1 $\mu$m, which is considered adequate (according to Mellin [21]) for a frequency response up to 10 kHz.

The digital images are recorded with $1280\times1024$ pixels 12 bit charge coupled device (CCD) cameras (PCO SensiCam SVGA). The pixel size and pitch are $6.7\times6.7$ $\mu m^2$ and 9 $\mu$m, respectively. The cameras are set, taking into account the Scheimpflug condition (Zang and Prasad [22]). Nikon AF Micro Nikkor lenses with a focal length of 60 mm are used for camera optics. A double-cavity (Nd:YAG) laser (Solo120PIV, New Wave Research) is used as a light source. The laser generates a maximum energy of 120 mJ/pulse of 532 nm wavelength green visible light. The pulse width is 10 ns, and the repetition rate is 15 Hz. The bursts of laser light are synchronized with cameras via a Dantec FlowMap system hub. The laser beam is delivered to a laser endoscope (Intelligent Laser Applications (ILA)) through an articulated mirror arm. The laser endoscope both generates the laser sheet through a cylindrical lens and bends the laser sheet by 90 deg through a prism in its tip. The outer diameter of the laser endoscope is 8 mm, and the divergence angle of the laser sheet is approximately 16 deg. The cameras and laser endoscope are mounted on a motor-controlled one-axis linear stage so that cameras and the light sheet can be moved together in the radial direc-

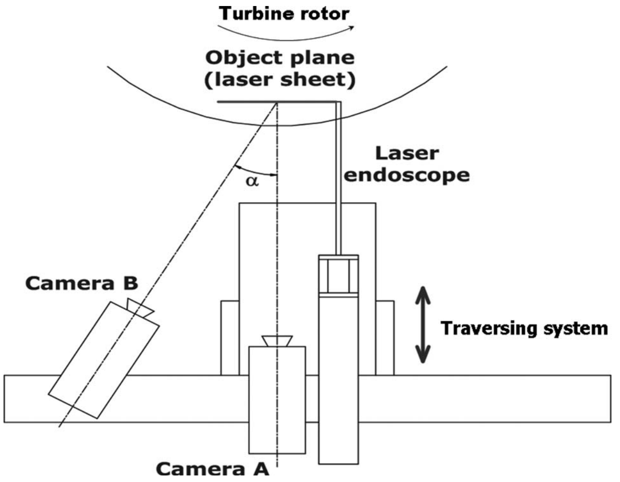

Fig. 3 Stereoscopic camera configuration in the test turbine

tion (Fig. 3).

By traversing radially, several blade-to-blade planes can be illuminated with the laser endoscope. Camera A is positioned such that its axis is perpendicular to the light sheet plane to avoid an interference with the laser endoscope. Camera B is tilted by different angles ($\alpha$=22 deg, 25 deg, and 30 deg), as shown in Fig. 3. The image plane (CCD plane) of Camera B is further rotated by 5 deg to satisfy the Scheimpflug condition, which ensures that all particles in the object field will be in good focus in the image plane (Prasad [19]). To compensate for the perspective distortion of the field of view due to the tilt angle of Camera B as well as the optical distortion through the double-curvature windows, a three-dimensional calibration method is used.

However, in the interstage area, the window has an abrupt change of curvature, which results in a severe optical distortion that could not be corrected by the calibration procedure. Therefore, data measured in this region are blanked out. The details of the calibration method can be found in Soloff et al. [23], while the description of the calibration procedure applied for these measurements is reported in detail in Porreca et al. [24].

Figure 4 shows the FRAP and five hole probe (5HP) measurement planes and the region of PIV measurements at the interstage and at the turbine exit region. The first stator is not shown in the figure in order to better highlight the measurement areas. Regarding the interstage region, measurements were taken in 15 blade-to-blade planes from 66% to 97%. One blade passing period is divided into 20 time steps, and between 60 and 100 digital image pairs are recorded for each measurement plane at each time step of a $50\times40$ mm$^2$ area. For the downstream region, measurements are made on three planes inside the shroud cavity and 17 blade-to-blade planes (from 60% to 96%) downstream of the second rotor. One blade passing period is divided into ten time steps, and 100 image pairs are recorded on each plane at each time step. The time interval between two laser bursts varies between 2 $\mu$s and 4 $\mu$s depending on the average flow field velocity. Each pair of images is interrogated using a cross-correlation analysis of $32\times32$ pixel subareas with an overlap of 50% between adjacent interrogations. An advanced interrogation method of window offset is used (Westerweel et al. [25]; Scarano and Riethmuller [26]). The theoretical analysis and simulations performed by Westerweel [27] show that the signal-to-noise ratio for PIV measurements with window offset is approximately three times larger than that without window offset when the flow has high turbulence intensity. Furthermore, the method of window offset is effective in reducing the error due to loss of pairs. To filter out spurious data, a criterion based on the local median is used (Westerweel [27]). Figure 5 shows a typical recorded image in the interstage measurement region. Visible in the picture are the blade trailing edge, the shroud platform, and the seeding particles that have been illuminated by the laser sheet.

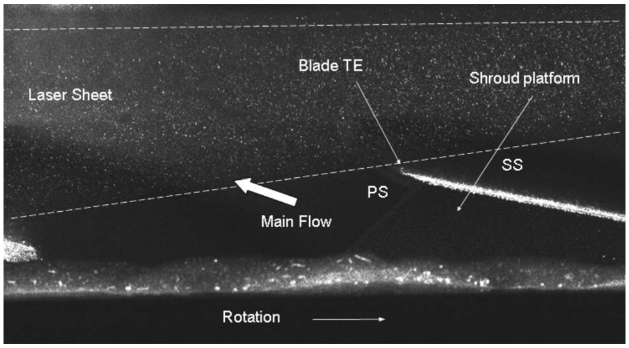

Fig. 5 Recorded image of seeded flow in the interstage measurement region

*Uncertainty Analysis of PIV Measurements*. For the estimation of the uncertainty in the PIV velocity measurements, many parameters have to be considered (Raffel et al. [28]; Willert and Gharib [29]). These include

- particle image diameter
- displacement of the particle relative to the size of the interrogation area
- particle image density
- local velocity gradients
- out-of-plane motion of tracer particles
- background noise

There is no established method to analytically evaluate the uncer-

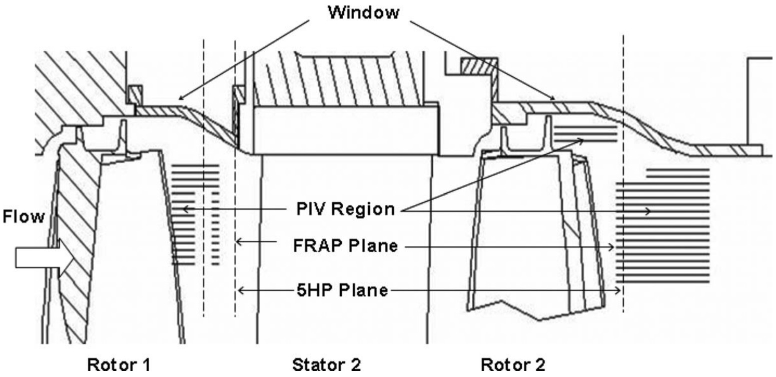

Fig. 4 Measurement regions: PIV, FRAP, and 5HP

**Table 2 Uncertainty analysis of stereoscopic PIV measurements**

| | | Velocity (m/s) | | | |
|---|---|---|---|---|---|
| Span | | Tangential velocity | Axial velocity | Radial velocity | Yaw angle |
| | | Interstage region | | | |
| 96% | Actual values | 30 | −5 | 10 | 80.54 |
| | Mean | 28.31 | −3.91 | 8.31 | 82.16 |
| | Standard deviation (m/s) | 0.92 | 0.71 | 2.47 | 1.30 deg |
| | Bias error (m/s) | 1.7 | −1.09 | 1.7 | −1.63 deg |
| 66% | Actual values | 30 | 65 | 10 | 24.7 |
| | Mean | 28.32 | 62.99 | 16.59 | 24.22 |
| | Standard deviation (m/s) | 2.25 | 2.69 | 5.97 | 1.92 deg |
| | Bias error (m/s) | 1.68 | 2.01 | −6.59 | 0.55 deg |
| | | Turbine exit region | | | |
| 85% | Actual values | 10 | 30 | 5 | 18.43 |
| | Mean | 13.09 | 31.10 | 1.08 | 22.83 |
| | Standard deviation (m/s) | 1.99 | 3.48 | 0.59 | 3.31 deg |
| | Bias error (m/s) | 3.09 | 1.10 | −3.92 | 4.40 deg |

tainty in PIV measurements due to the above factors. Therefore, the assessment of PIV accuracy may be done for each PIV system by using one of the following three methods. The first method is to make PIV measurements in a flow field with an exact solution (e.g., Poiseuille flow or three-dimensional rotating disk flow) and then evaluate uncertainty for the flow field. However, it is difficult to guarantee that the uncertainty determined in a canonical flow field can be applied to other more general flow fields. Also, it is not always possible to introduce such canonical flows with exact solutions in a specific environment such as the current test rig. The second method is to conduct a Monte Carlo simulation of particle displacements (Keane and Adrian [30]; Raffel et al. [28]). This approach allows the uncertainty of PIV measurements in a broad range of flow fields to be assessed. Third, PIV results can be compared against data obtained with hot wire or pneumatic probe methods or from direct numerical simulation (Scarano and Riethmuller [26]). However, a rigorous evaluation of uncertainty is difficult with this method since the measurement techniques are different and the direct numerical simulation itself has uncertainties.

In the current investigation, a Monte Carlo simulation has been conducted to evaluate measurement errors of PIV. To carry out a Monte Carlo simulation, tracer particle images must be artificially generated. The light intensity scattered from individual tracer particles is assumed to have a Gaussian profile in both the in-plane $(x,y)$ and out-of-plane $(z)$ directions,

$$I(x,y,z) = I_0 \exp\left[\frac{-(x-x_0)^2-(y-y_0)^2}{(1/8)d^2}\right]\exp\left[-\frac{{z_0}^2}{(1/8)\Delta {z_0}^2}\right] \tag{1}$$

The location of each tracer particle $(x_0,\ y_0,\ z_0)$ is set by using a random number generator. Then, the light intensity scattered from the particle at each location in an interrogation area can be defined from Eq. (1). Four parameters—particle image diameter, number of particles, maximum light intensity $I_0$, and actual displacement—must be given a priori. The diameter of tracer particles is set such that the particle fills a $2\times 2$ pixels pixel or $3\times 3$ pixels pixel region. The number of particles used here is 50. Both of these parameters were determined via a trial-and-error process so that the artificially generated images look similar to the measured images. Based on these artificial images, the first and second image frames with a time interval between 2 $\mu$s and 4 $\mu$s can be generated. The actual displacements of the particle $(\Delta x, \Delta y, \Delta z)$ are taken from a representative averaged velocity value measured with PIV at each point of interest. Based on these displacements, the image pairs of tracer particles in the object plane can be generated.

The images are not generated for the entire field of view (for the current investigation, $50\times 40\ \text{mm}^2$) but at three points (as shown in Table 2). A point in the field of view corresponds to a $32\times 32$ pixel interrogation area in the image plane. However, the images are generated in a $96\times 96$ pixel pixel region to properly account for the particles that enter and exit the $32\times 32$ pixel interrogation area that is located at the center of the $96\times 96$ pixel pixel region. With stereoscopic PIV, the displacement values seen by the two cameras are different, particularly when there are out-of-plane displacement components. Also, perspective and optical distortions of the images occur when the particle images are projected onto the image planes. The calibration procedure is used to estimate both the image distortion and the displacements seen in both cameras' image planes. The interrogation area is also subject to background noise due to reflection on solid surfaces and the light that is scattered from tracer particles located outside the light sheet. Therefore, the background noise has a static intensity level (from the reflection) as well as a randomly moving pattern (from the scattering of particles outside the light sheet). To obtain a spatially random intensity pattern, a random number generator has been used. Then, the background noise is superimposed on the particle images. Because there is a randomly moving pattern in the background, the noise patterns for the first and the second frames are separately generated. Three hundred particle image pairs for each point are generated to carry out statistical evaluations. The stereoscopic PIV error is then evaluated by comparing the imposed displacements to the displacements calculated from the artificially generated images. The measurement error consists of two parts, *bias error* and *root-mean-square (rms) error* (Raffel et al. [28]),

$$\varepsilon_{\text{PIV}} = \varepsilon_{\text{bias}} + \varepsilon_{\text{rms}}$$

The bias error is defined as the difference between the actual velocity value and the averaged value measured with PIV. This bias error originates from loss of pairs and velocity gradients in the interrogation areas.

rms error is the standard deviation of the values measured with PIV and can be regarded as measurement uncertainty of PIV. Table 2 shows the results of the uncertainty analysis expressed in terms of the bias and rms errors at the interstage and turbine regions. The bias error at the interstage region for the axial and tangential velocities (in-plane components with respect to the laser light sheet) is always in the range of $\pm 2$ m/s. Standard deviation is in the lower range of 4–7% and higher close to the tip

**Table 3 Uncertainty in measurements of 5HP and FRAP**

| Probe type | $\varphi$ (deg) | $\beta$ (deg) | $P_t$ (Pa) | $P$ (Pa) | Ma |
|---|---|---|---|---|---|
| 5HP | 0.3 | 0.3 | 60 | 130 | 0.4% |
| 2S-FRAP | 0.3 | 0.3 | 100 | 150 | 0.5% |

where the absolute velocity magnitude is smaller. In the turbine exit region, the magnitudes of the bias errors are similar, but the rms errors are larger.

The bias error of the radial velocity (out-of-plane component) is more than 10% in all the planes; therefore, the radial velocity measurements ought to be assessed only qualitatively. Another trend is that the errors of the in-plane components (tangential and axial velocities) are similar for all three locations while the error of the out-of-plane component increases as the measurement location is farther from the optical window. Measurement planes farther from the window suffer from more severe optical distortion. Thus, the error of the out-of-plane component appears to be more susceptible to optical distortion.

*FRAP and 5HP*. Flow parameters, including total and static pressures, flow angles, velocity components, and Mach numbers, are measured at frequencies of up to 40 kHz using a two-sensor FRAP. This probe is a modified version of the conventional single sensor probe; a second sensor that is sensitive to pitch angle variations of the flow is incorporated. This two-sensor FRAP has been used in previous investigations (Porreca et al. [31]). The FRAP also provides unsteady temperature measurements at a low frequency of up to 10 Hz. The absolute uncertainties in the measurements are listed in Table 3. Temperature measurements obtained with FRAP have an absolute uncertainty of the order of ±0.3 K.

The FRAP probe has been developed in the Turbomachinery Laboratory at ETH Zurich in the last 20 years of research. Time resolved measurements have been compared with laser Doppler velocimetry measurements taken at the exit of a centrifugal compressor facility [32]. The agreement of the time mean velocities was found in the range of 0–4% while the time resolved velocities were within 2–5%. Furthermore, acomparison with nonintrusive measurements is presented in this paper. An additional comparison between FRAP and pneumatic probe can be found in Refs. [33,18]. In the latter publication, the FRAP and 5HP data are compared at the exit of the first rotor and second stator of an axial turbine with exactly the same blade profile geometry of the one employed in the current work. The comparison shows that the pneumatic averaged data lay always in the minima and maxima of the FRAP measurement and therefore confirms the accuracy of this measurement technique.

The measurement grid comprises 1502 points that are distributed uniformly in the circumferential direction at every 3.5% pitch (32 points in a pitch range of 1.1) and 47 points clustered toward the end walls in the radial direction. Data from the sensors are sampled at 200 kHz, which corresponds to 109 samples for each blade passing period. Phase-locked averaging of the data is done over 80 rotor revolutions.

Steady state measurements are performed using miniaturized pneumatic 5HPs with a 0.9 diameter cobra head shape (Treiber et al. [34]). The probe is calibrated for ranges of ±14 deg in yaw and ±30 deg in pitch angle. The uncertainty of pneumatic probe measurements is reported in Table 3 for angles of ±10 deg in yaw and ±10 deg in pitch. For higher pitch angles, higher uncertainty is detected.

## FRAP–3D PIV Comparison and Analysis

Figure 6 shows a comparison between the velocity measured by the 3D PIV (Fig. 6(*a*)) and the FRAP (Fig. 6(*b*)) data. The FRAP data are presented over the same region as the PIV measurements. Regions of the PIV measurements that have insufficient laser illumination are blanked out at the left and right borders. Both data sets are presented with the same scale and levels. The higher tangential velocity region in the middle of the pictures shows the presence of the tip passage vortex that is located between 0.8 and 0.9 of the span height. The comparison shows good agreement between the two measurement techniques. In the PIV plot, the core with a high tangential velocity is slightly larger compared to the FRAP measurements. However at the location of the vortex core the differences in absolute magnitudes of velocity are comparable and are within the range of ±1.5 m/s, which is comparable to the uncertainty of the PIV measurements as discussed in the previous section.

Figure 7 shows the pitchwise yaw angle distribution at different axial planes downstream of the second rotor blade. The time averaged FRAP and PIV data are presented together with 5HP measurements. The FRAP and 5HP measurements are made in the plane located at 153% of tip $C_{\text{ax}}$. At this plane, there are blanked out regions in the PIV data, and thus three other planes located at 171%, 196% and 208% tip $C_{\text{ax}}$ are presented for the PIV data.

A good agreement between the probe and the optical measurement techniques is again observed. An underturning/overturning behavior is observed from a 0.7 span up to the blade tip where the blade profile is designed to align the flow with the underturned leakage flow in order to minimize mixing losses. The yaw angle profiles measured with the probes (FRAP and 5HP) are in good agreement up to a 0.75 span. Discrepancies are observed from the 0.75 span up to the blade tip since the passage vortex in the region generates a high level of unsteadiness, which results in the time averaged signal of the fast response probe being different from the pneumatically averaged signal of the 5HP.

Overall the time averaged PIV data are in good agreement with the probe data. Differences are of the order of ±2.5 deg in the region from 0.6 up to 0.9 blade span. The largest differences are in

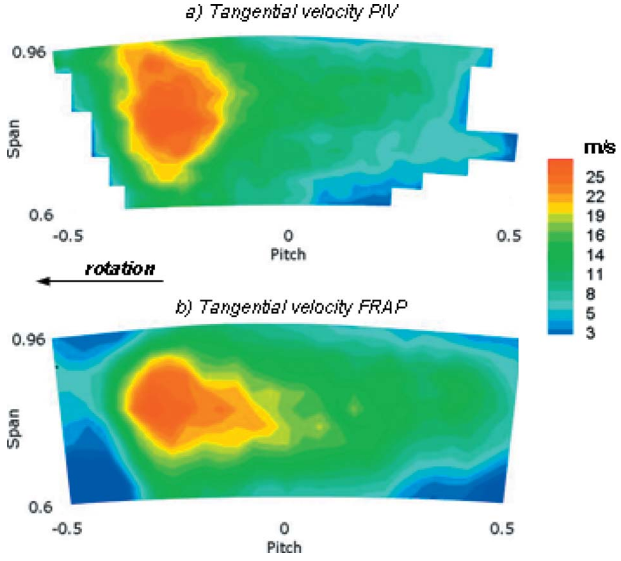

**Fig. 6 Measured absolute tangential velocity at one rotor blade position: (*a*) PIV and (*b*) FRAP—turbine exit region**

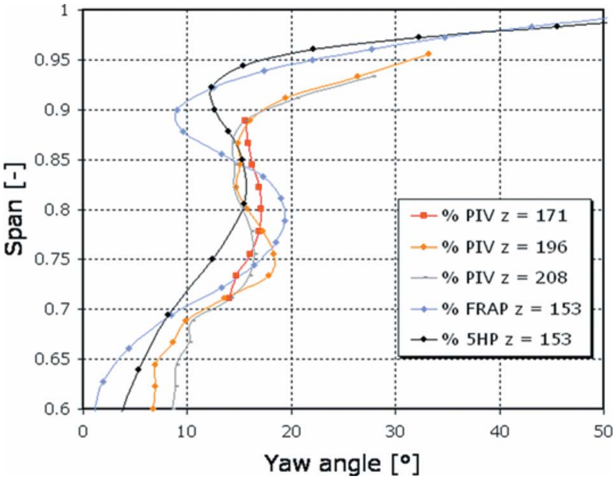

**Fig. 7 Comparison between FRAP, 5HP, and PIV time averaged pitchwise yaw angles—turbine exit region**

the vicinity of the passage vortex core, where perhaps the errors in the out-of-plane velocity component in the PIV data contribute to the observed differences.

Above a 90% span, in the region of overturning due to the leakage layer, the trend in the probe data is captured correctly by the PIV, but there are larger differences compared with the probe data. The PIV data appear to be displaced away from the blade tip. This is expected as the PIV data are measured further downstream of the blade row (171–208% tip $C_{ax}$) compared to the probe data that are measured at 153% tip $C_{ax}$. At the more downstream positions the leakage flow is entrained more into the main flow.

## Interstage Flow Analysis

Figure 8 shows the absolute yaw angles downstream of the first rotor blade. These PIV measurements are averaged in time and pitch and presented for axial planes located between 109% and 128% midspan $C_{ax}$. The passage vortex produces large flow underturning, and this is evident in all the measurement planes between 70% span and the tip. Further downstream, an increasing region of underturning is observed in the tip region due to the incoming tip leakage flow. Within the labyrinth seal, the flow retains its relatively high tangential momentum that has been imparted by the upstream nozzle guide vanes (NGVs) Therefore at the rotor exit, there is a relatively high difference in the tangential momentum of the main stream and the leakage flow. This difference in momentum increases the mixing losses, and it is for this reason that some designs adopt "bladelets" to turn the leakage flow in order to reduce the difference in tangential momentum and thus minimize the mixing losses. These devices have been found to be more effective when placed in the stationary frame (Rosic and Denton [35]) compared to the shroud (Wallis et al. [36]).

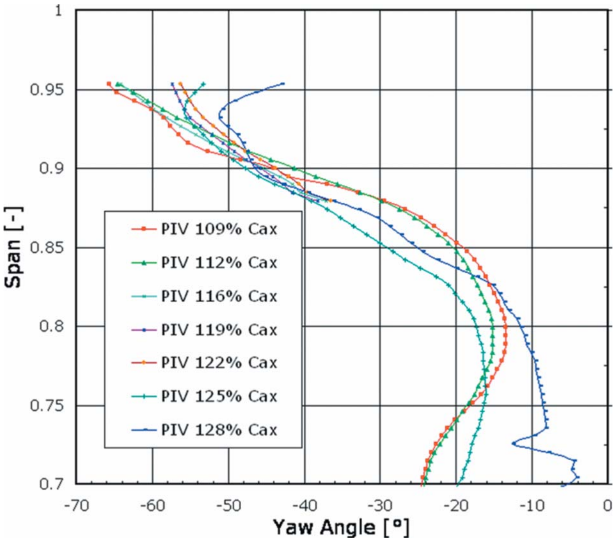

**Fig. 8 PIV measured time and pitchwise averaged absolute yaw angles at different axial planes**

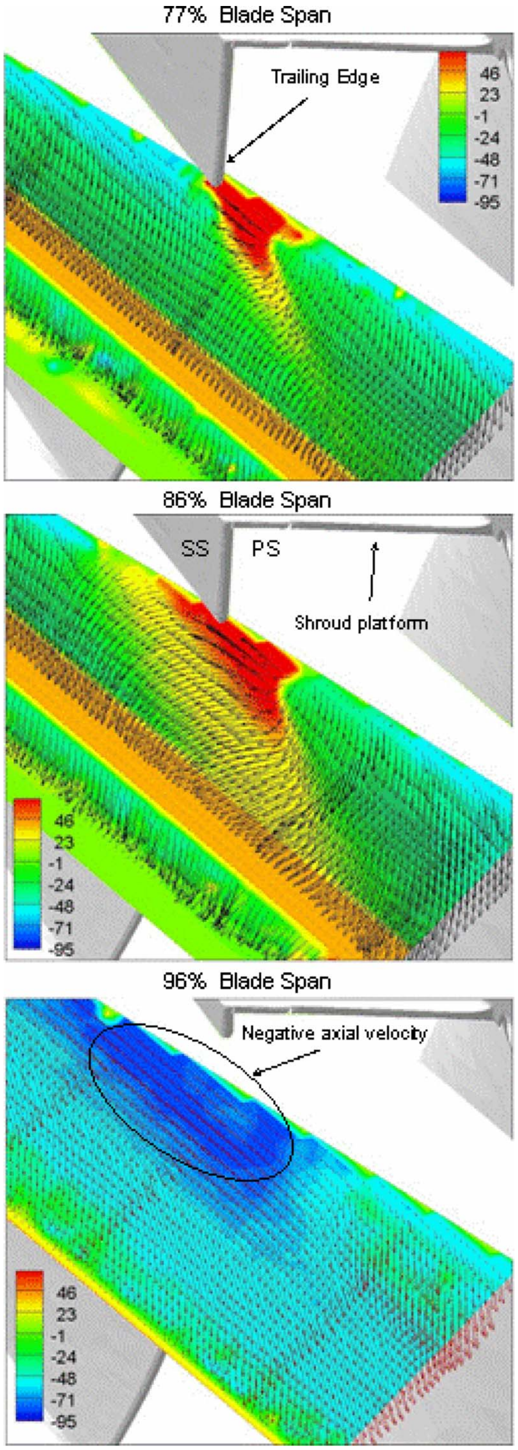

**Fig. 9 PIV measured absolute yaw angles at different tangential planes. Vectors show the in-plane velocity component—interstage region.**

Figure 9 shows contour plots at three blade span positions of the PIV measured yaw angle. Superimposed on the contour plots are vectors of the in-plane velocities. The contours in the middle of the measurement plane are blanked out, as shown in the orange region with zero length vectors; these PIV data are unusable due to the optical distortion through the window. All the measurements are derived from phase-locked data, which are averaged over 100 samples. At the 77% blade span plane, the measured yaw angle shows two distinct regions: the main "undisturbed" flow in the middle of the passage and the wake region that is close to the trailing edge. In the wake region the flow is underturned with yaw angles as large as 80 deg; the deficit in the axial velocity and the presence of the passage vortex cause this underturning. The wake region is highly confined, compared to the main flow, and thus there are large circumferential gradients in the yaw angle.

At the 86% and 96% blade span positions, the influence of the wake is reduced. At the 86% position, the region of underturned flow is significantly reduced compared to that at the 77% blade span position. At the 96% blade position, no region of underturned flow is observed. Rather the passage vortex results in a region with both strong overturning of the flow and measured negative axial velocities. The resultant yaw angles exceed 90 deg in this region. The negative velocities arise due to the rapid flow expansion as the shroud platform uncovers the blade passage. The passage vortex grows downstream of the blade throat and expands over the shroud platform. This growth and expansion results in an upward radial motion that is relatively weak in the middle of the blade passage and stronger downstream of the blade's trailing edge. A similar radial motion is observed in the leakage cavity that is downstream of the second rotor with a similar partial shroud geometry; these measurements in the cavity are detailed in Yun et al. [37].

Figure 10 shows contour plots of the PIV measured absolute yaw angles at two axial planes, 109% and 114% midspan $C_{ax}$. The in-plane velocity vectors are superimposed on the contour plots. The vertical dashed line shows the trailing edge of the rotor blade projected onto these downstream planes. The rotor motion is from right to left. In order to highlight the wake and secondary flow, only half of the blade pitch region is shown. The yaw angle varies between −80 deg and +40 deg due to the presence of the passage vortex. In the region between the 80% span and the blade tip, these variations result in large gradients of the yaw angle.

These gradients are larger closer to the blade (109% mid $C_{ax}$ compared to 114% mid $C_{ax}$) since the mixing weakens the passage vortex as it evolves downstream.

The in-plane velocity vectors show the presence of a vortex at the trailing edge of the rotor blade. Its vorticity is of opposite sign to that of the passage vortex. This flow phenomenon is sometimes observed in turbomachinery blade flows and has been previously observed in a study of low aspect ratio, high turning NGVs (Pullan et al. [38]). The rotation of this observed vortex is consistent with the shedding of streamwise vorticity from the pressure side to suction side at the blade's trailing edge. The partial covering of the shroud platform decreases the blade loading on the blade tip and thus enhances the shed vorticity.

A combined effect of the passage vortex and the TE shed vortex is to displace the underturned low momentum flow toward the suction side. A comparison of the yaw angles in the upstream (109% mid $C_{ax}$) and downstream (114% mid $C_{ax}$) planes shows that the gradients in the yaw angle are substantially reduced. This is a result of the merging of the two vortices. The merging and subsequent dissipation of the vortical structures result in mixing losses that may be quantified in terms of the relative total pressure coefficient. This is accomplished from the FRAP measurements in the axial plane located downstream at 152% mid $C_{ax}$, as shown in Fig. 11.

Figure 12 shows a contour plot of the measured relative total pressure coefficient. The data are phase locked at a rotor blade position of $T/T_0=1.85$. The projected locations of the rotors' trailing edge are shown by the dashed lines, and the pressure and

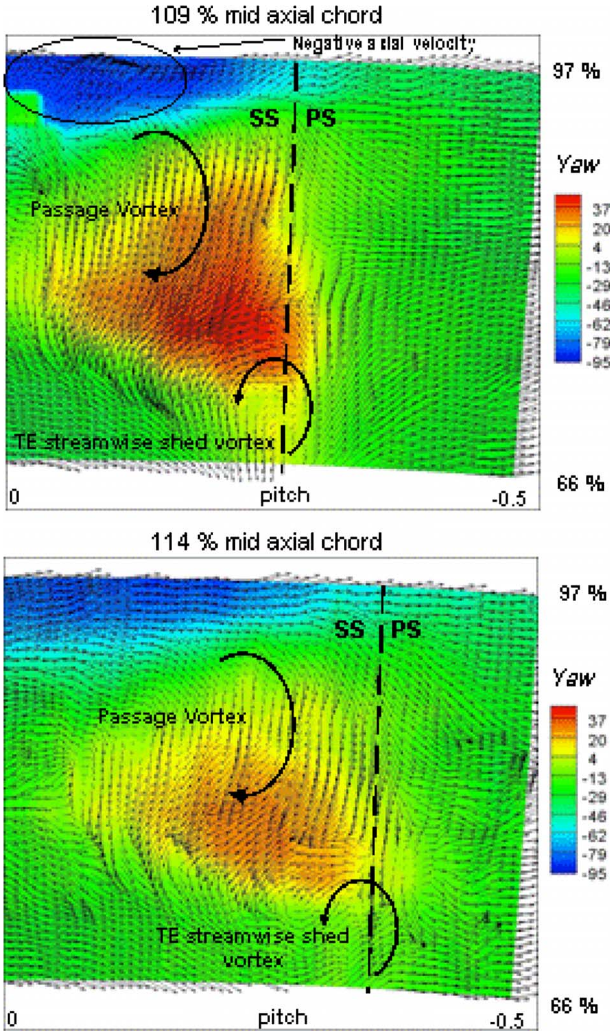

**Fig. 10** PIV measured absolute yaw angles at different axis-perpendicular planes. Vectors show the in-plane velocity component—interstage region

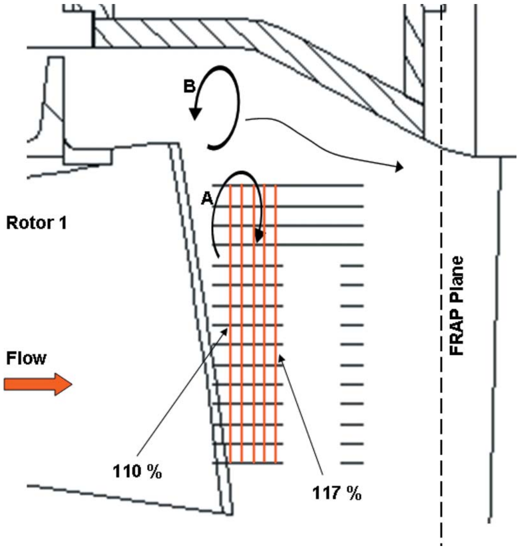

**Fig. 11** Schematic of flow structures and measurements in the interstage region

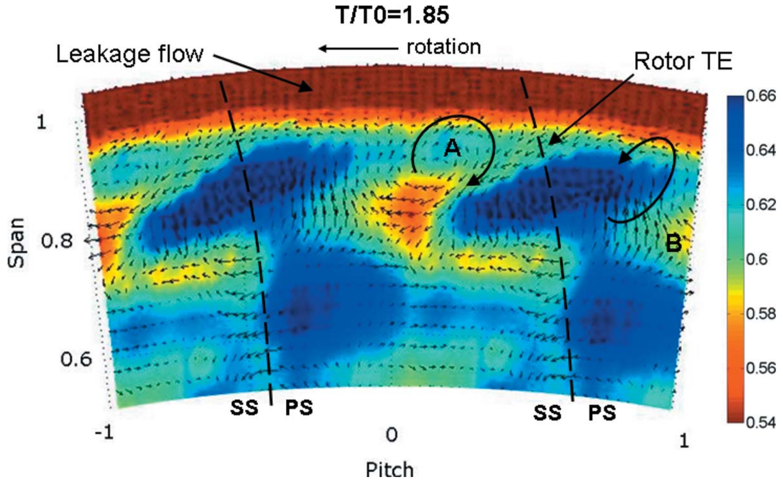

**Fig. 12 FRAP measurements of the relative total pressure coefficient $\mathrm{Cpt}_{\mathrm{rel}}$ and secondary flow vectors—interstage region**

suction sides are also identified. Superimposed on the contours are vectors of the local secondary flow velocities. The secondary flow velocity computed at each time step is defined as

$$\vec{u}_{\mathrm{sec}} = \vec{u}_i - (\vec{e}_{mean}\vec{u}_i)\vec{e}_{mean}$$

where $\vec{u}_i$ is the local flow vector and $\vec{e}_{\mathrm{mean}}$ is the circumferentially averaged mean unit vector. The contour plot shows that the total pressure is reduced in the wake region, downstream of the rotor's trailing edge, and in a circumferential region (0.95–1.05% blade height) that is associated with the cavity flow. Two counter-rotating structures are visible from the velocity vector field. They are labeled as structures A and B in Fig. 12 and can be seen to push low momentum fluid from the wake toward the suction side of the blade. The vortex that was shed from the rotor's trailing edge, and was identified in Fig. 10, is not seen in Fig. 12. A comparison of the PIV (Fig. 10) and FRAP (Fig. 12) data identifies structure A as the passage vortex and structure B as a vortex that originates from the sudden expansion downstream of the shroud cutback. A schematic of the flow structures is shown in the meridional view of the interstage region in Fig. 11. Also shown in the figure are the relative locations of the FRAP (vertical dashed line) and PIV (series of horizontal lines) measurements. Vortex B could not be observed in the PIV data since the measurement region does not extend above 96% span. However, this vortex is entrained into the main flow downstream of the PIV measurement region and seen in the FRAP plane. Evidence of this structure can be seen from the measured data in the cavity downstream of the second rotor, as described in Yun et al. [37].

In Fig. 13 the time evolution of the relative total pressure coefficient is plotted as a function of the measurement position with respect to the stator blade. The vertical dashed lines denote the position of the leading edge of the second stator, and a blade passing fraction of $T/T0=1.85$ (which is used in Fig. 12) is shown by the horizontal dashed line. The contour levels in Figs. 12 and 13 are the same in order to facilitate the interpretation of the plots. The regions of reduced relative total pressure associated with the vortical structure described previously in Fig. 12 are seen to lie along inclined lines in Fig. 13. This inclination indicates that regions of lower total pressure move together with the rotor blade. At 76% span, Fig. 13(*a*), the degree of interaction with secondary flow is relatively high.

However, no substantial differences between the passage vortex A and the leakage vortex B are seen in Fig. 13. Rather only a broad region of decreased relative total pressure is observed. As the leading edge of the second stator is approached by the flow structures, the size of the region of low relative total pressure decreases. In Fig. 13(*b*) the time-distance diagram is presented for the blade midspan location. At this position, no secondary flows are present and the flow field is dominated by the rotor wake and the potential field of the second stator. The rotor wake is shed at the trailing edge and is then convected downstream to impinge on the second stator blade row—first on the suction side of the blade and then on the pressure side of the following blade. As the wake passes through the passage of the stator (the middle of the passage corresponds to a stator pitch of approximately −0.4), there are very few disturbances. However, as the rotor is moving, the wake is periodically bowed and then compressed due to the potential field of the stator's leading edge.

The variation in the relative total pressure is higher for the passage vortex (Fig. 13(*a*))—note that the contour scales are the same in Figs. 13(*a*) and 13(*b*). In the region of interaction with the second stator leading edge (pitch=0.2), the time averaged relative total pressure coefficient deficit is about 6.6% with respect to the same averaged value at the pitch position equal to 0.6 where the wake is undisturbed. On the other hand, at 76% span the time averaged relative total pressure increase in this location is equal to 5.1% with respect to the position pitch=0.6. This concludes that in the case of the passage vortex (76% span), although variation is higher in the time domain, the variation of the relative total pressure in the second stator leading edge region is lower than in the wake.

At each measurement point the time dependent pressure can be written as

$$P(t) = \tilde{p}(t) + p'(t)$$

where $\tilde{p}(t)$ is the phase-locked measured pressure and $p'(t)$ is the nondeterministic part of the pressure signal. The pressure unsteadiness coefficient $P_u$ is then defined as the ratio of the rms value of the term $p'$ and the relative dynamic head,

$$P_u = \frac{\mathrm{rms}(p')}{0.5\rho V_{\mathrm{rel}}^2}$$

The rms value of $p'$ is determined from 80 instantaneous samples. Figure 14 shows a $P_u$ coefficient plotted in a time-distance diagram at 76% and mid span. The loss generation mechanism can be assessed from analysis of the phase-locked measured relative total pressure (Fig. 13) nondeterministic pressure unsteadiness $P_u$.

In Fig. 14(*a*), the levels of pressure unsteadiness are elevated in regions associated with the passage vortex, namely, the inclined lines that indicate the downstream convection of the passage vortex. When the passage vortex impinges on the leading edge of the second stator, the levels of pressure unsteadiness are significantly modulated and vary from 8% to 13%. On the other hand, in the

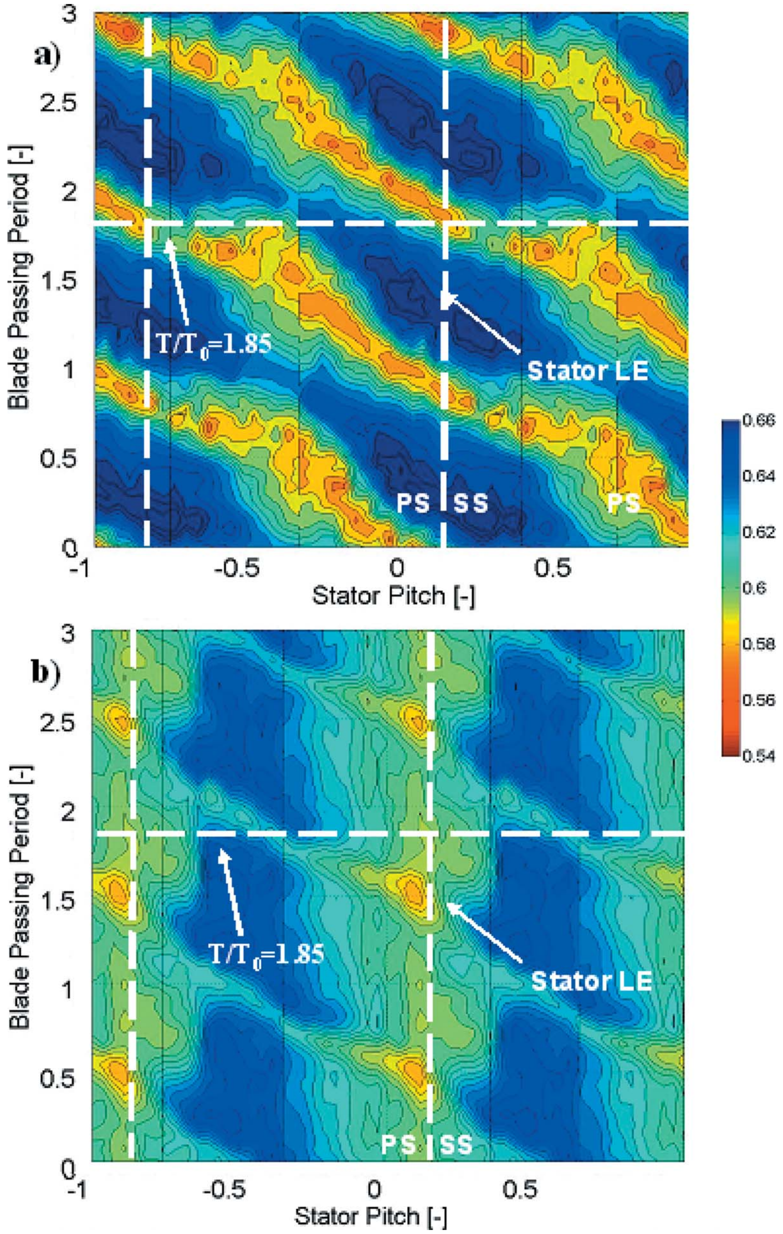

**Fig. 13 Time-distance plot of relative total pressure coefficient $Cpt_{rel}$ at (*a*) 76% span and (*b*) 50% span**

regions where the main flow is dominant, $P_u$ is as low as 2%. The effect of vortex stretching and growth when the passage vortex interacts with the second stator's leading edge can be observed. The stretching mechanism occurs when the vortex is accelerated in the stator passage, while vortex growth occurs due to the blockage effect of the potential field generated from the stator's leading edge. Within the stator passage (stator pitch of approximately −0.4) the levels of $P_u$ are as high as 13%; however at the stator leading edge (stator pitch around 0.2) the level of unsteadiness reduces to around 8%.

In Fig. 14(*b*) the time-distance plot of the pressure unsteadiness coefficient for the midspan location is shown. The effect of the secondary flow is negligible at this span, and thus the levels of unsteadiness are significantly lower than that in Fig. 14(*a*). Nevertheless regions with relatively higher unsteadiness are associated with the rotor wake structure and are seen to lie along inclined lines. In these regions, the level of unsteadiness is as high as 4%, whereas in the main flow the peak values decrease to no more than 1%. The trajectory of the rotor's wake, which is convected downstream through the passage of the second stator, can be inferred from the region of elevated $P_u$. When approaching the second stator's leading edge, the trajectory has a kink, which is also accompanied by a broad region of increased pressure unsteadiness.

A comparison of the relative pressure coefficient (shown in Fig. 13) and the pressure unsteadiness coefficient (Fig. 14) shows that regions of low relative total pressure coincide with the regions of high pressure unsteadiness both in the passage vortex region and in the wake region.

Since the measurement probe is in the stationary frame, i.e., fixed with the stator row, the relative total pressure varies (on the time and space domain) due to the combination of the rotor motion, the potential field created by the stator row, and the losses generated in the rotor flow passage. For this reason, losses cannot be isolated from the other effects. The quantification of loss can only be properly made by the measurement of entropy, which is

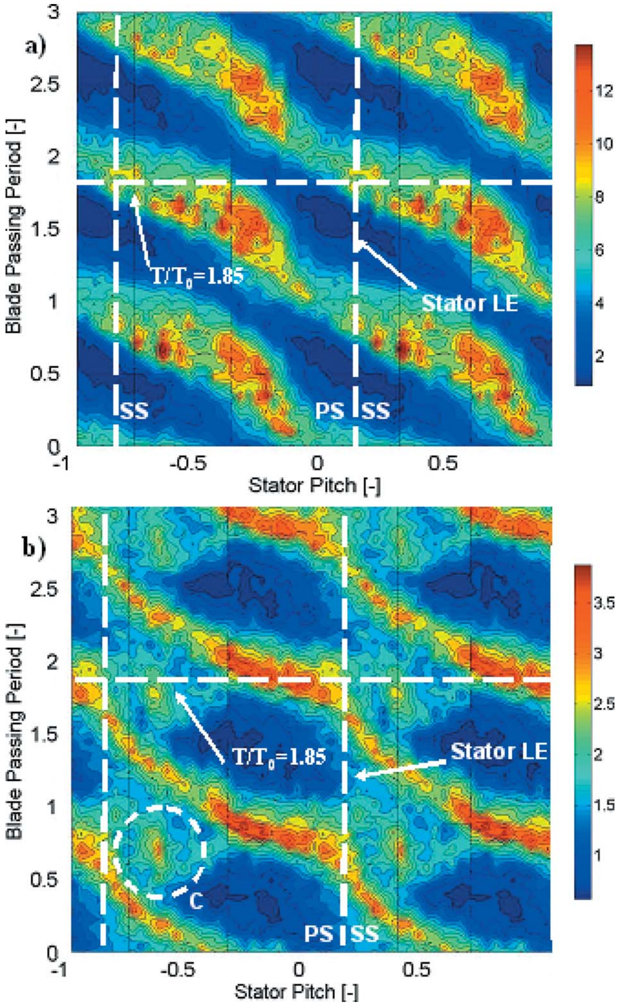

**Fig. 14 Time-distance plot of pressure unsteadiness coefficient Pu (%) at (*a*) 76% span and (*b*) 50% span**

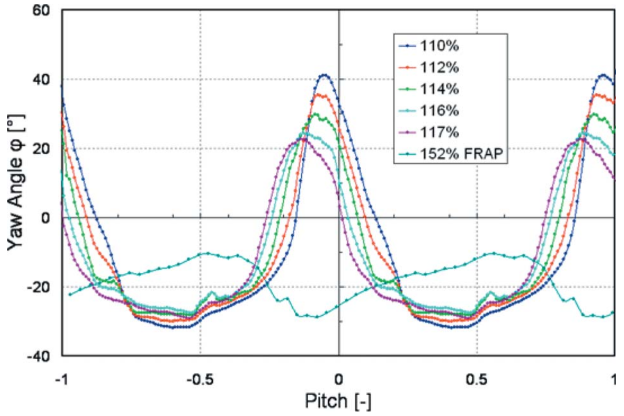

**Fig. 15 Circumferential evolution of yaw angle at different axial locations (110%–152% $C_{ax}$) at 80% span—one rotor blade position**

retrieved by the combination of instantaneous temperature and pressure. Although the FRAP can measure both quantities simultaneously, the frequency response of the temperature signal is several orders of magnitude lower than the pressure signal; thus these data cannot be used for unsteady entropy measurements.

The set of measured data presented in this work clearly show a strong correlation between region of low relative total pressure and high nondeterministic pressure unsteadiness. The combination of these two quantities can be considered as an indication of loss production, and thus unsteady loss mechanisms can be assessed.

Kelvin's theorem indicates that the circulation around a stream tube is constant. Thus in an incompressible flow, such as that in the present work, an increase in the vortex diameter is accompanied by a decrease in the kinetic energy. This induces a lower dissipation and thus lower rate of mixing and loss generation. This phenomenon occurs periodically when the vortex diameter grows due to the blockage effect of the second stator leading edge and is clearly observed from the measurement of relative total pressure at 76% span (Fig. 13(*a*)) together with the increased level of unsteadiness in Fig. 14(*a*). A similar approach can be used in the analysis of the wake mechanism. If the wake is considered as a vortical structure with two counter-rotating vortex sheets, according to Kelvin's theorem, the velocity difference is increased when the wake is compressed. This compression therefore results in an increased velocity gradient inside the wake, which in turn results in an increase in the mixing losses. This process is shown in Fig. 13(*b*) around a pitch of 0.2 where a broad area of increased relative total pressure drop, as well as an increased level of pressure unsteadiness (Fig. 14(*b*)), is measured. Thus there is a clear link between the loss production mechanism and the kinking of wake's structure as the wake is turned and successively compressed around the stator leading edge.

It is also noteworthy to point out the concentrated region of high unsteadiness in the middle of the rotor blade passage—this is labeled as C in Fig. 14(*b*). Its periodic appearance suggests that it is associated with the chopped wake shed from the first NGV. This chopped wake is convected downstream through the rotor blade passage. Further analysis is required to confirm the source of this concentrated region since the equal number of blade counts does not make it possible to clearly separate the effect of flow structures generated in the NGV or in the rotor.

The measurements of the relative total pressure and pressure unsteadiness coefficients that were presented above show that the unsteady loss generation mechanisms at the midspan are different from those in the secondary flow region. In the region of secondary flow, the mechanisms are driven by the stretching and growth of passage vortex, and from the measured data, this mechanism is more pronounced at 76% span compared to the midspan region. Thus, modifications to the characteristics of the secondary flow deserve more attention in the aerodynamic design. For example, a rotor/stator design that increases the mixing in the tip region and thus reduces the diffusion of the unsteady vortex should improve the aerodynamic performance. This can be accomplished by including forward sweep in the blade stacking on the second stator's tip as a means to increase the axial distance between the rotor and stator.

The degree of mixing of the flow in the interstage region can be studied by observing the variation of the measured yaw angle at one fixed rotor blade position at different axial location in the volume shown in Fig. 11. The yaw angle variation, derived from the PIV measurements, as a function of the blade pitch is shown in Fig. 15 for five axial positions (from 110% $C_{ax}$ to 117% $C_{ax}$). At all positions the data are measured at 80% blade span. Also shown in the figure is the yaw angle derived from the more downstream located FRAP. It can be seen that the largest changes in the yaw angle occur at the most upstream position (110% $C_{ax}$). The peak value occurs at a pitch of approximately −0.1, and significant underturning occurs in the pitch range of −0.15 to 0.1. At the more downstream positions, the peak value decreases and occurs at a more negative pitch as the passage vortex convects downstream. However, the region of the main flow (seen in the pitch ranges of −0.75 to −0.4 and 0.2–0.65) remains almost unchanged. The location of the peak value in the yaw angle that is observed in the FRAP measurements is expected due to its more downstream location. It is also noted that at this more downstream position the pitch range of underturning is broader due to the increased mixing of the vortex into the main flow.

## Conclusion

A unique set of steady and unsteady data has been acquired by means of different measurement techniques (3D-PIV and FRAP) in a partially shrouded multistage axial turbine. Owing to the combination of flow velocimetry and pressure measurements, the flow kinematics and loss generation mechanism have been verified. Stereoscopic PIV has been compared with FRAP unsteady pressure measurements and 5HP at the exit of the turbine section, and they show a good agreement.

The interaction of vortex structures has been studied in the interstage tip region. The passage vortex grows downstream of the blade throat and then passes over the shroud platform due to the uncovering of the blade throat. Together with the passage vortex, a vortex is formed due to a sudden flow expansion at the trailing edge of the shroud. The interaction of the two vortex structures entrains low momentum fluid from the wake and thus generates a core of local pressure losses that are measured downstream throughout the interstage region. The analysis of time-distance plots shows that this interaction is triggered by the blade passing period.

Unsteady loss generation has been discussed from the combination of measured relative total pressure and the nondeterministic pressure unsteadiness in the interstage region. Flow structure interaction, with the second stator's leading edge such as vortex stretching and wake bending mechanisms have been observed and found to be a primary source of unsteady losses.

This work presents a unique combination of velocity and pressure data and detailed flow analysis, which enables the possibility to enhance flow modeling used in the design process and provides improved understanding of loss generation mechanisms.

## Acknowledgment

The support of the Alstom-ETH research and development forum "Center of Energy Conversion" and the financial support of Alstom Power are acknowledged. The authors gratefully acknowledge Alstom Power Switzerland and Rolls Royce Deutschland for their kind permission to publish the results presented in this paper. In particular, thanks are due to Michael Loetzerich and Erik Janke for their support and suggestions during the course of this research activity.

## Nomenclature

$C_{\mathrm{ax}}$ = rotor blade axial chord
Cpt = total pressure coefficient $(P_{0\mathrm{meas}}-P_{S\mathrm{exit}})/(P_{0\mathrm{inlet}}-P_{S\mathrm{exit}})$
$d$ = diameter of the seeding particle in Eq. (1)
$I$ = scattered light intensity
$I_0$ = maximum light intensity in Eq. (1)
Ma = Mach number
NGV = nozzle guide vane
$P$ = static pressure
PS = blade pressure side
SS = blade suction side
$u, v, w$ = axial, tangential, radial flow velocities
$T/T_0$ = blade passing period fraction
TE = trailing edge
$x_0$, $y_0$, $z_0$ = location of tracer particles in Eq. (1)
$z$ = turbine axial coordinate

### Greek

$\alpha$ = angle between cameras A and B
$\Delta z_0$ = laser beam thickness
$\varepsilon$ = measurement error
$\beta$ = pitch angle
$\varphi$ = yaw angle
$\rho$ = density

### Subscripts

0 = stagnation quantity
rel = relative quantity
sec = secondary flow vector
mean = mean unit vector

## References

[1] Schlienger, J., Kalfas, A. I., and Abhari, R. S., 2005, "Vortex-Wake-Blade Interaction in a Shrouded Axial Turbine," ASME J. Turbomach., **127**, pp. 633–707.
[2] Miller, R. J., Moss, R. W., Ainsworth, R. W., and Horwood, C. K., 2003, "Time-Resolved Vane-Rotor Interaction in a High-Pressure Turbine Stage," ASME J. Turbomach., **125**, pp. 1–13.
[3] Pfau, A., Schlienger, J., Rusch, D., Kalfas, A. I., and Abhari, R. S., 2005, "Unsteady Flow Interaction Within the Inlet Cavity of a Turbine Rotor Tip Labyrinth Seal," ASME J. Turbomach., **127**, pp. 679–688.
[4] Gaetani, P., Persico, G., Dossena, V., and Osnaghi, C., 2006, "Investigation of the Flow-Field on a HP Turbine Stage for Two Stator-Rotor Axial Gaps. Part II: Unsteady Flow Field," ASME Paper No. IGTI GT2006-90556.
[5] Wernet, M. P., 2000, "Application of DPIV to Study Both Steady State and Transient Turbomachinery Flows," Opt. Laser Technol., **32**, pp. 497–525.
[6] Balzani, N., Scarano, F., Riethmuller, M. L., and Breugelmans, F. A. E., 2000, "Experimental Investigation of the Blade-to-Blade in a Compressor Rotor by Digital Particle Image Velocimetry," ASME J. Turbomach., **122**, pp. 743–750.
[7] Sanders, A. J., Papalia, J., and Fleeter, S., 2002, "Multi-Blade Row Interactions in a Transonic Axial Compressor: Part I—Stator Particle Image Velocimetry (PIV) Investigation," ASME J. Turbomach., **124**, pp. 10–18.
[8] Uzol, O., Chow, Y. C., Katz, J., and Meneveau, C., 2002, "Experimental Investigation of Unsteady Flow Field Within a Two-Stage Axial Turbomachine Using Particle Image Velocimetry," ASME J. Turbomach., **124**, pp. 542–552.
[9] Ibaraki, S., Matsuo, T., and Yokoyama, T., 2006, "Investigation of Unsteady Flow Field in Vaned Diffuser of a Centrifugal Compressor," ASME Paper No. GT2006-90268.
[10] Estevadeordal, J., Gogineni, S., Goss, L., Copenhaver, W., and Gorrell, S., 2002, "Study of Wake-Blade Interactions in a Transonic Compressor Using Flow Visualization and DPIV," ASME J. Fluids Eng., **124**, pp. 166–175.
[11] Liu, B., Wang, H., Liu, H., Yu, H., Jiang, H., and Chen, M., 2004, "Experimental Investigation of Unsteady Field in the Tip Region of an Axial Compressor Rotor Passage at Near Stall Condition with Stereoscopic Particle Image Velocimetry," ASME J. Turbomach., **126**, pp. 360–370.
[12] Göttlich, E., Woisetschläger, J., Pieringer, P., Hampel, B., and Heitmeir, F., 2005, "Investigation of Vortex Shedding and Wake-Wake Interaction in a Transonic Turbine Stage using Laser-Doppler-Velocimetry and Particle Image Velocimetry," ASME Paper No. GT2005-68579.
[13] Dorris, A. R., North, W. E., and Malandra, A. J., 1996, "Gas Turbine Blade Having a Cooled Shroud," U.S. Patent No. 5,482,435.
[14] Tomita, Y., 1998, "Gas Turbine Rotor," U.S. Patent No. 5785496.
[15] Nirmalan, N. V., and Bailey, J. C., 2005, "Experimental Investigation of Aerodynamic Losses of Different Shapes of a Shrouded Blade Tip Section," ASME Paper No. IGTI GT2005-68903.
[16] Harvey, N. W., and Ramsden, K., 2001, "A Computational Study of a Novel Turbine Rotor Partial Shroud," ASME J. Turbomach., **123**, pp. 534–543.
[17] Willer, L., Harvey, N. W., Haselbach, F., and Newman, D. A., 2006, "An Investigation Into Novel Turbine Rotor Winglet—Part II: Numerical Results and Experimental Results," ASME Paper No. IGTI GT2006-90459.
[18] Porreca, L., Behr, T., Schlienger, J., Kalfas, A. I., Abhari, R. S., Ehrhard, J., and Janke, E., 2005, "Fluid Dynamics and Performance of Partially and Fully Shrouded Axial Turbines," ASME J. Turbomach., **127**, pp. 668–678.
[19] Prasad, A. K., 2000, "Stereoscopic Particle Image Velocimetry," Exp. Fluids, **29**, pp. 103–116.
[20] Kähler, C. J., Sammler, B., and Kompenhans, J., 2002, "Generation and Control of Tracer Particles for Optical Flow Investigations in Air," Exp. Fluids, **33**, pp. 736–742.
[21] Mellin, A., 1997, "Tracer Particles and Seeding for Particle Image Velocimetry," Meas. Sci. Technol., **8**, pp. 1496–1416.
[22] Zang, W. J., and Prasad, A. K., 1997, "Performance Evaluation of a Scheimpflug Stereocamera for Particle Image Velocimetry," Appl. Opt., **36**, pp. 8738–8744.
[23] Soloff, S. M., Adrian, R. J., and Liu, Z.-C., 1997, "Distortion Compensation for Generalized Stereoscopic Particle Image Velocimetry," Meas. Sci. Technol., **8**, pp. 1441–1454.
[24] Porreca, L., Kalfas, A. I., Abhari, R. S., Yun, Y. I., and Song, S. J., 2006, "Stereoscopic PIV Measurements in A two-Stage Axial Turbine," *The 18th Symposium on Measurement Techniques in Transonic and Supersonic Flow in Cascades and Turbomachinery*, Thessaloniki, Greece, September.
[25] Westerweel, J., Dabiri, D., and Gharib, M., 1997, "The Effect of a Discrete Window Offset on the Accuracy of Cross-Correlation Analysis of Digital PIV Recordings," Exp. Fluids, **23**, pp. 20–28.
[26] Scarano, F., and Riethmuller, M. L., 1999, "Iterative Multigrid Approach in PIV Image Processing With Discrete Window Offset," Exp. Fluids, **26**, pp. 513–523.

[27] Westerweel, J., 1994, “Efficient Detection of Spurious Vectors in Particle Image Velocimetry,” Exp. Fluids, **16**, pp. 237–247.

[28] Raffel, M., Willert, C., and Kompenhans, J., 1998, *Particle Image Velocimetry: A Practical Guide*, Springer, Berlin.

[29] Willert, C. E., and Gharib, M., 1991, “Digital Particle Image Velocimetry,” Exp. Fluids, **10**, pp. 181–193.

[30] Keane, R. D., and Adrian, R. J., 1992, “Theory of Cross Correlation Analysis of PIV Images,” Appl. Sci. Res., **49**, pp. 191–215.

[31] Porreca, L., Hollenstein, M., Kalfas, A. I., and Abhari, R. S., 2007, “Turbulence Measurements and Analysis in a Multistage Axial Turbine,” J. Propul. Power, **23**(1), pp. 227–234.

[32] Gizzi, W. P., Roudener, C., Stahlecker, D., Köppel, P., and Gyarmathy, G., 1999, “Time-Resolved Measurements With Fast-Response Probes and Doppler Velocimetry at the Impeller Exit of a Centrifugal Compressor: A Comparison of Two Measurement Techniques,” Proc. Inst. Mech. Eng., Part A, **213**, pp. 291–318.

[33] Kupferschmied, P., Köppel, P., Gizzi, W., Roudener, C., and Gyarmathy, G., 1999, “Time-Resolved Measurements in Fast-Response Aerodynamic Probes in Turbomachines,” Meas. Sci. Technol., **11**, pp. 1036–1054.

[34] Treiber, M., Kupferschmied, P., and Gyarmathy, G., 1998, “Analysis of the Error Propagation Arising From the Measurements With a Miniature Pneumatic 5-Hole Probe,” *XIVth Symposium on Measuring Techniques for Transonic and Supersonic Flows in Cascade and Turbomachines*.

[35] Rosic, B., and Denton, J., 2006, “The Control of Shroud Leakage Loss by Reducing Circumferential Mixing,” ASME Paper No. GT2006-90949.

[36] Wallis, A. M., Denton, J. D., and Demargne, A. A. J., 2001, “The Control of Shrouded Leakage Flows to Reduce Aerodynamic Losses in a Low Aspect Ratio, Shrouded Axial Flow Turbine,” ASME J. Turbomach., **123**, pp. 334–341.

[37] Yun, Y. I., Porreca, L., Kalfas, A. I., Song, S. J., and Abhari, R. S., 2006, “Investigation of 3D Unsteady Flows in a Two Stages Shrouded Axial Turbine Using Stereoscopic PIV and FRAP—Part II: Kinematics of Shroud Cavity Flow,” ASME Paper No. GT2006-91020.

[38] Pullan, G., Denton, J., and Dunkley, M., 2003, “An Experimental and Computational Study of a Streamwise Shed Vortex in a Turbine Stage,” ASME J. Turbomach., **125**, pp. 291–297.

# Effect of Trench Width and Depth on Film Cooling From Cylindrical Holes Embedded in Trenches

**Yiping Lu**

**Alok Dhungel**

**Srinath V. Ekkad**
e-mail: ekkad@vt.edu

Mechanical Engineering Department,
Virginia Tech,
Blacksburg, VA 24061

**Ronald S. Bunker**
GE Global Research Center,
Niskayuna, NY 12301

*The present study is an experimental investigation of film cooling from cylindrical holes embedded in transverse trenches. Different trench depths are considered with two trench widths. Trench holes can occur when blades are coated with thermal barrier coating (TBC) layers. The film-hole performance and behavior will be different for the trench holes compared to standard cylindrical holes that are flush with the surface. The trench width and depth depend on the mask region and the thickness of the TBC layer. Detailed heat transfer coefficient and film effectiveness measurements are obtained simultaneously using a single test transient IR thermography technique. The study is performed at a single mainstream Reynolds number based on freestream velocity and film-hole diameter of 11,000 at four different coolant-to-mainstream blowing ratios of 0.5, 1.0, 1.5, and 2.0. The results show that film effectiveness is greatly enhanced by the trenching due to the improved two-dimensional nature of the film and lateral spreading. The detailed heat transfer coefficient and film effectiveness contours provide a clear understanding of the jet-mainstream interactions for different hole orientations. Computational fluid dynamics simulation using* FLUENT *was also performed to determine the jet-mainstream interactions to better understand the surface heat transfer coefficient and film effectiveness distributions.* [DOI: 10.1115/1.2950057]

## Introduction

Gas turbine blades need to be effectively cooled to increase component life and reduce maintenance costs. Typically, cooling a turbine blade involves long turbulated serpentine internal passages with ribs, impingement holes, and pin fins for heat transfer enhancement along with film cooling through discrete holes to protect the blades from direct contact with hot gases.

With increasing turbine inlet temperatures, modern hot gas path components may be coated with thin layers of thermal barrier coatings (TBCs) made of ceramic material, such as yttria with stabilized zirconia. The coatings are thin and on the order of film-hole sizes typically 0.5–2 mm. Typically, film holes are drilled on the surface before the TBC layer is applied. The hole area may be masked, then the TBC layer is sprayed, and then the mask will be removed revealing the holes embedded in 2D trenches. It was determined by Bunker [1] that film holes embedded in trenches showed very little variation in film effectiveness with increasing blowing ratio, revealing the possibility that the coolant flow exiting the cylindrical hole spreads into the trench and comes into contact with hot gas as a 2D film rather than 3D structures that exit the cylindrical hole. However, Bunker [1] provided only film effectiveness distributions and also the hole had a compound angle (radial injection) in the lateral direction. Lu et al. [2] studied the effect of trench exit area and edge shape on film cooling performance using an IR thermography method. They studied the effect of trench width and altered the exit edge of the slot. They also presented the heat transfer coefficients along with the film effectiveness results. Their results showed that the film cooling holes provide higher film effectiveness when embedded in a trench. However, in some geometries, when the trench began at the upstream edge of the hole, the film effectiveness diminished. The heat transfer coefficient enhancement due to the embedding was not significantly higher compared to the typical unembedded cylindrical hole. The overall heat flux ratio comparing film cooling with embedded holes to unembedded holes shows that the full trench and downstream trench spacing after the hole exit produce the highest heat flux reduction. Bunker [1] embedded compound angle holes in the trenches and Lu et al. [2] used simple angle holes. Both the studies were not parametric in nature to determine the optimum trench width and depth. Waye and Bogard [3] studied the presence of trenched holes on the suction side of a vane. The narrow trench configuration provided the best adiabatic effectiveness performance. In fact, the increasing adiabatic effectiveness levels with increasing blowing ratio indicated the trench suppressed coolant jet separation. This result is consistent from Bunker [1] and Lu et al. [2].

Previously, Blair [4] investigated the slot film cooling at the entry of a vane cascade endwall. Chyu et al. [5] provided the film effectiveness measurements downstream of 2D slots modeled as gap leakages, both aligned and misaligned. Wang et al. [6] was the first study to look at jets exiting into slots. They showed that the slot exit provides a uniform velocity distribution. Klinger and Hennecke [7] and Schulz [8] also studied the discrete holes feeding a trench for combustor applications. The trench is very different from a slot as the slot is a 2D geometry that is designed to produce a 2D film. However, the trench is a shallow slot where the holes are embedded in it.

In the present study, a transient infrared thermography technique is used for obtaining both heat transfer coefficient and film effectiveness from a single test. The transient IR technique is based on the two-equation, single test proposed by Vedula and Metzger [9] and was demonstrated successfully by Ekkad et al. [10]. Simultaneous $\eta$ and $h$ distributions are investigated and presented, on the flat surface downstream of injection, for various blowing ratios for regular cylindrical holes and for six different trench configurations. This paper also presents the computational fluid dynamics (CFD) predictions of film cooling for holes embedded in transverse trenches for one trench depth. The trenched hole results were compared with a standard simple angle cylindrical holes and a standard diffuser shaped hole configuration.

---

Contributed by the International Gas Turbine Institute of ASME for publication in the JOURNAL OF TURBOMACHINERY. Manuscript received June 11, 2007; final manuscript received July 13, 2007; published online September 25, 2008. Review conducted by David Wisler. Paper presented at the ASME Turbo Expo 2007: Land, Sea and Air (GT2007), 2007, Montreal, Quebec, Canada, May 14–17, 2007.

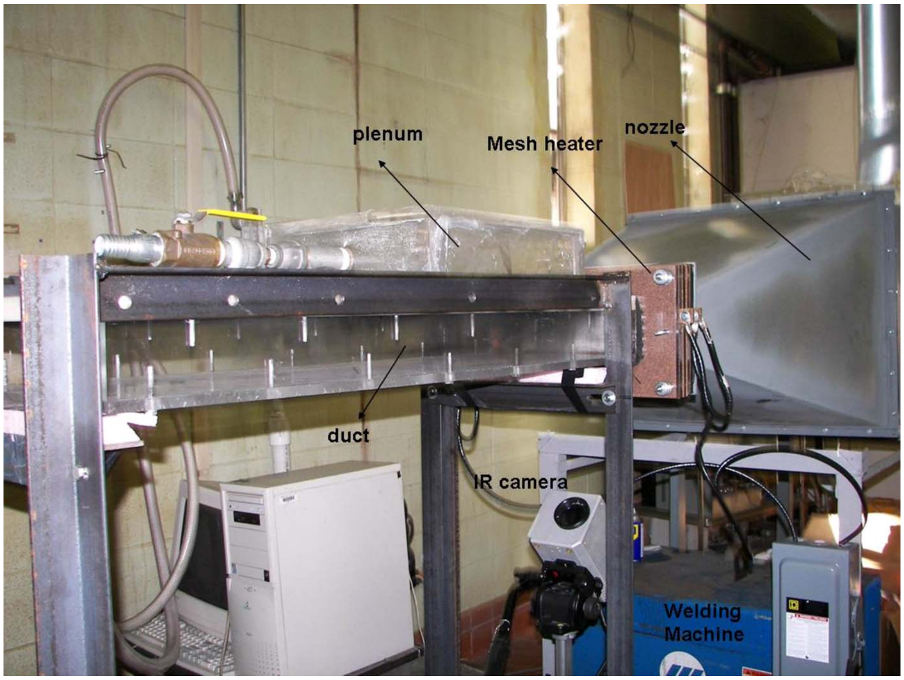

Fig. 1 Test rig setup

## Test Facility

Figure 1 shows the comprehensive view of the experimental arrangement. A fast response mesh heater was placed at the exit of the nozzle (Fig. 2). The mesh heater concept developed by Gillepsie et al. [11] has the capability of providing an instantaneous temperature step to the mainstream air. The mesh used to build the heater was 304 stainless steel woven wire mesh with a 20 $\mu$m wire diameter. The free area of the mesh was 33.6%, which helped in reducing the freestream turbulence before the test section.

The test section is made of plexiglass and has a cross section of 30 cm width and 9 cm height. The top plate of the test section is made of 3 cm thick ABS. This plate has a replaceable section about 25.4 cm downstream of the test section inlet. This replaceable section can be interchanged to change the hole geometry. The replacement section was also made of the same ABS material with same thickness. The edges were flush after the mounting of the test plate to ensure no trip at the edges. In addition, sealant was used to seal the edges to ensure no coolant leakage at the contact locations. A trip is placed at the entrance to the test section to produce a fully turbulent boundary layer over the test plate. The coolant air is provided from a separate compressed air supply and is metered for flow measurement. When the valve is flipped, the coolant enters a plenum below the test plate and is then ejected through the film cooling holes into the test section. Thermocouples are mounted upstream of the hole row to measure the mainstream temperature and inside one of the holes to measure the coolant exit temperature. The coolant temperature is measured inside only one hole because pretesting showed that all film holes had the same flow rate and temperature conditions. For all cases, the thickness of the test plate was the same. So the trench hole lengths were shorter than the base line and shaped hole lengths.

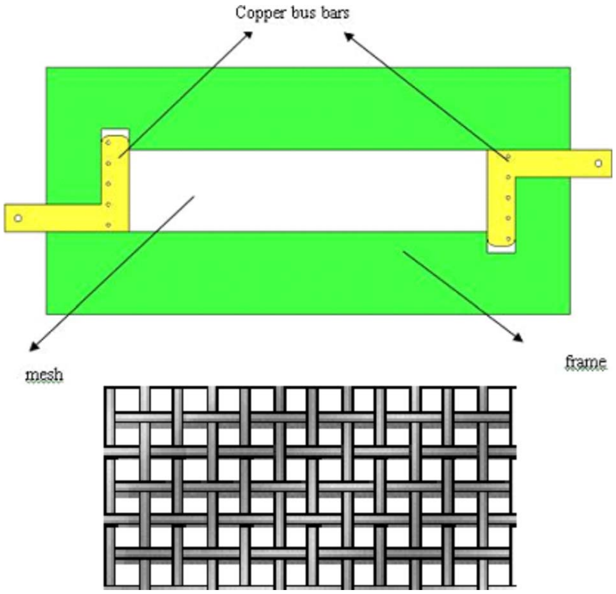

Fig. 2 Mesh heater

The blowing ratio, or the ratio of coolant mass flux to mainstream mass flux at injection location, was based on measuring the total coolant mass flow rate through the six holes and determining the mass flux for coolant by dividing with the total hole area.

The infrared thermography system used is a FLIR Systems ThermaCAM SC 500. The camera has a range of −40–500°C. The ThermaCAM 500 utilizes uncooled microbolometer long wave detectors to sense IR radiation. This makes them ideal for general thermal measurement applications. The SC 500 system provides real time 14 bit digital output, a 320×240 pixel detector, precision temperature measurement, internal data storage, and outstanding thermal sensitivity. The camera has following specifications: the field of view and minimum focus distance are 24 deg×18 deg and 0.5 m, respectively, the spectral range is 7.5–13 $\mu$m, and accuracy is ±2% or 2°C. The test surface is viewed through a stretched polyurethane sheet. The sheet is thin enough to cause very little effect on IR transmissivity. There is no fluttering of the sheet due to the stretching. The system calibration is conducted using a thermocouple placed on the black painted test surface to act as the benchmark. This thermocouple is used to estimate the emissivity of the test surface. The emissivity of the black painted test when viewed without the window is 0.98. The calibrated transmissivity for the polyurethane sheet was 0.75.

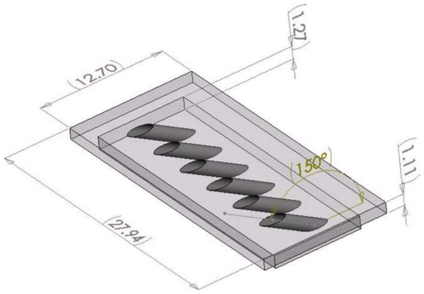

Fig. 3 Test plate geometry without trench

Figure 3 shows the test plate with film-hole geometry used in this study. There are six holes of 1.27 cm diameter in each row inclined at 30 deg along the flow direction. The hole spacing between the adjacent holes is three-hole diameters for all the holes. Figure 4 shows the trench film cases and shaped hole and Table 1 lists the film-hole geometry parameters. For shaped diffuser hole, the hole inclination angle is set as 30 deg and the length of cylindrical inlet portion is $l=2D$. The hole laidback angle is 15 deg.

Table 1 Film hole and flow geometry

| | Width | Depth |
|---|---|---|
| Case 1 (Fig. 4(*b*)) | 2 D | 0.5 D |
| Case 2 (Fig. 4(*c*)) | 3 D | 0.5 D |
| Case 3 (Fig. 4(*d*)) | 2 D | 0.75 D |
| Case 4 (Fig. 4(*e*)) | 3 D | 0.75 D |
| Case 5 (Fig. 4(*f*)) | 2 D | 1.0 D |
| Case 6 (Fig. 4(*g*)) | 3 D | 1.0 D |

The measured mainstream velocity and freestream turbulence intensity using a calibrated single hot wire probe are 13.8 m/s and 2%, respectively. The mainstream Reynolds number ($\mathrm{Re}_d$) based on film-hole diameter is 11,000. The boundary layer profile measured downstream of the trip is close to the fully turbulent flow profile (1/7th law). The numerical scheme used the same conditions as experiments. Four blowing ratios, $M=0.5$, 1.0, 1.5, and 2.0, are tested for all the eight cases. The coolant-to-mainstream density ratio for the entire study was 1.07.

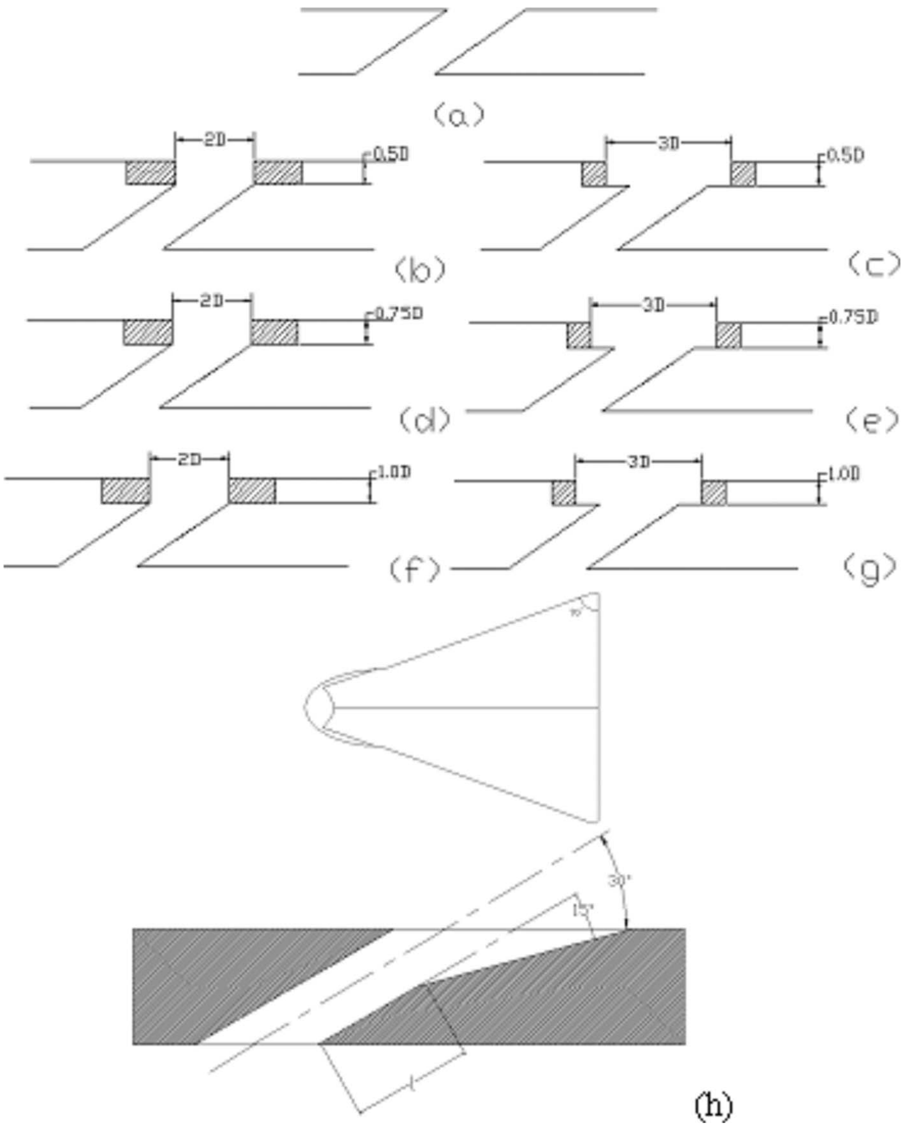

Fig. 4 Eight cases with different hole configurations studied

## Procedure

A thermocouple is attached to the test surface with aluminum tape. The thermocouple is located outside the measurement domain to prevent from interference caused by the aluminum tape. The test surface is then sprayed with black flat paint to increase the emissivity of the test surface. The IR camera is focused on the test surface (typically covers slightly larger than the region of interest and the thermocouple). Prior to the actual thermal measurement, calibration of the entire thermography system and the IR signal is required. The test surface is then heated with the hot air supplied by the blower through the mainstream heater. The temperatures of thermocouples are monitored until steady state is reached. The temperature measured by the thermocouple is then compared to that measured by the IR system. The factors required for an accurate IR measurement to compensate for the effects of several different sources of radiation include the distance between the test surface and the front lens of camera, the relative humidity, and the background temperature. Multiple temperature calibrations compensate for all other emitting sources of radiation within view of test article. A number of temperatures are used to establish the corrective value of emissivity. However, the temperature of the reference object must not be too close to the ambient temperature for this to work. During the emissivity calculation, polyethylene sheet window was not used. So, the transmissivity value used was 1.

Typically, the mainstream temperature undergoes a step change increase due to the mesh heater. The coolant temperature is, however, maintained at the initial temperature. The wall temperature monitored by the thermocouple used for emissivity estimation rises as the outside surface is heated during the transient test at a more gradual rate than mainstream temperature. The inside wall temperature is unaffected by the heating on the opposite side confirming the usage of the semi-infinite solid assumption. The test surface was modeled as a semi-infinite solid medium imposed by a sudden transient heating. The entire solid medium was initially at a uniform temperature before the transient test. During the transient heating test, each point on the surface will respond with different temperatures at different times due to different heat transfer coefficients. Faster time of temperature change in response to the prescribed temperature during the transient test will produce higher heat transfer coefficient and vice versa. The test surface is modeled as undergoing 1D transient conduction with convective boundary conditions at the wall. Applying the prescribed boundary conditions and initial conditions to the problem and solving for the wall temperature response with time at the wall produce a solution of the form [12]

$$\frac{T_w - T_i}{T_\infty - T_i} = 1 - \exp\left(\frac{h^2 \alpha t}{k^2}\right)\operatorname{erfc}\left(\frac{h\sqrt{\alpha t}}{k}\right) \tag{1}$$

where $h$ is the unknown quantity in the equation and $T_w$ is the wall temperature at time $t$ after the initiation of the transient test. The material properties, $\alpha$ ($7.157 \times 10^{-8}\ \mathrm{m^2/s}$) and $k$ ($0.15\ \mathrm{W/m\,K}$), dictate the applicability of the semi-infinite solid solution.

In film cooling situations, the basic convective heat load equation is modified to include the film temperature based on the definition of the local heat flux. The equation becomes

$$\frac{T_w - T_i}{T_f - T_i} = 1 - \exp\left(\frac{h_f^{\,2} \alpha t}{k^2}\right)\operatorname{erfc}\left(\frac{h_f\sqrt{\alpha t}}{k}\right) \tag{2}$$

where $T_f$ is the local film temperature and is a function of the local mixing between the mainstream and coolant jet near the surface.

Vedula and Metzger [9] presented a method wherein two color change times can be obtained from a single transient test at every location. If during the transient, the liquid crystal coating indicates one surface temperature ($T_{w1}$) at time $t_1$ and another surface temperature ($T_{w2}$) at time $t_2$. Basically, two events are measured at every point leading to the solution of both $h$ and $T_f$ from the simultaneous solution of the two equations:

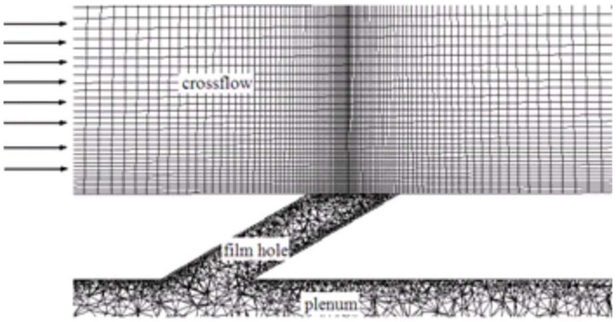

(a) within film hole

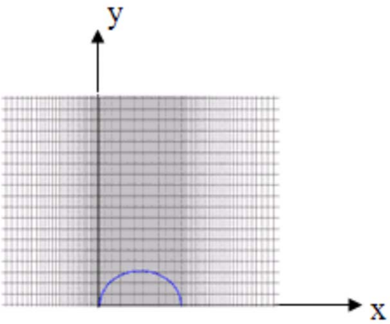

(b) jet exit plane

**Fig. 5 Computational grid details**

$$\frac{T_{w1} - T_i}{T_f - T_i} = 1 - \exp\left(\frac{h_f^{\,2} \alpha t_1}{k^2}\right)\operatorname{erfc}\left(\frac{h_f\sqrt{\alpha t_1}}{k}\right)$$

$$\frac{T_{w2} - T_i}{T_f - T_i} = 1 - \exp\left(\frac{h_f^{\,2} \alpha t_2}{k^2}\right)\operatorname{erfc}\left(\frac{h_f\sqrt{\alpha t_2}}{k}\right) \tag{3}$$

In the proposed transient test, the mainstream will be heated and the coolant supply will be cold or similar to room temperature. The wall temperatures are captured at set instants of time over the entire surface. The mesh heater was designed to provide a true step change in air temperature at the start of a test. The true step change in mainstream temperature allows the use of the original solution to the transient heating of the wall, Eq. (1). The regression technique used to reduce uncertainty in experimental measurements was to collect multiple wall temperature-time data pairs over a broad range of temperatures to use in an overconstrained system of equations to solve for $h$. The regression analysis put all terms of the conduction equation to the right hand side of the equation and was solved for all points of data for each pixel. This resulted in a residual error for each time-temperature data pair. The residual error was minimized in a least squares sense solving for the heat transfer coefficient that best fit all data.

Uncertainty in the calculation comes from measurement of initial, mainstream, and coolant temperatures. Estimated uncertainty in the initial and wall temperature ($\Delta T_i$) is $\pm 0.5°\mathrm{C}$, the mainstream temperature ($\Delta T_\infty$) is $\pm 0.5°\mathrm{C}$, and the coolant temperature ($\Delta T_c$) is $\pm 0.5°\mathrm{C}$. The camera frame rate is 60 Hz resulting in a time error of ±1.6% and the test surface property uncertainty is estimated at ±3%. The resulting *average* uncertainties using the methodology proposed by Kline and McClintock [13] for heat transfer coefficient and film effectiveness are ±4.5% and ±7.0%, respectively. However, uncertainty for local film effectiveness depends on the local value. Uncertainty for effectiveness measurements is ±0.03. Overall uncertainties in regions affected by two-dimensional conduction in regions such as sharp corners at trench edges and hole exit edges are higher. The affected region is within less than a quarter hole diameter region around the edges.

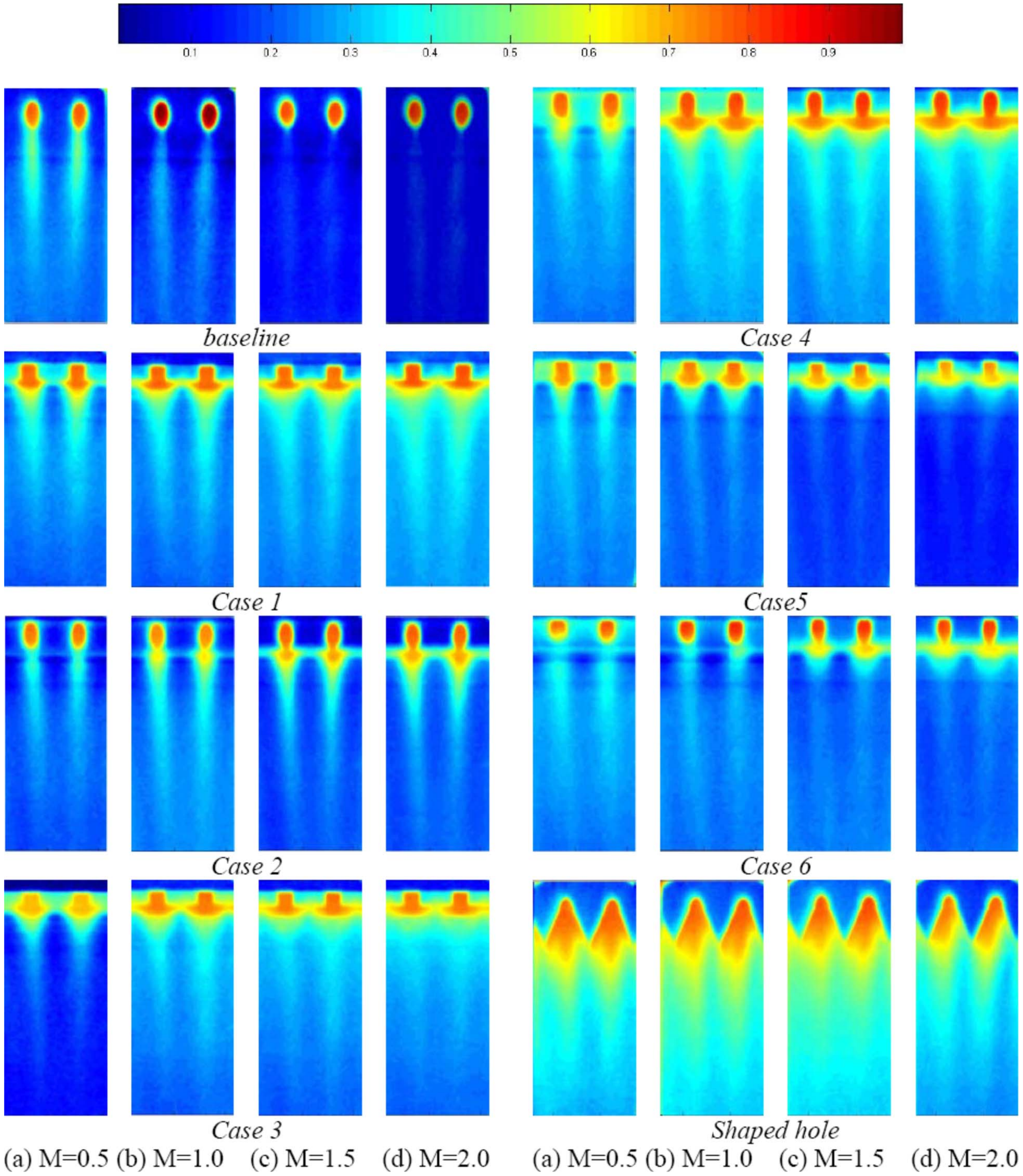

**Fig. 6 Detailed film effectiveness distributions for all cases at different blowing ratios**

## Numerical Procedure

A highly orthogonalized, nonuniform, fine grid mesh was generated with grid nodes clustered in the immediate vicinity of the discrete film cooling jet. The most difficult region for the grid generation and also the most critical portion of the entire mesh is the region near the film hole [14]. Other important grid parameters are considered. The grid aspect ratio, especially near the coolant jet, was kept under 10. The nodes near the test plate surface was adjusted so that average $y^+$ value was about 30 in the crossflow and 30–100 within the film hole. The overall extents of the computation domain in the lateral, vertical, and streamwise directions were 24.25 D, 15.875 D, and 80 D, respectively. The numerical computation area was matched to the experimental domain instead of computing only one hole with symmetry boundary conditions. The grid was created using GAMBIT and the simulation was run using FLUENT computer code. Figure 5 shows the grid used in the present study.

Boundary conditions are prescribed at all three boundary surfaces of the computation domain. Mainstream conditions were maintained the same in all cases and the coolant flow rate was altered to change the blowing ratios. The coolant temperature was set at 296 K and the mainstream temperature was set at 321 K. At

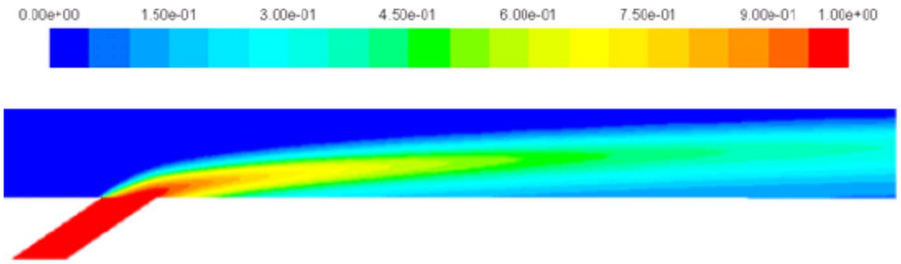

(a) Flat plate case

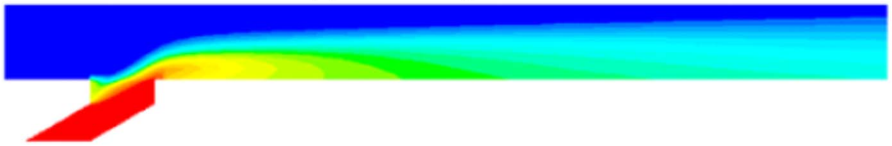

(b) Case 3

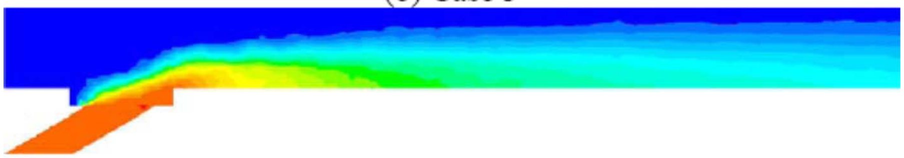

(c) Case 4

**Fig. 7 Computed centerline nondimensional temperature contours demonstrating effect of hole width at $M=1.0$**

the exit plane, pressure level was specified along with zero streamwise gradient for all other dependent variables.

The standard high Re $k$-$\varepsilon$ model was used in this study. The model is widely used and no additional details are provided here. Standard smooth-wall function is used to represent the near-wall behavior, and roughness effects have not been incorporated. All the cases presented here converged to residual levels of the order of $10^{-5}$ and to better than 0.03% error in the mass flow rate between the inlet and exit of the computational domain. Typically, 500 iterations were necessary to attain a converged solution. Grid independence was checked by comparing the solutions obtained with 85,562 nodes and the solutions obtained with 53,771 nodes for Case 1. In both cases, the grids were clustered near the film-hole region. The differences in the solution on two grids were found to be minimal. These results were presented in a CFD only study by Lu and Ekkad [14]. The numerical technique employed in this study was rather crude but provides some valuable insight to the film cooling behavior due to the presence of the trenches. Wall functions and a sparse grid near the wall are not adequate to obtain accurate wall temperature predictions but could provide sufficient detail of flow behavior away from the wall in the mixing region. The mixing flow behavior has been used to describe the wall measurements of heat transfer coefficients and film effectiveness.

## Results and Discussion

Figure 6 presents the effect of blowing ratio on detailed film effectiveness distributions for all the eight cases. For base line case, the jet streaks are clearly visible with the highest effectiveness occurring at $M=0.5$ near the hole exits. At higher blowing ratios, there is a jet lift-off resulting in lower coverage. For Case 1, the coolant enters a shallow (0.5 D) and narrow trench (2 D) before mixing with the mainstream. It appears that the coolant exiting the holes develops sideways and fills the trench before exiting as a more two-dimensional film. The spanwise mixing in the trench is clearly evident with higher effectiveness between the jets inside the trench. As the blowing ratio increases, the effectiveness increases inside the slot and outside, and the coverage distance is also enhanced. For Case 2, the coolant enters a shallow (0.5 D) and a wider trench (3 D). The lateral spreading into the slot is clearly missing for this wider trench. The jet streaks along the hole are evident similar to the cylindrical hole except at the trench edge where the flow hits the edge and shows a sudden increase in effectiveness outside the trench. Also, the effectiveness increases with increasing blowing ratio unlike the standard base line case where jet lift-off caused lower effectiveness at higher blowing ratios. For Case 3, the coolant enters a medium (0.75 D) and a narrow (2 D) trench. The coolant again appears to spread into the trench after exiting the hole similar to Case 1. A two-dimensional film appears to exit the trench. The lateral spreading is higher for Case 3 compared to Case 1. The deeper trench enables in reducing the three-dimensional structure exiting the holes more efficiently. With increasing blowing ratio, the film effectiveness increases especially in the downstream coverage and not much in the peak effectiveness. For Case 4, the coolant enters a medium (0.75 D) and a wider (3 D) trench. The deeper trench improves the lateral mixing for the wider trench compared to Case 2 with a shallow depth. The jets appear to mix laterally inside the trench and exit more two dimensionally in this case. The local peak effectiveness is higher for this case than Case 3 with the narrow trench. For Case 5, the coolant enters a deep (1 D) and a narrow (2 D) trench. The coolant exits the holes and mixes freely inside the 2D trench and forms a sheet before exiting the trench and interacting with the mainstream. The deeper slot increases the effectiveness inside the trench but seems to perform very poorly downstream of the trench. The coolant may pick up heat inside the trench due to some interaction with the mainstream inside the trench as the mainstream can enter the trench along the outer sides of the trench. The trapped coolant eventually exits but with very little effectiveness downstream. Also, the cooling effectiveness decreases with higher blowing ratio unlike Cases 1–4. For Case 6, the coolant enters a deep (1 D) and a wider trench (3 D). The trends are similar to that for Case 5. The coolant, however, mixes less inside the trench compared to Case 5 due to the increased trench area. The coolant exiting the holes also does not hit the

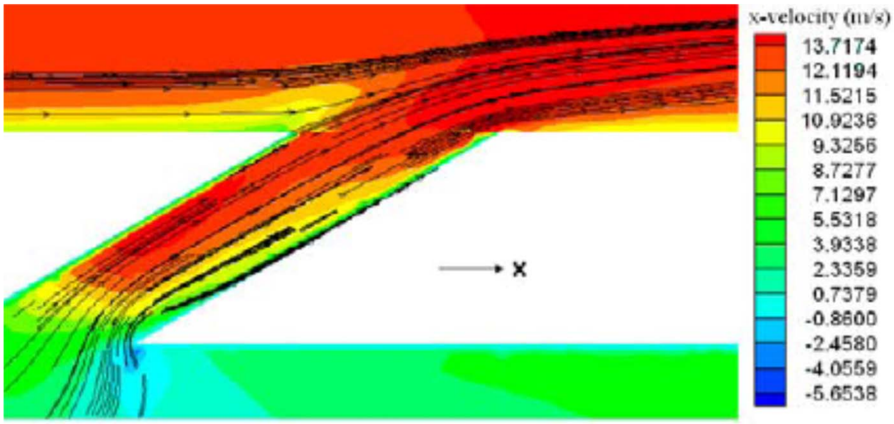

(a ) baseline

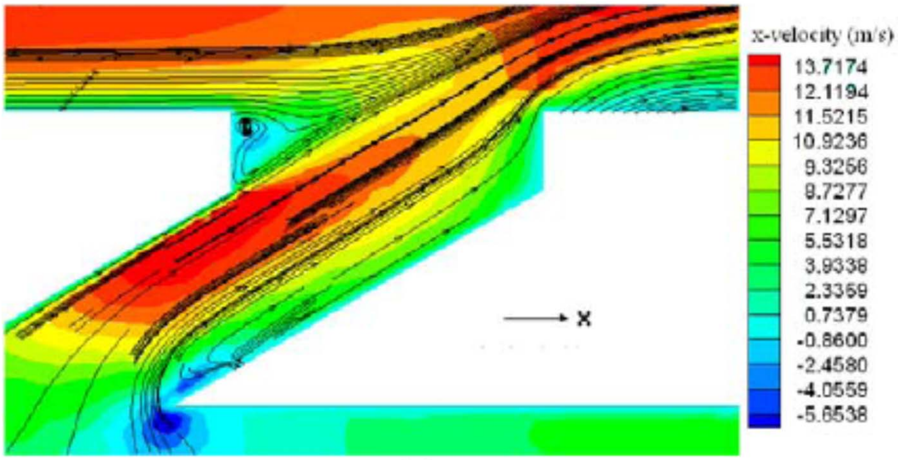

(a) Case 3

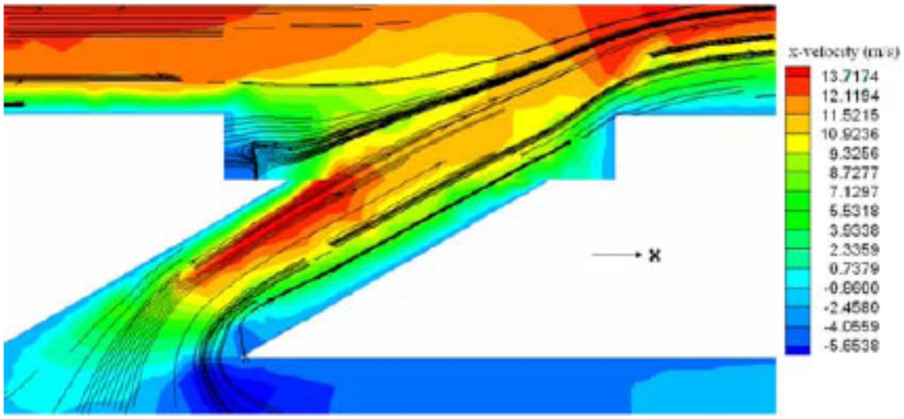

(b) Case 4

**Fig. 8 Mainstream-jet interactions for (*a*) base line, (*b*) Case 3, and (*c*) Case 4 at $M=1.0$**

trench sidewall as in Case 5. The blowing ratio effect increases the effectiveness inside the trench but decreases downstream with increasing blowing ratio.

For the shaped diffuser hole exit, the wide exit reduces the upward momentum of the jets and keeps the coolant closer to the surface. The lateral flaring enhances the lateral coverage of the coolant producing higher effectiveness overall. The shaped hole exit is typically created by employing a counterdrill that stamps the footprint at the exit by removing material from the cylindrical hole exit. Also interesting is the presence of classic diffuser separation at higher flow velocities through the shaped holes. The diffuser angle is significantly large for the shaped hole causing flow separation along one of the diffuser walls.

Figure 7 presents the computed centerline nondimensional temperature ($\theta$) profiles for the base line and Cases 3 and 4 at $M=1.0$. The coolant temperature profile away from the wall clearly shows an attached jet for both trench widths. The coolant from the

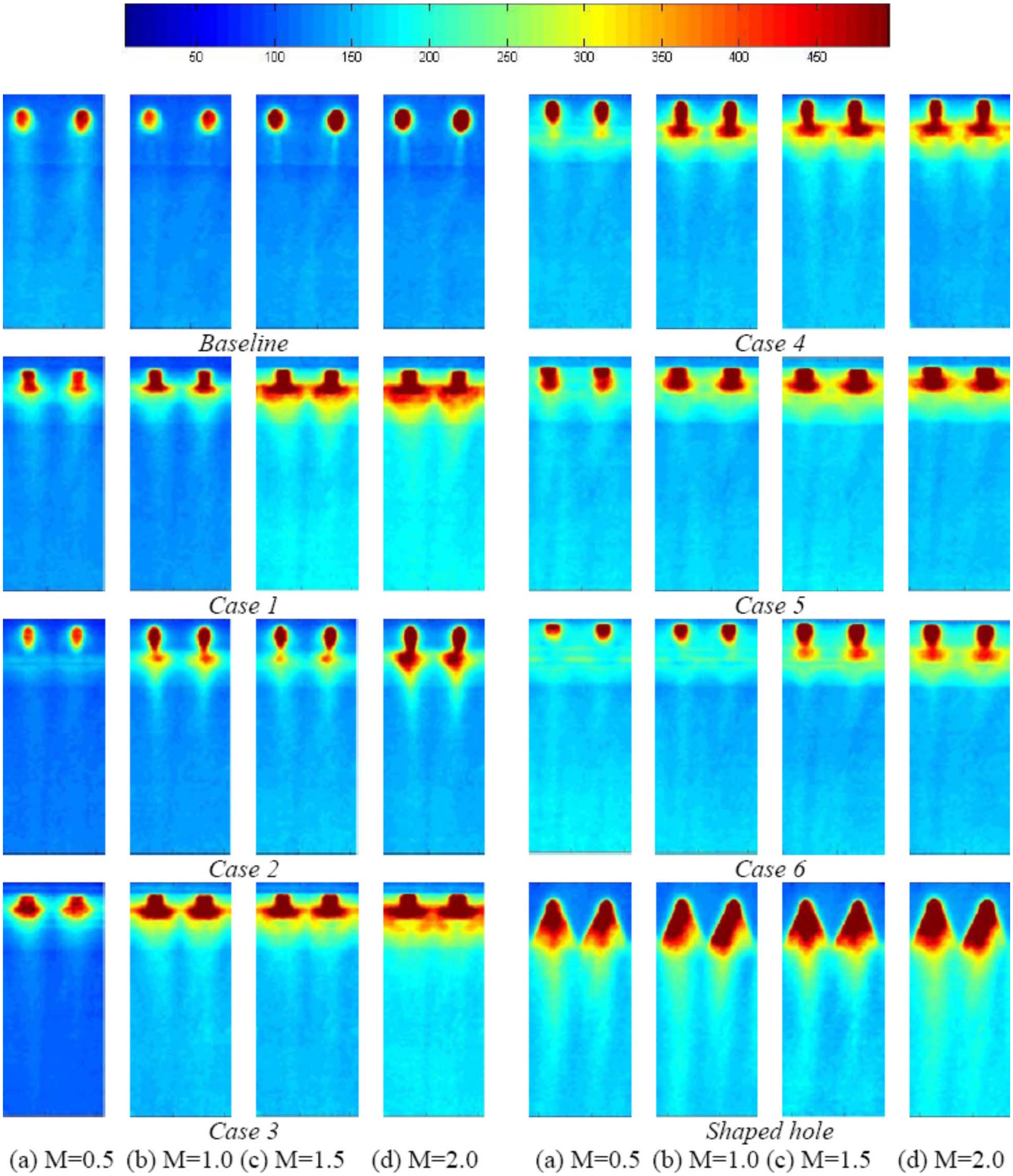

**Fig. 9 Detailed heat transfer coefficient ratio distributions for all cases at different blowing ratios**

cylindrical holes enter a 2D slot before they exit and make contact with the mainstream. Due to the presence of this 2D slot, the coolant tends to fill the slot and provides a more two-dimensional film that spreads laterally compared to the base line case. As the depth of the slot is increased, the coolant appears to provide a more two-dimensional jet with less and less lift-off. This hugging of the coolant with the surface results in higher cooling effectiveness of the trenched holes. The trenching of the holes due to TBC may not necessarily be a negative due to the significantly improved coolant trajectories. The resultant effect is a two-dimensional low momentum jet at the slot area exit. It is expected that, in some situations, the holes could be embedded in slots to improve film effectiveness and at the same time maintain the mechanical integrity as the slot is relatively shallow compared to the hole length. The trench appears to improve cooling farther downstream compared to baseline due to more coolant accumulation near the surface.

Figure 8 presents the path lines of coolant and mainstream imposed on velocity contours for base line and Cases 3 and 4 at $M=1.0$. Base line shows that the jet exits uniformly out of the hole and interacts with the mainstream. The jet displaces the

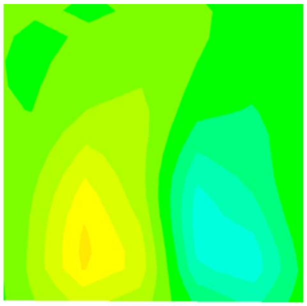

(a) Baseline

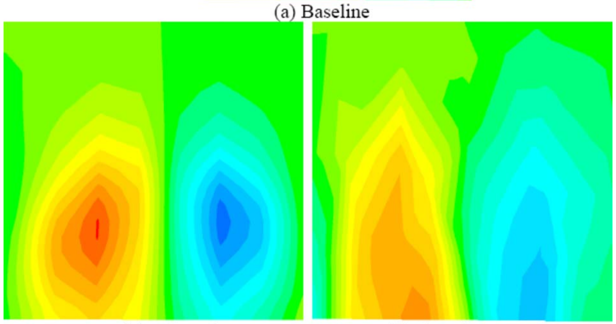

(b) Case 3 (c) Case 4

**Fig. 10 Vorticity contours downstream of injection $x/D=3$ for base line, Case 3, and Case 4**

mainstream and this displacement depends on the momentum of the jet with respect to the mainstream. For the narrow trench case (Case 3), the jet exits the cylindrical hole and slows down as it enters the trench due to the area increase and exits out of the trench at a much lower velocity than for the base line case. The exit velocity for Case 3 is about 30% lower than for the base line case indicating that the jet will have a lower momentum and thus will tend to stay closer to the surface or "hug" the surface better. Also, the downstream edge of the jet interacts with the trench edge and pushes coolant toward the upstream side resulting in a larger displacement of the mainstream from the surface. There is, however, a small recirculation zone on the upstream edge of the trench. For the wider trench (Case 4), the jet expands into the slot and slows down with only a 20% reduction in exit velocity. There is very minimal interaction with the upstream edge of the trench as the edge is now farther downstream than for Case 3. The recirculation zone on the upstream side is also significantly larger due to the larger space. Overall, the computed flow characteristics help in describing the detailed surface behavior obtained from the experiments.

Figure 9 presents the effect of blowing ratio on detailed heat transfer coefficient ($h$) distributions for the all eight cases. Nearly all the trenched holes appear to enhance the heat transfer coefficient compared to the base line case. It appears that there is significantly more interaction between the mainstream and jet primarily in the slot exit region resulting in higher turbulence production and subsequently higher heat transfer coefficient. This may be because of the creation of a new mixed boundary layer at the slot edge. The effect appears to extend in the downstream region of the slot for all Cases 1–6. However, Case 3 provides the higher enhancement than all the other cases. With larger coolant exit area, there is more regional mixing resulting in higher heat transfer coefficient for shaped hole case. The narrow trench for any depth creates a stronger trip to the boundary layer than the wider trench because the coolant is pushed back by the upstream edge back into the slot for the narrow trench. That does not occur for wider trench where the coolant blows directly into the trench and mixes with the mainstream.

Figures 10($a$)–10($c$) also show the cross-plane vorticity contours for base line, Case 3, and Case 4 for $M=1$ as the film moves downstream. One of the first studies by Leylek and Zerkle [15] indicated the presence of counter-rotating bean-shaped vortex pairs (CRVPs) exiting the jet holes and pushing downward resulting in the coolant moving away from the surface as the blowing ratio increased. They captured the vortex pair clearly as it moved downstream and dissipated into the mainstream. Since that study, efforts in film cooling studies has been to reduce the effect of this CRVP as it exits the holes by shaping the hole exit or reducing the upward jet momentum on exit. The presence of the CRVP for different width trenches are shown at $x/D=5$ downstream of the hole exit. The CRVP shown for Cases 3 and 4 are significantly stronger than for the base line case. With increase of trench width, it appears to have reduced the upstream momentum of the jets and has widened the CRVP and thus produced a squashed film that stays closer to the surface. The lift-off is thus reduced and there is no hot mainstream entrained near the wall as for the base line case resulting in better overall coolant coverage. The lateral mixing is also significantly higher for the trench cases compared to the base line.

The hole area region shows significantly higher heat transfer coefficient and film effectiveness results that may be contaminated by lateral conduction and edge effects. To avoid this, spanwise and area average results are only presented for region above $X/D>2$ as the region around the hole is subject to higher uncertainty. Figure 11 presents the effect of hole geometry on spanwise averaged film effectiveness for each blowing ratio. The average results are plotted against normalized streamwise distance indicated from upstream edge of the film hole. Results are presented from the downstream edge of the cylindrical holes for the base line and trench cases and beyond the actual exit of the shaped hole. This is done to avoid the issues associated with the uncertainty of data collected during the experiment inside the film holes and trenches. At a low blowing ratio of $M=0.5$, shaped diffuser hole provides the highest effectiveness clearly but the downstream decay is also rapid. All the trench cases except Case 3 show higher film effectiveness than the base line. For $M=1.0$, shaped hole still provided higher effectiveness than all the cases. However, Case 4 shows higher performance than other trench cases. The base line is the lowest among all the cases. Case 4 has a medium depth (0.75 D) and a wider trench (3 D). For $M=1.5$, shaped hole is the highest among all cases. Cases 3 and 4 are higher than other trench cases indicating an optimum depth of 0.75 D. All other cases are lower than these two cases. For $M=2.0$, there is a larger spread among the cases. Shaped hole is not as significantly higher than the trench cases, with Cases 1,3, and 4 showing comparable film effectiveness. Cases 5 and 6 are the lowest trench cases indicating that a deeper trench may not be a solution. The thickness of the TBC layer should not be too thin (0.5 D) and or too thick (1.0 D) to obtain the best cooling effectiveness. Klinger and Hennecke [7] provided a correlation for adiabatic film effectiveness for normal slot injection with blowing ratios below 2. However, their equation is valid only for $x/s>20$, where $s$ is the slot width. In the present study, most of the measured region is inside $x/s<20$.

Figure 12 presents the effect of hole geometry on spanwise averaged heat transfer coefficient ratio $(h/h_0)$ for each blowing ratio. The local heat transfer coefficient with film cooling ($h$) is normalized by the measured heat transfer coefficient without holes on a flat surface ($h_0$). The heat transfer coefficients without holes are consistently higher ($\sim$10–15%) than the turbulent boundary layer heat transfer correlation due to the enhanced freestream turbulence for the present study. At $M=0.5$, the heat transfer coefficient ratios are similar for all trench cases and base line except for shaped hole, which shows a bump immediately downstream of injection. As blowing ratio increases to $M=1.0$, the differences between the cases are enhanced. At $M=1.5$, all the trench cases show higher heat transfer coefficient ratio than the base line. The shaped hole is at a similar level to the trench cases. At $M=2.0$, the

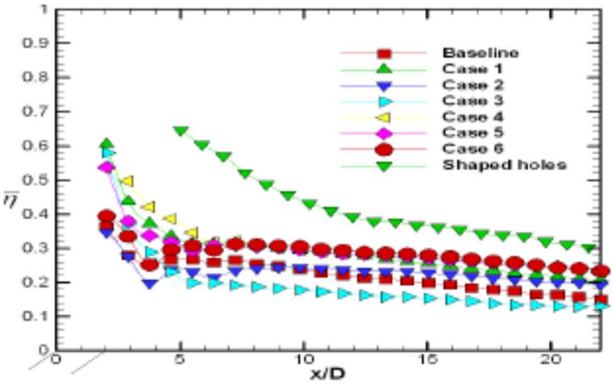

(a) M=0.5

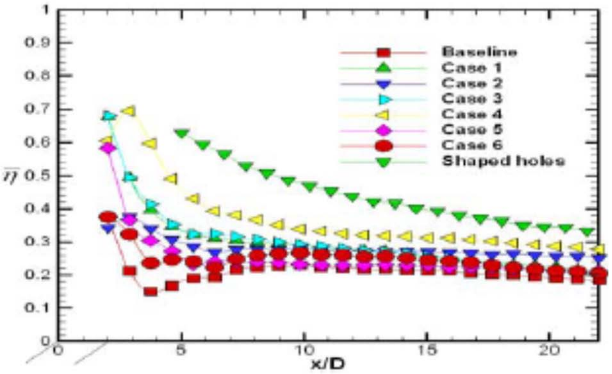

(b) M=1.0

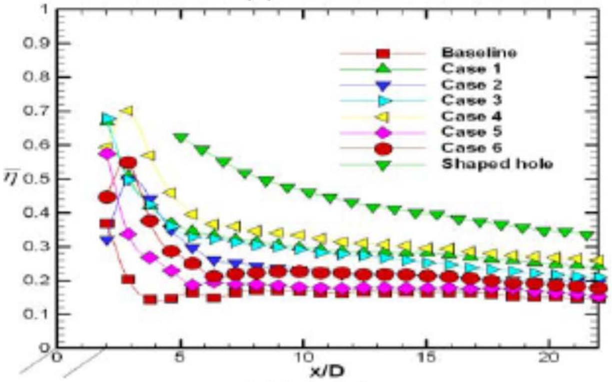

(c) M=1.5

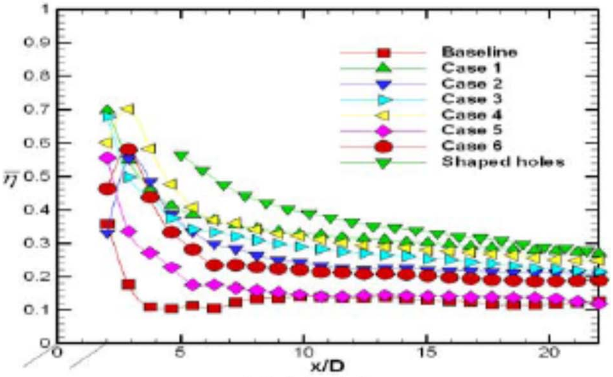

(d) M=2.0

**Fig. 11 Effect of hole configuration on spanwise averaged film effectiveness distributions at each blowing ratio**

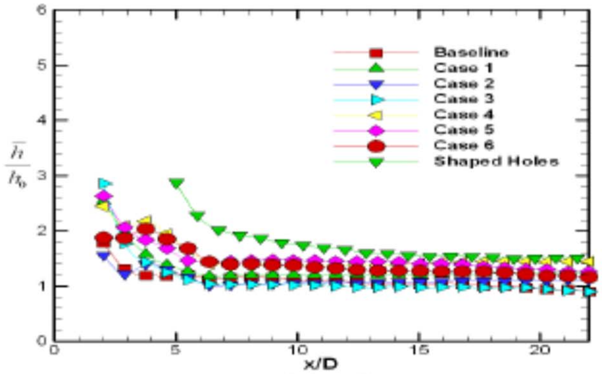

(a ) M=0.5

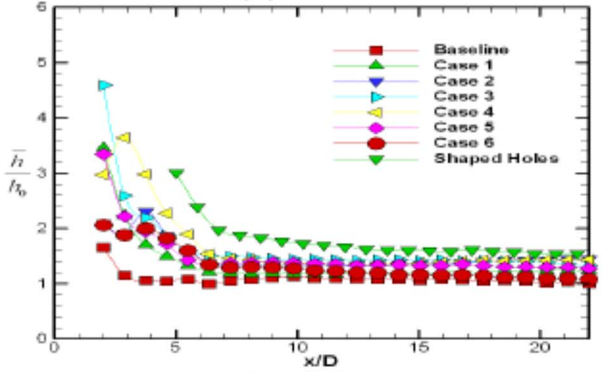

(b) M=1.0

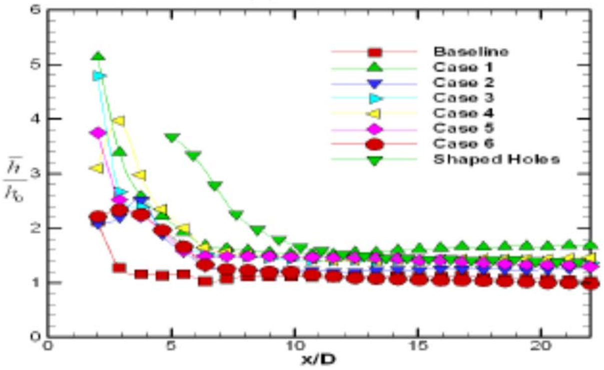

(c) M=1.5

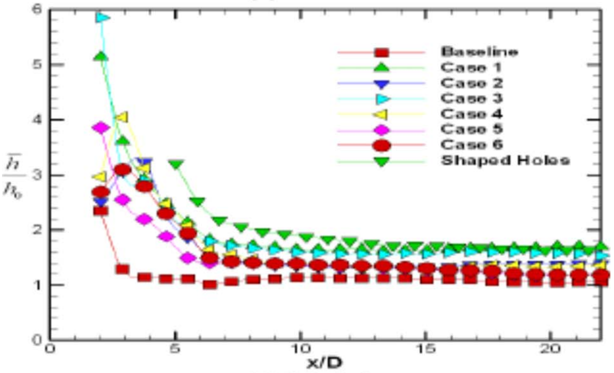

(d) M=2.0

**Fig. 12 Effect of hole configuration on spanwise averaged heat transfer coefficient ratio distributions at each blowing ratio**

trends are similar to that for $M=1.5$. It appears that the film exiting the trenches creates a new boundary and enhances heat transfer coefficients immediately downstream of the trench. Further downstream, the effect of trench width and depth is negligible unlike that for the film effectiveness results where medium depth trenches provided the best results.

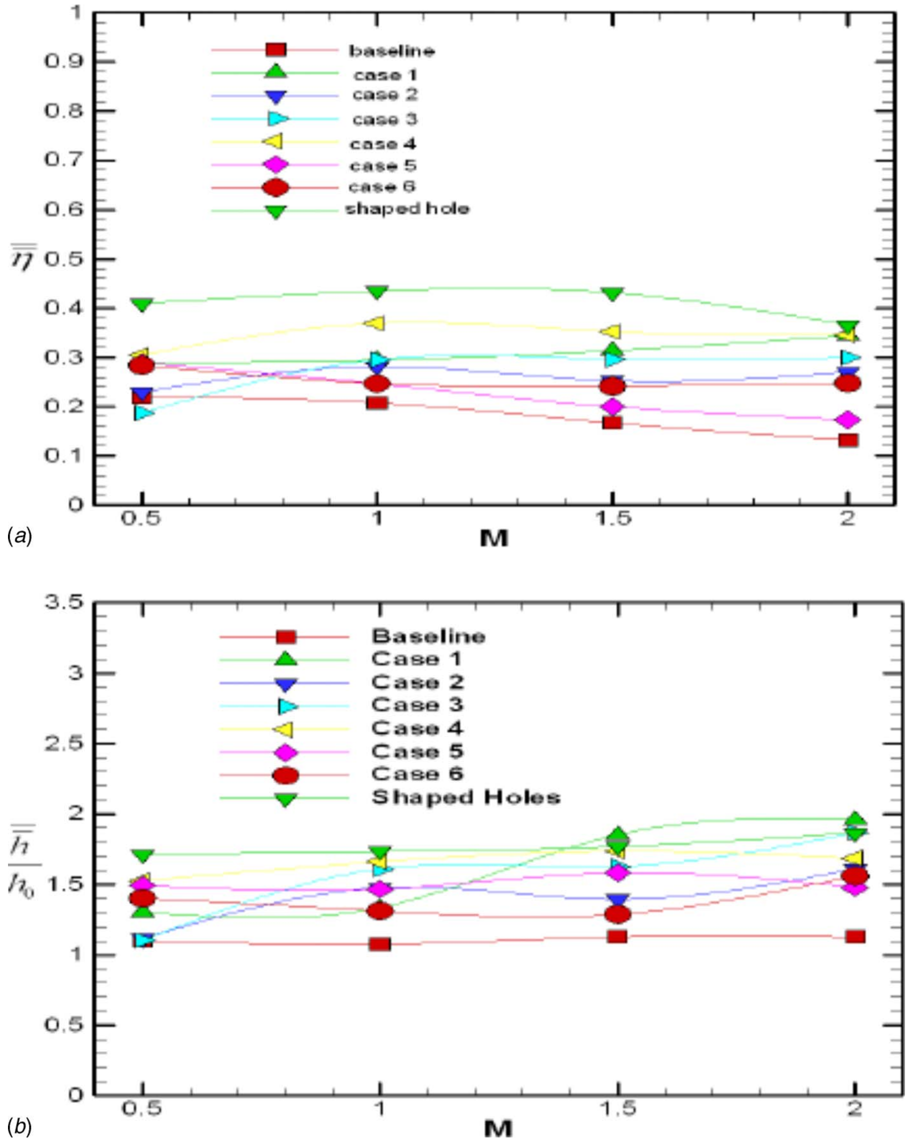

**Fig. 13 Effect of blowing ratio on overall area-averaged (*a*) film effectiveness, and (*b*) heat transfer coefficient ratios for all cases**

Figure 13 presents the effect of blowing ratio on the overall area-averaged film effectiveness and heat transfer coefficient ratios for all cases. As seen clearly from the plot, shaped diffuser hole shows much higher overall area-averaged effectiveness than the other cases. For Cases 3 and Case 4, it shows higher overall effectiveness within the trench cases. The shaped hole shows the highest heat transfer coefficient and the base line is the lowest. Importantly, the effect of blowing ratio on most of the trench cases is minimal. This was reported by Bunker [1] and Lu et al. [2]. The base line shows a decrease with increase in blowing ratio and the shaped hole peaks at $M=1.5$. the overall averaged heat transfer coefficient ratios show an increase with blowing ratio for all geometries. This is expected as the higher coolant flow interacts with the mainstream more and produces local turbulence and thus enhances heat transfer coefficient. Shaped hole and Case 1 show the highest heat transfer coefficient ratios. Base line shows the lowest enhancement ratios because of least interaction of jets with mainstream in the lateral direction.

Figure 14 presents the effect of blowing ratio on overall area-averaged heat flux ratio $(q''/q''_0)$ for all cases. This ratio indicates the reduction in heat flux obtained by introduction of film cooling over the surface. If the value is below 1.0, the effect is positive. If the value is greater than 1.0, then the presence of film cooling is detrimental. The heat flux ratio is calculated based on the formulation presented by Ekkad et al. [16].

The heat transfer ratio with and without film injection $(h/h_0)$ and the local film effectiveness are used to calculate the local heat flux ratio. The local heat transfer coefficient without film injection $(h_0)$ was experimentally determined by using a test plate without holes.

$$\frac{q''}{q''_0} = \frac{h}{h_0}\left(1 - \frac{\eta}{\phi}\right)$$

The term $\phi$ is the overall cooling effectiveness and ranges between 0.5 and 0.7 for typical blade cooling systems. In this study, a typical value of 0.6 is chosen. Changing the $\phi$ value will not change the trends but will only move the curves up or down. It is clear from the plot that most cases at $M=1.0$ provide low heat flux ratios except for Case 5. It appears that Cases 4 provides better protection at all blowing ratios and as does shaped diffuser hole except at higher blowing ratio of 2.0. Case 5 seems to show the worst performance.

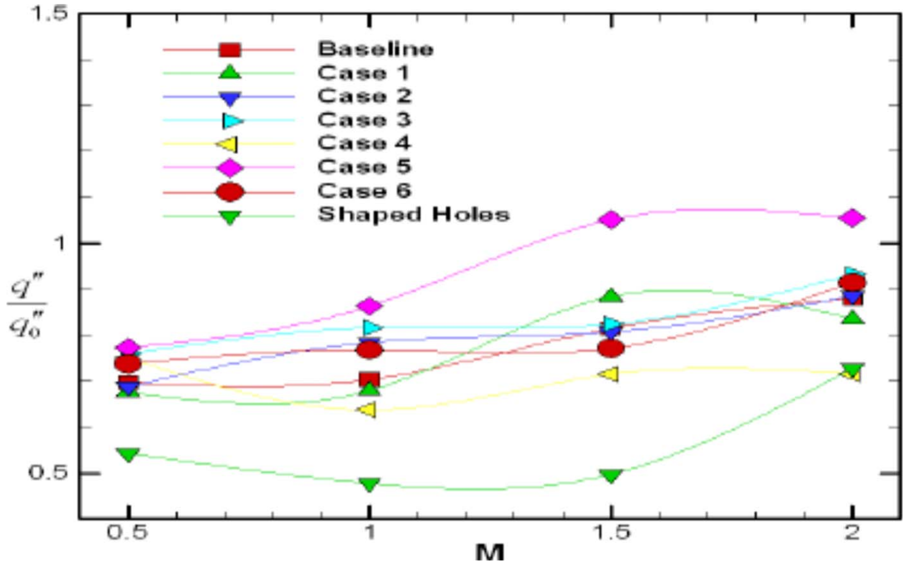

Fig. 14 Effect of blowing ratio on overall heat flux ratio for different cases

## Conclusions

A detailed study on the effects of trench width and depth in a 2D trench slot has been presented. Different slot dimensions were studied with varied trench widths, depths, and hole exit geometry. Both heat transfer coefficients and film effectiveness were measured using a transient infrared thermography technique. CFD results are also presented to understand the surface measurements. It appears that trenching the holes in a slot reduces the jet momentum at exit and also spreads the jets and provides two-dimensional slot jet coverage compared to the three-dimensional nature of individual jets. The wider spread of jets provides a better overall film effectiveness with increases in heat transfer coefficients. The trench wherein the jets come in and spread evenly into the slot before exiting especially Cases 3 and 4 performs better than other four trench cases and the base line case. An optimum trench depth exists at 0.75 D as shallow and deep trenches show worse performance. This is confirmed by the flow distributions obtained from CFD predictions. Shaped diffuser hole reduces the jet momentum at hole exit and outperforms the trench cases. The presence of a TBC on a shaped hole configuration is bound to change the dynamics of interaction between coolant and mainstream. In this study, the shaped holes are not trenched. Shaped holes are more expensive to manufacture and trenching of holes due to TBC can improve coolant performance without additional cost.

## Acknowledgment

This work was funded through a broader study on film cooling by General Electric Global Research Center, Niskayuna, NY. The sponsor is Dr. Ron Bunker.

## Nomenclature

$c_p$ = specific heat (kJ/kg K)
$d$ = hole diameter (m)
$h_0$ = local heat transfer coefficient without film injection ($\mathrm{W/m^2\,K}$)
$h$ = local heat transfer coefficient with film injection ($\mathrm{W/m^2\,K}$)
$k$ = thermal conductivity of test surface (W/m K)
L = length of film hole (m)
$M$ = blowing ratio$=\rho_c V_c/\rho_\infty V_\infty$
$q''$ = surface heat flux ($\mathrm{W/m^2}$)
Re = free-stream Reynolds number ($V_\infty d/\nu$)
$\rho_c$ = coolant density ($\mathrm{kg/m^3}$)
$\rho_\infty$ = mainstream density ($\mathrm{kg/m^3}$)
$t$ = time (s)
$T_c$ = coolant temperature (K)
$T_f$ = film temperature (K)
$T_i$ = test surface initial temperature (K)
$T_r$ = reference temperature (K)
$T_\infty$ = mainstream temperature (K)
Tu = free-stream mean turbulence intensity (%)
$T_w$ = local wall temperature (K)
$U_c$ = coolant velocity (m/s)
$U_\infty$ = mainstream velocity (m/s)
$x$ = streamwise distance along the test plate (m)
$y$ = coordinate normal to surface (m)
$\alpha$ = thermal diffusivity ($\mathrm{m^2/s}$)
$\eta$ = film cooling effectiveness$=(T_{\mathrm{aw}}-T_c)/(T_\infty-T_c)$
$\phi$ = nondimensional temperature$=(T_c-T_\infty)/(T_w-T_\infty)$
$\nu$ = kinematic viscosity of mainstream ($\mathrm{m^2/s}$)
$\theta$ = nondimensional film temperature$=(T_f-T_c)/(T_\infty-T_c)$

## References

[1] Bunker, R. S., 2002, "Film Cooling Effectiveness due to Discrete Holes Within a Transverse Surface Slot," ASME Paper No. GT-2002-30178.
[2] Lu, Y., Nasir, H., and Ekkad, S. V., 2005, "Film Cooling From a Row of Holes Embedded in Transverse Slots," ASME Paper No. IGTI2005-68598.
[3] Waye, S. K., and Bogard, D. G., 2006, "High Resolution Film Cooling Effectiveness Measurements of Axial Holes Embedded in a Transverse Trench With Various Trench Configurations," ASME Paper No. GT2006-90226.
[4] Blair, M. F., 1974, "An Experimental Study of Heat Transfer and Film Cooling on Large-Scale Turbine Endwalls," ASME J. Heat Transfer, **96**, pp. 524–529.
[5] Chyu, M. K., Hsing, Y. C., and Bunker, R. S., 1998, "Measurements of Heat Transfer Characteristics of Gap Leakage Around a Misaligned Component Interface," ASME Paper No. 98-GT-132.
[6] Wang, T., Chintalapati, S., Bunker, R. S., and Lee, C. P., 2000, "Jet Mixing in a Slot," Exp. Therm. Fluid Sci., **22**, pp. 1–17.
[7] Klinger, H., and Hennecke, D. K., 1993, "The Effect of Mainstream Flow Angle on Flame Tube Film Cooling," *AGARD Conference Proceedings CP-527, Heat Transfer and Cooling in Gas Turbines*.
[8] Schulz, A., 2001, "Combustor Liner Cooling Technology in Scope of Reduced Pollutant Formation and Rising Thermal Efficiencies," Ann. N.Y. Acad. Sci., **934**, pp. 135–146.
[9] Vedula, R. J., and Metzger, D. E., 1991, "A Method for the Simultaneous Determination of Local Effectiveness and Heat Transfer Distributions in a Three Temperature Convective Situations," ASME Paper No. 91-GT-345.
[10] Ekkad, S. V., Ou, S., and Rivir, R. B., 2004, "A Transient Infrared Thermography Method for Simultaneous Film Cooling Effectiveness and Heat Transfer Coefficient Measurements From a Single Test," ASME J. Turbomach., **126**,

pp. 546–553.

[11] Gillespie, D. R. H., Wang, Z., Ireland, P. T., and Kohler, S. T., 1996, "Full Surface Local Heat Transfer Coefficient Measurements in a Model of an Integrally Cast Impingement Cooling Geometry," *Proceedings of the International Gas Turbine and Aeroengine Congress & Exhibition*, Birmingham, UK, Jun.

[12] Incropera, F. P., and Dewitt, D., 2006, *Fundamentals of Heat Transfer*, Wiley, New York.

[13] Kline, S. J., and McClintock, F. A., 1953, "Describing Uncertainties in Single Sample Experiments," Mech. Eng. (Am. Soc. Mech. Eng.), **75**, pp. 3–8.

[14] Lu, Y., and Ekkad, S. V., 2006, "Predictions of Film Cooling from Cylindrical Holes Embedded in Trenches," AIAA-ASME Joint Thermophysics Conference, San Francisco, Jun. Paper No. AIAA-2006-3401.

[15] Leylek, J. H., and Zerkle, R. D., 1994, "Discrete Jet Film Cooling: A Comparison of Computational Results With Experiments," ASME J. Turbomach., **116**, pp. 358–368.

[16] Ekkad, S. V., Zapata, D., and Han, J. C., 1997, "Film Effectiveness Over a Flat Surface with Air and $CO_2$ Injection Through Compound Angle Holes Using a Transient Liquid Crystal Image Method," ASME J. Turbomach., **119**(3), pp.587–593.

# Effect of the Leakage Flows and the Upstream Platform Geometry on the Endwall Flows of a Turbine Cascade

**E. de la Rosa Blanco**

**H. P. Hodson**

Whittle Laboratory,
University of Cambridge,
Madingley Road,
Cambridge CB3 0DY, UK

**R. Vazquez**
ITP,
Industria de Turbo Propulsores S.A.,
Avda. Castilla 2.
Parque Empresarial San Fernando-Edificio
Japon,
San Fernando de Henares,
Madrid, 28830, Spain

*This work describes the effect that the injection of leakage flow from a cavity into the mainstream has on the endwall flows and their interaction with a large pressure surface separation bubble in a low-pressure turbine. The effect of a step in hub diameter ahead of the blade row is also simulated. The blade profile under consideration is a typical design of modern low-pressure turbines. The tests are conducted in a low speed linear cascade. These are complemented by numerical simulations. Two different step geometries are investigated, i.e., a backward-facing step and a forward-facing step. The leakage tangential velocity and the leakage mass flow rate are also modified. It was found that the injection of leakage mass flow gives rise to a strengthening of the endwall flows independently of the leakage mass flow rate and the leakage tangential velocity. The experimental results have shown that below a critical value of the leakage tangential velocity, the net mixed-out endwall losses are not significantly altered by a change in the leakage tangential velocity. For these cases, the effect of the leakage mass flow is confined to the wall, as the inlet endwall boundary layer is pushed further away from the wall by the leakage flow. However, for values of the leakage tangential velocity around 100% of the wheel speed, there is a large increase in losses due to a stronger interaction between the endwall flows and the leakage mass flow. This gives rise to a change in the endwall flows' structure. In all cases, the presence of a forward-facing step produces a strengthening of the endwall flows and an increase of the net mixed-out endwall losses when compared with a backward-facing step. This is because of a strong interaction with the pressure surface separation bubble.* [DOI: 10.1115/1.2950052]

## Introduction

Nowadays, the design of modern low-pressure turbines is a compromise between efficiency, cost, weight, and noise. A solid-thin profile gives rise to a reduction of cost when compared with a hollow-thick profile. However, a solid-thin profile can produce an increase in the losses. de la Rosa Blanco et al. [1] showed that a solid-thin profile could reduce the weight and the cost in low-pressure turbines while maintaining the efficiency, so long as the interaction between the endwall flows and the pressure surface separation bubble is suppressed. This occurs when the inlet endwall boundary layer is laminar. Thus, it was concluded that the state of the inlet endwall boundary layer plays a major role in the above interaction.

General reviews of endwall flows are given by Sieverding [2], Gregory-Smith [3], and Langston [4]. In a real low-pressure turbine, close to the endwall and between the platforms of two adjacent blade rows (one moving and one stationary), there are bound to be steps and gaps. de la Rosa Blanco et al. [5] showed that the presence of the step ahead of the blade row can significantly alter the structure and the strength of the endwall flows. Figure 1 shows the results of the oil flow visualization experiments on the endwall for two different steps. The flow structure changes greatly between the two cases. The separation line ($S_{e1}$) corresponding to the separation of the passage vortex from the endwall moves further from the blade pressure surface for the case of the backward-facing step. As a consequence, a strong interaction between the endwall flows and the pressure surface separation bubble does not happen. It was found that under certain inlet flow conditions, a backward-facing step gives rise to lower losses when compared with a flat endwall.

The fact that stationary and rotating parts are encountered in the turbine implies the existence of gaps. Hot gas path flow can enter the disk cavities causing thermal fatigue. To prevent the ingestion of hot gas, relatively cold air from the compressors is directed to the turbine disks. The effect of this air is to cool the disk cavities and to avoid the ingestion of hot gas due to the pressure difference between the cooling air and the mainstream. This cooling air leaks into the mainstream at the hub of the blade rows. For modern low-pressure turbines, the amount of mass flow that leaks into the mainstream is of the order of 0.5% of the inlet mass flow. The leakage flows are usually considered to be injected with a tangential velocity equal to 50% of the hub speed.

The effect of the leakage flows on the endwall flows has been studied in compressors and turbines. Wellborn and Okiishi [6], Wellborn et al. [7], Demargne and Longley [8], and Wellborn [9] have all investigated leakage flows in compressors. They found that the leakage tangential velocity was a key parameter in the interaction of the leakage flows and the endwall flows. Hunter and Manwaring [10], McLean et al. [11], Gier et al. [12], Schlienger et al. [13], and Bohn et al. [14] focused their work on turbines. They found that the injection of leakage mass flow in turbines gives rise to a strengthening of the endwall flows.

Hunter and Manwaring [10] performed simulations for a turbine with and without the cavities and they compared the results with the experimental findings. They showed the importance of including the leakage flows and the real endwall geometry in the computational calculations to obtain accurate results. The same conclusions were drawn by Shabbir et al. [15] in experimental and

---

Contributed by the International Gas Turbine Institute of ASME for publication in the JOURNAL OF TURBOMACHINERY. Manuscript received February 11, 2007; final manuscript received December 3, 2007; published online October 2, 2008. Review conducted by David Wisler. Paper presented at the ASME Turbo Expo 2006: Land, Sea and Air (GT2006), Barcelona, Spain, May 8–11, 2006.

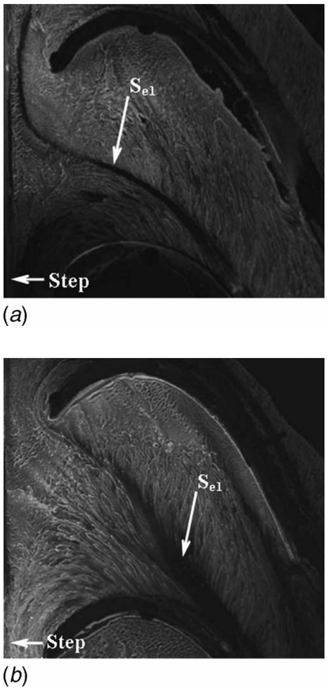

**Fig. 1 Oil flow visualization experiments on the endwall. Turbulent inlet boundary layer. (*a*) Backward-facing step. (*b*) Forward-facing step.**

computational simulations made in a high-speed compressor rotor and by Cherry et al. [16] in a low-pressure turbine of a high bypass turbofan engine. It is important to understand the influence of the main flowpath endwall details on the engine performance to take it into account during the design process.

The aim of this paper is to investigate the effect of an upstream step and the injection of leakage mass flow on the endwall flows and their interaction with the pressure surface separation bubble in the case of a solid-thin profile. The effect of a change of the leakage mass flow and the leakage tangential velocity is also analyzed.

## Experimental Methods

Experiments were undertaken in a linear cascade of solid-thin profiles that is characterized by a large pressure surface separation bubble. Figure 2 shows the solid-thin profile and the measured static pressure distribution at midspan. The result is compared with a hollow-thick profile. On the solid-thin profile, a separation bubble on the pressure surface (PS bubble) is observed to extend from close to the leading edge to a position approximately 50% $C_{ax}$. This is the same cascade and tunnel that was used by de la Rosa Blanco et al. [1] and de la Rosa Blanco et al. [5]. Details of the cascade geometry and the flow conditions are given in Table 1.

**Table 1 Profile details and flow conditions**

| | |
|---|---|
| Profile details | |
| $\alpha_1$ | 32 deg |
| $\alpha_2$ | 63 deg |
| $C_{ax}$ | 127 mm |
| Pitch/$C_{ax}$ | 0.96 |
| $h/C_{ax}$ | 2.95 |
| Flow conditions | |
| $Re_2$ | 232,000 |
| Incidence | 0 deg |
| Inlet Tu | 0.5% |
| Exit Mach No. | 0.07 |

Figure 3 shows a schematic representation of the cascade and cavity layout. The slot is 14% $C_{ax}$ wide. The upstream edge of the slot was placed at 18.6% $C_{ax}$ upstream of the blade leading edge. The cavity is made of Plexiglas and positioned under the endwall, forward of the blade leading edge. The leakage tangential velocity and the leakage mass flow rate were varied independently. The cavity and the control mechanisms that have been employed are the same as those used by Demargne [17]. The periodicity of the flow within the cavity was assessed by means of static pressure measurements. The static pressure inside the cavity is measured at six different points along the cavity. During the experiments, the difference in static pressure between these tappings was less than 3% of the dynamic head of the cavity flow in each experiment. A step can be placed upstream of the blade leading edge. Two different types of steps were tested, i.e., a forward-facing step and a backward-facing step. The step was 1.2% of the span high. A schematic representation is shown in Fig. 4.

The inlet endwall boundary layer was measured at 50% $C_{ax}$ upstream of the blade leading edge by means of a flattened Pitot tube. It was a turbulent boundary layer that was 3% of the span in thickness.

The choices of the values of the leakage tangential velocity and the leakage mass flow rate that have been tested are based on industrial experience. Three different leakage tangential velocities

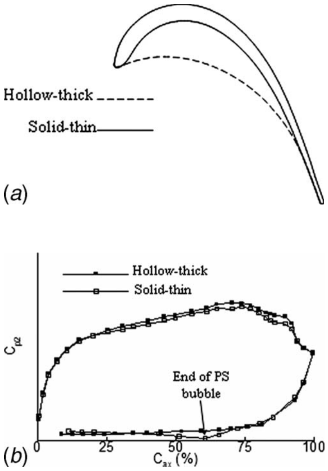

**Fig. 2 Profile sections and static pressure distributions**

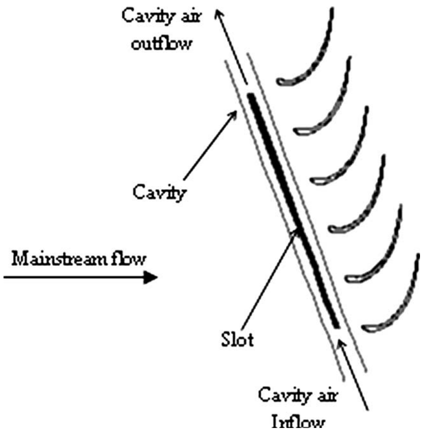

**Fig. 3 Schematic representation of the cascade and cavity layout**

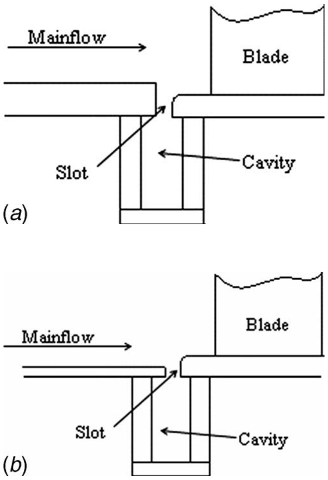

**Fig. 4 Cross-sectional view of the cavity. (*a*) Backward-facing step. (*b*) Forward-facing step.**

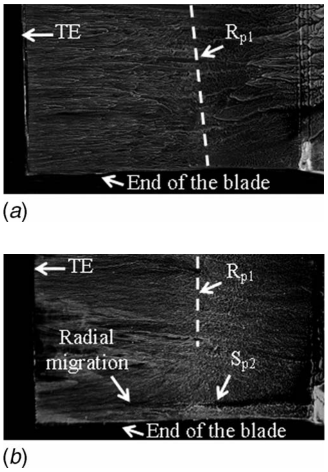

**Fig. 5 Oil flow visualization experiments on the blade pressure surface with cavity but with no net leakage flow. (*a*) Backward facing step. (*b*) Forward facing step.**

have been tested for the two step geometries. The one corresponding to $56\% U$ is similar to the value that is found in modern low-pressure turbines. Then, tests were performed with a leakage tangential velocity lower than the design value $(11\% U)$ and another one higher than the design value (around $100\% U$). The two values of the leakage mass flow rate $(0.7\% \ \dot{m}_1$ and $0.3\% \ \dot{m}_1)$ correspond to those used in modern low-pressure turbines.

The area traverses were performed with a five-hole probe (diameter 2 mm) at 50% $C_{\mathrm{ax}}$ downstream of the blade trailing edge. Measurements were performed over one-half of the span. The losses were calculated on a mass-averaged basis having performed a constant-area mixing calculation. The reference inlet total pressure that has been used to define the losses is shown as follows:

$$P_0 = \frac{\dot{m}_1 P_{01} + \dot{m}_{\mathrm{leak}} P_{0\mathrm{cav}}}{(\dot{m}_1 + \dot{m}_{\mathrm{leak}})} \tag{1}$$

where $P_{01}$ is the freestream inlet stagnation pressure, $P_{0\mathrm{cav}}$ is the stagnation pressure of the flow within the cavity, $\dot{m}_1$ is the inlet mass flow, and $\dot{m}_{\mathrm{leak}}$ is the leakage mass flow. The inlet loss is the mass-averaged loss at the inlet due to the presence of the endwall boundary layer. In the breakdown of the losses that is presented later, the profile loss is defined as the loss at midspan. The mixing loss is calculated from a position half of an axial chord length downstream of the blade trailing edge, assuming that the flow mixes at constant flow area with no external forces to uniform conditions downstream. The net mixed-out endwall loss is the difference between the measured loss and the sum of the profile loss and the inlet loss.

Flow visualization experiments similar to those in Fig. 1 were carried out using a mixture of diesel oil and fluorescent powder. The pictures were taken with a digital camera in dark conditions with the help of UV light to illuminate the patterns.

## Computational Method

The measurements have been complemented by computational fluid dynamics (CFD) calculations in order to help us the understand the flow physics. Fluent version 10 was used for the calculations. The Reynolds-averaged Navier–Stokes (RANS) method is employed with a $k$-$\varepsilon$ realizable turbulence model [18]. No wall functions were used because the resolution of the mesh was such that $y^+$ was always approximately unity. The number of cells was approximately $4.5 \times 10^6$.

The mesh was extended from 135% $C_{\mathrm{ax}}$ upstream of the blade leading edge to 100% $C_{\mathrm{ax}}$ downstream of the blade trailing edge in the axial direction. A plane of symmetry was applied so half of span was used for the simulations. No transition model was employed so the calculations are run as fully turbulent. It should be noted that the geometry in the calculations has a square lip to the cavity while the experimental measurements were made on a cascade where the lip geometry had a large radius. This can be seen in Fig. 4. The rounded lip avoids the presence of a separation bubble that happens just behind a square lip.

## Results and Discussion

**Effect of the Presence of the Cavity.** In this section, the effect of the presence of the cavity and a step on the endwall flows and their interaction with the pressure surface separation bubble is analyzed. For this case, there is no net leakage mass flow.

Figure 5 shows the flow visualization on the blade pressure surface for the two different steps when the cavity is present. For the case of the backward-facing step, there is a reattachment line $(R_{p1})$ that runs along the blade pressure surface. This corresponds to the attachment of the blade pressure surface separation bubble. However, for the case of the forward-facing step, there is a radial migration of flow in the region close to the endwall. This is a consequence of a strong interaction between the endwall flows and the pressure surface separation bubble. Similar behavior was observed by de la Rosa Blanco et al. [5] when the steps were placed ahead of the blade leading edge. To assess the effect of the cavity on the endwall flows' structure, the measurements at 50% $C_{\mathrm{ax}}$ downstream of the blade trailing edge are presented next for the two steps with the two different configurations, i.e., the case with no cavity and the case with cavity and no net leakage mass flow.

The pitchwise mass-averaged gross stagnation pressure loss coefficient is shown in Fig. 6(*a*). The values of the gross stagnation pressure loss are obtained from the area traverses. These losses include the contribution from the inlet endwall boundary layer. The presence of the cavity does not change the number of loss peaks. However, significant differences associated with their position and their intensity can be appreciated for the two step geometries. For the backward-facing step, the loss peak closer to the midspan gets stronger while the opposite trend happens for that closer to the wall. For the forward-facing step, the changes due to the presence of the cavity are more significant. In this case, both loss peaks get stronger. The losses close to the endwall decrease noticeably when the cavity is present for both step geometries, thus, suggesting a weaker suction side corner vortex. The cause of these flow features is discussed next in more detail.

The gross stagnation pressure loss contours, the streamwise

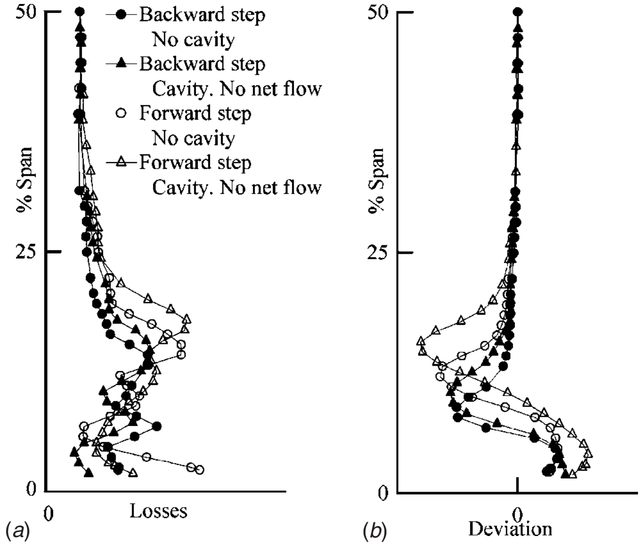

**Fig. 6 Measured pitchwise mass-averaged gross stagnation pressure loss and deviation at 50% $C_{ax}$ downstream of the blade trailing edge**

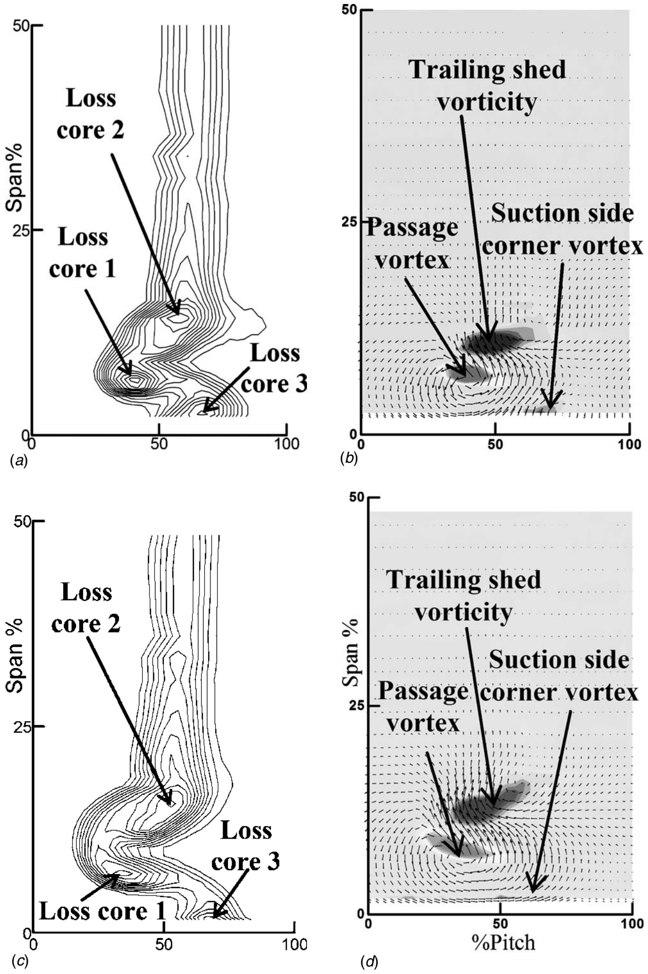

**Fig. 7 Measured loss contours, streamwise vorticity contours, and secondary velocity vectors at 50% $C_{ax}$ downstream of the blade trailing edge. Backward facing step. (*a*) and (*b*) No cavity. (*c*) and (*d*) Cavity. No net leakage flow.**

vorticity contours, and the secondary velocity vectors at 50% $C_{ax}$ downstream of the blade trailing edge are shown for all the cases in Figs. 7 and 8. The secondary velocity vectors represent the deviation from the flow at midspan at each pitchwise position. The streamwise vorticity is the projection of the total vorticity in the direction of the flow at midspan at each pitchwise position. To calculate the total vorticity from the five-hole probe data, the method proposed by Gregory-Smith et al. [19] based on the incompressible form of the Helmholtz equation was applied.

For each of the cases, in Figs. 7 and 8, there are two Loss Cores (Loss Core 1 and Loss Core 2) in the region away from the wall. These are associated with two regions of high streamwise vorticity. The area of high positive streamwise vorticity that is closer to the endwall corresponds to the passage vortex. This can be observed in the secondary velocity vectors, which rotate in the anticlockwise direction. It is associated with Loss Core 1. The region of high negative streamwise vorticity is located closer to the midspan. It corresponds to the trailing shed vorticity and Loss Core 2.

For the backward-facing step with the cavity, the loss core associated with the trailing shed vorticity is stronger when compared with the case with no cavity. Furthermore, the region of high positive streamwise vorticity is larger. However, the loss core at the endwall (Loss Core 3) and the loss core associated with the passage vortex (Loss Core 1) are weaker. This is due to an interaction between the flow inside the cavity and the inlet endwall boundary layer. Even when there is no net leakage flow, there is an exchange of flow between the mainstream and the flow within the cavity. This effect has been also highlighted in investigations by other researchers, i.e., Demargne [17]. In the region of high pressure in the mainstream, part of the fluid is swept into the cavity. This results in a reduction in the strength of the pressure side leg of the horseshoe vortex. However, in the region of low pressure, part of the flow from the cavity leaks into the mainstream, thus strengthening the suction leg of the horseshoe vortex. Additionally, the suction side corner vortex gets weaker as its associated region of high negative streamwise vorticity becomes smaller. This is because part of the fluid from the inlet endwall boundary layer that takes part in the vortex is swept into the cavity. This explains the reduction of the strength of the Loss Core 3 for the case with the cavity.

For the forward-facing step with the cavity, the two main loss cores and the passage vortex are closer to the midspan when compared with the case with no cavity. Furthermore, the peak values are higher and the passage vortex and the trailing shed vorticity are stronger as the regions of high streamwise vorticity appear to be more intense, which is indicative of the stronger endwall flows. The suction side corner vortex and its associated loss core (Loss Core 3) get weaker.

Figure 6(*b*) shows the spanwise distribution of the pitchwise mass-averaged deviation for the four cases. The deviation is defined as the difference of the yaw angle at each spanwise position and the yaw angle at midspan. For both step geometries, the case with the cavity shows the peak of the underturning moving closer to the midspan. For the backward-facing step, the peak value of the underturning does not show a significant difference. This is a consequence of the combination of a stronger trailing shed vorticity and a weaker passage vortex when compared with the case with no cavity. However, the region affected by the underturning spreads further in the spanwise direction for the case with the cavity. For the forward-facing step, the peak of the underturning increases with the cavity as a consequence of the stronger endwall flows. It is noticeable that in the two configurations that have been studied, the case of the forward-facing step shows stronger endwall flows than that of the backward-facing step. This is a consequence of the strong interaction between the endwall flows and the pressure surface separation bubble that happens for the forward-facing step. This was observed in the results of the flow visualization on the blade pressure surface that were performed for each of the cases.

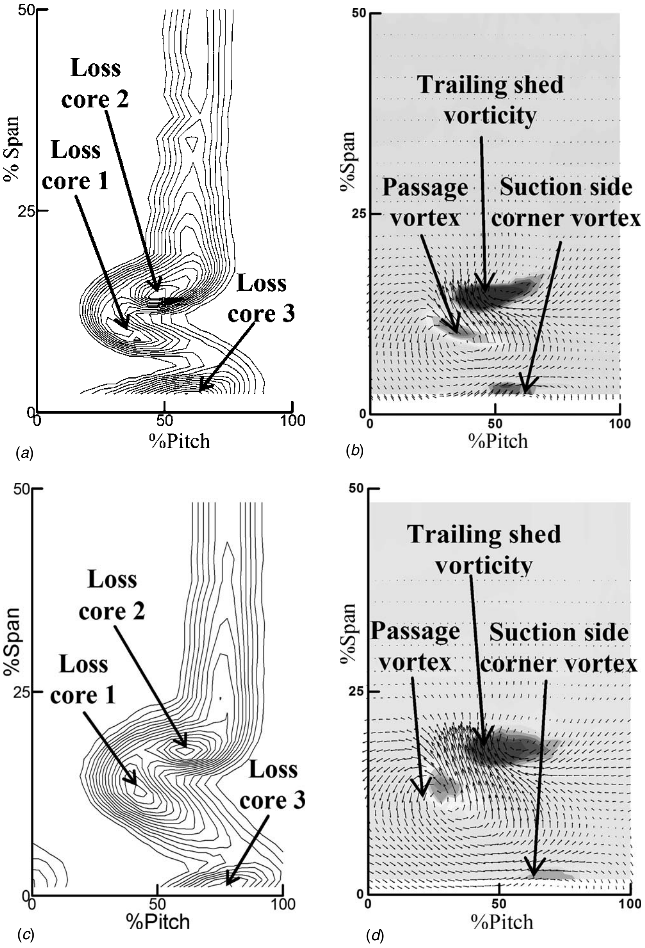

**Fig. 8 Measured loss contours, streamwise vorticity contours, and secondary velocity vectors at 50% $C_{ax}$ downstream of the blade trailing edge. Forward facing step. (*a*) and (*b*) No cavity. (*c*) and (*d*) Cavity. No net leakage flow.**

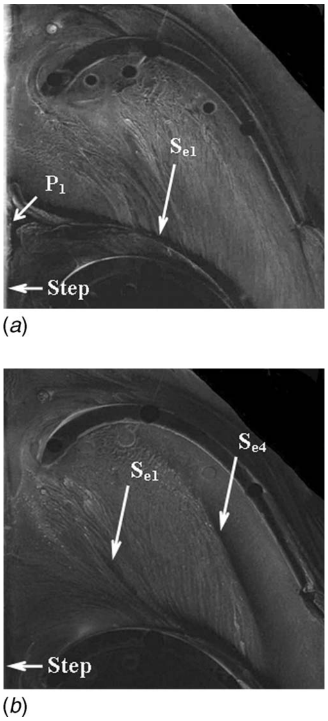

**Fig. 9 Oil flow visualization experiments on the endwall. $\dot{m}_{leak}=0.7\%\ \dot{m}_1 \cdot V_{leak}=56\%U$. (*a*) Backward-facing step. (*b*) Forward-facing step.**

**Effect of the Injection of Leakage Flow.** This section presents the effect of the injection of the leakage flow on the endwall flows and their interaction with a large pressure surface separation bubble. The effect of two different parameters is analyzed, i.e., the leakage mass flow and the leakage tangential velocity.

Figure 9 shows the results of the oil flow visualization experiments on the endwall for the two different steps with a leakage mass flow of 0.7% $\dot{m}_1$ and a leakage tangential velocity of 56% $U$. For the case of the backward-facing step, the injection of leakage flow pushes the separation line ($S_{e1}$) closer to the blade suction surface when compared with the case with no cavity (Fig. 1(*a*)). The flow separates at the separation point ($P_1$) that is located at the downstream edge of the cavity and close to the suction surface of the adjacent blade. For the forward-facing step, the separation line ($S_{e1}$) can also be distinguished within the blade passage although not as clearly as for the backward-facing step case (Fig. 9(*a*)). There is a separation line ($S_{e4}$), which is associated with the interaction with the pressure surface separation bubble.

Figure 10 shows the net mixed-out endwall loss for the two step geometries at different leakage conditions. The values of the net mixed-out endwall losses are nondimensionalized with respect to the case of a forward-facing step with a leakage mass flow rate of 0.7% $\dot{m}_1$ and a leakage tangential velocity of 92.5% $U$. There is a greater impact on the losses that are generated when the leakage flow is injected with respect to the case with no net leakage flow. This happens except for the cases with a forward-facing step with a leakage mass flow rate of 0.3% $\dot{m}_1$ and a leakage tangential velocity below 60% $U$. No explanation has been found for this.

At leakage tangential velocities below 56% $U$, a change in the leakage tangential velocity does not appear to significantly affect the losses. Nevertheless, the step geometry does have an influence. The forward-facing step gives rise to higher net mixed-out endwall losses than the backward-facing step at the same leakage conditions. This is due to the strong interaction that happens with the pressure surface separation bubble for the case of the forward-facing step, as observed on the results of the oil flow visualization experiments on the blade pressure surface that were performed for each of the cases. At the highest tested leakage tangential velocity, there is a large increase of the net mixed-out endwall losses for both step geometries. These results suggest that the leakage tan-

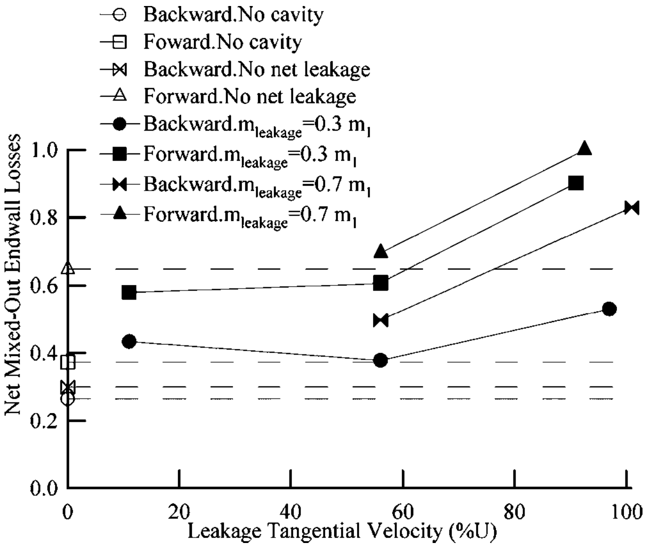

**Fig. 10 Measured net mixed-out endwall losses**

gential velocity plays a major role in creating the net mixed-out endwall losses for this linear cascade. Additionally, there appears to exist a value of the leakage tangential velocity beyond which a large increase of the losses occurs. Demargne and Longley [8] also found that the leakage tangential velocity was a key parameter in a linear compressor cascade. Furthermore, an increase of the leakage mass flow gives rise to an increase of the net mixed-out endwall losses. The cause of these flow features is explained next with the assistance of the computational results.

The flow around the slot involves the interaction and mixing of two streams with different velocities, both in magnitude and direction. A mixing shear layer forms between the leakage flow and the mainstream so an interaction between the two streams is possible.

In Fig. 11, the calculated path lines of the flow around the slot are presented for the cases under investigation. At the lower leakage tangential velocity and independently of the step geometry (Figs. 11(*b*) and 11(*d*)), the leakage flow is seen to push the inlet boundary layer away from the endwall. As a consequence, there is a thickening of the inlet endwall boundary layer ahead of the blade leading edge. This gives rise to an increase of the net mixed-out endwall losses at this leakage tangential velocity relative to the case with no cavity.

Simulations with different leakage tangential velocities have shown that when this parameter is increased above 44% for the backward-facing step or 37% for the forward-facing step, the flow structure around the cavity changes significantly (Figs. 11(*a*) and 11(*c*)). This effect occurs independently of the step geometry. Figures 11(*a*) and 11(*c*) show that there is a strong interaction between the inlet endwall boundary layer and the leakage flow. Figure 12 shows that the inlet flow separates at the upstream edge of the cavity and at three different points, $P_1$, $P_2$, and $P_3$, the inlet endwall boundary layer rolls up into three discrete vortical structures. These vortices have the same sense of rotation as the passage vortex. Within the blade passage, these vortices merge with the passage vortex under the influence of the blade pressure gradient. As a consequence, stronger endwall flows are found.

The formation of the discrete vortical structures at certain leakage tangential velocities could be caused by an increase of the velocity gradients at the interface between the cavity and the flow path. Kelvin–Helmholtz instabilities are amplified and breakdown into the roll-up vortices observed in Fig. 11. In the present investigation, it is believed that the vortex sheet that forms between the mainstream and the leakage flow at the slot tends to roll up. However, at the lower leakage tangential velocity, the length scale over which this process takes place is different to that at $101\%U$. It could happen further downstream, but the presence of the blade cascade and the endwall flows would inhibit the roll-up.

From the discussion above, it can be inferred that the penetration of the leakage flow into the mainstream is significantly influenced by the leakage tangential velocity. At the lower leakage tangential velocity, the flow leaking out through the cavity slot remains entirely near the endwall. However, at $101\%U$, the leakage flow interacts more strongly with the inlet boundary layer and the mainstream. As a consequence, vortical flow structures form. These structures have been also observed by other authors, such as Demargne and Longley [8], Wellborn [9] in compressors, and Anker and Mayer [20] and Gier et al. [12] in axial turbines.

The physical mechanism that has been described in this section can be generalized for other kinds of geometries. However, it is not possible to ensure that the sharp increase of losses will happen in all the cases at $56\%U$.

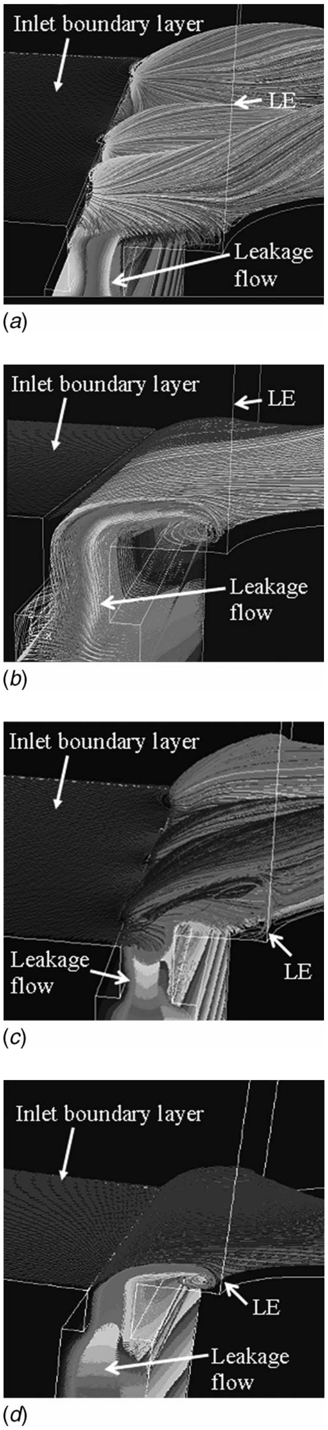

(*a*)

(*b*)

(*c*)

(*d*)

**Fig. 11 Calculated particle path lines around the slot. $\dot{m}_{\mathrm{leak}}=0.9\%\ \dot{m}_1$. (*a*) $V_{\mathrm{leak}}=101\%U$, backward step. (*b*) $V_{\mathrm{leak}}=44\%U$, backward step. (*c*) $V_{\mathrm{leak}}=101\%U$, forward step. (*d*) $V_{\mathrm{leak}}=37\%U$, forward step.**

*Flow Field at 50% $C_{\mathrm{ax}}$ Downstream of the Blade Trailing Edge*. To assess the effect of the leakage tangential velocity on the endwall flows' structure and the net mixed-out endwall losses, the measurements at 50% $C_{\mathrm{ax}}$ downstream of the blade trailing edge are presented next. The results are presented for two different values of the leakage tangential velocity and a leakage mass flow rate of 0.7% $\dot{m}_1$. Results for both step geometries are shown.

The spanwise distribution of the pitchwise mass-averaged gross stagnation pressure loss coefficient is illustrated in Fig. 13. The values of the leakage tangential velocity are shown in the figure. These losses include the contribution from the inlet endwall boundary layer. It should be noted that the difference in losses at the midspan is because the reference inlet total pressure in every case changes depending on the total pressure of the leakage flow (see Eq. (1)). For both step geometries, the injection of leakage

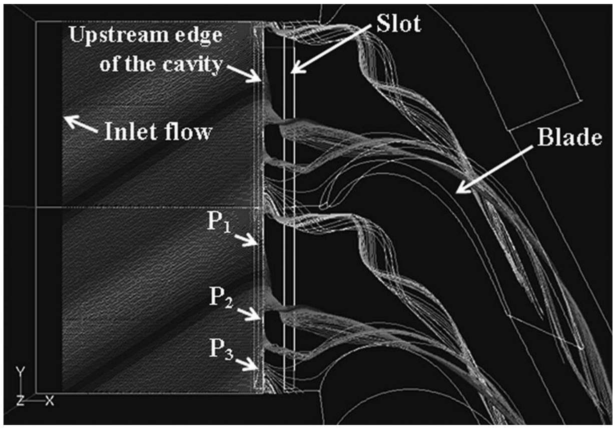

**Fig. 12 Calculated path lines of the inlet endwall boundary layer. Forward step, $V_{\text{leak}}$: 101% $U$. $\dot{m}_{\text{leak}}$=0.9% $\dot{m}_1$.**

mass flow gives rise to two loss peaks, except for the case of the forward-facing step at 92.5% $U$ where both loss peaks coalesce. For both step geometries, an increase in the leakage tangential velocity gives rise to a strengthening of the two loss peaks. They also move closer to the midspan. At the leakage tangential velocities shown, the loss peaks for the forward-facing step are higher than those for the backward-facing step. The cause of these flow features is explained next.

Figures 14 and 15 show the gross stagnation pressure loss contours, streamwise vorticity contours, and secondary velocity vectors at 50% $C_{\text{ax}}$ downstream of the blade trailing edge for the backward-facing and the forward-facing step, respectively.

When compared with the cases with no net leakage mass flow (Figs. 7(*c*) and 8(*c*)), the loss core associated with the passage vortex (Loss Core 1) and Loss Core 2 get larger. Additionally, the Loss Core 1 and the passage vortex move closer to the midspan. There is a strengthening of the passage vortex. This is because the passage vortex sweeps the leakage mass flow that is injected into the mainstream. This was observed in the computational results. The region of high negative streamwise vorticity associated with the trailing shed vorticity gets larger when the leakage mass flow is injected. The losses close to the endwall associated with the suction side corner vortex appears to be stronger for the cases with no cavity. This might be caused by the removing of the flow from the inlet endwall boundary layer that usually takes part in the suction side corner vortex. This occurs because this fluid together with the leakage flow is swept up by the passage vortex and convected into its associated loss core (Loss Core 1). An increase of the leakage tangential velocity for both of the step geometries causes Loss Core 1 and Loss Core 2 to spread further in the pitchwise direction.

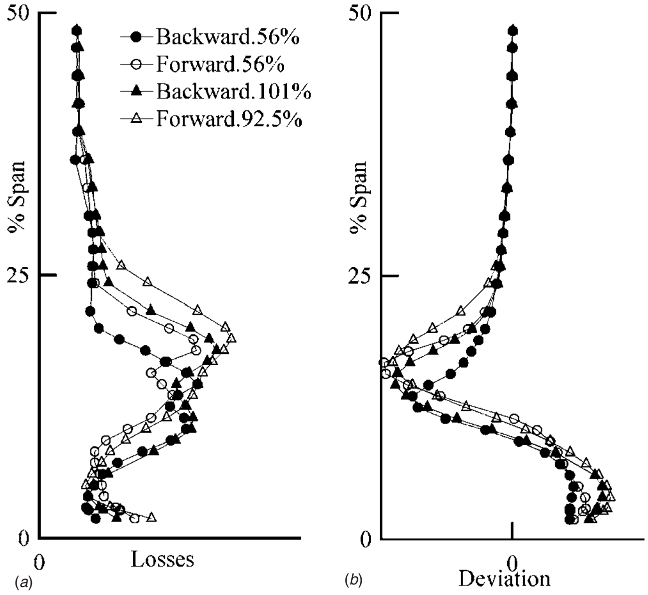

**Fig. 13 Measured pitchwise mass-averaged gross stagnation pressure loss and deviation at 50% $C_{\text{ax}}$ downstream of the blade trailing edge. $\dot{m}_{\text{leak}}$=0.7% $\dot{m}_1$.**

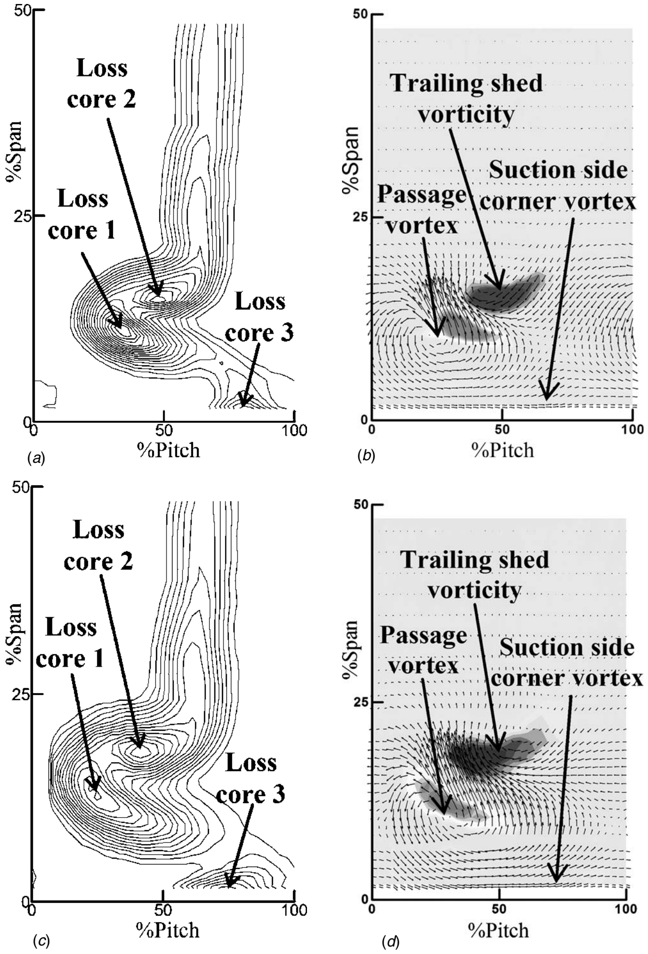

**Fig. 14 Measured loss contours, streamwise vorticity contours, and secondary velocity vectors at 50% $C_{\text{ax}}$ downstream of the blade trailing edge. Backward facing step. $\dot{m}_{\text{leak}}$=0.7% $\dot{m}_1$. (*a*) and (*b*) Leakage tangential velocity: 56% $U$. (*c*) and (*d*) Leakage tangential velocity: 101% $U$.**

At all of the leakage tangential velocities that were tested, the forward-facing step shows a larger Loss Core 1 and Loss Core 2 that additionally move closer to the midspan. The passage vortex is also placed closer to the midspan for both of the leakage tangential velocities tested. These features happen because of the strong interaction with the pressure surface separation bubble that occurs for the cases with a forward-facing step, as observed in the results of the oil flow visualization on the blade pressure surface.

The spanwise distribution of the pitchwise mass-averaged deviation is shown in Fig. 13. For both step geometries, the injection of leakage mass flow gives rise to an increase of the underturning as a consequence of stronger endwall flows. For the backward-facing step, an increase of the leakage tangential velocity from 56% $U$ to 101% $U$ gives rise to a higher peak of underturning that moves closer to the midspan. However, for the forward-facing step, even though the region affected by the underturning spreads

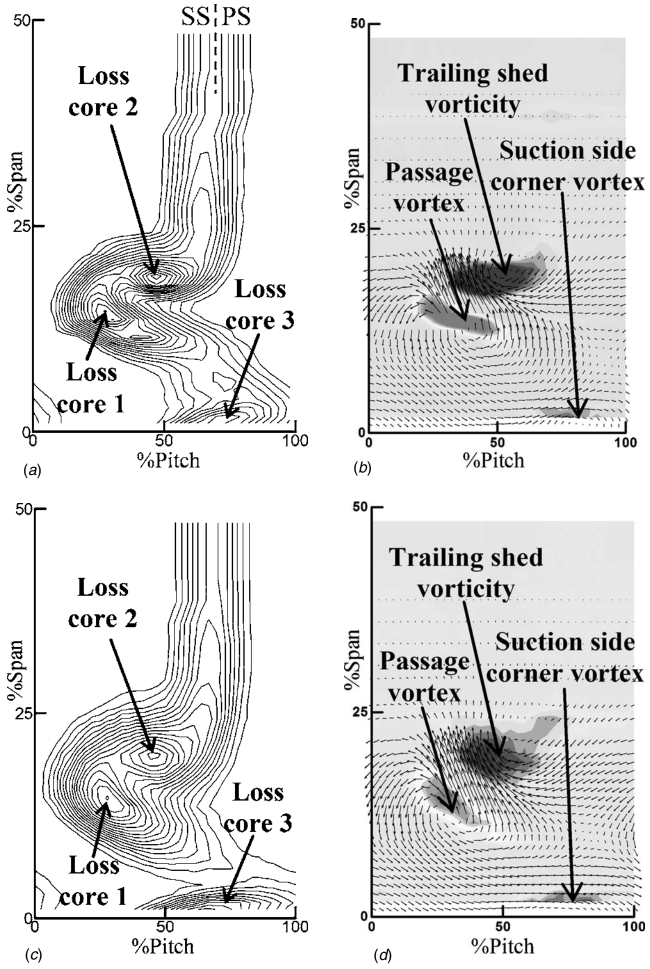

**Fig. 15 Measured loss contours, streamwise vorticity contours, and secondary velocity vectors at 50% $C_{ax}$ downstream of the blade trailing edge. Forward facing step, $\dot{m}_{leak}=0.7\%\ \dot{m}_1$. (*a*) and (*b*) Leakage tangential velocity: 56% *U*. (*c*) and (*d*) Leakage tangential velocity: 92.5% *U*.**

further in the spanwise direction, the peak of underturning at 92.5%*U* is slightly lower when compared to the case at 56%*U*. From these figures, it can be inferred that the injection of 0.7% $\dot{m}_1$ of leakage mass flow gives rise to a more nonuniform flow field at the exit. This would be detrimental to the performance of the following blade row in a low-pressure turbine. At all the leakage conditions that have been tested, the forward-facing step gives rise to higher values of underturning and overturning as well as higher losses when compared with the backward-facing step.

## Endwall Losses

This section discusses the effect on the net mixed-out endwall losses of the injection of leakage mass flow and the presence of a step ahead of the blade leading edge. Additionally, the effect of the leakage tangential velocity and the leakage mass flow rate is investigated. Table 2 shows the gross overall mixed-out losses and the net mixed-out endwall losses for each of the cases. Figure 10 shows the net mixed-out endwall losses for each of the cases. The losses are nondimensionalized with respect to the net mixed-out losses corresponding to a forward-facing step with a leakage mass flow of 0.7% $\dot{m}_1$ and a leakage tangential velocity of 92.5%*U*. An estimate of the uncertainty levels for the normalized loss values that are presented in this paper is 0.01.

When the cavity is present and no net leakage flow is injected, there is a noticeable impact on the net mixed out endwall losses when compared with the case with no cavity. The losses increase by 0.17 with a forward-facing step and by 0.02 with a backward-facing step. This increase in losses that happens for the two step geometries is because of the exchange of mass flow and momentum between the flow in the cavity and the mainstream that happens even when no net leakage flow is injected. The large difference between the two step geometries is due to the strong interaction with the pressure surface separation bubble that happens for the case of the forward-facing step.

**Table 2 Breakdown of the losses**

| Step | Leakage mass flow | Leakage tangential velocity | Gross overall mixed-out losses | Net mixed out endwall losses |
|---|---|---|---|---|
| Backward | No cavity | — | 0.84 | 0.26 |
| Forward | No cavity | — | 0.94 | 0.37 |
| Backward | 0% $m_1$ | ≈0%*U* | 0.90 | 0.30 |
| Forward | 0% $m_1$ | 56%*U* | 1.33 | 0.65 |
| Backward | 0.7% $m_1$ | 56%*U* | 1.07 | 0.50 |
| Forward | 0.7% $m_1$ | 56%*U* | 1.35 | 0.69 |
| Backward | 0.7% $m_1$ | 101%*U* | 1.47 | 0.83 |
| Forward | 0.7% $m_1$ | 92.5%*U* | 1.64 | 1.00 |
| Backward | 0.3% $m_1$ | 11%*U* | 1.03 | 0.43 |
| Forward | 0.3% $m_1$ | 11%*U* | 1.26 | 0.58 |
| Backward | 0.3% $m_1$ | 56%*U* | 0.98 | 0.38 |
| Forward | 0.3% $m_1$ | 56%*U* | 1.25 | 0.61 |
| Backward | 0.3% $m_1$ | 97%*U* | 1.16 | 0.53 |
| Forward | 0.3% $m_1$ | 91%*U* | 1.55 | 0.90 |

The injection of leakage mass flow gives rise to a significant increase in the net mixed-out endwall losses. This is caused by the loss generated during the mixing process of the two streams. These losses depend on the leakage tangential velocity and the leakage mass flow rate.

As was stated in a previous section and shown in Fig. 10, when the leakage tangential velocity is increased from 56%*U* to approximately 100%*U*, there is a large increase in the net mixed-out endwall losses for both step geometries and at any of the leakage mass flow rates tested. The cause of this rise is a stronger interaction between the leakage flow and the mainstream around the cavity slot. Furthermore, an increase of the leakage mass flow rate from 0.3% $\dot{m}_1$ to 0.7% $\dot{m}_1$ at fixed leakage tangential velocity causes an increase of the net mixed-out endwall losses.

At all of the leakage conditions that have been tested, the forward-facing step produces higher losses with respect to the case with a backward-facing step. This is a consequence of a strong interaction with the pressure surface separation bubble.

## Conclusions

A series of experiments was performed on a solid-thin profile linear cascade to study the effect of the injection of leakage flow from a cavity into the mainstream on the endwall flows and their interaction with a large pressure surface separation bubble. The profile is characterized by a large pressure surface separation bubble. A step of 1.2% of the span high was placed 18.6% $C_{ax}$ upstream of the blade leading edge. The inlet boundary layer was turbulent and the thickness was 3% of the span. Two different step geometries were analyzed, i.e., a backward-facing step and a forward-facing step. The effect of the leakage tangential velocity and the leakage mass flow rate were investigated.

For a backward-facing step at any of the leakage conditions that have been tested, there is not a strong interaction between the pressure surface separation bubble and the endwall flows. However, this interaction happens for the forward-facing step. Consequently, a forward-facing step gives rise to stronger endwall flows and higher net mixed-out endwall losses than the backward-facing step.

The presence of the cavity, even when no net leakage flow is injected, has an effect on the endwall flows and on the net mixed-out endwall losses. This is because of the exchange of mass and momentum between the leakage flow and the mainstream that happens around the slot. As a consequence, an increase of the net mixed-out endwall losses occurs although the presence of the cavity does not cause a change on the endwall flows, structure at 50% $C_{\mathrm{ax}}$ downstream of the blade trailing edge.

The injection of leakage mass flow gives rise to a strengthening of the endwall flows. This is enhanced when the leakage tangential velocity or the leakage mass flow rate is increased.

The injection of leakage mass flow from the cavity gives rise to the formation of a skewed shear layer between the leakage flow and the mainstream at the interface of the cavity with the mainflow path. A limit value of the leakage tangential velocity has been found. Above this value, a stronger interaction occurs between the leakage flow and the mainstream, which results in the formation of a number of roll-up vortices in the skewed shear layer. This gives rise to a strengthening of the endwall flows and an increase of the mixed-out endwall losses. This phenomenon happens independently of the step geometry. From this set of experiments and computational results, it is possible to conclude that the leakage tangential velocity is a key parameter that determines the endwall flows structure within the blade passage.

## Acknowledgment

The authors would like to thank T. Chandler for his work on the experimental setup. The authors would also like to thank ITP for the funding of the project and the permission to publish this paper.

## Nomenclature

$C_{\mathrm{ax}}$ = axial chord
$C_{p2}$ = static pressure coefficient $C_{p2}=(P_{01}-P_{\mathrm{blade}})/(P_{01}-P_{s2})$
$h$ = step height
$H$ = shape factor
LE = blade leading edge
$\dot{m}_1$ = inlet mass flow
$\dot{m}_{\mathrm{leak}}$ = leakage mass flow
$P_1$ = separation point
$P_{01}$ = inlet total pressure
$P_{0\mathrm{cav}}$ = total pressure of the leakage flow
$P_{\mathrm{blade}}$ = static pressure on the blade surface
$P_{s2}$ = exit static pressure
PS = blade pressure surface
$R_{p1}$ = reattachment line of the pressure surface separation bubble
SS = blade suction surface
$S_{e1}$ = separation line of the passage vortex from the endwall
$S_{e4}$ = separation line on the endwall
$S_{p2}$ = separation line on the blade pressure surface
TE = blade trailing edge
Tu = turbulence intensity
$U$ = Speed of the hub
$V_{\mathrm{leak}}$ = leakage tangential velocity
$u_\tau$ = wall friction velocity defined as $\sqrt{\tau_\omega/\rho}$
$y^+$ = dimensionless wall normal distance $yu_\tau/\nu$
$y$ = distance from the wall
$\delta_{99}$ = thickness of the inlet endwall boundary layer
$\alpha_1$ = inlet blade angle from the axial direction
$\alpha_2$ = exit blade angle from the axial direction
$\delta^*$ = displacement thickness
$\theta$ = momentum thickness
$\nu$ = kinematic viscosity
$\tau_w$ = wall shear stress
$\rho$ = density

## References

[1] de la Rosa Blanco, E., Hodson, H. P., Vazquez, R., and Torre, D., 2003, "Influence of the State of the Inlet Endwall Boundary Layer on the Interaction Between the Pressure Surface Separation and the Endwall Flows," Proc. Inst. Mech. Eng., Part A, **217**, pp. 413–420.
[2] Sieverding, C. H., 1985, "Recent Progress in the Understanding of Basic Aspects of Secondary Flows in a Turbine Blade Cascade," ASME J. Eng. Gas Turbines Power, **107**(2), pp. 248–252.
[3] Gregory-Smith, F. G., 1997, "Secondary and Tip-Clearance Flows in Axial Turbines," VKI LS 1997-01, Von Karman Institute for Fluid Dynamics, Rhode St. Genese, Belgium.
[4] Langston, L. S., 2001, "Secondary Flows in Axial Turbines—A Review," Ann. N.Y. Acad. Sci., **934**, pp. 11–26.
[5] de la Rosa Blanco, E., Hodson, H. P., and Vazquez, R., 2003, "Effect of Upstream Platform Geometry on the Endwall Flows of a Turbine Cascade," ASME Paper No. GT2005-68938.
[6] Wellborn, S. R., and Okiishi, T. H., 1999, "The Influence of Shrouded Stator Cavity Flows on Multistage Compressor Performance," ASME J. Turbomach., **121**, pp. 486–497.
[7] Wellborn, S. R., Tolchinsky, I., and Okiishi, T. H., 2000, "Modelling Shrouded Stator Cavity Flows in Axial-Flow Compressors," ASME J. Turbomach., **122**, pp. 55–61.
[8] Demargne, A. A. J., and Longley, J. P., 2000, "The Aerodynamic Interaction of Stator Shroud Leakage and Mainstream Flows in Compressors," ASME Paper No. 2000-GT-570.
[9] Wellborn, S. R., 2001, "Details of Axial-Compressor Shrouded Stator Cavity Flows," ASME Paper No. 2001-GT-0495.
[10] Hunter, S. D., and Manwaring, S. R., 2000, "Endwall Cavity Flow Effects on Gaspath Aerodynamics in an Axial Flow Turbine: Part I—Experimental and Numerical Investigation," ASME Paper No. 2000-GT-651.
[11] McLean, C., Camci, C., and Glezer, B., 2001, "Mainstream Aerodynamic Effects Due to Wheelspace Coolant Injection in a High-Pressure Turbine Stage: Part II-Aerodynamic Measurements in the Rotational Frame," ASME J. Turbomach., **123**, pp. 697–703.
[12] Gier, J., Stubert, B., Brouillet, B., and De Vito, L., 2003, "Interaction of Shroud Leakage Flow and the Main Flow in a Three-Stage, LP Turbine," ASME Paper No. 2003-GT-38025.
[13] Schlienger, J., Pfau, A., Kalfas, A. I., and Abhari, R. S., 2003, "Effects of Labyrinth Seal Variation on Multistage Axial Turbine Flow," ASME Paper No. 2003-GT-38270.
[14] Bohn, D. E., Balkowski, I., Ma, H., and Tummers, C., 2003, "Influence of Open and Closed Shroud Cavities on the Flow Field in a 2-Stage Turbine With Shrouded Blades," ASME Paper No. 2003-GT-38436.
[15] Shabbir, A., Celestina, M. L., Adamczyk, J. J., and Strazisar, A. J., 1997, "The Effect of Hub Leakage Flow on Two High Speed Axial Flow Compressor Rotors," ASME Paper No. 97-GT-346.
[16] Cherry, D., Wadia, A., Beacok, R., Subramanian, M., and Vitt, P., 2005, "Analytical Investigation of a Low Pressure Turbine With and Without Flowpath Endwall Gaps, Seals and Clearance Features," ASME Paper No. GT2005-68492.
[17] Demargne, A. A. J., 2000, "Aerodynamics of Stator-Shroud Leakage," Ph.D. thesis, University of Cambridge, Canbridge.
[18] Shih, H., Liou, W. W., Shabbir, A., and Zhu, J., 1995, "A New $k$-$\varepsilon$ Eddy-Viscosity Model for High Reynolds Number Turbulent Flows-Model Development and Validation," Comput. Fluids, **24**(3), pp. 227–238.
[19] Gregory-Smith, D. G., Graves, C. P., and Walsh, J. A., 1988, "Growth of Secondary Losses and Vorticity in an Axial Turbine Cascade," ASME J. Turbomach., **110**, pp. 1–8.
[20] Anker, J. E., and Mayer, J. F., 2002, "Simulation of the Interaction of Labyrinth Seal Leakage Flow and Main Flow in an Axial Turbine," ASME Paper No. 2002-GT-30348.

# Film Cooling Measurements for Cratered Cylindrical Inclined Holes

**Yiping Lu**

**Alok Dhungel**

**Srinath V. Ekkad**
e-mail: sekkad@vt.edu

Mechanical Engineering,
Virginia Tech,
Blacksburg, VA 24061

**Ronald S. Bunker**
GE Global Research Center,
Niskayuna, NY 12301

*Film cooling performance is studied for cylindrical holes embedded in craters. Different crater geometries are considered for a typical crater depth. Cratered holes may occur when blades are coated with thermal barrier coating layers by masking the hole area during thermal barrier coating (TBC) spraying, resulting in a hole surrounded by a TBC layer. The film performance and behavior is expected to be different for the cratered holes compared to standard cylindrical holes. Detailed heat transfer coefficient and film effectiveness measurements are obtained simultaneously using a single test transient IR thermography technique. The study is performed at a single mainstream Reynolds number based on freestream velocity and film-hole diameter of 11,000 at four different coolant-to-mainstream blowing ratios of 0.5, 1.0, 1.5, and 2.0. The results show that film cooling effectiveness is slightly enhanced by cratering of holes, but a substantial increase in heat transfer enhancement negates the benefits of higher film effectiveness. Three different crater geometries are studied and compared to a base line flush cylindrical hole, a trenched hole, and a typical diffuser shaped hole. Computational fluid dynamics simulation using FLUENT was also performed to determine the jet-mainstream interactions associated with the experimental surface measurements.* [DOI: 10.1115/1.2950055]

## Introduction

Gas turbine blades need to be effectively cooled to increase component life and reduce maintenance costs. Modern blades also use film cooling in addition to turbulated internal cooling to protect the blade's outer surface from hot gases. With increasing turbine inlet temperatures, there is a need for more effective cooling techniques to maintain the blades below failure conditions during operation. Discrete holes are drilled at several locations on the blade exterior surface so as to allow some of the internal cooling air to eject out and form a protective cooler film on the surface. For low temperature operations, simple angle holes, which are angled only along the flow direction, are used and are sufficient. Typically, most blades are additionally coated with ceramic thermal barrier coating (TBC) coatings to protect the metal surface from direct contact with hot gases.

The focus of this investigation is to study cratered cooling hole geometries on film cooling heat transfer and cooling effectiveness over flat surfaces. The TBC coatings are thin and on the order of film-hole sizes. The hole area is masked off before TBC spraying on to the blade metal surface. The mask coverage area produces different types of hole geometries. The masks can produce holes embedded in trenches or in craters. The size and depth of the trench/crater with respect to the hole size plays an important role in providing different film cooling characteristics. The effect of trenching/cratering may be to convert the three-dimensional nature of the mainstream-coolant interaction into a more 2D phenomenon, resulting in a more uniform cooling film on the surface. This study focuses on understanding the behavior of the film exiting cratered cylindrical holes.

Fric and Campbell [1] investigated a so-called cratered film hole in which the circular hole exits into a shallow circular surface cup or depression. This was the first study on this concept. They indicated that flow actually impinges on the edge of this depression, causing it to deflect and fill the depression prior to issuing onto the external surface. They also indicated that flat plate tests showed about a 50% improved effectiveness over round holes at $M=1$ and a greater increase as the blowing ratio increases. Effectiveness improvement of 100% and more was observed at $M=5$. A suggested application in Ref. [1] is the full coverage film cooling of combustor liners. However, they did not study the crater geometry and did not provide any understanding of the heat transfer coefficient enhancement associated with it. Bunker [2] investigated film effectiveness for geometries wherein the coolant from discrete holes enters a slot before mixing with the mainstream. The holes embedded in the trench provided higher film effectiveness distributions than the ones on the plane surface. However, Bunker [2] provided only film effectiveness distributions and also the hole had a compound angle (radial injection) in the lateral direction. Bunker [2] based his study on an earlier study by Wang et al. [3]. Wang et al. [3] were the first to study jets exiting into slots. They showed that the slot exit provides a uniform velocity distribution.

Lu et al. [4] studied the effect of trench exit area and edge shape on film cooling performance using an IR thermography method. Their results showed that the film cooling holes provide higher film effectiveness when embedded in a trench. However, in some geometries when the trench began at the upstream edge of the hole, the film effectiveness diminished. The heat transfer coefficient enhancement due to the embedding was not significantly higher compared to the typical unembedded cylindrical hole. The overall heat flux ratio comparing film cooling with embedded holes to that with unembedded holes shows that the full trench and downstream trench spacing after the hole exit produce the highest heat flux reduction. Recently, Lu and Ekkad [5] presented a computational fluid dynamics (CFD) study of cratered holes. They showed that the cratered holes show the presence of a weaker counter-rotating vortex pair that is typical of cylindrical holes and seems to show stronger film dissipation downstream. The turbulence intensity due to mixing between the mainstream and coolant jets is at similar levels as the base line case.

In the present study, a transient infrared thermography technique is used for obtaining both heat transfer coefficient and film effectiveness from a single test. The transient IR technique is

---

Contributed by the International Gas Turbine Institute of ASME for publication in the JOURNAL OF TURBOMACHINERY. Manuscript received June 11, 2007; final manuscript received June 21, 2007; published online October 2, 2008. Review conducted by David Wisler. Paper presented at the ASME Turbo Expo 2007: Land, Sea and Air (GT2007), Montreal, QC, Canada, May 14–17, 2007.

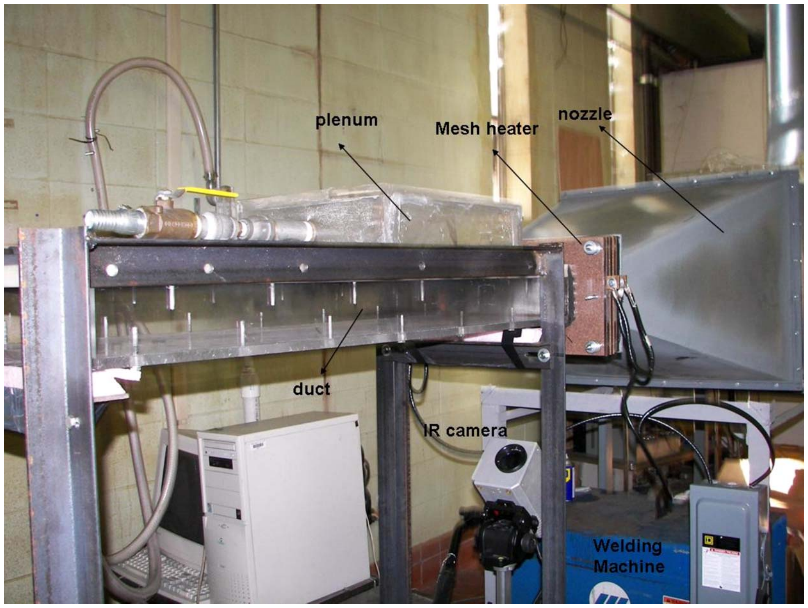

Fig. 1 Test rig setup

based on the two-equation single test proposed by Vedula and Metzger [6] and was demonstrated successfully by Ekkad et al. [7]. Simultaneous $\eta$ and $h$ distributions are investigated and presented on the flat surface downstream of injection for various blowing ratios for unembedded cylindrical holes and for three different cratered hole configurations. This paper also presents CFD predictions of film cooling for cratered holes.

## Test Facility

Figure 1 shows a comprehensive view of the experimental arrangement. A fast response mesh heater was placed at the exit of the nozzle. The mesh heater concept developed by Gillepsie et al. [8] has the capability of providing an instantaneous temperature step to the mainstream air. The mesh used to build the heater was a 304 stainless steel woven wire mesh with a 20 $\mu$m wire diameter. The free area of the mesh was 33.6%, which helped in reducing the freestream turbulence before the test section.

Figure 2 shows the layout of the mesh heater. The low electrical resistance of the dense wire mesh necessitated the use of a low voltage, high amperage power source. Power was supplied to the heater using a Miller Dialarc 250 ac/dc welding machine. It was found that when the heater was turned on, the steady state of the temperature of the mesh was achieved immediately. The test section is made of Plexiglass and has a cross section of 30 cm width and 9 cm height. The top plate of the test section is made of 3 cm thick ABS. This plate has a replaceable section about 25.4 cm downstream of the test section inlet. This replaceable section can be interchanged to change the hole geometry. A trip is placed at the entrance to the test section to produce a fully turbulent boundary layer over the test plate. The coolant air is provided from a separate compressed air supply and is metered for flow measurement. When the valve is flipped, the coolant enters a plenum below the test plate and is then ejected through the film cooling holes into the test section. Thermocouples are mounted upstream of the hole row to measure the mainstream temperature and inside one of the holes to measure the coolant exit temperature. The coolant temperature is measured inside only one hole because pretesting showed that all film holes had the same flow rate and temperature conditions.

The infrared thermography system used is a FLIR Systems ThermaCAM SC 500. The camera has a range of −40°C to 500°C. The ThermaCAM 500 utilizes uncooled microbolometer long wave detectors to sense IR radiation. This makes them ideal for general thermal measurement applications. The SC 500 system provides real time 14 bit digital output, a $320\times240$ pixel detector, precision temperature measurement, internal data storage, and outstanding thermal sensitivity. The camera has the following specifications: the field of view and minimum focus distance are $24\times18$ deg$^2$ and 0.5 m, respectively, the spectral range is 7.5–13 $\mu$m, and the accuracy is $\pm2\%$ or 2°C. The test surface is viewed through a stretched polyurethane sheet. The sheet is thin enough to cause very little effect on IR transmissivity. The system calibration is conducted using a thermocouple placed on the black painted test surface to act as the benchmark. This thermocouple is used to estimate the emissivity of the test surface. The emissivity of the black painted test when viewed without the window is 0.98. The calibrated transmissivity for the polyurethane sheet is 0.75.

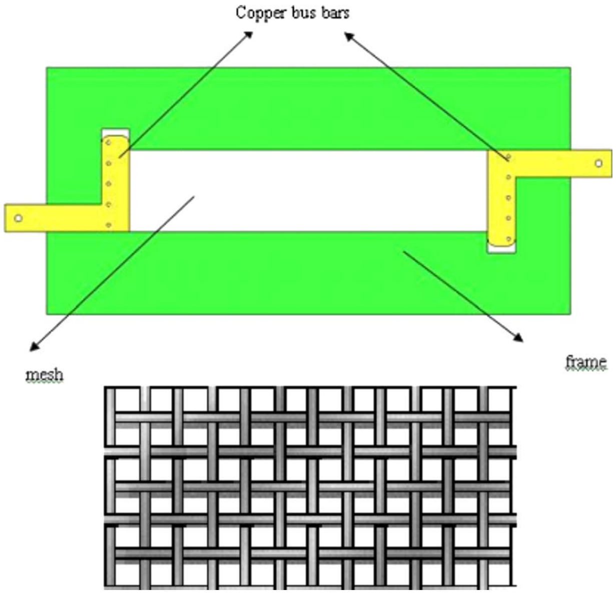

Fig. 2 Mesh heater

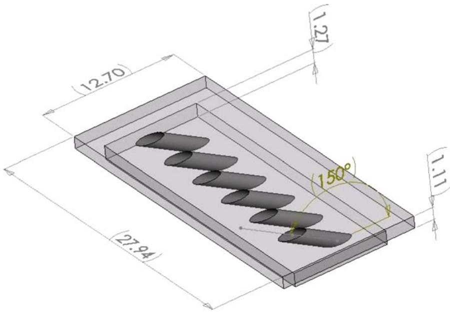

**Fig. 3 Test plate geometry for base line holes**

Figure 3 shows the test plate with a fil99 m hole geometry used in this study. There are six holes of 1.27 cm diameter in each row inclined at 30 deg along the flow direction. The hole spacing between adjacent holes is three-hole diameters for all the holes. Figures 4(*a*)–4(*d*) show the four cases studied. The first is the base line case (Fig. 4(*a*)) where the holes are flushed with the surface. All the crater holes have the same crater depth of 0.5-hole diameter. Case 1 (Fig. 4(*b*)) is the cratered holes where the hole is offset in the crater such that the crater and hole downstream edge match. There is a crater region downstream of the hole, which is one hole diameters long. The width of the crater is two-hole diameters wide. Case 2 (Fig. 4(*c*)) is the concentric geometry where the hole and the crater center are matched. The crater is all around the hole exit. Case 3 (Fig. 4(*d*)) is when the crater is truly circular and both the upstream and downstream edges of the holes and craters match. There is crater area only around the sides of the hole. The base line and three crater geometries are clearly indicative of some of the masking strategies for the TBC coated surfaces. Case 4 (Fig. 4(*e*)) is a 2D trench inside which the flow enters from the cylindrical hole [8]. The trench has a $2D$ width in the flow direction and a $0.75D$ depth. For shaped diffuser hole (Fig. 4(*f*)), the hole inclination angle is set as 30 deg and the length of the cylindrical inlet portion is $l=2D$. The hole laidback angle is 15 deg. For all cases, the thickness of the test plate was the same. So the trench hole lengths were shorter than the base line and shaped hole lengths.

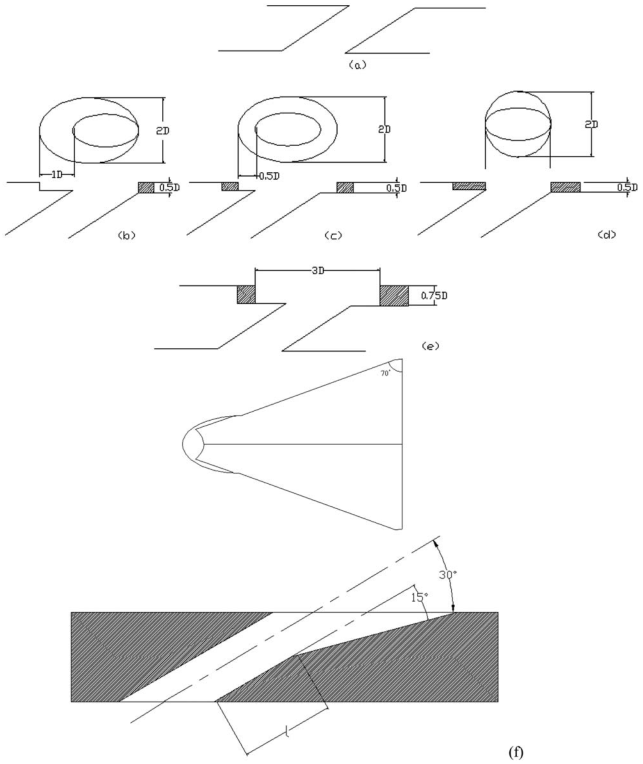

**Fig. 4 All cases with different hole configurations studied**

The measured mainstream velocity and freestream turbulence using a calibrated single hot wire probe are 13.8 m/s and 2%, respectively. The mainstream Reynolds number ($\mathrm{Re}_d$) based on film-hole diameter is 11,000. The boundary layer profile measured downstream of the trip is close to the fully turbulent flow profile (1/7th law). Four blowing ratios, $M=0.5$, 1.0, 1.5, and 2.0, are tested for six cases. The trench results are from Lu et al. [9].

## Procedure

The basic procedure is to initiate the main flow through the test section at the beginning. The coolant flow is set to the required rate to match the test blowing ratio. The heater is switched on when the flows are uniform and steady, thus beginning a transient heating test of the test surface. A thermocouple is attached to the test surface with aluminum tape. The thermocouple is located outside the measurement domain to prevent from interference caused by the aluminum tape. The test surface is then sprayed with black flat paint to increase the emissivity like a perfect blackbody with a known emissivity of unity. The IR camera is focused on the test surface (typically covers slightly larger than the region of interest and the thermocouple). Prior to the actual thermal measurements, calibration of the entire thermography system and the IR signal is required. The test surface is then heated with the hot air supplied by the blower through the mainstream heater. The temperatures of thermocouples are monitored until steady state is reached. The temperature measured by the thermocouple is then compared to that measured by the IR system. The factors required for an accurate IR measurement to compensate for the effects of several different sources of radiation include the distance between the test surface and the front lens of the camera, the relative humidity, and the background temperature. Multiple location temperatures are used for calibration to compensate for all other emitting sources of radiation within view of the test article. A number of temperatures are used to establish the corrective value of emissivity. However, the temperature of the reference object must not be too close to the ambient temperature for this to work. During the emissivity calculation, polyethylene sheet window was not used. So, the transmissivity value used was 1. The temperature change of the air environment is not large enough to affect the IR signal.

Typically the mainstream temperature increases from the initial temperature to set temperature immediately and then steadies. The coolant temperature is, however, maintained at the initial temperature. The wall temperature monitored by the thermocouple used for emissivity estimation rises as the outside surface is heated during the transient test at a more gradual rate than mainstream temperature. The inside wall temperature is unaffected by the heating on the opposite side, confirming the usage of the semi-infinite solid assumption. The test surface was modeled as a semi-infinite solid medium imposed by a sudden transient heating. The entire solid medium was initially at a uniform temperature before the transient test. During the transient heating test, each point on the surface will respond with different temperatures at different times due to different heat transfer coefficients. Faster time of temperature change in response to the prescribed temperature during the transient test will produce higher heat transfer coefficient and vice versa. The test surface is modeled as undergoing 1D transient conduction with convective boundary conditions at the wall. Applying the prescribed boundary conditions and initial conditions to the problem and solving for the wall temperature response with time at the wall produces a solution of the form

$$\frac{T_w - T_i}{T_\infty - T_i} = 1 - \exp\left(\frac{h^2 \alpha t}{k^2}\right)\operatorname{erfc}\left(\frac{h\sqrt{\alpha t}}{k}\right) \qquad (1)$$

where $h$ is the unknown quantity in the equation and $T_w$ is the measured wall temperature at time $t$ after the initiation of the transient test. The material properties $\alpha$ ($7.157 \times 10^{-8}$ m/s) and $k$ (0.15 W/m K) dictate the applicability of the semi-infinite solid solution on the test surface.

In film cooling situations, the basic convective heat load equation is modified to include the film temperature based on the definition of the local heat flux. The equation becomes

$$\frac{T_w - T_i}{T_f - T_i} = 1 - \exp\left(\frac{{h_f}^2 \alpha t}{k^2}\right)\operatorname{erfc}\left(\frac{h_f\sqrt{\alpha t}}{k}\right) \qquad (2)$$

where $T_f$ is the local film temperature, which is a function of the local mixing between the mainstream and coolant jet near the surface.

The mesh heater was designed to provide a true step change in air temperature at the start of a test. The true step change in mainstream temperature allows the use of the original solution to the transient heating of the wall (Eq. (1)). The regression technique used to reduce uncertainty in experimental measurements was to collect multiple wall temperature–time data pairs over a broad range of temperatures to use in an overconstrained system of equations to solve for $h$. The regression analysis put all terms of the conduction equation to the right hand side of the equation and was solved for all points of data for each pixel. This resulted in a residual error for each time-temperature data pair. The residual error was minimized in a least squares sense solving for the heat transfer coefficient that best fit all data.

Uncertainty in the calculation comes from the measurement of initial, mainstream, and coolant temperatures. The estimated uncertainty in initial and wall temperatures ($\Delta T_i$) is $\pm 0.5°$C, the mainstream temperature ($\Delta T_\infty$) is $\pm 1.1°$C, and the coolant temperature ($\Delta T_c$) is $\pm 0.5°$C. The camera frame rate is 60 Hz, resulting in a time error of $\pm 1.6\%$, and the test surface property uncertainty is estimated at $\pm 3\%$. The resulting *average* uncertainties using the methodology proposed by Kline and McClintock [10] for heat transfer coefficient and film effectiveness are $\pm 4.5\%$ and $\pm 7.0\%$, respectively. However, the uncertainty for local film effectiveness depends on the local value. The uncertainty for effectiveness measurements is $\pm 0.03$.

## Numerical Procedure

A highly orthogonalized nonuniform fine grid mesh was generated with grid nodes clustered in the immediate vicinity of the discrete film cooling jet. The most difficult region for the grid generation and also the most critical portion of the entire mesh is the region near the film hole [5]. Other important grid parameters are considered. The grid aspect ratio, especially near the coolant jet was kept under 10. The nodes near the test plate surface was adjusted so that the average $y^+$ value was about 30 in the crossflow and 30–100 within the film hole. The overall values of the computation domain in the lateral, vertical, and streamwise directions were 24.25$D$, 15.875$D$, and 80$D$, respectively. The grid was created using GAMBIT, and the simulation was run using the FLUENT computer code.

Boundary conditions are prescribed at all three boundary surfaces of the computation domain. Mainstream conditions were maintained the same in all cases, and the coolant flow rate was altered to change the blowing ratios. The coolant temperature was set at 296 K. A cross-stream turbulence intensity of 3% and $x$-direction velocity were specified and were similar to experimental conditions to produce the desired oncoming mainstream Reynolds number at a temperature of 321 K. At the exit plane, pressure level was specified along with zero streamwise gradient for all other dependent variables.

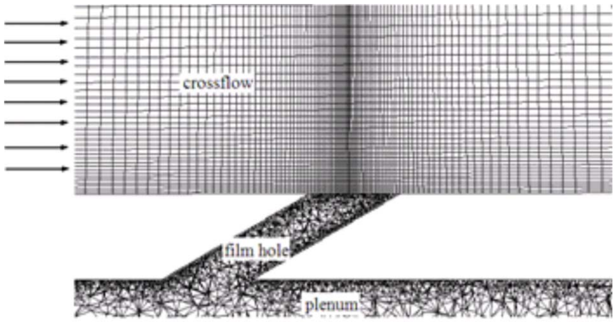

(a) within film hole

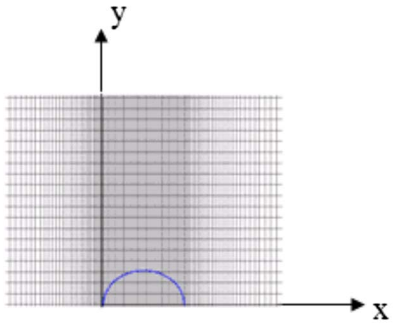

(b) jet exit plane

**Fig. 5 Computational grid details**

The standard high Re $k$-$\varepsilon$ model was used in this study. The model is widely used, and no additional details are provided here. A standard smooth-wall function is used to represent the near-wall behavior, and roughness effects have not been incorporated. All the cases presented here converged to residual levels of the order of $10^{-5}$ and to better than 0.03% error in the mass flow rate between the inlet and exit of the computational domain. Typically, 500 iterations were necessary to attain a converged solution. Grid independence was checked by comparing the solutions obtained with 855,625 nodes and the solutions obtained with 537,714 nodes for Case 1. In both cases the grids were clustered near the film-hole region. Figure 5 shows the grid used in the present study. The differences in the solution on two grids were found to be minimal. These results were presented in a CFD only study by Lu and Ekkad [5]. The CFD results are mainly used to determine the flow characteristics and mixing away from the wall to better understand the measured wall heat transfer distributions. The turbulence modeling used is rather crude with a relatively coarse grid to provide accurate wall heat transfer characteristics.

## Results and Discussion

Figure 6 presents the effect of blowing ratio on detailed film effectiveness distributions for five cases. For the base line case, the jet streaks are clearly visible, with the highest effectiveness occurring at $M = 0.5$ near the hole exits. At higher blowing ratios, there is a jet lift-off resulting in a lower coverage. For Case 1, the effectiveness is higher than the base line case for all blowing ratios. This may be due to the reduced exit momentum of the jets when they interact with the mainstream. The jets exit the cylindrical holes and expand into the crater, resulting in lower momentum jets. As the blowing ratio increases, the jet streaks expand more laterally and reduced effectiveness is seen downstream. The lateral spreading is due to the accumulation of the coolant inside the crater and then diffusing out of the larger area of the crater than is observed for the base line. For Case 2, the effectiveness is higher than for the base line case. However, there is a very limited spreading in the lateral direction immediately downstream of the

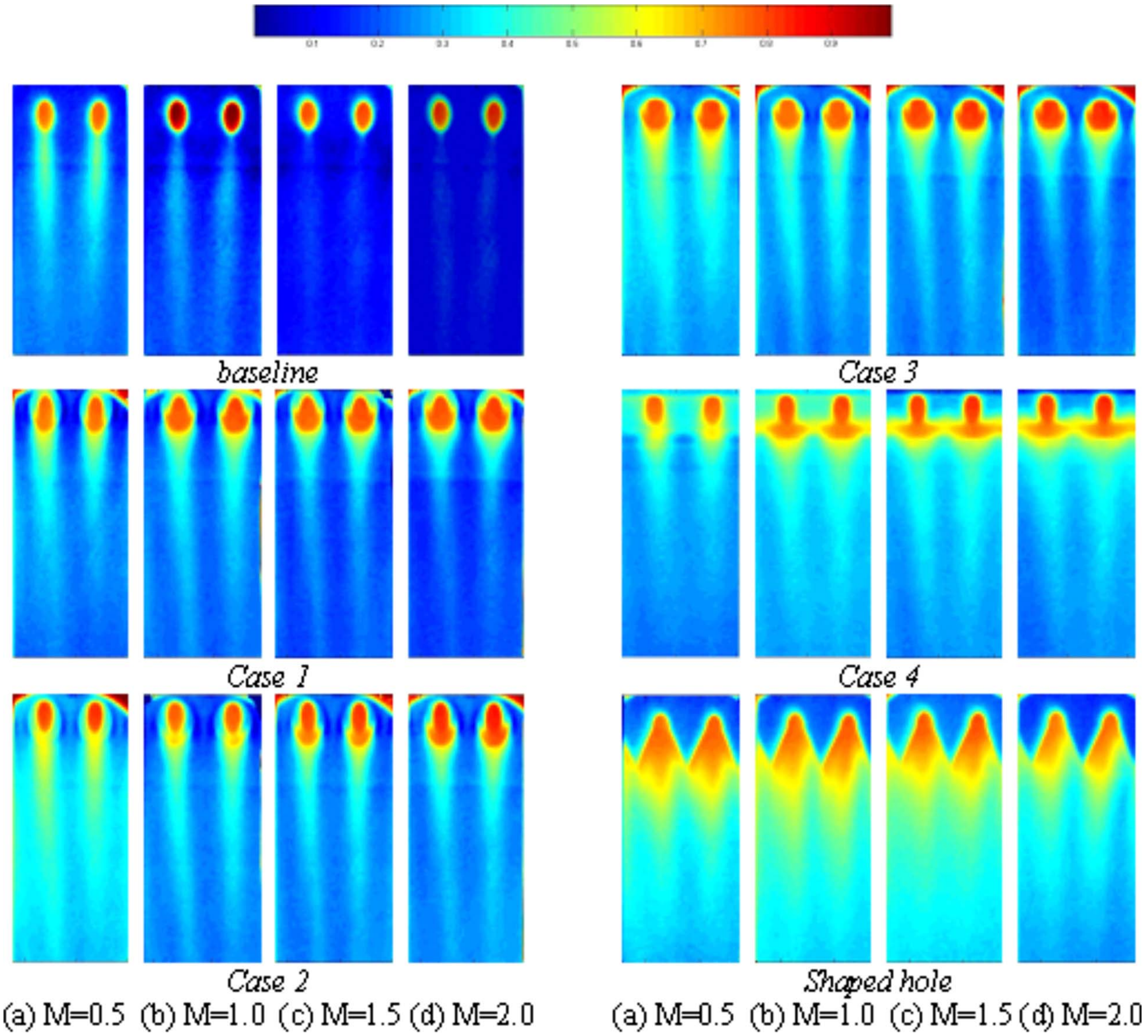

**Fig. 6 Detailed film effectiveness distributions for all cases at different blowing ratios**

crater, as seen for Case 1. However, there is a higher cooling effectiveness downstream compared to Case 1. Effectiveness decreases with increasing blowing ratio for Case 2. For Case 3, the jets show improved effectiveness over the base line and Cases 1 and 2. There appears to be more lateral spreading than for Case 2, and the jets appear to provide coverage farther downstream than for Cases 1 and 2. This may be due to the circular shape of the crater, where the jet streak is maintained because of the streamwise length of the hole and the additional area in the lateral direction. The trench case (Case 4) from Ref. [8] is shown for comparison. The trench shows a two-dimensional behavior unlike the cratered holes. The trenched hole also shows an increase in film effectiveness for higher blowing ratios. The diffuser shaped hole is far superior in performance than all the other cases due to the significantly reduced momentum of the jets and the coolant hugging the surface even at high blowing ratios. However, the shaped hole is not a good comparison for the crater holes as the shaped hole may be cratered in real applications, and this should be considered in the comparisons. The asymmetric behavior of the shaped hole for higher blowing ratios indicates classic diffuser separation along one wall. This may indicate an otherwise stronger diffuser angle chosen in this configuration.

Figure 7 presents the pathlines of coolant and mainstream imposed on velocity contours for the base line and Cases 1–3 at $M=1.0$. The base line case shows that the jet exits uniformly out of the hole and interacts with the mainstream. The jet displaces the mainstream, and this displacement depends on the momentum of the jet with respect to the mainstream. Case 1 shows the offset cratered hole. The jets appear to be slightly slower, exiting the crater but largely unaffected except at the downstream edge where the coolant seems entrained, resulting in a lower velocity region. A large recirculation zone is also seen upstream of the hole exit inside the crater. This region may also entrain some hot mainstream gases and may be detrimental to the blade metal surface. Case 2 shows more bending of the jet along the hole inclination angle and less interaction with the downstream edge of the crater wall compared to Case 1. There is a very low velocity zone after the downstream edge, indicating some possibility of separation at the downstream edge. Case 3 shows the lowest jet exit velocity out of the crater among all the cases. There are smaller recirculation zones inside the crater in the flow direction as there is no area to expand. The separation zone is less evident for this case on the downstream edge.

Figures 8(*a*)–8(*d*) show centerline nondimensional temperature ($\theta$) contours for all cases at $M=1$ to demonstrate the effect of

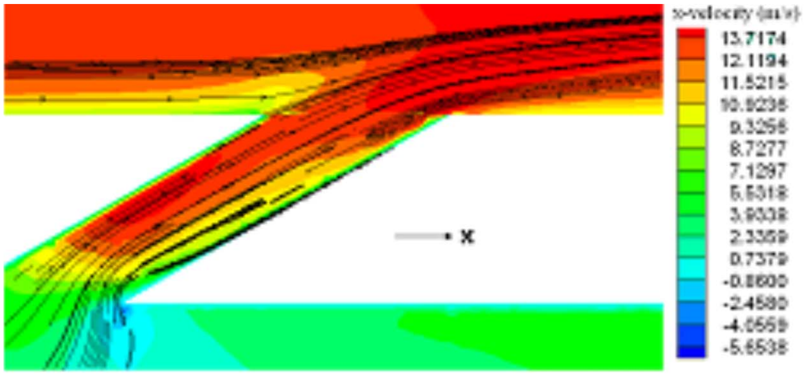

(a) Baseline

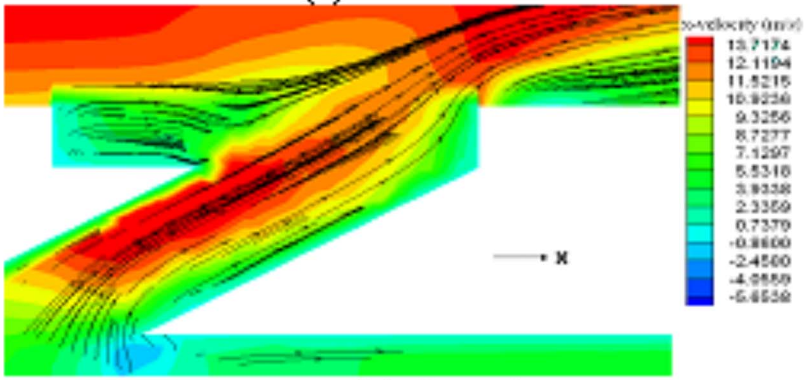

(b) Case 1

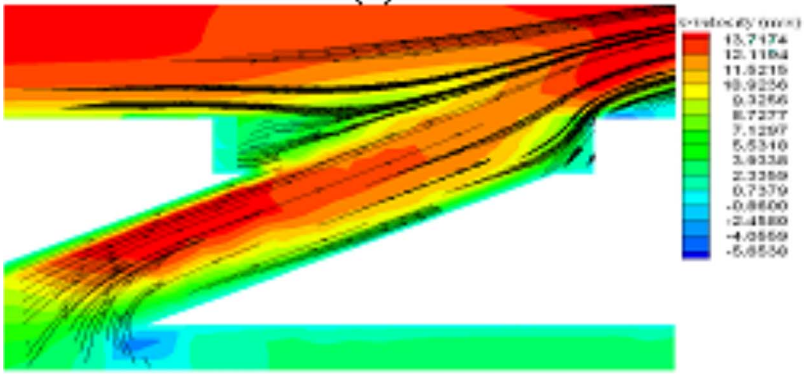

(c) Case 2

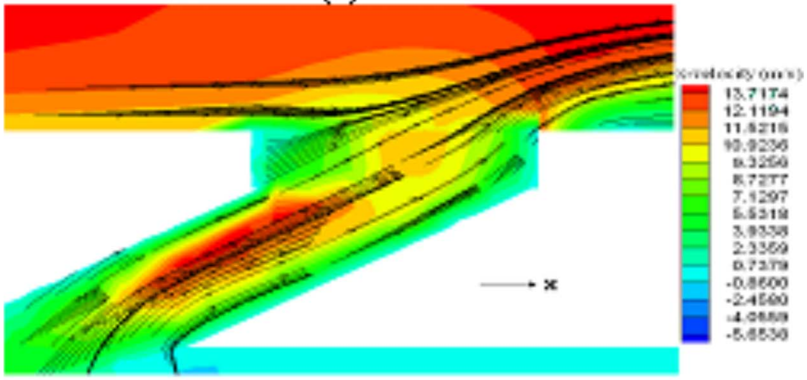

(d) Case 3

**Fig. 7** **Mainstream-jet interactions for (*a*) the base line, (*b*) Case 1, (*c*) Case 2, and (*d*) Case 3**

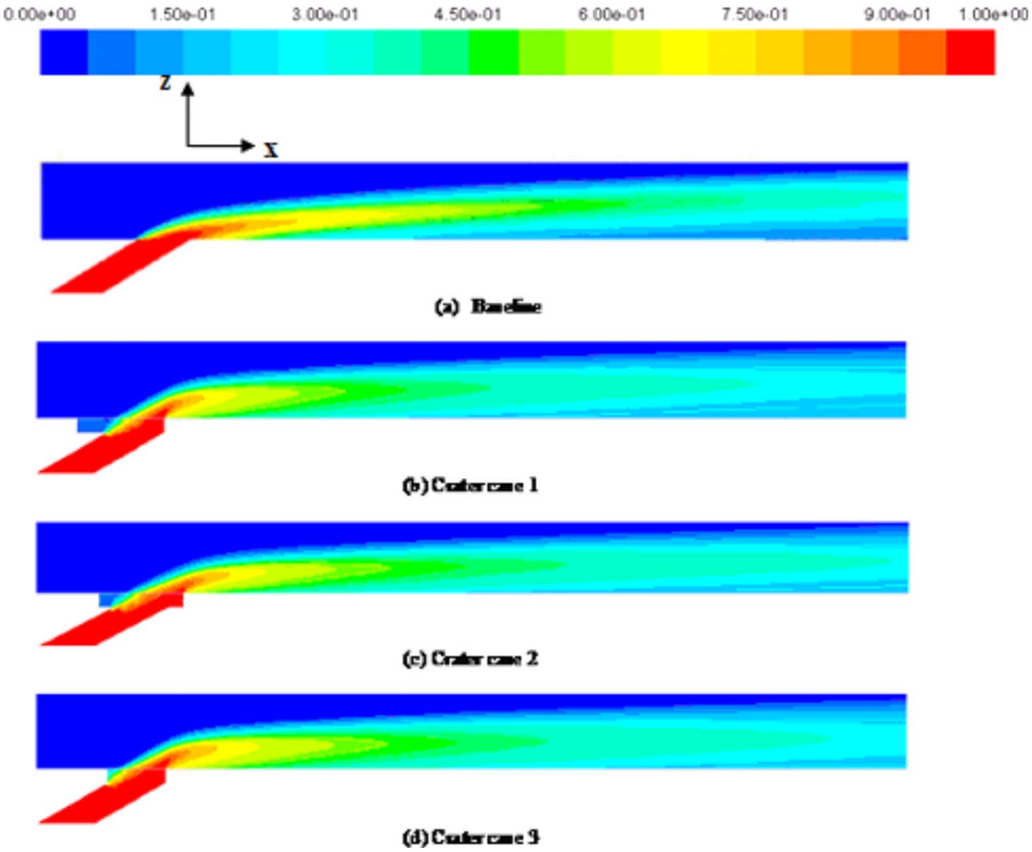

**Fig. 8 Computed nondimensional temperature contours of the film temperature ($\theta$) and mixing downstream of the holes**

crater shape on jet trajectory. It is seen that the base line case shows the jet lift-off from the surface, resulting in little coolant attached to the surface a bit downstream of the hole exit. The cooling air is away from the surface with mainstream entrainment under the jet. The cratered holes actually show a separation region just downstream of the craters, resulting in a reduced coolant velocity and thus leading to a better attachment to the surface farther downstream. Case 1 seems to show the least effectiveness downstream. Case 2 is slightly better than Cases 1 and 3. One interesting point to note is that the downstream region film is clearly attached to the crater regions. The separation near the downstream edge seems to cause reattachment of the jets downstream, resulting in higher effectiveness farther downstream than for the base line case at all blowing ratios.

Figure 9 presents the effect of blowing ratio on detailed heat transfer coefficient ($h$) distributions for the same five cases. Nearly all the cratered holes appear to enhance the heat transfer coefficient compared to the base line case. It appears that there is significantly more interaction between the mainstream and jet primarily in the slot exit region, resulting in higher turbulence production and subsequently higher heat transfer coefficient. The effect of blowing ratio on heat transfer coefficient enhancement appears diminished for the cratered hole Cases 1–3. This may be due to increased lateral spreading and lesser interaction with mainstream, which is typical for high momentum jets when injected directly through a cylindrical hole. The trench case (Case 4) shows increasing heat transfer coefficient ratios with increasing blowing ratio, but overall enhancement is limited to a relatively small region downstream of the trench exit. The shaped hole also shows higher heat transfer coefficient farther downstream. This may be a direct result of the flow separation in the diffuser walls, leading to much higher heat transfer coefficients than expected for typical shaped hole designs. Typically, shaped hole designs have been shown to provide higher film effectiveness distributions and slightly elevated heat transfer coefficients over the base line geometry.

Figures 10(*a*)–10(*d*) show the cross-plane vorticity contours for three cratered hole cases as the film moves downstream. One of the first CFD studies by Leylek and Zerkle [11] indicated the presence of counter-rotating bean-shaped vortex pairs (CRVP) exiting the jet holes and pushing downward, resulting in the coolant moving away from the surface as the blowing ratio increased. They captured the vortex pair clearly as it moved downstream and dissipated into the mainstream. Since that study, efforts have been made to reduce the effect of this CRVP as it exits the holes by shaping the hole exit or reducing the upward jet momentum on exit. The interesting issue for the crater holes is the increased strength of the vortex pair due to cratering. All three crater geometries show stronger vortices. The strength of the vortex is almost double that for the base line case. This may explain several factors that contribute to higher film effectiveness and higher heat transfer coefficients for cratered holes. Case 3 shows the vortex closer to the surface than for Cases 1 and 2.

The hole area region shows significantly higher heat transfer coefficient and film effectiveness results that may be contaminated by lateral conduction and edge effects. To avoid this, spanwise and area averaged results are only presented for the region above $X/D > 2$ as the region around the hole is subject to higher uncertainty. Figure 11 presents the effect of hole geometry on spanwise averaged film effectiveness for each blowing ratio. The average results are plotted against normalized streamwise distance upstream of the film-hole edge regardless of the crater and trench size and shape. At a low blowing ratio of $M = 0.5$, the shaped diffuser hole provides the highest effectiveness clearly but the downstream decay is also rapid. Case 2 also provides high effectiveness. Except for the base line case, Cases 1 and 4 clearly

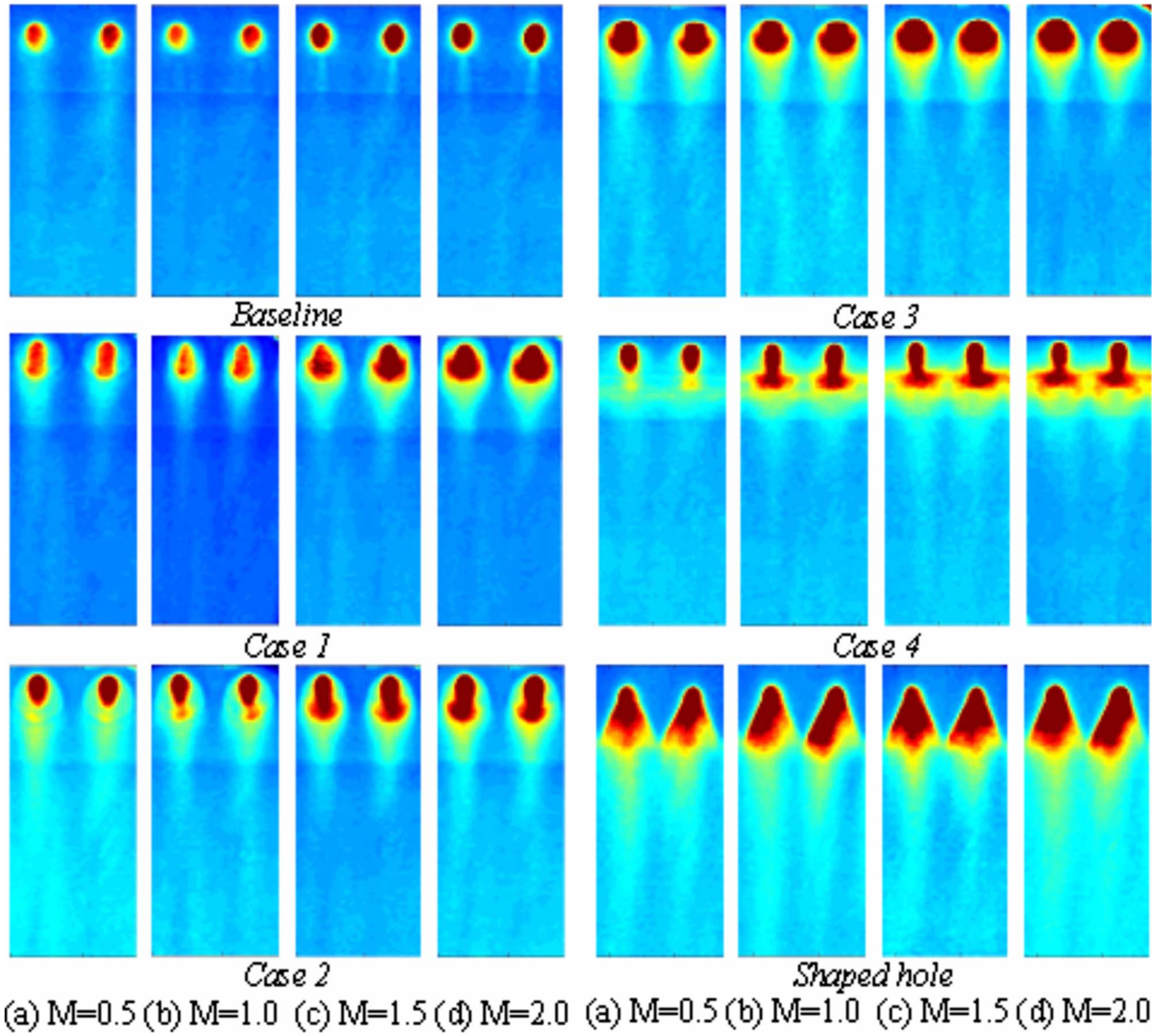

**Fig. 9 Detailed heat transfer coefficient ratio distributions for all cases at different blowing ratios**

provide the lowest effectiveness. As the blowing ratio increases to $M=1.0$, the shaped diffuser hole still remains at the highest level. All crater cases show similar effectiveness levels, with the trench case performing better. At $M=1.5$, the shaped hole is clearly better than all the cases, with the trench case slightly above Cases 2 and 3. Case 1 is lowest among all the crater cases. All the crater cases are still significantly higher than the base line case. For a high blowing ratio of $M=2$, Case 2 outperforms all the other cratered hole cases. It appears that the shaped hole and Case 4 provide better coverage.

Figure 12 presents the effect of hole geometry on spanwise averaged heat transfer coefficient ratio $(h/h_0)$ for each blowing ratio. The local heat transfer coefficient with film cooling $(h)$ is normalized by the heat transfer coefficient without holes on a flat surface $(h_0)$. Results are only presented downstream of the hole edge. At a low blowing ratio of $M=0.5$, the heat transfer coefficients for Cases 2–4 are at similar levels to those for all cases, with Case 1 and the base line relatively lower. The shaped hole shows the highest heat transfer coefficient ratios immediately downstream of the exit but decreases rapidly downstream. At $M=1.0$, all three cratered hole cases produce similar higher heat transfer coefficient enhancements due to increases in local interactions between the mainstream and jets, but still lower than the trench case (Case 4) and shaped hole case. For $M=1.5$, the shaped hole produces the highest heat transfer coefficient enhancement, with the base line case producing the lowest enhancement. The crater holes and the trenched hole produce similar levels of enhancement. At $M=2.0$, the trends are similar to $M=1.5$. The crater geometry seems to have very little effect on heat transfer coefficient enhancement, which may indicate that all geometries generate similar levels of turbulence due to jet-mainstream mixing. The craters/trenches also tend to disrupt the coolant flow at the downstream edge after initial diffusion into the crater/trench, resulting in discontinuous boundary layer growth.

Figure 13 presents the effect of blowing ratio on the overall area-averaged film effectiveness and heat transfer coefficient for all cases. Only the region beyond $X/D>1$ is considered for overall averaging. As seen clearly from the plot, the shaped diffuser hole shows much higher overall area-averaged effectiveness than the other cases. The trench case (Case 4) also shows slightly higher effectiveness compared to the crater cases at higher blowing ratios. There is a slight decrease in film effectiveness with increasing blowing ratio for all cratered hole cases. The heat trans-

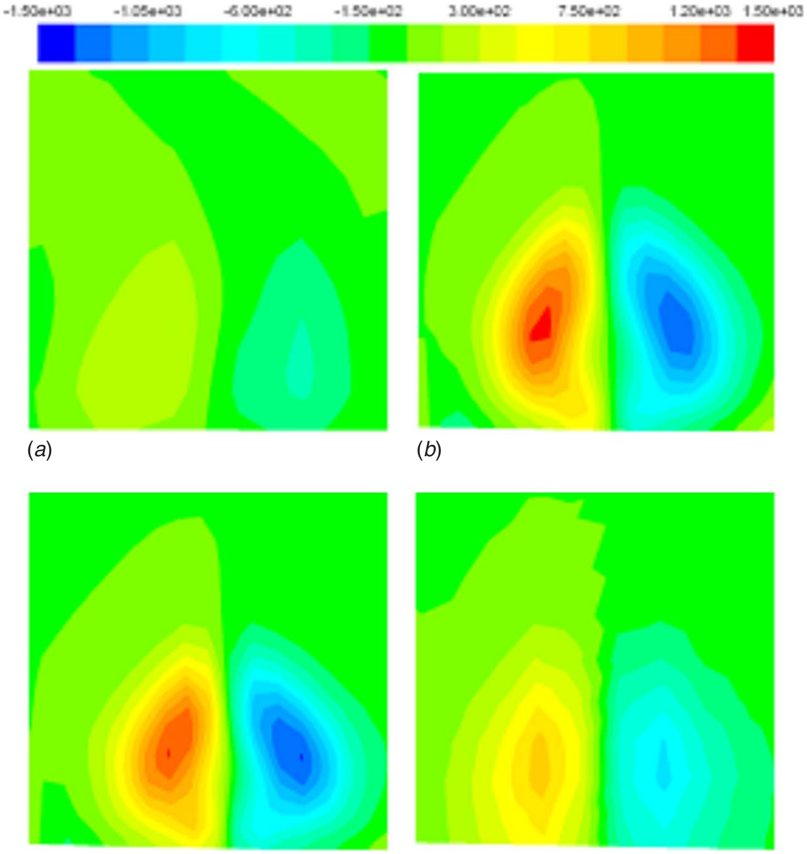

(*a*) (*b*) (*c*) (*d*)

**Fig. 10 Vorticity contours (1/s) downstream of injection for (*a*) the base line, (*b*) Case 1, (*c*) Case 2, and (*d*) Case 3**

fer coefficient ratios show minimal effect of the blowing ratio for all the cases. The shaped hole shows the highest heat transfer coefficient, and the base line is the lowest.

Figure 14 presents the effect of the blowing ratio on the overall area-averaged heat flux ratio ($q''/q''_0$) for all three cases. This ratio indicates the reduction in heat flux obtained by the introduction of film cooling over the surface. If the value is below 1.0, the effect is positive. If the value is greater than 1.0, then the presence of film cooling is detrimental. The heat flux ratio is calculated based on the formulation presented by Ekkad et al. [12]. The heat transfer ratio with and without film injection ($h/h_0$) and the local film effectiveness are used to calculate the local heat flux ratio,

$$\frac{q''}{q''_0} = \frac{h}{h_0}\left(1 - \frac{\eta}{\phi}\right)$$

The term $\phi$ is the overall cooling effectiveness and ranges between 0.5 and 0.7 for typical blade cooling systems. In this study, a typical value of 0.6 is chosen. The base line and Case 3 seem to show the worst performance. All cratered holes show heat flux ratios close to 1.0 for $M=1.5$ and higher blowing ratios. It appears that cratered holes may perform better at lower blowing ratios but are clearly not effective at higher blowing ratios. The trench may be the more optimum choice for masking rather than craters, as indicated by the overall performance especially at higher blowing ratios.

## Conclusions

Film cooling for cratered holes has been explored. Both heat transfer coefficients and film effectiveness were measured using a transient infrared thermography technique. The cratered holes increase film effectiveness over the base line case by about 50%. However, they do not provide significant lateral spreading, as seen for trenched holes. The jets still maintain a three-dimensional structure although the vortex strength is weaker than the base line case, as seen in the CFD predictions. Overall, the cratered holes do not perform as good as the trenched holes but clearly show a significant improvement at low blowing ratios over the base line. This is the first study that focused on cratered holes and provided a better understanding of the film behavior for these types of holes. The effect of crater depth may have an impact as the present study only investigated a shallow crater of 0.5$D$ depth.

## Acknowledgment

This work was funded through a broader study on film cooling by General Electric Global Research Center, Niskayuna, NY. The sponsor is Dr. Ron Bunker.

## Nomenclature

$c_p$ = specific heat (kJ/kg K)
$d$ = hole diameter (m)
$h_0$ = local heat transfer coefficient without film injection ($\mathrm{W/m^2\,K}$)
$h$ = local heat transfer coefficient with film injection ($\mathrm{W/m^2\,K}$)
$k$ = thermal conductivity of test surface (W/m K)
$L$ = length of film hole (m)
$M$ = blowing ratio$=\rho_c V_c/\rho_\infty V_\infty$
$q''$ = surface heat flux ($\mathrm{W/m^2}$)
Re = freestream Reynolds number ($V_\infty d/\nu$)
$\rho_c$ = coolant density ($\mathrm{kg/m^3}$)
$\rho_\infty$ = mainstream density ($\mathrm{kg/m^3}$)

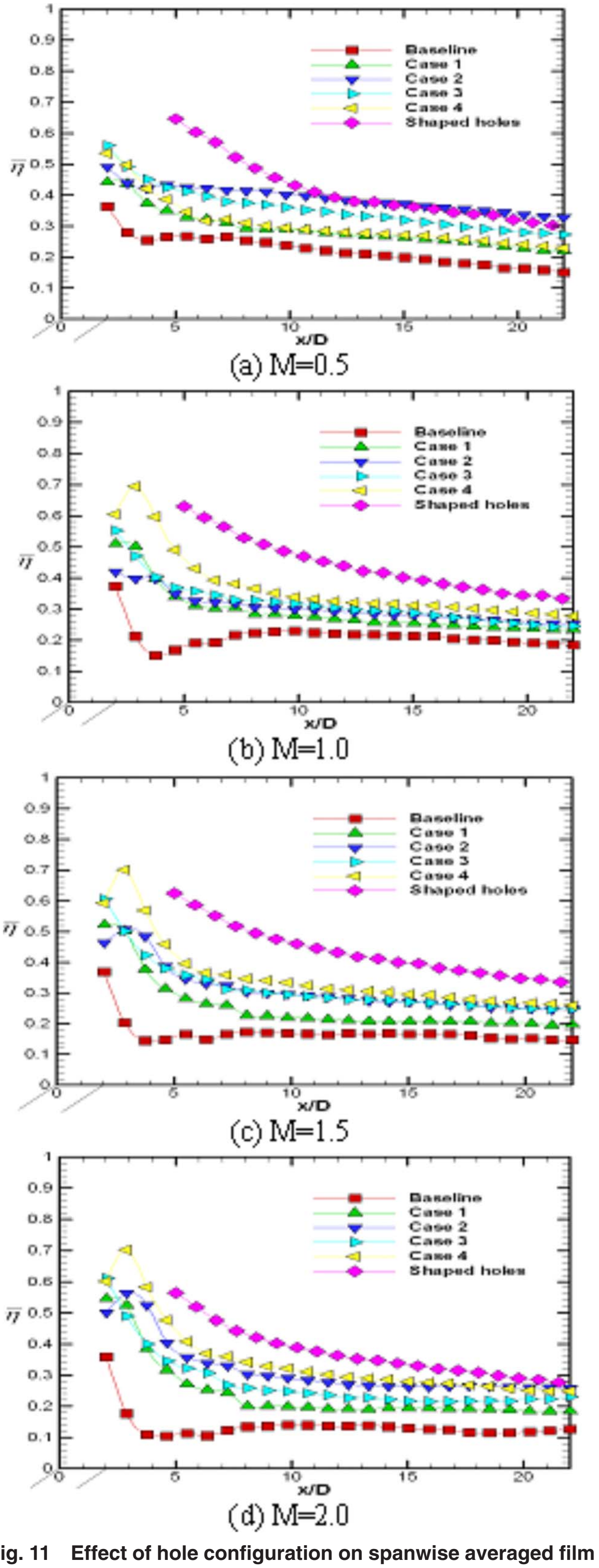

**Fig. 11 Effect of hole configuration on spanwise averaged film effectiveness distributions at each blowing ratio**

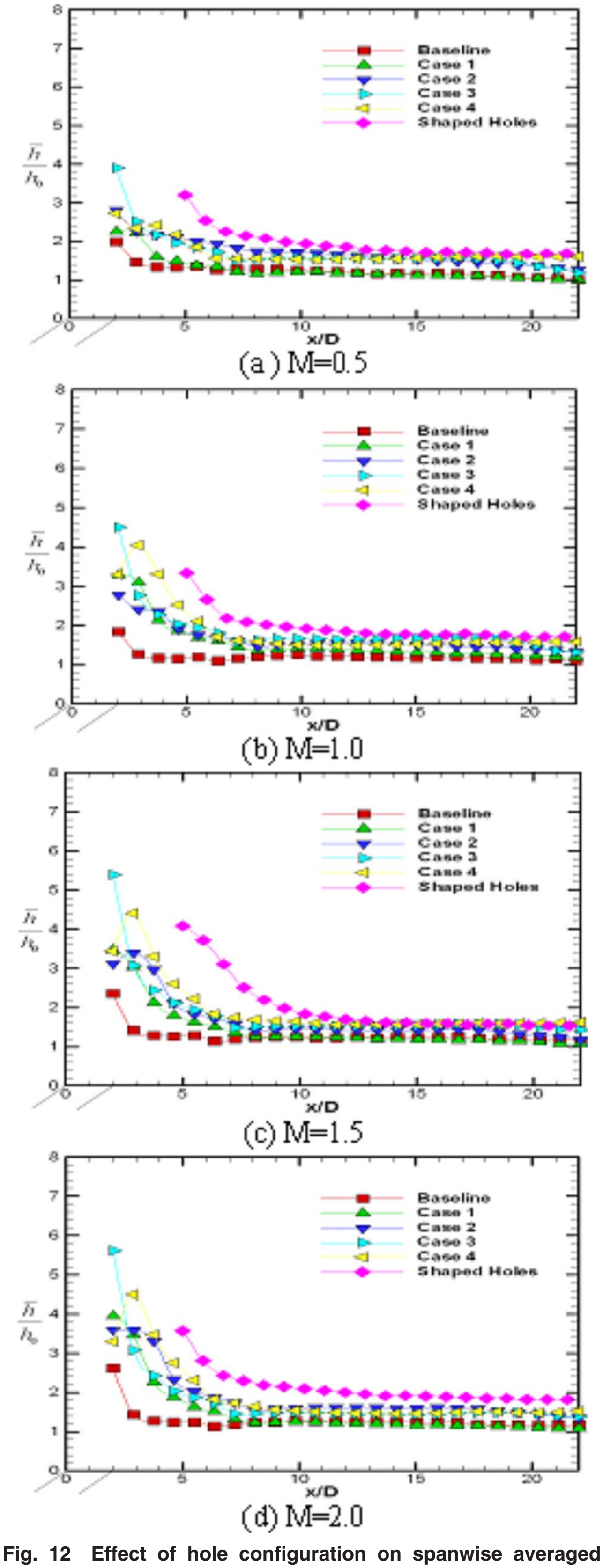

**Fig. 12 Effect of hole configuration on spanwise averaged heat transfer coefficient ratio distributions at each blowing ratio**

$t$ = time (s)
$T_c$ = coolant temperature (K)
$T_f$ = film temperature (K)
$T_i$ = test surface initial temperature (K)
$T_r$ = reference temperature (K)
$T_\infty$ = mainstream temperature (K)
Tu = freestream mean turbulence intensity (%)

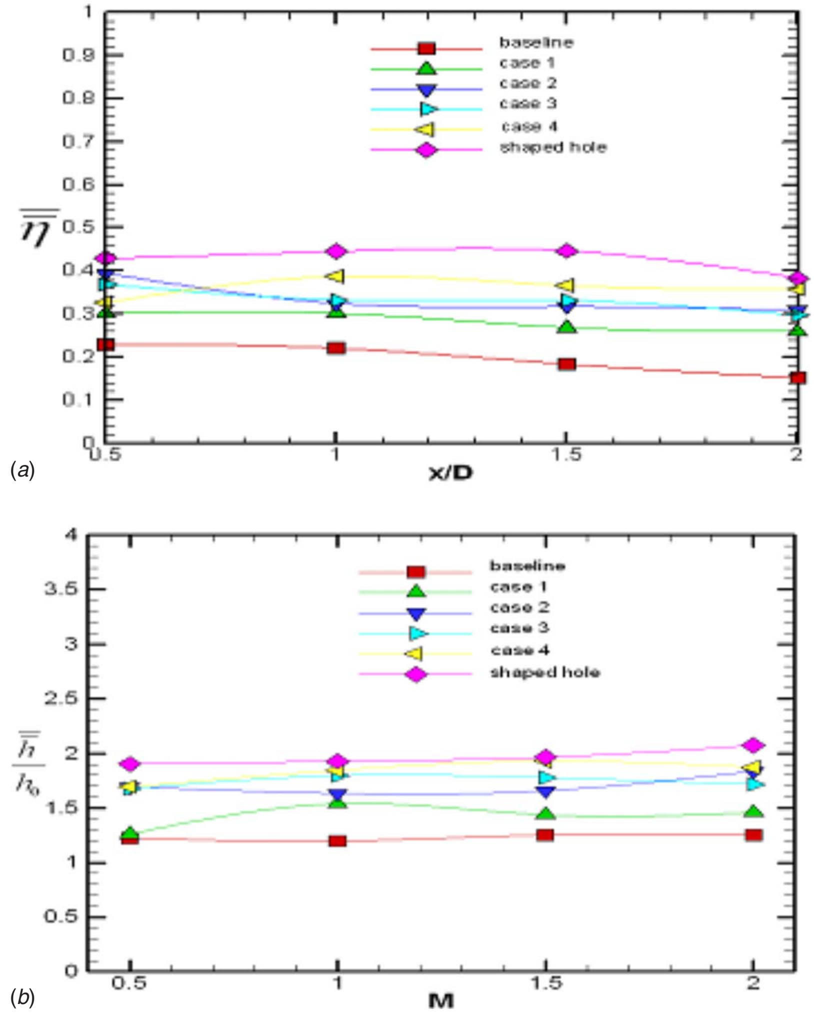

**Fig. 13 Effect of blowing ratio on overall area-averaged (*a*) film effectiveness and (*b*) heat transfer coefficient ratios for all cases**

$T_w$ = local wall temperature (K)
$U_c$ = coolant velocity (m/s)

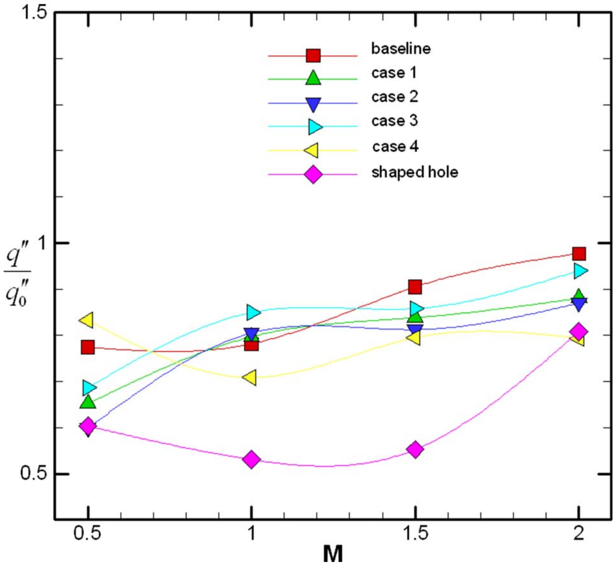

**Fig. 14 Effect of blowing ratio on the overall heat flux ratio for different cases**

$U_\infty$ = mainstream velocity (m/s)
$x$ = streamwise distance along the test plate (m)
$y$ = coordinate normal to surface (m)
$\eta$ = film cooling effectiveness
$\phi$ = nondimensional temperature$=(T_c-T_\infty)/(T_w-T_\infty)$
$\nu$ = kinematic viscosity of mainstream $(\mathrm{m}^2/\mathrm{s})$
$\alpha$ = thermal diffusivity $(\mathrm{m}^2/\mathrm{s})$
$\tau$ = time (s)

## References

[1] Fric, T. F., and Campbell, R. P., 2002, "Method for Improving the Cooling Effectiveness of a Gaseous Coolant Stream Which Flows Through a Substrate, and Related Articles of Manufacture," U.S. Patent No. 6,383,602.
[2] Bunker, R. S., 2002, "Film Cooling Effectiveness Due to Discrete Holes Within a Transverse Surface Slot," ASME Paper No GT-2002-30178.
[3] Wang, T., Chintalapati, S., Bunker, R. S., and Lee, C. P., 2000, "Jet Mixing in a Slot," Exp. Therm. Fluid Sci., **22**, pp. 1–17.
[4] Lu, Y., Nasir, H., and Ekkad, S. V., 2005, "Film Cooling From a Row of Holes Embedded in Transverse Slots," ASME Paper No. IGTI2005-68598.
[5] Lu, Y., and Ekkad, S. V., 2006, "Film Cooling Predictions for Cratered Cylindrical Holes," ASME Paper No. IMECE2006-14406.
[6] Vedula, R. J., and Metzger, D. E., 1991, "A Method for the Simultaneous Determination of Local Effectiveness and Heat Transfer Distributions in a Three Temperature Convective Situations," ASME Paper No. 91-GT-345.
[7] Ekkad, S. V., Ou, S., and Rivir, R. B., 2004, "A Transient Infrared Thermography Method for Simultaneous Film Cooling Effectiveness and Heat Transfer Coefficient Measurements From a Single Test," ASME J. Turbomach., **126**, pp. 546–553.
[8] Gillespie, D. R. H., Wang, Z., Ireland, P. T., and Kohler, S. T., 1996, "Full

Surface Local Heat Transfer Coefficient Measurements in a Model of an Integrally Cast Impingement Cooling Geometry," *Proceedings of the International Gas Turbine and Aeroengine Congress and Exhibition, June*, Birmingham, UK.

[9] Lu, Y., Dhungel, A., Ekkad, S. V., and Bunker, R. S., 2007, "Effect of Trench Width and Depth on Film Cooling From Cylindrical Holes Embedded in Trenches," ASME Paper No. GT2007-27388.

[10] Kline, S. J., and McClintock, F. A., 1953, "Describing Uncertainties in Single Sample Experiments," Mech. Eng. (Am. Soc. Mech. Eng.), **75**, pp. 3–8.

[11] Leylek, J. H., and Zerkle, R. D., 1994, "Discrete Jet Film Cooling: A Comparison of Computational Results With Experiments," ASME J. Turbomach., **116**, pp. 358–368.

[12] Ekkad, S. V., Zapata, D., and Han, J. C., 1997, "Film Effectiveness Over a Flat Surface With Air and $CO_2$ Injection Through Compound Angle Holes Using a Transient Liquid Crystal Image Method," ASME J. Turbomach., **119**(3), pp. 587–593.

**S. K. Krishnababu**[1]
Department of Engineering,
University of Cambridge
Cambridge CB2 1PZ, UK

**P. J. Newton**
Department of Mechanical Engineering,
University of Bath
Bath BA2 7AY, UK

**W. N. Dawes**
Department of Engineering,
University of Cambridge
Cambridge CB2 1PZ, UK

**G. D. Lock**
Department of Mechanical Engineering,
University of Bath
Bath BA2 7AY, UK

**H. P. Hodson**
Department of Engineering,
University of Cambridge
Cambridge CB2 1PZ, UK

**J. Hannis**
Siemens Industrial Turbomachinery Ltd.,
Lincoln LN5 7FD, UK

**C. Whitney**[2]
Alstom Power Technology Centre,
LN5 7SD, UK

# Aerothermal Investigations of Tip Leakage Flow in Axial Flow Turbines—Part I: Effect of Tip Geometry and Tip Clearance Gap

*A numerical study has been performed to investigate the effect of tip geometry on the tip leakage flow and heat transfer characteristics in unshrouded axial flow turbines. Base line flat tip geometry and squealer type geometries, namely, double squealer or cavity and suction-side squealer, were considered. The performances of the squealer geometries, in terms of the leakage mass flow and heat transfer to the tip, were compared with the flat tip at two different tip clearance gaps. The computations were performed using a single blade with periodic boundary conditions imposed along the boundaries in the pitchwise direction. Turbulence was modeled using three different models, namely, standard k-ε, low Re k-ω, and shear stress transport (SST) k-ω, in order to assess the capability of the models in correctly predicting the blade heat transfer. The heat transfer and static pressure distributions obtained using the SST k-ω model were found to be in close agreement with the experimental data. It was observed that compared to the other two geometries considered, the cavity tip is advantageous both from the aerodynamic and from the heat transfer perspectives by providing a decrease in the amount of leakage, and hence losses, and average heat transfer to the tip. In general, for a given geometry, the leakage mass flow and the heat transfer to the tip increased with increase in tip clearance gap. Part II of this paper examines the effect of relative casing motion on the flow and heat transfer characteristics of tip leakage flow. In Part III of this paper the effect of coolant injection on the flow and heat transfer characteristics of tip leakage flow is presented.*
[DOI: 10.1115/1.2950068]

## Introduction

In unshrouded axial turbines, clearance gaps between the rotor blades and the stationary shroud are necessary to prevent the physical rubbing between them. The pressure difference between the pressure and the suction sides of the blade causes an undesirable leakage of fluid through the clearance gap, see Fig. 1. This affects the stage performance. Typically a clearance of 1% of blade span causes 1–2% of primary flow to leak and hence a loss of 1–3% on stage efficiency [1].

There are two distinct aspects of tip leakage flows [2]. First, as the flow passes through the tip gap without being properly turned, there is a reduction in work done and second, due to mixing, there is generation of entropy within the gap, in the blade passage, and downstream of the blade row. Apart from these losses, the rapid acceleration of hot mainstream flows into the tip gap followed by the separation and reattachment of the hot gas on the tip results in high heat transfer to the tip. This high heat transfer to the tip together with that to the suction and pressure side of the blade must be removed by the blade internal and external cooling flows. The compressor supplies this cooling flow, which imposes a further penalty on the engine performance. Hence considerable research has been done to understand and quantify the losses and the heat transfer associated with the tip leakage flows.

A review of research quantifying the losses and heat transfer associated with tip clearance flow is provided by Bunker [3]. Much of the early work used idealized models, e.g., Kim and Metzger [4], Chen et al. [5], and, more recently, Krishnababu et al. [6]. Using linear cascades, Bunker et al. [7] measured heat transfer for sharp and radiused-edged blades for different clearance gaps; Kwak and Han [8,9] used the transient liquid crystal technique and Jin and Goldstein [10] the naphthalene technique to determine the effects of clearance gap, turbulence intensity, and Reynolds number on the mass/heat transfer from the tip and near-tip surfaces.

In recent years, three-dimensional numerical simulation of flow and heat transfer of tip leakage flow past blades with flat and squealer tip geometries has been reported. Ameri et al. [11] performed a three-dimensional numerical simulation of flow and heat transfer over a turbine blade with cavity tip. Turbulence was modeled using the $k$-$\omega$ turbulence model. The provision of cavity was found to reduce the mass flow rate through the tip gap by as much as 14%. However, only a meager change in efficiency was noticed. This was reported to be due to the increase in heat transfer to the blade in the case of the cavity tip as compared to the case of the flat tip. Ameri and Bunker [12] performed a numerical simulation to investigate the distribution of heat transfer coefficient on the tip of flat and radiused edge blades. The results using the radiused edge tip agreed better with their experimental data [7]. This improved agreement was attributed to the absence of edge separation on the tip of the radiused edge blade. Yang et al. [13,14] performed a numerical study of tip leakage flow and heat transfer past a turbine blade for three different tip gaps. They

---

[1] Present address: VUTC, Department of Mechanical Engineering, Imperial College, London, UK.

[2] Present address: E.O.N UK, Power Technology, Radcliffe-on-Soar, Nottingham, UK.

Contributed by the International Gas Turbine Institute of ASME for publication in the Journal of Turbomachinery. Manuscript received June 30, 2007; final manuscript received January 4, 2008; published online October 3, 2008. Review conducted by David Wisler. Paper presented at the ASME Turbo Expo 2007: Land, Sea and Air (GT2007), Montreal, Quebec, Canada, May 14–17, 2007.

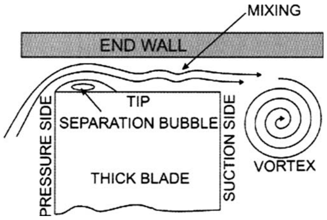

**Fig. 1 A schematic of tip leakage flow**

compared the performance of the cavity tip with that of the flat tip. Acharya et al. [15] and Saha et al. [16] investigated the flow and heat transfer characteristics of tip leakage flow using different tip gap geometries. Of all the geometries they considered, the lowest mass flow rates and tip heat transfer coefficients were obtained in the case of the suction-side squealer geometry followed by the cavity geometry. Mumic et al. [17] studied the aerothermal performance of flat and cavity geometries at three different tip gaps. Both in the case of the flat tip and cavity tip, the overall heat transfer to the tip and the leakage mass flow rate increased with an increase in tip gap height. Compared to the flat tip, the overall heat transfer to the cavity tip was found to be lower.

In this paper, a numerical investigation that was carried out to study the flow and heat transfer in the tip region of flat and squealer type geometries is reported. The performances of the squealer geometries (double squealer or cavity and suction-side squealer) in terms of the leakage mass flow and heat transfer to the tip were compared with the flat tip at two different tip clearance gaps (1.6%C and 2.8%C). The computational code used is validated using the experimental data from Newton et al. [18]. The heat transfer experiments were performed on a polycarbonate replica of the cascade blades. In the experiments hot mainstream flow was generated using an upstream wire mesh. Heat transfer was measured using thermochromic liquid crystal (TLC). The method of analysis is explained by Newton et al. [18]. It was found that the cavity tip is advantageous both from the aerodynamic and from the heat transfer perspectives by providing a decrease in the amount of leakage, and hence losses and average heat transfer to the tip. In Part II of this paper the effect of relative casing motion on the flow and heat transfer characteristics of tip leakage flow is investigated. In Part III of this paper the effect of coolant injection on the flow and heat transfer characteristics of tip leakage flow is presented.

## Computational Details

The simulations reported in this investigation were performed using CFX 5.6 [19], a commercially available computational fluid dynamics (CFD) solver. The solutions were obtained by solving the Navier–Stokes equations using a finite-volume method to discretize the equations. Structured meshes generated using the commercial mesh generation program ICEM-HEXA were used. The computations were performed using a single blade with periodic boundary conditions imposed along the boundaries in the pitchwise direction. The computational domain of a flat tip blade with a clearance gap of 1.6%C is shown in Fig. 2. The grids were clustered in the tip gap region and toward the pressure and suction surfaces of the blade. At the inlet, which is placed at half a chord upstream of the leading edge, total temperature and total pressure were specified. The inlet flow angle is 32.5 deg. At the exit, which is placed at a distance equal to a chord downstream of the trailing edge, static pressure was specified. The flow conditions correspond to an exit Reynolds number of $2.3\times10^5$, which is the same as that in the experiments. The flow is incompressible. No-slip isothermal wall conditions (wall temperature being 94% of inlet total temperature) were imposed on the blade and the casing. The hub located far away from the tip was inviscid with adiabatic conditions imposed. The salient features of the cascade are shown in Table 1.

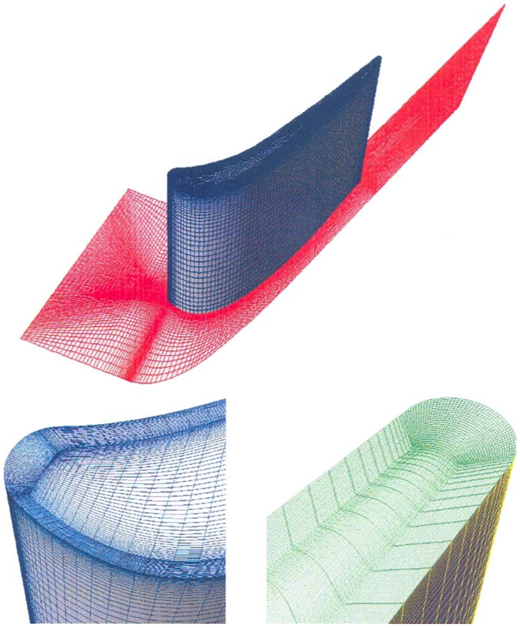

**Fig. 2 Computational domain with a typical mesh superimposed**

The grid independence test was carried out by computing the flow past a flat tip blade with a clearance of 1.6%C. Three different meshes, namely, G1–G3, were considered. Average $Y^+$ values on the tip, number of cells across the tip gap, and total number of cells for the three meshes considered are given in Table 2.

The contours of heat transfer coefficient on the tip obtained by the computations performed using Meshes G1–G3 are shown in Figs. 3(*b*)–3(*d*), respectively. Since the flow is incompressible the heat transfer coefficient is defined as $q_w=h(T_{o\ \mathrm{in}}-T_w)$. The experimental distribution is shown in Fig. 3(*a*) for comparison. The differences between the solutions obtained using the three meshes considered are seen to be small. The computed contours are in close agreement with the experimental contour. The comparison of the computed contours with the experimental contour shows that a continuous region of high heat transfer marked A in Fig. 3(*a*) is rather broken near the midchord region in all the computed contours. A ridge of high heat transfer near the leading edge

**Table 1 Cascade properties [18]**

| | |
|---|---|
| No. of blades | 5 |
| Chord, $C$ | 225 mm |
| Axial chord, $C_x$ | 103 mm |
| Pitch/chord ratio, $s/C$ | 0.824 |
| Aspect Ratio | 2.11 |
| Stage exit $\mathrm{Re}_c$ | $2.3\times10^5$ |
| Inlet flow angle, $\alpha_1$ | 32.5 deg |
| Blade exit angle, $\alpha_2$ | 75.6 deg |
| Practical tip clearance,%C | 1.6–2.8 |

**Table 2 Mesh details: flat tip blade ($H/C=1.6\%$)**

| Mesh | Average $Y^+$ on tip | No. of cells across the tip | Total No. of cells (million) |
|---|---|---|---|
| G1 | 4.37 | 25 | 2.2 |
| G2 | 2.26 | 35 | 2.8 |
| G3 | 1.15 | 40 | 2.5 |

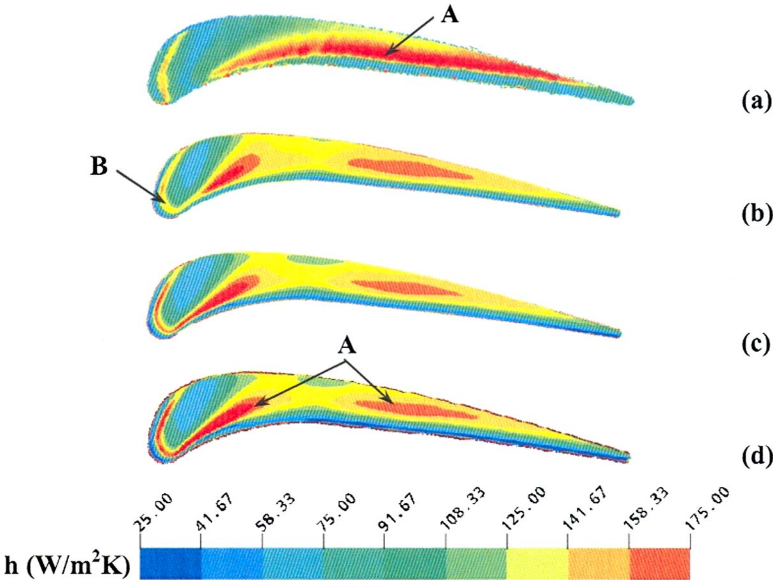

**Fig. 3 Grid independence study: contours of heat transfer coefficient on flat tip with *H/C* of 1.6%: (*a*) experiment, (*b*) G1, (*c*) G2, and (*d*) G3 using SST *k*-*ω***

marked B and the high heat transfer region A are connected in the computed contours, whereas they are separated by a region of low heat transfer in the experimental contours. It is also seen that the computations overpredict the heat transfer near the leading edge and underpredict it elsewhere. A description of this inaccuracy associated with the computation is provided in the next section. Comparing the contours obtained using the three meshes it is seen that the differences between the solutions obtained using G2 and G3 are the smallest. The average values of heat transfer coefficient on the tip as obtained by the computations using the three meshes and the experiment are given in Table 3. It is seen that, on average, the computations underpredict the heat transfer to the tip by 5–10%. It is also seen that the differences in the average values obtained using G2 and G3 are smaller. Hence further comparisons with the experiments are made using the solutions obtained on the coarser mesh G2.

The blade loading at midspan, for the flat tip geometry, obtained by the computations using G2 and the experiment are shown in Fig. 4. The quantity plotted is the coefficient of pressure $C_p=(P_{o\ \mathrm{in}}-p)/(P_{o\ \mathrm{in}}-p_{\mathrm{exit}})$. The computed distribution is seen to agree closely with the experimental distribution.

The computations reported above were performed using the shear stress transport (SST) *k*-*ω* model of Menter [20], which encompasses the low Reynolds number *k*-*ω* model and the *k*-*ε* model, with the original low Reynolds number *k*-*ω* model activated near the wall and the standard *k*-*ε* model activated away from the wall. However, in order to assess the capability of the models to correctly predict the blade heat transfer, additional computations were performed using the standard *k*-*ε* model and the *k*-*ω* model. Automatic wall functions [21], which shift gradually between a low Reynolds number formulation and wall functions based on the grid density, were used in the case of *k*-*ω* and the SST *k*-*ω* models, whereas a standard wall function was used in the case of the computations performed with *k*-*ε* model. An upper limit on the production of turbulent kinetic energy was imposed in the case of all the three turbulence models used [19].

The contours of heat transfer coefficient on the tip obtained using the three models are shown in Fig. 5. From the figure it is seen that, compared to the case of other two models, the heat transfer to the tip is significantly higher in the case of the computation using *k*-*ε* model. The levels of heat transfer predicted by the other two models are in close agreement with each other. However, compared to Fig. 5(*c*), in Fig. 5(*b*) the high heat transfer region marked A occurs closer to the suction-side edge. This shows that the *k*-*ω* model predicts a larger separated region compared to the SST *k*-*ω* model.

The average values of heat transfer to the tip, as predicted by the three models, are compared in Table 4. Comparing the values obtained using Mesh G2, it is seen that the *k*-*ε* model overpredicts the average value by nearly 50%, the *k*-*ω* model underpredicts it by nearly 20%, and the SST *k*-*ω* model underpredicts by nearly 10%. A similar overprediction of heat transfer by the *k*-*ε* model was also noticed by Krishnababu et al. [6]. The differences in the levels of heat transfer predicted by these three models can be

**Table 3 Average *h* on tip: flat tip blade (*H/C*=1.6%)**

| | Average $h$ (W/m$^2$ K) | |
|---|---|---|
| Mesh | Expt. | CFD |
| G1 | 110.4 | 106.2 |
| G2 | — | 100.2 |
| G3 | — | 100.5 |

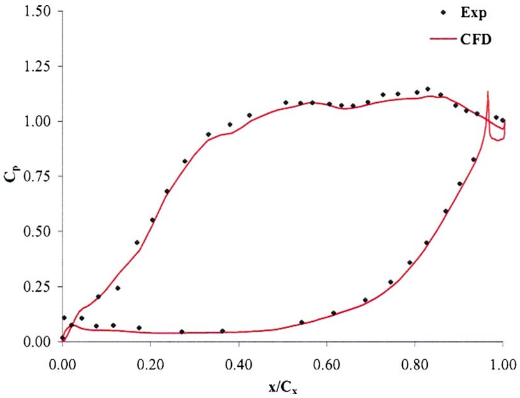

**Fig. 4 Blade loading at midspan: flat tip (*H/C*=1.6%)**

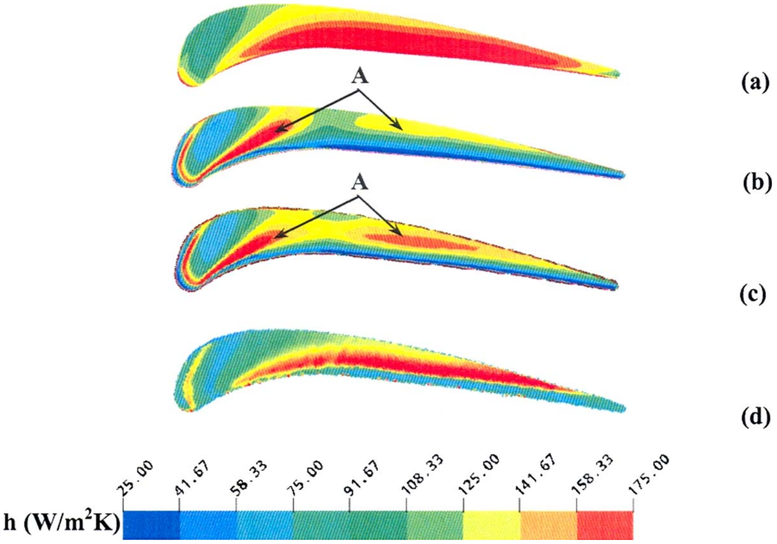

**Fig. 5 Dependence of *h* on turbulence model: contours of *h* on flat tip with *H/C* of 1.6% as predicted by (*a*) *k*-$\varepsilon$, (*b*) *k*-$\omega$, (*c*) SST *k*-$\omega$ models, and (*d*) experiment**

explained with the help of the contours of turbulent kinetic energy ($k$) values of the first grid point from the tip (Fig. 6). It is seen that compared to the other two models the $k$-$\varepsilon$ model predicts very large values of $k$. In Table 4, also it is seen that the average value of $k$ in the first grid point from the tip, obtained in the case of the $k$-$\varepsilon$ model, is approximately 25 times larger than that obtained in the case of the $k$-$\omega$ model. The overprediction of heat transfer coefficient by the $k$-$\varepsilon$ model is linked to these large values of $k$ [6]. The levels of $k$ predicted by the other two models are comparable and hence the heat transfer coefficient predicted by these models. From now on, unless specified, all the computational plots and contours presented are those obtained using the SST $k$-$\omega$ model on Mesh G2.

**Table 4 Dependence of *h* on the turbulence models: flat tip blade (*H/C*=1.6%)**

| | Average $h$ (W/m$^2$ K) | | | | Average $k$ (m$^2$/s$^2$) on tip | | |
|---|---|---|---|---|---|---|---|
| Mesh | Expt. | $k$-$\varepsilon$ | $k$-$\omega$ | SST $k$-$\omega$ | $k$-$\varepsilon$ | $k$-$\omega$ | SST $k$-$\omega$ |
| G1 | 110.4 | — | 98.7 | 106.2 | — | 0.13 | 0.26 |
| G2 | — | 145.1 | 89.4 | 100.2 | 2.83 | 0.10 | 0.21 |
| G3 | — | — | 86.5 | 100.5 | — | 0.08 | 0.18 |

## Investigation of Tip Leakage Flow

**Flat Tip.** The computed flow patterns at the two tip gaps of 1.6%C and 2.8%C considered are shown in Figs. 7(*a*) and 7(*b*), where streamlines crossing the tip, colored by the flow velocity, are presented. At both the clearance gaps considered, a horseshoe vortex is formed on the tip near the leading edge. The pressure side arm of this vortex moves from the leading-edge region toward the trailing edge along the chord staying closer to the pressure side edge of the tip. The suction-side arm moves along the suction-side edge and exits the tip gap at a distance of about 10% of axial chord from the leading edge in an almost axial direction. This flow, on exiting the tip gap, shears with the mainstream flow and forms the tip leakage vortex (marked in Fig. 7). The strength

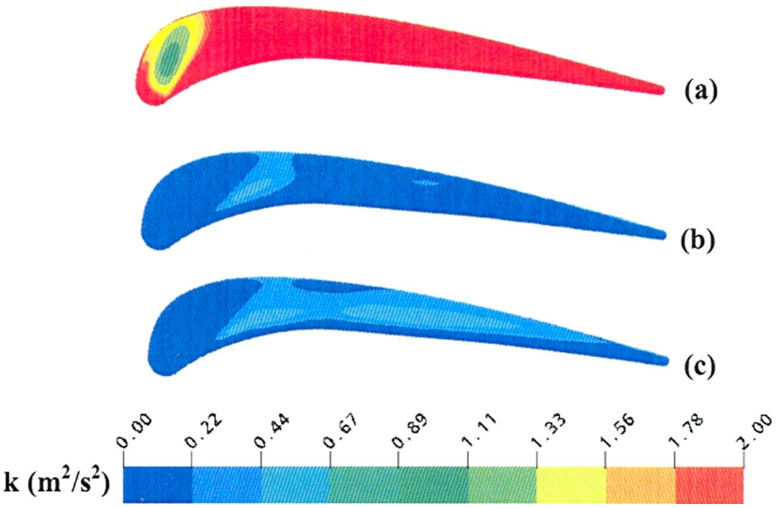

**Fig. 6 Contours of turbulence kinetic energy on flat tip with *H/C* of 1.6% as predicted by (*a*) *k*-$\varepsilon$, (*b*) *k*-$\omega$, and (*c*) SST *k*-$\omega$ models using Mesh G2**

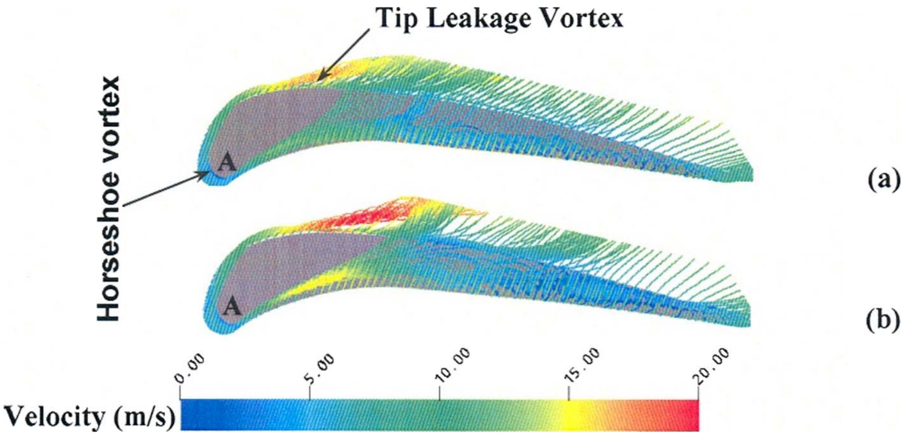

Fig. 7 Flow pattern across tip using SST $k$-$\omega$ model: flat tip with $H/C$ of (*a*) 1.6% and (*b*) 2.8%

of the tip leakage vortex is higher at higher clearance gap. High heat transfer coefficients are expected in the regions immediately downstream of the two arms of the horseshoe vortex due to flow reattachment. Figure 7 also shows that, at the higher clearance gap, the pressure side arm of the horseshoe vortex moves away from the pressure side edge closer to the tip gap exit.

Figures 8(*a*) and 8(*b*) show the contours of the pressure coefficient, $C_p$, on the tip at both the clearance gaps considered. In the region $0.2 < x/C_x < 0.9$, high values of $C_p$ (or low values of pressure) are noticed. This is associated with the flow separation from the pressure side edge and located underneath the pressure side arm of the horseshoe vortex, as shown in Fig. 7. This low pressure region is observed to be larger in the computed distribution (compared to the experimental distribution) at both the clearance gaps. The flow subsequently reattaches on the tip surface and then decelerates before reaching the suction surface. It is also evident that with a larger clearance gap, the region of separation increases in size. A region of relatively low $C_p$ is observed near the leading edge of the blade tip, $x/C_x < 0.2$, where there is less pressure differential to drive flow across the gap.

In Figs. 9(*a*) and 9(*b*) the contours of the heat transfer coefficient on the tip at the two clearance gaps considered are shown. It is observed that the maximum heat transfer coefficient occurs in the region of reattachment on the blade tip (region marked A in Figs. 9(*a*) and 9(*b*). This region is more extensive for the larger tip gap. A ridge of high heat transfer is observed near the leading edge of the blade (marked B in Figs. 9(*a*) and 9(*b*)) where the flow, which is driven into the tip gap by high pressure existing near the stagnation point of the blade, separates and then reattaches (see A in Figs. 7(*a*) and 7(*b*)). Generally there is low heat transfer in the leading-edge region (marked C in Figs. 9(*a*) and 9(*b*)) where there is less pressure difference to drive flow across the gap. In the computations the location of peak heat transfer coefficient occurs further toward the suction side of the blade. This is due to the larger separated region predicted by the computations, as was noticed previously from the distribution of $C_p$ on the tip. In CFX 5.6, a limiter is imposed on the production of turbulent kinetic energy in all the SST $k$-$\omega$ model simulations to eliminate the excessive unphysical production of $k$ in the stagnation regions. This limiter is similar to the production limiter used in the $k$-$\omega$ model simulation by Krishnababu et al. [6]. The larger size of the separation bubble and the underprediction of the heat transfer coefficient are thus believed to be due to possible excessive clipping on the overproduction of turbulent kinetic energy. The average value of heat transfer to the tip as obtained by the experiments and the computations for the two tip gaps is shown in Table 5. It is seen that while the experiment shows an increase, the computations show a decrease, although close to 1%, in the value

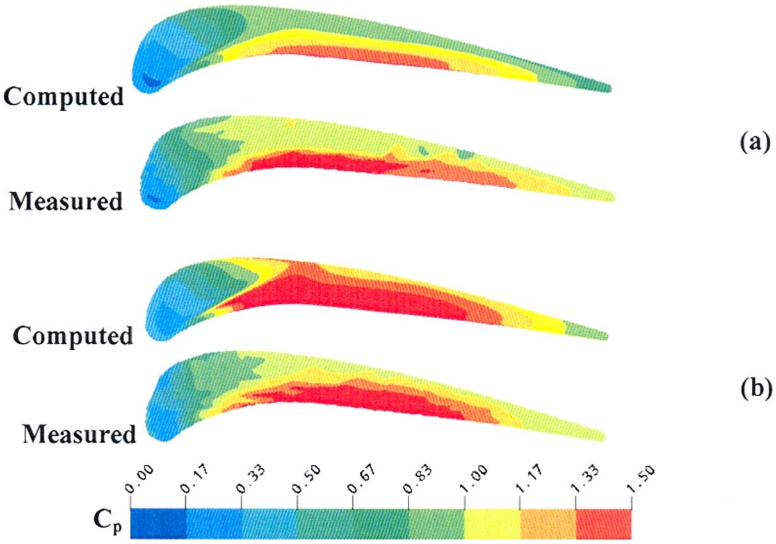

Fig. 8 Contours of $C_p$ on tip: flat tip with $H/C$ of (*a*) 1.6% and (*b*) 2.8%

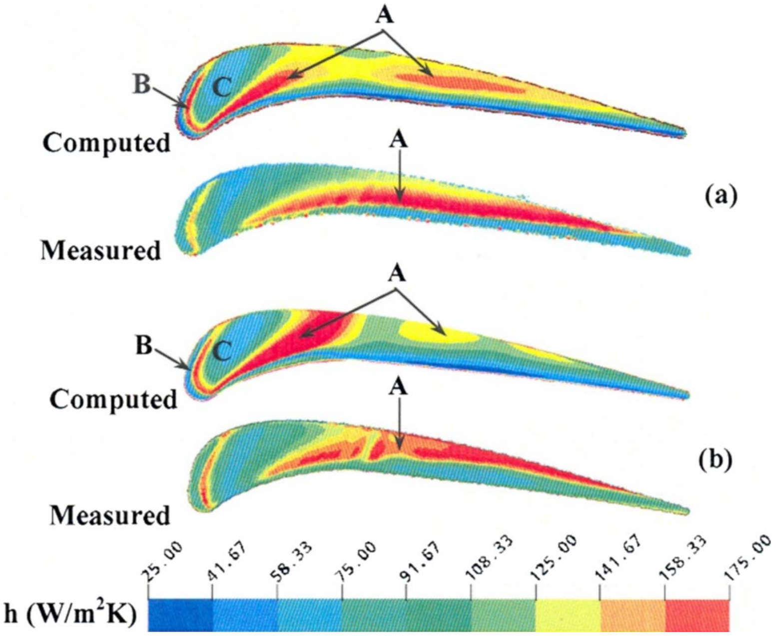

**Fig. 9** Contours of *h* on tip: flat tip with *H*/*C* of (*a*) 1.6% and (*b*) 2.8%

of average heat transfer to the tip at higher tip gap. Previous investigators, namely, Yang et al. [13], Mumic et al. [17], and Azad et al. [22], observed an increase in heat transfer to the tip with increase in tip gap height. While the present experimental data are in agreement with the observation made by the previous investigators the computed data do not agree. The discrepancy in the computed data is due to the overprediction of the size of the separated region. The larger separated region causes the peak heat transfer to occur further downstream and closer to the suction-side edge. This means that the actual metal area available for heat transfer downstream of reattachment is smaller in the computation compared to that in the experiment. This in turn implies a reduction in the extent of the high heat transfer region downstream of the peak heat transfer and hence the average value. This is more pronounced in the regions near the trailing edge.

Figures 10(*a*) and 10(*b*) show the computed contours of heat transfer coefficient on the tip, suction side, and pressure side of the blade for the two clearance gaps considered. On the pressure surface of the blade the distribution of heat transfer coefficient is largely two dimensional except for the region in the vicinity of the tip (approximately six times the height of tip gap), which is affected by the flow accelerating into the tip gap from the pressure side. On the suction side of the blade the footprint of the leakage vortex is visible as a region of higher *h*. The extent of the high heat transfer region on the suction surface is higher at the higher clearance gap. This is caused by the increase in mass flow leaking through the tip gap.

**Cavity Tip.** The computational domain for the case of a cavity tip is shown in Fig. 11. The depth of the cavity, $H_{sq}$, is 1.35*H* for both the tip gaps. The cavity and suction-side squealer geometries were designed in consultation with Siemens and Alstom. The flow patterns across the tip for the two tip gaps considered are shown in Figs. 12(*a*) and 12(*b*), where streamlines crossing the tip colored by the flow velocity are presented. At both the clearance gaps considered, unlike in the case of the flat tip, two horseshoe vortices are formed, one on the top of the squealer (marked V1) and one on the cavity floor (marked V2). The pressure side arm of the vortex, V1, moves on the top of the pressure side squealer from the leading-edge region toward the trailing edge. A part of this vortex flows into the cavity (near point marked A1) and interacts with the pressure side arm of V2. The combination then moves across the blade and impinges on the suction-side squealer (near point marked A2). A part of this combination leaves the tip gap near the region of impingement and the remaining moves (staying closer to the suction-side squealer) toward the trailing edge from where it exits the tip gap. Another part of the pressure side arm of V1 flows into the cavity near Point B and travels cross chord toward the suction side and then exits the tip gap near the midchord region. The suction-side arm of V1 moves along the suction-side edge on the squealer and interacts with the suction-side arm of V2 near Point C from where it exits the tip gap in an almost axial direction. This flow, on exiting the tip gap, shears with the mainstream flow and forms the tip leakage vortex (as marked in Fig. 12). The strength of the tip leakage vortex is higher at higher clearance gap. At both of the clearance gaps considered, although, the flow separates off the pressure side corner of the tip, generally, there is no subsequent reattachment prior to reaching the suction-side squealer.

The computed contours of $C_p$ on the tip at both of the clearance gaps are shown in Fig. 13. Relatively lower values of $C_p$ are noticed in the latter two-thirds part of the cavity along the chord. Lower heat transfer coefficients are expected in this region due to the existence of low velocity. A high pressure/low $C_p$ region is observed near the leading edge of the cavity (marked E in Fig. 13). This corresponds to the location of flow impingement on the cavity floor. Higher values of $C_p$ are noticed in the regions underneath the arms of the horseshoe vortices V1 and V2.

In Figures 14(*a*) and 14(*b*) the contours of the heat transfer coefficient on the tip at clearance gaps of 1.6%C and 2.8%C are shown. High heat transfer coefficients occur in the regions of flow impingement on the top of the squealer and on the cavity floor (corresponding to regions marked D–H in Figs. 12(*a*) and 12(*b*). Generally there is low heat transfer in the trailing edge regions

**Table 5** Average *h* on flat tip: effect of tip gap height (mesh G2 using SST *k*-*ω* model)

| *H*/*C* (%) | Average *h* (W/m² K) | |
|---|---|---|
| | Expt. | CFD |
| 1.6 | 110.4 | 100.2 |
| 2.8 | 122.8 | 98.8 |

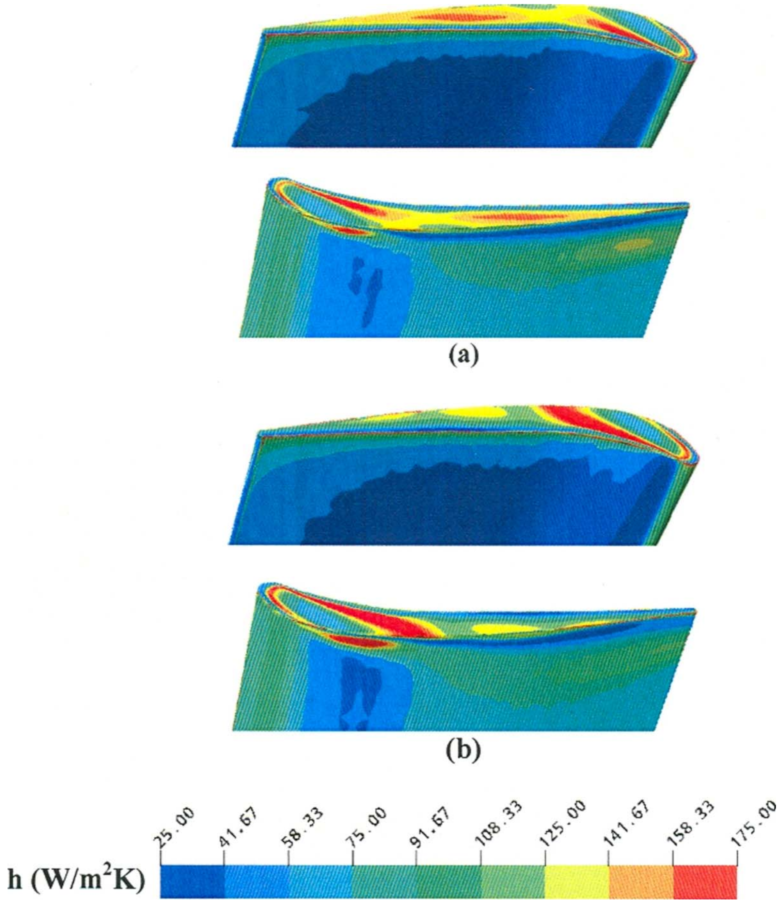

**Fig. 10 Contours of *h* on blade: flat tip with *H/C* of (*a*) 1.6% and (*b*) 2.8%—region near the tip**

where the flow velocities are lower. The computed distribution is in general in close agreement with the experimental distribution of heat transfer coefficients. However, in the leading-edge region closer to the pressure side (in the vicinity of H in Fig. 12) the heat transfer coefficients are overpredicted.

Compared to the case of flat tip, the cavity tip eliminated the peak in heat transfer associated with the reattachment of flow separated from the pressure side rim. However, high heat transfer coefficients are observed at positions on the squealers that corresponded to flow impingement. The average values of heat transfer to the tip as obtained by the experiments and the computations for the two tip gaps are shown in Table 6. Since the heat transfer to the squealer faces was not measured in the experiments, the average values reported in Table 6 are those obtained without including the heat transfer to the squealer faces in the averaging process. From Table 6 it is seen that there is not much change in average heat transfer to the tip with changes in tip clearance.

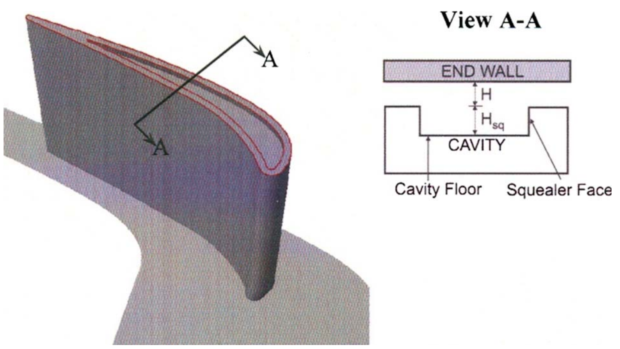

**Fig. 11 Computational domain: cavity tip**

Figures 15(*a*) and 15(*b*) show the computed contours of heat transfer coefficient on the tip and suction surface of the blade for the two clearance gaps considered. As observed in the case of the flat tip the distribution of heat transfer coefficient on the pressure side (not shown here) was also found to be two dimensional except for the region in the vicinity of the tip. The footprint of the leakage vortex is visible on the suction side of the blade as a region of higher $h$. Compared to the case of the flat tip (Figs. 10(*a*) and 10(*b*)) this region is observed to be smaller and closer to the tip at both the clearance gaps considered. This is caused by the decrease in mass flow leaking through the tip gap (see next section).

**Suction-Side Squealer Tip.** The computational domain of suction-side squealer tip considered is shown in Fig. 16. The height of the squealer ($H_{sq}$ is $1.35H$) is the same as that for the cavity tip for both the tip gaps. The flow patterns across the tip for the two tip gaps considered are shown in Figs. 17(*a*) and 17(*b*). The flow pattern shows a vortical structure with three arms (marked V1–V3) formed at the leading-edge stagnation region. The two suction-side arms V1 and V2 exit the tip gap near point marked A. They interact with each other and with the mainstream flow and form the tip leakage vortex. The pressure side arm V3 moves cross chord and impinges on the face of the squealer (near B) and then moves along the chord toward the trailing edge from where it exits the tip. In the vicinity of B, a part of the flow (arm V3) accelerates over the squealer, impinges on the top of the squealer (marked C), and then exits the tip gap. This flow, on

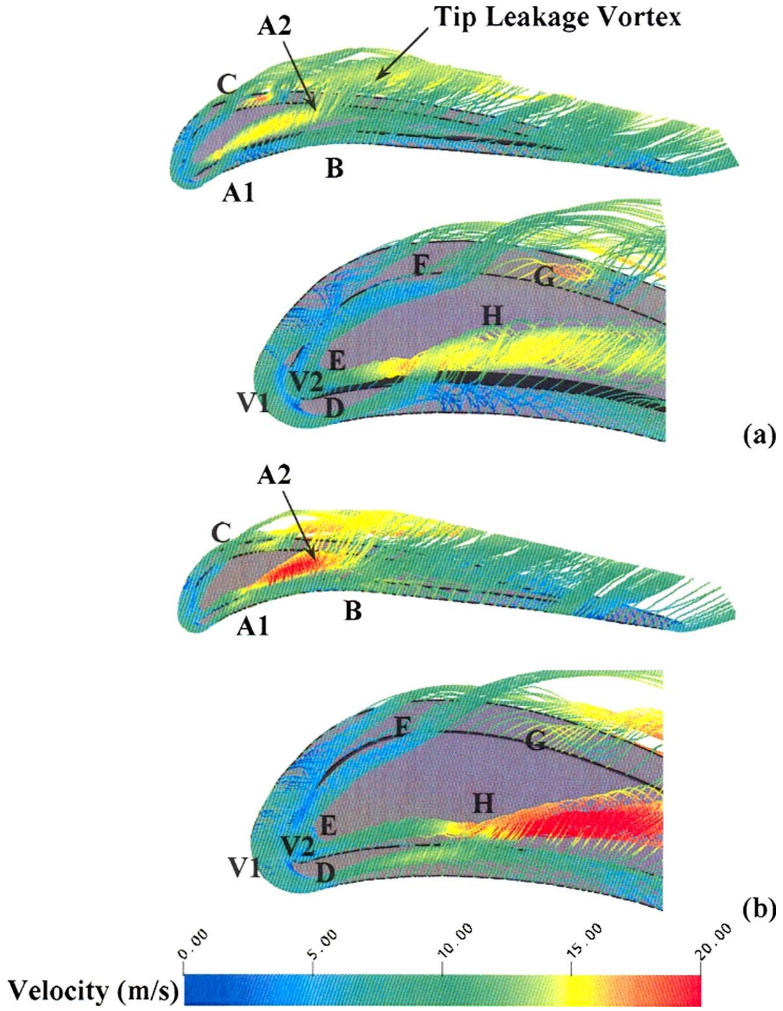

Fig. 12 Flow pattern across tip: cavity tip with *H*/*C* of (*a*) 1.6% and (*b*) 2.8%

exiting the tip gap, becomes part of the tip leakage vortex. Enhanced rates of heat transfer are expected at these locations of impingement (B and C). The vortices formed are more intense at the larger tip gap.

The computed contours of $C_p$ on the tip at the two clearance gaps considered are shown in Fig. 18. Relatively lower values of $C_p$ are noticed on the tip surface upstream of the squealer. Lower heat transfer coefficients are expected in this region due to the existence of low velocity. The region of high values of $C_p$ on the top of the squealer indicates the existence of low pressure, separated region.

In Figs. 19(*a*) and 19(*b*) the contours of the heat transfer coefficient on the tip at clearance gaps of 1.6%C and 2.8%C are shown. High heat transfer coefficients occur in the regions of flow impingement on the top of the squealer and on the tip surface upstream of the squealer (regions marked C–F in Figs. 17(*a*) and 17(*b*). The computed distribution of heat transfer coefficients is in general in close agreement with that obtained by the experiment. Low heat transfer coefficients are observed in the trailing edge regions due to low leakage flow velocities. Compared to the case

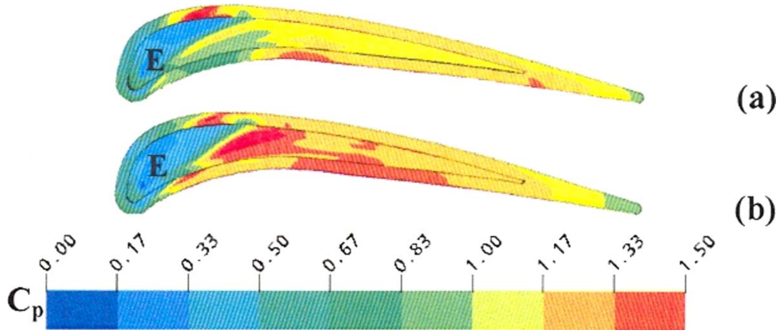

Fig. 13 Contours of $C_p$ on tip: cavity tip with *H*/*C* of (*a*) 1.6% and (*b*) 2.8%

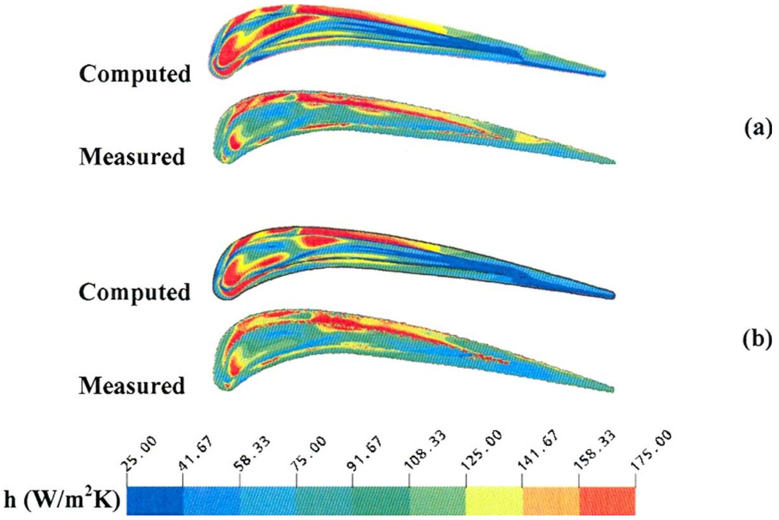

Fig. 14 Contours of $h$ on tip: cavity tip with $H/C$ of (*a*) 1.6% and (*b*) 2.8%

of the other two geometries considered, a considerable decrease in heat transfer to the tip is noticed from Fig. 19. This is indicated by the decrease in the amount of the red region and the average values of heat transfer to the tip shown in Table 7. Again the average values reported in Table 7 are those obtained without including the heat transfer to the squealer faces in the averaging process. Both the experiment and the computation show an increase in the average heat transfer to the tip at higher tip gap.

Figures 20(*a*) and 20(*b*) show the computed contours of heat transfer coefficient on the tip and suction surface of the blade at the two clearance gaps considered. As was observed in the case of the flat tip the distribution of heat transfer coefficient on the pressure side (not shown here) was also found to be two dimensional except for the region in the vicinity of the tip. The footprint of the leakage vortex is visible on the suction side of the blade as a region of higher $h$. Compared to the cases of the flat tip and cavity tip (Figs. 10 and 15) this region is observed to be larger and further away from the tip at both the clearance gaps considered. This is caused by an increase in mass flow leaking through the tip gap (see next section).

Table 6 Average $h$ on cavity tip: effect of tip gap height

| $H/C$ (%) | Average $h$ (W/m$^2$ K) | |
|---|---|---|
| | Expt. | CFD |
| 1.6 | 111.8 | 98.9 |
| 2.8 | 112.3 | 98.1 |

## Comparison of Tip Geometries

The contraction coefficient, $\sigma$ (=unblocked height available for leakage flow at the vena contracta/tip gap height), tip leakage mass flow as a percentage of inlet mass flow, and the area weighted average heat transfer to the tip in the case of the three geometries considered for the two tip clearance gaps are given in Tables 8 and 9. Area weighted average values are used to compare the different geometries as the total metal area exposed to the fluid changes with changes in geometry. The contraction coefficients presented are those obtained from the contours of total pressure loss coefficient ($Y_p$) such as that shown in Fig. 21.

From Tables 8 and 9, it is seen that for a given tip clearance gap, compared to the case of the flat tip, the leakage mass flow decreases in the case of the cavity tip and increases in the case of the suction-side squealer tip. Previous investigators, namely Yang et al. [13], Ameri et al. [11], Mumic et al. [17], and Azad et al. [22], have also noticed a similar reduction in leakage mass flow in the case of the cavity tip compared to that of the flat tip. Acharya et al. [15] and Kwak et al. [23] reported a decrease in leakage mass flow in the case of the suction side squealer compared to the

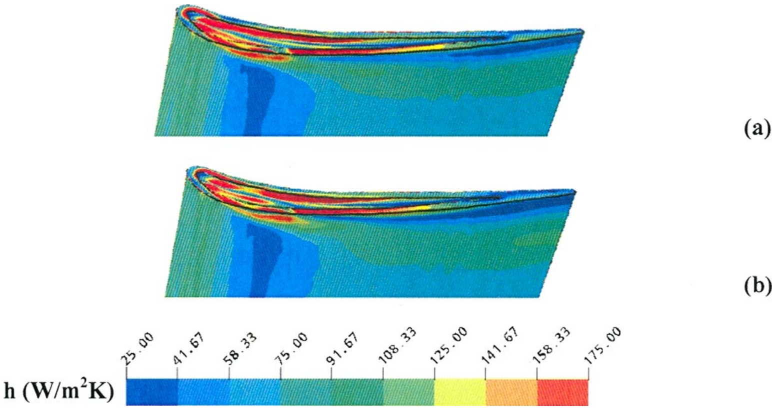

Fig. 15 Computed contours of $h$ on blade: cavity tip with $H/C$ of (*a*) 1.6% and (*b*) 2.8%—region near the tip

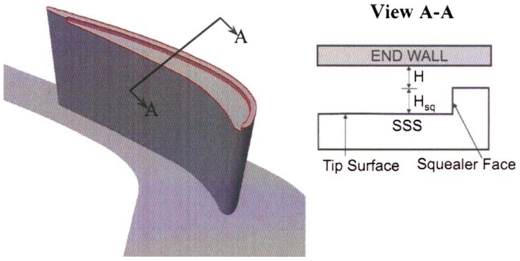

**Fig. 16 Computational domain: SSS tip**

flat tip, whereas, Heyes et al. [24] reported an increase in leakage mass flow in the case of the suction-side squealer. These discrepancies in relative aerodynamic performance of the suction-side squealer are due to the differences in the ratio of the thickness of the squealer to the local thickness of the blade among the different studies. The decrease in leakage mass flow (by 8% and 3%, respectively, at clearance gaps of 1.6%C and 2.8%C) in the case of the cavity tip is because the flow is blocked twice by the separation bubbles, once each on top of the two squealers. The increase in leakage mass flow (by 17% and 7%, respectively, at clearance

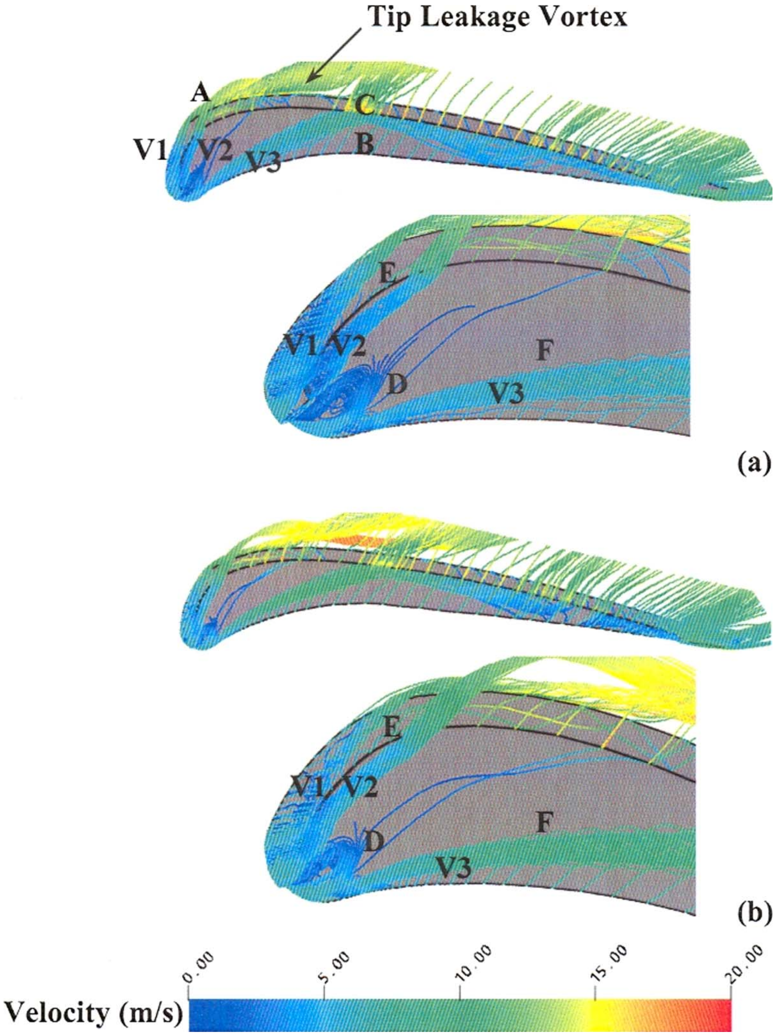

**Fig. 17 Flow pattern across tip: SSS tip with *H/C* of (*a*) 1.6% and (*b*) 2.8%**

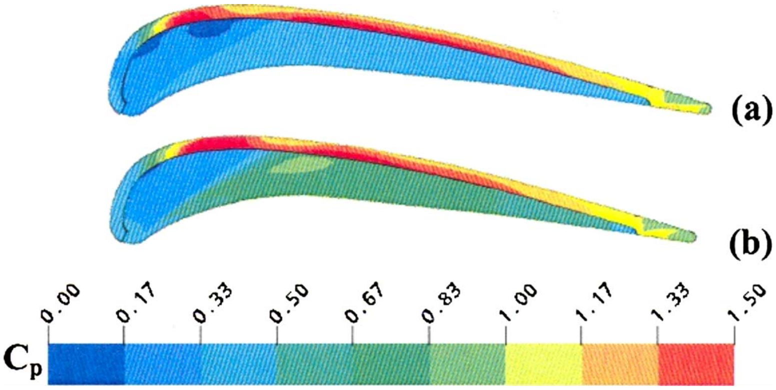

**Fig. 18 Contours of $C_p$ on tip: SSS tip with *H/C* of (*a*) 1.6% and (*b*) 2.8%C**

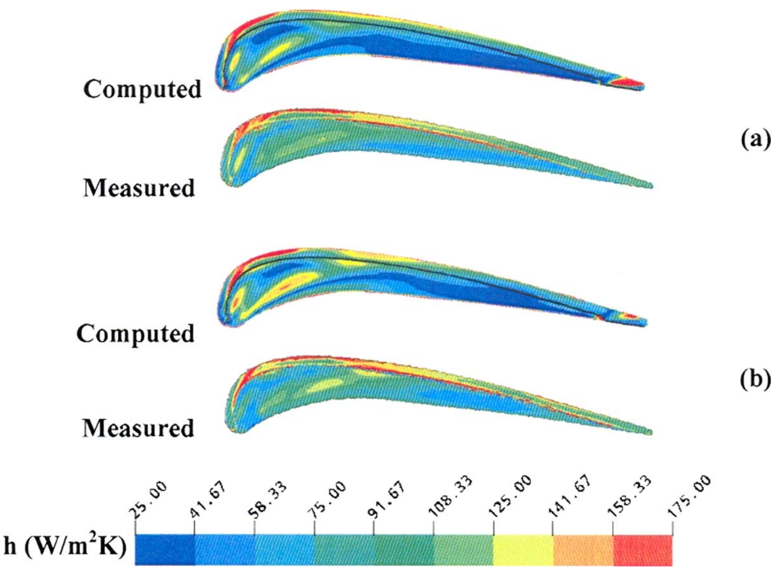

Fig. 19 Contours of *h* on tip: SSS tip with *H*/*C* of (*a*) 1.6% and (*b*) 2.8%

gaps of 1.6%C and 2.8%C) in the case of the suction-side squealer tip is due to the decrease in blockage as indicated by the larger values of the contraction coefficient compared to the case of the flat tip. The increase in leakage mass flow at higher tip clearance gap is due to the increase in the tip exit area and exit velocity. This ranking of tip geometries in terms of the leakage mass flow is in agreement with the ranking obtained using idealized models by Krishnababu et al. [6].

Tables 8 and 9 also show that for a given tip clearance gap, compared to the flat tip, the area weighted average heat transfer to the tip decreases in the case of both the squealer geometries considered. A similar decrease in average heat transfer to the tip in the case of the squealer geometries was also noticed by Ameri et al. [11], Yang et al. [13], Acharya et al. [15], Mumic et al. [17], Azad et al. [22], and Kwak et al. [23]. The decrease in area weighted average heat transfer to the tip (by 9% and 2%, respectively, at clearance gaps of 1.6%C and 2.8%C) in the case of cavity tip is due to the low values of heat transfer to the cavity floor. In the case of the suction-side squealer the decrease in area weighted average value (by 32% and 17%, respectively, at clearance gaps of 1.6%C and 2.8%C) is due to the low values of heat transfer to the tip surface upstream of the squealer caused by low flow velocities in these regions. Compared to the cavity, the suction-side squealer provides a larger decrease in the average value. This is due to comparatively lower heat transfer to the tip surface upstream of the squealer. Acharya et al. [15] and Kwak et al. [23] also reported the superior heat transfer performance of the suction-side squealer geometry compared to the cavity and flat tip.

Table 7 Average *h* on SSS tip: effect of tip gap height

| *H*/*C* (%) | Average *h* (W/m$^2$ K) | |
|---|---|---|
| | Expt. | CFD |
| 1.6 | 94.03 | 94.90 |
| 2.8 | 99.33 | 99.15 |

In contrast to the above observations, in the case of the investigation using idealized models ([6]) the average heat transfer had increased in the case of the cavity tip and decreased only marginally in the case of the suction-side squealer tip. This is because in the case of the idealized models the flow reattached on the top of the squealers and on the cavity floor (or tip surface upstream of the squealer in the case of suction-side squealer). In the case of the geometries considered in this investigation the flow in general does not reattach for most part of the squealers, thus reducing the

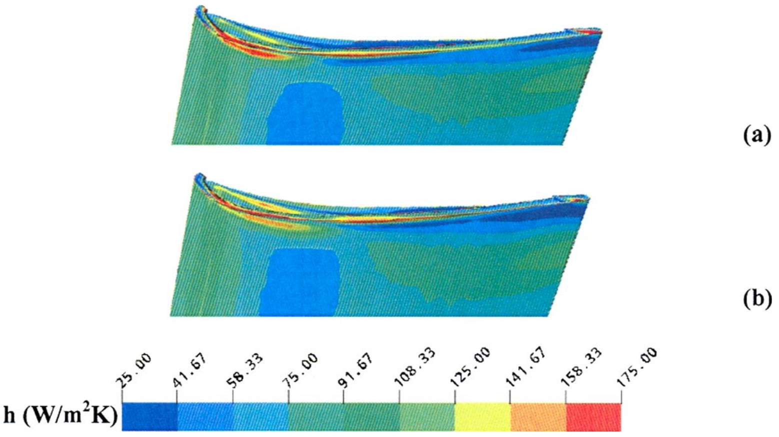

Fig. 20 Computed contours of *h* on blade: SSS tip with *H*/*C* of (*a*) 1.6% and (*b*) 2.8%—region near the tip

**Table 8  Effect of geometry: $H/C$ of 1.6%**

| Geometry | $\sigma$ PS | $\sigma$ SS | Leakage mass flow (% inlet) | Area weighted average $h$ on tip $(\mathrm{W/m^2\,K})$ |
|---|---|---|---|---|
| Flat | 0.56 | — | 2.81 | 116.7 |
| Cavity | 0.60 | 0.6 | 2.40 | 106.3 |
| SSS | — | 0.70 | 3.07 | 79.4 |

average heat transfer to the tip. Thus it can be said that the performance of the squealer geometries depends on the state of the separated flow, which in turn depends on the thickness of the squealer relative to the local thickness of the blade. In this case and in the case of practical industrial blades, the ratio of the thickness of the squealer to the local thickness of the blade varies widely along the chord. Thus it can be said that although the two-dimensional idealized models provide insight into the nature of flow field in the squealer geometries, from heat transfer perspective, they do not always provide the information needed to rank the tip gap geometries. The differences in relative aerodynamic performance of the suction-side squealer, between the data from the available literature and the present study, are also due to this phenomenon as the state of the separated flow defines the contraction on the top of the squealer and hence the leakage mass flow.

**Table 9  Effect of geometry: $H/C$ of 2.8%**

| Geometry | $\sigma$ PS | $\sigma$ SS | Leakage mass flow (% inlet) | Area weighted average $h$ on tip $(\mathrm{W/m^2K})$ |
|---|---|---|---|---|
| Flat | 0.60 | — | 4.26 | 109.7 |
| Cavity | 0.58 | 0.88 | 4.13 | 107.5 |
| SSS | — | 0.79 | 4.59 | 91.1 |

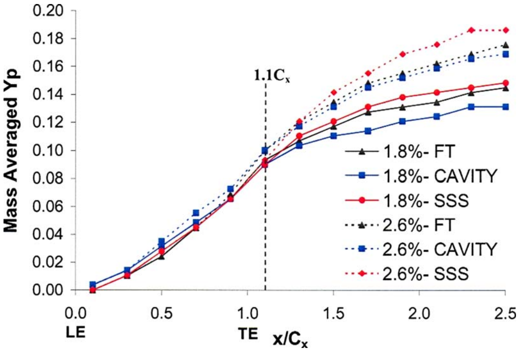

**Fig. 22  Variation of mass averaged $Y_p$ along the axial direction**

From Tables 8 and 9, it is seen that an increase in the tip clearance gap decreases the area weighted average heat transfer in the case of the flat tip and increases in the case of the cavity (although marginal) and suction-side squealer tips. The decrease in the case of the flat tip is caused by the formation of larger separated region at large tip gap. The larger separated region causes the peak heat transfer to occur further downstream and closer to the suction-side edge, thus reducing the extent of the high heat transfer region downstream of the peak heat transfer hence the average value. In the case of the squealer geometries the increase in average values at higher clearance gap is due to the increase in flow velocities (see Figs. 12 and 17).

The distribution of total pressure loss coefficient, $Y_p$, mass averaged about the axial planes, along the axial direction is shown in Fig. 22. The trend in the variation of losses is very similar to the trend reported by Bindon [25], Basson and Lakshminarayana [26],

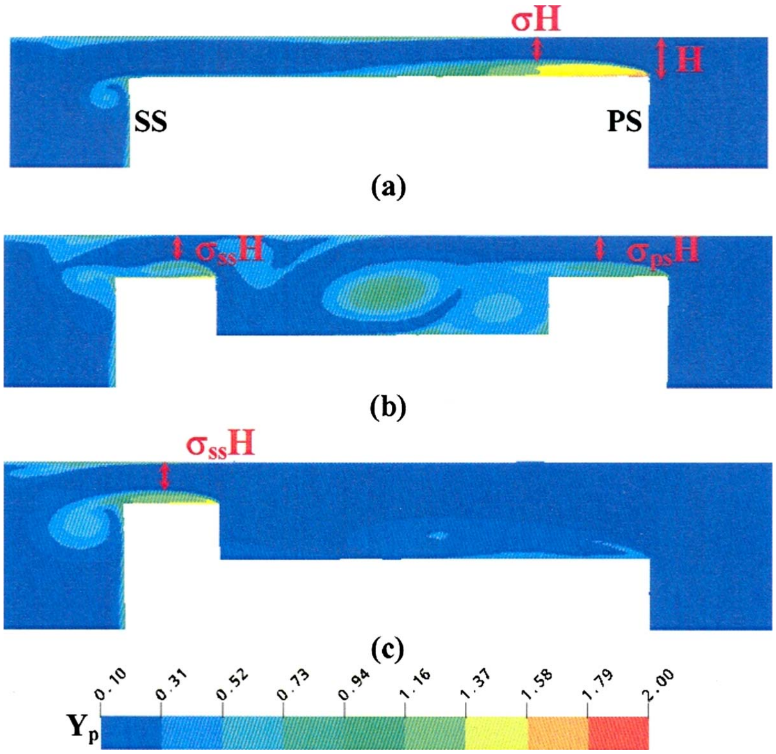

**Fig. 21  Contours of total pressure loss coefficient on an axial plane at $x/C_x$ of 0.5: region near the tip gap: (*a*) flat tip, (*b*) cavity tip, and (*c*) SSS tip with $H/C$ of 1.6%**

and Zamri [27]. The trends for all the three geometries at both the tip gaps are similar up to 10% axial chord downstream of the trailing edge. The loss coefficient continues to increase, although at different rates, for all the cases. Compared to the case of flat tip, the losses are smaller in the case of the cavity tip and larger in the case of the suction-side squealer tip. These are caused by correspondingly larger or smaller amount of leakage mass flow through the tip gap. Zamri [27] similarly reported that, compared to the case of flat tip geometry, the losses are smaller in the case of the cavity geometry. Figure 22 also shows that for a given tip gap geometry, the losses are larger at larger tip gap heights. This is due to the increase in leakage mass flow with increase in tip gap height. Heyes et al. [24] and Bindon [25] also reported a similar increase in loss due to the increase in tip gap.

In summary, compared to the flat tip, the cavity tip proves to be advantageous both from the aerodynamic perspective and from the heat transfer perspective by providing a decrease in the amount of leakage (and hence losses) and average heat transfer to the tip. The suction-side squealer tip although provides a larger reduction in the average heat transfer to the tip, increases the leakage mass flow and hence the losses.

## Conclusions

A numerical study has been performed to investigate the effect of tip geometry on the tip leakage flow and heat transfer characteristics in unshrouded axial flow turbines. The computational code used, CFX 5.6, was validated using the data measured (by Newton et al. [18]) on a flat tip blade with a tip clearance gap of 1.6%C. The computations performed using SST $k$-$\omega$ model were found to be in close agreement with the experiment. However, the predicted separated region near the pressure side edge was found to be larger than that observed in the experiment, and the computations underpredicted the average heat transfer to the tip by 5–10%. The larger size of the separation bubble and the underprediction of the heat transfer coefficient were believed to be due to excessive clipping on the overproduction of turbulent kinetic energy.

The effects of geometry of the blade tip on the leakage mass flow and heat transfer to the tip were investigated. Two different squealer geometries, at two tip gaps of 1.6%C and 2.8%C, were compared with the base line flat tip in terms of leakage mass flow and the average heat transfer to the tip.

At both the tip gaps considered, provision of the cavity reduced the leakage mass flow, whereas the suction-side squealer increased it. This was found to be due to the increase/decrease in blockage as indicated by the corresponding decrease/increase in the values of contraction coefficient. This ranking of tip geometries in terms of the leakage mass flow is in agreement with the ranking obtained using the idealized two-dimensional models by Krishnababu et al. [6].

Compared to the flat tip, the area weighted average heat transfer to the tip decreased in the case of both the squealer geometries considered. The decrease in area weighted average heat transfer to the tip in the case of the cavity tip was found to be due to the low values of heat transfer to the cavity floor. In the case of the suction-side squealer, the decrease in area weighted average heat transfer was found to be due to the low values of heat transfer to the tip surface upstream of the squealer caused by low flow velocities in these regions. It was also noticed that, compared to the cavity, the suction-side squealer provided a larger decrease in average value due to comparatively lower heat transfer to the tip surface upstream of the squealer. However, this ranking of tip geometries in terms of average heat transfer to the tip does not agree with the ranking obtained in the case of the investigation using idealized two-dimensional models by Krishnababu et al. [6]. It was noted that although the two-dimensional idealized models provide insight into the nature of flow field in the squealer geometries, from heat transfer perspective, it is unlikely that they can always provide the information needed to rank the tip gap geometries.

In general, for a given geometry, the leakage mass flow and the heat transfer to the tip increased with increase in tip clearance gap due to the increase in flow velocities and tip gap exit area.

## Acknowledgment

The work presented in this paper was carried out as a part of a project funded by EPSRC, Alstom Power Ltd., UK, and Siemens Industrial Turbomachinery Ltd., Lincoln, UK. Their support is gratefully acknowledged.

## Nomenclature

$C$ = chord
$C_p$ = $(P_{o\ \mathrm{in}}-p)/(P_{o\ \mathrm{in}}-p_{\mathrm{exit}})$
$C_x$ = axial chord
G1, G2, G3 = mesh used for computations
$h$ = heat transfer coefficient$=q_w/(T_{o\ \mathrm{in}}-T_w)$
$H$ = tip gap height
$k$ = turbulent kinetic energy
$P_{o\ \mathrm{in}}$ = total pressure at inlet
$p_{\mathrm{exit}}$ = exit static pressure
$q_w$ = heat flux from air to wall
SSS = suction-side squealer
$T_{o\ \mathrm{in}}$ = inlet total temperature
$T_w$ = wall temperature
$Y_p$ = $(P_{o\ \mathrm{in}}-P_o)/(P_{o\ \mathrm{in}}-p_{\mathrm{exit}})$
$\varepsilon$ = rate of dissipation of $K$
$\omega$ = turbulence frequency
$\sigma$ = unblocked height available for leakage flow/tip gap height

## References

[1] Booth, T. C., Dodge, P. R., and Hepworth, H. K., 1982, "Rotor-Tip Leakage: Part 1-Basic Methodology," ASME J. Eng. Power, **104**, pp. 154–161.
[2] Denton, J. D., and Cumpsty, N. A., 1987, "Loss Mechanisms in Turbomachines," *Proceedings of ImechE, Turbomachinery-Efficiency and Improvement*, Paper No. C260/87.
[3] Bunker, R. S., 2001, "A Review of Turbine Blade Tip Heat Transfer in Gas Turbine Systems," Ann. N.Y. Acad. Sci., **934**, pp. 64–79.
[4] Kim, Y. W., and Metzger, D. E., 1993, "Heat Transfer and Effectiveness on Film Cooled Turbine Blade Tip Models," ASME Paper No. 93-GT-208.
[5] Chen, G., Dawes, W. N., and Hodson, H. P., 1993, "A Numerical and Experimental Investigation of Turbine Tip Gap Flow," *Proceedings of the 29th Joint Propulsion Conference and Exhibit*, AIAA Paper No. 93-2253.
[6] Krishnababu, S. K., Newton, P., Dawes, W. N., Lock, G. D., and Hodson, H. P., 2005, "An Experimental and Numerical Investigation of the Tip Leakage Flow and Heat Transfer Using a Rotor Tip Gap Model," *Proceedings of the Fifth European Turbomachinery Conference*, Lille, France.
[7] Bunker, R. S., Bailey, J. C., and Ameri, A. A., 1999, "Heat Transfer and Flow on the First Stage Blade Tip of a Power Generation Gas Turbine. Part I: Experimental Results," ASME Paper No. 99-GT-169.
[8] Kwak, J. S., and Han, J. C., 2002, "Heat Transfer Coefficient and Film-Cooling Effectiveness on a Gas Turbine Blade Tip," ASME Paper No. 2002-GT-30194.
[9] Kwak, J. S., and Han, J. C., 2002, "Heat Transfer Coefficient and Film-Cooling Effectiveness on the Squealer Tip of a Gas Turbine Blade," ASME Paper No. 2002-GT-30555.
[10] Jin, P., and Goldstein, R. J., 2002, "Local Mass/Heat Transfer on Turbine Blade Near-Tip Surfaces," ASME Paper No. 2002-GT-30556.
[11] Ameri, A. A., Steinthorsson, E., and Rigby, D. L., 1998, "Effect of Squealer Tip on Rotor Heat Transfer and Efficiency," ASME J. Turbomach., **120**, pp. 753–759.
[12] Ameri, A. A., and Bunker, R. S., 1999, "Heat Transfer and Flow on the First Stage Blade Tip of a Power Generation Gas Turbine. Part II: Simulation Results," ASME Paper No. 99-GT-283.
[13] Yang, H., Acharya, S., Ekkad, S. V., Prakash, C., and Bunker, R., 2002, "Flow and Heat Transfer Predictions for a Flat Tip Turbine Blade," ASME Paper No. 2002-GT-30190.
[14] Yang, H., Acharya, S., Ekkad, S. V., Prakash, C., and Bunker, R., 2002, "Numerical Simulation of Flow and Heat Transfer Past a Turbine Blade With a Squealer Tip," ASME Paper No. 2002-GT-30193.
[15] Acharya, S., Yang, H., Prakash, C., and Bunker, R., 2003, "Numerical Study of Flow and Heat Transfer on a Blade Tip With Different Leakage Reduction Strategies," ASME Paper No. 2003-GT-38617.

[16] Saha, A. K., Acharya, S., Prakash, C., and Bunker, R., 2003, "Blade Tip Leakage Flow and Heat Transfer With Pressure Side Winglet," ASME Paper No. 2003-GT-38620.

[17] Mumic, F., Eriksson, D., and Sunden, B., 2004, "On Prediction of Tip Leakage Flow and Heat Transfer in Gas Turbines," ASME Paper No. 2004-GT-53448.

[18] Newton, P. J., Krishnababu, S. K., Lock, G. D., Hodson, H. P., Dawes, W. N., Hannis, J., and Whitney, C., 2005, "Heat Transfer and Aerodynamics of Turbine Blade Tips in a Linear Cascade," ASME Paper No. 2005-GT-69034.

[19] Stubley, G. D., 2004, CFX User Manual.

[20] Menter, F. R., 1994, "Two-Equation Eddy-Viscosity Turbulence Models for Engineering Applications," AIAA J., **32**, pp. 269–289.

[21] Menter, F. R., and Esch, T., 2001, "Elements of Industrial Heat Transfer Predictions." *Proceedings of the 16th Brazilian Congress of Mechanical Engineering (COBEM)*, Uberlandia, Brazil, Nov.

[22] Azad, G. S., Han, J., Teng, S., and Boyle, R. J., 2000, "Heat Transfer and Pressure Distribution on a Gas Turbine Blade Tip," ASME J. Turbomach., **122**, pp. 717–724.

[23] Kwak, J. S., Ahn, J., Han, J., Lee, C. P., Boyle, R., Bunker, R. S., and Gaugler, R., 2003, "Heat Transfer Coefficients on the Squealer Tip and Near Tip Regions of a Gas Turbine Blade With Single or Double Squealer," ASME Paper No. 2003-GT-38907.

[24] Heyes, F. J. G., Hodson, H. P., and Dailey, G. M., 1992, "The Effect of Blade Tip Geometry on the Tip Leakage Flow in Axial Turbine Cascade," ASME J. Turbomach., **114**, pp. 643–651.

[25] Bindon, J. P., 1988, "The Measurement and Formation of Tip Clearance Loss," ASME Paper No. 88-GT-203.

[26] Basson, A., and Lakshminarayana, B., 1993, "Numerical Simulation of Tip Clearance Effects in Turbomachinery," ASME Paper No. 93-GT-316.

[27] Zamri, M. Y., 1994, "Numerical and Experimental Investigation of Transonic Turbine Over Tip Leakage Flow," M.Phil. thesis, University of Cambridge, UK.

**S. K. Krishnababu**[1]

**W. N. Dawes**

**H. P. Hodson**

Department of Engineering,
University of Cambridge,
Cambridge CB2 1TN, UK

**G. D. Lock**

Department of Mechanical Engineering,
University of Bath,
Bath BA2 7AY, UK

**J. Hannis**

Siemens Industrial Turbomachinery Ltd.,
P.O. Box 1,
Waterside South,
Lincoln LN5 7FD, UK

**C. Whitney**[2]

Alstom Power Technology Centre,
Cambridge Road,
Whetstone,
Leicester LE8 6LH, UK

# Aerothermal Investigations of Tip Leakage Flow in Axial Flow Turbines—Part II: Effect of Relative Casing Motion

*A numerical study has been performed to investigate the effect of casing motion on the tip leakage flow and heat transfer characteristics in unshrouded axial flow turbines. The relative motion between the blade tip and the casing was simulated by moving the casing in a direction from the suction side to the pressure side of the stationary blade. Base line flat tip geometry and squealer type geometries, namely, double squealer or cavity and suction side squealer, were considered at a clearance gap of 1.6%C. The computations were performed using a single blade with periodic boundary conditions imposed along the boundaries in the pitchwise direction. Turbulence was modeled using the shear stress transport k-ω model. The flow conditions correspond to an exit Reynolds number of $2.3\times10^5$. The results were compared to those obtained without the relative casing motion reported in Part I of this paper. In general, the effect of relative casing motion was to decrease the tip leakage mass flow and the average heat transfer to the tip due to the decrease in leakage flow velocity caused by a drop in driving pressure difference. Compared to the computations with stationary casing, in the case of all the three geometries considered, the average heat transfer to the suction surface of the blade was found to be larger in the case of the computations with relative casing motion. At a larger clearance gap of 2.8%C, in case of a flat tip, while the tip leakage mass flow decreased due to relative casing motion, only a smaller change in the average heat transfer to the tip and the suction surface of the blade was noticed.* [DOI: 10.1115/1.2952378]

## Introduction

In unshrouded axial turbines, clearance gaps between the rotor blades and the stationary shroud are necessary to prevent the physical rubbing between them. The pressure difference between the pressure and the suction sides (SSs) of the blade causes an undesirable leakage of fluid through the clearance gap. This affects the stage performance. Typically, a clearance of 1% of blade span causes 1–2% of primary flow to leak and hence a loss of 1–3% on stage efficiency (Booth et al. [1]).

There are two distinct aspects of tip leakage flows (Denton and Cumpsty [2]). First, as the flow passes through the tip gap without being properly turned, there is a reduction in work done, and second, due to mixing, there is generation of entropy within the gap, in the blade passage, and downstream of the blade row. Apart from these losses, the rapid acceleration of hot mainstream flows into the tip gap followed by the separation and reattachment of the hot gas on the tip results in high heat transfer to the tip. This high heat transfer to the tip, together with that to the suction and pressure sides of the blade, must be removed by the blade internal cooling flows. The compressor supplies this cooling flow, which imposes a further penalty on the engine performance. Hence, considerable research has been done to understand and quantify the losses and the heat transfer associated with the tip leakage flows.

A review of research quantifying the losses and heat transfer associated with tip clearance flow is provided by Bunker [3]. Much of the early work used idealized models, e.g., Kim and Metzger [4] and Chen et al. [5], and a more recent Krishnababu et al. [6]. More recently, using linear cascades, Bunker et al. [7] measured heat transfer for sharp and radiused-edged blades for different clearance gaps; Kwak and Han [8,9] used the transient liquid crystal technique, and Jin and Goldstein [10] used the naphthalene technique to determine the effects of clearance gap, turbulence intensity, and Reynolds number on the mass/heat transfer from the tip and near-tip surfaces.

In recent years, three-dimensional numerical simulation of flow and heat transfer of tip leakage flow past blades with flat and squealer tip geometries have been reported. Ameri et al. [11] performed a three-dimensional numerical simulation of flow and heat transfer over a turbine blade with cavity tip. Turbulence was modeled using a $k$-$\omega$ turbulence model. The provision of cavity was found to reduce the mass flow rate through the tip gap by as much as 14%. However, only a meager change in efficiency was noticed. This was reported to be due to the increase in heat transfer to the blade in the case of the cavity tip as compared to the case of the flat tip. Ameri and Bunker [12] performed a numerical simulation to investigate the distribution of heat transfer coefficient on the tip of flat and radiused-edged blades. The results using the radiused-edge tip agreed better with their experimental data (Bunker et al. [7]). This improved agreement was attributed to the absence of edge separation on the tip of the radiused-edged blade. Yang et al. [13,14] performed a numerical study of tip leakage flow and heat transfer past a turbine blade for three different tip gaps. They compared the performance of the cavity tip to that of the flat tip. Acharya et al. [15] and Saha et al. [16] investigated the flow and heat transfer characteristics of tip leakage flow using different tip gap geometries. Of all the geometries they considered, the lowest mass flow rates and tip heat transfer coefficients were obtained in the case of the suction side squealer (SSS) ge-

---

[1] Present address: VUTC, Department of Mechanical Engineering, Imperial College, London, UK.

[2] Present address: E.O.N UK, Power Technology, Radcliffe-on-Soar, Nottingham, UK.

Contributed by the International Gas Turbine Institute of ASME for publication in the JOURNAL OF TURBOMACHINERY. Manuscript received August 27, 2007; final manuscript received January 4, 2008; published online October 3, 2008. Review conducted by David Wisler. Paper presented at the ASME Turbo Expo 2007: Land, Sea and Air (GT2007), Montreal, QC, Canada, May 14–17, 2007.

ometry followed by the cavity geometry. Mumic et al. [17] studied the aerothermal performance of flat and cavity geometries at three different tip gaps. Both in the case of the flat tip and cavity tip, the overall heat transfer to the tip and the leakage mass flow rate increased with the increase in tip gap height. Compared to the flat tip, the overall heat transfer to the cavity tip was found to be lower.

In Part I of this paper (Krishnababu et al. [18]), a numerical study performed to investigate the effect of tip geometry on the tip leakage flow and heat transfer characteristics in unshrouded axial flow turbines is reported. Base line flat tip geometry and squealer type geometries, namely, double squealer or cavity and SSS, were considered. The performances of the squealer geometries, in terms of the leakage mass flow and heat transfer to the tip, were compared to the flat tip. It was observed that compared to the other two geometries considered, the cavity tip is advantageous both from the aerodynamic and from the heat transfer perspectives by providing a decrease in the amount of leakage, and hence losses, and in the average heat transfer to the tip.

Very few studies have investigated the effect of relative casing motion on the tip leakage flow. Morphis and Bindon [19] and Yaras and Sjolander [20] have shown that the tip leakage mass flow can reduce significantly as a result of motion of the casing relative to the tip. Srinivasan and Goldstein [21] have noticed a small but definite reduction in heat transfer to the tip at smaller tip gap due to the relative casing motion. At larger tip gaps, the effect of the relative casing motion on the heat transfer to the tip was found to be negligible. Rhee and Cho [22,23] have also reported a decrease in leakage flow and heat transfer to the tip due to the casing motion. However, in the open literature, the effect of relative casing motion on the aerodynamic and the heat transfer characteristics of the tip leakage flows is rarely investigated in a single study using the same geometry and hence were rarely linked.

In this paper, an attempt has been made to link the effect of relative casing motion on the tip leakage mass flow and heat transfer to the blade. The effect of relative casing motion on the performances of the flat and squealer geometries (double squealer or cavity and SSS) in terms of the leakage mass flow and heat transfer to the tip was investigated at a tip clearance gap of 1.6% chord. The effect of relative casing motion at a larger clearance gap of 2.8% chord is studied using the flat tip blade. It is shown that the effect of relative casing motion is to decrease the tip leakage mass flow and the average heat transfer to the tip.

Although the relative wall motion considerably increases the realism of the simulation, the flow is still idealized in many aspects. The casing motion does not simulate the real engine effects such as centrifugal forces leading to radial flows in the blade passage. However, in and around the tip gap region, the casing motion is believed to be a dominant factor compared to the other effects of rotation.

## Computational Details

The simulations reported in this investigation were performed using CFX 5.6 (Stubley [24]), a commercially available computational fluid dynamics (CFD) solver. The solutions were obtained by solving the Navier–Stokes equations using a finite-volume method to discretize the equations. Structured meshes generated using the commercial mesh generation program ICEM-HEXA were used. The computational code was validated using the data measured by Newton et al. [25] on a linear cascade with stationary casing. The computations were performed using a single blade with periodic boundary conditions imposed along the boundaries in the pitchwise direction. The computational mesh of the flat tip blade with a clearance gap of $1.6\% C$ used for validation is shown in Fig. 1. At the inlet, which is placed at half a chord upstream of the leading edge, total temperature and total pressure were specified. The inlet flow angle is 32.5 deg. At the exit, which is placed at a distance equal to a chord downstream of the trailing edge, static pressure was specified. The flow conditions correspond to an exit Reynolds number of $2.3 \times 10^5$, which is the same as that in the experiments. The flow is incompressible. No-slip isothermal wall conditions (wall temperature being 94% of inlet total temperature) were imposed on the blade and the casing. The hub located far away from the tip was inviscid with adiabatic conditions imposed. The computations were performed using the shear stress transport (SST) $k$-$\omega$ model of Menter [26], which encompasses the low Reynolds number $k$-$\omega$ model and the $k$-$\varepsilon$ model, with the original low Reynolds number $k$-$\omega$ model activated near the wall and the standard $k$-$\varepsilon$ model activated away from the wall.

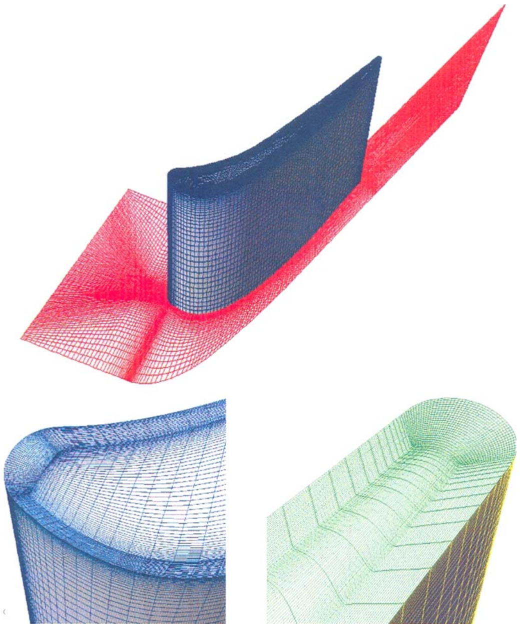

**Fig. 1 Computational domain with a typical mesh superimposed**

Three different meshes, namely, G1, G2, and G3, were used in the validation process. Average $Y^+$ values on the tip, number of cells across the tip gap, and total number of cells for the three meshes considered are given in Table 1. It should be noted that only small changes in the values of $Y^+$ occurred with the introduction of relative casing motion.

The contours of heat transfer coefficient on the tip obtained by the computations performed using the meshes G1, G2, and G3 are shown in Figures 2(*b*)–2(*d*), respectively. The experimental distribution (Newton et al. [25]) is shown in the Fig. 2(*a*) for comparison. The differences between the solutions obtained using the three meshes, considered are seen to be small and the computed contours are in close qualitative agreement with the experimental contours. Comparing the contours obtained using the three meshes it is seen that the differences between the solutions obtained using G2 and G3 are smallest. The average values of heat transfer coefficient on the tip as obtained by the computations using the three meshes and the experimental value are given in Table 2. It is seen that, on average, the computations underpredict the heat transfer to the tip by 5–10%. It is also seen that the differences in the

**Table 1 Details of the meshes G1, G2, and G3**

| Mesh | Average $Y^+$ on tip | Number of cells across the tip | Total number of cells (million) |
|---|---|---|---|
| G1 | 4.37 | 25 | 2.2 |
| G2 | 2.26 | 35 | 2.5 |
| G3 | 1.15 | 40 | 2.8 |

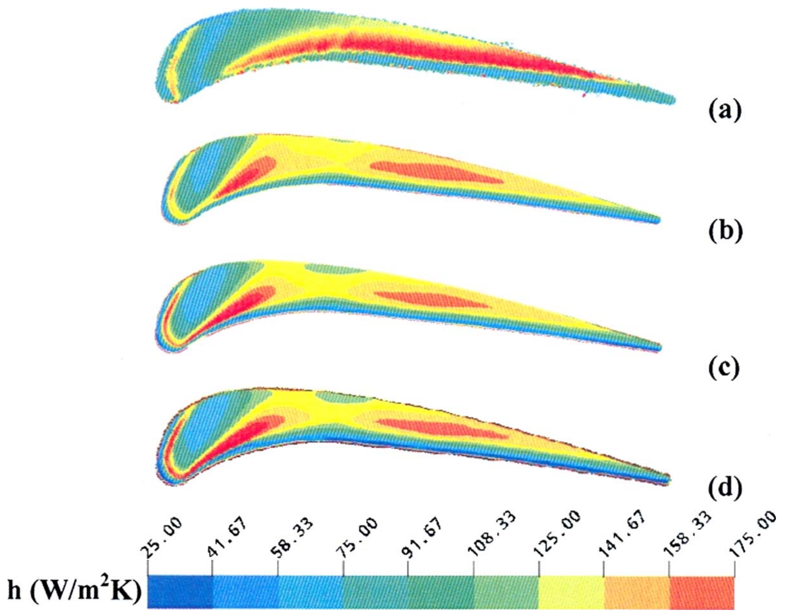

Fig. 2 Validation study: Contours of heat transfer coefficient on tip: (*a*) experimental, (*b*) G1, (*c*) G2, and (*d*) G3

average values obtained using G2 and G3 are smaller. Hence, further comparisons with the experiments are made using the solutions obtained on the coarser mesh G2.

The blade loading at midspan, for the flat tip geometry, obtained by the computations using G2 and the experiment are shown in Fig. 3. The quantity plotted is the coefficient of pressure, $C_p$. The computed distribution is seen to agree closely with the experimental distribution. Further details of the validation are provided in Part I of this paper (Krishnababu et al. [18]).

Table 2 Average *h* on tip

| | Average $h$ (W/m$^2$ K) | |
|---|---|---|
| Mesh | Expt.<br>(Newton et al. [25]) | CFD |
| G1 | 110.4 | 106.2 |
| G2 | — | 100.2 |
| G3 | — | 100.5 |

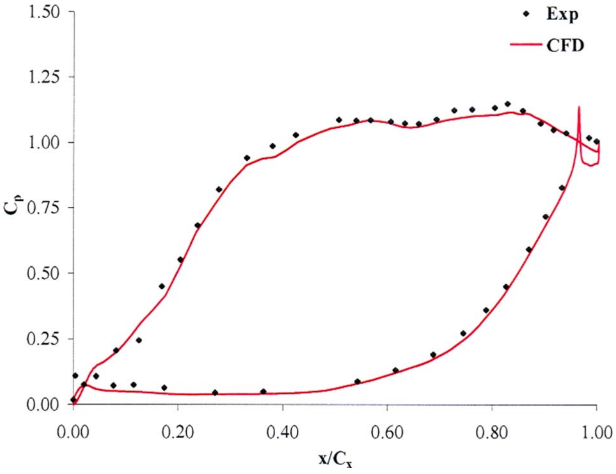

Fig. 3 Blade loading at midspan

The relative motion between the blade tip and the casing was simulated by moving the casing at a velocity, $U$, in a direction from the SS to the pressure side of the stationary blade. The casing is moved at twice the inlet flow velocity, $V_x$. The flow coefficient, $V_x/U$, of 0.5 is comparable to that of an industrial turbine blade investigated by Krishnababu [27]. The results of the computations with relative casing motion are compared to those obtained without the relative casing motion reported in Part I of this paper (Krishnababu et al. [18]).

## Investigation of Tip Leakage Flow: Effect of Relative Casing Motion

**Flat Tip.** The computed streamlines, colored by flow velocity, across the tip at the tip gap of 1.6%$C$ obtained in the simulation with casing motion is compared to those obtained without casing motion in Fig. 4. The flow patterns remain similar; however, the tip leakage vortex in the case with casing motion is seen to be closer to the SS of the blade than in the case with stationary casing. Also, in the case with casing motion, the separated region on the tip, near the pressure side edge, is observed to have reduced in size. Furthermore, the strength of this separated region is seen to be smaller in the case with casing motion. This can be observed by comparing the colors of the streamlines in this region.

In Fig. 5, the contours of heat transfer coefficient on the tip obtained in the simulation with relative casing motion are compared to those obtained without relative motion. Compared to the heat transfer distribution obtained in the case with stationary casing, in the case with relative casing motion, the region of high heat transfer (marked A) between $0.1<x/C_x<0.65$ is seen to have moved upstream toward the pressure side edge; however, not much change is noticed in the regions $x/C_x<0.1$ and $x/C_x>0.65$.

Figures 6(*a*) and 6(*b*) show the contours of heat transfer coefficient on the suction and pressure surfaces of the blade for the two clearance gaps considered. On the pressure surface of the blade, at both the tip clearance gaps, the distribution of heat transfer coefficient obtained by the computation with relative casing motion is the same as that obtained in the simulation without relative motion. On the suction surface of the blade, at the smaller tip clearance gap (Figure 6(*a*)), the magnitude of heat transfer

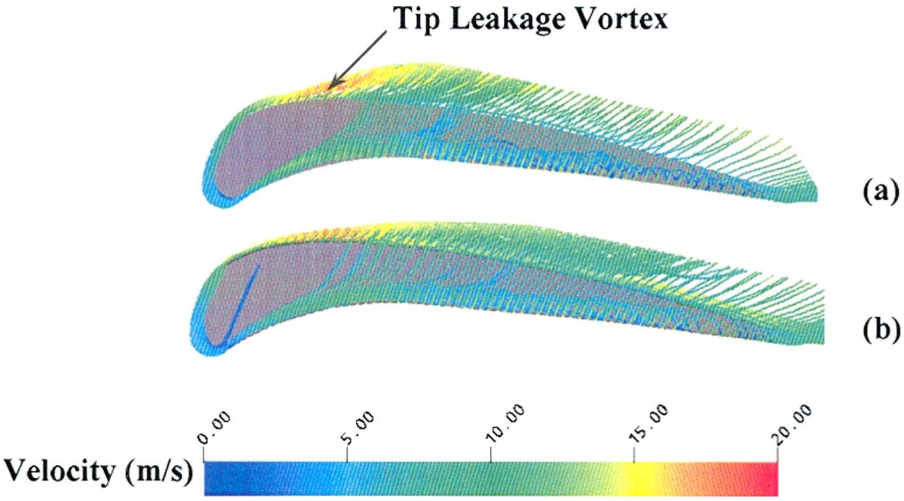

**Fig. 4 Streamlines across flat tip at *H* of 1.6% *C*: (*a*) stationary casing and (*b*) with casing motion**

coefficients along the footprint of the tip leakage vortex is much larger in the computations with relative casing motion, whereas the differences in the magnitude of heat transfer are smaller at the higher tip clearance gap (Fig. 6(*b*)).

The reasons for the above differences can be explained with the help of Figs. 4 and 7. Figure 7 shows the computed contours of total pressure loss coefficient on an axial plane at $x/C_x$ of 0.7. From these figures, it is seen that the viscous dragging effect of the casing motion (scrapping effect) has moved the tip leakage vortex closer to the suction surface of the blade. This movement is more pronounced at the smaller clearance gap, in which case the tip leakage vortex is observed to impinge on the suction surface of the blade (see Fig. 7(*a*)). The impingement of the tip leakage vortex increases the heat transfer on this surface. The contours of total pressure loss coefficient across the tip gap also shows that in the computation with relative casing motion, the separated region near the pressure side edge have reduced in size. The associated earlier reattachment of the flow causes the upstream movement of the high heat transfer region closer to the pressure side edge observed in Figs. 5(*a*) and 5(*b*).

The tip leakage mass flows, area weighted average heat transfer coefficient on the tip, and the suction surface of the blade obtained in the case of the computations with and without relative casing motion are shown in Table 3. It is seen that compared to the case with stationary casing, in the case of the computations with relative casing motion, the tip leakage mass flows had decreased by about 15% and 8%, respectively, at the clearance gaps of 1.6% $C$ and 2.8% $C$.

The mechanism, which causes the reduction in leakage mass

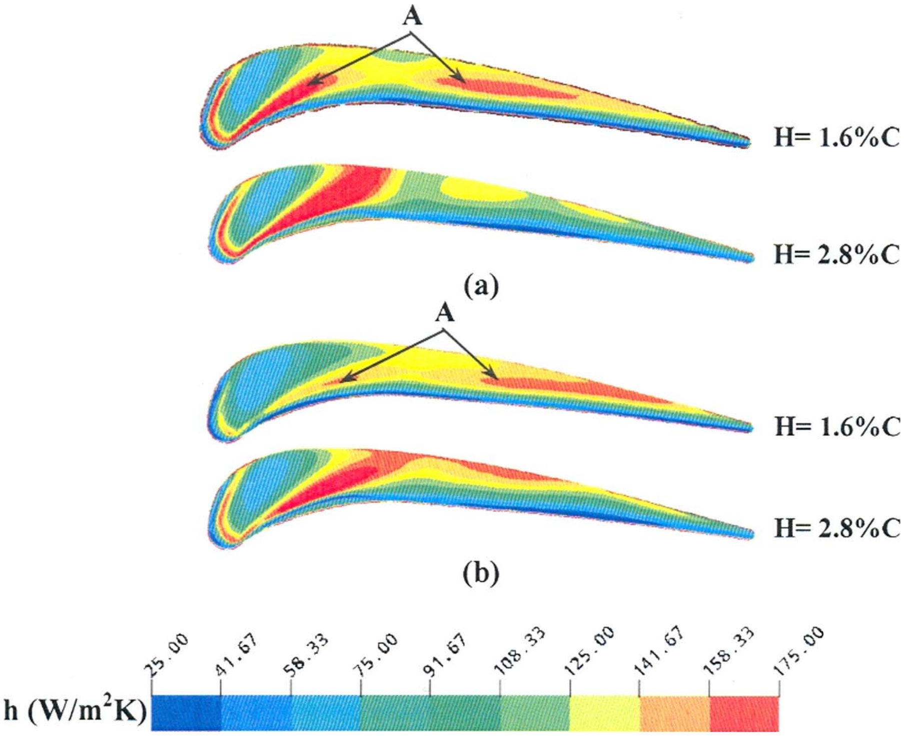

**Fig. 5 Contours of *h* on flat tip: (*a*) stationary casing and (*b*) with casing motion**

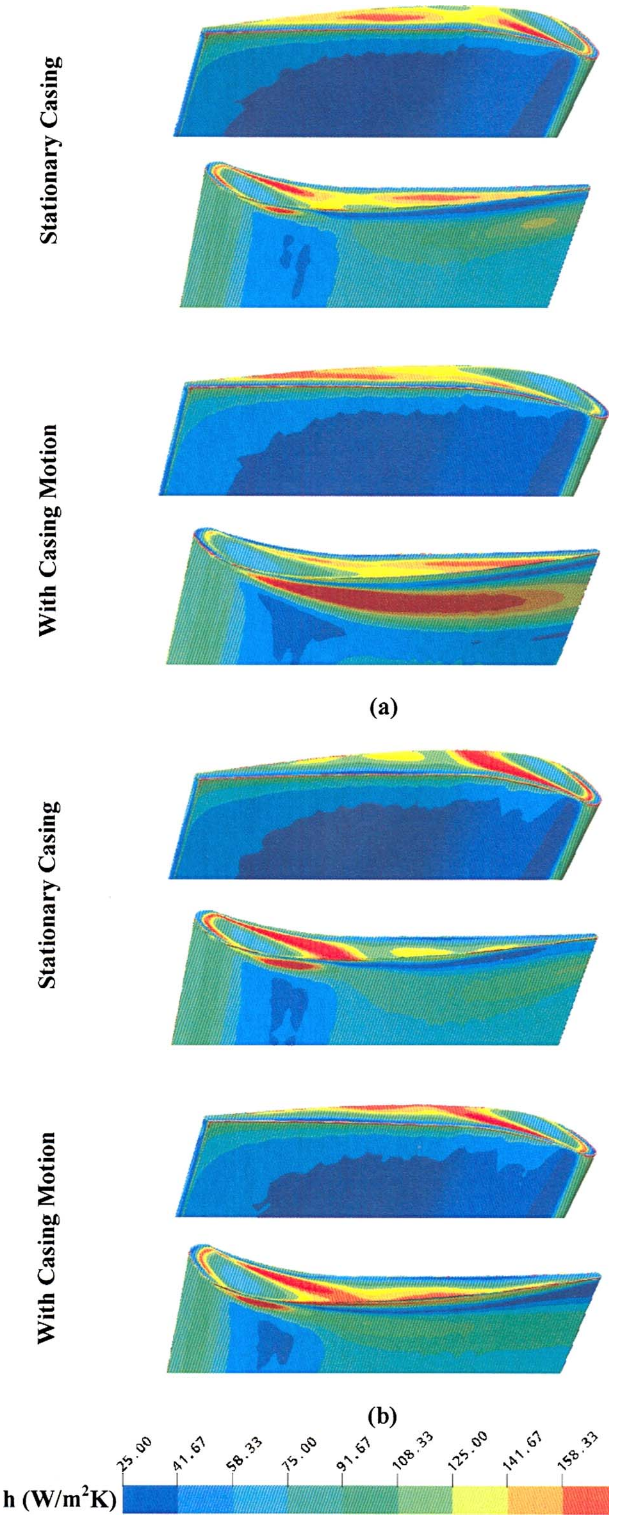

**Fig. 6 Contours of *h* on flat tip blade with *H*/*C* of (*a*) 1.6% and (*b*) 2.8%—region near the tip**

flow rate, is evident from Figs. 4 and 7. The tip leakage vortex, which has moved closer to the suction surface by scraping effect of the relative casing motion, partly blocks the tip gap exit. This increases the pressure at tip gap exit, thereby reducing the driving pressure difference for the leakage flow. For example, at a lower tip gap of $1.6\% C$, the difference in coefficient of pressure between the pressure and suction surfaces of the blade, which drives the flow through the tip gap, is observed to decrease from 0.44 in the case of the stationary casing to 0.33 in the case of the computation with relative casing motion. A similar decrease in the driving pressure difference was also noticed by Morphis and Bindon [19].

Table 3 also shows that at lower tip gap, compared to the case of the computation with stationary casing, in the case of the simulation with relative casing motion, the area weighted average heat transfer to the tip decreases by about 8% and the area average heat transfer to the suction surface of the blade increases by about 6%. The decrease in the average heat transfer to the tip is caused by the decrease in the leakage flow velocity, which is due to the decrease in driving pressure difference. The increase in average heat transfer to the suction surface of the blade is due to the increase in the magnitude of heat transfer coefficients along the footprint of the tip leakage vortex (see Fig. 6). The differences are smaller at the larger tip gap.

**Squealer Tips.** The computed streamlines, colored flow velocity, across the squealer tips at the tip gap of $1.6\% C$ obtained in the simulation with casing motion, is compared to those obtained without casing motion in Fig. 8. The flow patterns remain similar; however, the tip leakage vortex in the case with casing motion is seen to be closer to the SS of the blade than in the case with stationary casing. Furthermore, the strength of the horseshoe vortices V1 and V2 (cavity and SSS tip) and of the vortical structure V3 (SSS tip) is seen to be smaller in the case with casing motion, as observed by comparing the colors of the streamlines in this region.

In Figs. 9(*a*) and 9(*b*), the contours of heat transfer coefficient on the squealer tips obtained in the simulation with relative casing motion are compared to those obtained without relative motion. The distribution of heat transfer coefficient obtained by the computation with casing motion remains almost the same as that obtained in the computation with stationary casing.

Figures 10(*a*) and 10(*b*) show the contours of heat transfer coefficient on the suction and pressure surfaces of the blades with cavity and SSS tips. As was observed in the case of the blade with flat tip, on the pressure surface of the blade, the distribution of heat transfer coefficient obtained by the computation with relative casing motion remains similar to that obtained in the simulation without relative motion. On the suction surfaces of the blades, the magnitudes of heat transfer coefficients along the footprint of the tip leakage vortex are larger in the computations with relative casing motion. From the contours of total pressure loss coefficient (see Figs. 11(*a*) and 11(*b*)) on an axial plane at $x/C_x$ of 0.7, it is seen that the scrapping effect has moved the tip leakage vortex closer to the suction surface of the blade. The resulting impingement of this tip leakage vortex formed by the flow leaking through the tip gap increases the heat transfer to this surface. In the case of the cavity tip (Fig. 10(*a*)), compared to the computation with stationary casing, the heat transfer to the squealer face is observed to have decreased in the computation with relative casing motion. In the case of the SSS tip, not much change in the distribution of heat transfer on the squealer face is noticed.

The tip leakage mass flows, and area weighted average heat transfer to the tip and to the suction surface of the blade obtained in the case of the computations with and without relative casing motion are shown in Table 4. It is seen that, compared to the computations with stationary casing, in the computations with relative casing motion, the tip leakage mass flows have decreased by about 12% and 8% in the case of the cavity and SSS tips, respectively. This is due to the decrease in the magnitude of the pressure difference driving the flow through the tip gap, which is caused by the blockage created by the movement of the tip leakage vortex closer to the suction surface.

It is also seen that in the case of the cavity tip, compared to the computation with stationary casing, in the computation with relative casing motion, the area weighted average heat transfer to the tip decreases by about 5%. The average heat transfer to the tip decreases by about 3% in the case of the SSS tip. The decrease in

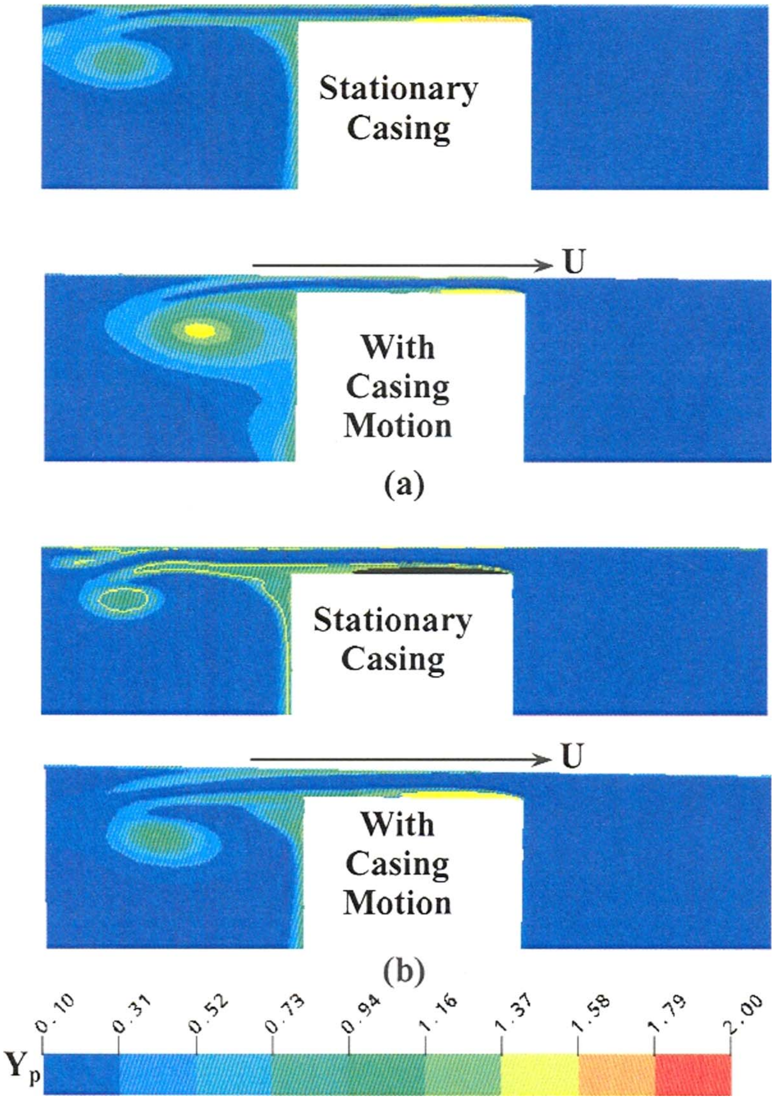

**Fig. 7 Contours of total pressure loss coefficient on an axial plane at $x/C_x=0.7$: Flat tip with $H/C$ of (*a*) 1.6% and (*b*) 2.8%—region near the tip**

the average heat transfer to the tip in the case of the cavity tip is due to the decrease in heat transfer to the squealer face. In both cases of the squealer geometries, the average heat transfer to the suction surface of the blade increases. This increase in average heat transfer to the suction surface of the blade is due to the large increase in the magnitude of heat transfer coefficients along the footprint of the tip leakage vortex (see Fig. 10).

The tip leakage mass flow as a percentage of inlet mass flow and the area weighted average heat transfer to the tip in the case of the computations with relative casing motion of the three geometries considered are compared in Table 5. From the table, it is seen that, compared to the case of the flat tip, the leakage mass flow decreases in the case of the cavity tip and increases in the case of the SSS tip. It is also seen that, compared to the flat tip, the average heat transfer to the tip have decreased in the case of both the squealer geometries. It should be noted that this ranking of tip geometries in terms of the leakage mass flow and average heat transfer to the tip is in agreement with the ranking obtained previously in the simulations with stationary casing (Krishnababu et al. [18]). Thus, from the experimental point of view, considering

**Table 3 Effect of relative casing motion—flat tip**

| | $H/C=1.6\%$ | | $H/C=2.8\%$ | |
|---|---|---|---|---|
| Parameter | With casing motion | Stationary casing | With casing motion | Stationary casing |
| Leakage mass flow (% inlet) | 2.21 | 2.61 | 3.93 | 4.26 |
| Area weighted Average *h* on tip ($W/m^2 K$) | 108.99 | 116.71 | 109.39 | 109.07 |
| Area weighted Average *h* on SS ($W/m^2 K$) | 67.75 | 63.52 | 64.22 | 63.69 |

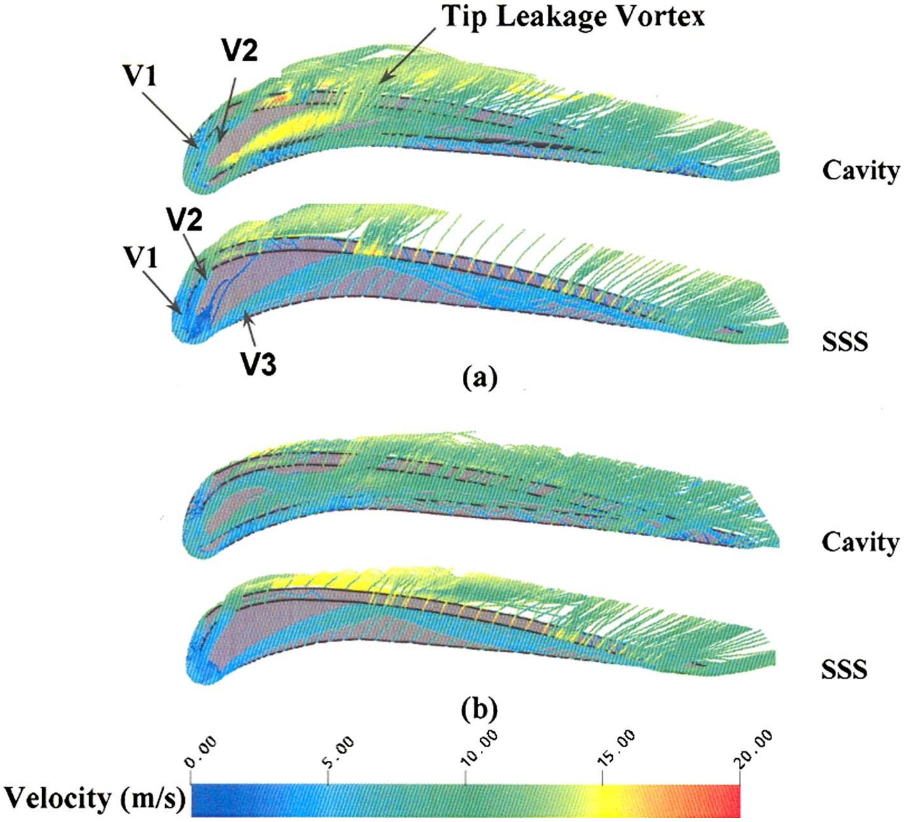

**Fig. 8 Streamlines across squealer tips with *H*/*C* of 1.6%: (*a*) stationary casing and (*b*) with casing motion**

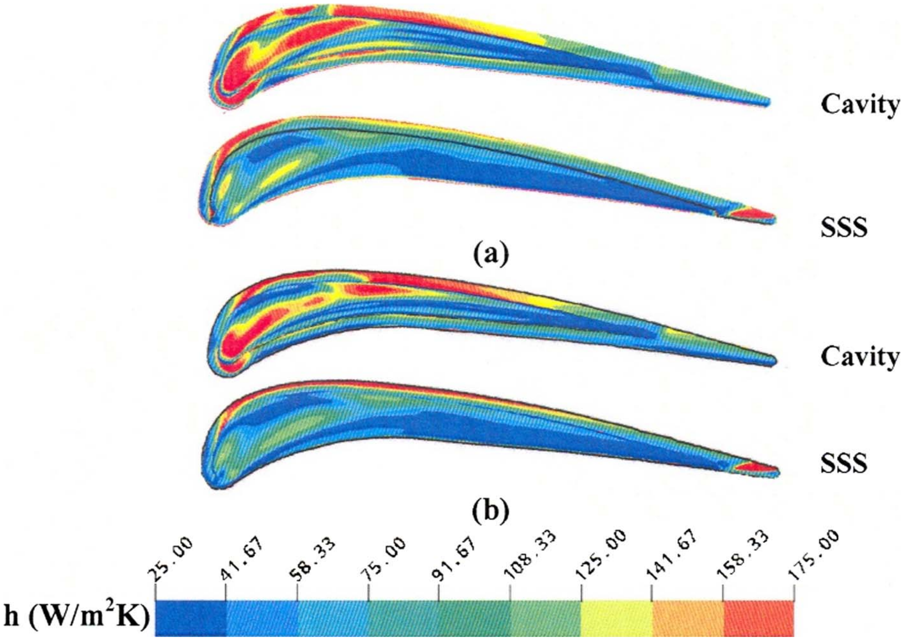

**Fig. 9 Contours of *h* on squealer tips with *H*/*C* of 1.6%: (*a*) stationary casing and (*b*) with casing motion**

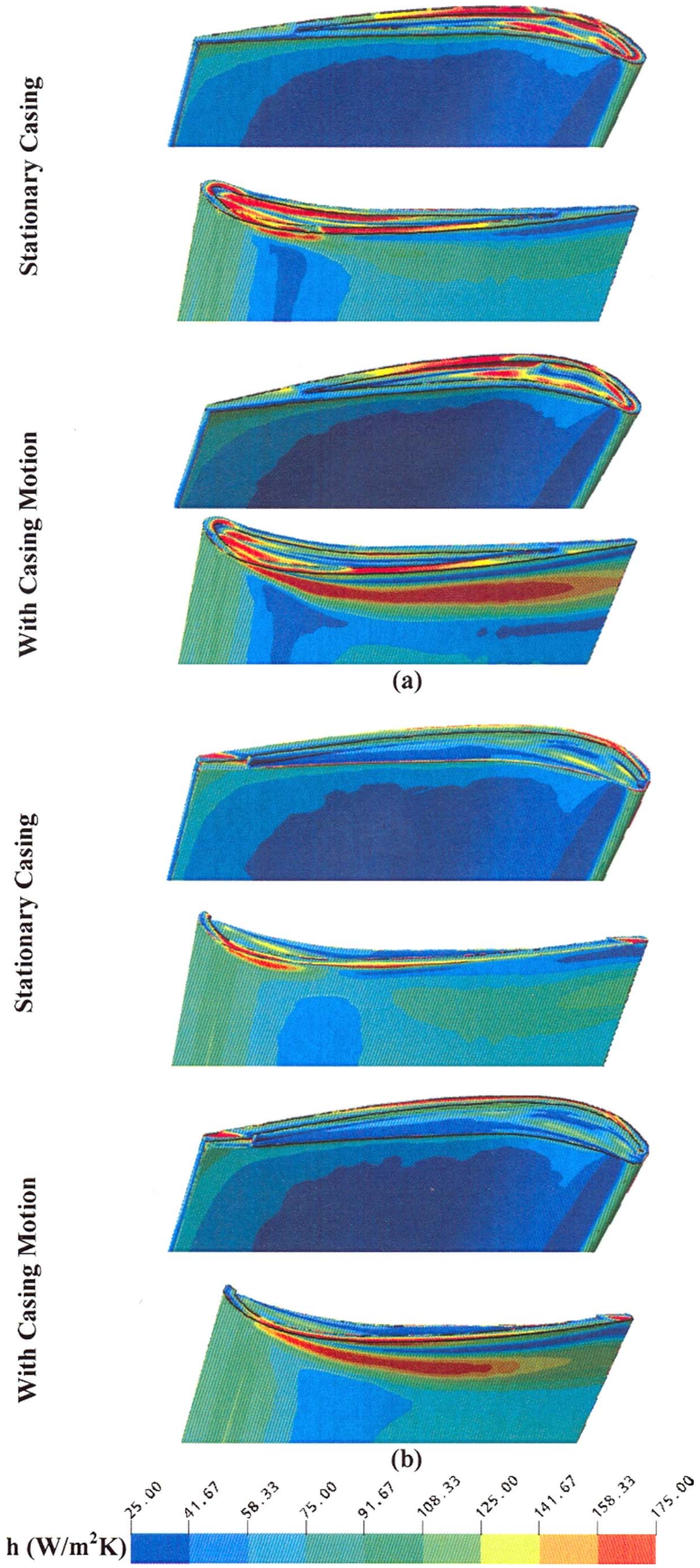

**Fig. 10** **Contours of *h* on squealer tips with *H*/*C* of 1.6%: (*a*) cavity tip and (*b*) SSS tip—region near the tip**

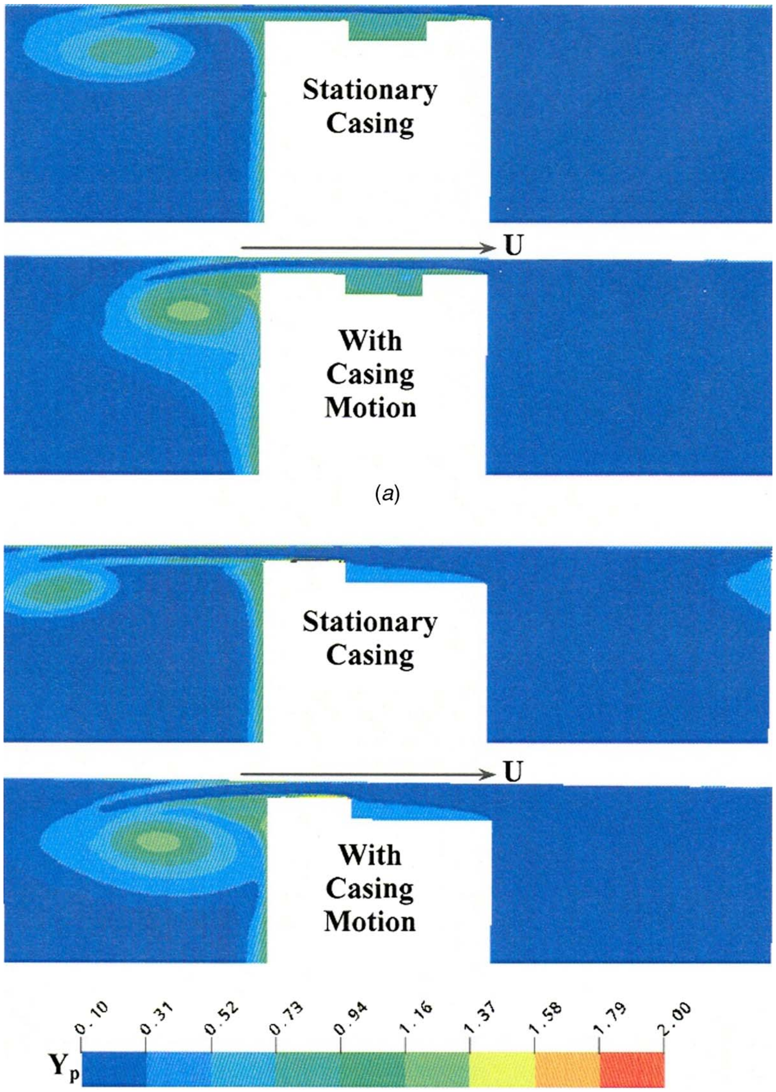

(*a*)

(*b*)

**Fig. 11 Contours of total pressure loss coefficient on an axial plane at $x/C_x=0.7$: Squealer tips with $H/C$ of 1.6%: (*a*) cavity tip and (*b*) SSS tip**

the additional cost of moving the endwall relative to the blades, it can be said that very little harm is done by neglecting the relative endwall motion unless the gap is very small and/or the focus is on the suction surface of the blade.

## Conclusions

A numerical study has been performed to investigate the effect of casing motion on the tip leakage flow and heat transfer characteristics in unshrouded axial flow turbines. The relative motion between the blade tip and the casing was simulated by moving the casing in a direction from the SS to the pressure side of the stationary blade. The computations were performed using the commercial code, CFX 5.6, which was validated using the data measured by Newton et al. [25] on a flat tip blade with a tip clearance gap of 1.6%$C$. Turbulence was modeled using the SST $k$-$\omega$ model. Base line flat tip geometry and squealer type geometries, namely, cavity and SSS, were considered at a clearance gap of 1.6%$C$. The effect of relative casing motion at a larger clearance

**Table 4 Effect of relative casing motion—squealer tips**

| | Cavity | | SSS | |
|---|---|---|---|---|
| Parameter | With casing motion | Stationary casing | With casing motion | Stationary casing |
| Leakage mass flow (% inlet) | 2.1 | 2.4 | 2.8 | 3.1 |
| Area weighted average $h$ on tip ($\mathrm{W/m^2\,K}$) | 101.5 | 106.3 | 76.8 | 79.4 |
| Area weighted average $h$ on SS ($\mathrm{W/m^2\,K}$) | 65.5 | 60.9 | 68.3 | 64.8 |

**Table 5 Comparison of tip geometry: $H/C=1.6\%$**

| Geometry | Leakage mass flow (% inlet) | Area weighted average $h$ on tip $(\mathrm{W/m^2\,K})$ |
|---|---|---|
| Flat | 2.21 | 108.9 |
| Cavity | 2.11 | 101.5 |
| SSS | 2.82 | 76.8 |

gap of $2.8\%C$ was studied using the flat tip blade.

At the smaller tip clearance gap, the effect of relative casing motion was to decrease the tip leakage mass flow and the average heat transfer to the tip due to the decrease in leakage flow velocity caused by the drop in driving pressure difference. However, in the case of the SSS, the change in the average heat transfer to the tip was found to be marginal. Compared to the computations with stationary casing, in the case of all the three geometries considered, the average heat transfer to the suction surface of the blade was found to increase in the case of the computations with relative casing motion due to the large increase in heat transfer along the footprints of the tip leakage vortex.

In the case of the flat tip at the larger tip clearance gap, while the tip leakage mass flow was found to decrease compared to the case with stationary casing, only a smaller change in the average heat transfer to the tip and the suction surface of the blade was noticed.

The ranking of the tip geometries in terms of the leakage mass flow and average heat transfer to the tip was in agreement with the ranking obtained in the simulations with stationary casing reported in Part I of this paper (Krishnababu et al. [18]). Thus, considering the additional cost of moving the endwall, it can be said that very little harm is done to the ranking of the geometries by neglecting the relative endwall motion, unless the gap is very small and/or the focus is on the suction surface of the blade.

## Acknowledgment

The work presented in this paper was carried out as a part of a project funded by EPSRC, Alstom Power Ltd, UK and Siemens Industrial Turbomachinery Ltd, Lincoln, UK. Their support is gratefully acknowledged.

## Nomenclature

$C$ = chord
$C_p$ = $(P_{\mathrm{oin}}-p)/(P_{\mathrm{oin}}-p_{\mathrm{exit}})$
$C_x$ = axial Chord
G1, G2, G3 = mesh used for computations
$h$ = heat transfer coefficient, $q_w/(T_{\mathrm{oin}}-T_w)$
$H$ = tip gap height
$k$ = turbulent kinetic energy
$P_{\mathrm{oin}}$ = total pressure at inlet
$p_{\mathrm{exit}}$ = exit static pressure
$q_w$ = heat flux from air to wall
$T_{\mathrm{oin}}$ = inlet total temperature
$T_w$ = wall temperature
$Y_p$ = $(P_{\mathrm{oin}}-P_o)/(P_{\mathrm{oin}}-p_{\mathrm{exit}})$
$\varepsilon$ = rate of dissipation of $k$
$\omega$ = turbulence frequency

## References

[1] Booth, T. C., Dodge P. R., and Hepworth, H. K., 1982, "Rotor-Tip Leakage: Part 1-Basic Methodology," ASME J. Eng. Power, **104**, pp. 154–161.
[2] Denton, J. D., and Cumpsty, N. A., 1987, "Loss Mechanisms in Turbomachines," *Proceedings of the ImechE, Turbomachinery-Efficiency and Improvement*, Paper No. C260/87.
[3] Bunker, R. S., 2001, "A Review of Turbine Blade Tip Heat Transfer in Gas Turbine Systems," Ann. N.Y. Acad. Sci., **934**, pp. 64–79.
[4] Kim, Y. W., and Metzger, D. E., 1993, "Heat Transfer and Effectiveness on Film Cooled Turbine Blade Tip Models," ASME Paper No. 93-GT-208.
[5] Chen, G., Dawes, W. N., and Hodson, H. P., 1993, "A Numerical and Experimental Investigation of Turbine Tip Gap Flow," AIAA Paper No. 93-2253.
[6] Krishnababu, S. K., Newton, P., Dawes, W. N., Lock, G. D., and Hodson, H. P., 2005, "An Experimental and Numerical Investigation of the Tip Leakage Flow and Heat Transfer Using a Rotor Tip Gap Model," *Proceedings of the Fifth European Turbomachinery Conference*, Lille, France.
[7] Bunker, R. S., Bailey, J. C., and Ameri, A. A., 1999, "Heat Transfer and Flow on the First Stage Blade Tip of a Power Generation Gas Turbine. Part I: Experimental Results," ASME Paper No. 99-GT-169.
[8] Kwak, J. S., and Han, J. C., 2002, "Heat Transfer Coefficient and Film-Cooling Effectiveness on a Gas Turbine Blade Tip," ASME Paper No. 2002-GT-30194.
[9] Kwak, J. S., and Han, J. C., 2002, "Heat Transfer Coefficient and Film-Cooling Effectiveness on the Squealer Tip of a Gas Turbine Blade," ASME Paper No. 2002-GT-30555.
[10] Jin, P., and Goldstein, R. J., 2002, "Local Mass/Heat Transfer on Turbine Blade Near-Tip Surfaces," ASME Paper No. 2002-GT-30556.
[11] Ameri, A. A., Steinthorsson, E., and Rigby, D. L., 1998, "Effect of Squealer Tip on Rotor Heat Transfer and Efficiency," ASME J. Turbomach., **120**, pp. 753–759.
[12] Ameri, A. A., and Bunker, R. S., 1999, "Heat Transfer and Flow on the First Stage Blade Tip of a Power Generation Gas Turbine—Part II: Simulation Results," ASME Paper No. 99-GT-283.
[13] Yang, H., Acharya, S., Ekkad, S. V., Prakash, C., and Bunker, R., 2002a, "Flow and Heat Transfer Predictions for a Flat Tip Turbine Blade," ASME Paper No. 2002-GT-30190.
[14] Yang, H., Acharya, S., Ekkad, S. V., Prakash, C., and Bunker, R., 2002b, "Numerical Simulation of Flow and Heat Transfer Past a Turbine Blade With a Squealer Tip," ASME Paper No. 2002-GT-30193.
[15] Acharya, S., Yang, H., Prakash, C., and Bunker, R., 2003, "Numerical Study of Flow and Heat Transfer on a Blade Tip With Different Leakage Reduction Strategies," ASME Paper No. 2003-GT-38617.
[16] Saha, A. K., Acharya, S., Prakash, C., and Bunker, R., 2003, "Blade Tip Leakage Flow and Heat Transfer With Pressure Side Winglet," ASME Paper No. 2003-GT-38620.
[17] Mumic, F., Eriksson, D., and Sunden, B., 2004, "On Prediction of Tip Leakage Flow and Heat Transfer in Gas Turbines," ASME Paper No. 2004-GT-53448.
[18] Krishnababu, S. K., Newton, P. J., Dawes, W. N., Lock, G. D., Hodson, H. P., Hannis, J., and Whitney, C., 2009, "Aerothermal Investigations of Tip Leakage Flow in Axial Flow Turbines—Part I: Effect of Tip Geometry and Tip Clearance Gap," ASME J. Turbomach., **131**, p. 011006.
[19] Morphis, G., and Bindon, J. P., 1988, "The Effects of Relative Motion, Blade Edge Radius and Gap Size on the Blade Tip Pressures Distribution in an Annular Turbine Cascade With Clearance," ASME Paper No. 88-GT-256.
[20] Yaras, M. I., and Sjolander, S. A., 1992, "Effects of Simulated Rotation on Tip Leakage in a Planar Cascade of Turbine Blades—Part I: Tip Gap Flow," ASME J. Turbomach., **114**, pp. 652–659.
[21] Srinivasan, V., and Goldstein, R. J., 2003, "Effect of Endwall Motion on Blade Tip Heat Transfer," ASME J. Turbomach., **125**, pp. 267–273.
[22] Rhee, D. H., and Cho, H. H., 2006, "Local Heat/Mass Transfer Characteristics on a Rotating Blade With Flat tip in Low-Speed Annular Cascade—Part I: Near Tip Surface," ASME J. Turbomach., **128**, pp. 96–109.
[23] Rhee, D. H., and Cho, H. H., 2006, "Local Heat/Mass Transfer Characteristics on a Rotating Blade With Flat Tip in Low-Speed Annular Cascade—Part II: Tip and Shroud," ASME J. Turbomach., **128**, pp. 110–119.
[24] Stubley, G. D., 2004, CFX User Manual.
[25] Newton, P. J., Krishnababu, S. K., Lock, G. D., Hodson, H. P., Dawes, W. N., Hannis, J., and Whitney, C., 2005, "Heat Transfer and Aerodynamics of Turbine Blade Tips in a Linear Cascade," ASME Paper No. 2005-GT-69034.
[26] Menter, F. R., 1994, "Two-Equation Eddy-Viscosity Turbulence Models for Engineering Applications," AIAA J., **32**, pp. 269–289.
[27] Krishnababu, S. K., 2005, "A Computational Investigation of Tip Leakage Flow and Heat Transfer in Unshrouded Axial Flow Turbines," Ph.D. thesis, University of Cambridge, Cambridge, UK.

**P. J. Newton**

**G. D. Lock**

Department of Mechanical Engineering,
University of Bath,
Bath BA2 7AY, UK

**S. K. Krishnababu**

**H. P. Hodson**

**W. N. Dawes**

Whittle Laboratory,
Department of Engineering,
University of Cambridge,
Cambridge CB2 1PZ, UK

**J. Hannis**
Siemens Industrial Turbomachinery Ltd.,
Lincoln LN5 7FD, UK

**C. Whitney**
Alstom Power Technology Centre,
Leicester LN5 7FD, UK

# Aerothermal Investigations of Tip Leakage Flow in Axial Flow Turbines—Part III: TIP Cooling

*Contours of heat transfer coefficient and effectiveness have been measured on the tip of a generic cooled turbine blade, using the transient liquid crystal technique. The experiments were conducted at an exit Reynolds number of* $2.3\times 10^5$ *in a five-blade linear cascade with tip clearances of 1.6% and 2.8% chord and featuring engine-representative cooling geometries. These experiments were supported by oil-flow visualization and pressure measurements on the tip and casing and by flow visualization calculated using* CFX, *all of which provided insight into the fluid dynamics within the gap. The data were compared with measurements taken from the uncooled tip gap, where the fluid dynamics is dominated by flow separation at the pressure-side edge. Here, the highest levels of heat transfer are located where the flow reattaches on the tip surface downstream of the separation bubble. A quantitative assessment using the net heat flux reduction (NHFR) revealed a significant benefit of ejecting coolant inside this separation bubble. Engine-representative blowing rates of approximately 0.6–0.8 resulted in good film-cooling coverage and a reduction in heat flux to the tip when compared to both the flat tip profile and the squealer and cavity tip geometries discussed in Part 1 of this paper. Of the two novel coolant-hole configurations studied, injecting the coolant inside the separation bubble resulted in an improved NHFR when compared to injecting coolant at the location of reattachment.* [DOI: 10.1115/1.2950060]

*Keywords: turbine tip, heat transfer, novel cooling strategy*

## 1 Introduction

In a gas turbine, a gap between the rotating blade tip and the stationary casing is needed to allow relative motion. In an unshrouded turbine stage, this tip gap is nominally of the order 1% of blade height, though manufacturing tolerances, centrifugal expansion, and dissimilarity between the thermal loading of the blade row and casing lead to a variation in the clearance during the operating cycle. The difference in pressure between the pressure and suction aerofoil surfaces drives hot mainstream flow through the gap between the tip of the rotating blade and the surrounding casing. (Since the pressure difference across the gap is of the order of the exit dynamic pressure and the gap height-to-axial-length ratio is ~1, then the flow is driven by the pressure difference rather than viscous forces.) The leakage is essentially axial, i.e., orthogonal to the casing motion. The flow separates at the pressure-side edge and, depending on the blade thickness, reattaches downstream. At the exit of the clearance, the mixed-out flow meets the mainstream on the suction side (SS) and rolls up into a vortex. Geometric changes to the blade tip can be effective in reducing the leakage flow. Current design often features a recessed tip, known as a squealer, where the tip gap can be made smaller without the risk of significant tip contact with the casing. In addition to mechanical benefits, the recess also acts as a labyrinth seal, increasing resistance to the flow.

The tip leakage has a detrimental effect on the stage efficiency. Aerodynamic losses occur due to viscous effects within the tip gap itself and due to mixing losses when the leakage flow interacts with the passage flow. Furthermore, there is a reduction in work output from the stage as the leakage flow exits unturned, though some of this work may be recovered in latter stages of a multistage turbine. Another important consequence is the deterioration of the blade-tip surface due to regions of high local heat transfer in the narrow gap. The high velocity and thin boundary layers create a region in the engine that limits performance and demands frequent inspection. It is therefore important to understand the aerodynamics and heat transfer within the gap in order to introduce new tip designs and cooling configurations that might reduce the impact of this leakage flow.

This three-part paper presents experiments and computations relating to such flows modeled using generic, blade-tip geometries in an engine-simulated environment. Part 1 [1] explores the effects of introducing SS and cavity squealers. No relative motion between the tip and casing is present in the experiments conducted in this study and it is assumed that the flow through such clearances is essentially driven by pressure difference. Part 2 [2] explores the effects of relative motion computationally. The computations were performed using a single blade with periodic boundary conditions imposed along the boundaries in the pitchwise direction. Turbulence was modeled using three different models, viz., standard $k$-$\varepsilon$, low Re $k$-$\omega$, and standard $k$-$\omega$, in order to assess the capability of the models in correctly predicting the blade heat transfer.

A squealer geometry is one means of reducing heat transfer to the tip of the blade. An alternate method is to use cooling, and this is the focus of this paper. Film cooling is introduced at locations designed to optimize, in terms of both aerodynamics and heat transfer, the performance of the tip gap. Experimental measurements of heat transfer coefficient and film-cooling effectiveness using the transient liquid crystal technique are described. Pressure measurements, flow visualization, and computational results are used to link the aerodynamic and heat transfer characteristics of the flow.

Bunker [3] provided a review of research quantifying the losses and heat transfer associated with tip clearance flow. The science of

---

Contributed by the International Gas Turbine Institute of ASME for publication in the JOURNAL OF TURBOMACHINERY. Manuscript received June 14, 2007; final manuscript received July 5, 2007; published online October 3, 2008. Review conducted by David Wisler. Paper presented at the ASME Turbo Expo 2007: Land, Sea and Air (GT2007), Montreal, QC, Canada, May 14–17 2007.

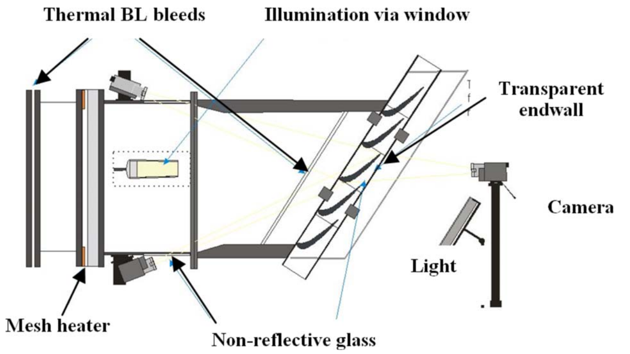

Fig. 1 Low-speed cascade modified for heat transfer measurements

Table 1 Details of low-speed cascade

| | |
|---|---|
| Number of blades | 5 |
| Chord, $c$ | 225 mm |
| Axial chord, $C_x$ | 103 mm |
| Pitch/chord ratio, $s/C$ | 0.824 |
| Aspect ratio | 2.11 |
| Stage exit $\mathrm{Re}_c$ | $2.3\times 10^5$ |
| Inlet flow angle, $\alpha_1$ | 32.5 deg |
| Blade exit angle, $\alpha_2$ | 75.6 deg |
| Practical tip clearance | 3.7–6.35 mm |
| Mass flow rate | 1.6 kg/s |
| Max thickness/chord | 14% |

tip leakage flow develops rapidly. There are, however, still relatively few studies of experimental cases that support heat transfer measurements with aerodynamic data. Due to the complexities of heat transfer studies, there have also been few parametric studies.

Haselbach and Schiffer [4] described a multinational five-year research initiative to address, in part, the shortage of cooled tip and shroud heat transfer understanding. Much of the early research used idealized models, as described in the Introduction to Part 1 [1]. Recently, some studies have been performed on cascade geometries. Kwak and Han have studied heat transfer and effectiveness on plain [5] and cavity [6] tip profiles in a blowdown cascade with compressible flow, where coolant was injected from the pressure-side corner and tip camber line. Increasing the coolant-blowing rate had the effect of partially blocking the tip clearance gap, thus reducing heat transfer upstream of ejection. The addition of pressure-side holes yielded marginally reduced heat transfer and improved effectiveness. Ahn et al. [7] performed similar tests using pressure sensitive paint to determine film-cooling effectiveness, obtaining broadly agreeable conclusions. Yang et al. [8] performed FLUENT calculations for the geometries investigated by Ahn et al. It was found that the numerical results tended to overpredict effectiveness but trends were fairly well matched. Kuwabara et al. [9] measured effectiveness on a 1.3× scale blade with film cooling, at a number of clearance heights using an infrared (IR) camera. Holes were located along a locus on the pressure-side surface near the corner. Effectiveness was shown to increase with blowing ratio for the range of blowing ratios tested, with no influence on the leakage trajectories witnessed in an oil-flow visualization. Nasir et al. [10] performed heat transfer and effectiveness measurements on a linear cascade model using cartridge heaters located inside the blade and a transient IR camera technique. Low values of effectiveness, which were localized to the immediate vicinity of the holes, indicating a poor cooling design, were recorded.

The purpose of this paper is to design a successful strategy to cool the tip of a generic turbine blade. The design is to be informed by the contours of heat transfer coefficient measured using an uncooled blade tip and also by knowledge of the fluid dynamics governing the flow through the tip gap. This fluid-dynamic information was obtained from pressure measurements, surface-shear oil-flow visualization, and streamline flow visualization using CFX. The new cooling strategy evolved from a comprehensive series of tests conducted in a 1D test rig, as opposed to the linear cascade data presented here [11].

## 2 Experimental Procedure

The experiments were conducted in the Whittle Laboratory at the University of Cambridge. A schematic of the low-speed linear cascade is shown in Fig. 1 and salient features are listed in Table 1. Further details are available in the works of Newton et al. [12] and Heyes et al. [13], who used the same cascade. The blades were cantilevered from the hub by a screw arrangement that allows the tip clearance gap to be set. All measurements were made about the central blade in the cascade. The Reynolds number, based on exit velocity and chord, was $2.3\times 10^5$.

The cascade has the same geometry as a two-stage high pressure (HP) version of the Peregrine turbine rig [14], which itself is based on an actual HP turbine. Three tip-gap geometries were tested: plain tip, SS squealer, and cavity squealer. Referring to Part 1 [1], two tip-gap heights, $H=3.7$ mm and 6.35 mm (1.6% and 2.8% chords) were used. The cavity and SS squealer geometries were designed in consultation with Siemens and Alstom—further details are available in Ref. [12]. Other details of the cascade are as follows: inlet mainstream stagnation temperature, pressure, and flow velocity—318 K, 137 Pa (gauge), and 4.5 m/s; exit pressure and velocity—1 atm and 15 m/s; coolant total temperature 293 K; and mainstream turbulence intensity <0.5%.

Most aerodynamic measurements were made on the casing but tip and aerofoil surface data were available for the plain-tip geometry. Static pressure data were also gathered using a pitchwise traversable end wall. This end wall was traversed using a computer-controlled stepper motor. Two rows of 21 pressure tapping holes, located one blade pitch apart, were used to measure end wall static pressure over the tip of the central blade and adjacent passages. All aerodynamic measurements were carried out using two cross-calibrated Scanivalve units.

The heat transfer experiments were performed on a polycarbonate replica of the cascade blades. Two replicas were made: a solid, plain-tip blade, and a hollow blade with interchangeable tips for the film-cooling and squealer investigations. Tip pieces were also constructed from Rhoacell, a low-conductivity machinable foam used to create an adiabatic surface. Heat transfer was measured using thermochromic liquid crystal (TLC)—the method of analysis is described in the next section. Both narrowband and wideband liquid crystals were used. Small uncertainties in the temperature obtained from calibration were ±0.2°C.

A hot mainstream flow was generated using an upstream wire mesh powered by a 15 kW dc supply from a welding unit. Due to the large mass flow through the cascade (~1.6 kg/s), only the flow entering the tip gap was heated, the remaining flow passing through a cold mesh adjacent (in a spanwise direction) to the heater mesh. Traverse profiles indicated minimal mixing between heated and unheated flows and a homogeneous temperature profile entering the blade row. Boundary layer bleeds were implemented on the end wall to eliminate the thermal boundary layer. Area traverses upstream of the blade row have shown temperature field distortion within the region of interest to be less than 0.1°C with the heater mesh active. The freestream turbulence intensity was less than 0.5% and no attempt has been made to reproduce engine-representative turbulence characteristics.

**Film Cooling Strategy.** Two cooling strategies were devised, both based on the data collected on the uncooled tip. In the *first* configuration, the coolant holes were located 5 mm from the

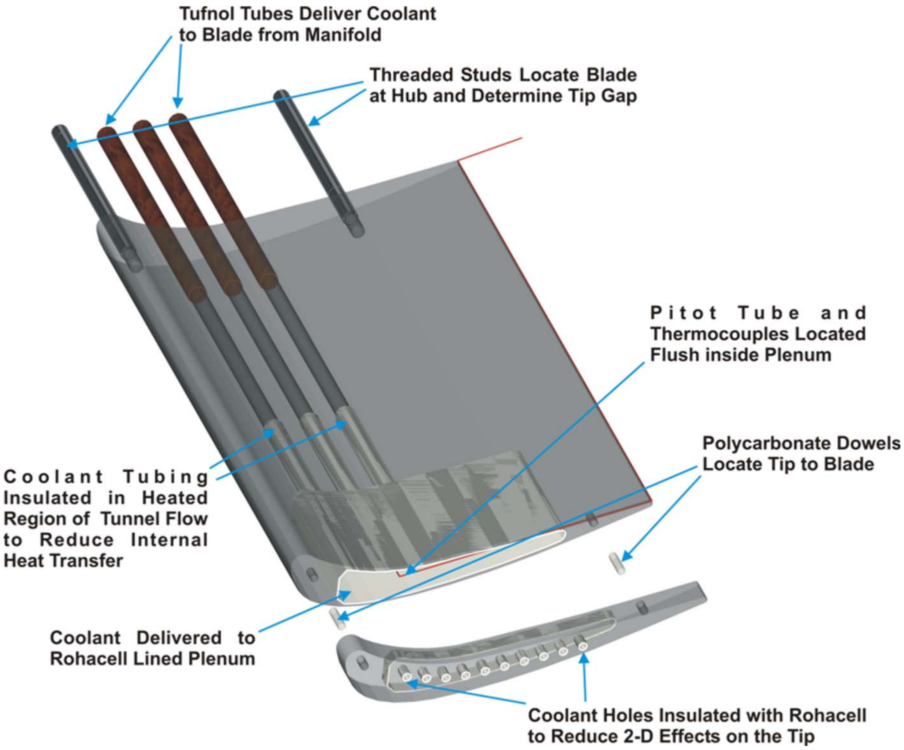

Fig. 2 Cooled blade subassembly

pressure-side corner perpendicular to the camber line ($x_c/C = 2.2\%$), in order to inject coolant into the separation bubble. The holes spanned from 15% to 70% chord to coincide with the regions of heightened heat transfer. This design was expected to have the secondary benefit of avoiding the regions of high static pressure at the leading edge of the blade, which would have resulted in coolant ingestion at low blowing rates. The *second* design injected coolant 10 mm from the pressure side edge ($x_c/C = 4.4\%$), to correspond with the line of reattachment. The 5 mm and 10 mm coolant geometries had 11 and 10 coolant holes, respectively. In both designs, the coolant holes were positioned exactly along a path perpendicular to the camber line. The hole pitch-to-diameter ratio was 3. The coolant-hole diameter was 4 mm, which scales to engine-representative film-cooling geometries, as suggested by Siemens and Alstom. Note that a coolant mass flow equal to 1% of the mainstream flow is typically used in the turbine. To reduce the edge effects around the holes, each 4 mm diameter hole was lined with a 1 mm thick Rhoacell ring of outer diameter 6 mm.

The coolant volumetric flow rate was measured by an inline flow meter. This controlled, pressurized flow passed through a Peltier unit [15] and required 20 min to reach the steady-state temperature of the tunnel air. The cooled tests were performed after completion of the uncooled test program and the blade used for the uncooled tests was hollowed to facilitate coolant flow to the tip. The dowels used to locate the uncooled blade were replaced with hollow tubes that delivered the compressed air from a manifold. A large chamber was created at the tip end of the blade to provide a uniform flow to the tip. The interior of the hollowed-out blade was lined with Rhoacell to prevent the convectively heated blade from heating the coolant during the transient experiment. A total pressure probe and two thermocouples were sealed inside the chamber, as shown in Fig. 2. No attempt was made to measure heat transfer on the blade aerofoil surfaces under coolant injection as the blade walls were very thin.

Due to the low speed nature of the cascade and the varying static pressure/leakage flow velocity about the blade-tip surface, cooled experiments were parametrized by coolant total pressure ratio, $Cp_{t,c}$, defined as

$$Cp_{t,c} = \frac{P_t - P_{t,c}}{P_t - P_e}$$

where $P_t$ and $P_{t,c}$ are the upstream and coolant total pressures and $P_e$ the static pressure at the cascade exit. Using the static pressure data available from the end wall measurements, it was possible to infer a mean blowing rate, $\bar{B}$ from $Cp_{t,c}$. The calculation uses the measured static pressure above the coolant holes to determine a local velocity ratio, which is then averaged to obtain $\bar{B}$. For completeness, cases are parametrized in terms of both $Cp_{t,c}$ and $\bar{B}$.

## 3 Transient Heat Transfer Technique

This section describes the experimental technique used to measure the heat transfer coefficient using TLCs. Further details of the theory are available in Refs. [16–18].

The heat transfer coefficient, $h$, is defined as

$$q_w = h(T_{\mathrm{aw}} - T_w) \tag{1}$$

where $q_w$ is the surface heat flux from the air to the wall, $T_w$ is the surface temperature of the wall, and $T_{\mathrm{aw}}$ is the adiabatic-wall temperature. $T_{\mathrm{aw}}$ depends on the total temperature of the air, $T_a$, and, in cases where compressibility is an issue, on the fluid dynamics.

In a typical transient test, an abrupt change in air temperature is generated, and a narrowband TLC is used to determine the surface temperature, $T_w$, of the test piece. Knowing the time, $t$, at which the surface reaches $T_w$, $h$ (assumed time invariant) can be calculated from the solution of Fourier's one-dimensional conduction equation for the case of a semi-infinite plate.

In the tests reported here, the mesh heater created an effective step change in the air temperature, but at the test section an exponential-type rise in air temperature was produced. Newton et

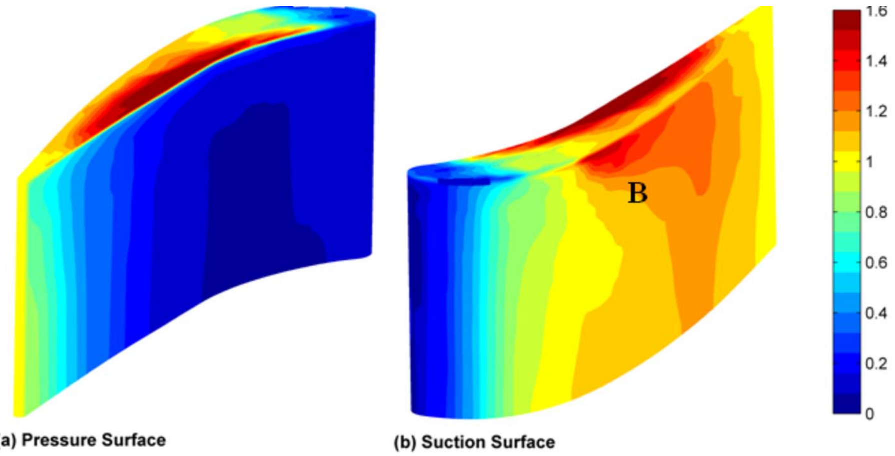

(a) Pressure Surface (b) Suction Surface

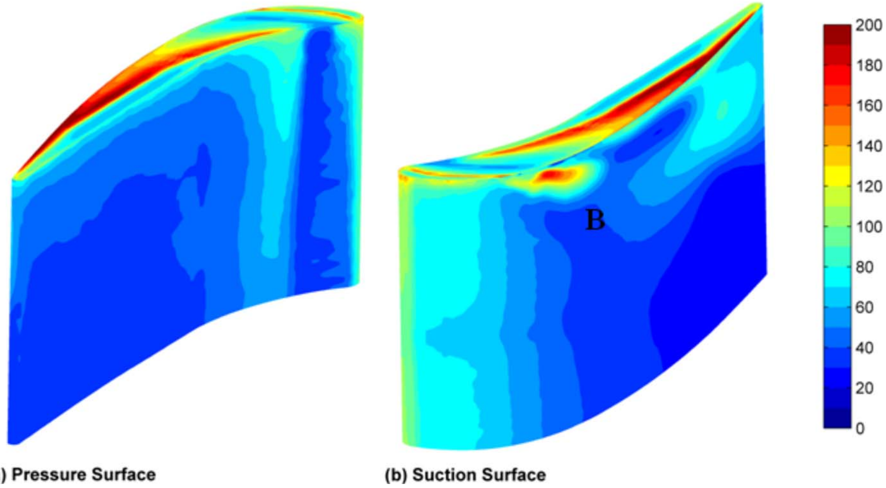

(a) Pressure Surface (b) Suction Surface

**Fig. 3 (*a*) Pressure coefficient for tip and aerofoil surfaces—colored version available in Ref. [24]. (*b*) Heat transfer coefficient (W m$^{-2}$ K$^{-1}$) for tip and aerofoil surfaces—colored version available in Ref. [24].**

al. [18] showed that the adiabatic wall temperature, $T_{\mathrm{aw}}$, could be fitted by an exponential series of $m$ terms, such that

$$T_{\mathrm{aw}}(t) = T_{a,0} + \sum_{j=1}^{m} T_{a,j}(1 - e^{-t/\tau_j}) \tag{2}$$

where $T_{a,0}$ is the air temperature at $t=0$, and $T_{a,j}$ and $\tau_j$ are the constant amplitudes and time constants, respectively. As $t \rightarrow \infty$,

$$T_{\mathrm{aw},\infty} = T_0 + \sum_{j=1}^{m} T_{a,j} \tag{3}$$

where $T_0$ is the initial temperature of the wall, such that

$$T_0 = T_{a,0} \tag{4}$$

Fourier's conduction equation for a semi-infinite slab has been solved by Gillespie et al. [19] for the case where there is a simple exponential increase in the air temperature, corresponding to the case where $m=1$ in Eq. (3). The solution is

$$\theta = \frac{T_w - T_0}{T_{\mathrm{aw},\infty} - T_0} = g(\beta,\beta_\tau) \tag{5}$$

where

$$g(\beta,\beta_\tau) = 1 - \frac{1}{1+\beta_\tau^2} e^{\beta^2} \operatorname{erfc}(\beta) - e^{-t/\tau} \frac{\beta_\tau^2}{1+\beta_\tau^2} \times \left\{ 1 + \frac{1}{\beta_\tau} \left[ \frac{1}{\pi} \sqrt{\frac{t}{\tau}} + \frac{2}{\pi} \sum_{n=1}^{\infty} \frac{1}{n} e^{-n^2/4} \sinh\left( n \sqrt{\frac{t}{\tau}} \right) \right] \right\} \tag{6}$$

$$\beta = \frac{h\sqrt{t}}{\sqrt{\rho c k}} \tag{7}$$

and

$$\beta_\tau = \frac{h\sqrt{\tau}}{\sqrt{\rho c k}} \tag{8}$$

For the case where $\tau=0$, Eq. (5) simplifies to

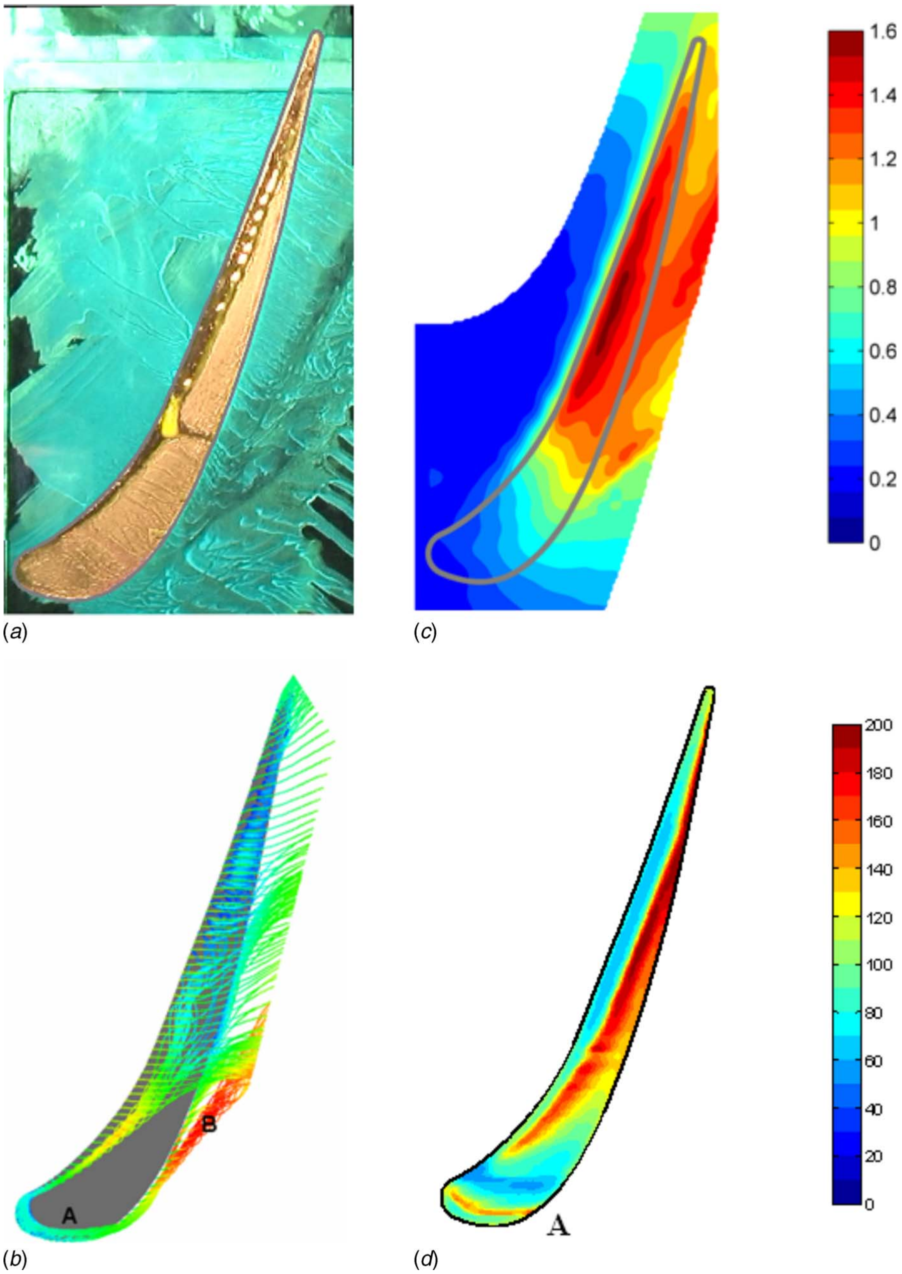

**Fig. 4** ((*a*) and (*b*)) Oil-flow visualization and pressure coefficient on casing—colored version available in Ref. [24]. ((*c*) and (*d*)) CFX streamlines and heat transfer coefficient ($Wm^{-2}K^{-1}$) on tip—colored version available in Ref. [24].

$$\theta = f(\beta) \tag{9}$$

where, from Eq. (6),

$$f(\beta) = 1 - e^{\beta^2}\,\mathrm{erfc}(\beta) \tag{10}$$

which is the well-known solution of Fourier's equation for a step change in the air temperature.

The general solution for an exponential series, corresponding to Eq. (3), is given by Newton et al. [18] as

$$\theta = \sum_{j=1}^{m} \frac{T_{a,j}}{T_{\mathrm{aw},\infty} - T_0} g(\beta, \beta_{\tau j}) \tag{11}$$

For the special case where $m=1$, $T_{a,1}=T_{\mathrm{aw},\infty}-T_0$ and Eq. (11) reduces to Eq. (6).

It has been verified that $h$ is time independent under similar conditions (within experimental uncertainty) using liquid crystals, which are activated at different temperatures [18].

The presence of cooling, i.e., injected air at a second temperature $T_c$, introduces the film-cooling effectiveness, $\eta=(T_{\mathrm{aw}}-T_c)/(T_a-T_c)$ as a variable in addition to $h$. Like $h$, it is assumed that $\eta$ is only a function of the aerodynamics and so is time invariant.

The cooled heat transfer measurements were performed in two stages. Film-cooling effectiveness was measured on a Rhoacell tip with the wideband TLC. Heat transfer coefficient was then obtained by a separate experiment using a narrowband crystal and polycarbonate tip. The heat transfer coefficient was deduced using the locally measured $\eta$.

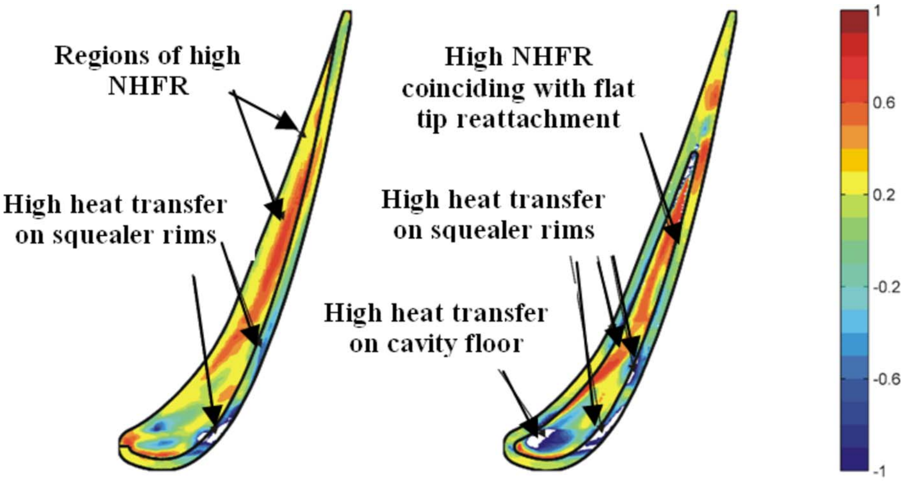

(*a*) SSS (*b*) CAVITY

**Fig. 5** ((***a***) **and** (***b***)) **NHFR for SS squealer and cavity tips—colored version available in Ref.** [**24**]

In order to evaluate the influence of the coolant in an engine environment, a net heat flux reduction (NHFR) similar to that used by Sen et al. [20] is used. The NHRF is the ratio of the reduction in heat flux due to film cooling to the heat flux without cooling,

$$\Theta_E = \frac{T_a - T_c}{T_r - T_w} \tag{12}$$

$$\text{NHFR} = \frac{q_w - q_{w,c}}{q_w} = 1 - \frac{h_c}{\overline{h_{\text{uc}}}}(1 - \eta\Theta_E) \tag{13}$$

Here, $\overline{h_{\text{uc}}}$ is the mean uncooled heat transfer coefficient. The objective of film cooling is to increase the NHFR by reducing the heat transfer coefficient and increasing $\eta$. The NHFR is most meaningful at engine-representative conditions. The value of $\theta_E$ was selected as 1.5, comparable to that of Sargison et al. [21] and based on an air total temperature $T_a$=1900 K, a blade metal temperature $T_w$=1200 K, a coolant total temperature $T_c$=880 K, and a transonic air recovery temperature $T_r$=1880 K. An integrated average of the NHFR may be used to determine the overall performance of a cooled geometry by means of a summation over all $i$=1 to $n$ pixels present for the cooled geometry. The reduction in tip surface area resulting from the holes is approximately 3% and this acts so as to increase the measured NHFR. No data are acquired from the Rhoacell ring surrounding the holes so the numerator of Eq. (15) is scaled so as to assume an average value in this region as follows:

$$S = \frac{A_{\text{tip,unmeasured}} + A_{\text{tip,measured}}}{A_{\text{tip,measured}}} \tag{14}$$

$$\overline{\text{NHFR}} = 1 - \frac{S}{n_{\text{uc}}\overline{h_{\text{uc}}}} \sum_{i=1}^{n_c} h_{c,i}(1 - \eta\Theta_E) \tag{15}$$

Note that this definition of $\overline{\text{NHFR}}$ differs slightly from that of Newton et al. [12]. The inclusion of $S$ and the area of the coolant holes in Eq. (15) yield a slightly higher NHFR.

Experimental uncertainties have been calculated using the method described by Owen et al. [22] and Newton [23], which introduces an amplification parameter. If $P_T$ is the uncertainty in temperature, then this is amplified (via the solution of Fourier's equation) to a larger uncertainty in $h$, $P_h$, depending on the crystal activation time, and exponential time constants in the gas-temperature history. Uncertainties in $\eta$ and NHFR were determined in a similar manner. Typical uncertainties are as follows: $h$, 7%; $\eta$, 8%; and NHFR, 10%.

## 4 Experimental Results

A comprehensive parametric study of turbine tip aerodynamics and heat transfer by experiment has been conducted by Newton [23] and further details are available in this thesis. Three *uncooled* tip geometries, at three gap heights, were tested: plain tip, SS squealer, and cavity (the latter two geometries are shown in Fig. 5). Aerodynamic and heat transfer measurements were made on the casing and tip, and aerofoil surfaces. These experiments are supported by flow visualization experiments and information computed using the CFX code. The *cooled* experiments were conducted using only the plain tip configuration, with two different cooling geometric arrangements as described above and shown in Fig. 6. The data were collected at three nominal coolant blowing rates and at three gap heights.

**Aerodynamics of Uncooled Plain Tip.** Figure 3(*a*) illustrates measurements of the pressure coefficient, $C_p$, on the plain tip blade at a dimensionless clearance height $H/C$=2.2%. The view also shows the pressure and suction surfaces of the aerofoil, though only 33% of the blade span is shown. The impingement of the leakage vortex is visible on the SS aerofoil surface (marked B). The leakage vortex was observed to increase in intensity as clearance gap increased. Figure 4(*a*) is an oil-flow visualization on the tip and end wall—the images are superimposed. These figures clearly illustrate that between $0.2<x/C<0.9$ there is a region of high velocity associated with the flow separating from the pressure-side edge of the tip gap. The flow subsequently decelerates as it reattaches to the tip surface before reaching the suction surface. A region of low leakage velocity is observed near the leading edge of the blade tip, where there is less pressure differential to drive flow across the gap. Figure 4(*b*) shows the corresponding $C_p$ measured on the casing, indicating similar features.

Figure 4(*c*) illustrates the trajectory of leading-edge streamlines, obtained by CFX. The streamlines are color-coded to indicate the magnitude of the velocity. These computational flow visualization predictions support the experimental data, indicating high leakage velocities in the regions of high $C_p$. The computational fluid dynamics (CFD) has captured the pressure-side separation discussed above and also reveals a similar separation near the leading edge of the blade ($x/C$=0), marked A where flow is

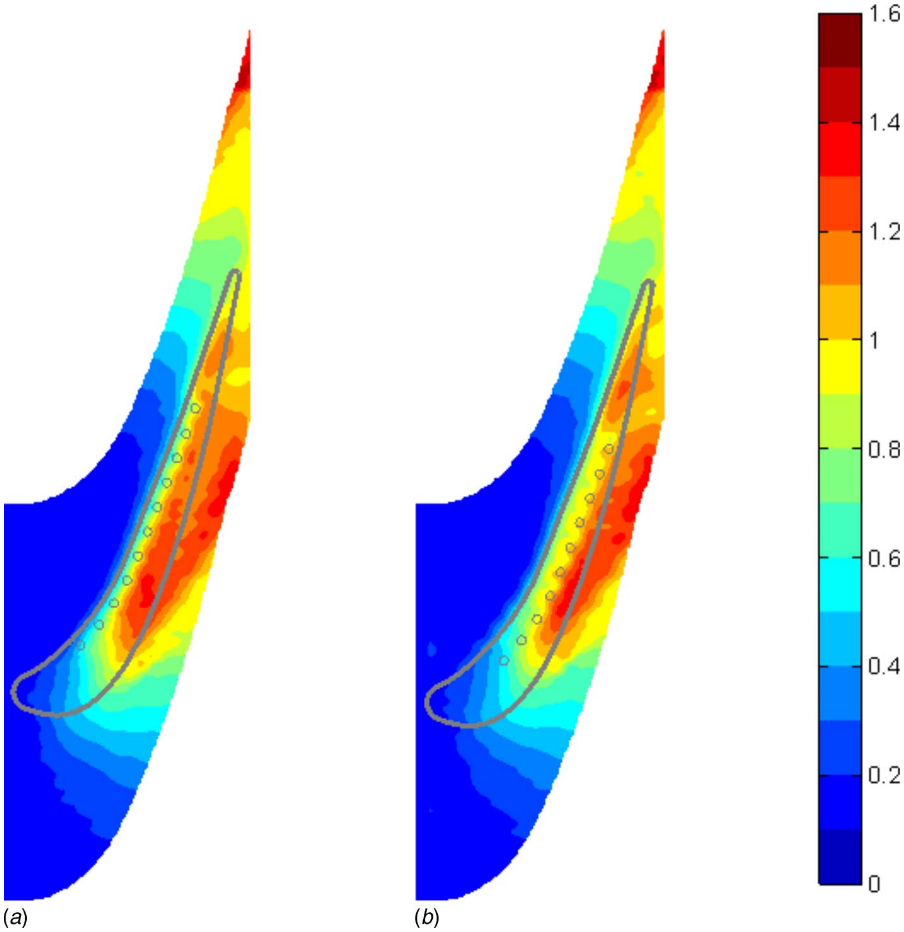

**Fig. 6 Casing $C_p$ for first (*a*) and second (*b*) cooling configurations—colored version available in Ref. [24]**

driven into the tip gap by HP near the stagnation point of the blade. The highest velocities are calculated in the tip leakage vortex on the SS of the tip, marked B in the figure. As described in Part 1 [1], two other uncooled tip-gap geometries were tested: a SS squealer and a cavity squealer. The reader is referred to this paper for a detailed discussion of how the pressure fields for these configurations differ to that associated with the plain tip.

**Uncooled Heat Transfer Experiments.** Figure 3(*b*) illustrates measurements of the heat transfer coefficient on the plain tip blade as well as data on the suction and pressure aerofoil surfaces at a clearance height of $H/C=2.2\%$. Again note that only 33% of the blade span is shown. The most striking observation is that the highest heat transfer coefficient on any surface (including the stagnation region on the pressure and suction aerofoil surfaces) is observed on the tip of the blade. Figure 4(*d*) shows the heat transfer coefficient contours on the tip only, which will be used to directly compare with the film-cooled experiments discussed below. The data in close proximity to the aerofoil edges are less accurate than elsewhere due to edge effects.

**Uncooled Heat Transfer Experiments.** Figure 3(*b*) illustrates measurements of the heat transfer coefficient on the plain tip blade as well as data on the suction and pressure aerofoil surfaces at a clearance height of $H/C=2.2\%$. Again note that only 33% of the blade span is shown. The most striking observation is that the highest heat transfer coefficient on any surface (including the stagnation region on the pressure and suction aerofoil surfaces) is observed on the tip of the blade. Figure 4(*d*) shows the heat transfer coefficient contours on the tip only, which will be used to directly compare with the film-cooled experiments discussed below. The data in close proximity to the aerofoil edges are less accurate than elsewhere due to edge effects.

The associated pressure field, oil-flow visualization, and CFD flow visualization are shown in Figs. 3(*a*) and 4(*a*)–4(*c*). It is observed that the maximum heat transfer coefficient occurs in the region of reattachment on the blade tip essentially along a line parallel to the pressure-side rim. A ridge of high heat transfer is also observed near the leading edge of the blade where flow, driven into the tip gap by high pressure near the stagnation point of the blade, separates and then reattaches (see A in Fig. 4(*d*)). Generally there is low heat transfer in this leading-edge region where there is less pressure differential to drive flow across the gap.

The impingement of the tip leakage vortex (marked B in Figs. 3(*a*) and 3(*b*)) is visible on the SS aerofoil surface where high heat transfer is observed. Though not shown here, the area of the region influenced by the leakage vortex is observed to increase as the intensity of the vortex increases with the increase in clearance gap [23]. It is interesting to note that the origin of the leakage vortex appears to be the flow over the leading edge of the suction surface.

**NHFR in Uncooled Experiments.** The distribution of heat transfer coefficient over the uncooled SS squealer and a cavity squealer blade tips is described in Part 1 [1]. The reader is referred to this paper for a detailed discussion of how the temperature fields for these configurations differ to that associated with the

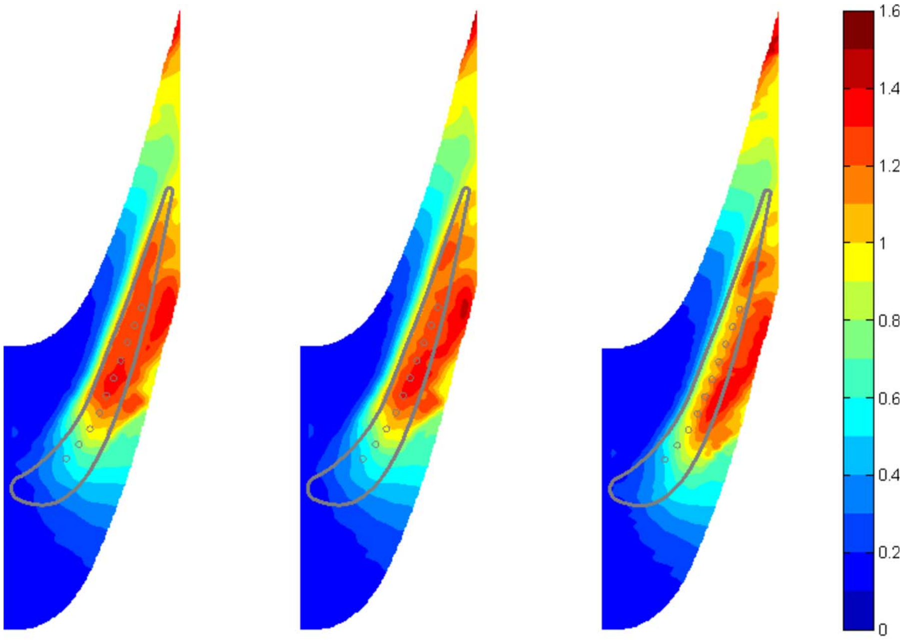

($a$) $\bar{B}$ = 0.6 ($b$) $\bar{B}$ = 0.8 ($c$) $\bar{B}$ = 1.0

**Fig. 7 (($a$)–($c$)) Pressure coefficient on casing for $B$=0.6, 0.8, and 1.0, second cooling configuration—colored version available in Ref. [24]**

plain tip. However, to put into context the performance of the cooled tip profiles described below, the uncooled SS squealer and cavity tip profiles have been assessed in terms of the NHFR.

In the absence of coolant, the NHFR (Eq. (13)) becomes

$$\mathrm{NHFR}_{\mathrm{uc}} = 1 - \frac{\overline{h_{\mathrm{squealer}}}}{h_{\mathrm{plain}}} \qquad (16)$$

The SS squealer case at $H/C=2.2\%$ (Fig. 5($a$)) is dominated by large regions of high positive NHFR, corresponding to low local heat transfer relative to the flat tip case. This result is due to the enlarged flow area away from the squealer resulting in lower velocity and increased regions of separation on the tip floor. Only on the squealer rim is there a significant level of elevated heat transfer relative to the flat tip case and this occurs in a relatively small region. The area averaged value of NHFR, $\overline{\mathrm{NHFR}}$, was calculated as 0.15.

For the cavity tip profile, Fig. 5($b$) (again at $H/C=2.2\%$), the leading-edge region and SS cavity rim are subjected to elevated heat transfer relative to the flat tip profile. The heat transfer on the internal cavity walls was not measured. Therefore the average value of surface $h$ was assumed to be present on the cavity walls and Eq. (16) was scaled by the scaling factor of Eq. (13), yielding $\overline{\mathrm{NHFR}}$ of −0.01 for the cavity tip, implying no net gain in terms of heat transfer.

**Aerodynamics of Cooled Tip.** Aerodynamic measurements were performed over a range of blowing rates for the two cooled tip geometries. Only the data for a tip clearance height $H/C=2.2\%$ are shown here, though data have also been collected at $H/C=1.6\%$ and 2.8% [23].

Figure 6($a$) shows the end wall pressure coefficient for a fixed blowing rate of $\bar{B}\approx 1.0$, corresponding to $Cp_{t,c}=0$, for the *first* cooling strategy, $x_c/C=2.2\%$. It compares directly to Fig. 4($b$) where no coolant was employed. The influence of injecting the coolant into the tip leakage flow is twofold: There is a reduction in the pressure coefficient within the tip gap and also a reduction in the size and intensity of the leakage vortex. A particularly strong reduction in pressure coefficient is notable over the coolant holes, coinciding with the separation bubble in the uncooled case. Regions of low pressure coefficient are evident immediately upstream of the holes, near the pressure-side corner, indicating the removal of this separation bubble. The reduction in the intensity and size of the leakage vortex suggests a reduction in tip leakage losses and a likely reduction in discharge coefficient.

Figure 6($b$) shows similar data for the *second* coolant geometry, where $x_c/C=4.4\%$. As with the case for $x_c/C=2.2\%$, a dramatic reduction in pressure coefficient on the tip surface upstream of the coolant holes is evident. Though not shown here (see Ref. [23]), increasing the clearance height decreases the reduction in pressure coefficient and this is due to the coolant filling proportionally less of the tip gap.

Figure 7 shows similar data for a fixed tip gap height at three different coolant blowing rates: 0.6, 0.8, and 1.0. Increasing the coolant blowing rate, by means of increasing the coolant plenum total pressure, is seen to shift the peak region and reduce the pressure coefficient on the casing. At low blowing rates, the coolant flow is more inclined to remain attached to the tip surface and has less influence on the leakage flow. However, even at these low blowing rates, a reduction in peak pressure coefficient above the separation and in the leakage vortex is evident.

**Cooled Heat Transfer Experiments.** Heat transfer experiments were performed at a number of blowing rates for the two different coolant configurations at the same three gap heights investigated in the uncooled experiments. Only data for the case of $H/C=2.2\%$ are shown here.

Figure 8 is an oil-flow visualization for the first cooling configuration, with holes located at $x_c/C=2.2\%$. The average coolant blowing rate was $\bar{B}=0.74$, which corresponded to a coolant mass flow equal to ~0.5% of the mainstream flow—a percentage not untypical of that used in engineering practice. The corresponding film-cooling effectiveness, heat transfer coefficient, and NHFR plots are shown in Fig. 9. The faded (dry) regions from the flow visualization closely match the regions of high heat transfer on the tip. Similarly the regions near the leading-edge (i.e., $x/C<0.2$) and the trailing-edge region both demonstrate low surface shear

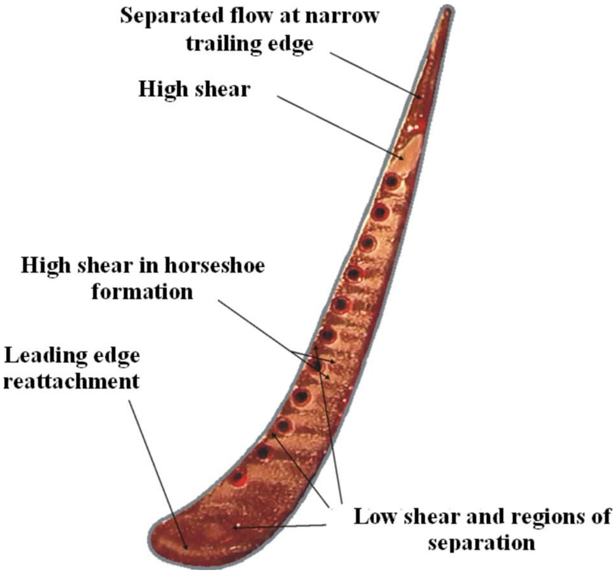

**Fig. 8 Oil-flow visualization on tip: first cooling geometry, $x_c/C=2.2\%$—colored version available in Ref. [24]**

and this manifests itself as low heat transfer. Note that Figs. 4(*a*) and 4(*b*) are the equivalent oil-flow visualization and heat transfer maps for the uncooled tip.

The salient flow features are labeled in Fig. 9. The holes have been positioned to inject coolant into the separation bubble and this has successfully avoided the high heat transfer associated with reattachment present in the uncooled case (Fig. 4(*d*)), as planned. The classic cooling footprints shown in the effectiveness plot indicate that the flow is essentially perpendicular to the chord and that the coolant remains attached. Away from the holes, the footprints are relatively narrow and significant regions exist between the holes where effectiveness is close to zero. There are regions of high heat transfer surrounding the coolant holes where the tip leakage flow accelerates around the emerging plumes of coolant. Downstream of the holes, there is elevated heat transfer where the passage flow mixes with the coolant. The coolant emerges normal to the tip surface into a region of turbulent unattached flow, a scenario which is antithetical to typical film cooling practice. The effectiveness data suggest that some of the coolant becomes entrained into the vortex within the separation and is drawn upstream towards the pressure-side edge. Figure 8, the oil-flow visualization, supports this observation. (Note that the inside of the blade is well insulated using a low-conductivity foam and conduction will be small—see also Fig. 12.)

The NHFR provides a quantification of the reduction in heat transfer to the tip with film cooling compared to that heat transfer without cooling. The objective of film cooling is to increase the NHFR by reducing heat transfer coefficient and increasing effectiveness. This cooling geometry exhibits high positive NHFR under the coolant footprints. Some regions of negative NHFR are observed in areas where the effectiveness is low but the heat transfer coefficient has been elevated due to increased turbulent mixing with the cooling present and the impingement of the coolant jet vortices back to the surface. The overall result is a noticeable reduction in heat flux to the blade tip, with an integrated average $\overline{\text{NHFR}}=0.37$, indicating an effective cooling design.

Figures 10 and 11 illustrate the effect of decreased ($\bar{B}=0.58$) and increased ($\bar{B}=0.99$) blowing rates for the first cooling geometry. The marginal decrease in blowing rate is observed to create little change to the effectiveness, heat transfer, or NHFR plots detailed in Fig. 9 ($\bar{B}=0.74$). Indeed, reducing the blowing rate resulted in an identical $\overline{\text{NHFR}}=0.37$. However, increasing the blowing rate to unity results in a detriment to $\overline{\text{NHFR}}=0.28$ the effectiveness plots of Fig. 11 indicate that the coolant has lifted off the tip surface. In terms of heat transfer, increasing the blowing rate beyond $\bar{B}=0.58$ has not improved the cooling characteristics, implying a waste of coolant.

Figure 12 illustrates the results for the second cooling configuration with holes located at $x_c/C=4.4\%$, corresponding with the region of reattachment and highest heat transfer in the uncooled experiments. The blowing rate, $\bar{B}=0.8$, is nominally similar to that used in Fig. 9. This heat transfer coefficient figure illustrates that the cooling design has been less successful in removing the band of high heat transfer associated with the flow reattachment in the uncooled case. The even distribution of film coolant about the tip surface, without a dramatic change in heat transfer coefficient, results in $\overline{\text{NHFR}}=0.23$, significantly less than when coolant is injected into the bubble (the first cooling configuration) but still an enhancement over the uncooled profiled tips.

This paper has presented data for the most successful cases tested, i.e., those with at tip clearance to chord ratio, $H/C=2.2\%$. Table 2 summarizes $Cp_{t,c}$, $\bar{B}$, and $\overline{\text{NHFR}}$ for all investi-

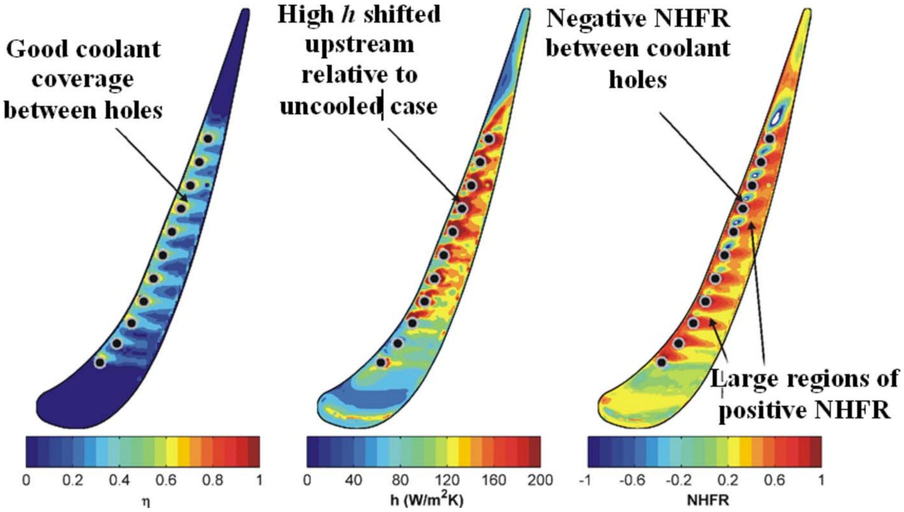

**Fig. 9 Cooled tip $x_c/C=2.2\%$, $h$, $\eta$, NHFR, and $\bar{B}=0.74$—colored version available in Ref. [24]**

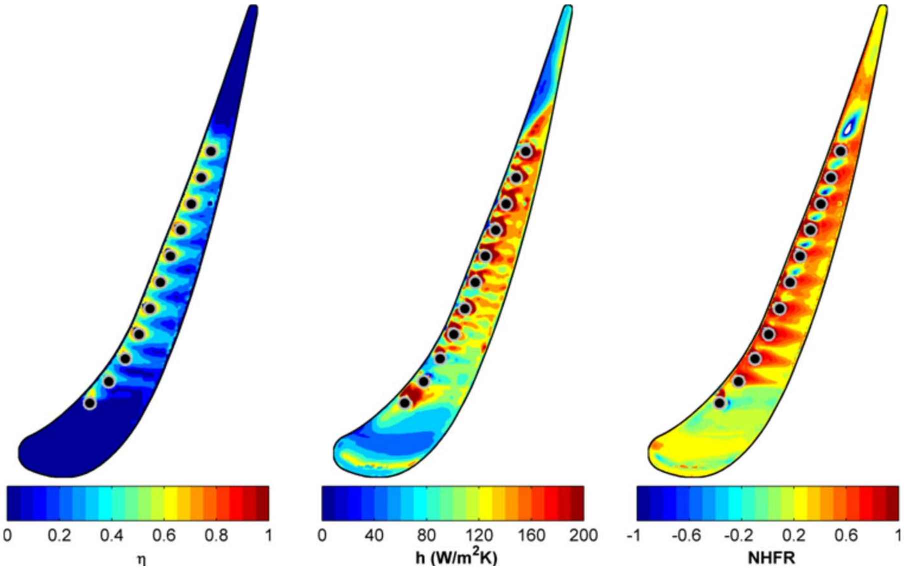

**Fig. 10 Cooled tip $x_c/C$=2.2%, $h$, $\eta$, NHFR, and $\bar{B}$=0.58—colored version available in Ref. [24]**

gated geometries and blowing rates, details of which can be found in Ref. [23]. Increasing the ratio $H/C$ to 2.8% or reducing this ratio to 1.6% produced qualitatively similar features to those presented here but quantitatively poorer performances in terms of $\overline{\text{NHFR}}$ for a given geometry and $\bar{B}$.

## 5 Conclusions

Two successful and novel strategies to cool the tip of a generic turbine blade have been presented. The film cooling designs were informed by the contours of heat transfer coefficient measured using an uncooled blade tip. It was observed that the highest heat transfer coefficients on any surface (including the stagnation region on the pressure and suction aerofoil surfaces) were measured on the tip of this uncooled blade. Supporting fluid-dynamic information, which included pressure measurements, surface-shear oil-flow visualization, and streamline flow visualization using CFX, revealed that the fluid dynamics of the tip gap was governed by a separation bubble near the pressure-side entrance to the gap; here, the leakage flow separated from the tip surface and reattached in a region parallel to the pressure-side rim. The highest heat transfer coefficients were located in this region of reattachment.

Flow visualization and pressure data revealed that injecting coolant inside this separation bubble significantly altered the fluid dynamics of the overtip flow. Experiments using TLC illustrated the successful elimination of the region of high heat transfer associated with the reattachment present in the uncooled case. Measurements of heat transfer coefficient and cooling effectiveness led to a calculation of the net heat flux reduction (NHRF) to the blade tip. High levels of film-cooling effectiveness were observed at engine-representative blowing rates of approximately 0.5–0.8. The blockage effect of the plumes of emerging coolant resulted in localized accelerations of the leakage flow surrounding the holes

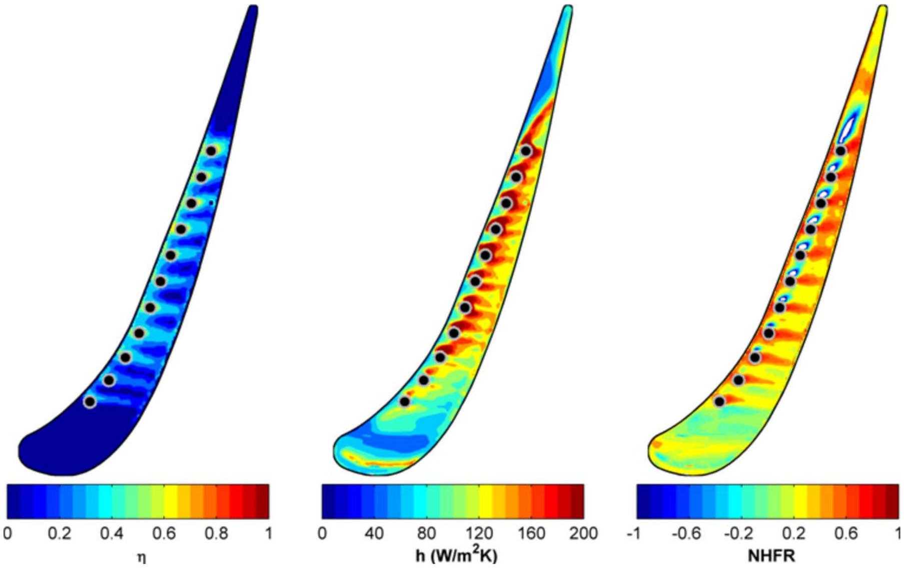

**Fig. 11 Cooled tip $x_c/C$=2.2%, $h$, $\eta$, NHFR, and $\bar{B}$=0.99—colored version available in Ref. [24]**

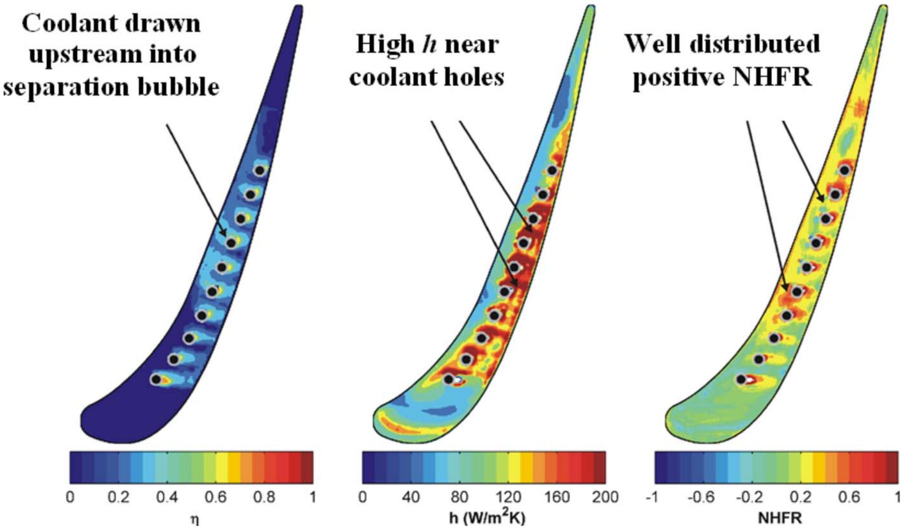

Fig. 12 Cooled tip $x_c/C=4.4\%$, $h$, $\eta$, NHFR, and $\bar{B}=0.8$—colored version available in Ref. [24]

with associated elevated heat transfer. However, an integrated average of the NHFR revealed that the net heat flux to the tip at engine-level temperatures would be reduced by 37% for a coolant mass flow equivalent to 0.5% of the mainstream, indicating an effective cooling design.

A second design featured the injection of coolant at the reattachment region, rather than inside the separation bubble. This configuration was again found to be a successful means of reducing the heat flux to the tip, but less effective than the first strategy. Both cooling configurations featured a superior NHFR when compared with the SS squealer and cavity squealer discussed in Part 1.

## Nomenclature

$B$ = blowing rate, $B=\rho_c v_c/\rho_a v_a$
$C$ = specific heat of wall
$C$ = chord, 225 mm
$C_p$ = pressure coefficient, $C_p=(P_t-P)/(P_t-P_e)$
$f(\beta)$ = step-change solution of Fourier's equation
$g(\beta,\beta_\tau)$ = exponential solution of Fourier's equation
$h$ = heat transfer coefficient $(q_w/(T_{\mathrm{aw}}-T_w))$
$H$ = tip clearance gap
$k$ = thermal conductivity of wall
$m$ = number of terms in exponential series
$P$ = pressure
$q_w$ = heat flux from air to wall
$t$ = time, blade thickness
$T$ = temperature
$v$ = freestream velocity
$x$ = distance along the chord
$\beta$ = parameter in the step-change solution $\beta=(h\sqrt{t/\rho ck})$
$\beta_\tau$ = parameter in the exponential solution $\beta_\tau=(h\sqrt{\tau/\rho ck})$
$\rho$ = density
$\eta$ = film-cooling effectiveness, $\eta=(T_{\mathrm{aw}}-T_c)/(T_a-T_c)$
$\theta$ = nondimensional temperature $\theta=(T_w-T_0)/(T_{\mathrm{aw},\infty}-T_{w0})$
$\Theta_E$ = nondimensional engine temperature $\Theta_E=(T_a-T_c)/(T_r-T_w)$
$\tau$ = time constant

### Subscripts

0 = value at $t=0$
$\infty$ = value as $t\to\infty$
$a$ = mainstream air
aw = adiabatic wall
$c$ = coolant, cooled
$e$ = cascade exit
$j$ = $j$th term in series
$r$ = recovery
$t$ = upstream stagnation condition
uc = uncooled

Table 2 Net heat flux reduction

| | | Net heat flux reduction | | |
|---|---|---|---|---|
| Profile | $H/C$ | $Cp_{t,c}$ | $\bar{B}$ | $\overline{NHFR}$ |
| SSS | 2.2% | N/A | N/A | 0.15 |
| CAVITY | 2.2% | N/A | N/A | 0.0 |
| $x_c/C=2.2\%$ | 1.6% | 0.32 | 0.78 | 0.28 |
| $x_c/C=2.2\%$ | 1.6% | 0.13 | 0.91 | 0.29 |
| $x_c/C=2.2\%$ | 1.6% | 0.04 | 0.97 | 0.22 |
| $x_c/C=2.2\%$ | 2.2% | 0.62 | 0.58 | 0.37 |
| $x_c/C=2.2\%$ | 2.2% | 0.43 | 0.74 | 0.37 |
| $x_c/C=2.2\%$ | 2.2% | 0.02 | 0.99 | 0.28 |
| $x_c/C=2.2\%$ | 2.8% | 0.57 | 0.50 | 0.3 |
| $x_c/C=2.2\%$ | 2.8% | 0.18 | 0.88 | 0.31 |
| $x_c/C=4.4\%$ | 1.6% | 0.82 | 0.38 | 0.06 |
| $x_c/C=4.4\%$ | 1.6% | 0.23 | 0.85 | 0.06 |
| $x_c/C=4.4\%$ | 1.6% | −0.30 | 1.17 | 0.03 |
| $x_c/C=4.4\%$ | 2.2% | 0.98 | 0.20 | 0.23 |
| $x_c/C=4.4\%$ | 2.2% | 0.72 | 0.49 | 0.26 |
| $x_c/C=4.4\%$ | 2.2% | 0.30 | 0.8 | 0.23 |
| $x_c/C=4.4\%$ | 2.8% | 0.79 | 0.42 | 0.31 |
| $x_c/C=4.4\%$ | 2.8% | 0.52 | 0.67 | 0.2 |
| $x_c/C=4.4\%$ | 2.8% | −0.06 | 1.04 | 0.19 |

## References

[1] Krishnababu, S. K., Newton, P. J., Dawes, W. N., Lock, G. D., Hodson, H. P., Hannis, J., and Whitney, C., 2009, "Aerothermal Investigations of Tip Leakage Flow in Axial Turbines—Part I: Effect of Tip Geometry and Tip Clearance Gap," ASME J. Turbomach., **131**, p. 011006.

[2] Krishnababu, S. K., Dawes, W. N., Hodson, H. P., Lock, G. D., Hannis, J., and Whitney, C., 2009, "Aerothermal Investigations of Tip Leakage Flow in Axial Turbines—Part II: Effect of Relative Casing Motion," ASME J. Turbom-

ach., **131**, p. 011007.
[3] Bunker, R. S., 2001, "A Review of Turbine Blade Tip Heat Transfer, Heat Transfer in Gas Turbine Systems," Ann. N.Y. Acad. Sci., **934**, pp. 64–79.
[4] Haselbach, F., and Schiffer, H. P., 2004, "Aerothermal Investigations on Turbine Endwalls and Blades (AITEB)," ASME Paper No. GT-2003-53078.
[5] Kwak, J. S., and Han, J. C., 2002, "Heat Transfer Coefficient and Film-Cooling Effectiveness on a Gas Turbine Blade Tip," ASME Paper No. GT-2002-30194.
[6] Kwak, J. S., and Han, J. C., 2002, "Heat Transfer Coefficient and Film-Cooling Effectiveness on the Squealer Tip of a Gas Turbine Blade," ASME Paper No. GT-2002-30555.
[7] Ahn, J., Mhetras, S., and Han, J., 2004, "Film Cooling Effectiveness on a Gas Turbine Blade Tip Using Pressure Sensitive Paint," ASME Paper No. GT-2004-53249.
[8] Yang, H., Chen, H., and Han, J., 2004, "Numerical Prediction of Film Cooling and Heat Transfer with Different Film Hole Arrangements on the Plane and Squealer Tip of a Gas Turbine Blade," ASME Paper No. GT-2004-53199.
[9] Kuwabara, H., Tsukagoshi, K., and Arts, T., 2004, "High Coverage Blade Tip Film Cooling," ASME Paper No. GT-2004-53226.
[10] Nasir, H., Ekkad, S. V., Bunker, R. S., and Prakash, C., 2004, "Effects of Tip Gap Film Injection From Plain and Squealer Blade Tips," ASME Paper No. GT-2004-53455.
[11] Krishnababbu, S. K., Newton, P. J., Dawes, W. N., Lock, G. D., and Hodson, H. P., 2005, "An Experimental and Numerical Investigation of the Tip Leakage Flow and Heat Transfer Using a Rotor Tip Gap Model," Sixth European Turbomachinery Conference, Lille, France.
[12] Newton, P. J., Lock, G. D., Krishnababbu, S. K., Hodson, H. P., Dawes, W. N., Hannis, J., and Whitney, C., 2007, "Heat Transfer and Aerodynamics of Turbine Blade Tips in a Linear Cascade," ASME J. Turbomach., **128**, pp. 300–309.
[13] Heyes, F. J. G., Hodson, H. P., and Dailey, G. M., 1991, "The Effect of Blade Tip Geometry on the Tip Leakage Flow in Axial Turbine Cascades," ASME Paper No. 91-GT-135.
[14] Hodson, H. P., Banieghbal, M. R., and Dailey, G. M., 1995, "3-Dimensional Interactions in the Rotor of an Axial Turbine," AIAA J., **11**(2), pp. 196–204.
[15] Friedrichs, S., Hodson, H. P., and Dawes, W. N., 1995, "Distribution of Film-Cooling Effectiveness on a Turbine Endwall Measured Using the Ammonia and Diazo Technique," ASME Paper No. 95-GT-1.
[16] Schultz, D. L., and Jones, T. V., 1973, "Heat Transfer Measurements in Short Duration Hypersonic Facilities," Paper No. AGARD-AG-165.
[17] Ireland, P. T., and Jones, T. V., 2000, "Liquid Crystal Measurements of Heat Transfer and Surface Shear Stress," Meas. Sci. Technol., **11**, pp. 969–986.
[18] Newton, P. J., Yan, Y., Stevens, N. E., Evatt, S. T., Lock, G. D., and Owen, J. M., 2003, "Transient Heat Transfer Measurements Using Thermochromic Liquid Crystal. Part 1: An Improved Technique," Int. J. Heat Fluid Flow, **24**, pp. 14–22.
[19] Gillespie, D. R. H., Wang, Z., Ireland, P. T., and Kohler, S. T., 1998, "Full Surface Local Heat Transfer Measurements in a Model of an Integrally Cast Impingement Cooling Geometry," ASME J. Turbomach., **120**, pp. 92–99.
[20] Sen, B., Schmidt, D. L., and Bogard, D. G., 1994, "Film Cooling With Compound Angle Holes: Heat Transfer," ASME Paper No. 94-GT-311.
[21] Sargison, J. E., Guo, S. M., Oldfield, M. L. G., Lock, G. D., and Rawlinson, A. J., 2002, "A Converging Slot-Hole Film-Cooling Geometry—Part 2: Transonic Nozzle Guide Vane Heat Transfer and Loss," ASME J. Turbomach., **124**, pp. 461–471.
[22] Owen, J. M., Newton, P. J., and Lock, G. D., 2003, "Transient Heat Transfer Measurements Using Thermochromic Liquid Crystal. Part 2: Experimental Uncertainties," Int. J. Heat Fluid Flow, **24**, pp. 23–28.
[23] Newton, P. J., 2005, "Aerodynamic and Heat Transfer Measurements in Turbine Tip Leakage Flow Models," Ph.D. thesis, University of Bath, Bath, UK.
[24] Newton, P. J., Lock, G. D., Krishnababbu, S. K., Hodson, H. P., Dawes, W. N., Hannis, J., and Whitney, C., 2007, "Aerothermal Investigations of Tip Leakage Flow in Axial Flow Turbines—Part III: Tip Cooling," ASME Paper No. GT-2007-27368.

# Identification of the Stability Margin Between Safe Operation and the Onset of Blade Flutter

**Tim Rice**

**David Bell**

**Gurnam Singh**

ALSTOM,
Newbold Road,
Rugby CV21 2NH, England

*The introduction of longer last stage blading in steam turbine power plant offers significant economic and environmental benefits. The modern trend, adopted by most leading steam turbine manufacturers, is to develop long last stage moving blades (LSMBs) that feature a tip shroud. This brings benefits of improved performance due to better leakage control and increased mechanical stiffness. However, the benefits associated with the introduction of a tip shroud are accompanied by an increased risk of blade flutter at high mass flows. The shroud is interlocked during vibration, causing the first axial bending mode to carry an increased, out of phase, torsional component. It is shown that this change in mode shape, compared to an unshrouded LSMB, can lead to destabilizing aerodynamic forces during vibration. At a sufficiently high mass flow, the destabilizing unsteady aerodynamic work will exceed the damping provided by the mechanical bladed-disk system, and blade flutter will occur. Addressing the potential for flutter during design and development is difficult. Simple tests prove inadequate as they fail to reveal the proximity of flutter unless the catastrophic condition is encountered. A comprehensive product validation program is presented, with the purpose of identifying the margin for safe operation with respect to blade flutter. Unsteady computational fluid dynamics predictions are utilized to identify the mechanisms responsible for the unstable aerodynamic condition and the particular modes of vibration that are most at risk. Using this information, a directed experimental technique is applied to measure the combined aerodynamic and mechanical damping under operating conditions. Results that demonstrate the identification of the aeroelastic stability margin for a new LSMB are presented. The stability margin predicted from the measurements demonstrates a significant margin of safety.* [DOI: 10.1115/1.2812339]

## Introduction

Significant advances in the understanding of blade flutter have been achieved through numerous experimental and theoretical modeling investigations. Most attention has been focused on compressors due to their well documented predisposition to blade flutter under certain operation regimes, see Sisto [1]. In recent years, the risk of blade flutter in turbine applications has received attention due to increasing operational demands and aggressive design requirements, for example, high lift and low mass designs in aeroengines.

There are many examples of experimental investigations into blade flutter, which have improved fundamental understanding and provided valuable data for the validation of modeling techniques, see Carta and St. Hilaire [2], Bölcs and Fransson [3], and Bell and He [4]. Most of these investigations have been forced vibration experiments, performed in a controlled environment, normally a linear or annular cascade. Unfortunately, there are relatively little experimental data available in open literature that are obtained from real turbomachinery applications, though some notable exceptions are provided by Barton and Halliwell [5] and Scalzo et al. [6].

Several computational fluid dynamics computational fluid dynamics (CFD) investigations and theoretical flutter design methods, applied to real turbine applications, are reported in open literature. For turbine applications, it has been consistently demonstrated that mode shape, which is directly constrained by the number and type of mechanical interconnections, plays a significant role in determining aeroelastic stability, see, for example, Corral et al. [7], Cherysheva et al. [8], Kielb et al. [9], and Huang et al. [10]. In several instances, the results presented by these authors indicate unstable unsteady aerodynamic conditions for realistic turbine configurations. It therefore appears likely that there are many real applications that operate in an unstable aerodynamic environment and rely on the mechanical damping of the bladed assembly to maintain aeroelastic stability. Under such conditions, there may be no evidence of the proximity of the critical aeroelastic instability. Small changes in operational conditions, such as an increase in mass flow, could lead to catastrophic instability. The present work is fundamentally intended to close the gap between the predicted unsteady aerodynamic stability and actual operational aeroelastic stability. A method for determining the margin of safety in real turbomachinery applications is demonstrated.

**Flutter in Low Pressure Steam Turbine Development.** Historically, blade flutter has not been a major concern for steam turbine manufacturers. The only part of the bladed flow path considered at risk to flutter is the last stage moving blade in low pressure (LP) cylinders. There are no cases of blade failure due to flutter reported in open literature, and none known to the authors' knowledge, within ALSTOM. However, it remains feasible that blade failures, or reliability problems, may well be associated with flutter or at least due to turbine operation in close proximity to the stability margin, leading to increased levels of vibration.

The risk of blade flutter must be acknowledged in the development and validation of new last stage blade products in LP steam turbines, much like in their aeroengine counterparts. This is because the requirements for new last stage moving blade (LSMB) products are constantly extending the envelope of operational ex-

---

Contributed by the International Gas Turbine Institute of ASME for publication in the JOURNAL OF TURBOMACHINERY. Manuscript received June 8, 2007; final manuscript received July 19, 2007; published online October 17, 2008. Review conducted by David Wisler. Paper presented at the ASME Turbo Expo 2007: Land, Sea and Air (GT2007), Montreal, Quebec, Canada, May 14–17, 2007.

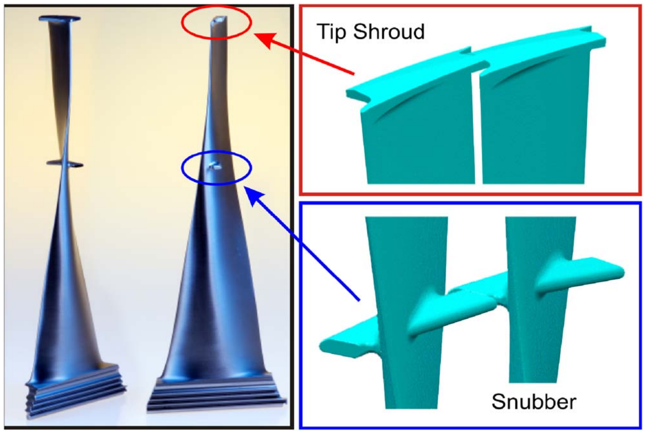

**Fig. 1 ND45A (50 Hz) last stage moving blade**

perience. The trend is for longer LSMBs, delivering greater exhaust area, elevated performance levels, and significant cost savings through reduction of the number of LP flows required in a power plant. New design features are often applied to improve performance levels and mechanical characteristics in the development of these new LSMBs. In recent developments, most leading manufacturers now offer long LSMBs with tip shrouds in order to improve performance, through control of the leakage flow, and increase mechanical stiffness. Since the first family of vibration characteristically occurs at relatively low frequencies, even for LSMBs with one or more mechanical interconnections, the operating reduced frequency is at a level that flutter may occur. Although flutter appears to have been avoided in more mature LSMB designs, it is important to understand and assess the impact of new design features, such as tip shrouds, on aeroelastic stability in order to ensure delivery of a robust, high performance product.

Blade flutter analysis based on CFD predictions has been routinely applied in recent LSMB developments undertaken by ALSTOM. This has been intended to qualitatively assess risk, prior to final product validation in a model test turbine and the subsequent commissioning of new products in the field. CFD flutter analysis is documented here for the development of a new LSMB, along with the fundamental understanding gained during this part of the investigation. The theoretical analysis leads to a novel test technique, applied during the product validation phase, in a model turbine test. The test method, which is directed by the findings of the CFD analysis, provides evaluation of both aerodynamic and mechanical damping at operational conditions. Simple processing of the measurements also yields an assessment of the aeroelastic stability margin for the LSMB. The results demonstrate that the new LSMB will operate well within safe limits.

**ND45A Low Pressure Last Stage Moving Blading.** The present investigation was conducted as part of the development program for new last stage blading for a LP steam turbine, which is identified as the "ND45A" (for 50 Hz applications). Following successful product validation that is documented in part within this paper, this blade is now available for both new and retrofit steam turbine applications.

The investigation was initiated with the demanding objective of quantitatively determining the risk of blade flutter, i.e., the margin of safety, for the ND45A LSMB. The final design for this new LSMB, to which all CFD analysis and testing are applied, is shown in Fig. 1, and basic properties are summarized in Table 1.

The ND45A LSMB in steel has two mechanical interconnections: a snubber (part span shroud) at 65% height and a tip shroud. Significant operational experience exists for ALSTOM in the application of snubbers for long LSMBs and for shrouds in relatively short LSMBs. However, the application of a tip shroud on such a long LSMB must be considered as a significant technological development by all manufacturers. While the benefits are very clear with respect to reduced leakage losses (typically worth around 2–3% on total-total isentropic efficiency of the last stage) and enhanced blade stiffness, the impact of the tip shroud on aeroelastic stability of LSMBs in LP steam turbines was relatively unknown, although it was expected to be significant due to its influence on mode shape.

**Table 1 ND45A and datum LSMB properties**

| LSMB properties | ND45A | Datum |
|---|---|---|
| Rotational speed (Hz) | 50 | 50 |
| Exhaust area ($m^2$) | 10.7 | 9.1 |
| Number of blades per circle | 67 | 71 |
| Hub diameter (mm) | 1884 | 1680 |
| Blade length (mm) | 1130 | 1055 |
| Mechanical interconnections | 2<br>Snubber<br>tip shroud | 1<br>Snubber |
| Snubber location (% height) | 65 | 76 |

For the purposes of the CFD flutter analysis, a mature LSMB was also assessed to provide a stable datum. This blade, which has an unblemished service record, has been used on 57 turbines worldwide (115 rows) and the lead units have amassed in excess of 100,000 hours operation. This LSMB was chosen since it has a snubber (albeit at a different fractional height) but is unshrouded. Comparison of predictions for these two blades would give insight into the influence of the tip shroud on the aeroelastic stability. It would also enable qualitative assessment of the relative stability of the ND45A against a known stable base line.

The last stage of LP steam turbines operate in a challenging environment, which is characterized by a predominantly supersonic/transonic flow regime, with very high operational pressure ratios over the last stage. The flow is choked through the last two stages, and changes in mass flow or condenser pressure only affect the exit flow in the LSMB in nondimensional terms (excluding Reynolds number). For a nominal turbine mass flow, inlet flow conditions to the LSMB are therefore fixed over a range of exit pressure.

**Computational Fluid Dynamics Flutter Analysis.** CFD flutter analysis was performed for both the ND45A and datum LSMB at their respective design mass flows and over a range of exit velocities (condenser pressures) in order to adequately cover normal operating conditions. At each exit velocity, a range of nodal diameters in the first family of vibration was considered, with separate computations performed for forward and backward traveling waves at each nodal diameter. A matrix of the CFD computations performed is provided in Table 2.

**Computational Method.** The CFD analysis was performed using an unsteady 3D inviscid explicit time-marching code, which was originally developed by He [11] and subsequently adapted by the authors to handle the complex vibration mode shapes that characterize LSMBs with mechanical interconnections. The CFD method uses a moving grid to accommodate the blade vibration and applies shape correction, developed by He [11], to handle phase-shifted boundary conditions, thus permitting solutions within a single passage domain. The fundamental accuracy of the code has been extensively validated against standard test configurations, see Bölcs and Fransson [3] and Bell and He [4].

**Computational Domain.** All computations were performed in an isolated, single passage rotor domain for the LSMB. The inlet plane is located approximately midway between the last stage fixed blade and the LSMB, and the exit plane is located several blade chord lengths downstream. The same mesh density was employed for both the ND45A and datum LSMB, which was a simple H mesh of dimensions $13 \times 110 \times 25$ (pitchwise

**Table 2 Matrix of CFD computations**

| CFD computations<br>○ ND45A LSMB<br>× Datum LSMB | $N_u$: +/−20 | $N_u$: +/−15 | $N_u$: +/−11 | $N_u$: +/−8 | $N_u$: +/−5 | $N_u$: +/−2 |
|---|---|---|---|---|---|---|
| $C_z$: 180 m/s | ○ | ○ | ○ | ○ | ○ | ○ |
| $C_z$: 240 m/s | ○ × | ○ | ○ × | ○ × | ○ × | ○ |
| $C_z$: 280 m/s | ○ | ○ | ○ | ○ | ○ | ○ |

× streamwise × radial). This is relatively coarse but was established to be reasonably mesh insensitive for the purposes of the inviscid CFD modeling, at least in terms of predicting aerodynamic damping. The moving grid extends five cells in the pitchwise direction away from the blade surface and five cells up and downstream of the blade. The computational domain does not include modeling of the snubber blockage, although this is not considered to be an important factor in determining the aeroelastic stability, as indicated by Huang et al. [12], nor is the shroud leakage included in the domain, but this again is considered to be of secondary importance. Nonetheless, these issues were implicitly addressed by the subsequent test investigation.

**Boundary Conditions and Vibration Description.** Standard aerodynamic boundary conditions were applied at the inlet and exit to the computational domain. Inlet conditions were defined by total pressure, total temperature, flow, and angles. These were held constant for all calculations and were extracted from a 3D stage CFD model of the last stage configuration. Exit conditions were prescribed by a static pressure at the hub and application of simple radial equilibrium. The exit pressure condition was adjusted to obtain the variation in exit velocity defined in Table 2. The pressure ratio across the computational domain was typically 3:1.

The mode of vibration is applied as a boundary condition in the CFD analysis. Complex components of axial, tangential, and radial bendings and torsions are specified at each radial grid station. The vibration frequency and interblade phase angle (IBPA) are also defined to complete the specification. This effectively means that the mode shape is an approximate solid body vibration definition at each radial grid section, since displacements are not defined for individual surface nodes. In all cases, the vibration mode shape data were obtained from 3D finite element analysis (FEA) and the results processed to deliver the approximated data for each radial grid section. This approximation of the mode shape was considered satisfactory because there is very little deformation of the blade in the first family of vibration. This was also verified to be correct through comparison of the approximated data with the FEA mode shapes, up to 20 nodal diameters in the first family of vibration.

The vibration modes are summarized in Figs. 2 and 3 for the ND45A and datum LSMB, respectively. For consistent comparison, the mode shapes are plotted for a nominal maximum amplitude in axial bending of 1.0 mm. Only the axial bending and torsional components are defined in these figures since these are the dominant components when compared to the tangential and radial bending components. Figures 2(*a*), 2(*b*), 3(*a*), and 3(*b*) show the amplitude of axial bending and amplitude of torsion along the height of the blades for the ND45A and datum LSMB. Figures 2(*c*) and 3(*c*) show the phase angle between axial bending and torsional components of vibration along the blade height for the ND45A and datum LSMB. It should be noted that Figs. 2(*c*) and 3(*c*) only show the phase difference for the backward traveling waves. The forward traveling waves are defined by applying the complex conjugate of the mode shape description shown in these diagrams and opposite sign of IBPA. The opposite sign of phase difference should therefore be applied to Figs. 2(*c*) and 3(*c*) to obtain the corresponding forward traveling wave.

The first family of vibration is typically referred to as the "first flap," because without interconnections, the mode is described by a simple flapping or bending motion, predominantly in the axial direction. However, as can be seen in Figs. 2 and 3, there is also a significant torsional component of vibration, which increases with nodal diameter for both these LSMBs. This is because the mechanical interconnections must remain interlocked during vibration. As the nodal diameter increases, the amplitude of torsion must increase in order to preserve the interconnections. The phase angle between the torsional component of vibration and the axial bending is also constrained at the interconnections, as can be seen in Figs. 2(*c*) and 3(*c*). Since the ND45A has a tip shroud as well as a snubber, a significantly higher amplitude of the torsion can be observed toward the tip when compared to the datum LSMB, see

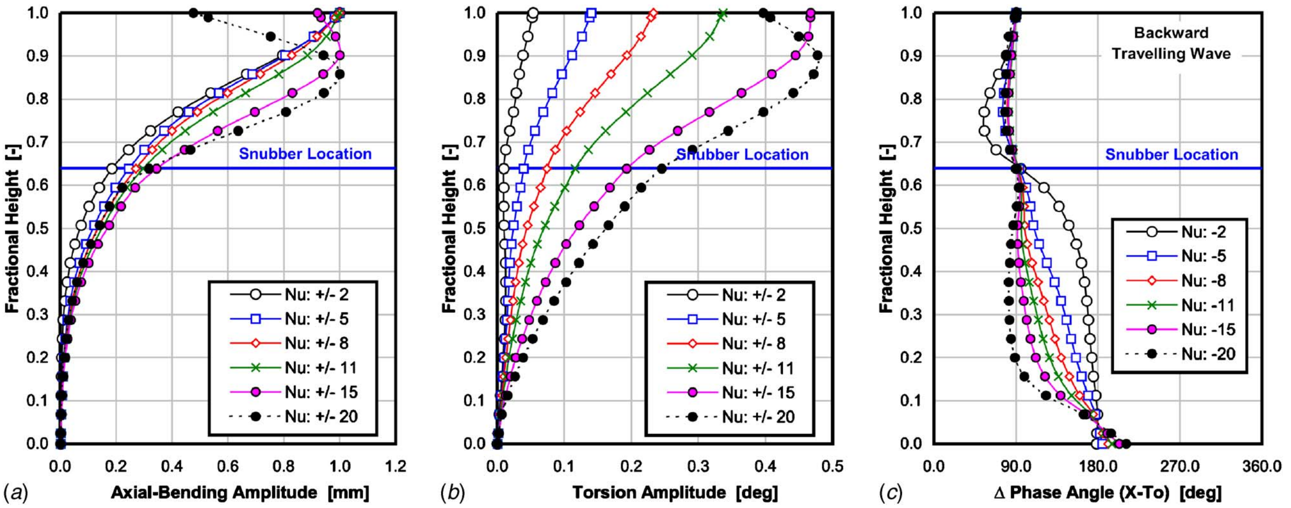

**Fig. 2 ND45A LSMB mode description**

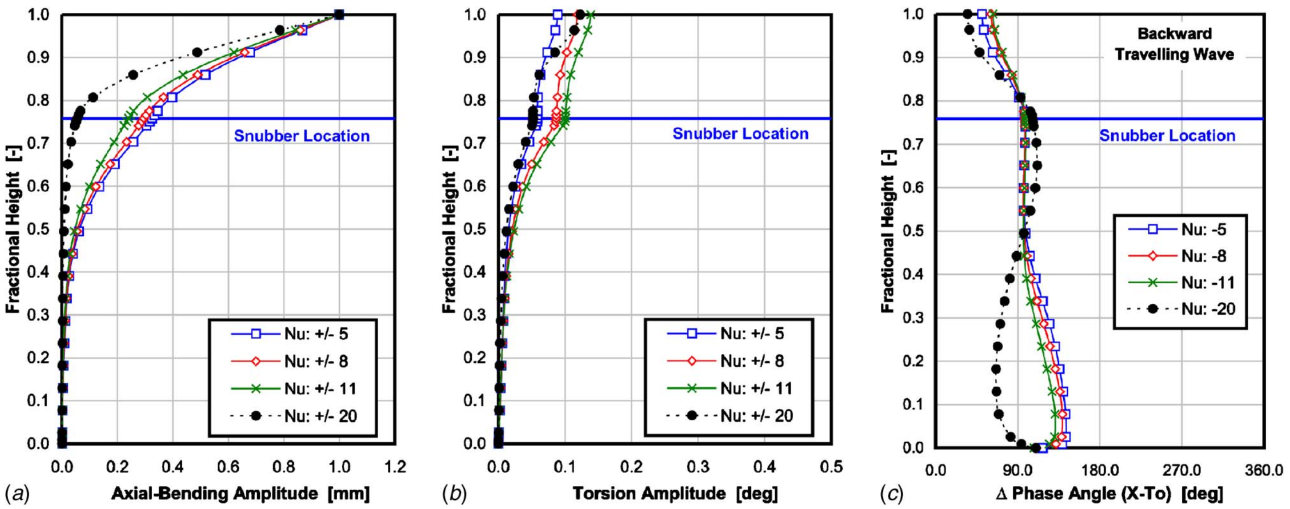

Fig. 3 Datum LSMB mode shape description

Figs. 2(*a*), 2(*b*), 3(*a*), and 3(*b*). The phase angle between axial bending and torsion is also much greater in the tip region for the ND45A relative to the datum LSMB due to the tip shroud.

**Results: Blade Flutter Predictions.** All CFD flutter predictions are presented in terms of aerodynamic logarithmic decrement, see Fig. 4. This defines the predicted stability of the LSMB at design mass flow in the absence of mechanical damping. Negative values indicate an unstable aerodynamic condition. The figure shows the results for both the ND45A and datum LSMB for a range of nodal diameters (both forward and backward traveling waves) and for a practicable operating range of exit velocity ($C_z$).

The datum LSMB is aerodynamically stable throughout the operating range at all nodal diameters, whereas the ND45A is aerodynamically unstable for backward traveling above seven nodal diameters. The peak unstable aerodynamic condition occurs around −15 nodal diameters at the intermediate exit velocity (240 m/s). It is clear that changes in nodal diameter exert a significantly greater influence on the aerodynamic stability than changes in exit velocity.

In addition to the overall aerodynamic damping, Fig. 5 shows the predicted local aerodynamic damping for the ND45A LSMB. It can be seen from this figure that the most significant contribution to the overall aerodynamic stability comes toward the tip section, where the amplitudes of vibration are greatest.

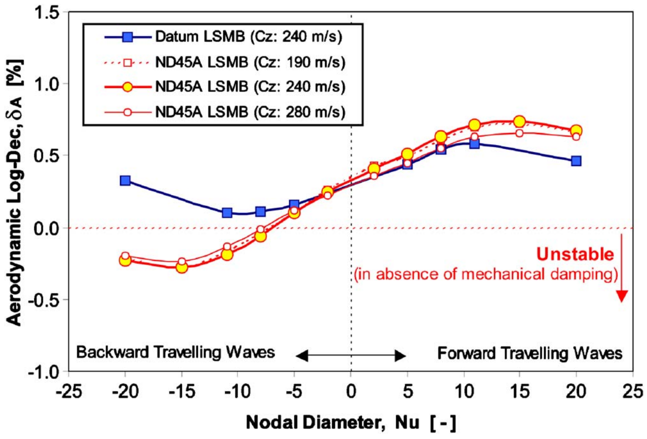

Fig. 4 Predicted aerodynamic stability (log-dec) for the ND45A and datum LSMB (design mass flow)

**Influence of the Tip Shroud.** Further CFD analysis was performed on the ND45A LSMB to assess the influence of the tip shroud. In this analysis, the vibration mode description was transposed from the datum LSMB to see whether a significant stabilizing behavior would be observed. These computations were performed in two steps. In the first, just the frequency of vibration was transposed in order to qualitatively assess the role of reduced frequency. In the second part, the frequency and mode shape were transposed. The results of these computations are presented in Fig. 6. This figure clearly shows that the mode shape of the ND45A LSMB, associated with the tip shroud, exerts a significant destabilizing influence. The predictions of the ND45A with the datum LSMB mode shape and frequency applied are stable at all conditions. Conversely, it also shows that the increased first family frequencies of the ND45A LSMB exert a stabilizing influence due the corresponding increase in reduced frequency.

In understanding why the mode shape associated with the ND45A tip shroud exerts a destabilizing influence on the aeroelastic stability, it is important to consider why the forward traveling waves are stable and the backward traveling waves are unstable. To explain the overall behavior, a simple quasisteady argument is proposed. The argument concerns the phase angle between the

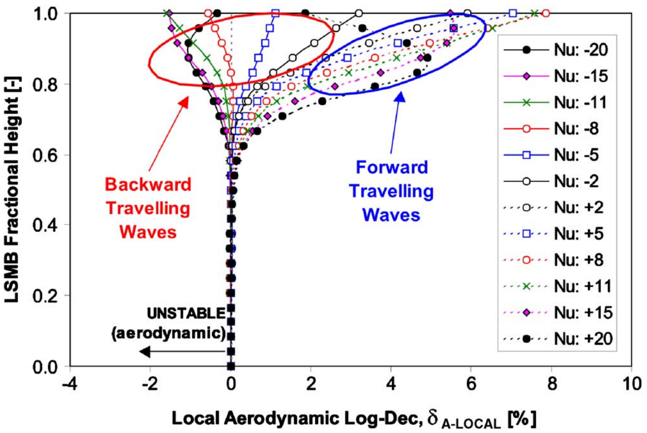

Fig. 5 Predicted local aerodynamic damping for the ND45A LSMB (log-dec), defined as

$$\delta_{A-\mathrm{local}} = \frac{\text{(aerodynamic work per cycle per unit span)}}{2 \times \text{(overall strain energy)}}$$

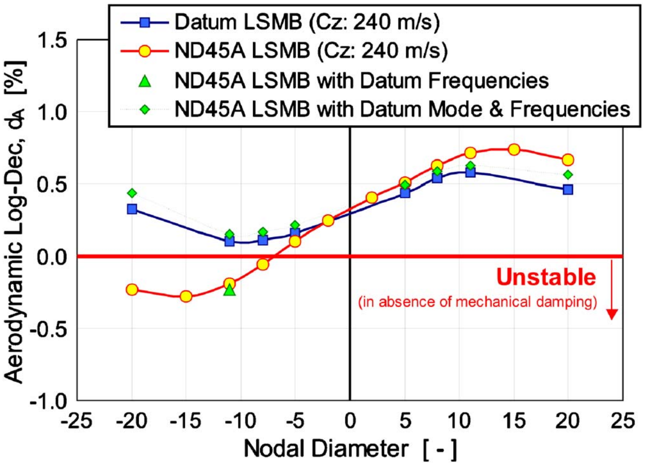

**Fig. 6 Predicted aerodynamic stability of the ND45A with the datum LSMB frequency and mode shape applied**

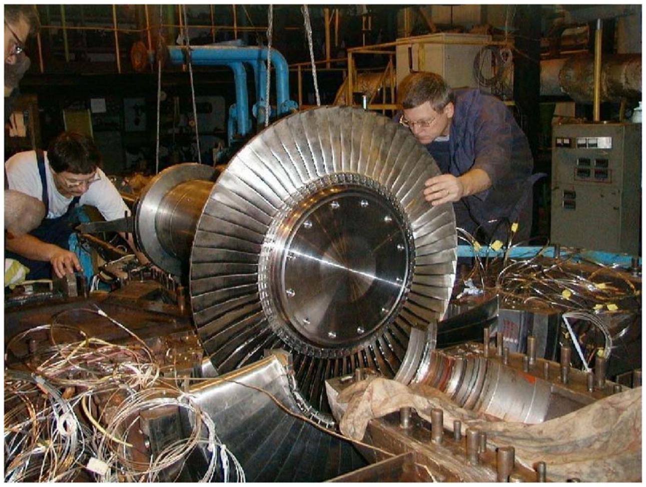

**Fig. 8 Assembly of the model turbine**

torsional and axial bending components of vibration and the cross coupling of the unsteady flow field induced by these vibration components. In the case of backward traveling waves, as the blade deflects upstream through its mean position with the axial bending component, the blade section is already rotated to a lower stagger angle compared to its mean orientation. This means that there is reduced axial force on the blade section, and the unsteady blade force is directed upstream, momentarily in the same direction as the axial bending. This unsteady force associated with the torsional component of vibration thereby excites the axial bending component. Conversely, for the forward traveling waves, as the blade deflects upstream through its mean position, the blade section is already rotated to a higher stagger by virtue of the change in phase angle between the two components of vibration. The unsteady axial force induced by the torsional component of vibration therefore opposes the axial bending motion and exerts a stabilizing influence. This argument is presented diagrammatically in Fig. 7.

## Analysis of Blade Flutter Predictions

Despite the apparent destabilizing influence of the tip shroud predicted by the CFD analysis, the benefits of this feature remain significant in terms of the performance improvement and increased mechanical stiffness. It was therefore a clear objective of the development project to retain the tip shroud if at all possible. Several different design concepts for the aerofoil and conventional shroud were therefore assessed, but none could exert an appreciable improvement over the present design. In fact, the present design is a more optimal solution in this respect due to the long tip chord length and relatively high frequencies, which combine to increase the operating reduced frequency and improve stability. Although the other design variants are not presented, it should be noted for reference that the ND45A LSMB is significantly more aerodynamically stable than the similar sized, shrouded LSMB previously investigated by Huang et al. [12].

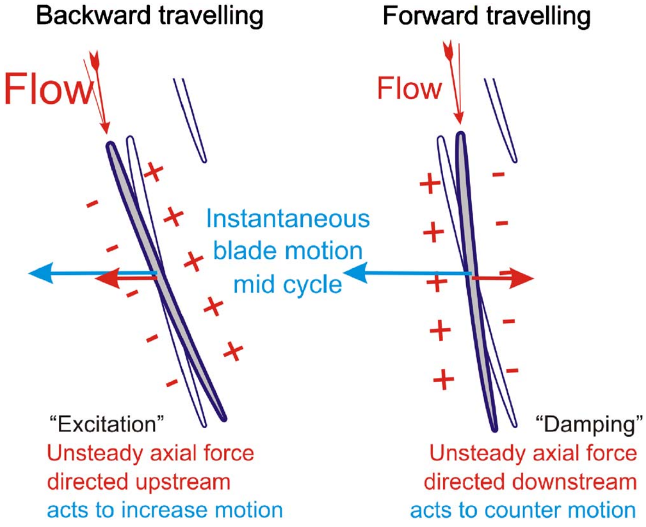

**Fig. 7 Quasisteady illustration of cross-coupling of unsteady pressure due to axial bending and torsional vibration components**

Aeroelastic stability is not determined solely by the unsteady aerodynamics. Blade flutter will only occur if the destabilizing aerodynamic damping exceeds the complete damping of the material, mechanical, and nodal system (herein now referred to as mechanical damping). Unfortunately, there are very little reliable data available to define accurate values of mechanical damping for such a complicated mechanical system. At this point in the flutter investigation, it was therefore not possible to establish whether blade flutter would occur within or beyond the intended operational conditions. Nonetheless, there was a clear indication as to which operating conditions were most at risk: backward traveling waves above seven nodal diameters.

The CFD work has demonstrated how negative aerodynamic damping can occur. The physical explanation of these results suggests that this effect is probably present on any LSMB incorporating a tip shroud. Based on previous experience, it was considered likely that there would be sufficient mechanical damping for the ND45A LSMB, such that flutter would not be encountered during the product development tests. However, it was also considered important to measure quantitatively the margin of safety in terms of application mass flow to ensure stable operation in the field.

## Measurement Technique

The aim of the next stage in the investigation was to determine the margin of safety from flutter for the ND45A LSMB. This was carried out in a model steam turbine, operated at CKTI, St. Petersburg, Russia. The small scale model rotor is shown during assembly in Fig. 8. Excitation was provided with an electromagnet and the blade response was measured using strain gauge sensors. Analysis of these responses was carried out to establish the measured aggregate damping. To separate the mechanical and aerodynamic components of the aggregate damping, tests were carried out at two different mass flows. While these flows were at

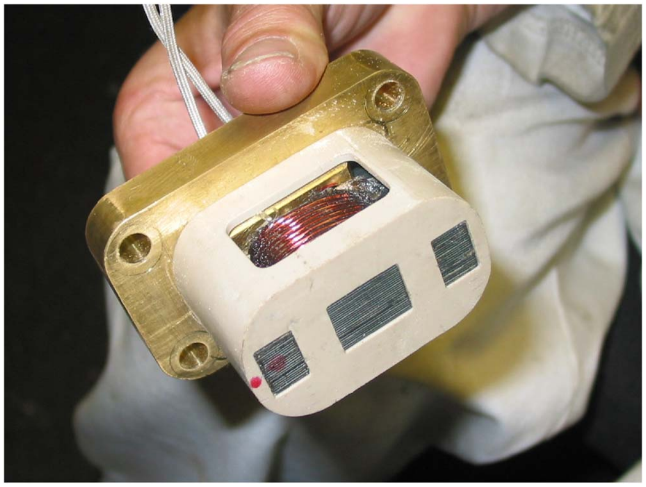

Fig. 9 Magnet assembly

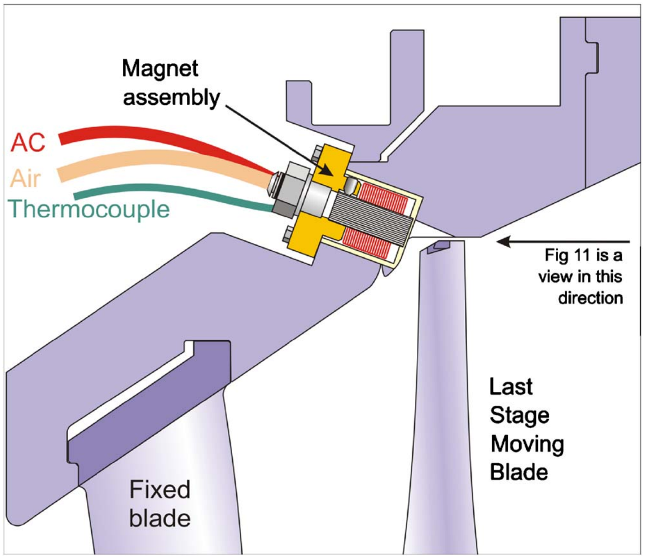

Fig. 10 Magnet assembly installed in upstream blade carrier

different Reynolds numbers, the pressure ratios were specified and controlled to give the same volumetric flow for both cases. This means that both flow regimes contain the same distribution of Mach numbers. At low amplitudes of vibration, the mechanical damping is regarded as constant for the purposes of this investigation. Therefore, the change in damping is all aerodynamic and is due to the change in density between the two otherwise similar flow cases. The use of two flows is simply an expedient way of generating data at two different density levels. This means that it is reasonable to assume linear behavior to calculate the fixed mechanical damping and hence the aerodynamic component of damping at the two flows tested. Finally, the margin of safety can be established by extrapolating from the measurements forward to the flow where the aggregate damping would change sign, the point at which the onset of blade flutter is predicted.

The flows selected for testing were as follows:

(a) A high flow (140% of the nominal design flow and the maximum mass flow possible at the test facility). This was beyond the initial operational range of the design.
(b) A low flow (70% of the nominal design flow).

The intended operational envelope for the blade design lay within these two test flows.

**AC Magnet.** A compact magnet was specifically developed for installation in the test turbine. The magnet was assembled by winding turns of insulated wire onto an E core. A thermocouple pocket was included under the windings so that the magnet temperature could be monitored during operation. Initial tests showed that cooling would be required if sufficient magnetic flux was to be generated at the frequencies of interest. Forced air cooling was found to be effective. The E core was firmly mounted onto a brass back plate, providing a solid mounting and a heat sink path. The magnet is shown in Fig. 9.

The magnet assembly was bolted into a recess machined into the upstream blade carrier, oriented to direct the magnetic force onto the mass of the blade shroud. The flow path profile was carefully maintained, with some local hand dressing of the plastic front face in situ. A small local cavity was made in the cylindrical portion over the blade to remove ferritic material from the direct line of sight between the magnet and the blade. Figure 10 is a cross section through the turbine showing the positioning of the magnet and the tip shroud.

Figure 11 is a view looking upstream on the blade trailing edges. The magnet can just be seen through the tip gap with the blades stationary. The lower blade in the picture carries a strain gauge, encapsulated to reduce damage due to moisture.

**AC Magnet Drive.** A high voltage ac magnet drive was constructed around an amplifier unit commonly used for medical magnetic imaging. The input signal wave form was constructed from square switched pulses generated from a software. By including periods of zero excitation within each cycle, high voltage and high current operation could be achieved with significantly reduced magnet temperatures. While the amplifier switches polarity on the magnet (pull and push in a cycle), the blade rotating in the flux field only experiences "pull pull;" therefore, the magnet is driven at half the frequency required for direct excitation.

## Measurement and Analysis of Damping

There are two main methods for measuring damping:

(1) In the time domain, measurement can be made of an amplitude decay curve following a tap test (or in the present case, switching off the magnet excitation).
(2) In the frequency domain, excitation can be slowly swept across a resonant condition and the shape of the response curve can be used with the "half power point" method to determine the level of damping present, as applied by Manwaring and Krikeng [13].

Measurements are presented in terms of logarithmic decrement (log-dec) ($\delta$). Many different definitions of damping are in com-

Fig. 11 The installed magnet can just be seen through the tip gap over the blade (see arrow)

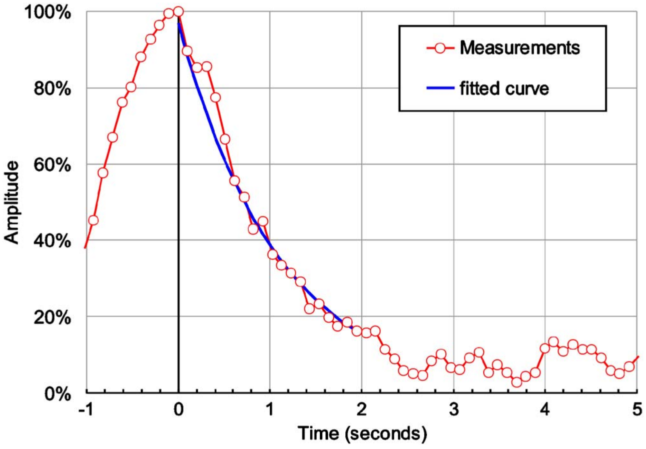

**Fig. 12 An example of a magnet off decay curve**

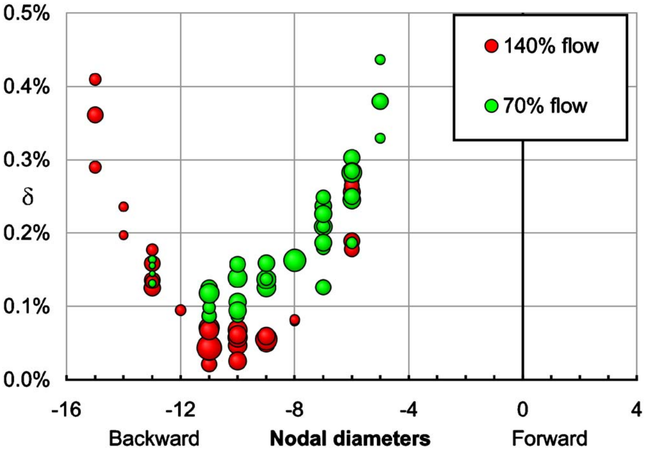

**Fig. 13 The individual $\delta$ values from the analysis**

mon use. A concise collection of these terms and relationships is presented by Folkman [14]. Such standard relationships enable comparison of results obtained by the two different methods above.

Initial trials were carried out in the laboratory on a bladed wheel in a vacuum. During these tests, the frequency sweep method was found to be very effective. However, at the test turbine, the "magnet off" method was found to be more applicable due to the regime of turbine speed control that could be achieved.

At both the mass flows tested, a sequence of nodal diameters were individually excited while the blade response signals were recorded. The range of nodal diameters with negative aerodynamic damping had largely been identified by the CFD predictions and the measurements were focused on this area.

The magnet excitation frequency would be adjusted to excite the nodal diameter at precisely the turbine nominal speed. This would also reveal the likely response amplitude. The controls of the excitation could be adjusted, either to obtain more energy input or to reduce the rate of magnet temperature rise. For each nodal diameter, the following test procedure was repeated a number of times. The turbine speed was swept slowly over the target speed. The magnet would be switched on as the shaft speed approached the nominal condition. The response of a strain gauge would be watched, and as it rose above an achievable threshold level, the magnet would be suddenly switched off, providing a period of time where the previously imposed blade vibration decayed in the presence of the correct aerodynamic environment.

Evaluation of the damping values was carried out after the testing. A long continuous series of data points was recollected from the tape recorder and stored in a data file, covering the periods where the magnet off tests had been successfully performed. This extended time series was then analyzed in small sections to build up the time history of the resonant frequency amplitude. This second series of values was examined to analyze the decay curve periods immediately after the magnet had been turned off.

For decay data identified as a genuine magnet off event, an exponential decay curve was fitted to the data. The $\delta$ value and initial amplitude were determined by minimizing errors between the fitted curve and the measured data. An example of how the curve fit was applied to the analyzed sequence of amplitudes is shown in Fig. 12. The magnet was turned off at the time marked 0 s. The curve fit was applied to the data for the following 2 s, after which the signal returned to normal background noise levels.

Figure 13 shows the individual results obtained set out against the nodal diameters tested. Both flows are shown. This provides an indication of the scatter and repeatability encountered with this type of measurement. The size of the symbol is used to indicate the initial amplitude of the fitted decay curve, with the larger amplitudes being viewed as less susceptible to error.

The data were reduced to a single point for each flow and nodal diameter by carrying out a weighted average, according to the initial amplitudes of the decay curves. These values are shown in Fig. 14, where curves have been fitted through the data with very little residual error. The lowest damping value found is at 11 nodal diameters for both flows.

Having obtained consistent measurements at two different flows, the data were then used to separate the components of mechanical and aerodynamic dampings. Extrapolating the results at each nodal diameter back to zero flow establishes the underlying mechanical damping values for the rotating assembly. The difference between the mechanical damping and the aggregate damping measurement then gives the aerodynamic damping at each flow. Figure 15 outlines this process in graphical form. The linear extrapolation back to zero flow is marked 1 and the evaluation of the aerodynamic components, at the two flows tested, are marked 2.

In a similar way, the measurements can be extrapolated forward to higher flows to predict where blade flutter would occur for the unstable nodal diameters. While there may be some nonlinearity associated with the actual onset of flutter, this predicted value is of great use in assessing the margin of safety inherent in a blade design. Even if the nonlinearities meant that full blade flutter did not occur until a slightly higher flow, the intercept of zero aggre-

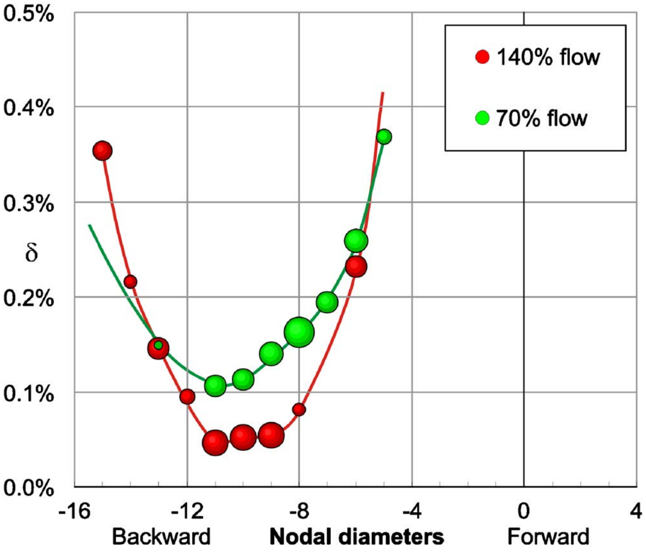

**Fig. 14 Averaged values for aggregate damping**

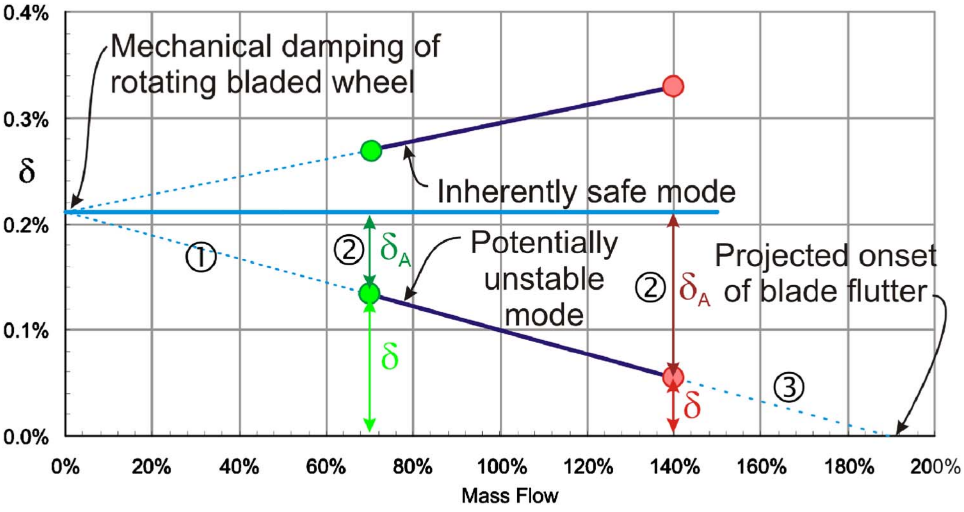

**Fig. 15 Method to determine the aerodynamic damping from the aggregate damping measurements**

gate damping should remain in the position from which the margin is gauged. At the least, high vibration levels must be expected when operating beyond the projected intercept. The extrapolation forward to the onset of flutter is indicated with the symbol 3 in Fig. 15.

The use of a simple linear model is based on the fact that the single effective difference between the two sets of measurements is the density level. The difference in Reynolds numbers or wetness exerts second order effects and are not considered large enough to invalidate this linear evaluation.

The results obtained for the underlying mechanical damping are shown in Fig. 16, revealing a reduction with additional backward traveling nodal diameters. The curve drawn on Fig. 16 follows previous experience indicating that the mechanical damping will be symmetrical about the zero nodal diameter axis. The values obtained suggest that the mechanical damping follows a form of periodic curve with nodal diameter.

Establishing the mechanical damping leads to evaluation of the aerodynamic damping components. These values are shown in Fig. 17. Symbols with no color are used to indicate that only one mass flow was tested at this particular nodal diameter. In these cases, the value for the aerodynamic damping was obtained by reading the mechanical damping off the curve in Fig. 16. The method for obtaining the aerodynamic damping imposes the ratio of mass flows at each nodal diameter. The two curves drawn in Fig. 17 are therefore simply scales of each other.

Figure 18 gives the comparison between the values obtained from the measurements and those calculated with the CFD. The aerodynamic damping figures from the two sources are given for 140% flow. The CFD can be seen to have correctly identified the presence of an area of negative aerodynamic damping, however, the magnitude and the corresponding number of nodal diameters are both larger than indicated by analysis of the measurements.

The physical simplifications in the CFD modeling (absence of overshroud leakage, no snubber, no upstream fixed blades, and inviscid flow) may each have an influence on the predicted overall aerodynamic stability.

In comparing the overall shape of the curves, it can be seen that an inviscid code has succeeded in capturing the significant trends.

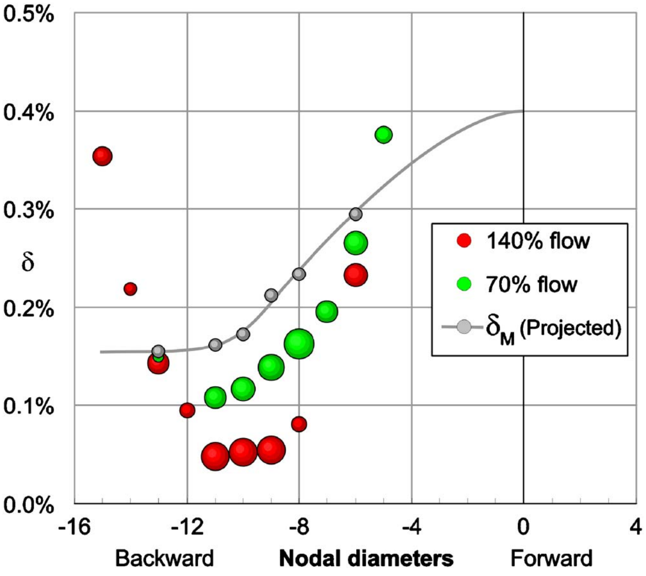

**Fig. 16 Extrapolating the measurements back to zero flow gives $\delta_M$, the projected mechanical damping**

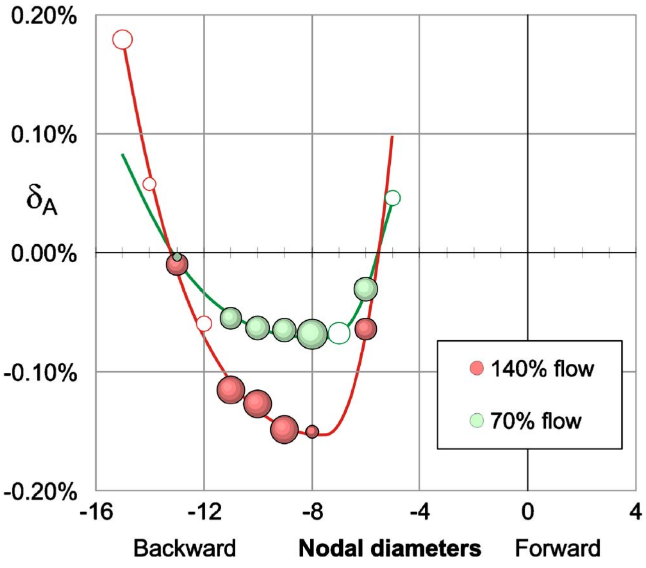

**Fig. 17 Calculated values of aerodynamic damping**

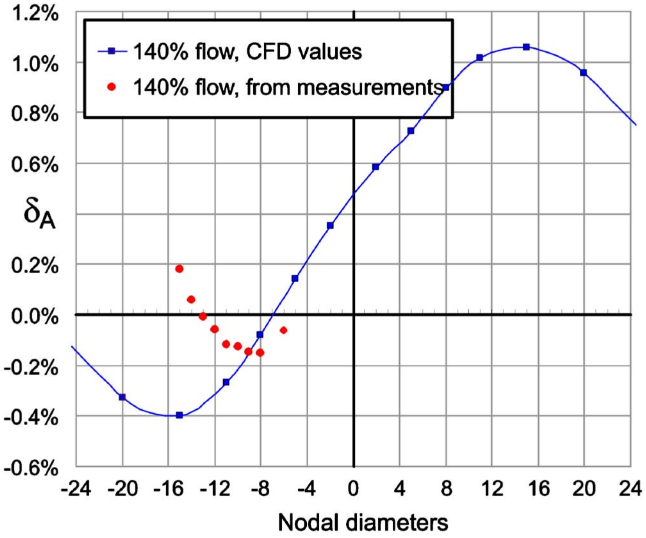

**Fig. 18 Comparison of the aerodynamic damping values from the measurements with the CFD predictions**

This would imply that viscous effects are of secondary importance, lending support to the use of linear extrapolations in this work.

It can be seen that the CFD represents a substantially cautious prediction of the aerodynamic stability.

## Predicting the Onset of Blade Flutter

Projecting the test measurements forward to zero aggregate damping indicates the mass flow at which the unstable modes are predicted to encounter blade flutter. Figure 19 is a 3D view of the averaged measurements together with the extrapolations to lower and higher mass flows. Projecting back through the measurements onto the wall of the plot gives the mechanical damping curve, found at zero flow, as shown previously in Fig. 16. Projecting to higher flows identifies the position where the aggregate damping is predicted to cross zero for unstable modes. Flows higher than this point would then operate with negative aerodamping in excess of the mechanical damping, leading to blade flutter. The area where flutter is predicted to occur is shown in red on the floor of Fig. 19. This is also shown as a conventional diagram in Fig. 20. The lowest flow where flutter is predicted is found at 190% of the design flow with nine nodal diameters. The two nodal diameters either side of the nine are only slightly more stable. Outside this range, other nodal diameters are found to be more stable and project out to very high flows. It is found that 5 and 14 nodal diameters are inherently stable. For these two cases, the aggregate damping increases with mass flow, as indicated by lines rising with flow in Fig. 19.

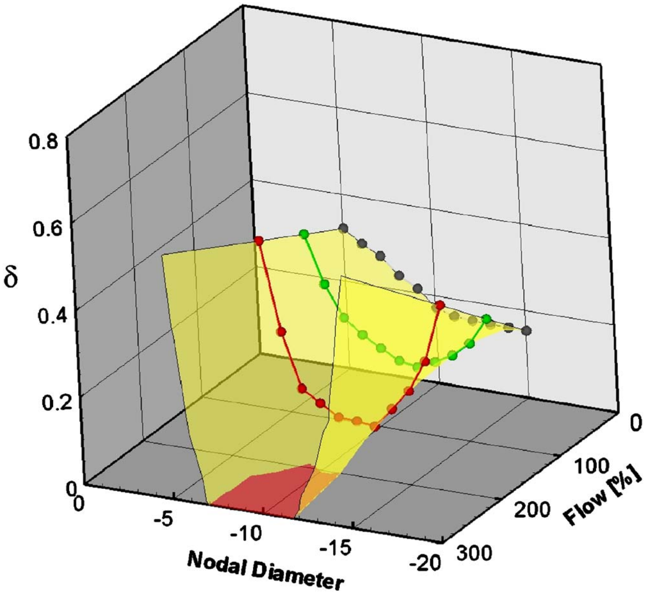

**Fig. 19 3D visualization of the measurements obtained and the extrapolated information for mechanical damping and the location of the onset of flutter**

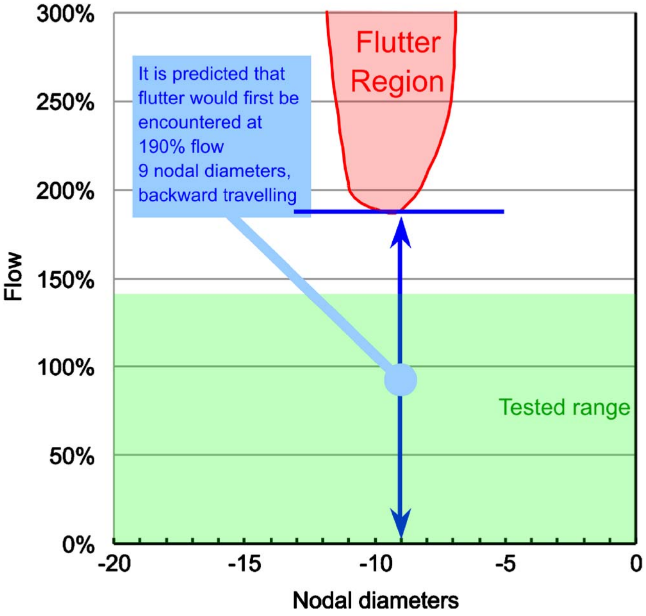

It is predicted that flutter would first be encountered at 190% flow 9 nodal diameters, backward travelling

**Fig. 20 Identification of the predicted location of the onset of blade flutter**

If there were no knowledge of the proximity of blade flutter, there would remain a possibility that flutter might be encountered just beyond the highest mass flow tested. To cope with this possibility, it would be necessary to apply a suitable factor of safety and only permit application of the blade up to a fraction of the highest mass flow tested. The knowledge that blade flutter would not occur with the ND45A until well beyond the tested range is in this case sufficient to remove this restriction and allow the new blade to be offered up to the maximum flow tested.

## Conclusions

Steam turbine last stage moving blades with tip shrouds are inherently at risk from flutter. CFD flutter modeling has shown why this arises and has been largely successful in predicting which modes will carry negative aerodynamic damping. In operation, the overall system remains stable because of the mechanical damping of the bladed disk assembly. Conventional testing or even successful application of a design does not prove that the design is stable for the complete application range and does not give any indication of the safety margin. In order to provide this critical information, measurements have been made of the aggregate damping during turbine operation. The measurements were designed to enable the separation of the mechanical and aerodynamic components of damping. The results have been used to identify the stability margin between safe operation and the onset of blade flutter. This approach represents a significant step forward in the analysis and understanding of flutter in steam turbines.

The CFD analysis and novel testing technique were applied in the product validation of the ALSTOM ND45A blade, demonstrating a large factor of safety from flutter.

## Acknowledgment

This investigation was made possible through the valuable contributions of many engineers.

Our thanks are extended to all our ALSTOM colleagues involved in the development of our LP blading technology and the ND45A LSMB. In particular, we are grateful for the support and assistance provided by Paul Gruau, Luca Ripamonti, Pierre Alain Masserey, and Ralf Greim.

The LP test turbine facility is situated in St. Petersburg, and the excellent assistance provided by our colleagues in Russia during the test program is gratefully acknowledged.

The authors are also very grateful for contributions of Andy Brown in developing and constructing the magnets and of James Mason for his work before and during the tests with the electromagnet drive.

Considerable assistance with the test program was given by Thorsten Osterhage, Peter Weiss, and Michael Mossom.

We would also like to acknowledge the contribution of Professor Li He for providing the original CFD code and many useful discussions on the subject of blade flutter.

Finally, we would like to thank Peter Walker and Mike McGuire for their constructive input and advice.

## Nomenclature

$C_z$ = 1D, axial, exit velocity (trailing edge of the LSMB)
FEA = finite element analysis
IBPA = interblade phase angle (deg)
$k$ = reduced frequency
log-dec = logarithmic decrement
LP = low pressure (as in LP steam turbine)
LSMB = last stage moving blade in LP steam turbine
$N_u$ = nodal diameter (negative values: backward traveling waves)
to = denotes torsional component of vibration
$X$ = denotes axial bending component of vibration
$\delta_A$ = aerodynamic damping, expressed as log-dec (%)
$\delta_{A\text{-local}}$ = local aerodynamic damping, expressed as log-dec (%)
$\delta_M$ = mechanical damping, expressed as log-dec (%) (this describes the damping provided by the complete material, mechanical, and nodal system)
$\delta$ = aggregate damping, $\delta = \delta_M + \delta_A$, expressed as log-dec (%)

## References

[1] Sisto, F., 1987, “AGARD Manual on Aeroelasticity in Axial Flow Turbomachines,” Unsteady Turbo-machinery Aerodynamics Report No. AGARD-AG-298, Vol. 1.

[2] Carta, F. O., and St. Hilaire, A. O., 1980, “Effects of Interblade Phase Angle on Cascade Pitching Stability,” ASME J. Eng. Power, **102**, pp. 391–396.

[3] Bölcs, A., and Fransson, T. H., 1986, “Aeroelasticity in Turbomachines: Comparison of Theoretical and Experimental Cascade Results,” Communication du Laboratoire de Thermique Appliquée et de Turbomachines No. 13, EPFL, Lusuanne.

[4] Bell, D. L., and He, L., 2000, “Three Dimensional Unsteady Flow for an Oscillating Turbine Blade and the Influence of Tip Leakage,” ASME J. Turbomach., **122**(1), pp. 93–101.

[5] Barton, H. A., and Halliwell, D. G., 1987, “Detailed On-Blade Measurements on a Transonic Fan in Unstalled Supersonic Flutter,” *Proceedings of the fourth International Symposium on Unsteady Aerodynamics and Aeroelasticity of Turbomachines (ISUAAT)*, Aachen, Germany.

[6] Scalzo, A. J., Allen, J. M., and Antos, R. J., 1986, “Analysis and Solution of a Nonsynchronous Vibration Problem of the Last Row Turbine Blade of a Large Industrial Combustion Turbine,” ASME J. Eng. Gas Turbines Power, **108**, pp. 591–598.

[7] Corral, R., Cerezal, N., and Vasco, C., 2003, “Flutter Boundaries for Pairs of Low Pressure Turbine Blades,” *Proceedings of the tenth International Symposium on Unsteady Aerodynamics, Aeroacoustics and Aeroelasticity of Turbomachines (ISUAAAT)*, Durham, NC, pp. 3–16.

[8] Cherysheva, O. V., Fransson, T. H., Kielb, R. E., and Barter, J., 2003, “Influence of a Vibration Amplitude Distribution on the Aerodynamic Stability of a Low-Pressure Turbine Sectored Vane,” *Proceedings of the tenth ISUAAAT*, Durham, NC, pp. 17–30.

[9] Kielb, R., Barter, J., Chernysheva, O., and Fransson, T., 2003, “Flutter Design of Low Pressure Turbine Blades With Cyclic Symmetric Modes,” *Proceedings of the tenth International Symposium on Unsteady Aerodynamics, Aeroacoustics and Aeroelasticity of Turbomachines (ISUAAAT)*, Durham, NC, pp. 41–52.

[10] Huang, X. Q., He, L., and Bell, D. L., 2006, “Influence of Upstream Stator on Rotor Flutter Stability in a Low Pressure Steam Turbine Stage,” Proc. Inst. Mech. Eng., Part A, **220**(1), pp. 25–35.

[11] He, L., 1990, “An Euler Solution for Unsteady Flow Around Oscillating Blades,” ASME J. Turbomach., **12**, pp. 714–722.

[12] Huang, X. Q., He, L., and Bell, D. L., 2006, “Experimental and Computational Study of Oscillating Turbine Cascade and Influence of Part-span Shrouds,” ASME J. Fluids Eng., submitted.

[13] Manwaring, S. R., and Krikeng, K. L., 1997, “Forced Response Vibrations of a Low Pressure Turbine due to Circumferential temperature Distortions,” *Proceedings of the eighth ISUAAAT*, Stockholm, Sweden.

[14] Folkman, S., “Damping Terms and Relationships,” www.mae.usu.edu/faculty/stevef/info/

# Effects of Obstructions and Surface Roughness on Film Cooling Effectiveness With and Without a Transverse Trench

**Ruwan P. Somawardhana**

**David G. Bogard**

Mechanical Engineering Department,
University of Texas at Austin,
Austin, TX 78712

*Recent studies have shown that film cooling with holes embedded in a shallow trench significantly improves cooling performance. In this study, the performance of shallow trench configurations was investigated for simulated deteriorated surface conditions, i.e., increased surface roughness and near-hole obstructions. Experiments were conducted on the suction side of a scaled-up simulated turbine vane. Results from the study indicated that as much as 50% degradation occurred with upstream obstructions, but downstream obstructions actually enhanced film cooling effectiveness. However, the transverse trench configuration performed significantly better than the traditional cylindrical holes, both with and without obstructions and almost eliminated the effects of both surface roughness and obstructions.* [DOI: 10.1115/1.2950063]

*Keywords: surface roughness, obstructions, transverse trench, film cooling, adiabatic effectiveness, vane*

## Introduction

Film cooling on turbine components has been studied since the 1970's, and there have been numerous studies on optimizing this technology. The majority of these tests are conducted with pristine surface conditions, something one might expect from a brand new component. However, it is well known that in-service turbine components can quickly develop rough surfaces from surface deposition, corrosion, and spallation. The root cause of surface deposition is from molten impurities in the combustion fuel and air impacting on a surface and being cooled, thereby hardening on a surface. Oxidation of metal surfaces or the erosion of thermal barrier coatings (TBCs) can cause spallation [1–3]. In the near-hole region, larger than average film cooling obstructions can also form due to the cooler surface as well as manufacturing defects [4,5]. Surface roughness and obstructions are both factors that can lead to significant film cooling degradation.

Though the effects of surface roughness on adiabatic effectiveness have been studied since the 1980's, the investigations into this have been limited in number, especially using actual vane geometry. Goldstein et al. [6], Schmidt and Bogard [7], and Schmidt et al. [8] all studied the effects of surface roughness on adiabatic effectiveness using a flat plate and saw little degradation in adiabatic effectiveness. Surface roughness effects on the suction side of simulated nozzle guide vanes were investigated by Guo et al. [9], Bogard et al. [10], and Rutledge et al. [11]. Guo et al. [9] found that roughness had little influence on film cooling effectiveness. Both Bogard et al. [10] and Rutledge et al. [11] used the same facilities that were used for this study, but at a location of higher surface curvature ($s/C=0.208-0.367$). Bogard et al. [10] found that a fully rough surface degraded adiabatic effectiveness by about 25% for all blowing ratios except for the high end, where performance began to converge. Rutledge et al. [11] found a definite degradation of around 30% at low blowing ratios but found an increase in adiabatic effectiveness due to the rough surface at high blowing ratios.

The previous rough surface studies all had uniform levels of roughness. However, depositions can accumulate around the edges of coolant holes, leading to near-hole obstructions that are somewhat larger than the general surface roughness. These near-hole obstructions can also be from manufacturing imperfections. Bunker [4] found that TBC applied incorrectly can cause as much as 50% centerline adiabatic effectiveness reduction due to film-hole blockage. Sundaram and Thole [5] studied large depositions that spanned multiple holes. They found that on the end wall, deposits downstream of the holes in the leading edge area caused increases up to 25%, but on the pressure side end wall, obstruction upstream and downstream of the holes caused nominally 35% degradation. Demling and Bogard [12] performed an obstruction study on the suction side of a turbine vane in the same facility used for the current study. They used obstructions that had a span of one coolant hole diameter and placed them upstream and downstream of the cooling hole. During that study, it was observed that at low blowing ratios there was a spatially averaged degradation of nominally 30% for both obstruction configurations. At high blowing ratios, upstream obstructions caused 55% degradation in adiabatic effectiveness and the downstream obstructions had no effect. The shape of the obstruction seemed to have little effect, although sharp edges seemed to degrade less than rounded edges. Changing the size of the obstructions (constant spanwise width while scaling height and streamwise length) showed $1/8d$ obstructions causing no change in performance relative to the no obstruction case, $1/2d$ and $1d$ obstructions causing large degradation and performing similarly, and $1/4d$ performing between the base line and the large obstructions. Finally, it was found that when placing obstructions at varying distances upstream of the coolant hole, placement of the obstruction two hole diameters upstream of the hole eliminated the effects of the upstream obstruction.

Bunker [13] and Waye and Bogard [14] found that embedding cylindrical holes in a narrow transverse trench can increase maximum adiabatic effectiveness by as much as 50%. Consequently the shallow trench performed similar to shaped holes, but with the

---

Contributed by the International Gas Turbine Institute of ASME for publication in the JOURNAL OF TURBOMACHINERY. Manuscript received June 20, 2007; final manuscript received October 17, 2007; published online October 17, 2008. Review conducted by David Wisler. Paper presented at the ASME Turbo Expo 2007: Land, Sea and Air (GT2007), Montreal, QC Canada, May 14–17, 2007.

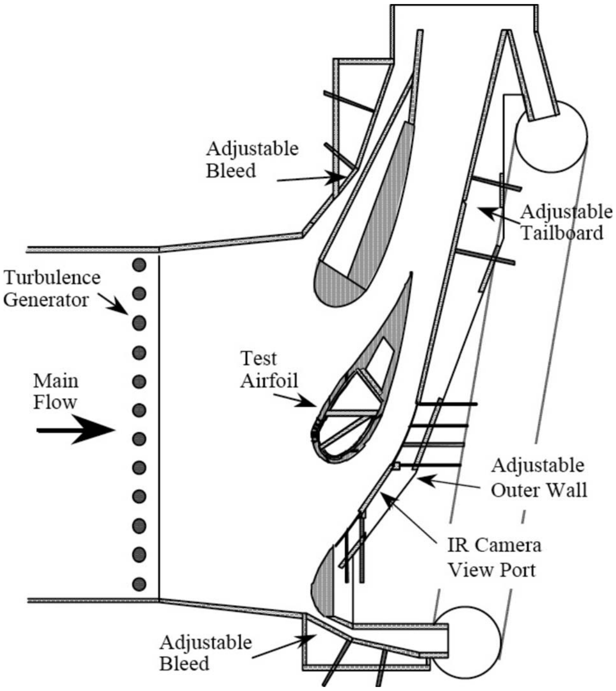

**Fig. 1 Schematic of the simulated turbine vane cascade test section**

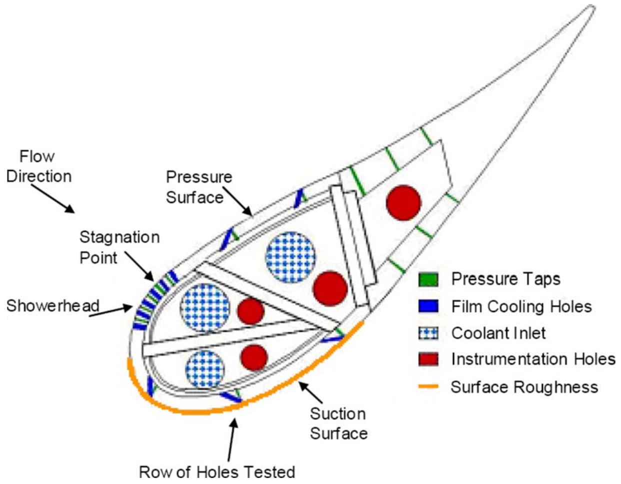

**Fig. 2 Schematic of test vane in detail**

advantage of cheaper manufacturing. While Bunker's [13] test was on a flat plate, Waye and Bogard's [14] tests were conducted in the same facility used for this study and in the same location on the suction side of the vane.

The current study involves an investigation of the effects of surface roughness and obstructions in the near-hole vicinity for film cooling on the suction side of a simulated turbine vane. A key part of this study was the investigation of the use of a narrow transverse trench for the film cooling holes to determine if it would mitigate the detrimental effects of surface roughness and obstructions. This is a companion paper to Somawardhana and Bogard [15] in which surface roughness and obstruction effects on cylindrical holes were investigated. This study is similar to that of Demling and Bogard [12], but is conducted farther downstream on the suction side of the vane where there are less curvature effects. A fully rough surface was used and high and low mainstream turbulence levels were tested.

## Experimental Facilities and Procedures

The facility used in this study consisted of a closed loop wind tunnel powered by a 50 hp variable speed blower. The nine times scale, three-vane linear cascade was placed in the test section of the wind tunnel, as shown in Fig. 1. The center vane, shown in Fig. 2, was used for test measurements, while the outer wall of the test section was adjusted to achieve a nondimensional pressure distribution around the vane that matched an inviscid computational fluid dynamics (CFD) simulation of the actual engine geometry and conditions. The inlet velocity to the cascade was set at 5.8 m/s and the exit velocity was accelerated to 28 m/s, producing an exit Reynolds number of $1.06 \times 10^6$ (based on a true chord length of $C=594$ mm) to match realistic engine conditions. A removable passive turbulence generator consisting of 38 mm diameter rods spaced 85 mm apart was located 0.5 m upstream of the cascade. Hot-wire measurements [14] showed an approach high turbulence level of $\text{Tu}_{\text{app}}=21\%$ with $\Lambda_f/d=10$, measured 107 mm ($0.18C$) upstream of the vane leading edge. For the low turbulence case an array of 19 mm rods were placed at nominally 1 m upstream of the vane. Low turbulence levels were $\text{Tu}_{\text{app}}=5.2\%$ with $\Lambda_f/d=10.7$. Due to the flow acceleration, at the test location $s/C=0.367$–$0.540$, the high and low turbulence levels were $\text{Tu}_\infty=3.9\%$ and $\text{Tu}_\infty=1.0\%$, respectively. Local turbulence length scales were similar to the length scales in the approach flow [14].

The test airfoil was machined in sections out of a low conductivity polyurethane foam, $k=0.048$ W/(m K), to mimic an adiabatic wall for adiabatic effectiveness measurements. The current study was conducted on the second row of cooling holes on the suction side of the vane located at $s/C=0.367$. The base line case had $d=4.11$ mm cylindrical holes with a 30 deg injection angle spaced $p/d=2.775$ apart.

The original section of the suction side tested already had an overlying transverse trench milled into the second row of cooling holes with a height of $h/d=0.5$ and a width of $w/d=4.0$, with the holes centered in the trench. Because the trench was milled into the surface, it actually moved the film cooling hole location $1d$ upstream, but the $x/d=0$ location was always defined at the trailing edge of the film cooling holes. Of the nine different trench configurations studied by Waye and Bogard [14], the one that performed best was the "narrow trench" configuration with depth and width of $h/d=0.5$ and $w/d=2$. This trench width was such that the walls of the trench were at the upstream and downstream edges of the coolant holes. To accomplish this geometry, preformed styrene strips were used ($k=0.17$ W/m K) and positioned with a double-sided tape to obtain the correct geometry. For the base line configuration (no trench), a styrene insert was manufactured to fill the trench with the appropriate hole geometry and was also positioned with a double-sided tape to achieve a uniform surface.

For the rough wall condition, sandpaper was used to simulate roughness. Bogard et al. [10] characterized typical surface roughness and created a plate with uniform cones having a precise geometry to obtain a hydrodynamic representation for the nine times scale facility used in their study. The representative surface roughness created by Bogard et al. [10] had an equivalent sand grain roughness of $k_s=0.5$ mm. The sandpaper used in this study had a CAMI grit designation of 36, which corresponds to an average grit diameter of 0.53 mm, close to $k_s$ of Bogard et al. [10]. In addition, an extensive study conducted by Dees [16] showed that the 36-grit sandpaper had similar hydrodynamic effects to the conical roughness. A summary of all test conditions is presented in Table 1.

The sandpaper along with all other surfaces were painted flat black to ensure a uniform emissivity for the IR camera, and the sandpaper was attached $29d$ upstream of the row of cooling holes and $34d$ downstream of the holes using a double-sided tape, with the edge of the sandpaper aligned with the leading or trailing edge

**Table 1 Test conditions**

| | |
|---|---|
| True chord length | 594 mm |
| Vane span | 549 mm |
| Vane pitch | 457 mm |
| Inlet velocity | 5.8 m/s |
| Exit Reynolds number | $1.06\times10^{6}$ |
| Test location | $s/C=0.367-0.540$ |
| High mainstream turbulence at inlet/test location | $\mathrm{Tu}_{\mathrm{app}}=21\%$ $\mathrm{Tu}_{\infty}=3.9\%$<br>$\Lambda_f=41$ mm |
| Low mainstream Turbulence at inlet/test location | $\mathrm{Tu}_{\mathrm{app}}=5.2\%$ $\mathrm{Tu}_{\infty}=1.0\%$<br>$\Lambda_f=44$ mm |
| Film cooling hole diameter | 4.11 mm |
| Hole length (base line) | 27.5 mm ($L/d=6.7$) |
| Hole length (trench) | 23.4 mm ($L/d=5.7$) |
| Trench height/Width | 2.1 mm ($h/d=0.5$) |
| Trench width | 4.2 mm ($w/d=2.0$) |
| Injection angle | 30 deg |
| Hole pitch | 11.4 mm ($p/d=2.78$) |
| Surface roughness | CAMI 36 grit |
| Obstructions | $2-1/2d\times1d\times1/2d$ |
| Density ratio | 1.3 |

of the holes. A microscopic inspection was used to confirm that the added paint did not alter the roughness profile. An example of the setup is given in Fig. 3. No sandpaper was attached between the holes, but contour plots showed that the $0.15d$ step change did not affect the film cooling performance as far as the coolant impinging and spreading between the holes before going downstream was concerned, as evidenced by the distinct jets with no lateral spreading due to the sandpaper edge.

In the study of Demling and Bogard [12], the shape 2 obstruction, shown in Fig. 4, was found to have the most significant effects, and so this same shape was used for this study. The obstructions were created out of quarter round styrene strips and the obstruction size used was $1/2d\times1d\times1/2d$, (*height* × *spanwise width* × *streamwise length*). The width was chosen to replicate the obstructions used by Demling and Bogard [12], and the $\frac{1}{2}d$ height and respectively scaled length was chosen based on a study by Wammack et al. [17]. Wammack et al. [17] found peak deposition levels of 310 $\mu$m; when scaled to this study, deposition heights did not exceed $1d$, but $1/2d$ was easily justified. These obstructions were placed on top of the sandpaper with the sand grains removed beneath the obstructions and were painted flat black for uniform emissivity.

All tests with obstructions were conducted with three consecutive holes, in the center of the row with 18 holes, containing the obstructions. There were two reasons for this; the first was to ensure the consistency between the three obstructed holes to verify the uniformity of the obstruction placement during each experiment. The second reason was to improve the accuracy of the laterally averaged values by having three holes available to average. To ensure that the results produced by obstructing three consecutive holes did not affect the results in any way compared to blocking just one hole, a test was run, obstructing only one hole. Results from this test confirmed that the obstructions on three holes had the same effects as a single hole [15].

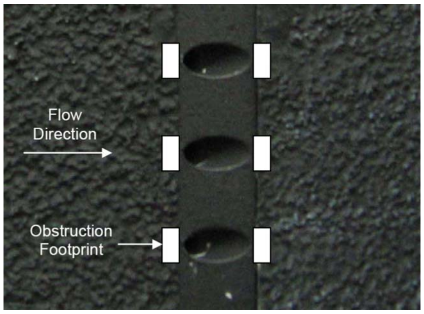

Fig. 3 Photograph of coolant holes showing sandpaper placement

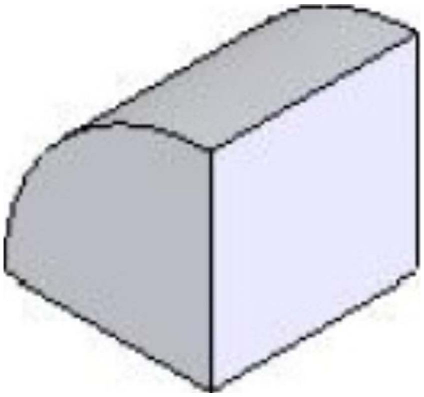

Fig. 4 Isometric view of shape 2

As previously mentioned, all laterally averaged data were averaged in the spanwise direction across three pitches in order to improve the accuracy of the data. The spatially averaged data were calculated by averaging the laterally averaged data streamwise from $x/d=0$ to 25, the same range shown in all laterally averaged plots.

Adiabatic effectiveness measurements were obtained from surface temperature measurements using infrared thermography via a FLIR ThermaCAM P20 camera. The camera was calibrated using type E ribbon thermocouples that were embedded between the sand grains and the foam surface (the paper portion of the sandpaper was removed due to its insulating effects). The camera resolution was 1.5 pixels/mm, and the usable field of view when set up and viewed through a circular NaCl IR window was 260 × 240 pixels. Beaded wire type E thermocouples were used to obtain the coolant and mainstream temperatures. The coolant temperature was obtained using two thermocouples, with the thermocouple junctions at the center of different coolant holes, just outside the field of view. The two mainstream thermocouples were placed upstream of the vane. Two thermocouples for each temperature measurement were used to identify any instrumentation errors, and the measurements were averaged between the two thermocouples. All thermocouple data were collected using a National Instruments data acquisition (NI DAQ) system. Adiabatic effectiveness, $\eta$, was calculated using the following definition:

$$\eta=\frac{T_\infty-T_{aw}}{T_\infty-T_c} \qquad (1)$$

Liquid nitrogen was used to cool the secondary loop air that was used for the coolant. A density ratio of DR=1.3 was used for all tests. Though density ratios closer to 2 are more common in actual engines, Cutbirth and Bogard [18] found that low density ratio coolant jets can give a good approximation of adiabatic effectiveness results and are on the order of only 10% lower than the high density ratio case when using high mainstream turbulence.

A range of blowing ratios were used, $M=0.4-1.6$, but the majority of the data presented are for $M=0.4$, 0.6, and 1.2. These blowing ratios were chosen based on $M=0.6$ being the peak value for the rough walled base line case, with $M=0.4$ and 1.2 representing lower and upper bounds, respectively. With the low temperatures used, although the foam vane has a low conductivity, there is still a slight conduction through the foam, making the surface temperatures slightly cooler than they should be. Radia-

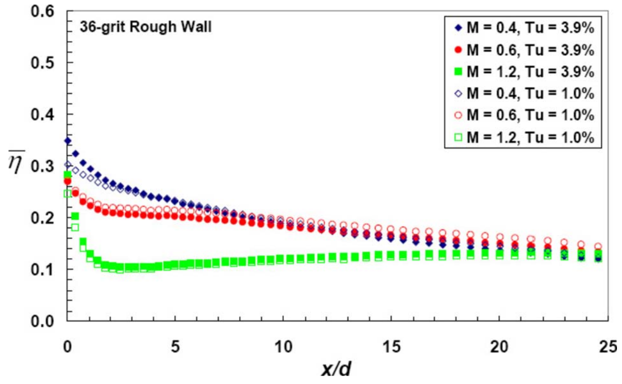

**Fig. 5 Laterally averaged adiabatic effectiveness comparison of high and low turbulence levels on the base line configuration with a rough wall**

tion was determined to be negligible, and a conduction correction was calculated using steady state values with no blowing. A constant conduction correction of $\eta_o=0.04$ was used for both high and low Tu on smooth wall tests, and $\eta_o=0.02$ or $\eta_0=0.03$ was used for high and low Tu on rough walled tests, respectively. The conduction correction values were calculated using a 1D conduction model described by Ethridge et al. [19],

$$\eta = \frac{\eta_{\text{measured}} - \eta_o}{1 - \eta_o} \tag{2}$$

The uncertainty used was based on test-to-test repeatability. A statistical analysis produced an uncertainty of $\delta\bar{\eta}=\pm 0.015$ and $\delta\bar{\bar{\eta}}=\pm 0.012$ over 11 repeated experiments of the base line case with a rough wall over the full range of blowing ratios. For the tests with obstructions, it was the standard to also run a case without obstructions within the same test. This practice allowed both to help get a good basis to calculate test-to-test repeatability and to check between tests to ensure that testing conditions were the same between tests. Systematic errors from individual thermocouples, the IR camera temperature calibration, and the conduction correction used in the data reduction produce an additional $\delta\bar{\eta}=\pm 0.006$ using a propagation of uncertainty. If the data in this study were to be compared to other studies, the total uncertainty of the data would be $\delta\bar{\eta}=\pm 0.021$.

## Results

**Effect of Mainstream Turbulence.** All tests were run at both high and low turbulence. However, as noted earlier, the difference between the turbulence at the testing location of the vane was small due to the flow acceleration [14]. From Fig. 5, it is apparent that the small differences in mainstream turbulence produce negligible changes in laterally averaged adiabatic effectiveness. Because high mainstream turbulence models actual turbine conditions better, the remainder of the data shown will be with high mainstream turbulence only.

**Surface Conditions.** The two surface conditions tested were a smooth wall and a rough wall. Surface roughness tends to significantly degrade effectiveness for low blowing ratios and enhance effectiveness for high blowing ratios, shown in Fig. 6. At low blowing ratios, degradation was found to be around 30%, similar to the results of Bogard et al. [10] and Rutledge et al. [11] although both Bogard et al. [10] and Rutledge et al. [11] performed their studies on the same simulated vane but at the upstream position of the first row of coolant holes. A 45% increase in adiabatic effectiveness was observed in the current study at high blowing ratios. This is consistent with Rutledge et al. [11] who found almost a 70% increase in adiabatic effectiveness due to roughness at high blowing ratios. Dees [16] showed a significant thickening of the boundary layer from $\delta=1.26$ mm to $\delta=3.46$ mm at $s/C=0.367$ for the smooth and rough walls, respectively, and at the same facility used for the current study. In addition, Dees [16] showed that roughness causes an increase in turbulence. With roughness, the thicker boundary layer allows for more separation of the coolant at low blowing ratios as well as dispersion due to turbulence, thereby causing degradation in spatially averaged adiabatic effectiveness. At the high blowing ratios, where separation would be expected even on the smooth case, the added turbulence from the surface roughness works in favor of increasing the adiabatic effectiveness by mixing the coolant and mainstream, thereby bringing back some of the separated coolant to the surface.

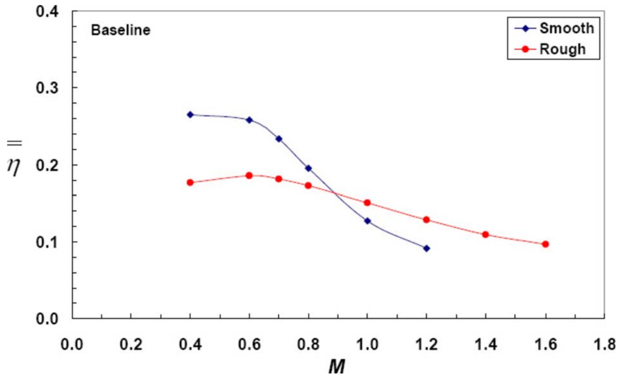

**Fig. 6 Spatially averaged adiabatic effectiveness comparison of the base line case with smooth and rough walls**

**Obstructions With a Rough Wall.** If the driving mechanism for obstruction formation is through deposition, it can be presumed that if obstructions are present, then the overall surface condition will also be rough. However, to distinguish the effects between surface roughness and obstructions on film cooling, a comparison between a smooth wall with obstructions and a rough wall with obstructions is presented in Fig. 7. An examination of this figure shows that in many cases, the difference between the smooth and rough surfaces with obstructions is within uncertainty or close to it. This leads to the conclusion that when obstructions are present, effects from surface conditions are minimized and the obstructions dominate the adiabatic effectiveness. As with the mainstream turbulence levels, because a rough surface is more likely with obstructions, considering actual turbine conditions, only rough wall cases will be presented in the following results.

Of the three obstruction configurations tested, upstream, downstream, and upstream+downstream, it is apparent in Fig. 7 that

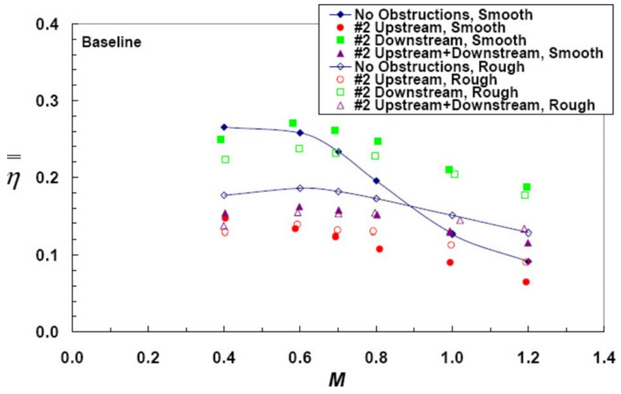

**Fig. 7 Spatially averaged adiabatic effectiveness of the base line case with smooth or rough walls and varying obstruction configurations**

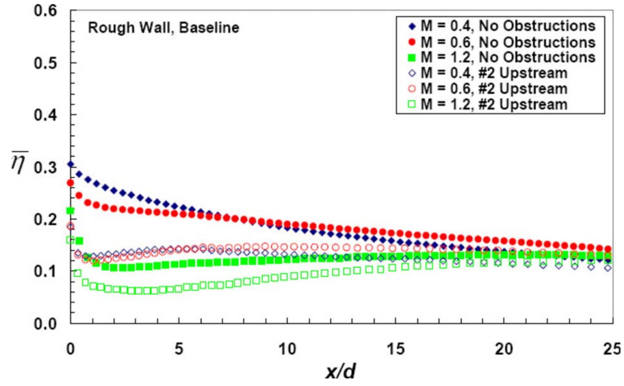

Fig. 8 Laterally averaged adiabatic effectiveness of the base line case with a rough wall and upstream obstructions

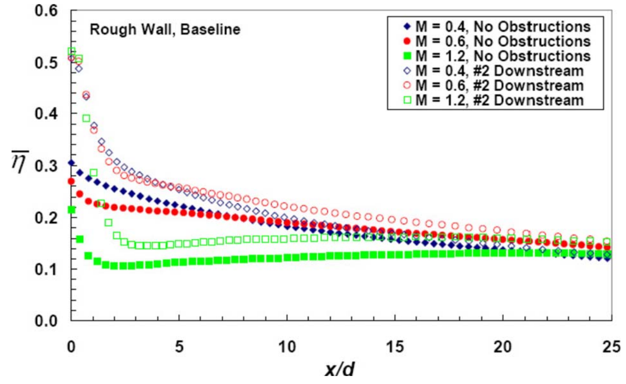

Fig. 9 Laterally averaged adiabatic effectiveness of the base line case with a rough wall and downstream obstructions

upstream obstructions cause the largest degradation, i.e., a 50% decrease with respect to the smooth surface and a 25% decrease relative to the rough surface. Similar results were found by Sundaram and Thole [5] and Demling and Bogard [12] who both found upstream obstructions to cause the most degradation, although in Sundaram and Thole's [5] experiment, the upstream +downstream case performed mostly the same as the upstream case. In addition, the upstream+downstream case, although in between the upstream and downstream configurations, performs closer to the results from the upstream configuration, leading to the conclusion that upstream obstructions dominate, again seen by Sundaram and Thole [5].

The decrease in adiabatic effectiveness due to upstream obstructions may be attributed to the blocking of the mainstream. The blocking of the mainstream prevents the mainstream from pushing the coolant jets to the surface, which in turn allows separation. Furthermore, the obstructions likely generate increased turbulence, which would increase dispersion of the coolant and bring some of the separated coolant back to the surface. These two differing characteristics can be seen in laterally averaged adiabatic effectiveness values, shown in Fig. 8. Separation and a return of some of the coolant to the surface at all blowing ratios for the cases with the upstream obstructions can be deduced from the laterally averaged adiabatic effectiveness distribution. Separation is suggested by the very low values of laterally averaged adiabatic effectiveness immediately downstream of the hole and a gradual increase in laterally averaged adiabatic effectiveness farther downstream.

Downstream obstructions generally improved adiabatic effectiveness for all blowing ratios, as shown in Fig. 7. From the laterally averaged values shown in Fig. 9, it is clear that the near-hole region dominates the significant increase in spatially averaged adiabatic effectiveness, while further downstream the adiabatic effectiveness converges and is essentially the same across all blowing ratios. Comparing contour plots (Fig. 10) at a blowing ratio of $M=0.6$, the coolant can be seen to spread in the spanwise direction as it is forced to flow around the downstream obstruction. This spreading of the coolant jets due to downstream obstructions was also seen in Demling and Bogard [12].

It was noted that the upstream+downstream case performed between the upstream and downstream cases, but closer to the upstream configuration. From the laterally averaged data, shown in Fig. 11, in the near-hole region across all blowing ratios with upstream+downstream obstructions, the adiabatic effectiveness is elevated and then followed by a sharp decrease. The initial elevated levels are due to the spreading of the coolant from the downstream obstruction, as previously discussed. The sharp decrease in adiabatic effectiveness near the hole can be attributed to the upstream obstruction blocking the mainstream, allowing for

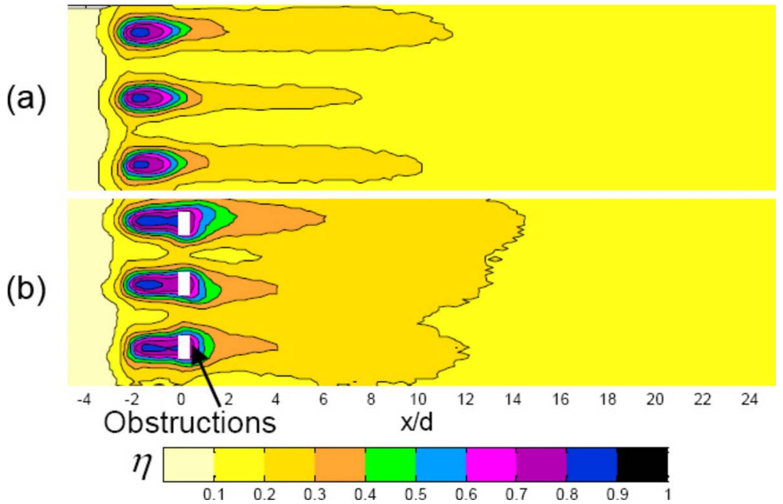

Fig. 10 Contour plots of adiabatic effectiveness for the base line case at $M=0.6$ with a rough wall and (*a*) no obstructions and (*b*) downstream obstructions

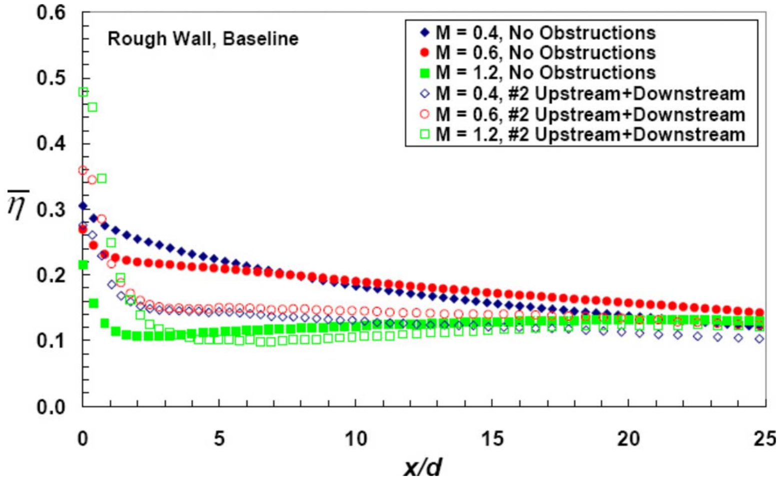

**Fig. 11 Laterally averaged adiabatic effectiveness of the base line case with a rough wall and both upstream and downstream obstructions simultaneously**

the coolant to separate. At high blowing ratios, it seems that the upstream+downstream obstructions have little effect. The obstructed case does perform better in the near-hole region, but by $x/d=3$ it performs the same as the unobstructed case. The process here involves the downstream obstructions entraining part of the coolant, thereby increasing the near-hole adiabatic effectiveness, evidenced by the bulb shape downstream of the hole in Fig. 12. However, even though the upstream obstruction would normally cause a blow-off, the nonobstructed case is already expected to separate due to the high blowing ratio, leading to both cases exhibiting the same level of separation despite different configurations.

**Narrow Trench With Smooth and Rough Surfaces.** The narrow trench provides uniform film cooling coverage and therefore better adiabatic effectiveness levels than cylindrical holes, as shown in Ref. [14], and the current study observed similar results. The major advantage of the narrow trench is that it inhibits separation, causing the coolant jets to fill the trench first, and then exit the trench as a sheet rather than as individual jets [14]. The increased performance due to the trench over standard cylindrical holes was also observed when roughness and obstructions were present.

Unlike the base line case, adiabatic effectiveness with the narrow trench is relatively constant across the range of blowing ratios, as shown in Fig. 13. Furthermore, this constant level occurs for smooth and rough surfaces. The largest difference between smooth and rough surfaces when using a narrow trench is at low blowing ratios, with a degradation of only 15%, which is quickly eliminated with increasing blowing ratio. This leads to the conclusion that film cooling performance with a trench is insensitive to the effects of surface roughness, especially at the mid to high blowing ratios.

**Narrow Trench With Obstructions and a Rough Surface.** Knowing that the trench mitigates rough surface effects, the next determination was how obstructions affect trench performance. These results are presented in Fig. 14, which shows the spatially averaged adiabatic effectiveness for obstructions normalized by the no obstruction case. Figure 14 shows that upstream obstructions cause degradation across all blowing ratios, downstream obstructions cause a slight increase at high blowing ratios, and obstructions upstream and downstream simultaneously fall between upstream and downstream configurations for most blowing ratios.

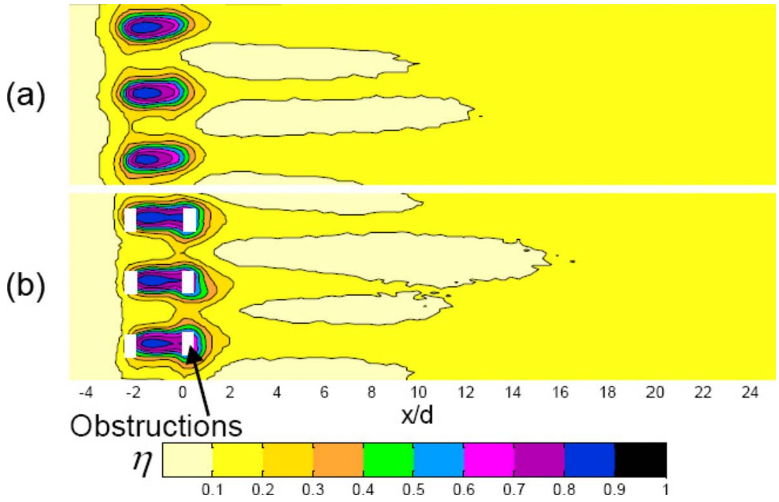

**Fig. 12 Contour plots of adiabatic effectiveness for the base line case at $M=1.2$ with a rough wall and (*a*) no obstructions and (*b*) both upstream and downstream obstructions simultaneously**

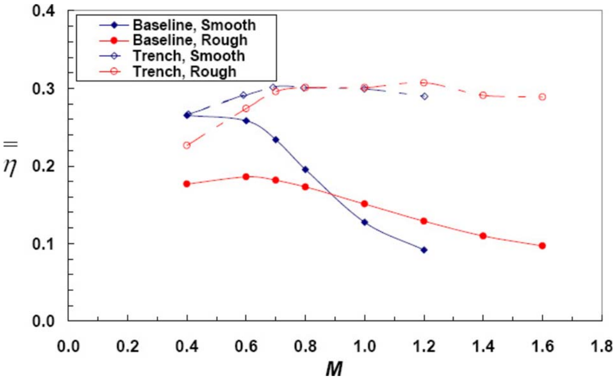

**Fig. 13 Spatially averaged adiabatic effectiveness of both base line and trench cases with both smooth and rough surfaces**

Overall, the variation from unity due to obstructions is relatively small, with a maximum degradation of 15% compared to a maximum degradation of almost 40% for the base line case. Compared to the base line, the trench significantly minimizes most of the effects due to obstructions.

A further comparison of the trench and base line cases shows that regardless of the obstruction configuration with a rough wall, the worst performing trench case still achieves higher adiabatic effectiveness values than the best case for the base line, shown in Fig. 15. Figure 15 shows the trench case configurations normalized by the optimal blowing ratio yielding the highest spatially averaged adiabatic effectiveness of the base line case with similar obstruction configurations. As the blowing ratio increases, the benefits of the trench also increase, and up to a 140% increase in spatially averaged adiabatic effectiveness was observed. This is significant because it shows that based on adiabatic effectiveness, embedding cylindrical holes in a trench will always give a benefit over standard cylindrical holes, whether the surface is smooth or degraded to a rough surface with obstructions near holes.

## Conclusions

In this study, the performance of shallow trench configurations was investigated for simulated deteriorated surface conditions, i.e., increased surface roughness and near-hole obstructions. The study involved determining the effects on cylindrical holes and then seeing how cylindrical holes embedded in a trench performed in comparison. It was found that regardless of the surface conditions, embedding cylindrical holes in a trench will always outperform standard cylindrical holes.

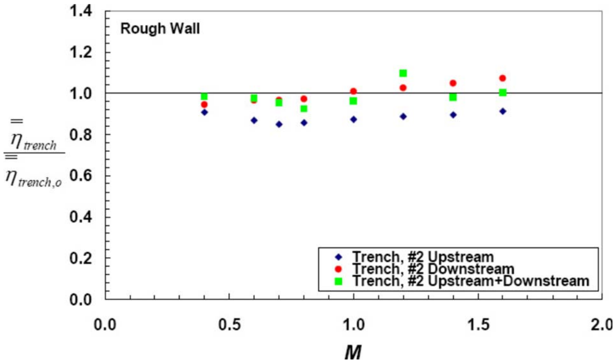

**Fig. 14 Spatially averaged adiabatic effectiveness of the trench case with a rough wall and various obstruction configurations normalized by the rough wall trench case with no obstructions**

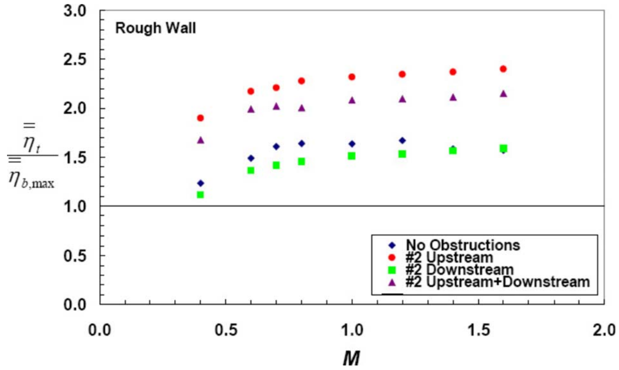

**Fig. 15 Spatially averaged adiabatic effectiveness of the trench case with a rough wall with and without obstructions normalized by the maximum base line value for each obstruction configuration**

From the cylindrical hole study, it was determined that when $0.5d$ high obstructions are present, degrading effects from surface roughness are overshadowed by the dominating effects of near-hole obstructions. With no trench, obstructions upstream of the coolant holes produced as much as 50% degradation, while downstream obstructions actually enhanced adiabatic effectiveness. When both upstream and downstream obstructions were present simultaneously, the upstream obstruction effects dominated.

The trench showed the most promising results. Not only did the narrow trench significantly improve adiabatic effectiveness relative to the base line, it eliminated the degrading effects from surface roughness. For rough wall conditions the trench more than doubled the adiabatic effectiveness. Furthermore, when a narrow trench was used, the degrading effects due to near-hole obstructions were negligible. As the blowing ratio increased, the benefits of the trench over cylindrical holes also increased, similar to the performance of shaped holes.

## Acknowledgment

The authors gratefully acknowledge support from the University Turbine Systems Research (UTSR) program (Contract No. 03-01-SR110) directed through the South Carolina Institute for Energy Studies and the Office of Naval Research through the Electric Ship consortium.

## Nomenclature

$C$ = chord length
$d$ = film cooling hole diameter
DR = density ratio, $\rho_c/\rho_\infty$
$h$ = trench height
HTu = high turbulence
$k$ = thermal conductivity
$k_s$ = equivalent sand grain roughness
LTu = low turbulence
$M$ = blowing ratio, $\rho_c U_c/\rho_\infty U_\infty$
$p$ = coolant hole pitch distance
$s$ = streamwise coordinate from the stagnation line
Tu = turbulence intensity, $u_{\mathrm{rms}}/U_{\mathrm{mean}}$
$U$ = flow velocity
$w$ = trench width
$x$ = streamwise distance from the downstream edge of the coolant holes

### Greek

$\Lambda_f$ = integral length scale
$\delta$ = uncertainty or boundary layer thickness
$\eta$ = adiabatic effectiveness, $(T_\infty - T_{aw})/(T_\infty - T_c)$

## Subscripts and Superscripts

app = approach condition
$b$ = base line
$c$ = coolant
$o$ = without film cooling or without obstructions
rms = root mean square
$t$ = trench
$\infty$ = local mainstream
$\overline{\ }$ = laterally averaged
$\overline{\overline{\ }}$ = spatially averaged

## References

[1] Bogard, D. G., Schmidt, D. L., and Tabbita, M., 1998, "Characterization and Laboratory Simulation of Turbine Airfoil Surface Roughness and Associated Heat Transfer," ASME J. Turbomach., **120**, pp. 337–342.

[2] Bons, J. P., Taylor, R. P., McClain, S. T., and Rivir, R. B., 2001, "The Many Faces of Turbine Surface Roughness," ASME J. Turbomach., **123**, pp. 739–748.

[3] Hamed, A., Tabakoff, W., and Wenglarz, R., 2006, "Erosion and Deposition in Turbomachinery," J. Propul. Power, **22**(2), pp. 350–360.

[4] Bunker, R. S., 2000, "Effect of Partial Coating Blockage on Film Cooling Effectiveness," ASME Paper No. 2000-GT-0244.

[5] Sundaram, N., and Thole, K. A., 2006, "Effects of Surface Deposition, Hole Blockage, and TBC Spallation on a Vane Endwall Film-Cooling," ASME Paper No. GT2006-90379.

[6] Goldstein, R. J., Eckert, E. R. G., Chiang, H. D., and Elovic, E., 1985, "Effect of Surface Roughness on Film Cooling Performance," ASME J. Eng. Gas Turbines Power, **107**, pp. 111–116.

[7] Schmidt, D. L., and Bogard, D. G., 1996, "Effects of Free-stream Turbulence and Surface Roughness on Film Cooling," ASME Paper No. 96-GT-462.

[8] Schmidt, D. L., Sen, B., and Bogard, D. G., 1996, "Effects of Surface Roughness on Film Cooling," ASME Paper No. 96-GT-299.

[9] Guo, S. M., Lai, C. C., Jones, T. V., Oldfield, M. L. G., Lock, G. D., and Rawlinson, A. J., 2000, "Influence of Surface Roughness on Heat Transfer and Effectiveness for a Fully Film Cooled Nozzle Guide Vane Measured by Wide Band Liquid Crystals and Direct Heat Flux Gauges," ASME Paper No. 2000-GT-0204.

[10] Bogard, D. G., Snook, D., and Kohli, A., 2003, "Rough Surface Effects on Film Cooling of the Suction Side Surface of a Turbine Vane," ASME Paper No. IMECE2003-42061.

[11] Rutledge, J. L., Robertson, D., and Bogard, D. G., 2006, "Degradation of Film Cooling Performance on a Turbine Vane Suction Side Due to Surface Roughness," ASME J. Turbomach., **128**, pp. 547–554.

[12] Demling, P., and Bogard, D. G., 2006, "The Effects of Obstructions on Film Cooling Effectiveness on the Suction Side of a Gas Turbine Vane," ASME Paper No. GT2006-90577.

[13] Bunker, R. S., 2002, "Film Cooling Effectiveness Due to Discrete Holes Within a Transverse Surface Slot," ASME Paper No. GT-2002-30178.

[14] Waye, S. K., and Bogard, D. G., 2006, "High Resolution Film Cooling Effectiveness Measurements of Axial Holes Embedded in a Transverse Trench With Various Trench Configurations," ASME Paper No. GT2006-90226.

[15] Somawardhana, R. P., and Bogard, D. G., 2007, "Study on Obstruction Geometry, Obstruction Location, and Varying Surface Roughness on Adiabatic Effectiveness," ASME Paper No. GT2007-28004.

[16] Dees, J. A., 2006, "Effects of Regular and Random Roughness on the Heat Transfer and Skin Friction Coefficient on the Suction Side of a Gas Turbine Vane," MS thesis, University of Texas at Austin.

[17] Wammack, J. E., Crosby, J., Fletcher, D., Bons, J. P., and Fletcher, T. H., 2006, "Evolution of Surface Deposits on a High Pressure Turbine Blade, Part I: Physical Characteristics," ASME Paper No. GT2006-91246.

[18] Cutbirth, J. M., and Bogard, D. G., 2003, "Effects of Coolant Density Ratio on Film Cooling Performance on a Vane," ASME Paper No. GT2003-38582.

[19] Ethridge, M. I., Cutbirth, J. M., and Bogard, D. G., 2001, "Scaling of Performance for Varying Density Ratio Coolants on an Airfoil With Strong Curvature and Pressure Gradient Effects," ASME J. Turbomach., **123**, pp. 231–237.

# Aeroelastic Analysis of Rotors With Flexible Disks and Alternate Blade Mistuning

**James M. Bleeg**
e-mail: james.bleeg@pw.utc.com

**Ming-Ta Yang**
e-mail: ming-ta.yang@pw.utc.com

**James A. Eley**
e-mail: james.eley@pw.utc.com

Pratt & Whitney,
400 Main Street,
East Hartford, CT 06108

*A new reduced-order aeroelastic model using the principal shapes (AMPSs) of modes is presented. Rotors with flexible disks and alternate blade mistuning can challenge the fidelity of flutter prediction techniques that assume uniform blade-to-blade geometry and mode shape invariance with nodal diameter pattern. The AMPS method, however, accounts for alternating blade geometry as well as varying blade mode shapes, providing accurate flutter predictions for a large number of modes from a small number of computational fluid dynamics simulations. AMPS calculations on rotors with alternate blade mistuning are presented and compared to other prediction techniques. The results provide insight into how alternate blade mistuning affects aerodynamic coupling and the flutter characteristics of a rotor.* [DOI: 10.1115/1.2812957]

## 1 Introduction

As modern jet engines trend toward lighter-weight designs, rotor loading and flexibility increase, increasing flutter risk. Effective flutter prediction tools and an understanding of flutter mitigation strategies are therefore critical to successful engine design.

The object of any flutter analysis is stability prediction, and for many modern rotors, aerodynamic damping almost completely determines the aeroelastic stability. Aerodynamic damping is very sensitive to mode shape and the local flow field, thus a thorough flutter analysis requires the consideration of dozens of modes at multiple operating conditions. Aerodynamic damping can be determined for many modes simultaneously by solving the flutter eigenvalue problem, which requires the input of an aerodynamic coupling matrix. Computational fluid dynamics (CFD) simulations are often used to populate this matrix. For rotors with stiff disks and negligible structural coupling between blades, simulating one or two blade mode shapes is usually enough to construct the full aerodynamic coupling matrix. However, if the disk is flexible and there is significant frequency veering between mode families, more blade mode shapes need to be considered, requiring many more CFD simulations. If the rotor is mistuned with significant blade-to-blade geometry variations, the computational requirements increase further.

Alternate blade mistuning (ABM) is a specific type of mistuning in which two distinct blade types are alternated around the wheel. ABM increases the damping of lightly damped modes, in turn increasing flutter margin [1–3]. Flutter analysis can help maximize the ABM stability benefit while minimizing performance costs. To that end, the objective of this study is a set of fast and reliable flutter prediction tools for rotors with ABM, especially those with flexible disks and substantial geometric differences between the two blade types.

Many flutter prediction methods are reported in the literature. CFD-based methods have demonstrated success when applied to tuned rotors [4,5]. These methods can be extended to capture the effects of mistuning on rotors with stiff disks using reduced-order models that neglect structural coupling, such as the one described by Crawley and Hall [1]. In recent years, structural mistuning models have advanced to account for structural coupling [6–8]. Kielb et al. [9] combined the fundamental mistuning model (FMM) with influence coefficients computed from CFD to create a prediction method that works well for mistuned rotors with moderate structural coupling; however, the method does not account for large geometric variability blade to blade and is restricted to isolated mode families with negligible blade mode shape variation. When geometry or mode shape variations are significant, a different approach is needed. The direct method approach, which involves directly simulating each mistuned rotor mode of interest with CFD, captures the effect of these variations, but many CFD simulations are required and the computational cost can be prohibitive.

A new flutter prediction method called the aeroelastic model using principal shapes (AMPSs) of modes is presented. It was developed to compute the aerodynamic damping for a large set of modes from a reduced number of CFD calculations, while still capturing the effects of structural coupling, cyclic blade geometry variation, and blade mode shape changes due to veering. To do this, AMPS takes the set of structural mode shapes from a rotor cyclic symmetry model and defines a smaller set of principal shapes, which approximately spans the set of actual mode shapes. Using the influence coefficient method [10], the principal shapes of the modes (PSM) are simulated with CFD calculations and the motion dependent forces are recorded. Finally, using linear superposition, the aerodynamic coupling matrix is constructed for the set of actual modes. The eigenvalue problem is then solved to determine the aerodynamic damping distribution.

AMPS aerodynamic damping predictions are presented for two ABM rotors and their tuned counterparts. The new method is validated by comparison with direct method predictions. AMPS results are then analyzed and compared with results from other prediction techniques to gain insight into how ABM affects rotor stability.

## 2 Mathematical Formulation

**2.1 Eigenvalue Problem for the Flutter Analysis.** The equation of motion of a bladed-disk structure subject to aerodynamic forces can be written as the following.

$$\mathbf{M}\ddot{\mathbf{x}} + \mathbf{C}\dot{\mathbf{x}} + \mathbf{K}\mathbf{x} = \mathbf{f}_m + \mathbf{f}_e \tag{1}$$

where $\mathbf{x}$ is the displacement of the structure from its equilibrium position, $\mathbf{M}$, $\mathbf{C}$, and $\mathbf{K}$ are the mass, damping, and stiffness matrices of the structure, $\mathbf{f}_m$ is the motion-dependent (vibration-induced) aerodynamic force, and $\mathbf{f}_e$ is the external aerodynamic force that is not vibration induced. Note that the damping matrix

---

Contributed by the International Gas Turbine Institute of ASME for publication in the JOURNAL OF TURBOMACHINERY. Manuscript received June 20, 2007; final manuscript received July 19, 2007; published online October 17, 2008. Review conducted by David Wisler. Paper presented at the ASME Turbo Expo 2007: Land, Sea and Air (GT2007), Montreal, Quebec, Canada, May 14–17, 2007.

$\mathbf{C}$ represents only the structural damping such as material and frictional damping. The aerodynamic damping effect is represented by the motion-dependent force $\mathbf{f}_m$.

For the purpose of flutter analysis, the structural damping and the external excitation force are assumed to be zero, i.e.,

$$\mathbf{C} = \mathbf{0} \quad \text{and } \mathbf{f}_e = \mathbf{0} \tag{2}$$

The structural vibration, $\mathbf{x}$ and the motion-dependent force $\mathbf{f}_m$ are assumed to be sinusoidal. Equation (1) can then be transformed to the following equation in the frequency domain.

$$(\mathbf{K} - \omega^2\mathbf{M})\mathbf{y} = \mathbf{p} \tag{3}$$

where $\mathbf{y}$ is the complex amplitude of $\mathbf{x}$, $\mathbf{p}$ the complex amplitude of $\mathbf{f}_m$, and $\omega$ the oscillation frequency. For small amplitude oscillation, the motion-dependent aerodynamic force can be approximated as a linear function of $\mathbf{y}$, i.e.,

$$\mathbf{p} = \mathbf{A}\mathbf{y} \tag{4}$$

where $\mathbf{A}$ is the aerodynamic coupling matrix, which describes the aerodynamic coupling among blades. $\mathbf{A}$ can be numerically estimated based on the following equation:

$$\mathbf{A} = \nabla_{\mathbf{y}}\mathbf{p}|_{\mathbf{y}=\mathbf{0}} \tag{5}$$

Substituting Eq. (4) into Eq. (3) yields the eigenvalue problem for the flutter analysis of a fluid-structural system:

$$(\mathbf{K} - \omega^2\mathbf{M} - \mathbf{A})\mathbf{y} = \mathbf{0} \tag{6}$$

For a limited frequency range of interest, the size of Eq. (6) can be significantly reduced. Based on the theory of modal interaction developed by Yang and Griffin [6], the structural amplitude can be approximated by the following equation:

$$\mathbf{y} = \mathbf{\Phi}\boldsymbol{\beta} \tag{7}$$

where $\mathbf{\Phi}$ is the mode shape matrix containing the set of modes with frequencies that are close to the frequency of interest, i.e.,

$$\mathbf{\Phi} = \lfloor \boldsymbol{\phi}_1 \boldsymbol{\phi}_2 \boldsymbol{\phi}_3 \cdots \boldsymbol{\phi}_{\hat{N}} \rfloor \tag{8}$$

where $\hat{N}$ is the number of down selected modes and $\boldsymbol{\beta}$ denotes the participation of the modes. The mode shape $\boldsymbol{\phi}_r$ and its corresponding eigenvalue $\lambda_r$ satisfy the following structural eigenvalue problem:

$$(\mathbf{K} - \lambda_r\mathbf{M})\boldsymbol{\phi}_r = \mathbf{0} \tag{9}$$

Substituting Eq. (7) into Eq. (6) and applying the orthogonality of modes, the flutter eigenvalue problem in the modal form can be expressed as

$$(\hat{\mathbf{K}} - \omega^2\hat{\mathbf{M}} - \hat{\mathbf{A}})\boldsymbol{\beta} = \mathbf{0} \tag{10}$$

where $\hat{\mathbf{K}}$ and $\hat{\mathbf{M}}$ are the diagonal modal stiffness and mass matrices of the structure and $\hat{\mathbf{A}}$ is the modal aerodynamic coupling matrix with the following expression:

$$\hat{\mathbf{A}} = \mathbf{\Phi}^H\mathbf{A}\mathbf{\Phi} \tag{11}$$

The dimension of the modal matrices in Eq. (10) is $\hat{\mathbf{N}} \times \hat{\mathbf{N}}$, where $\hat{\mathbf{N}}$ is typically on the order of the number of blades.

The flutter eigenvalue problem posed in Eq. (10) can be solved much more efficiently than its equivalent posed in Eq. (6) because the size of the problem has been significantly reduced.

**2.2 Characteristics Implied by Rotational Periodicity.** Consider a bladed disk with a rotational periodicity of $N$.[1] One can write the aerodynamic coupling matrix $\mathbf{A}$ in the following block-circulant form [1]:

$$\mathbf{A} = \begin{bmatrix} \mathbf{A}_0^{[0]} & \mathbf{A}_1^{[0]} & \cdots & \mathbf{A}_{N-1}^{[0]} \\ \mathbf{A}_{N-1}^{[0]} & \mathbf{A}_0^{[0]} & \cdots & \mathbf{A}_{N-2}^{[0]} \\ \vdots & \vdots & \ddots & \vdots \\ \mathbf{A}_1^{[0]} & \mathbf{A}_2^{[0]} & \cdots & \mathbf{A}_0^{[0]} \end{bmatrix} \tag{12}$$

where $\mathbf{A}_r^{[s]}$ is the effect of a unit vibration of the $r$th sector on the $s$th sector and, for all $r = 0, \ldots, N-1$,

$$\mathbf{A}_r^{[r]} = \mathbf{A}_0^{[0]} \tag{13}$$

$$\mathbf{A}_r^{[0]} = \mathbf{A}_0^{[N-r]} \tag{14}$$

Note that, though the sectors are numbered from 0 to $N-1$ in Eq. (12), because of rotational periodicity, sector $N$ and sector 0 refer to the same sector, sector $(N-1)$ and sector $-1$ refer to the same sector, and so on.

The $r$th mode shape vector $\boldsymbol{\phi}_r$ of the rotor can be written as

$$\boldsymbol{\phi}_r = \begin{Bmatrix} \boldsymbol{\phi}_r^{[0]} \\ \boldsymbol{\phi}_r^{[1]} \\ \vdots \\ \boldsymbol{\phi}_r^{[N-1]} \end{Bmatrix} \tag{15}$$

where $\boldsymbol{\phi}_r^{[s]}$ is the component of $\boldsymbol{\phi}_r$ that is associated with the $s$th sector. The rotational periodicity of the structure implies

$$\boldsymbol{\phi}_r^{[s]} = \boldsymbol{\phi}_r^{[q]} e^{i2\pi(s-q)n/N} \tag{16}$$

with $n$ being the phase index (or, nodal diameter pattern) of mode $\boldsymbol{\phi}_r$, and $s, q = 0, 1, \ldots, N-1$.

Similarly, with $\mathbf{\Phi}^{[s]}$ being defined as the component of $\mathbf{\Phi}$ that is associated with the $s$th sector

$$\mathbf{\Phi}^{[s]} = \lfloor \boldsymbol{\phi}_1^{[s]} \ \boldsymbol{\phi}_2^{[s]} \ \boldsymbol{\phi}_3^{[s]} \ \cdots \ \boldsymbol{\phi}_N^{[s]} \rfloor \tag{17}$$

the mode shape matrix $\mathbf{\Phi}$ can be written as

$$\mathbf{\Phi} = \begin{bmatrix} \mathbf{\Phi}^{[0]} \\ \mathbf{\Phi}^{[1]} \\ \vdots \\ \mathbf{\Phi}^{[N-1]} \end{bmatrix} \tag{18}$$

The mode shape matrix components $\mathbf{\Phi}^{[s]}$ and $\mathbf{\Phi}^{[q]}$ are correlated by a phase transformation matrix $\mathbf{E}$

$$\mathbf{\Phi}^{[s]} = \mathbf{\Phi}^{[q]}\mathbf{E}^{s-q} \tag{19}$$

Without losing generality, let $\mathbf{\Phi}^{[0]}$ denote the mode shape matrix component associated with the reference sector. $\mathbf{\Phi}^{[0]}$ can be derived using standard cyclic symmetry modal analyses.

**2.3 Principal Shapes of the Modes.** For the set of modes within a frequency range of interest, the columns of $\mathbf{\Phi}^{[0]}$, namely, $\boldsymbol{\phi}_r^{[0]}$ $(r = 1, 2, \ldots, \hat{N})$, have a lot of similarities. For example, in the extreme case of a perfectly rigid disk, all $\boldsymbol{\phi}_r^{[0]}$ within a single blade mode family are identical. In the case of a flexible disk, the $\boldsymbol{\phi}_r^{[0]}$ within a blade mode family would have characteristics similar to the corresponding cantilever blade mode, but also differences due to blade root motion. Mathematically, $\mathbf{\Phi}^{[0]}$ can be expressed in terms of a singular value decomposition.

$$\mathbf{\Phi}^{[0]} = \mathbf{U}\mathbf{S}\mathbf{V}^H \tag{20}$$

$\mathbf{U}$ and $\mathbf{V}$ are unitary orthonormal matrices which represent the column and row spaces of $\mathbf{\Phi}^{[0]}$. The columns of $\mathbf{U}$, $\mathbf{u}_r$ $(r = 1, 2, \ldots, \hat{N})$, are the principal shapes for the modes (PSMs) of interest, and $\mathbf{S}$, the singular value matrix, is diagonal with each singular value denoting the importance of its corresponding PSM.

Suppose the first $\tilde{N}$ PSM can be used as a basis to represent $\mathbf{\Phi}^{[0]}$ with acceptable errors. One can write

---

[1] In the case of a tuned rotor, $N$ is the number of blades. In the case of a rotor with ABM, $N$ is the number of blades divided by 2.

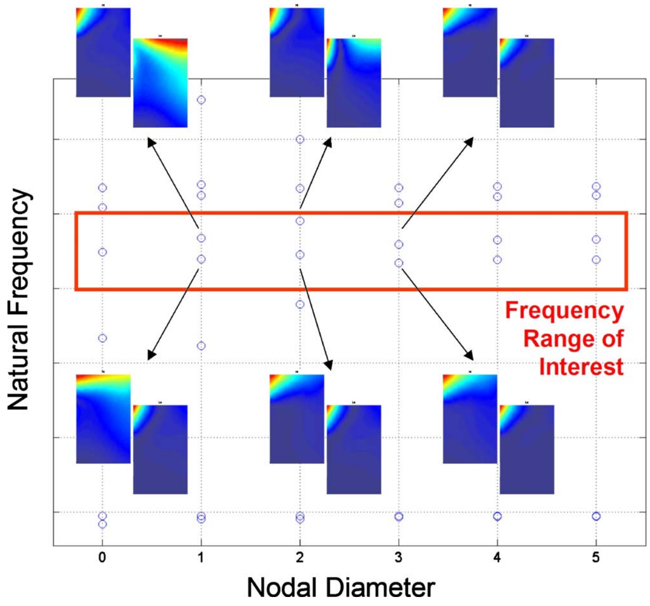

**Fig. 1 Nodal diameter map and mode shapes, ABM Rotor X**

$$\mathbf{\Phi}^{[0]} = \widetilde{\mathbf{U}}\mathbf{Z} \tag{21}$$

where $\widetilde{\mathbf{U}}$ is the matrix containing a reduced set of PSM, the $\widetilde{N}$ most significant columns of $\mathbf{U}$, and $\mathbf{Z}$ is the corresponding coefficient matrix.

**2.4 Computing the Aerodynamic Coupling Matrix.** Substituting Eqs. (12)–(14), (18), and (19) into Eq. (11), the modal aerodynamic coupling matrix $\hat{\mathbf{A}}$ can be expanded as

$$\hat{\mathbf{A}} = \sum_{r=0}^{N-1}\sum_{s=0}^{N-1} (\mathbf{E}^{r+1})^H \mathbf{\Phi}^{[0]^H} \mathbf{A}_0{}^{[s]} \mathbf{\Phi}^{[0]} \mathbf{E}^{r-s+1} \tag{22}$$

Now, substitute Eq. (21) into Eq. (22) and let

$$\widetilde{\mathbf{P}}^{[s]} = \mathbf{A}_0{}^{[s]}\widetilde{\mathbf{U}} = [\widetilde{\mathbf{p}}_1{}^{[s]}\widetilde{\mathbf{p}}_2{}^{[s]} \cdots \widetilde{\mathbf{p}}_{\widetilde{N}}{}^{[s]}] \tag{23}$$

The modal aerodynamic coupling matrix can be computed by

$$\hat{\mathbf{A}} = \sum_{r=0}^{N-1}\sum_{s=0}^{N-1} (\mathbf{E}^{r+1})^H \mathbf{\Phi}^{[0]^H} \mathbf{P}^{[s]} \mathbf{Z} \mathbf{E}^{r-s+1} \tag{24}$$

In Eq. (24), $\tilde{p}_r{}^{[s]}$, the $r$th column of $\widetilde{\mathbf{P}}^{[s]}$, is the aerodynamic force on the $s$th sector induced by the reference sector vibrating in a unit of the $r$th PSM, $\mathbf{u}_r$. $\tilde{p}_r{}^{[s]}$ can be computed by CFD routines with prescribed blade structural motion. Equations (24) and (10) are the general equations that form the backbone of the AMPS method. They account for structural coupling, blade mode shape changes with nodal diameter, and cyclically varying geometry.

Equations (24) and (10) can take the form of other reduced-order methods when simplifying assumptions are used. For example, Eq. (24) reduces to the influence coefficient method when only a limited number of passages neighboring the reference sector are modeled in the CFD analysis [10]. If it is assumed that only one blade type and one blade mode shape are needed to compute the aerodynamic coupling matrix, then only one PSM is required and the equations can approximate well-known reduced-order methods for mistuned rotors. For example, when the disk is assumed to be perfectly rigid, the modal stiffness and mass matrices $\hat{\mathbf{K}}$ and $\hat{\mathbf{M}}$ in Eq. (10) become $\hat{k}\mathbf{I}$ and $\hat{m}\mathbf{I}$, with $\hat{k}$ and $\hat{m}$ being the blade alone modal stiffness and mass. In this case, Eq. (10) is similar to the method described by Crawley and Hall [1]. When the disk is assumed to be slightly flexible, $\hat{\mathbf{K}}$ and $\hat{\mathbf{M}}$ can be constructed according to Feiner and Griffin [8]. In this case, the equations are similar to the method described by Kielb et al. [9].

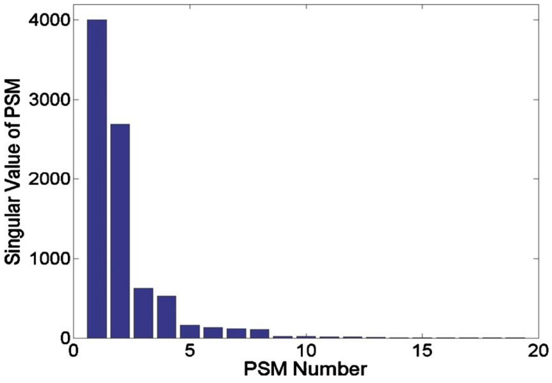

**Fig. 2 Singular values of PSM, ABM Rotor X**

## 3 Numerical Results

**3.1 Procedure.** The preceding mathematical treatment of the AMPS method was written for general application to any rotor or vane with rotational periodicity. The remainder of the paper focuses on application of the AMPS method to two compressor rotors with ABM. Rotor X, the first ABM rotor discussed, was designed to remedy subsonic stall flutter observed in the tuned rotor. This rotor has 20 blades with two geometrically distinct blade types alternated around the wheel. Subsequent engine tests showed that ABM substantially increased Rotor X flutter margin.

Figure 1 is a nodal diameter map for ABM Rotor X derived from a cyclic symmetry finite element model (FEM) of a two-blade sector. It exhibits several traits that complicate flutter analysis of the rotor, traits which are absent from tuned rotors with stiff disks. For example, within the frequency range of interest, there are several mode dyads, defined in this paper as two modes with the same nodal diameter but separated by a small frequency difference[2]. Also, the A- and B-blade deflection shapes, depicted for a few representative modes, vary within the frequency range of interest[3].

Singular value decomposition indicates that the full set of select Rotor X modes can be approximated with a subset of PSM (Eq. (21)). Figure 2 plots the singular values of the mode shape matrix $\mathbf{\Phi}^{[0]}$. It shows that the first few singular values are much greater than the rest of the singular values. Therefore, $\mathbf{\Phi}^{[0]}$ can be represented by a reduced set of principal shapes, $\widetilde{\mathbf{U}}$, without incurring significant approximation errors. Figure 3 shows how the errors drop quickly as the number of PSM increases. Later, it is shown that the first four PSMs are sufficient to represent the modes of interest in this case.

Since the structural modes can be reconstructed with linear combinations of PSM, the unsteady aerodynamic forces associated with the structural modes can be derived, using linear superposition, from the forces associated with the PSM. Therefore, the entire modal aerodynamic coupling matrix $\hat{\mathbf{A}}$ can be generated from the motion-dependent forces computed from the simulation of just a few PSMs. With $\hat{\mathbf{K}}$ and $\hat{\mathbf{M}}$ already known from the FEM,

---

[2] For tuned rotors with stiff disks, mode families are usually isolated with large frequency differences between modes at the same nodal diameter. However, ABM rotors with flexible disks can have two or more modes per nodal diameter within a relatively narrow frequency range. Dyadic modes are discussed further in Sec. 3.3.

[3] Significant geometric differences between the two blade types are not evident in the contour plots because all the contour plots presented herein are mapped to rectangles to protect proprietary rotor designs.

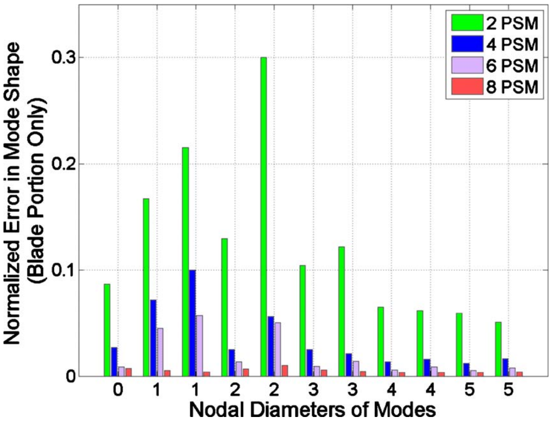

**Fig. 3 Errors of mode shapes approximated by PSM, ABM Rotor X. The normalized error for the *r*th mode is defined as $\|\phi_r - \phi_r\| / \max_r \|\phi_r\|$ where $\phi_r$ is the mode shape approximated by PSM and $\phi_r$ is the baseline mode shape. $\|\cdot\|$ is the Euclidean norm of a vector.**

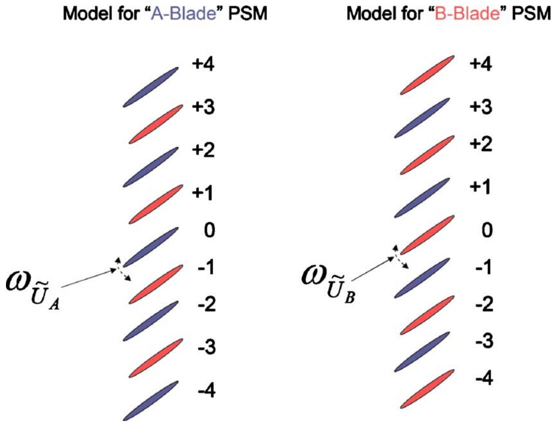

**Fig. 4 IC CFD Models for ABM rotors**

Eq. (10) is then solved for the aeroelastic modes, frequencies, and damping.

The influence coefficient (IC) method was used to compute the PSM induced aerodynamic forces. The CFD models are depicted in Fig. 4. The IC method uses linear superposition and assumes the unsteady aerodynamic forces induced by the vibration of the reference Blade 0 diminish to negligible levels beyond the ±4 blades. One IC calculation is run for each PSM[4], and $\tilde{\mathbf{P}}^{[s]}$ is constructed from the aerodynamic forces recorded on each blade.

**3.2 Validation of the Aeroelastic Model Using Principal Shapes.** AMPS and direct method flutter analyses were conducted on ABM Rotor X. Multirow steady CFD calculations provided boundary and initial conditions for the time-marching, isolated-row IC flutter calculations. The CFD system described by Silkowski et al. [4], since expanded to include AMPS and the direct method for mistuned rotors, was used for this study. As depicted by the pressure ratio versus flow map in Fig. 5, the CFD calculations were run at operating conditions where tuned Rotor X fluttered in test.

AMPS aerodynamic damping predictions using two, four, and

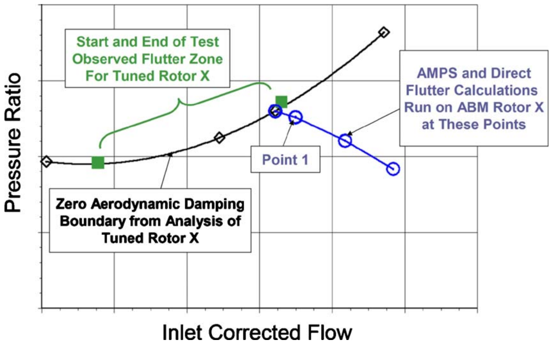

**Fig. 5 Pressure ratio versus flow, Rotor X**

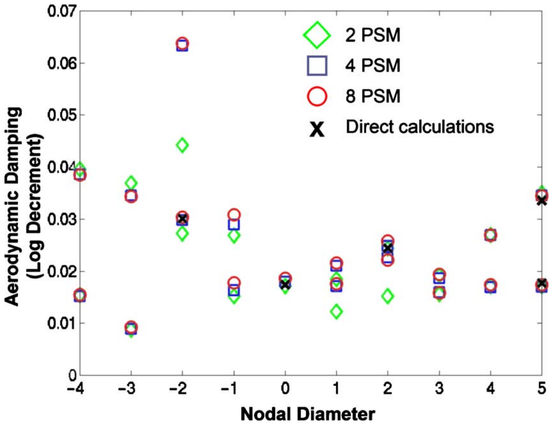

**Fig. 6 Aerodynamic damping, ABM Rotor X**

eight PSMs were made for the modes highlighted in Fig. 1. The set of modes included forward and backward traveling wave patterns. Direct method predictions were made for the 0, ±2, and 5 nodal diameter (ND) modes[5]; these modes were most amenable to direct simulation using periodic boundary conditions. Figure 6 plots predicted aerodynamic damping versus nodal diameter pattern at Point 1 on the performance map. The eight PSM AMPS results agree very well with the direct method results, as do the four PSM AMPS results. In turn, agreement is good between the eight PSM and four PSM results, even for the ±1 ND modes, which suffer from the largest mode shape approximation differences between four PSMs and eight PSMs (Fig. 3). The two PSM damping predictions, which employ much larger approximation errors, agree reasonably well with the other predictions for some modes (e.g., three and 5 ND modes), but not others (e.g., one and two ND modes). For Rotor X, the two PSM mode shape approximations are too coarse to reliably predict aerodynamic damping for all the modes of interest. This is an indication of mild blade mode shape changes with nodal diameter. Four PSMs are sufficient to capture the effect of these mode shape changes on damping and consistently match direct method predictions, not just for overall damping, but for the details of the unsteady flow fields as well.

Figure 7 compares Blade B contours of motion-dependent unsteady pressure for the lightly damped 5 ND mode, as predicted by the AMPS and direct methods. The two results are nearly identical and so in turn are the predicted contours of aerodynamic damping density (Fig. 8).

When the aeroelastic system is linear, agreement between AMPS and the direct method is very good; however, at severe

---

[4] For this application, the PSMs were constructed in pairs: For the first PSM of a given pair, the A blade deflects and the B blade is stationary and vice versa for the second PSM. Constructing the PSM in this way allowed for a more straightforward implementation of the method.

[5] Nodal diameters > 0 travel in the direction of the rotor spin. Nodal diameters < 0 travel in the opposite direction.

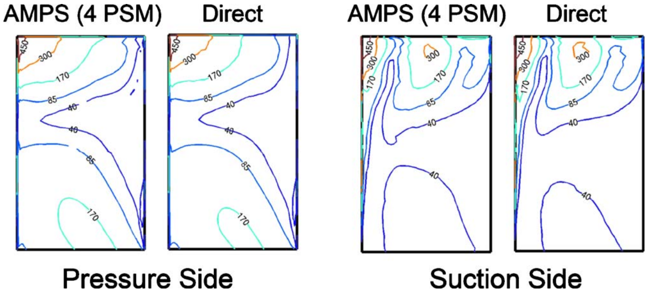

**Fig. 7 Magnitude of unsteady pressure, ABM Rotor X, B blade, 5 ND mode**

off-design conditions where nonlinear aeroelastic behavior is present, agreement between the methods deteriorates. Figure 9 plots predicted damping versus inlet corrected flow for the two 5 ND modes and the 0 ND mode. The agreement between AMPS (four PSMs) and direct method results is very good at the two highest flow points. However, the agreement begins to break down at the lowest flow. In this study, the AMPS and direct method simulate blade vibrations with prescribed small amplitudes, and linear aerodynamic response is assumed (i.e., the damping coefficients are independent of vibration amplitude). Further investigation of the comparison between the two methods in Fig. 9 reveals that while damping is insensitive to vibration amplitude at higher flows, at the lowest flow, the damping varies significantly with amplitude. Thus, the AMPS and direct method results differ at the lowest flow because the unsteady aerodynamic response and, resultantly, the flutter behavior are nonlinear for the range of amplitudes simulated. The AMPS method, with its liberal use of linear superposition, does not apply well to situations where capturing nonlinear flutter is important. The precise manner in which nonlinear flutter analyses should be run is a research topic unto itself and beyond the scope of this paper.

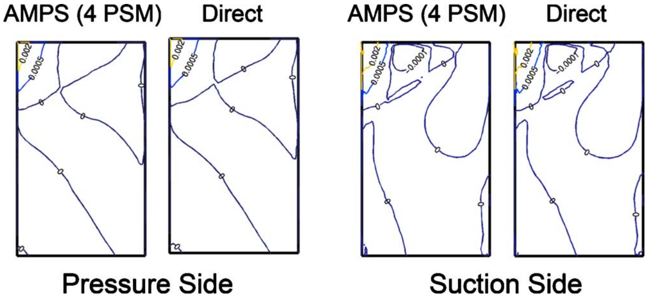

**Fig. 8 Aerodynamic damping density, ABM Rotor X, B BLADE, 5 ND mode**

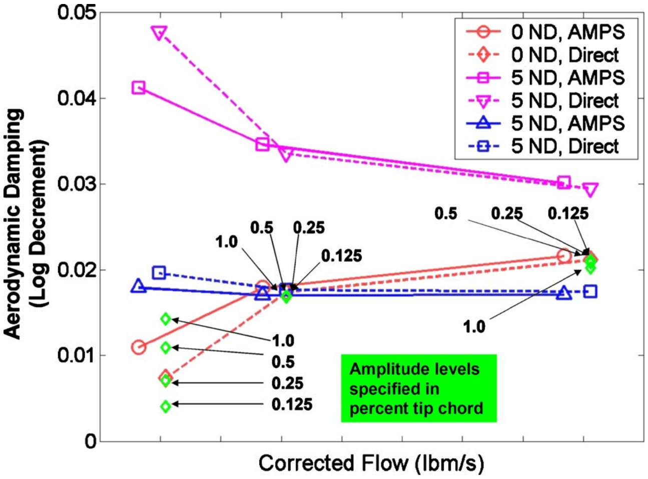

**Fig. 9 Comparison of AMPS and direct method, ABM Rotor X**

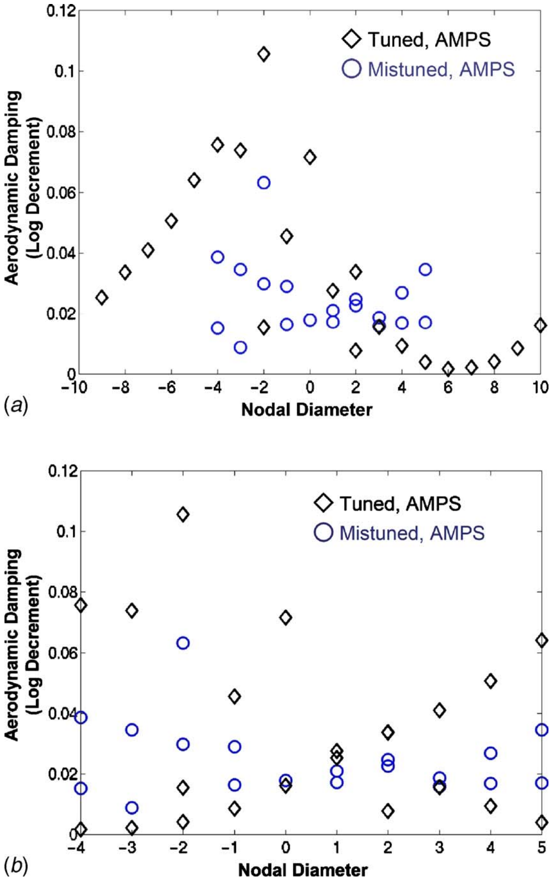

**Fig. 10 (*a*) Comparison of aerodynamic damping, Rotor X, not aliased and (*b*) comparison of aerodynamic damping, Rotor X, aliased**

**3.3 Impact of Alternate Blade Mistuning on Flutter.** ABM can be an effective flutter remedy [1–3,11]. By reducing aerodynamic coupling between neighboring blades and increasing the aerodynamic damping of otherwise lightly damped modes, ABM augments rotor flutter margin relative to its tuned counterpart. ABM Rotor X was created by replacing every other A-type blade on tuned Rotor X with a higher frequency B-type blade. Tuned and ABM damping distributions at map Point 1 are plotted in Fig. 10(*a*). The two rotors have the same number of blades, but tuned Rotor X has 20 identical sectors while ABM Rotor X has 10 sectors, and thus only 10 unique nodal diameter patterns. To make a more direct comparison with ABM Rotor X, tuned Rotor X is aliased to ten sectors in Fig. 10(*b*). For most of the nodal diameter patterns, each rotor has two modes within the frequency range of interest. For the tuned rotor, the two modes are distinguished primarily by interblade phase angle ($\Delta\text{IBPA}=180$ deg). For the ABM rotor, dyadic modes are distinguished by IBPA too, but more prominently by frequency and blade participation: Typically, the A blades vibrate with greater amplitude than the B blades for one mode, and the B blades vibrate with greater amplitude for the other mode.

Test data and AMPS identified the lightly damped −4 ND mode[6] as a flutter concern for the tuned rotor. Figure 11(*a*) breaks down the damping contributions blade by blade. The bars on this

---

[6] Predicted damping levels vary significantly with mode (e.g., Fig. 10). In this paper, modes with predicted aerodynamic damping levels clearly below the damping distribution mean are labeled *lightly damped*. Modes with predicted damping levels clearly above the mean are labeled *heavily damped*.

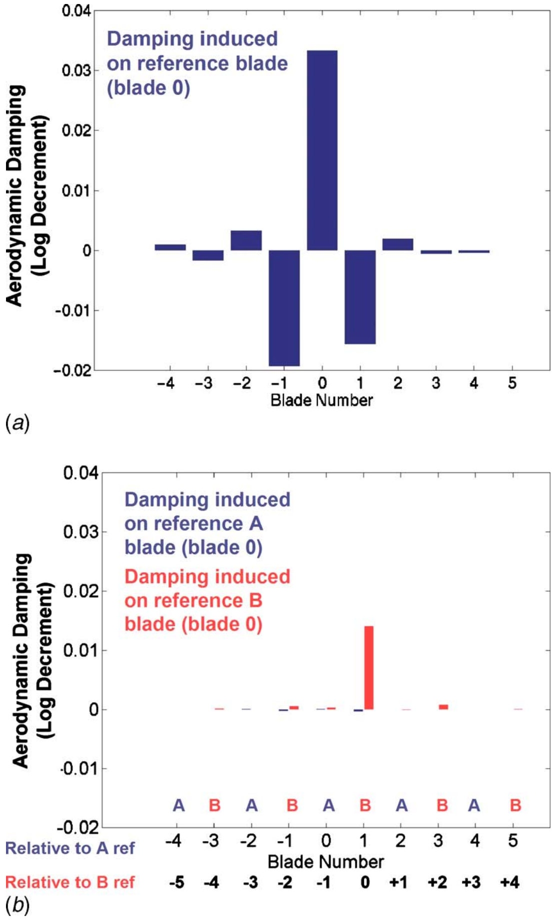

**Fig. 11** (*a*) **Blade-by-blade damping breakdown, −4 ND mode, lightly damped, tuned Rotor X and** (*b*) **blade-by-blade damping breakdown, −4 ND mode, lightly damped, ABM Rotor X**

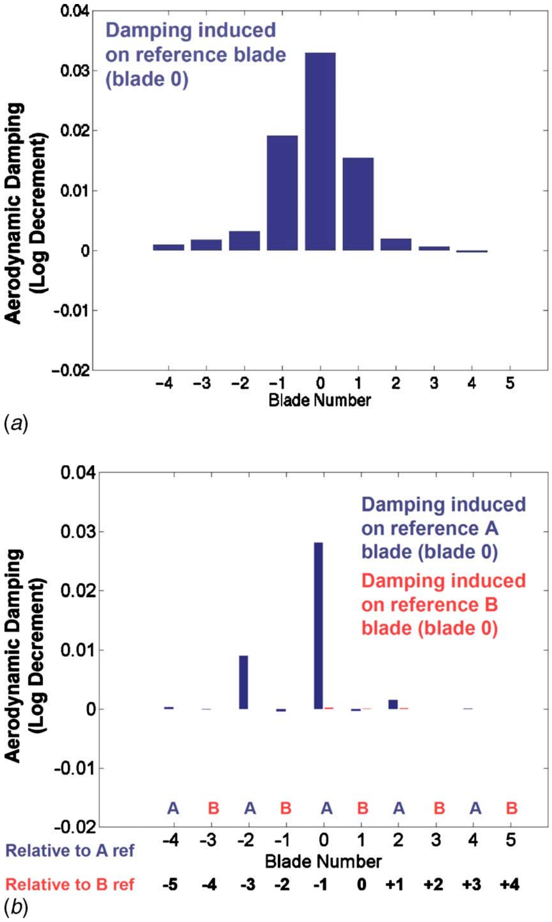

**Fig. 12** (*a*) **Blade-by-blade damping breakdown, −4 ND mode, heavily damped, tuned Rotor X and** (*b*) **blade-by-blade damping breakdown, −4 ND mode, heavily damped, ABM Rotor X**

plot represent the damping on the reference Blade 0 induced by the vibration of Blade $n$. The sum of the blade-by-blade contributions equals the overall tuned rotor damping for the −4 ND mode. The reference blade is nearly always self-damped. In other words, when the reference blade vibrates, it induces unsteady aerodynamic forces on its surface that serve to damp its vibration. The $\pm 1$ blades can induce destabilizing unsteady aerodynamic forces on the reference blade, which is the case for this mode. The influence of the $\pm 2$, $\pm 3$, and $\pm 4$ blades on the reference blade is relatively weak for this case. The blade-by-blade damping breakdown for the ABM rotor mode is plotted in Fig. 11(*b*). In some respects, the ABM damping breakdown looks similar to the tuned rotor breakdown: The reference blade is self-damped and the contributions from the peripheral blades are small. However, unlike the tuned Rotor X breakdown, damping contributions from $\pm 1$ blades are negligible for the ABM rotor—their destabilizing effect has been virtually eliminated. As a result, the overall damping for this mode increases.

By the same mechanism that stabilizes the lightly damped modes, ABM reduces the damping of the more heavily damped modes. The heavily damped −4 ND tuned and mistuned modes provide a good example. The tuned mode is broken down blade by blade in Fig. 12(*a*). In this case, $\pm 1$ blades induce stabilizing unsteady aerodynamic forces on the reference blade. As depicted in Fig. 12(*b*), ABM nearly eliminates the influence of $\pm 1$ blades, decreasing the overall damping relative to that of the tuned mode.

Explanations for how mistuning increases the aerodynamic damping of lightly damped modes can be approached from a number of directions including symmetry breaking [12] and coupling between different traveling waves [13,14]. An intuitive and accessible explanation, which centers on alternating blade-by-blade modal deflection amplitudes and their effect on aerodynamic coupling, was chosen for this paper as it fits naturally with the methods and results described herein. For a given mode, all of the blades on a perfectly tuned rotor vibrate with the same amplitude, but on a mistuned rotor, the blades vibrate with different amplitudes. Figure 13 plots ABM Rotor X A-to-B-blade ratios of maximum deflection for all modes of interest. Figure 11 considered along with Fig. 13 illustrates how A/B amplitude ratio affects aerodynamic coupling. For this −4 ND mode, the destabilizing effect of the $\pm 1$ blades on the reference blade has been significantly reduced because the A blades are barely moving.

Accounting for aerodynamic coupling between dyadic structural modes has little practical effect on the computed amplitude ratios. The weak aerodynamic coupling between dyadic modes is due to the relatively large frequency differences between them, a reflection of the substantial frequency separation between the A and B blades. Consequently, structural coupling largely determines the modal amplitude ratios for ABM Rotor X.

The amplitude ratio distribution in Fig. 13 and its effect on aerodynamic coupling between blades (e.g., Figs. 11 and 12), explain much of the tuned-to-mistuned damping trends in Fig. 10. As suggested by Figs. 10–12, reference blade self-damping sets the mean of the damping versus nodal diameter distribution. Damping variation with nodal diameter pattern is chiefly influenced by the $\pm 1$ blades for most tuned rotors, including tuned Rotor X. For ABM rotors, with the influence of the $\pm 1$ blades diminished, damping variation with nodal diameter decreases and

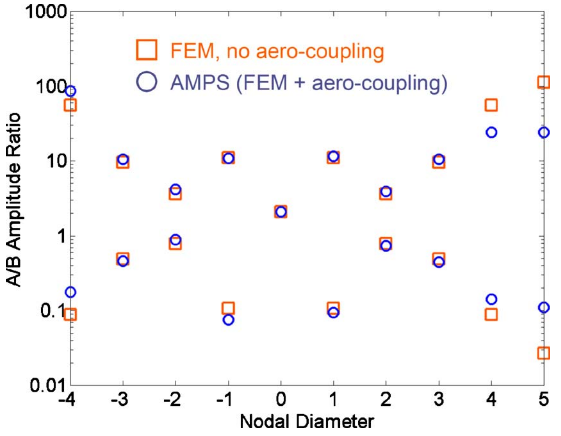

**Fig. 13 Ratios of maximum blade deflection amplitude, ABM Rotor X**

the relative influence of the ±2 blades increases. However, when the amplitude ratio between the A and B blades is close to 1.0, the ±1 blades can still make a significant contribution to the overall damping. The −3 ND mode has a B/A amplitude ratio of only 2.0, indicating significant structural coupling between the blades. As a result, the destabilizing effect of the ±1 blades is partially retained (Fig. 14), reducing the ABM damping benefit as compared to similar modes with less structural coupling. The finding that structural coupling can reduce the effectiveness of ABM echoes findings presented by Kielb et al. [15,9].

**3.4 Comparing the Aeroelastic Model Using Principal Shapes With Other Prediction Methods.** Comparisons to other prediction methods can provide further insight into ABM. A reduced-order model described by Crawley–Hall [1] (herein referred to as the CH method) computes ABM aerodynamic damping using just the tuned rotor aerodynamic influence coefficients and the A- and B-blade frequencies as inputs. No CFD or FE analyses of the mistuned geometry are required. Because it does not account for structural coupling, the method is more applicable to rotors with stiff disks; it is used here as a reference point. Kielb–Feiner [9] (herein referred to as the KF method) is a similar approach to CH, using the same IC and blade frequency inputs. However, KF accounts for structural coupling using the FMM technique [8] and requires only one additional input: the full set of frequencies from an isolated tuned mode family.

In the case of tuned Rotor X, the set of modes in the frequency range of interest (Figs. 15 and 1) is not quite an isolated mode family. Despite this, the KF predicted amplitude ratio trends agree reasonably well with AMPS results (Fig. 16). CH does not capture the amplitude ratio trends well because the structural coupling, which is substantial for some of the modes, is not accounted for, and the aerodynamic coupling is too weak to significantly affect the amplitude ratios. Nevertheless, the KF and CH aerodynamic damping predictions are in agreement for several modes (Fig. 17). This is because structural coupling is weak for these modes as evidenced by large amplitude ratios predicted by the FEM model. With weak aerodynamic and structural coupling between neighboring blades, dyadic mistuned modes collapse to the damping mean of the dyadic tuned modes. Alternately stated, damping for the dyadic mistuned modes approximates the sum of the tuned blade-by-blade damping breakdown minus the contributions of the ±1 and ±3 blades (Fig. 12). An exception is the 0 ND mode, which has significant structural coupling (A/B amplitude ratio from FEM is 2.1). The KF damping prediction for the lightly damped 0 ND mode is lower than the CH prediction because KF accounts for the structural coupling and captures the corresponding destabilizing impact of the ±1 blades.

Comparing the KF results to the validated AMPS results is more complicated and interesting. The KF damping distribution approximately tracks the AMPS damping distribution for the A-blade dominated modes, which in this case are the more heavily damped modes from each mode dyad. Recall that the A blades on the mistuned rotor are identical to the blades on the tuned rotor from which the ICs used in KF analysis were derived. However, the B-blade geometry is significantly different from the A-blade geometry. Consequently, the damping of the B-blade dominated

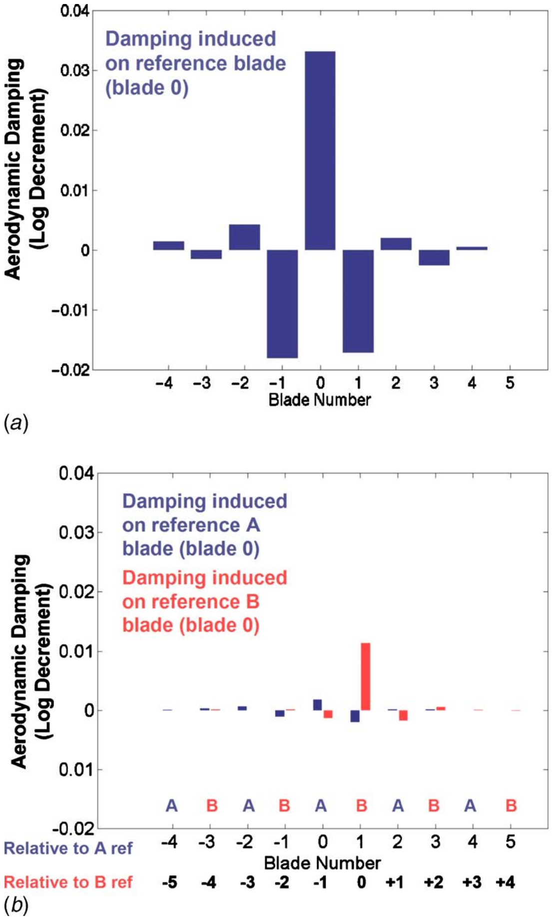

(*a*)

(*b*)

**Fig. 14 (*a*) Blade-by-blade damping breakdown, −3 ND mode, lightly damped, tuned Rotor X and (*b*) blade-by-blade damping breakdown, −3 ND mode, lightly damped, ABM Rotor X**

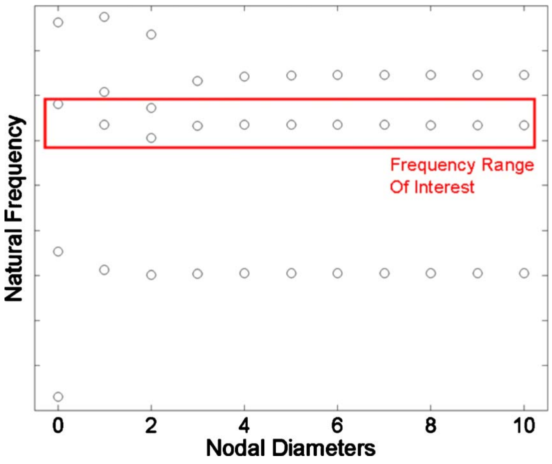

**Fig. 15 ND map of tuned Rotor X**

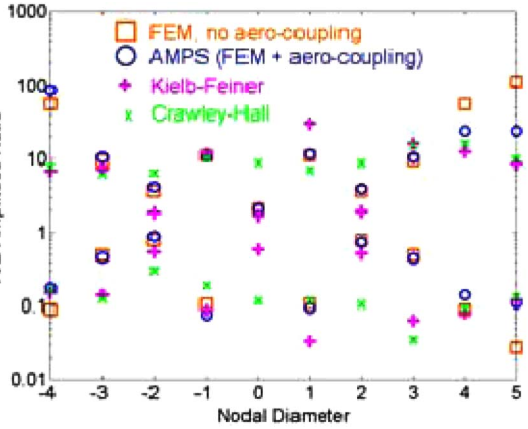

**Fig. 16 Ratios of maximum blade deflection amplitude, ABM Rotor X**

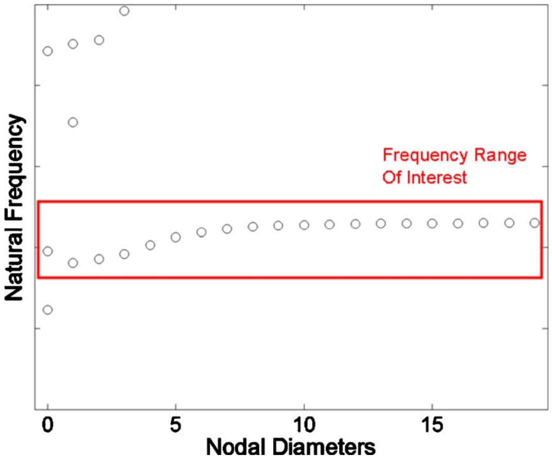

**Fig. 18 ND map, tuned Rotor Y (38 blades)**

modes is significantly different than that of the A-blade dominated modes. Consider, for example, the stark differences between the damping breakdowns of the B-blade dominated and A-blade dominated −4 ND modes (Figs. 11(*b*) and 12(*b*)). The coupling between like blades (influence of the ±2 blades) is much larger for the A blades than the B blades, partially explaining why the damping of the A-blade dominated modes varies slightly more with nodal diameter than that of the B-blade dominated modes. The difference in coupling between like blades may be related to the fact that the B blades are recessed axially relative to the A blades. In addition to like-blade coupling differences, the reference blade self-damping of the B-blade dominated modes is much lower than that of the A-blade dominated modes. As a result, the B-blade dominated modes have less overall damping. Aside from frequency, geometric differences between the A and B blades are not accounted for in the KF analysis, and consequently, the damping differences between the A- and B-blade dominated modes, as predicted by the AMPS method, are not captured by the KF method. There is also poor agreement between AMPS and KF for some of the ±2 and ±3 ND modes (Figs. 16 and 17). In this instance, the problem can be traced back to the fact that the set of modes in the frequency range of interest is not an isolated mode family.

Rotor Y, the second rotor considered in this study, is more well suited to application of the KF method. There is only one, isolated tuned mode family in the frequency range of interest (Fig. 18), and the high frequency B blades are geometrically similar to the A blades. The A blades in turn are equivalent to the tuned rotor blades. Figure 19 plots CF, KF, and AMPS (two PSMs, tuned and four PSMs, mistuned) aerodynamic damping predictions for Rotor Y. The KF results are clearly distinct from the CH predictions, especially for low nodal diameter patterns where structural coupling is significant as shown in the amplitude ratio versus nodal diameter plot in Fig. 20. The KF method captures the effect of structural coupling, and agreement between the AMPS and KF damping predictions is good.

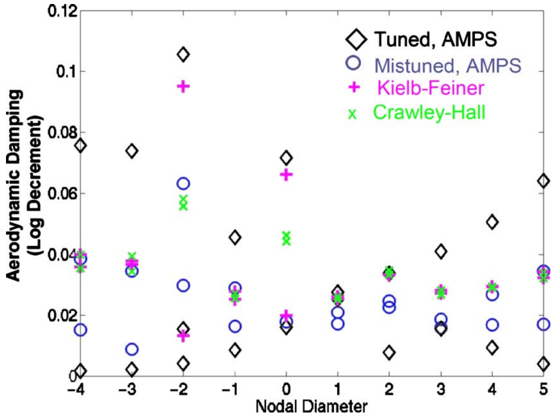

**Fig. 17 Aerodynamic damping, Rotor X. Aerodynamic input for the CH and KF methods is provided by AMPS analysis of tuned Rotor X.**

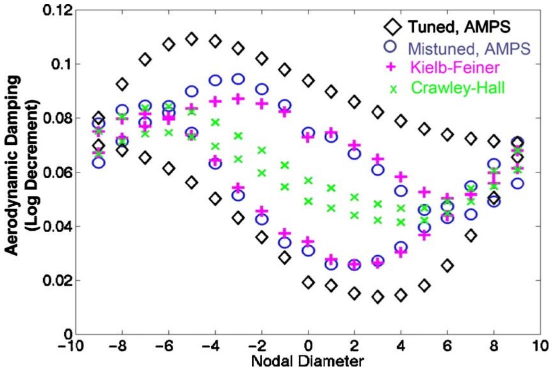

**Fig. 19 Aerodynamic damping, Rotor Y. Aerodynamic input for the CH and KF methods is provided by AMPS analysis of tuned Rotor Y.**

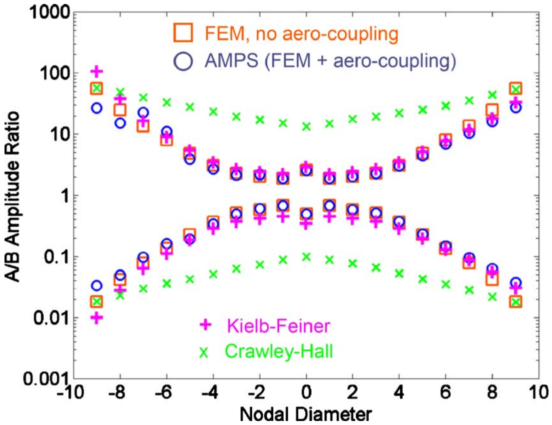

**Fig. 20 Ratios of maximum blade deflection amplitude, ABM Rotor Y**

## 4 Conclusions

A new reduced-order aeroelastic model called AMPS is presented. It is formulated generally to apply to any rotor or vane with rotational periodicity; however, this paper focuses on a specific application of this technique to rotors with flexible disks and ABM. The AMPS model is distinguished by its ability to capture structural coupling between blades, blade mode shape variation with nodal diameter, and alternating blade geometry—each of which can significantly affect aerodynamic damping. Numerical results show that when the aeroelastic system is linear, AMPS can compute the aerodynamic damping for a large number of modes, using just a few CFD calculations, to within the accuracy of the direct method.

Analysis of the AMPS results provides insight into the impact of ABM on rotor stability. ABM causes neighboring blades to vibrate with different amplitudes, reducing aerodynamic coupling. This has the effect of stabilizing the lightly damped modes while reducing the damping of the heavily damped modes. Thus, A-to-B-blade amplitude ratio has a first order influence on tuned-to-mistuned aerodynamic damping trends. Flexible disks increase structural coupling and decrease the amplitude differences between neighboring blades—reducing the ABM damping benefit. Therefore, accurate aerodynamic damping predictions for rotors with ABM and flexible disks must account for structural coupling effects.

Aerodynamic damping predictions were made with AMPS for two ABM rotors and compared to results from other flutter prediction methods. When applied to rotors with flexible disks, the reduced-order KF approach demonstrates clear advantages over approaches that do not account for structural coupling. Agreement between KF and AMPS is good when there is only one, isolated mode family in the frequency range of interest and the two ABM blade types are geometrically similar. However, when the modes of interest do not belong to a single, isolated mode family or when there are significant geometric differences between the A- and B-blade types, a higher order approach such as AMPS should be used.

## Acknowledgment

The authors would like to thank their colleagues William Owen, Jinzhang Feng, Peter Silkowski, Charles Gendrich, Chae Rhie, Yuan Dong, Robert Morris, George S. Copeland, Mark Stephens, Barry Ford, and Victor Filipenco for their important contributions to this work.

## References

[1] Crawley, E., and Hall, K., 1985, "Optimization and Mechanisms of Mistuning in Cascades." ASME J. Eng. Gas Turbines Power, **107**, pp. 418–426.

[2] Kaza, K. R. V., and Kielb, R. E., 1982, "Flutter and Response of a Mistuned Cascade in Incompressible Flow," AIAA J., **20**(8), pp. 1120–1127.

[3] Campobasso, M., and Giles, M., 2001, "Analysis of the Effect of Mistuning on Turbomachinery Aeroelasticity," *Unsteady Aerodynamics, Aeroacoustics and Aeroelasticity in Turbomachines* Ferrand, P., and Aubert, S., eds., Presses Universitaires de Grenoble, Grenoble, France, pp. 885–896.

[4] Silkowski, P., Rhie, C., Copeland, G. S., Eley, J., and Bleeg, J., 2002, "Computational-Fluid-Dynamics Investigation of Aeromechanics." J. Propul. Power, **18**(4), pp. 788–796.

[5] Sanders, A. J., Hassan, K. K., and Rabe, D. C., 2003, "Experimental and Numerical Study of Stall Flutter in a Transonic Flow—Low Aspect Ratio Fan Blisk," ASME Paper No. GT2003–38353.

[6] Yang, M.-T., and Griffin, J. H., 1997, "A Normalized Modal Eigenvalue Approach for Resolving Modal Interaction," ASME J. Eng. Gas Turbines Power, **119**(3), pp. 647–650.

[7] Yang, M.-T., and Griffin, J. H., 2001, "A Reduced Order Model of Mistuning Using a Subset of Nominal System Modes," ASME J. Eng. Gas Turbines Power, **123**(4), pp. 893–900.

[8] Feiner, D., and Griffin, J., 2002, "A Fundamental Model of Mistuning for a Single Family of Modes," ASME J. Turbomach., **124**, pp. 597–605.

[9] Kielb, R., Feiner, D., Griffin, J., and Miyakozawa, T., 2004, "Flutter of Mistuned Bladed Disks and Blisks With Aerodynamic and FMM Structural Coupling," ASME Paper No. GT2004-54315.

[10] Bakhle, M., Mahajan, A., Keith, T., and Stefko, G., 1991, "Cascade Flutter Analysis With Transient Response Aerodynamics." Comput. Struct., **41**(5), pp. 1073–1085.

[11] Sadeghi, M., and Liu, F., 2001, "Computation of Mistuning Effects on Cascade Flutter." AIAA J., **39**(1), pp. 22–28.

[12] Shapiro, B., 1998, "A Symmetry Approach to Extension of Flutter Boundaries via Mistuning." J. Propul. Power, **14**(3), pp. 354–366.

[13] Imregun, M., and Ewins, D., 1984, "Aeroelastic Vibration Analysis of Tuned and Mistuned Blade Systems," *Unsteady Aerodynamics of Turbomachines and Propellers Symposium Proceedings*, Cambridge University Press, Cambridge, UK, pp. 149–161.

[14] Martel, C., Corral, R., and Llorens, J., 2006, "Stability Increase of Aerodynamically Unstable Rotors Using Intentional Mistuning," ASME Paper No. GT2006–90407.

[15] Kielb, R., and Kaza, K., 1984, "Effects of Structural Coupling on Mistuned Cascade Flutter and Response." ASME J. Eng. Gas Turbines Power, **106**, pp. 17–24.

**Katharine L. Harrison**

**John R. Dorrington**

**Jason E. Dees**

**David G. Bogard**

Mechanical Engineering Department,
University of Texas at Austin,
Austin, TX 78712

**Ronald S. Bunker**
GE Global Research Center,
Niskayuna, NY 12309

# Turbine Airfoil Net Heat Flux Reduction With Cylindrical Holes Embedded in a Transverse Trench

*Film cooling adiabatic effectiveness and heat transfer coefficients for cylindrical holes embedded in a 1d transverse trench on the suction side of a simulated turbine vane were investigated to determine the net heat flux reduction. For reference, measurements were also conducted with standard inclined, cylindrical holes. Heat transfer coefficients were determined with and without upstream heating to isolate the hydrodynamic effects of the trench and to investigate the effects of the thermal approach boundary layer. Also, the effects of a tripped versus an untripped boundary layer were explored. For both the cylindrical holes and the trench, heat transfer augmentation was much greater for the untripped approach flow. A further increase in heat transfer augmentation was caused by use of upstream heating, with as much as a 180% augmentation for the trench. The tripped approach flow led to much lower heat transfer augmentation than the untipped case. The net heat flux reduction for the trench was found to be significantly higher than for the row of cylindrical holes.* [DOI: 10.1115/1.2812967]

## Introduction

Today's modern gas turbines are subjected to extremely high temperatures and thermal stresses during normal operation. The thermal conditions that turbine components are exposed to actually exceed the materials limits of the components. Cooling techniques must therefore be utilized to prevent failure and provide satisfactory component life.

Recently, studies by Bunker [1], Waye and Bogard [2], Lu et al. [3], and Dorrington and Bogard [4] conducted on cylindrical holes embedded in transverse trenches showed significant improvements in adiabatic effectiveness over standard inclined, cylindrical holes. Bunker [1] studied the effects of axial and radial holes embedded in a transverse trench with depths $s/d=0.43$ and $s/d=3$, respectively. This study showed that the centerline adiabatic effectiveness improved by 50–75% in the region of $x/d<40$ for the axial holes. Waye and Bogard [2] studied various upstream and downstream trench lip configurations with a constant trench depth of $s=0.5d$. They determined that the best performing configurations were those with a sharp rectangular trench lip immediately downstream of the coolant hole exit. Another important finding of Ref. [2] was that the trench appeared to suppress jet separation and increase lateral coolant spreading. Lu et al. [3] studied the adiabatic effectiveness of five trench configurations with a uniform trench depth of $0.4d$. One of their best configurations also had a sharp rectangular downstream trench lip.

More recently, Dorrington and Bogard [4] tested many trench configurations and determined that a $0.75d$ depth trench produced 40% greater average adiabatic effectiveness levels than a $0.5d$ depth trench, and a $1.0d$ depth trench performed similarly to the $0.75d$ depth trench. Furthermore, they found that the adiabatic effectiveness for the best trench configuration was similar to that for a row of shaped holes. This is important because the trench may prove to be significantly cheaper to manufacture than shaped holes.

In addition to determining adiabatic effectiveness, it is important to examine heat transfer coefficient augmentation, since increased mixing from injection can increase the heat transfer rate. Several heat transfer studies have been conducted on film cooled surfaces to determine heat transfer coefficient augmentation. Ericksen and Goldstein [5], Baldauf et al. [6], and Ammari et al. [7] measured augmentation that was less than 10% for a blowing ratio of $M=0.5$, except within the first few hole diameters downstream of the holes.

Most studies in open literature do not heat the surface upstream of the film cooling holes. It is generally assumed that upstream heating has a small effect on heat transfer coefficient augmentation. A few studies have examined the effects of an upstream thermal boundary layer. Mayhew et al. [8] measured heat transfer coefficient augmentation using upstream heating and, for $M=0.5$, found augmentation from 15% to 5%, which the authors claimed was higher than for previous studies with unheated starting length. The study attributed the elevated augmentation to the use of upstream heating. Kelly and Bogard [9] showed increased augmentation near the holes on a flat plate when upstream heating was used, but the effect subsided downstream. Coulthard et al. [10] found that the heat transfer coefficient augmentation was not significantly affected by upstream heating at high blowing ratios, but at low blowing ratios there was an increased augmentation, especially near the holes.

Heated and unheated starting lengths are both useful for fully characterizing heat transfer coefficient augmentation. For an unheated starting length with downstream heating alone, changes in the heat transfer coefficient are due solely to hydrodynamic effects because there is no upstream thermal boundary layer. However, since the actual airfoil will generally have heating (or cooling) of the flow upstream of the coolant holes, upstream heating is a more realistic simulation. In this study, heat transfer coefficient augmentation was examined for both heated and unheated starting length configurations.

Since it is possible to negate the benefits of film cooling if heat transfer coefficients are increased significantly by the injection process, the net effect on heat transfer rate to the surface is commonly estimated using the net heat flux reduction, $\Delta q_r$. This parameter is a measure of how much film cooling reduces the heat flux to the wall relative to the heat flux that would occur with no film cooling. The adiabatic effectiveness and heat transfer coefficients are combined to determine the net heat flux reduction, $\Delta q_r$, using the following equation (derivation shown in Ref. [11]):

---

Contributed by the International Gas Turbine Institute of ASME for publication in the JOURNAL OF TURBOMACHINERY. Manuscript received July 2, 2007; final manuscript received August 15, 2007; published online October 17, 2008. Review conducted by David Wisler. Paper presented at the ASME Turbo Expo 2007: Land, Sea and Air (GT2007), Montreal, Quebec, Canada, May 14–17, 2007.

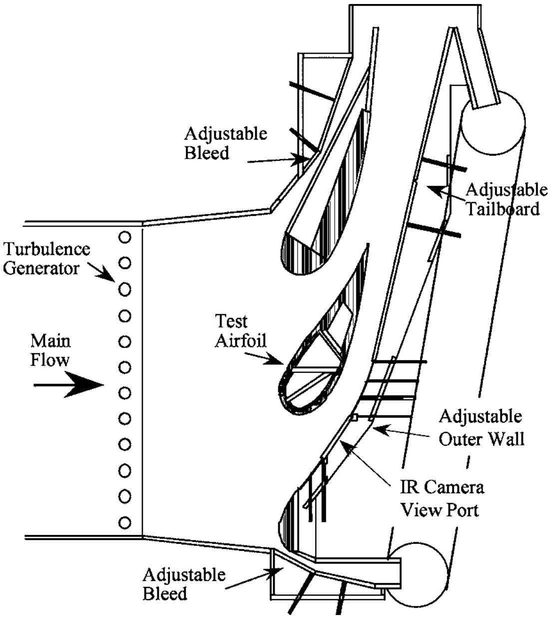

**Fig. 1 Schematic of test section**

$$\Delta q_r = 1 - \frac{h_f}{h_0}\left(1 - \frac{\eta}{\phi}\right) \tag{1}$$

The $\phi$ parameter in this equation, referred to as the overall effectiveness, is the normalized surface temperature for the actual airfoil. Generally, the overall effectiveness is assumed to be $\phi=0.6$ for calculation of the net heat flux reduction, and $\phi=0.6$ was assumed for this study.

The primary goal of this study was to determine the heat transfer coefficient augmentation caused by coolant injection through a 1*d* deep, 2*d* wide trench, and ultimately the net heat flux reduction that can be achieved with this trench. For reference, measurements were also made using a base line case consisting of a row of cylindrical, inclined holes. Since the approach boundary layer was transitional without a trip, measurements were also taken with an upstream trip to induce a turbulent boundary layer. Base line adiabatic effectiveness data from Waye and Bogard [2] and trench adiabatic effectiveness data from Dorrington and Bogard [4] were used to calculate the net heat flux reduction. The trench technology tested in this study is described in the U.S. Patent No. 6,234,755.

## Facilities and Procedures

All experiments were conducted in a closed loop wind tunnel driven by a 50 hp variable speed fan with adjustable pitch. The test section was a simulated three vane cascade schematically shown in Fig. 1. The tests were conducted on the center vane, a 9× scaled up version of an actual turbine vane, as shown in Fig. 2. The outer walls of the test section were carefully adjusted to match the nondimensional pressure distribution around the vane based on an inviscid CFD simulation of the cascade flow. The Reynold's number was matched to real engine conditions. A turbulence generator was located at the entrance of the test section. It was positioned 0.50 m upstream of the vane cascade and was comprised of 12 vertical rods with diameter of 38 mm and spaced 85 mm apart. The mainstream turbulence was previously measured by Robertson [12] to be 21% with an integral length scale of $\Lambda/d=10.0$.

The vane was manufactured from polyurethane foam with $k=0.048$ W/m K. A removable section of the vane, made of the same material, was used to vary configurations and test the trench and base line row of holes. The trench was milled in the removable section, which had a row of 18 coolant holes. For the base line configuration, the trench was filled by using an insert with cylindrical holes. The trench was 2*d* wide with the vertical trench lips being positioned flush with the upstream and downstream exits of the hole, as shown in Fig. 3. This trench configuration was the most effective of 15 different trench configurations tested in the companion study [4]. Only one row of holes was examined in this study, as shown in Fig. 2, and all other rows of holes were sealed off. Pertinent geometrical and flow parameters are presented in Table 1.

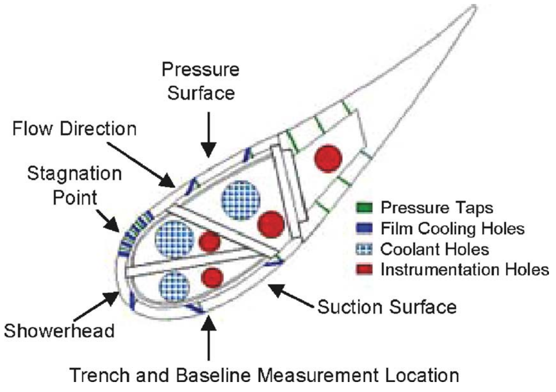

**Fig. 2 Detailed representation of the test vane**

The adiabatic effectiveness $\eta$ is a measure of how well the surface of the airfoil is being cooled. It is defined as follows:

$$\eta = \frac{T_{\text{aw}} - T_\infty}{T_{c,\text{exit}} - T_\infty} \tag{2}$$

The surface temperature $T_{\text{aw}}$, used for the adiabatic effectiveness was measured using a FLIR ThermaCAM P20 infrared camera. The camera was calibrated using ribbon E-type thermocouples located on the surface. The thermocouple data were acquired by a National Instruments Data Acquisition system.

The adiabatic effectiveness experiments were conducted with a coolant to mainstream density ratio of 1.3. This was achieved by

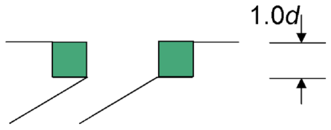

**Fig. 3 Narrow trench configuration**

**Table 1 Test condition data**

| | |
|---|---|
| Hole diameter | $d=4.11$ mm |
| Pitch | $p=2.775d$ |
| Trench depth | $s=1d$ |
| Trench width | $w=2d$ |
| Hole angle | $\alpha=30$ deg |
| Hole length (without trench) | $l=6.7d$ |
| Hole length (with trench) | $l=4.7d$ |
| Nominal mainstream temperature | $T=300$ K |
| Mainstream velocity (at tunnel inlet) | $U_\infty=5.8$ m/s |
| Mainstream Re (based on the chord length at the tunnel inlet) | $\text{Re}=2.2\times10^5$ |
| Mainstream turbulence (at tunnel inlet) | Tu=21% |
| Mainstream turbulence length scale | $\Lambda=10d$ |
| Chord length | $c=59.4$ cm |
| Vane span | 54.9 cm |
| Vane pitch | 45.7 cm |
| Position of trench | $X=0.367c$ |
| Position of trip | $X=0.285c$ |

using liquid nitrogen to cool the air before entering the vane plenum. There were three different independent plenums in the vane, but all tests conducted in this study were done on the suction side, and no coolant was allowed to enter the pressure side or showerhead plenums. The coolant air was bled off of the mainstream flow at a location just upstream of the wind tunnel fan. The air was then pumped into a heat exchanger where it was cooled by liquid nitrogen prior to entering the vane suction side plenum.

Due to the finite thermal conductivity of the polyurethane test section, a one dimensional conduction correction was employed when processing the adiabatic effectiveness data. The appropriate conduction correction was determined using measurements of the surface temperature with the exit of the coolant holes blocked to directly determine the conduction error. This conduction error, denoted $\eta_o$, was used to establish the conduction correction for the adiabatic effectiveness as follows:

$$\eta = \frac{\eta_{\text{measured}} - \eta_0}{1 - \eta_0} \tag{3}$$

The conduction correction was found to be $\eta_0 = 0.040 \pm 0.015$. More details on adiabatic effectiveness tests are available in Refs. [2,4].

Heat transfer experiments were run by securing 0.1 mm thick type 302 stainless steel heat flux foils to the surface of the vane upstream and downstream of the trench. The heat flux foils were attached to the surface directly upstream and downstream of the inserts. The heat flux foils were covered with a layer of flat black vinyl cardstock to smooth steps before and after the plates. This also provided a smooth wall and repeatable surface conditions. Heat transfer experiments were conducted using a $1d$ depth trench. Both heat flux plates were attached to the surface regardless of whether upstream heating was used so that the hydrodynamic approach conditions were the same with and without upstream heating. All heat transfer experiments were conducted using a density ratio of $DR=1.0$ to reduce measurement uncertainties.

The FLIR IR camera was used to record surface temperatures and was calibrated using two type E thermocouples on the surface of the vane. To produce a uniform heat flux, electrical current from a power supply was supplied to the heat flux foils. The voltage across a shunt resister was used to determine the current, and the voltage drop was measured across the downstream heat flux plate. The heat flux through the surface was found by the following equation, in which $A$ is the area of the heat flux plate:

$$q''_{\text{generated}} = \frac{IV}{A} \tag{4}$$

A thermocouple was attached to the interior surface of the vane to determine the internal temperature $T_i$, such that conduction corrections could be determined. The convective heat flux supplied to the surface was found by subtracting the losses due to conduction and radiation as follows:

$$q''_{\text{convection}} = q''_{\text{generated}} - q''_{\text{conduction}} - q''_{\text{radiation}} = \frac{IV}{A} - \frac{k}{L}(T_{\text{surf}} - T_i) - \varepsilon\sigma(T^4_{\text{surf}} - T^4_{\infty}) \tag{5}$$

The conduction and radiation corrections typically accounted for approximately 4% and 6% of the total heat flux, respectively.

The heat flux foils were attached in series so that the current through the upstream and downstream heat flux foils was equal. The upstream heat flux foil spanned $21.7d$ upstream of the upstream edge of the trench insert and the downstream heat flux foil spanned $27.0d$ downstream of the downstream edge of the insert, resulting in 25% greater heat flux upstream than downstream. This higher heat flux for the upstream foil was used because the upstream heat flux did not span all the way from the stagnation line. However, the 25% higher heat flux was arbitrary and represents only one of many possible upstream heating conditions.

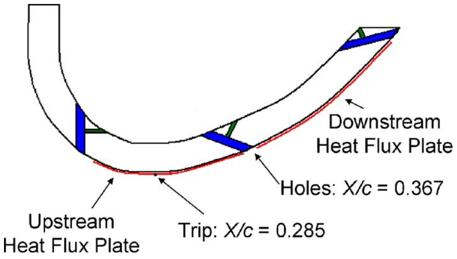

**Fig. 4 Location of trip and heat flux plates**

Heat transfer coefficients without film cooling $h_0$ were measured by filling the trench with an insert and covering the entire surface up to the stagnation line with cardstock. An insert with extensions of the cylindrical, inclined holes was used to test the base line configuration. For the tripped configurations, a 0.4 mm diameter trip was positioned at $X/c=0.285$, as shown in Fig. 4. One hole diameter upstream of the trench, the boundary layer thicknesseses with and without the trip were measured to be $\delta = 3.2$ mm and 1.2 mm, respectively. The tripped boundary profile was very close to a 1/7th power law correlation, and the untripped profile was transitional, as shown in Fig. 5.

The base line adiabatic effectiveness measurements used to calculate the net heat flux reduction were taken from Waye and Bogard Ref. [2]. Through analysis of data from Ref. [2], the boundary layer thickness was found to be 1.5 mm. The trench adiabatic effectiveness measurements were taken from Dorrington and Bogard [4]. The boundary layer thickness was not measured but the approach conditions were similar to the untripped heat transfer tests.

Uncertainty in the measurements was calculated using the sequential perturbation method described by Moffat [13]. The uncertainty in adiabatic effectiveness was found to be $\delta\overline{\eta} = \pm 0.02$ or less for all measurements by both sequential perturbation and test-to-test repeatability measurements. The following uncertainties were included in the analysis: the IR camera calibration, thermocouple measurements, the blowing ratio, and the conduction correction. See Refs. [2,4] for more information on the adiabatic effectiveness measurements.

Using sequential perturbation, the average uncertainty in heat transfer measurements with film cooling was found to be $\delta h_f = 5.7\%$, and the average uncertainty in heat transfer measurements without film cooling was found to be $\delta h_0 = 5.0\%$. The average uncertainty in heat transfer augmentation values was calculated to be $\delta(h_f/h_0) = 7.8\%$ and the average uncertainty in net heat flux reduction calculation was $\delta\overline{\Delta q_r} = \pm 0.06$. All uncertainty values

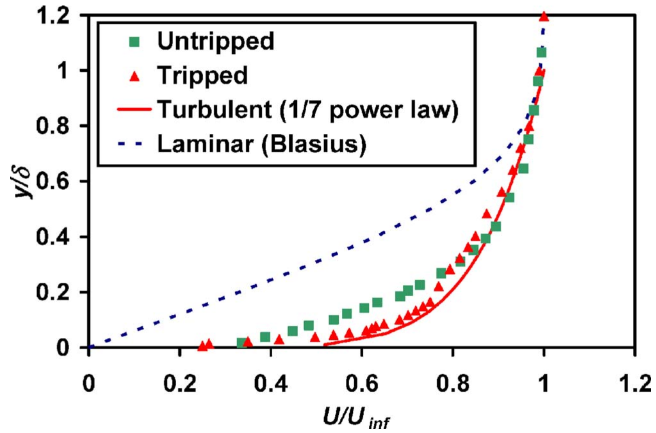

**Fig. 5 Boundary layer profiles for tripped and untripped heat transfer experiments**

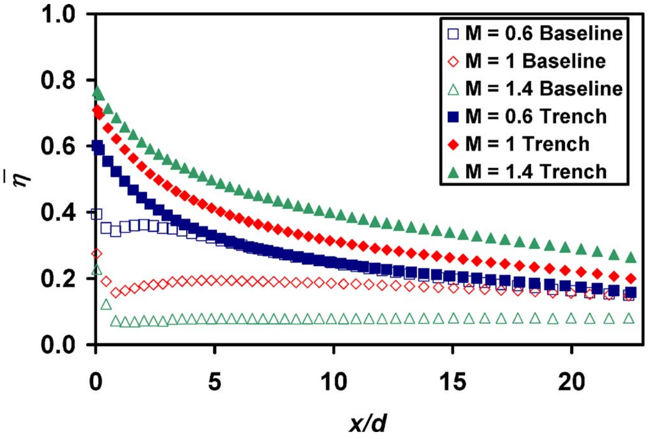

Fig. 6 Distributions of $\bar{\eta}$ for the base line and trench without a trip

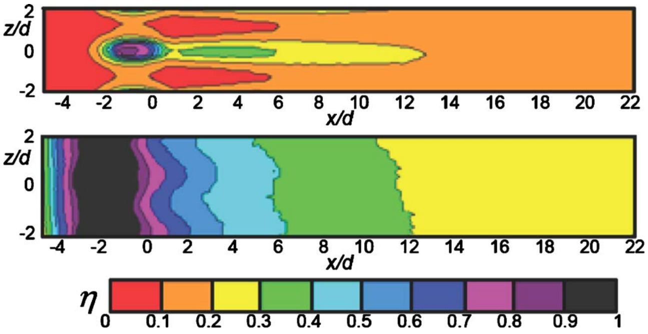

Fig. 7 Surface contours of $\eta$ without upstream heating and without a trip for the base line (top) and trench (bottom)

were determined at a 95% confidence level. Uncertainty calculations for heat transfer testing included: the IR camera calibration, thermocouples, the conduction correction, the radiation correction, and the uncertainties in the current and voltage measurements. The largest source of uncertainty was the surface temperature measurements in which the uncertainty was ±0.5 K. Bias errors due to conduction into the airfoil wall, 4%, and radiation to surroundings, 6%, were corrected as discussed previously. Repeatability of measurements within a test was checked in every experiment. In-test repeatability for the $h_f$ and $h_0$ measurements was found to be ±2–4%. The $h_0$ configurations were repeated in multiple tests, and the test-to-test repeatability was found to be ±5%.

## Results

To fully characterize film cooling performance, it is necessary to measure both the adiabatic effectiveness and heat transfer coefficient augmentation. Adiabatic effectiveness downstream of the narrow trench is compared to that for a base line row of cylindrical holes in Fig. 6. These results were taken from Refs. [2,4], and are presented in terms of laterally averaged effectiveness $\bar{\eta}$ for blowing ratios of $M=0.6$, 1.0, and 1.4. The trench exhibited increasing $\bar{\eta}$ levels with increasing blowing ratio, while $\bar{\eta}$ levels for the cylindrical holes decreased with increasing $M$. At the lowest blowing ratio shown of $M=0.6$, the performance for the cylindrical holes and the trench were comparable. However, at blowing ratios of $M=1.0$ and 1.4, for which cylindrical hole performance dropped dramatically because of jet separation, the trench performance continued to increase substantially. Ultimately for $M=1.4$, $\bar{\eta}$ levels for the trench were more than three times greater than that for base line cylindrical holes. Refer to Refs. [2,4] for more details.

To illustrate the differences between the trench and base line configurations, Fig. 7 presents contour plots of adiabatic effectiveness for $M=1$. The trench increased lateral coolant spreading and greatly increased adiabatic effectiveness. For the base line cylindrical hole configuration, streaks of higher $\eta$ are evident at the location of distinct coolant jets. The individual jets are much less visible on the contour plot for the trench configuration. Refer to Refs. [2,4] for more explanation on how the trench increased adiabatic effectiveness.

Examination of heat transfer coefficients is important because injection of coolant can lead to heat transfer coefficient augmentation. Heat transfer coefficient augmentation measurements are presented for four different configurations: heated and unheated starting lengths, and tripped and untripped approach boundary layers. An unheated starting length was used to isolate the hydrodynamic effects. This allowed the hydrodynamic boundary layer effects to be analyzed without being influenced by an upstream thermal boundary layer. Unheated starting length measurements are also useful because net heat flux reduction is commonly presented in literature for this configuration. Heated starting length measurements were taken to illustrate the effect of a heated upstream thermal boundary layer since operational airfoils are heated upstream.

There are two reasons for tripping the flow. First, rough surface conditions on operational airfoils and leading edge showerhead blowing would probably cause transition to turbulence on an actual airfoil. Second, a comparison between the tripped and untripped heat transfer coefficients with blowing to tripped and untripped $\overline{h_0}$ values allowed determination of whether blowing increased augmentation by essentially causing transition to turbulence. Base line heat transfer coefficient augmentation was also measured for comparison to the trench.

Heat transfer coefficient augmentation contour plots of the untripped base line and trench configurations for $M=1$ without upstream heating are shown in Fig. 8. Unlike the adiabatic effectiveness contour plots shown in Fig. 7, individual jets were not visible in the heat transfer coefficient augmentation contours. The contour plots demonstrate that augmentation was fairly uniform laterally. Thus, for the following results, only laterally averaged heat transfer coefficient augmentation will be discussed.

For reference, the heat transfer coefficients $\overline{h_0}$ for an airfoil surface with no film cooling holes or trench were measured. These reference cases are presented in Fig. 9 for all four heat transfer configurations, i.e., with and without upstream heating, and with and without a boundary layer trip. As expected, an unheated starting length resulted in much higher $\overline{h_0}$ initially because of the development of a new thermal boundary layer. Also, $\overline{h_0}$ values for the unheated starting length decayed faster than $\overline{h_0}$ for the heated starting length, such that the difference between the two values reduced with downstream distance. In theory, given sufficient de-

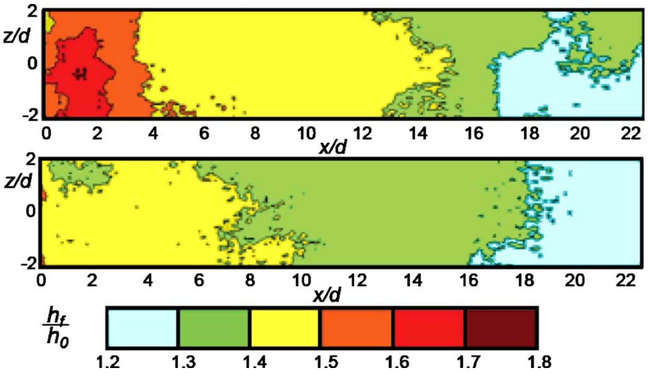

Fig. 8 Surface contours of $\overline{h_f/h_0}$ without upstream heating and without a trip for the base line (top) and the trench (bottom)

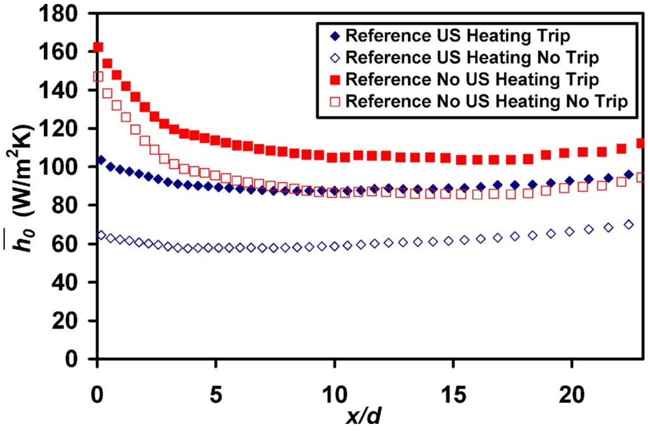

**Fig. 9 Reference smooth surface $\overline{h_0}$ values for four operating conditions**

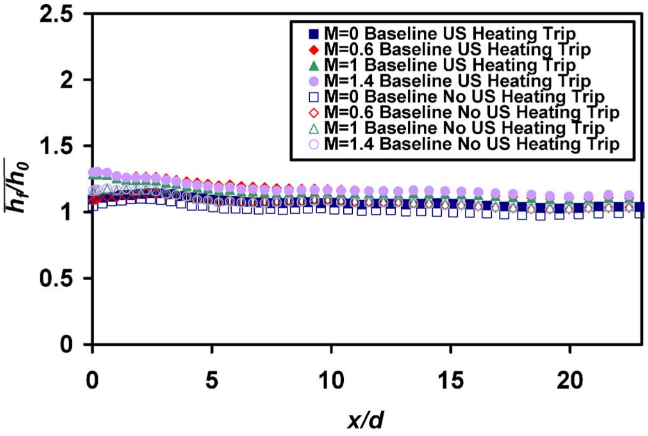

**Fig. 11 Base line $\overline{h_f/h_0}$ with and without upstream heating and with a trip**

velopment length, the unheated starting length $\overline{h_0}$ values would have become equivalent to those for the heated starting length. However, this did not occur over the distance of $x/d=23$ measured in these experiments.

Also evident in Fig. 9 are much lower $\overline{h_0}$ values for the cases without a boundary layer trip. With upstream heating, the trip caused 40%–60% increases in $\overline{h_0}$. This can be attributed to the trip causing the transitional boundary layer to become fully turbulent as noted earlier. Without upstream heating, tripping the flow caused a 10%–20% increase in $\overline{h_0}$.

Before presenting results of the effects of the shallow trench on enhancing heat transfer coefficients, it is informative to examine the effects of film injection from the base line cylindrical hole configuration. Figure 10 shows laterally averaged heat transfer coefficient augmentation, $\overline{h_f/h_0}$, for the base line with heated and unheated starting lengths and without a trip. Results for three blowing ratios, $M=0.6$, 1.0, and 1.4, are presented, in addition to a condition designated $M=0$, which indicates measurements with the holes exposed but without blowing. Immediately obvious from this figure is a significantly higher augmentation, $\overline{h_f/h_0}\approx 2$, with upstream heating compared to $\overline{h_f/h_0}\approx 1.5$ without upstream heating. This significant increase in the heat transfer coefficient can be attributed to the effect of the coolant jets displacing the upstream thermal boundary layer. Even for the unheated starting length condition, the coolant jets caused a 50% enhancement in the heat transfer coefficient. In this case, the increase is due to hydrodynamic effects and is likely due to the jets promoting transition of the boundary layer to fully turbulent flow.

Augmentation of the heat transfer coefficients for the base line row of holes with and without upstream heating and with a tripped approach flow is shown in Fig. 11. With no upstream heating the augmentation was at most 15%, significantly less than the no trip case. This can be attributed to the trip having caused transition of the boundary layer to fully turbulent flow so that the coolant jet injection had little additional impact on the flow. The case with upstream heating had a maximum augmentation of 30%, slightly larger than the unheated starting length case. Consequently, the displacement of the upstream thermal boundary layer did cause an additional increase in heat transfer coefficient, but the increase was smaller than that for an untripped approach flow.

Measurements of heat transfer coefficient augmentation for the trench showed trends similar to the base line case. Values of $\overline{h_f/h_0}$ for the trench with and without upstream heating and with no boundary layer trip are presented in Fig. 12. Data are presented for blowing ratios of $M=0$, 0.6, 1.0, 1.4, and 1.8. Augmentation values without upstream heating were as high as 50% near the holes and were still 25% by $20d$ downstream. Enhanced $\overline{h_f/h_0}$ in this case was due to the hydrodynamic effects of the trench since this configuration lacked an upstream thermal boundary layer. Coolant injection through the trench caused the boundary layer to transition to turbulent. With upstream heating, there was as much as 150% augmentation close to the trench, with still a 50% aug-

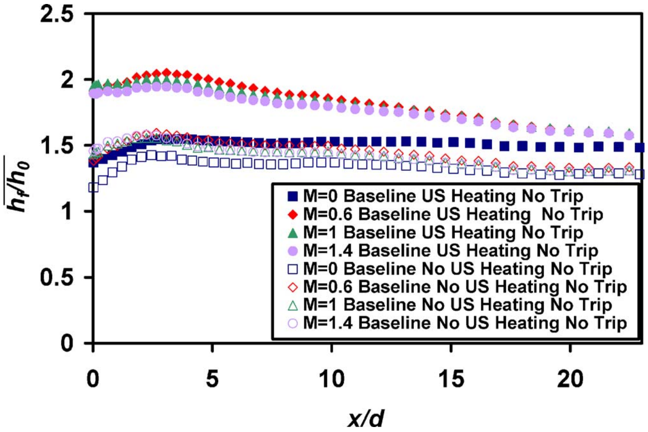

**Fig. 10 Base line $\overline{h_f/h_0}$ with and without upstream heating and without a trip**

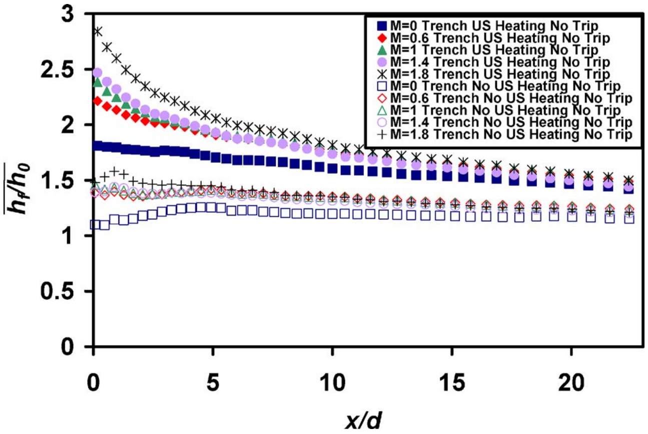

**Fig. 12 Trench $\overline{h_f/h_0}$ with and without upstream heating and without a trip**

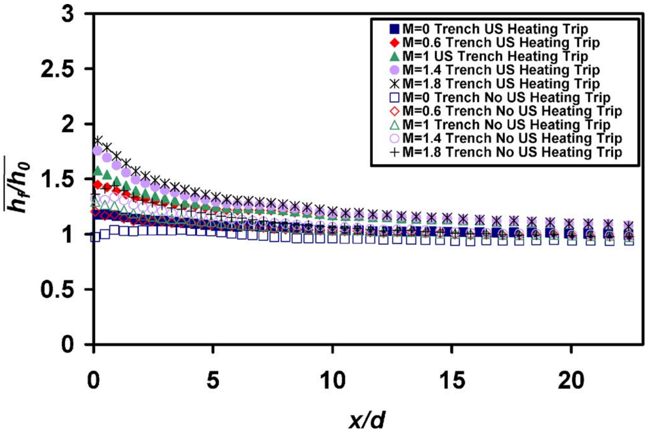

**Fig. 13 Trench $\overline{h_f/h_0}$ with and without upstream heating and with a trip**

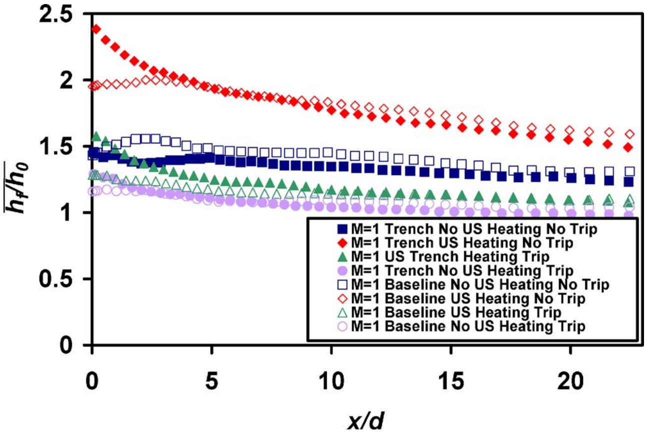

**Fig. 15 Comparison of $\overline{h_f/h_0}$ for the trench and base line at $M=1$**

mentation by $20d$ downstream. Enhancement over the unheated starting length case was due to displacement of the upstream thermal boundary layer. Similar to the base line row of holes, $\overline{h_f/h_0}$ was increased considerably by the presence of upstream heating.

Augmentations of heat transfer coefficients with and without upstream heating, and with a tripped approach flow, are presented in Fig. 13 for the trench. With an unheated starting length, augmentation was only 6% by $10d$ downstream, but augmentation was 20% with upstream heating at the same location. Close to the trench the augmentation was as much as 70%. Augmentation for the tripped approach boundary layer flow was much less than for the corresponding untripped cases. Without upstream heating, the $M=0$ (no blowing) data showed no augmentation because the flow was already fully turbulent due to the trip and the trench could not further stimulate transition. The higher blowing ratios showed augmented $\overline{h_f/h_0}$ values relative to the $M=0$ case, which can be attributed to interaction of the coolant flow with the mainstream.

Because the $\overline{h_f/h_0}$ ratio varies with changes in either $h_f$ or $h_0$, further insight can be gained by examining $\bar{h}_f$ alone for all four trench heat transfer configurations at $M=0$, as shown in Fig. 14. Immediately evident from the figure is that the $\bar{h}_f$ distributions were exactly the same for the tripped and untripped approach flows, for the same thermal approach conditions. This demonstrates that the effects of the trench on the boundary layer flow dominated to the extent that the approach flow was irrelevant. However, if the flow was already turbulent, the presence of the trench did not cause a further increase in $\bar{h}_f$.

The heat transfer coefficient augmentation due to injection from the trench is compared to the base line configuration in Fig. 15. This figure shows base line and trench $\overline{h_f/h_0}$ values at a blowing ratio of $M=1$ for all four heat transfer testing configurations: tripped and untripped, with and without upstream heating. As is clear from the figure, $\overline{h_f/h_0}$ values were very similar for the base line and trench configurations, for all operating conditions.

To determine the balance between the beneficial effects of lowered temperature due to film cooling injection and the detrimental effects of augmented heat transfer coefficients, the net heat flux reduction $\overline{\Delta q_r}$ was calculated. Since adiabatic effectiveness data with a trip were unavailable in Refs. [2,4], $\overline{\Delta q_r}$ was only calculated for the corresponding untripped heat transfer configurations.

The net heat flux reduction for the untripped base line configuration with and without upstream heating is presented in Fig. 16. The most striking results are the negative $\overline{\Delta q_r}$ values, which indicate that film cooling injection had a detrimental effect and could increase the net heat flux into the surface. The largest degradation in performance occurred at high blowing ratios, which can be attributed to the low $\bar{\eta}$ levels at high $M$. Also contributing to the low net heat flux reduction levels were the high $\overline{h_f/h_0}$ levels present for the untripped configurations. The lower $\overline{\Delta q_r}$ values for the upstream heated case can be attributed to larger $\overline{h_f/h_0}$ values with upstream heating than without.

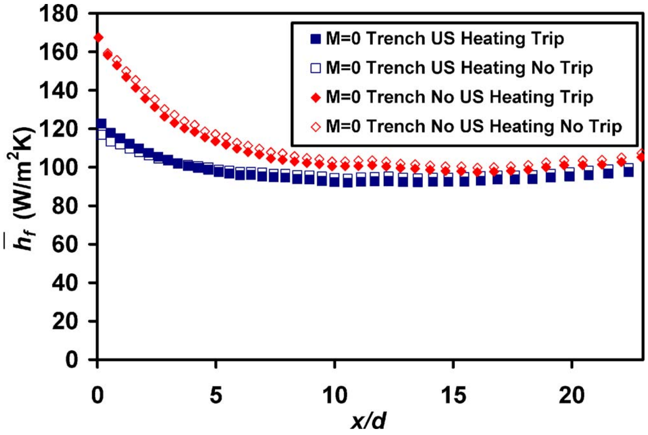

**Fig. 14 Distributions of $\bar{h}_f$ with an exposed trench but with no blowing ($M=0$)**

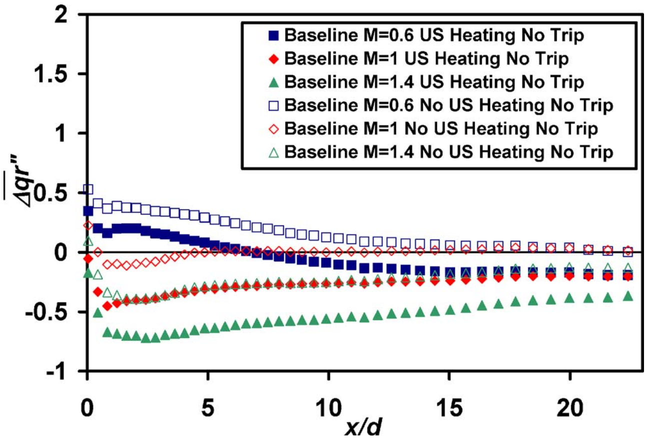

**Fig. 16 Base line $\overline{\Delta q_r}$ with and without upstream heating and without a trip**

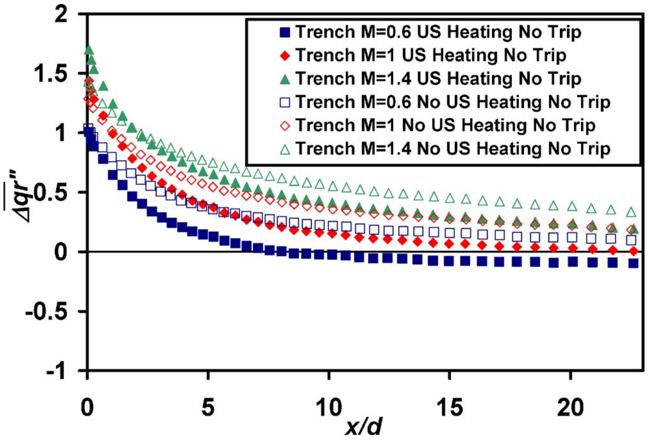

Fig. 17 Trench $\overline{\Delta q_r}$ with and without upstream heating and without a trip

Values for $\overline{\Delta q_r}$ obtained using a trench were distinctly higher than the base line results. Figure 17 shows the trench net heat flux reduction results, from which it is immediately obvious that $\overline{\Delta q_r}$ was essentially positive for all blowing ratios. The higher net heat flux reduction values were due to much higher $\overline{\eta}$ levels for the trench. In converse to the base line case, $\overline{\Delta q_r}$ for the trench increased with blowing ratio due to increasing $\overline{\eta}$ levels with increasing blowing ratio. The performance with and without upstream heating were similar, especially at high blowing ratios with high $\overline{\eta}$ levels. Despite the large differences in $\overline{h_f/h_0}$ for the heated and unheated approach conditions, the very high $\overline{\eta}$ levels dominated over the effects of $\overline{h_f/h_0}$ and the net heat flux reduction remained high.

Of the two untripped configurations, the heated starting length is more representative of actual airfoils. Figure 18 shows $\overline{\Delta q_r}$ for the base line and trench configurations with a heated starting length and an untripped boundary approach flow. At $M=0.6$, base line results after $x/d=5$ were only slightly lower than the trench configuration due to similar $\overline{\eta}$ and $\overline{h_f/h_0}$ levels. At $M=1$ and $M=1.4$, $\overline{\Delta q_r}$ levels for the trench were much higher than the base line, indicating the trench was much better at reducing heat flux into the surface.

## Conclusions

This study examined the adiabatic effectiveness, heat transfer coefficients, and net heat flux reduction for film cooling with inclined cylindrical holes and with holes buried within a shallow trench. Experiments were done using a wind tunnel facility incorporating a simulated vane using a single row of holes located on the suction side. This study complements a companion study, which showed significantly increased adiabatic effectiveness when coolant is injected into a shallow trench transverse to the flow.

To fully characterize heat transfer coefficient augmentation, four reference operating conditions were examined: tripped and untripped boundary layer approach flows, each with heated and unheated starting lengths. It was important to examine both heated and unheated starting lengths because upstream heating is more representative of actual airfoil conditions, but unheated starting length measurements are useful since they isolate the hydrodynamic effects of the trench. The four reference conditions resulted in four distinctly different distributions of heat transfer coefficients for the reference "no-holes" case, $h_0$. The $h_0$ distribution with no boundary layer trip was significantly lower, nominally 50%, than with a trip. Velocity profile measurements showed that this was due to a transitional boundary layer flow for the no-trip case, and a fully turbulent boundary layer for the tripped case. As expected, the unheated starting lengths resulted in higher $h_0$ distributions due to the delayed development of a thermal boundary layer.

The heat transfer augmentation obtained with inclined, cylindrical holes proved to be very dependent on the operating condition used. With no upstream trip, a significant augmentation occurred, 50%–100%, which was attributed to the coolant hole (with no injection) or the coolant injection accelerating boundary layer transition. This was confirmed by the observation that with an upstream trip, there was negligible augmentation of the heat transfer coefficient when using no upstream heating. There was a significant difference in heat transfer augmentation when comparing heated and unheated upstream flow cases with no trip. The augmentation with a heated upstream flow was double that for an unheated upstream flow, i.e., 100% augmentation compared to 50% augmentation. This only occurred with coolant injection. The large increase in augmentation was attributed to the displacement of the upstream thermal boundary layer by the injected coolant. With an upstream trip, there was an increased augmentation when using a heated upstream flow. However, the maximum augmentation was only 30% near the hole and decayed to less than 15% by $20d$ downstream, which was much less than for the untripped flow.

The heat transfer augmentations that were found with coolant injection from holes embedded in a shallow trench were very similar to that found for the standard inclined hole configuration. The main difference was an increased augmentation near the coolant injection point for the trench when using a heated approach flow.

The overall performance of the film cooling configurations was evaluated by estimating the net heat flux reduction using measurements of adiabatic effectiveness and heat transfer coefficient augmentation. Since the heat transfer coefficient augmentations for the trench and base line were similar, but the adiabatic effectiveness was much higher for the trench, the net heat flux reduction for the trench was much higher than for the base line. The average heat flux reduction for the trench configuration at high blowing ratios was greater than 50%, while the average heat flux reduction for standard holes at the optimum lower blowing ratio was less than 10%. The base line configuration produced negative net heat flux reductions (i.e., the coolant injection caused an increase in heat transfer to the surface) for the higher blowing ratios, and even for lower blowing ratios without a trip and with upstream heating. These negative net heat flux reduction values can be attributed to the large heat transfer augmentation that occurred for the no trip case. For the no trip case, the reference heat transfer coefficient was much lower because the boundary layer was transitional and not fully turbulent. The coolant injection process

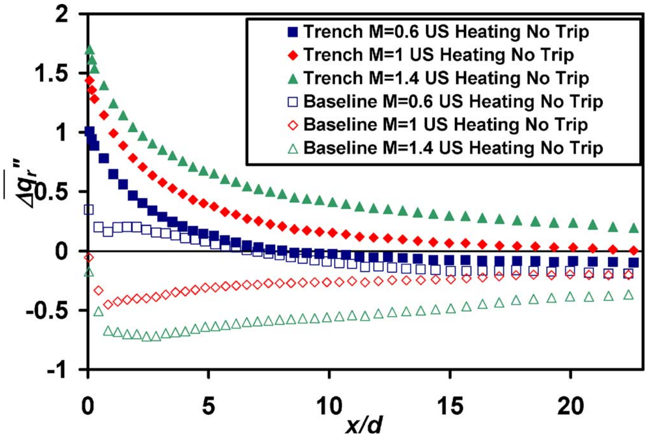

Fig. 18 Comparison of base line and trench $\overline{\Delta q_r}$ with upstream heating and without a trip

caused transition to fully turbulent flow, resulting in a large increase in the heat transfer coefficient. Consequently, for higher blowing ratios where the adiabatic effectiveness was poor, the large augmentation of the heat transfer coefficient caused an increase in the overall heat transfer to the wall. Although the trench configuration had similar, if not greater augmentation of the heat transfer coefficients than the standard hole configuration, the net heat flux reduction was significantly higher because of the much larger adiabatic effectiveness produced by the trench.

## Acknowledgment

The authors gratefully acknowledge the Office of Naval Research (ONR) and the General Electric Corporation for their support of this research. A special thanks also goes to Brian Mouzon for providing the adiabatic effectiveness data for the $s=1.0d$ trench configurations.

## Nomenclature

$c$ = chord length
$d$ = hole diameter
$DR$ = density ratio$=\rho_c/\rho_\infty$
$h_0$ = heat transfer coefficient without film cooling $=q''/(T_\infty-T_{\text{surf}})$
$h_f$ = heat transfer coefficient with film cooling $=q''/(T_\infty-T_{\text{surf}})$
$h_f/h_0$ = heat transfer coefficient augmentation
$I$ = current
$k$ = thermal conductivity
$l$ = hole length
$L$ = thickness of airfoil wall
$M$ = blowing ratio$=\rho_c U_c/\rho_\infty U_\infty$
$p$ = hole spacing
$q''$ = heat flux
$\Delta q_r$ = net heat flux reduction
Re = Reynolds number
$s$ = trench depth
$T$ = temperature
$Tu$ = mainstream turbulence intensity
$U$ = velocity
$V$ = voltage
$w$ = trench width
$X$ = streamwise coordinate originating at the stagnation line
$x$ = streamwise coordinate originating at downstream edge of the trench insert
$y$ = coordinate normal to the vane surface
$z$ = spanwise coordinate

### Greek

$\Lambda$ = mainstream turbulence length scale
$\alpha$ = injection angle
$\delta$ = boundary layer thickness
$\varepsilon$ = emissivity
$\phi$ = overall effectiveness$=(T_{\text{surf}}-T_\infty)/(T_{c,i}-T_\infty)$
$\eta$ = adiabatic effectiveness$=(T_{\text{aw}}-T_\infty)/(T_{c,\text{exit}}-T_\infty)$
$\eta_0$ = conduction error
$\rho$ = density
$\sigma$ = Stephan–Boltzmann constant

### Subscripts and Superscripts

- = laterally averaged
$\infty$ = mainstream
aw = adiabatic wall
$c$ = coolant
exit = evaluated at hole exit
$i$ = evaluated internally in the plenum
surf = wall surface

## References

[1] Bunker, R., 2002, “Film Cooling Effectiveness due to Discrete Holes Within a Transverse Surface Slot,” ASME Paper No. GT-2002-30178.
[2] Waye, S. K., and Bogard, D. G., 2006, “High Resolution Film Cooling Effectiveness Measurements of Axial Holes Embedded in a Transverse Trench With Various Trench Configurations,” ASME Paper No. GT-2006-90226.
[3] Lu, Y., Nasir, H., and Ekkad, S. V., 2005, “Film Cooling From a Row of Holes Embedded in Transverse Slots,” ASME Paper No. GT-2005-68598.
[4] Dorrington, J. R., and Bogard, D. G., 2007, “Film Effectiveness Performance for Coolant Holes Embedded in Various Shallow Trench and Crater Depressions,” ASME Paper No. GT2007-27992.
[5] Ericksen, V. L., and Goldstein, R. J., 1974, “Heat Transfer and Film Cooling Following Injection Through Inclined Circular Tubes,” ASME J. Heat Transfer, **107**, pp. 239–245.
[6] Baldauf, S., Scheurlen, M., Schultz, A., and Wittig, S., 2002, “Heat Flux Reduction From Film Cooling and Correlation of Heat Transfer Coefficients From Thermographic Measurements at Engine Like Conditions,” ASME Paper No. GT-2002-30181.
[7] Ammari, H., Hay, N., and Lampard, D., 1990. “The Effect of Density Ratio on the Heat Transfer Coefficient From a Film-Cooled Flat Plate,” ASME J. Turbomach., **112**, pp. 444–450.
[8] Mayhew, J. E., Baughn, J. W., and Byerley, A. R., 2002, “The Effect of Freestream Turbulence on Film Cooling Heat Transfer Coefficient,” ASME Paper No. GT-2002-30173.
[9] Kelly, G. B., and Bogard, D. G., 2003, “An Investigation of the Heat Transfer for Full Coverage Film Cooling,” ASME Paper No. GT2003-3876.
[10] Coulthard, S. M., Volino, R. J., and Flack, K. A., 2006, “Effect of Unheated Starting Lengths on Film Cooling Effectiveness,” ASME J. Turbomach., **128**, pp. 579–588.
[11] Sen, B., Schmidt, D. L., and Bogard, D. G., 1994, “Film Cooling With Compound Angle Holes: Heat Transfer,” ASME J. Turbomach., **118**, pp. 800–806.
[12] Robertson, D. R., 2004, “Roughness Impact on Turbine Vane Suction Side Film Cooling Effectiveness,” MS thesis, The University of Texas at Austin.
[13] Moffat, R. J., 1988, “Describing the Uncertainties in Experimental Results,” Exp. Therm. Fluid Sci., **1**, pp. 3–17.

**Jean Thomassin**
Pratt and Whitney Canada,
1000 Marie-Victorin,
Longueuil, QC, J4G 1A1, Canada

**Huu Duc Vo**

**Njuki W. Mureithi**

École Polytechnique de Montréal,
2500 Chemin de Polytechnique,
Montréal, QC, H3T 1J4, Canada

# Blade Tip Clearance Flow and Compressor Nonsynchronous Vibrations: The Jet Core Feedback Theory as the Coupling Mechanism

*This paper investigates the role of tip clearance flow in the occurrence of nonsynchronous vibrations (NSVs) observed in the first axial rotor of a high-speed high-pressure compressor in an aeroengine. NSV is an aeroelastic phenomenon where the rotor blades vibrate at nonintegral multiples of the shaft rotational frequencies in operating regimes where classical flutter is not known to occur. A physical mechanism to explain the NSV phenomenon is proposed based on the blade tip trailing edge impinging jetlike flow, and a novel theory based on the acoustic feedback in the jet potential core. The theory suggests that the critical jet velocity, which brings a jet impinging on a rigid structure to resonance, is reduced to the velocities observed in the blade tip secondary flow when the jet impinges on a flexible structure. The feedback mechanism is then an acoustic wave traveling backward in the jet potential core, and this is experimentally demonstrated. A model is proposed to predict the critical tip speed at which NSV can occur. The model also addresses several unexplained phenomena, or missing links, which are essential to connect tip clearance flow unsteadiness to NSV. These are the pressure level, the pitch-based reduced frequency, and the observed step changes in blade vibration and mode shape. The model is verified using two different rotors that exhibited NSV.*

[DOI: 10.1115/1.2812979]

## Introduction

Nonsynchronous vibrations (NSVs) have been observed in an axial compressor rotor blade. NSVs are characterized by being asynchronous to the rotor speed, i.e., the rotor blades vibrate at nonintegral multiples of the shaft rotational frequencies, and they occur in operating regimes not associated with classical flutter. This type of vibration was previously reported by Baumgartner et al. [1] and Kielb et al. [2].

Figure 1 shows the rotor blade under study. The observed NSV mode is the first torsion (1T) illustrated in the figure. Figure 2(*a*) shows engine experimental blade strain gauge data during NSV. The significant vibratory amplification is clearly evident. Figure 2(*b*) shows the unsteady pressure simultaneously measured on the casing of which the level is in agreement with the case reported by Baumgartner et al. [1].

Several authors have studied tip clearance flow unsteadiness as the source of noise and NSV, both using computational simulations and experimentation. Examples of work in this area can be found from Kameier and Neise [3,4], Mailach et al. [5], and Liu et al. [6], who studied the tip flow unsteadiness, known as rotating instabilities (RIs), inferred to excite the casing acoustic modes, which in turn can excite the blades. The reported acoustic wave to structure coupling mechanism is somewhat similar to the work of Yamaguchi et al. [7] who found NSV due to surrounding bleed cavity acoustic resonance, with the difference that the excitation source is attributed to a tip vortex interaction that increases with tip clearance. Fukano and Jang [8], März et al. [9], and Zhang et al. [10] all identified an interference of the tip clearance flow instability with the adjacent blade pressure face at high stage loading. Vo [11] showed that significant tip clearance flow unsteadiness exists at large tip clearance when only one of the two criteria for spike stall inception, namely, the trailing edge backflow, is met. This work suggested that the trailing edge backflow acts as an impinging jet on the pressure face of the second adjacent blade, and this is related to the known RI phenomenon.

Figure 3 from Vo [11] illustrates the impinging jetlike blade tip trailing edge flow feature, which laid the base for this work. This backflow is essentially a recirculation zone, as described by Kameier and Neise [3], with a circumferential velocity component. At large clearance, and under high blade loading, the tip clearance flow develops in a jetlike pattern that reaches below the blade tip in the adjacent passage to finally impinge on the pressure side near the trailing edge.

The trailing edge backflow described by Vo [11] and Vo et al. [18] has been verified experimentally by Deppe et al. [12] both in cascade and compressors.

Figures 4 and 5 show additional evidence of blade pressure side impingement both calculated by März et al. [9] and measured by Fukano and Jang [8], respectively, at conditions where RIs exist.

Figure 4 shows the velocity vectors for a span cut just below the blade tip seen during a RI cycle [9]. The velocity field circled in the figure is in good agreement with the impinging jetlike flow described in Fig. 3.

Figure 5 presents the measured rotor trailing edge velocity fluctuations ($V_f$) at large tip clearance and high stage loading [8], which are the typical conditions for RI. The presence of large velocity fluctuations (circled) is consistent with a flow impingement below the trailing edge tip.

The recent work cited points to the study of the dynamics of an impinging jet to elucidate the mechanism behind NSV. Further-

---

Contributed by the International Gas Turbine Institute of ASME for publication in the Journal of Turbomachinery. Manuscript received June 13, 2007; final manuscript received August 24, 2007; published online October 28, 2008. Review conducted by David Wisler. Paper presented at the ASME Turbo Expo 2007: Land, Sea and Air (GT2007), Montreal, Quebec, Canada, May 14–17, 2007.

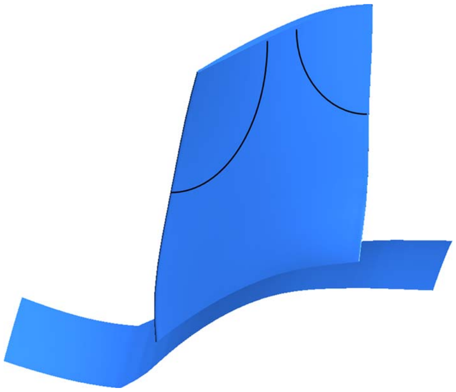

Fig. 1 Rotor blade and NSV mode shape

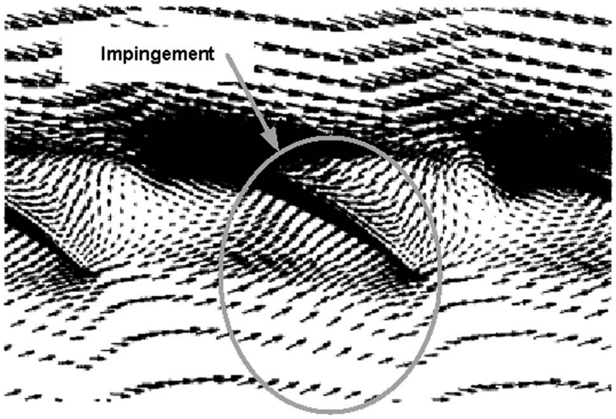

Fig. 4 Tip velocity vector during RI [9]

more, although tip clearance flow instabilities (RI) are generally accepted as the cause for NSV, some unexplained phenomena, or missing links, are noted between the RI only based NSV mechanism and the available experimental data on NSV.

First, the amplitudes of the tip pressure fluctuation during actual NSV conditions are experimentally measured to be between one and three orders of magnitude higher than during RI conditions of the fixed blade cases. Baumgartner et al. [1] reported NSV pressure fluctuations in the order of 150 dB, while typical near field RI induced noise data with nonvibrating blades are in the order of 110–120 dB [3]. The rotor considered in this study also exhibited casing pressure fluctuations in the order of 150 dB, as shown in Fig. 2.

Second, there seems to be a physical inconsistency on the scaling length for the reduced frequency of RI. The flow emanating from the tip clearance essentially involves a shear layer. Based on typical observations of shear layer induced instabilities, one would expect the reduced frequency to scale with geometric length scales related to the body such as the chord or the tip clearance from which the jetlike shear layer emanates. For example, the reduced frequency of a cylinder in cross-flow scales with the diameter ($\mathrm{St}_D = fD/U$) [13]. Similarly, for circular and planar jets, the reduced frequencies are, respectively, found to be $\mathrm{St}_D = fD/U$ and $\mathrm{St}_H = fH/U$, where $D$ and $H$ are the circular jet diameter and the planar jet width [14]. However, Kameier and Neise [3] deduced a reduced frequency from observations on RI that scales with the blade pitch when using half the blade tip velocity ($U_{\mathrm{tip}}/2$) as the velocity term.

Third, there is nothing in the RI based NSV mechanism to explain the frequency shift phenomena observed by Kielb et al. [2] where the blade vibration mode switched from the first torsion to the second torsion mode, which vibrated at around twice the first torsion mode frequency during NSV.

In this paper, a mechanism and associated model based on a resonant jet analogy is proposed to explain NSV and resolve the above three missing links.

A jet core acoustic feedback theory is developed. The theory is verified on a simple experimental apparatus. A model is formulated, based on this theory, to predict the critical rotor speed at which NSV may occur at high stage loading.

The model is validated against two different rotor blades that exhibited NSV. Additional implications of the inferred NSV mechanism are subsequently presented.

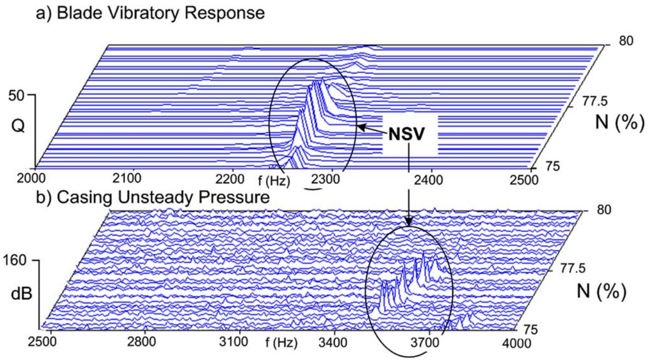

Fig. 2 NSV blade vibrations and casing pressure

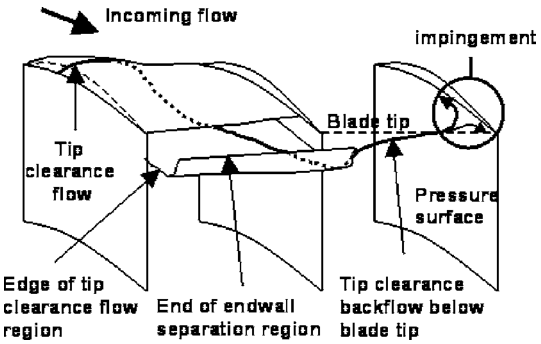

Fig. 3 Impinging trailing edge backflow [11]

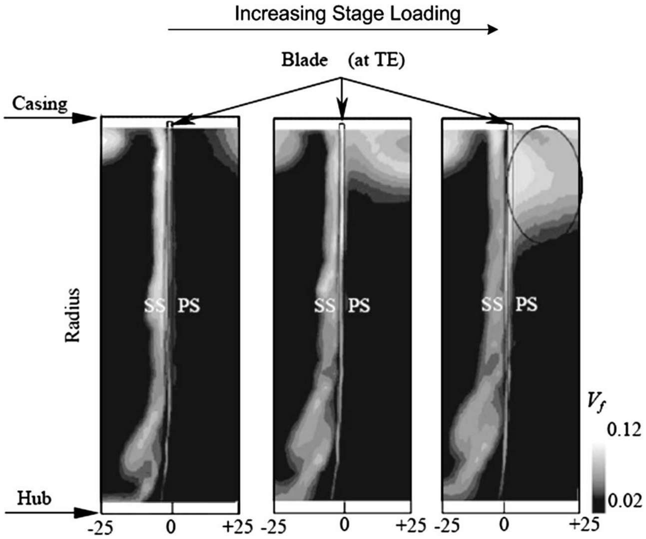

Fig. 5 Pressure side velocity fluctuation [8]

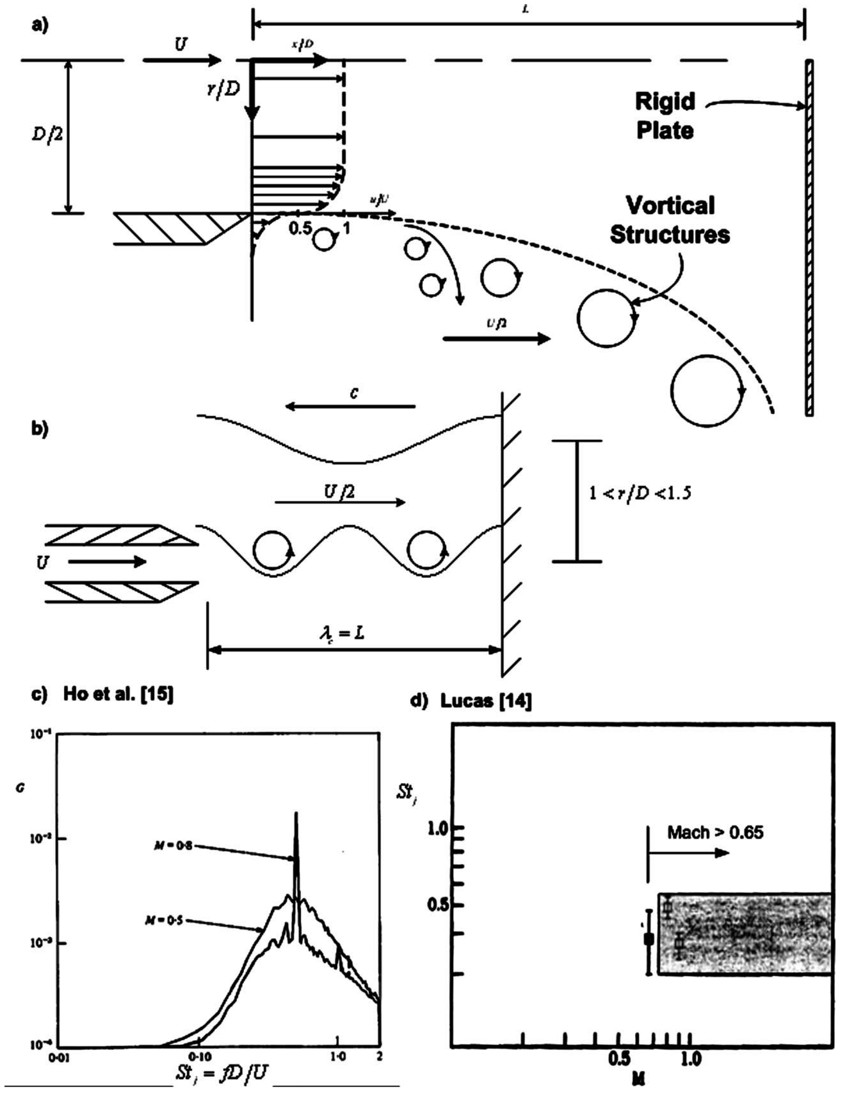

Fig. 6 Resonant jet on a rigid plate, Ho [15]

## Impinging Jet Resonance

In observing RI-type flow unsteadiness when the flow condition depicted in Fig. 3 arises at stable (unstalled) compressor operations, Vo [11] suggested that an explanation into the flow unsteadiness associated with NSV may lie in the dynamics of an impinging jet as studied by Ho and Nosseir [15].

Ho and Nosseir [15] conducted experimental work on high-speed subsonic jets impinging on a rigid flat plate. The shear layer, around the jet, produces vortical flow structures that scale with the jet velocity and diameter. When a rigid plate is introduced in the potential core of the jet, these impinging structures produce an acoustic reflection. As the jet velocity is increased, it eventually reaches a critical value where the acoustic feedback wavelength matches the jet-to-plate distance. The jet is then said to be resonant and significant amplification of the pressure unsteadiness is observed on the plate. The resonant jet conditions were found to occur at Mach numbers higher than 0.65, whereas jet velocities associated with NSV are often lower than this threshold. In fact, RIs have been measured to rotate at around half the rotor speed, depending on the stage loading condition, by Kameier and Neise [3,4]. At off-design conditions, where NSVs are often observed, the blade tip velocity ($U_{\text{tip}}$) is generally subsonic, and thus the inferred tip jet emanating from the tip clearance is expected to be below Mach 0.5 in the relative frame of reference.

**Jet Resonance When Impinging on a Rigid Plate.** Figure 6 shows a simplified view of Ho and Nosseir's [15] rigid plate acoustic feedback and resonant impinging jet observations. The exact details such as the reflecting wave angle, presented in Ref. [15], are omitted here for clarity.

When the fluid first exits the nozzle, small structures proportional to the thin shear layer thickness are produced. Those small structures merge very soon after leaving the nozzle lip into larger vortical structures that scale with the jet diameter ($D$). The structures are convected downstream at around half the jet velocity (Fig. 6(*a*)) and induce pressure fluctuations on the plate. If the rigid plate is inserted within the jet potential core ($L/D \sim < 7$), peak pressure fluctuations are observed on the plate at $1 < r/D < 1.5$. The pressure fluctuation is also null at the plate center ($r/D=0$), which is a stagnation point. The fluctuation reduced frequency ($\text{St}_j = fD/U$) is a constant at a given ratio of the plate distance to the jet diameter ($L/D$) [15]. The pressure fluctuations produce a sound wave that is reflected outside the jet potential core at the speed of sound ($c$). The reflected wave frequency is proportional to the jet velocity, and it is also equal to the ratio of the speed of sound over its wavelength ($f = \text{St}_j U/D = c/\lambda_c$). Thus, there exists a critical value of the jet velocity ($U$) for which the reflected wavelength ($\lambda_c$) equals the jet-to-plate distance ($L$), as

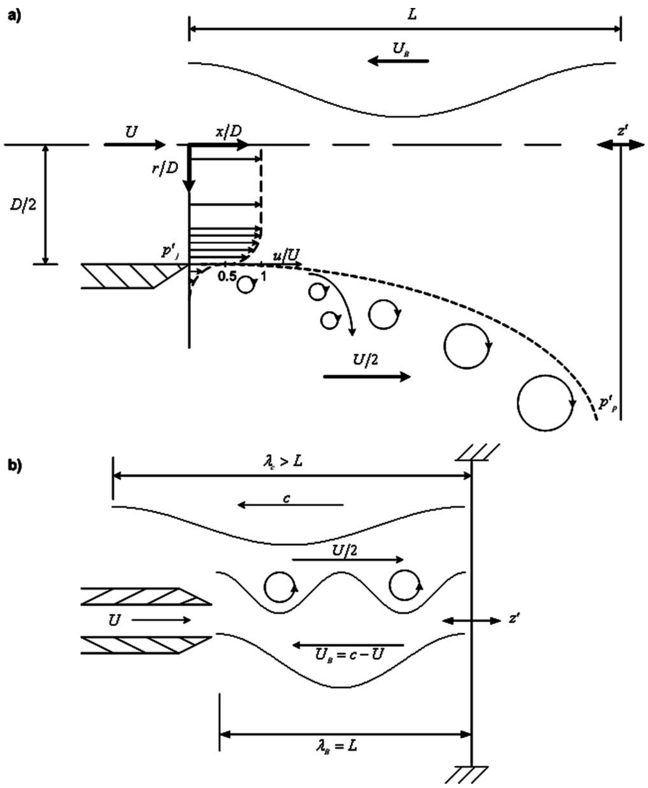

Fig. 7 Jet core feedback theory

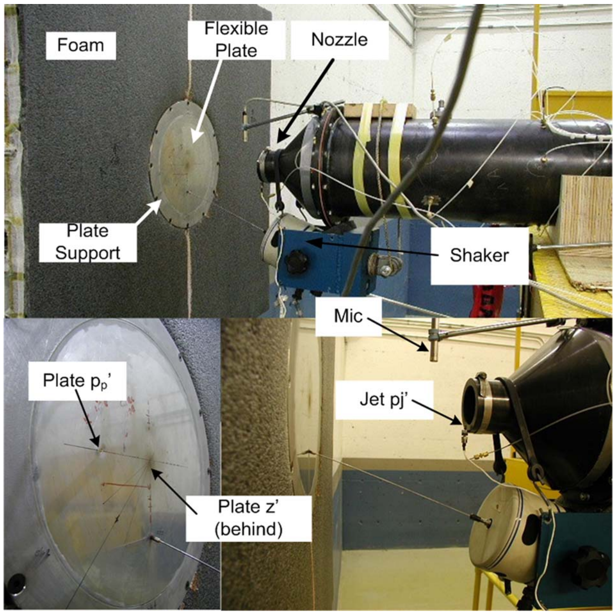

Fig. 8 Experimental setup

depicted in Fig. 6(*b*). At this critical condition, the jet vortical structures lock-on to the acoustic wave frequency and significant amplification of the pressure fluctuations is measured on the plate (Fig. 6(*c*)). Figure 6(*d*) presents the possible Strouhal number range of resonant impinging jets. It also shows that resonance on a rigid plate has not been reported below Mach 0.65 [14].

**Jet Core Feedback Theory.** This paper introduces the jet core feedback theory whose essence is shown in Fig. 7. When a jet impinges on a flexible plate, in contrast to the rigid plate case, the plate vibration ($z'$) induces a velocity, and thus a pressure fluctuation at $r/D=0$ (Fig. 7(*a*)). This in turn produces a pressure wave that propagates back inside the jet potential core at velocity $U_B$, where

$$U_B = c - U \tag{1}$$

with $c$ being the local speed of sound. This implies that for the jet-on flexible-plate system, there exists a critical velocity ($U$), for which the jet becomes resonant at the plate natural frequency. The critical condition is then

$$f = f_b = \mathrm{St}_j U/D = U_B/\lambda_B = (c-U)/\lambda_B \tag{2}$$

with $f_b$ being the plate vibration frequency and $\lambda_B$ the reflected wavelength. According to Eq. (2), and as shown in Fig. 7(*b*), the critical jet velocity at which the jet resonance can occur is when the feedback wavelength ($\lambda_B$) equals the distance between the jet lip and the plate ($L$). In parallel, this also implies that the core feedback wavelength ($\lambda_B=(c-U)f$) is smaller than the acoustic wavelength ($\lambda_c=c/f$) for any $U>0$. In the context of a compressor rotor, the critical jet velocity then becomes in the order of magnitude of the RI reported velocities [3,4]. Such a locked-on system will induce significant pressure amplification. Note also that the blade pitch ($s$) will naturally appear as the equivalent of the jet-to-plate distance ($L$) in the critical frequency calculation.

The reflected wave will cause velocity and pressure fluctuation at the jet lip. A wave crest, oscillating at the plate natural frequency, exists at the jet lip under the following condition:

$$L = n\lambda_B/2 \tag{3}$$

where $n$ is an integer.

Jet lip forced oscillation was also used in external impinging jet excitation studies to optimize the system heat transfer [16,17]. The excitation usually takes the form of a speakerphone located in a plenum upstream of the jet nozzle. It was found that the jet vortical structure formation can lock onto the external excitation provided that the forced oscillation frequency is close enough to the impinging jet natural frequency.

## Jet-Flexible-Plate Experiment

An experiment was conducted with a jet impinging on a flexible plate to demonstrate the proposed jet core feedback theory. Figure 8 shows the experimental apparatus.

The diameter of the circular jet ($D$) was 0.0635 m (2.5 in.). In order to obtain a peak displacement at $r/D=0$, and good frequency agreement between the plate and the jet, the circular plate was designed such that the first nodal circle mode (Mode 01) natural frequency coincided with the jet oscillation around Mach 0.4 per Eq. (2). The plate was made of mild steel with an outside diameter of 0.273 m (10.75 in.) and a thickness of 1.59 mm (0.0625 in.). The plate was clamped to the support at its circumference. Figure 9 shows the plate first two nodal circle modes, 00 and 01, which have their peak displacement at $r/D=0$.

The jet core feedback demonstration consists of setting the plate into vibration using an external shaker at the Mode 01 natural frequency. The jet velocity is then varied from Mach 0.2 to Mach 0.5 to locate the resonant jet condition. The resonant jet is characterized by the peak response of the plate pressure fluctuation ($p'_p$) located at $r/D=1.25$ to the jet lip pressure fluctuation ($p'_j$). Once the resonant jet Mach number is located, dwells are conducted around that point to determine the resonant conditions more accurately and to derive the backward propagating speed using the pressure and vibration signal phase relationships and Eqs. (1) and (2).

The experiment was conducted at different jet-to-plate distances ($L/D$) of 4.92, 4.75, and 2.52, where the nozzle lip pressure fluctuation is expected near a maximum per Eq. (3).

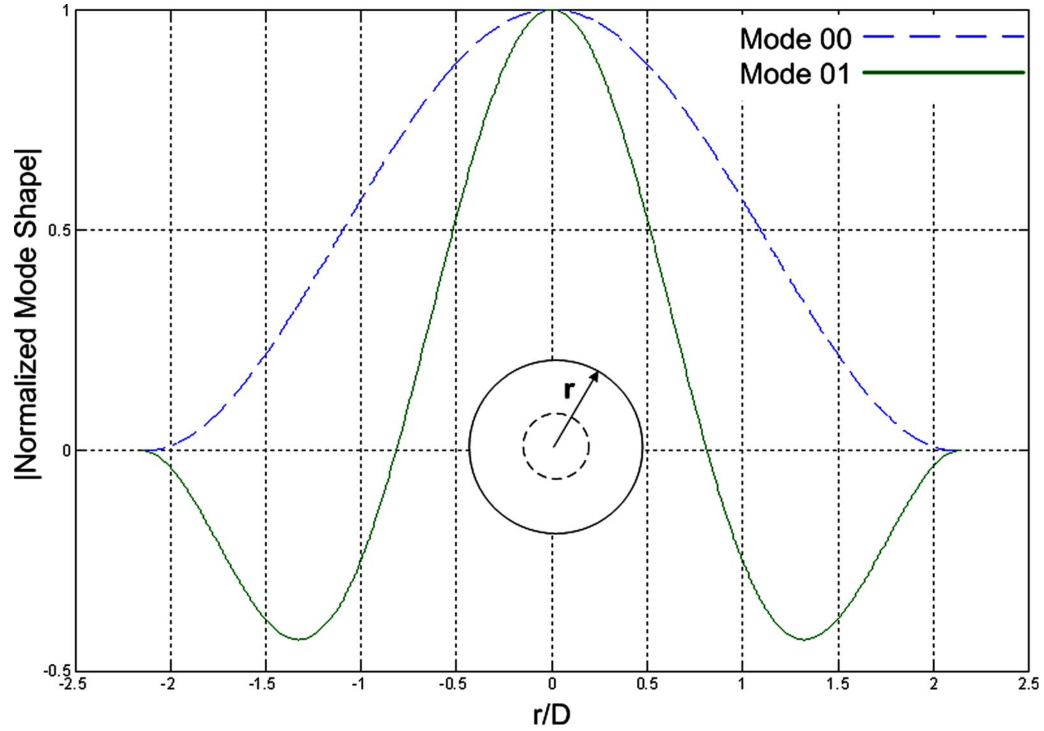

Fig. 9 Plate nodal circle mode shapes

Figure 10 shows the acoustic response $|p'_p/p'_j|$ to a slow jet Mach number sweep through the resonance at $L/D=4.75$. The strong amplification, 1000 times, shows the evidence of the jet acoustic lock-on at the plate natural frequency of 687 Hz. This is the first time, to the author's knowledge, that jet resonance has been shown to occur below Mach 0.65, and it confirms our hypothesis of a resonant impinging jet on a flexible structure. The speed of sound during the test ambient conditions was 345 m/s. The jet reduced frequency ($\mathrm{St}_j$) at the resonant condition (Mach 0.37) was 0.342.

Dwells were conducted in the vicinity of the localized resonant Mach number to conduct the phase analysis. The magnitude response seen during the dwells is used to accurately locate the resonant peak frequency for the phase analysis. The best accuracy of the resonant peak amplification is obtained from the sweepthrough, as shown in Fig. 10, since it is hardly possible to dwell at the exact maximum response, and thus steady-state running is always slightly off on either side of the resonant peak. On the other hand, best accuracy of the resonant frequency and Mach number is obtained from the dwells due to the inherent averaging of the response spectrum generation, which is more accurate in steady state than in transient. This is also true for a slow maneuver such as the slow sweepthrough used to generate Fig. 10.

Figure 11 shows the forward wave transfer function ($|p'_p/p'_j|$) for the three distance ($L/D$) configurations at their respective peak responses. It confirms the acoustic amplification at the plate natural frequency of 687 Hz and is used to accurately determine the resonance conditions.

No pressure measurement is available at $r/D=0$ where the accelerometer is installed. However, the pressure fluctuation at $r/D=0$ and $x=L$ is in phase with the plate displacement due to the no slip condition of the flow adjacent to the surface. Thus, the phase component of the plate vibration-to-jet lip pressure transfer

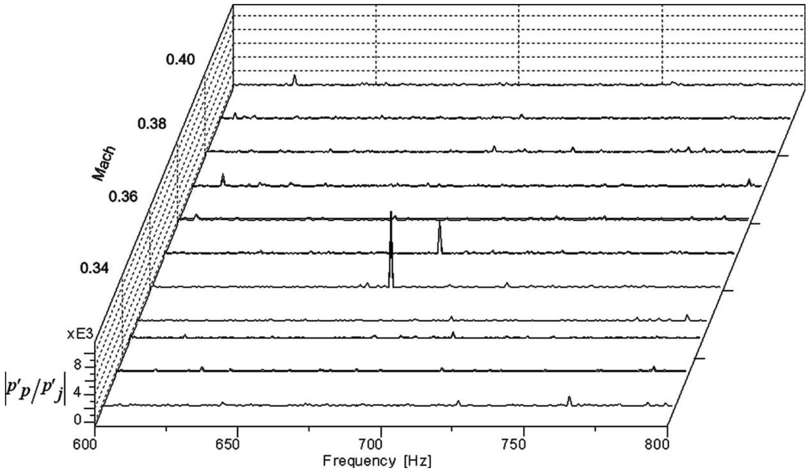

Fig. 10 Mach sweep through resonance

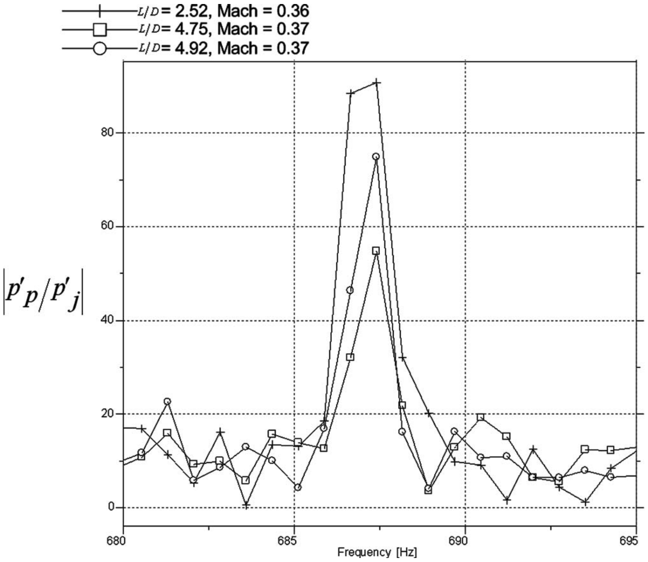

Fig. 11 Forward wave transfer function

function $(z'/p'_j)$ is used to derive the backward wave resulting propagation speed and wavelength at the plate resonant frequency.

Figure 12 shows the measured phase component of the backward wave transfer function $(\angle z'/p'_j)$ compared to the prediction at a given distance to wavelength ratio $(L/\lambda_B)$. The dashed line in Fig. 12 is the predicted phase of the backward wave. The prediction is obtained from the resulting distance to wavelength ratio $(L/\lambda_B)$ when assuming the wave propagating speed per Eq. (1) and calculating the wavelength $(\lambda_B)$ per Eq. (2). The experiment was conducted near acoustic resonances as per Eq. (3) with $(n \approx 1)$ and $(n \approx 2)$. The measured phase (square symbols), corresponding to three different nozzle-to-plate distances, agrees well with the prediction.

The above results experimentally confirm the jet core feedback theory, in which a plate vibration induces a feedback wave traveling upstream in the jet potential core at a velocity that is the difference between the local speed of sound and the jet forward velocity. This feedback wave then couples with the jet lip convected unsteadiness to cause an acoustic resonance at the plate natural frequency, and at jet velocity below Mach 0.65.

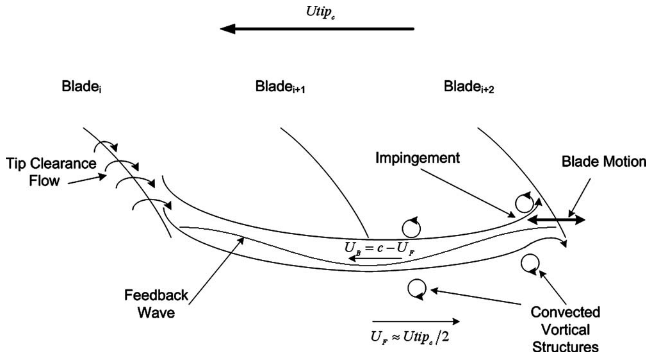

Fig. 13 Jet core feedback—NSV application

## Application to Rotor Blading

As described by Vo [11] and Vo et al. [18], and shown in Fig. 3, the trailing edge backflow impinges on the blade tip at the adjacent blade passage. This impinging flow, shown from a radially inward perspective above the blade tip in Fig. 13, travels forward, that is, from left to right in the figure, at velocity $(U_F)$.

The forward wave velocity $(U_F)$ is linked to the trailing edge backflow and in turn to the RI velocity [11] and has been established to be at around half the blade tip speed [3,4]. This is also confirmed with a single blade passage steady computational fluid dynamics (CFD) simulation of the rotor under study, which shows that the average normalized tip clearance tangential velocity $(U_F/U_{\text{tip}})$ is 0.484. Therefore, the general approximation $(U_F = U_{\text{tip}}/2)$ will be used.

The jet core feedback wave, traveling backward at velocity $U_B$ per Eq. (1), with $U = U_F$, is also shown in the figure. The critical NSV condition arises when the feedback wavelength equals twice the blade pitch $(s)$, as illustrated in Fig. 13 by the full wavelength within two pitches.

As also shown in Fig. 13, the blade$_i$ convected vortical structures, synchronized to the feedback wave, will impinge on the blade$_{i+2}$ pressure side. This in turn initiates strong amplification of both the pressure fluctuation and blade vibration, at the blade natural frequency, and can cause fatigue problems.

It should be noted that the resulting forward wavelength is not an integer multiple of two blade pitches, this condition being met only for the backward wave which travels at a different velocity,

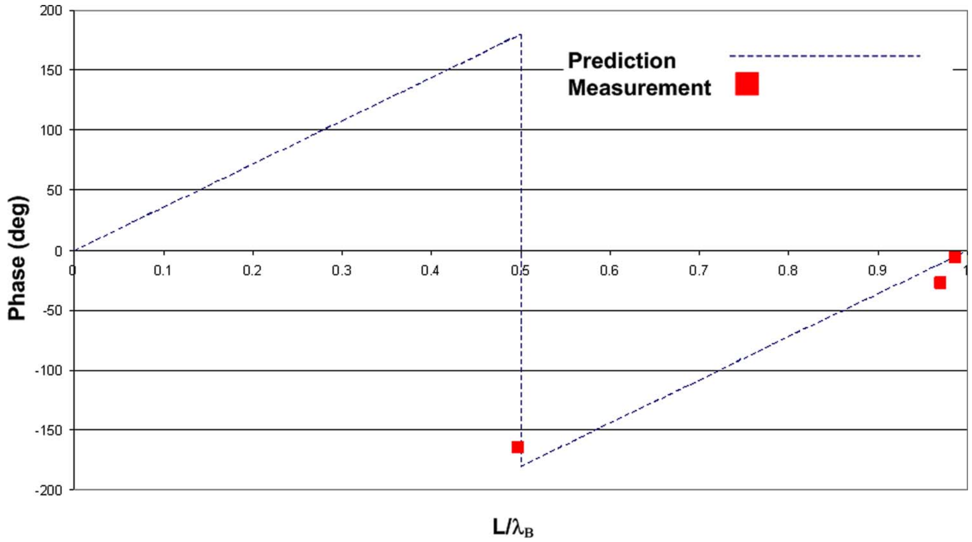

Fig. 12 Backward wave phase results

and thus its instantaneous phase may not appear synchronized to the blade movement. The forward wave is convected, that is, its velocity fluctuates around the mean jet velocity ($U_F$) and therefore does not require to either be an integer of a half or of a full blade pitch to generate the unsteady forcing on the blade. In contrast, an equivalent acoustic wave velocity would fluctuate around zero mean (an acoustic wave is propagated), thus requiring phase matching as does the feedback wave.

Equation (4) is derived to predict the critical tip velocity ($U_{\mathrm{tip}_c}$) at which NSV may occur at the blade natural frequency ($f_b$).

$$U_{\mathrm{tip}_c} = 2(c - 2sf_b/n) \tag{4}$$

where $c$ is the blade tip speed of sound, $s$ the blade pitch, and $n$ an integer that accounts for the superharmonics of the acoustic feedback wave, which results from the impinging flow "staging" phenomenon [14] and is discussed in the subsequent section.

**Critical Tip Speed Validation.** Equation (4) is now verified against the rotor under study along with Baumgartner et al. [1] rotor for which relevant information is available.

(i) Rotor Under Study
Based on the rotor blade characteristics, the blade pitch ($s$) is 0.042 m. The blade vibration frequency ($f_b$) was found to be around 2260 Hz during NSV. The blade tip region local speed of sound ($c$) was about 356 m/s during the NSV event. Substituting these values into Eq. (4), with $n=1$, the critical NSV tip velocity ($U_{\mathrm{tip}_c}$) predicted by Eq. (4) is 332 m/s and NSVs were actually measured at ($U_{\mathrm{tip}}$) between 310 m/s and 335 m/s. The critical NSV velocity is therefore accurately predicted by the proposed theory.

(ii) Baumgartner et al. Rotor [1]
Based on the rotor blade characteristics, the blade pitch ($s$) is 0.053 m. The blade vibration frequency ($f_b$) was found to be around 1372 Hz during NSV. The blade tip region local speed of sound ($c$) is estimated at 357 m/s, assuming standard day inlet, 30 K first stage off-design temperature rise from the given 400 K over ten stages at design speed, during the event. Substituting these values into Eq. (4), with $n=1$, the critical NSV tip velocity ($U_{\mathrm{tip}_c}$) predicted by Eq. (4) is 423 m/s and NSVs were actually measured at ($U_{\mathrm{tip}}$) near 411 m/s. Equation (4) prediction thus falls within 3% of the reported [1] NSV speed.

Unfortunately, for the rotor used by Kielb et al. [2], relevant characteristics are not available, and Eq. (4) cannot be verified against this supplementary case.

## NSV Model Implications

**Nonsynchronous Vibration Zone Prediction and Avoidance.** Equation (4) constitutes a straightforward tool to predict the critical NSV zones in the rotor operating envelope, and the above results show that it leads to a reasonable prediction of the critical NSV speed even with an approximation of the blade tip local speed of sound. This is explained by the speed of sound being proportional to the square root of the temperature.

There is some analytical work in determining more accurately the local speed of sound. If, however, the stage characteristic is known, either by analytical or experimental means, the tip temperature at the NSV condition can be approximated from the near stall temperature rise characteristic as a function of the corrected rotor speed and the inlet temperature. The inlet temperature can be derived from the ambient conditions and the upstream compression stages when applicable.

Equation (4) can be used to design the blade away from potential NSV. The critical NSV speed ($U_{\mathrm{tip}_c}$) can be designed outside the operating range, or at least matched at low stage loading. For example, the front and near stage $U_{\mathrm{tip}_c}$ should cross the blade modes, respectively, at the high and low ends of the operating speed range.

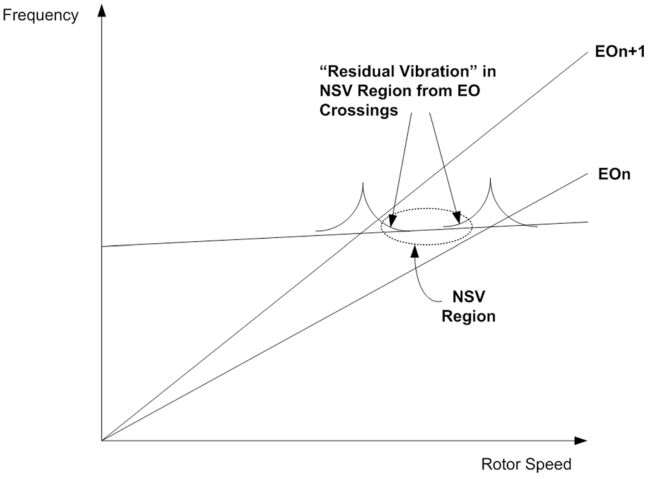

Fig. 14 NSV region on Campbell diagram

**Initial Blade Vibration.** The proposed model is based on the feedback wave from the blade vibration, and it assumes that the blade is actually vibrating when the NSV tip flow condition occurs. This is a reasonable assumption since, in practice, NSV inevitably occurs between two integer engine order (EO) crossings on the blade Campbell diagram. The Campbell diagram is a plot of the blade natural frequencies versus rotational speeds where potential crossings are represented by straight lines of slope EO, an integer, as shown in Fig. 14.

Small forced response residual vibration from the near EO crossing can initiate the feedback wave that in turn will synchronize the generation of the tip clearance flow shear layer vortical structures to the blade natural frequency with which the self-sustained NSV will lock on, as depicted in Figure 14. This is also well illustrated by Fig. 15, which shows actual engine blade strain gauge response during NSV just following EO6 crossing on a slow engine deceleration.

Close inspection of the engine strain gauge data of Kielb et al. [2] also shows the NSV occurrence in the vicinity of the 12EO crossing, of which some activity can be seen in the strain gauge data. More research work is required to determine the actual minimum blade vibration threshold to initiate the jet core feedback wave. It is possible that typical engine running small blade movement at their natural frequencies, or the RI condition itself, is enough to trigger the acoustic feedback phenomenon.

**Resonant Jet Staging and Vibration Frequency Shifts.** The general behavior of impinging shear layers has been characterized by Rockwell [19] and his work is summarized by Lucas [14]. One of the principal features common to impinging shear layers is the amplification of the pressure fluctuations in a narrowband of frequencies, as shown in Fig. 6($c$), caused by the acoustic feedback (also known as the upstream influence) of the unsteady pressure from impingement on the downstream body. The frequency of the impinging shear layer oscillations increases quasilinearly with the mean jet velocity over a limited range. It eventually "switches" from one feedback harmonic to the next in order to preserve the phase relationship between the source instability and the feedback wave. This phenomenon, causing discontinuities in the frequency versus jet velocity characteristic, is known as staging of the impinging shear layer.

The proposed mechanism is a particular type of impinging shear layer developing in the blade tip region for which the "jet" velocity is constant but the feedback wave is generated by the

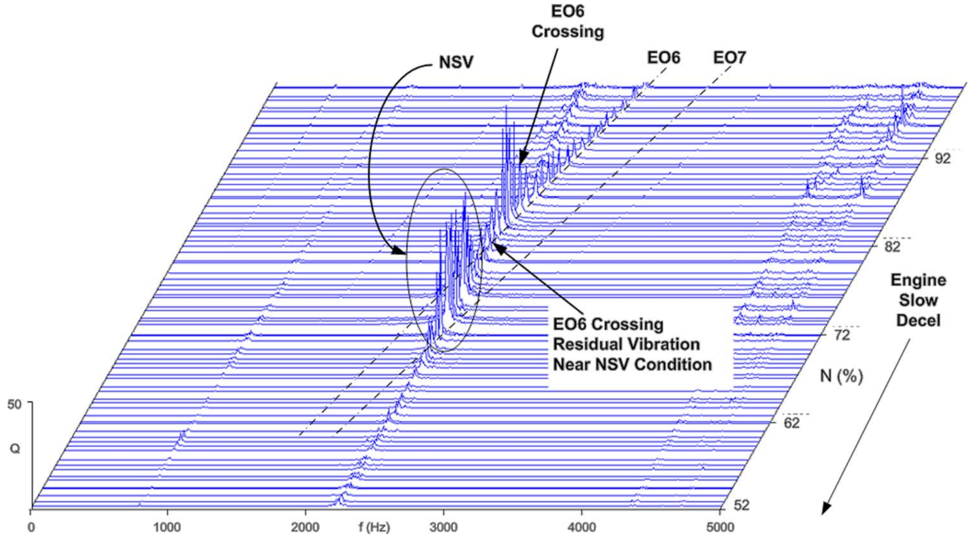

Fig. 15 NSV near EO6 on engine deceleration

blade vibratory motion. The phase relationship between the shear layer source blade and the adjacent vibrating blade will be preserved for any shorter feedback wavelength that is a superharmonic of the fundamental feedback wave. This will occur at frequencies that are integer multiples of the fundamental. This phenomenon could explain the observation by Kielb et al. [2] where NSV switches from the blade first torsional (1T) to second torsional (2T) vibration modes. In this case, the two blade vibration mode natural frequencies are apart by about a factor of 2. According to the proposed mechanism for NSV, the step change can be explained by the staging of the feedback wave as, illustrated in Fig. 16.

The staging causes the acoustic wave to switch from its first to second harmonic within the blade pitch. Its traveling speed remains constant, the resulting frequency would double and lock on to the 2T mode, which coincidentally vibrates at a frequency around twice the 1T mode frequency.

## Conclusion

The link between tip clearance flow unsteadiness (RI) and NSV has been explained with a mechanism based on a novel impinging resonant jet theory. Moreover, a simple model to predict the critical rotor speed of NSV occurrence has been introduced and verified against the rotor under study and the rotor studied by Baumgartner et al. [1].

The proposed jet core feedback theory shows the possibility of having impinging jet acoustic resonance below Mach 0.65 when the jet impinges on a flexible structure.

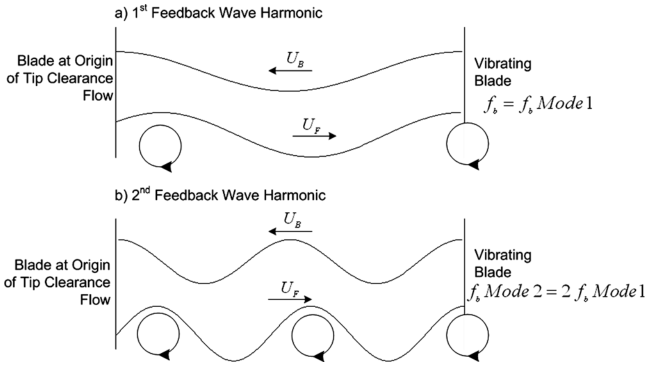

Fig. 16 Feedback staging and vibration frequency shift

Experimental work was conducted to demonstrate the jet core feedback theory using an impinging jet on a flexible-plate apparatus. The results demonstrate the presence of the jet core acoustic wave traveling at $c-U$ and its coupling with the shear layer vortical structures at the nozzle lip causing jet resonance below Mach 0.65.

The proposed model and associated physical NSV mechanism address the three missing links between RI and NSV that are identified from current knowledge: the required pressure unsteadiness amplification, the blade pitch as a main driving parameter, and the occasional vibration frequency and mode shift.

Equation (4) can be used to design a rotor critical NSV speed and blade mode crossings outside the operating range, or at least at low stage loading conditions.

This work suggested that damping the NSV surrounding EO crossing responses may prevent NSV occurrence. Further research is required to confirm the minimum blade vibration threshold that can trigger the acoustic feedback.

## Acknowledgment

The authors would like to thank Pratt and Whitney Canada for permission to publish this work.

## Nomenclature

$c$ = local speed of sound
CFD = computational fluid dynamics
$D$ = jet diameter, cylinder diameter
EO = engine order (1,2,3,…)
$f$ = natural frequency
$G$ = power spectral density
$H$ = planar jet width
HPC = high-pressure compressor
$N$ = rotor speed
NSV = nonsynchronous vibrations
$p'$ = pressure fluctuation
PS = pressure side
$Q$ = blade vibration amplification factor
$r$ = radial distance
RI = rotating instabilities
$s$ = blade pitch
SS = suction side
St = reduced frequency (Strouhal number)
$T$ = torsional vibration mode
TE = trailing edge

$u$ = instantaneous velocity
$U$ = average velocity
$U_{\mathrm{tip}}$ = blade tip velocity
$V_f$ = velocity fluctuation
$x$ = axial distance
$z'$ = center plate vibration
$\lambda$ = wavelength

## Subscripts

$B$ = backward traveling wave
$c$ = speed of sound, critical
$D$ = round jet
$H$ = planar jet
$F$ = forward traveling wave
$p$ = plate
$j$ = jet lip
$b$ = blade

## References

[1] Baumgartner, M., Kameier, F., and Hourmouziadis, J., 1995, "Non-Engine Order Blade Vibration in a High Pressure Compressor," 12th International Symposium on Airbreathing Engines, Melbourne, Australia.

[2] Kielb, R. E., Thomas, J. P., Barter, J. W., and Hall, K. C., 2003, "Blade Excitation by Aerodynamic Instabilities—A Compressor Blade Study," ASME Paper No. GT-2003-38634.

[3] Kameier, F., and Neise, W., 1997, "Rotating Blade Flow Instability as a Source of Noise in Axial Turbomachines," J. Sound Vib., **203**(2), pp. 833–853.

[4] Kameier, F., and Neise, W., 1997, "Experimental Study of Tip Clearance Losses and Noise in Axial Turbomachines and Their Reduction," ASME J. Turbomach., **119**, pp. 460–471.

[5] Mailach, R., Lehman, I., and Vogeler, K., 2001, "Rotating Instabilities in a Axial Compressor Originating From the Blade Tip Vortex," ASME J. Turbomach., **123**, pp. 453–463.

[6] Liu, J. M., Holste, F., and Neise, W., 1996, "On the Azimuthal Mode Structure of Rotating Blade Flow Instabilities in Axial Turbomachines," *AIAA and CEAS Aeroacoustics Conference*, AIAA Paper No. 96-1741.

[7] Yamaguchi, N., Sato, T., Umemura, S., and Ohwaki, T., "A Non-Synchronous Vibration of Moving Blades Coupled With the Bleed Chamber Resonance in an Axial Compressor," Takasago R&D Center, Mitsubishi Heavy Industries.

[8] Fukano, T., and Jang, C.-M., 2003, "Tip Clearance Noise of Axial Flow Fans Operating at Design and Off-Design Condition," J. Sound Vib., **275**, pp. 1027–1050.

[9] März, J., Hah, C., and Neise, W., 2002, "An Experimental and Numerical Investigation Into the Mechanism of Rotating Instability," ASME J. Turbomach., **124**, pp. 367–375.

[10] Zhang, H., Lin, F., Chen, J., Deng, X., and Huang, W., 2006, "A Study on the Mechanism of Tip Leakage Flow Unsteadiness in an Isolated Compressor Rotor," ASME Paper No. GT2006-91123.

[11] Vo, H. D., 2006, "Role of Tip Clearance Flow in the Generation of Non-Synchronous Vibrations," *Proceedings of the 44th AIAA Aerospace Sciences Meeting and Exhibit*, Reno, NV, AIAA Paper No. 2006-629.

[12] Deppe, A., Saathoff, H., and Stark, U., 2005, "Spike-Type Stall Inception in Axial-Flow Compressors," *Proceedings of the Sixth European Conference on Turbomachinery-Fluid Dynamics and Thermodynamics*, Lille, France.

[13] Blevins, R. D., 1990, *Flow Induced Vibrations*, 2nd ed., Krieger, Malabar, FL.

[14] Lucas, M. J., 1997, *Acoustic Characteristics of Turbomachinery Cavities*, ASME Press, New York.

[15] Ho, C.-M., and Nosseir, S., 1981, "Dynamics of and Impinging Jet Part I: The Feedback Phenomena," J. Fluid Mech., **105**, pp. 119–142.

[16] Tihon, J., Vejrazka, J., Marty, P., and Sobolik, V., 2005, "Effect of an External Excitation on the Flow Structure in a Circular Impinging Jet," Phys. Fluids, **17**, p. 105102.

[17] Hwang, S. D., and Cho, H. H., 2003, "Effects of Acoustic Excitation Positions on Heat Transfer and Flow in Axisymmetric Impinging Jet: Main Jet Excitation and Shear Layer Excitation," Int. J. Heat Fluid Flow, **24**, pp. 199–209.

[18] Vo, H. D., Tan, C. S., and Greitzer, E. M., 2005, "Criteria for Spike Initiated Rotating Stall," ASME Paper No. GT2005-68374.

[19] Rockwell, D., 1983, "Oscillations of Impinging Shear Layers," AIAA J., **21**(5), pp. 645–663.

# Film-Cooling Effectiveness on a Rotating Blade Platform

**A. Suryanarayanan**

**S. P. Mhetras**

**M. T. Schobeiri**

**J. C. Han**

Department of Mechanical Engineering,
Texas A&M University,
College Station, TX 77843-3123

*Film cooling effectiveness measurements under rotation were performed on the rotor blade platform using a pressure sensitive paint (PSP) technique. The present study examines, in particular, the film cooling effectiveness due to purging of coolant from the wheel-space cavity through the circumferential clearance gap provided between the stationary and rotating components of the turbine. The experimental investigation is carried out in a new three-stage turbine facility, recently designed and taken into operation at the Turbomachinery Performance and Flow Research Laboratory (TPFL) of Texas A&M University. This new turbine rotor has been used to facilitate coolant injection through this stator-rotor gap upstream of the first stage rotor blade. The gap was inclined at 25 deg to mainstream flow to allow the injected coolant to form a film along the passage platform. The effects of turbine rotating conditions on the blade platform film cooling effectiveness were investigated at three speeds of 2550 rpm, 2000 rpm, and 1500 rpm with corresponding incidence angles of 23.2 deg, 43.4 deg, and 54.8 deg, respectively. Four different coolant-to-mainstream mass flow ratios varying from 0.5% to 2.0% were tested at each rotational speed. Aerodynamic measurements were performed at the first stage stator exit using a radially traversed five-hole probe to quantify the mainstream flow at this station. Results indicate that film cooling effectiveness increases with an increase in the coolant-to-mainstream mass flow ratios for all turbine speeds. Higher turbine rotation speeds show more local film cooling effectiveness spread on the platform with increasing magnitudes.* [DOI: 10.1115/1.2752184]

## Introduction

Gas turbines typically run at high temperatures to maximize their thermal efficiency. Continuous operation at such high temperatures (~1500°C) though can increase the susceptibility to failure of the hot gas path components due to build up of thermal stresses. Thus, turbine components are designed such that high metal temperatures are avoided. Internal cooling of turbine components by supplying coolant through their hollow interior and also by coating their exterior with a ceramic layer preventing direct contact with the hot gases can help in lowering metal temperatures. This lowers the heat flux entering the turbine and its components. In addition to these two methods, film cooling is often employed as an active cooling method to further reduce contact between the metal and hot gas. The surface is perforated with holes through which high pressure coolant is injected over the hot blade surface. This injected coolant displaces the mainstream boundary layer to form a film of colder air over the surface thus reducing the temperature gradient. This active method of cooling is termed as film cooling and is expressed in terms of the film cooling effectiveness. A high and uniform effectiveness will increase the low cycle fatigue (LCF) life of the turbine component by reducing thermal stresses.

The present paper focuses on film cooling on the rotor hub platform through a circumferentially arranged slot that is positioned within the first stator-rotor axial gap of a three-stage multipurpose research turbine of the Turbomachinery Performance and Flow Research Laboratory (TPFL). The turbine has the capability to deal with aerodynamics, film cooling, and heat transfer issues described in Schobeiri et al. [1–3]. The secondary flow and its impact on efficiency and performance of turbine components are described in great detail by Lakshminarayana [4] and Schobeiri [5]. The 3D platform vortex pattern has been described in detail by Langston et al. [6], Goldstein and Spores [7], and Takeishi et al. [8]. Denton [9] gave an excellent overview of the effects of different mechanisms including the secondary flow on turbomachinery losses. In a very recent paper, Reid et al. [10] presented an investigation into the effect of the chordwise inter-platform leakage flow between vane segments on turbine performance. Their tests showed that the leakage flow can have a significant impact on turbine performance, but they pointed out that below a threshold leakage fraction the efficiency loss does not rise with increasing leakage flow rate. While the investigation in Ref. [10] and others deal with the effect of leakage flow on turbine aerodynamics, the present study deals primarily with film cooling aspect of coolant jet ejecting from a circumferential gap into the rotating blade passage.

The circumferential gap is designed to purge the turbine disk cavity to prevent hot gas ingestion and also to provide the hub platform with the necessary mass flow required for cooling it. In the absence of cooling flow injection, the platform is subjected to a low-energy boundary layer that causes a secondary flow motion of boundary layer fluid particles from pressure to suction surface. The secondary flow generates vortex systems that induce secondary flow losses. The low-energy boundary layer compounded with the high-temperature environment prevailing in the first few rows of a gas turbine engine contributes to thermal and mechanical stress buildup in the hub platform including inlet portion and throat region. As a result, the thin hub platform material subjected to the above stresses will become prone to cracking. To reduce the thermal stresses, coolant air is injected through the circumferential gap. As will be discussed in detail, depending on the engine rotational speed, the coolant jet injected through the gap can cover a major portion of the inlet platform and substantially decrease the heat flux into the turbine component by film cooling.

A compilation of the available cooling techniques prior to 2000 used in the gas turbine industry has been encapsulated by Han et al. [11]. Experimental investigations available in the open literature on film cooling and heat transfer on rotating turbine blades and their components are few and far between, primarily due to

---

Contributed by the International Gas Turbine Institute of ASME for publication in the Journal of Turbomachinery. Manuscript received September 18, 2006; final manuscript received October 17, 2006; published online October 28, 2008. Review conducted by David Wisler. Paper presented at the ASME Turbo Expo 2006: Land, Sea and Air (GT2006), Barcelona, Spain, May 8–11, 2006, Paper No. GT2006-90034.

the difficulty in instrumenting rotating parts. Dring et al. [12] investigated film cooling performance in a low-speed rotating facility. A film cooling hole was located on both the pressure and suction sides. They used ammonia and Ozalid paper to qualitatively observe the coolant trace while the quantitative tests were conducted using thermocouples. Their results show that the film coolant had only a small radial displacement, similar to flat plate results, on the suction side. On the pressure side, the film coolant trace had a large radial displacement toward the blade tip. Effectiveness distributions on the blade span for a rotating turbine blade were also provided by Takeishi et al. [13] and Abhari and Epstein [14] using gas chromatography and thin-film heat flux gauges, respectively.

Blair [15] studied the heat transfer on the pressure and suction sides as well as on the hub platform surface for a rotating turbine model. Enhanced heat transfer was observed on the platform due to the secondary flow effects. Recently, Ahn et al. [16,17] investigated the film cooling effectiveness on the leading edge of a rotating blade using the PSP technique. The same experimental facility has been used in this paper with a new turbine rotor to allow for stator-rotor gap cooling. They studied film cooling due to two row and three row coolant injection on the leading edge at design and off-design rotating conditions. Off-design conditions were found to significantly alter the film coolant traces on the leading edge.

A summary of film cooling effectiveness and heat transfer studies performed on the platforms of stationary cascades follows. Platform film cooling effectiveness investigations have been predominantly performed using cascade vanes. One of the earliest studies on platform film cooling was performed by Blair [18] using an upstream slot in a large scale turbine vane passage. Several papers have been published since then and only the most recent and relevant papers are quoted here. Harasgama and Burton [19] conducted heat transfer and aerodynamic measurements in an annular cascade fitted with vanes under representative engine flow conditions. Their results show that film cooling reduced the Nusselt numbers near the suction side by about 50% suggesting that the coolant was convected towards the suction side by the passage secondary flows.

Friedrichs et al. [20,21] detailed the aerodynamic aspects of platform film cooling and the effectiveness distributions using the ammonia and diazo technique. The tests were performed in a large scale low-speed turbine cascade fitted with four rows of film cooling holes at four axial stations on the platform. The presence of secondary flows was found to erode the coolant film near the surface necessitating a detailed investigation of the flow phenomenon in this region. The film cooling traces were observed to be pushed towards the suction side especially near the leading edge of the blade similar to that observed by Harasgama and Burton [19]. They also concluded that platform film cooling can increase aerodynamic losses. This increase is mainly due to losses during the mixing of the coolant with the mainstream.

A review of heat transfer on a turbine nozzle platform has been done by Chyu [22]. Slot injection was used on a turbine nozzle (vane) platform and film cooling effectiveness distributions were measured by Zhang and Jaiswal [23] using the PSP technique similar to the present study. The coolant film was found to be pushed towards the suction side decaying quickly for lower coolant-to-mainstream mass flow ratios. These observations compare well with those obtained by other researchers. Higher coolant-to-mainstream mass flow ratios gave a more uniform effectiveness distribution. Kost and Nicklas [24] and Nicklas [25] performed aerodynamic and thermodynamic measurements in a film cooled linear turbine cascade with transonic flow field with coolant injection through an upstream slot as well as through holes near the cascade entrance. They found that slot injection dramatically strengthened the horseshoe vortex due to proximity of the slot and the leading edge especially at high blowing ratios causing higher turbulence levels and heat transfer. Film cooling effectiveness near the pressure side is also found to be much lower due to the stronger horseshoe vortex. Film cooling through holes was also found to augment the heat transfer coefficients as compared to the unblown cases. Aerodynamic measurements with wheelspace coolant injection in a stationary as well as rotating frame were also compared by Mclean et al. [26,27].

Tests on film cooling effectiveness on contoured platforms were performed by Oke et al. [28–30] in a linear, low-speed cascade. Single and double slot injection was used upstream of the blades. Film cooling hole patterns on the platform with several holes along with slot injection were studied by Knost and Thole [31] in a low-speed cascade with nozzle guide vanes. Patterns with film cooling holes along iso-Mach lines were found to give much better film coverage. The effect of a back facing step before coolant injection was studied by Zhang and Moon [32] to simulate realistic engine geometry conditions. They used PSP to determine the film cooling effectiveness and found that a back facing step caused an unstable boundary layer and damages film coverage. Component misalignment with a forward as well as a backward step, at the upstream injection slot and on the slashface gap, was studied by Piggush and Simon [33]. They studied flow and loss characteristics associated with these features and noticed that blowing through the slashface gap has the most significant impact on the passage losses. Similar assembly features were also studied by Cardwell et al. [34]. Barigozzi et al. [35] examined film cooling using fan shaped holes instead of straight holes.

Film cooling on the rotor platform under rotating conditions is as yet an uninvestigated phenomenon in open literature. Thus, the primary focus of this research paper is to provide the reader with a comprehensive understanding of film cooling through the stator-rotor gap on the rotor hub under rotating conditions. Another important aspect of this paper is that it provides the reader/designer with a contour map of the local film cooling distribution on the platform surface under rotating conditions using the latest PSP technique rather than just a few discrete points that can be obtained from using heat flux gages or thermocouples. Instantaneous images of a PSP coated passage platform were captured in a stationary frame of reference through a transparent section on the shroud.

The PSP technique for film cooling effectiveness is based on mass transfer analogy and is free from heat conduction related errors frequently encountered with other heat transfer measurement techniques measuring adiabatic effectiveness. The turbine heat transfer research group from Texas A&M University has been actively involved in the development of this technique for film cooling effectiveness measurement. The results from this technique have been calibrated with other measurement techniques by Wright et al. [36] on a flat plate and Gao et al. [37] on a turbine blade leading edge model. A detailed working methodology of PSP to measure film cooling effectiveness has been described in Wright et al. [36]. PSP works by sensing the partial pressure of oxygen on the test surface. By displacing the oxygen on the platform via nitrogen injection from the stator-rotor gap and by measuring the relative difference between air and nitrogen injection, the film cooling effectiveness can be calculated. Since no heating is involved, errors resulting from lateral heat conduction in the test surface are avoided resulting in a clean and well-defined coolant trace. The results from this technique have been successfully demonstrated by Ahn et al. [38] and Mhetras et al. [39] on blade tip film cooling. Leading edge film cooling effectiveness tests in a rotating frame using the PSP method have also been performed by Ahn et al. [16,17].

The current investigation was performed in a multipurpose turbine research facility with a new turbine to accommodate film cooling between the stator-rotor circumferential gap. Several researchers studying turbine platform cooling have simulated this gap, meant to provide clearance for rotating components, using slot injection upstream of the cascade. Injecting coolant through this gap due to higher coolant pressure in the plenum than main-

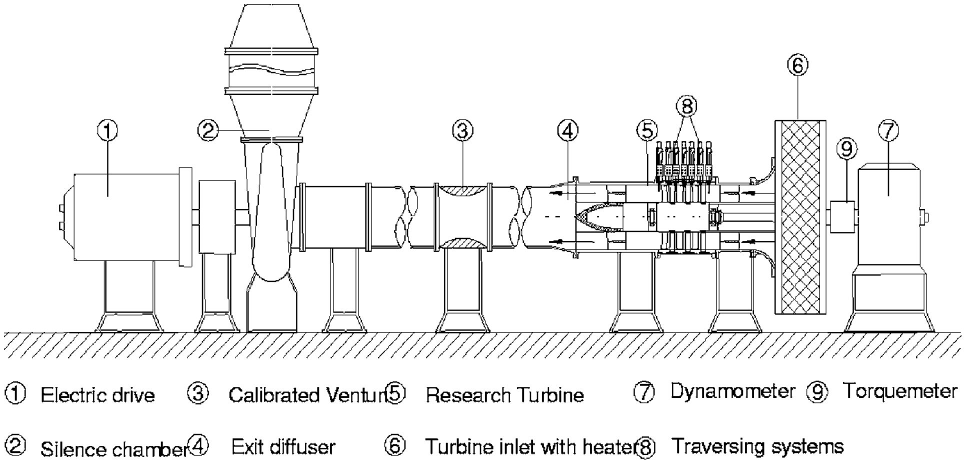

**Fig. 1 The overall layout of TPFL-research turbine facility, from Schobeiri et al. [1–3]**

stream prevents hot mainstream air from entering the turbine disk. The injected coolant provides an additional benefit of platform film cooling. The current investigation provides insightful information on the effect of blowing ratio on coolant distribution on the rotor platform as well as the effect of varying rotational speeds on the coolant distribution. Coolant was injected through this gap at four different mass flow ratios: 0.5%, 1.0%, 1.5%, and 2.0% of the mainstream core flow. The effect of rotation was studied at speeds of 2550, 2000, and 1500 rpm, respectively. The experimental results for flow and effectiveness will aid future engineers to design more efficient turbine components and help to calibrate CFD codes. Results can also be compared with data available from other researchers for stationary cascades and the resulting differences can be recognized and quantified.

## Experimental Facility

The experimental investigations have been carried out in a three-stage turbine research facility at the Turbomachinery Performance and Flow Research Laboratory of Texas A&M University. The turbine is the core component of the TPFL research facility designed by Schobeiri [1] in 1997 to address aerodynamics, efficiency, performance, and heat transfer issues of high pressure (HP), intermediate pressure (IP), and low pressure (LP) turbine components. Detailed aerodynamic, efficiency, loss, and performance measurements were carried out to verify and document the efficiency and performance of a high-efficiency 3D, bowed blading [1]. To compare the results of the investigations reported in Ref. [1] with those for 2D cylindrical blades, detailed measurement were conducted and summarized in the subsequent reports [2,3].

To determine the film cooling effectiveness under rotating conditions for leading edge film cooling [16,17], the turbine rotor was modified to integrate the coolant loop into the downstream section of the hollow turbine shaft and into the cylindrical hub cavity. The same rotor was not compatible with the new geometry which included the circumferential stator-rotor gap which provides for platform cooling. Hence, to perform the research reported in this paper, a further modification of the existing rotor unit did not seem to be feasible. A new rotor incorporating the stator-rotor gap was designed and manufactured.

The overall layout of the test facility is shown in Fig. 1. It consists of a 300 HP electric motor connected to a frequency controller which drives the compressor component. A three-stage centrifugal compressor supplies air with a maximum pressure difference of 55 kPa and a volume flow rate of 4 $m^3/s$. The compressor operates in suction mode and its pressure and volume flow rate can be varied by a frequency controller operating between 0 Hz and 66 Hz. A pipe with a transition piece connects the compressor to a Venturi mass flow meter used to measure the mass flow through the turbine component. The exit diffuser serves as a smooth transition piece between the turbine component and the Venturi, which is used for mass flow measurement. The three-stage turbine has an automated data acquisition system for detailed flow measurement at each blade row location. The turbine inlet has an integrated heater that prevents condensation of water from humid air expanding through the turbine during the test. The turbine shaft is connected through a flexible coupling with one end of a high precision torque meter that has a maximum rotational speed of 8500 rpm and a maximum torque rating of 677.9 N m. The other end of the torque meter is coupled via a second flexible coupling with an eddy current low inertia dynamometer with a maximum power capacity of 150 kW and a maximum torque of 500 N m.

**New Turbine Component Design.** A completely new advanced three-stage turbine component as shown in Figs. 2–4 was designed with the dimensions and operating conditions specified in Table 1 to replace the one discussed in Refs. [1–3,16,17]. In addition to the tasks performed by the old rotor, the new one was designed to operate at high speeds of 8500 rpm close to the transonic range. The first critical speed for vibration for the new rotor at its natural frequency occurs at 6500 rpm. Two independently controlled, concentric coolant loops provide the necessary mass flow for film cooling experiments. The outer loop supplies coolant for film cooling experiments in the blade passage section close to the trailing edge but is not used in this paper. The inner loop coolant jet ejecting from a circumferential gap between the first stator and rotor provides for hub platform cooling.

A concentric jet exits this circumferential gap at an angle of 25 deg into the mainstream (Figs. 3 and 5). The maximum normal gap width is designed to be 3 mm. However, it can be decreased to up to 0.5 mm by translating the entire rotor towards the front

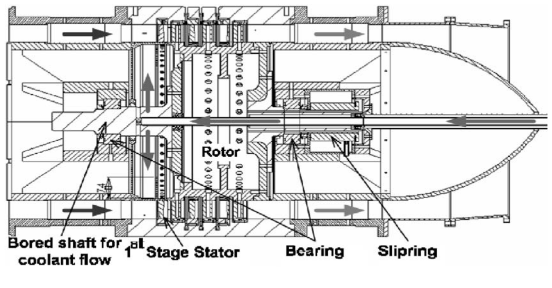

**Fig. 2 Section view of the modified stator-rotor turbine assembly**

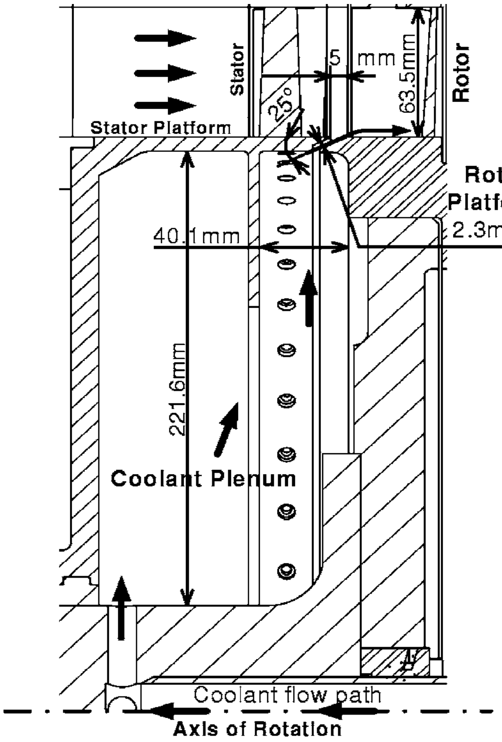

**Fig. 3 Detailed view of the stator-rotor gap**

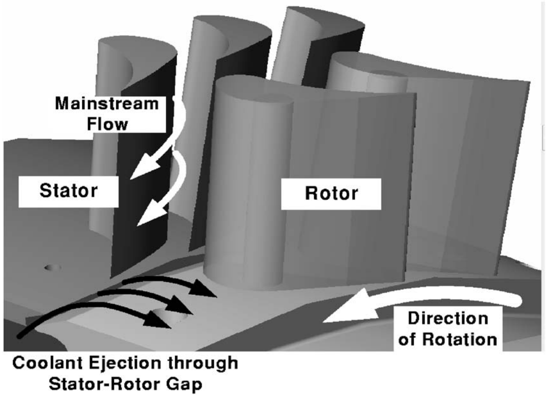

**Fig. 5 Schematic view of the stator-rotor gap design for the rotating endwall**

bearing. For the current study it was set to 2.3 mm. The axial stator-rotor gap for the first stage was measured at 5 mm. Similar to the optimization of the trailing edge slot ejection described in detail by Schobeiri [40] and Schobeiri and Pappu [41], the reduction of slot width is instrumental in establishing an optimum ejection ratio while keeping the cooling mass flow constant.

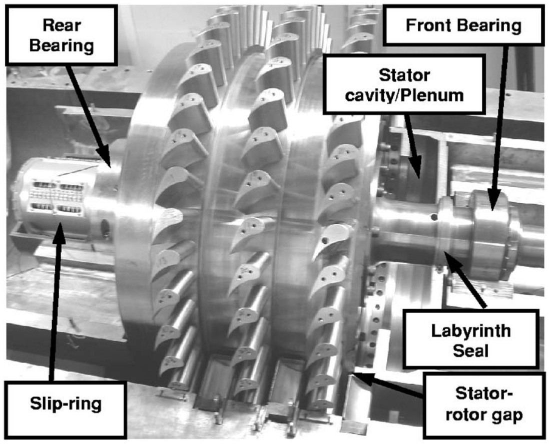

**Fig. 4 Turbine component with the 24-channel slip ring, casing cavity, and the front bearing**

**Table 1 Turbine dimensions and operating conditions**

| | | | |
|---|---|---|---|
| Stage no., $N$ | 3 | Mass flow | 3.728 kg/s |
| $D_t$ | 685.8 mm | $D_h$ | 558.8 mm |
| Reference speed | 2550 rpm | Current speed range | 1500 to 2550 rpm |
| Inlet pressure | 101.356 kPa | Exit pressure | 71.708 kPa |
| Blade height | 63.5 mm | Power | 80.0–110.0 kW |
| Blade no. | Stator 1=56 | Stator 2=52 | Stator 3=48 |
| Blade no. | Rotor 1=46 | Rotor 2=40 | Rotor 3=44 |
| $\alpha_2$ | 19 deg | $\phi$ | 0.353 |
| $\beta_3$ | 161 deg | $\lambda$ | 1.0 |
| $\alpha_3$ | 110 deg | $r$ | 0.5 |

The blades attached to the new rotor were taken from the rotor described in Refs. [1–3] and also used in Refs. [16,17]. They are typical HP-turbine blades used in steam turbines characterized by a relatively thick leading edge portion. This particular blade design allows reducing the total pressure losses due to the adverse off-design incidence changes caused by part-load operation. Thus, these blades are not typical of power generation or aircraft gas turbines. Given the considerable amount of manufacturing expenses that a new set of rotor and stator blades require and the lack of sufficient research funds, it was decided to use the same existing blades to carryout the current research. Although the blade geometry does not represent a typical gas turbine blade geometry, it provides the basic features to extract information relevant to gas turbine design community. These features are: (a) stator-rotor blade circulation and the exposure of the platform boundary layer to centrifugal and coriolis forces, and (c) the flow acceleration. Except for the last feature (c), none of the above features can be simulated in a cascade investigation.

To ensure that no coolant escapes through the rotary-stationary interfaces, the internal and external loops were sealed with labyrinths. The teeth spacing and the tip clearance were taken using the design instructions detailed by Schobeiri [5]. A 24-channel slip-ring is mounted to the rear shaft as shown in Figs. 2 and 4 to transfer temperature data from thermocouples from the rotating frame to the data acquisition system.

## Film-Cooling Effectiveness Measurement Theory and Data Analysis

Data for film cooling effectiveness was obtained by using the PSP technique. PSP is a photoluminescent material which emits light when excited, with emitted light intensity inversely proportional to the partial pressure of oxygen. This light intensity can be recorded using a charge coupled device (CCD) camera and can then be calibrated against the partial pressure of oxygen. Details of using PSP for pressure measurement are given in Ref. [42]. The image intensity obtained from PSP by the camera during data acquisition is normalized with a reference image intensity taken under no-flow conditions. Background noise in the optical setup is removed by subtracting the image intensities with the image intensity obtained under no-flow conditions without excitation. The resulting intensity ratio can be converted to pressure ratio using the previously determined calibration curve and can be expressed as

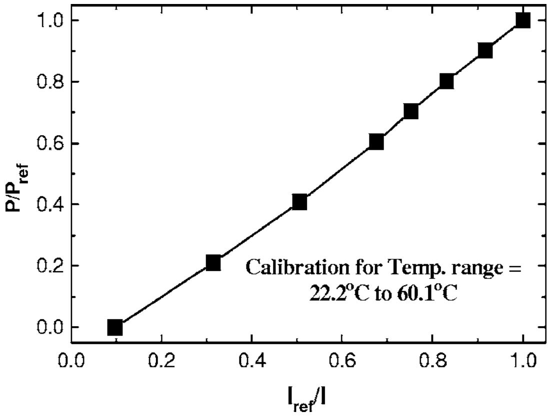

**Fig. 6 Calibration curve for PSP**

$$\frac{I_{\mathrm{ref}}-I_{\mathrm{blk}}}{I-I_{\mathrm{blk}}}=f\left(\frac{(P_{\mathrm{O_2}})_{\mathrm{air}}}{(P_{\mathrm{O_2}})_{\mathrm{ref}}}\right)=f(P_{\mathrm{ratio}}) \qquad (1)$$

where $I$ denotes the intensity obtained for each pixel and $f\ (P_{\mathrm{ratio}})$ is the relation between intensity ratio and pressure ratio obtained after calibrating the PSP.

Calibration for PSP was performed using a vacuum chamber at several known pressures varying from 0 atm to 1 atm with intensity recorded for each pressure setting. The same optical setup was chosen for calibration as well as for data acquisition during the experiments. A schematic of the calibration setup is shown in Fig. 6. PSP is sensitive to temperature with higher temperatures resulting in lower emitted light intensities. Hence, the paint was also calibrated for temperature. It was observed that if the emitted light intensity at a certain temperature was normalized with the reference image intensity taken at the same temperature, the temperature sensitivity can be removed. Hence, during data acquisition, the reference image was acquired immediately after the experiment was completed to avoid errors related to temperature variation. Reference images were acquired after the rotor came to a halt and the temperature change from loaded to stationary condition was small enough to disregard its effect on PSP measurement. Flow and surface temperatures were monitored by a thermocouple placed 2 mm above the surface close to the suction side and by another thermocouple placed underneath the platform surface, respectively. The thermocouples were wired through a slip-ring and connected to a microprocessor thermometer with a digital readout.

To obtain film cooling effectiveness, air and nitrogen were used alternately as coolant. Nitrogen which can be assumed to have the same molecular weight as that of air displaces the oxygen molecules on the surface causing a change in the emitted light intensity from PSP. By noting the difference in partial pressure between the air and nitrogen injection cases, the film cooling effectiveness can be determined using the following equation

$$\eta=\frac{C_{\mathrm{mix}}-C_{\mathrm{air}}}{C_{\mathrm{N_2}}-C_{\mathrm{air}}}=\frac{C_{\mathrm{air}}-C_{\mathrm{mix}}}{C_{\mathrm{air}}}=\frac{(P_{\mathrm{O_2}})_{\mathrm{air}}-(P_{\mathrm{O_2}})_{\mathrm{mix}}}{(P_{\mathrm{O_2}})_{\mathrm{air}}} \qquad (2)$$

where $C_{\mathrm{air}}$, $C_{\mathrm{mix}}$, and $C_{\mathrm{N2}}$ are the oxygen concentrations of mainstream air, air/nitrogen mixture, and nitrogen on the test surface, respectively. The definition of adiabatic film cooling effectiveness is

$$\eta=\frac{T_f-T_m}{T_c-T_m} \qquad (3)$$

The accuracy of the PSP technique for measuring film-cooling effectiveness has been compared by Wright et al. [36] on a flat plate with compound angled ejection holes using several measurement techniques such as steady and transient liquid crystal, infrared (IR) camera, and using a foil heater with thermocouples. Results were obtained for a range of blowing ratios and show consistency with each other. Wright et al. [36] found that IR, TSP, as well as PSP gave effectiveness results within 15% of each other. Larger uncertainties for heat transfer techniques such as IR and TSP methods were observed due to lateral conduction in the flat plate.

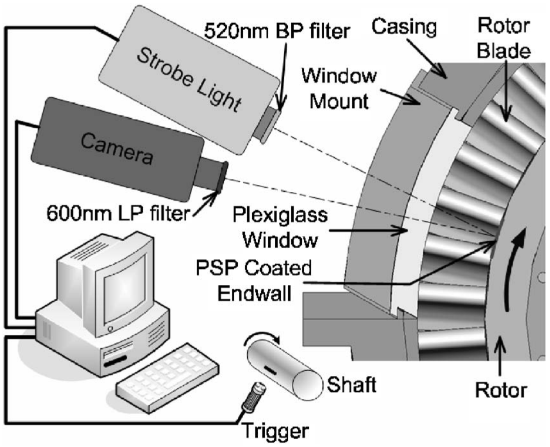

**Fig. 7 Optical components setup for the model turbine and PSP**

The platform passage under investigation was layered with PSP using an air brush. This coated surface was excited using a strobe light fitted with a narrow bandpass interference filter with an optical wavelength of 520 nm. Upon excitation from this green light, the PSP coated surface emitted red light with a wavelength higher than 600 nm. A 12-bit scientific grade CCD camera (high speed Sensicam with CCD temperature maintained at −15°C using two-stage Peltier cooler) was used to record images and was fitted with a 35 mm lens and a 600 nm longpass filter. The filters were chosen to prevent overlap between the wavelength ranges such that the camera blocked the reflected light from the illumination source. A schematic of the optical components setup is depicted in Fig. 7. The camera and the strobe light were triggered simultaneously from an angular position optical sensor offset to the shaft. By detecting the same angular position, the camera was able to view the same region of interest at every rotation, making it possible to average the image intensities without blurring the information. A minimum exposure time of 18 $\mu$s was used for image capture from the camera. Estimated rotor movement during image capture at 2550 rpm, for an 18 $\mu$s exposure time was 1.2 mm. A total of 150 TIF images were captured for each experiment with air and nitrogen injection and the pixel intensity for all images was averaged. The image resolution obtained from the camera was 1.5 mm/pixel with each image containing about 500 data points. The relatively low pixel resolution is a consequence of a binning of 8 used on the camera, as the emitted light intensity captured by the camera CCD in such a short exposure time was very low. A computer program was used to convert these pixel intensities into pressure using the calibration curve and then into film cooling effectiveness. The coolant flow rate was set using a rotameter based on prior calculation for the desired mass flow ratio. The coolant was heated to the same temperature as mainstream air (45°C) before injection through the gap.

Uncertainty calculations were performed based on a confidence level of 95% and are based on the uncertainty analysis method of Coleman and Steele [43]. Lower effectiveness magnitudes have higher uncertainties. For an effectiveness magnitude of 0.3, uncertainty was around ±2% while for effectiveness magnitude of 0.07, uncertainty was as high as ±10.3%. This uncertainty is the result of uncertainties in calibration (4%) and image capture (1%). The absolute uncertainty for effectiveness varied from 0.01 to 0.02 units. Thus, relative uncertainties for very low effectiveness

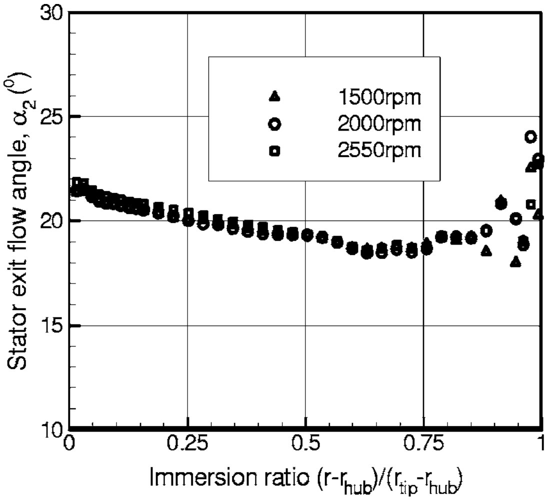

Fig. 8 Radial distribution of stator exit flow angle for varying rotor speeds

magnitudes can be very high (>100% at effectiveness magnitude of 0.01). However, it must be noted that very few data points exist with such high relative uncertainty magnitudes. Uncertainties for the blowing ratios are estimated to be 4%.

## Rotor Inlet Flow Measurement Results

Aerodynamic flow measurements were performed along the exit of the first stage stator to quantify the nature of the mainstream flow ahead of the stator-rotor platform gap. A five-hole probe calibrated ±20 deg in pitch and yaw was traversed radially from hub to tip at an interval of 1 mm up to 5% of the blade near the hub and tip and 2 mm in the central region to obtain accurate pressure, velocity, and flow-angle distributions at the stator exit. The precise alignment of the five-hole probe with the direction of flow ensures the accuracy of the data acquired. To enable accurate probe alignment, a stepper motor along with a worm-gear arrangement was used to actively rotate and adjust the five-hole probe inside the turbine. Figure 8 shows the direction of flow from the hub to tip for the three turbine operating speeds. As expected the flow exits the stator almost following the blade metal angle of 19 deg. However, near the casing the flow under the influence of strong secondary flows tends to deviate from the expected flow direction exhibiting higher angular fluctuations. Figures 9 and 10 show the radial distribution of total pressures and absolute velocities for varying turbine speeds. The total pressure distribution for all the three rotor speeds is similar with magnitudes increasing with operating speeds. The effects of the secondary flow at the hub and near the casing are distinctly seen in the radial velocity distributions for all three rotor speeds. Up to 5% of the flow in the radial direction near the hub and blade tip is affected by the secondary flow.

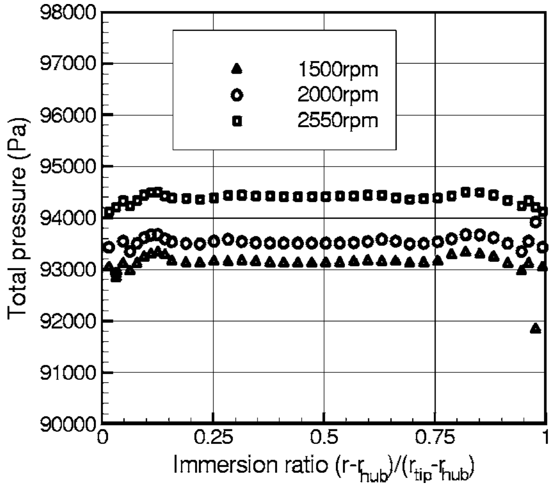

Fig. 9 Radial distribution of total pressure for varying rotor speeds

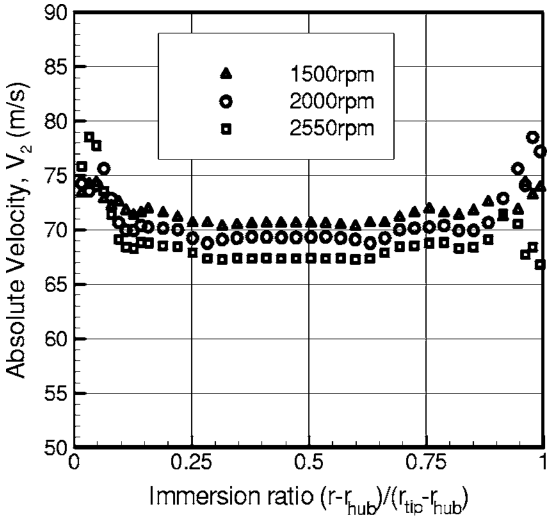

Fig. 10 Radial distribution of absolute velocity for varying rotor speeds

The absolute velocity (Fig. 10) at the first stage stator exit decreases by 3–4 m/s as the shaft speed is increased for 1500 – 2550 rpm. The overall average absolute and relative velocities for all speeds at the exit of the first stage stator were measured to be 69.3 m/s and 38.8 m/s, respectively, resulting in Mach numbers of 0.2 and 0.11, respectively. The Reynolds number based on the rotor axial chord length and the exit velocity was around 200,000 and the pressure ratio was 1.12 for the first stage. The rotation number corresponding to 2550 rpm, 2000 rpm, and 1500 rpm is 0.19, 0.15, and 0.11, respectively. The flow incidence angle change, *i*, relative to the incidence angle at the design operating condition (3000 rpm) shown in Fig. 12, for 2550 rpm, 2000 rpm, and 1500 rpm was determined as 23.2 deg, 43.4 deg, and 54.8 deg, respectively. This change in incidence angle causes the stagnation line on the blade leading edge to shift towards the pressure side affecting the static pressure distribution on the blade as well as the platform. Consequently, the coolant spread on the platform becomes affected with changing rotational speed. The inlet flow conditions thus help to better explain the film cooling effectiveness distributions on the blade platform.

## Film Cooling Effectiveness Results

Film cooling effectiveness measurements were performed for four coolant-to-mainstream mass flow ratios of 0.5%, 1.0%, 1.5%, and 2.0%. Film cooling data was also obtained for three rotational speeds, 2550 rpm (reference condition), 2000 rpm, and 1500 rpm. Total mass flow in the engine was 3.73 kg/s and was ensured to be the same for all three rpms by adjusting the blower frequency through the frequency controller. The four coolant-to-mainstream mass flow ratios approximately correspond to blowing ratios of 0.12, 0.24, 0.36, and 0.48, respectively, after assuming that the coolant exits the gap axially. Blowing ratios for each rotating speed differ slightly as the relative mainstream velocity at the rotor inlet changes with the rotating speed.

**Reference Rotating Condition.** Variation of rotational speed performed in the Ref. [16,17] showed that the location of the

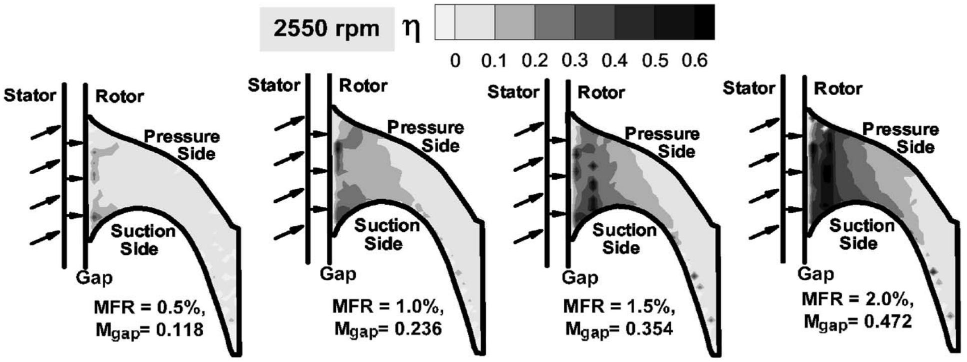

**Fig. 11 Film cooling effectiveness distribution on the rotating platform for 2550 rpm**

leading edge stagnation line, which yielded symmetric spreading of coolant on the suction and pressure surfaces of the leading edge was at an rpm of 2550. This rotational speed was chosen as the reference rotating condition for the current investigation. The effectiveness results obtained from using PSP for the reference rotating condition of 2550 rpm are plotted in Fig. 11. The figure shows the contour plots for all four mass flow ratios tested. The contour plots also show the location of the stator-rotor gap upstream of the passage and the path of the mainstream and coolant flow. The effectiveness in the gap, as the coolant escapes through it, could not be recorded as the plexiglass window through which the rotor platform was viewed was not wide enough.

Higher mass flow ratios result in coolant injection with higher momentum. As this momentum increases, it can be observed that the spread of the coolant as well as the effectiveness magnitudes are higher. The injected coolant is at the same density as the mainstream, i.e., the coolant to mainstream density ratio is 1. Hence, the injected coolant velocity is higher for higher mass flow ratios. This affects the secondary flow structure in the passage. At lower blowing ratios, the low momentum coolant is not capable of penetrating into the highly vortical secondary flow region on hub platform. It mixes with the main flow where its kinetic energy dissipates, making only a marginal contribution to effectiveness improvement. For the lowest mass flow ratio (MFR) = 1.5%, the maximum effectiveness magnitude is less than 0.2

As the mass flow ratio increases, the coolant injection velocity increases because the coolant can penetrate the complex secondary flows in the passage resulting in higher effectiveness on the platform. For the highest mass flow ratio of 2%, a region of high effectiveness can be observed near the entrance of the blade passage. The effectiveness from the gap to the beginning of this high effectiveness region is slightly lower. This indicates that the coolant probably detaches itself from the surface as it exits from the gap and then reattaches as it is pushed by the mainstream towards the surface which is marked by the high effectiveness spot (at around 15% of axial chord). Effectiveness magnitudes as high as 0.6 can be observed at this reattachment spot. Smaller reattachment spots can be observed for MFR = 1.5% too. Thus, as the mass flow ratio increases, the effectiveness magnitude and its spread become larger. The same phenomenon has been recorded by several researchers mentioned earlier with studies for slot film cooling on stationary, flat as well as curved platforms. Common to all blowing ratios investigated is that the suction surface is the location of inception of the effectiveness. Major parameters instrumental in making the suction surface the inception location are: (a) the platform secondary flow; (b) the Coanda effect that helps the injected coolant attach on the suction surface; and (c) the coolant injection angle.

The coolant distribution on the platform is predominantly governed by its flow characteristics. A strong pressure gradient exists within the passage from the pressure to the suction side with the static pressure near the pressure side being much higher due to lower mainstream velocities and blade curvature. The coolant traces show slightly higher effectiveness magnitudes toward the suction side near the leading edge. More coolant gets diverted away from the higher pressure stagnation region on the leading edge of the blade and finds its way towards the suction side. Effectiveness magnitudes on the pressure side begin to fade away rapidly as the coolant travels along the axial chord. As the passage vortex moves toward the suction side while gaining strength, it entrains the mainstream on the platform surface damaging the coolant film, which results in a sharp drop in effectiveness magnitudes. This sudden drop gives a good indication of the path traced by the passage vortex. Similar coolant spread profiles affected by secondary flows can be observed for stationary platform cooling through slots akin to the current design in turbine as well as vane cascades in the tests conducted by Blair [18] and Oke et al. [28].

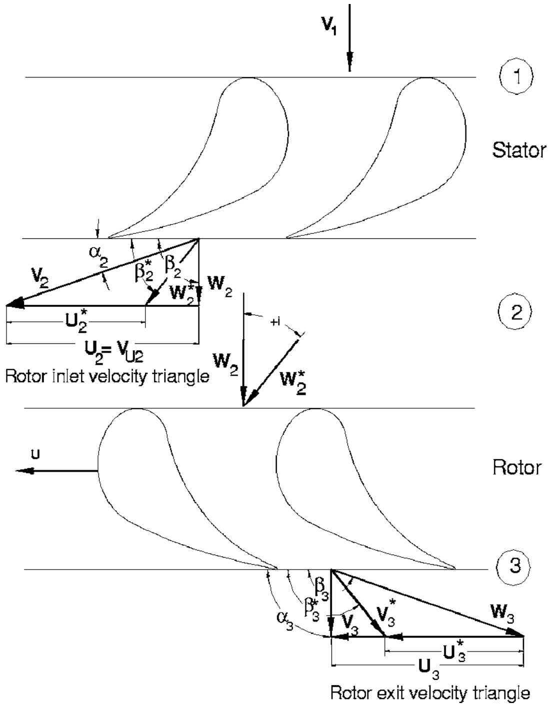

**Fig. 12 Velocity triangles and relative inlet and exit flow angles for design and off design rotating speeds**

**Variation of Rotating Conditions.** At rotational speeds lower than the design speed, the blade flow deflection becomes larger leading to higher specific stage load coefficient and the stagnation region moves toward the pressure side as the flow incidence angle

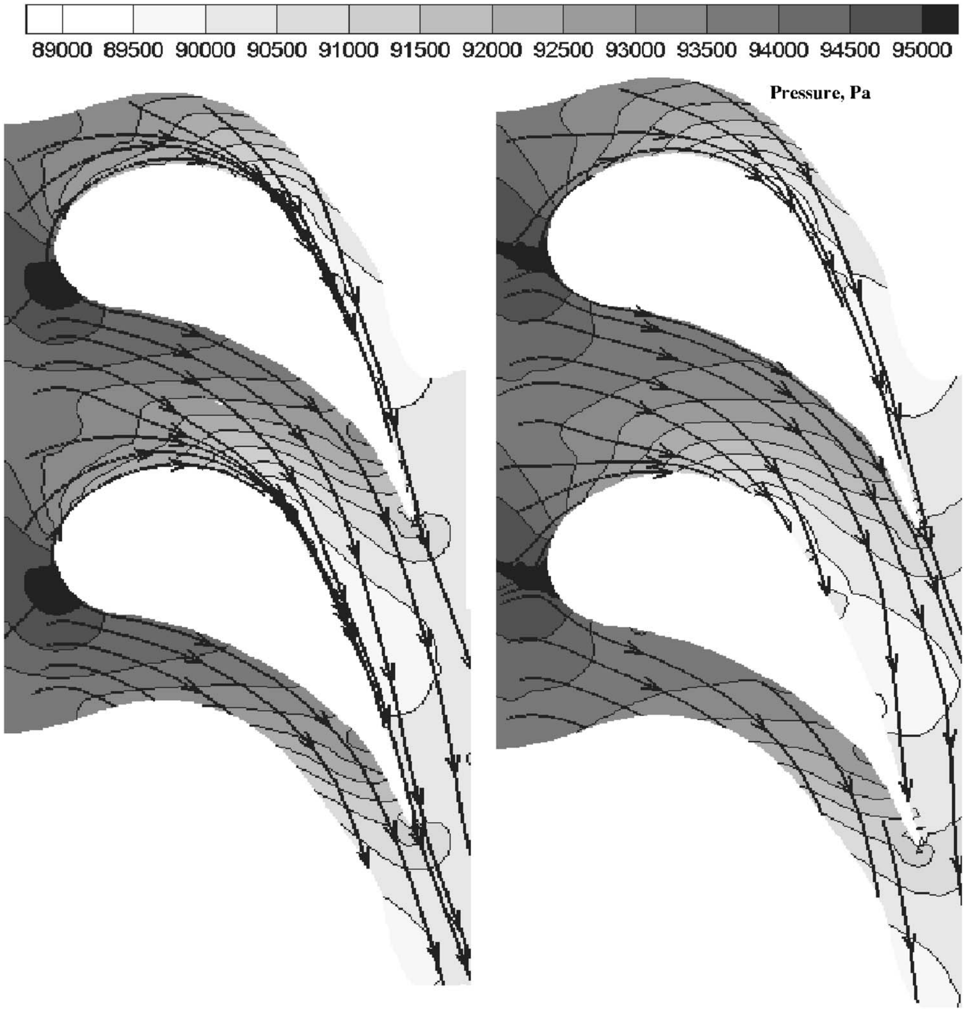

**Fig. 13 Numerical prediction of platform static pressure distribution (Pa) along with flow pathlines**

increases as sketched in Fig. 12. At progressively lower rotating speeds, the stagnation line will further move towards the blade pressure side, resulting in a higher pressure zone owing to higher flow deflection. The pressure gradient on the platform from the pressure to the suction side becomes affected by this shift in the stagnation region due to larger flow incidence angles. The pressure gradient becomes more nonuniform with decreasing rotational speeds as observed in Fig. 13. Figure 13 shows the numerical predictions of local static pressures on the platform surface with flow pathlines for 2550 rpm and 2100 rpm. These numerical predictions were performed using the CFD code, FLUENT, for the same geometry and flow conditions. About 1.1 million cells were used to grid 1.5 stages of the turbine. A sliding mesh was used to simulate rotation. A Reynolds stress model with a nonequilibrium wall function was used to solve the Reynolds averaged Navier-Stokes equations. From the figure, the movement of the stagnation region towards the pressure side for lower rpm can be easily discerned. Lower pressure at lower rotating speeds can be observed near the suction side. Figure 13 also shows the mainstream pathlines near the platform surface. The pathlines for 2100 rpm appear to converge together as the flow gets pushed to the suction side.

The larger gradients in the platform static pressure distribution for lower rotating speeds cause significant movement of the coolant film on the platform surface when it comes from the stator-rotor gap. The local mass flow of coolant from the stator-rotor gap depends on the pressure difference between the plenum and the mainstream static pressure. A higher pressure region near the blade pressure side close to the leading edge at lower rotating speeds as observed in Fig. 13 will result in a smaller pressure difference across the gap as compared to the reference condition. This will promote nonuniform coolant distribution from the stator-rotor gap with the coolant traces reorienting themselves toward the suction side of the platform. This phenomenon can be clearly observed from data taken for 2000 rpm and 1500 rpm as shown in Figs. 14 and 15. Both figures include contour plots for four different mass flow ratios. More coolant appears to come out from near the suction side of the platform where the pressure difference across the gap from inlet to outlet is larger with the lowest rotational speed of 1500 rpm showing the largest nonuniformity. Thus, the coolant film distribution and hence film cooling effectiveness strongly depend on the pressure distribution on the platform surface. As the blowing ratio increases, the traces become stronger due to the increase in the coolant momentum similar to that observed in Fig. 11.

After comparing Figs. 14 and 15 for lower rotating speeds with Fig. 11 at 2550 rpm (reference speed), it can be observed that the effectiveness magnitudes progressively decrease with lower rpm for the same mass flow ratio. This may be a result of stronger horseshoe vortices close to the suction side owing to the shift in the flow incidence angle at lower rpm. Very low effectiveness levels can be discerned for the lowest blowing ratio, MFR $=0.5\%$ for 1500 rpm, as compared to other rpms. Coolant traces can only be observed locally near the suction side of the blade.

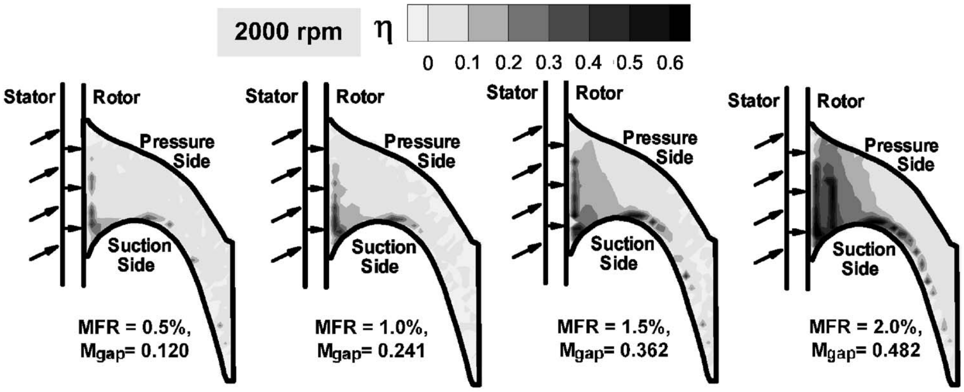

**Fig. 14 Film cooling effectiveness distribution on the rotating platform for 2000 rpm**

The coolant spread for MFR=2.0% is appreciably larger and some reattachment of coolant can also be observed for 2000 rpm similar to that observed for 2550 rpm. Effectiveness traces on the suction side though are more visible than that for 2550 rpm. Some coolant traces can even be observed close to the trailing edge near the suction side for higher mass flow ratios. For both reference and lower rotating speeds, the region downstream of the throat remains uncooled. Weak traces can be observed in this region for 2550 rpm for MFR=2.0% near the throat. This region experiences much higher velocities from the accelerating mainstream flow, resulting in high local heat transfer coefficients. The secondary flow vortices in the passage erode the coolant film before it reaches the throat.

In addition to the effect on static pressure distribution and film cooling due to inlet flow incidence angle change with rotational speed, rotation may also affect the coolant flow as it exits the stator-rotor gap. The gap and the disk cavity are bounded by two walls; stator endwall and the rotor platform. The enclosed coolant mass in the disk cavity will rotate with a certain frequency due to the cavity wall shear stress. High shear stresses, caused by relative motion in the circumferential gap, may introduce some swirl in the coolant flow as it exits. Hence, a tangential component may exist in the coolant flow as it exits the stator-rotor gap. This may cause some additional spreading of the coolant which cannot be achieved for film cooling studies in stationary cascades. This might also explain the larger coolant spread with increasing rotational speeds due to a larger tangential velocity component in the coolant as it exits the gap. The determination of the swirl angle as well as the measurement of this tangential velocity component was not the subject of the current paper. However, these are items of high importance along with the interstage measurements.

**Pitchwise Average Film Cooling Effectiveness.** The film cooling effectiveness results were averaged along the pitchwise direction and the averaged data for all coolant-to-mainstream mass flow ratios and rotational speeds are presented in Fig. 16 along the axial chord. The increase in effectiveness magnitudes with increasing mass flow ratio can be clearly observed from this figure. The averaged plots show a sharp decrease in effectiveness magnitude along the axial chord as indicated earlier with the region beyond $x/C_x=0.6$ remaining mostly uncooled with average effectiveness magnitudes below 0.1. The spikes occurring as a result of coolant jet reattachment at MFR=2.0% for 2550 rpm and 2000 rpm can also be observed. The decrease in effectiveness with lower rotational speeds can also be discerned. Figure 17 shows the same pitchwise averaged film cooling effectiveness results plotted for the four different coolant-to-mainstream mass flow ratios. The impact of turbine rotational speeds on film cooling effectiveness can be clearly perceived from this plot. As rpm increases, the effectiveness magnitudes increase for the same mass flow ratio. Figure 18 shows the average film cooling effectiveness plotted with $x/M_{\text{gap}}S$ as the abscissa. The figure compares the data with a correlation from Goldstein [44] for an equivalent two-dimensional slot on a flat stationary surface as given in Eq. (4)

$$\bar{\eta} = (1 + 0.249 \cdot (x/M_{\text{gap}}S)^{0.8})^{-1} \tag{4}$$

This correlation works well for $x/M_{\text{gap}}S > 10$, where the flow regime is more two dimensional. For $x/M_{\text{gap}}S < 10$, the three-dimensional flow regime due to mixing of the coolant jet with mainstream results in lower effectiveness than that predicted by the correlation. When compared to current data, for reference rotating condition, it shows relatively good comparison with the

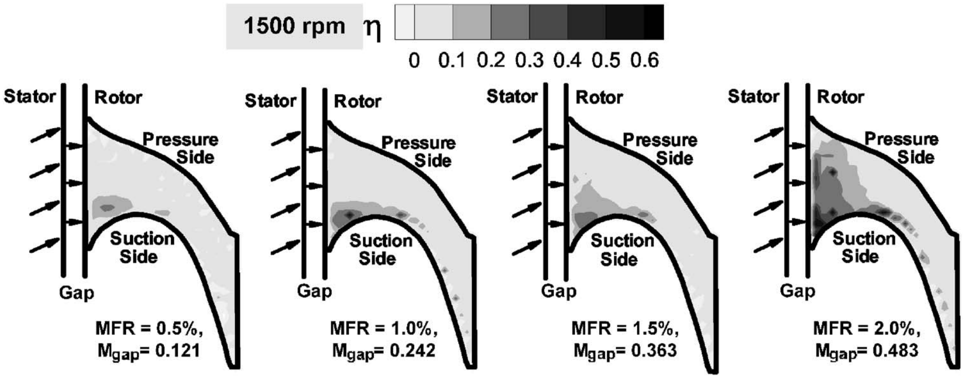

**Fig. 15 Film cooling effectiveness distribution on the rotating platform for 1500 rpm**

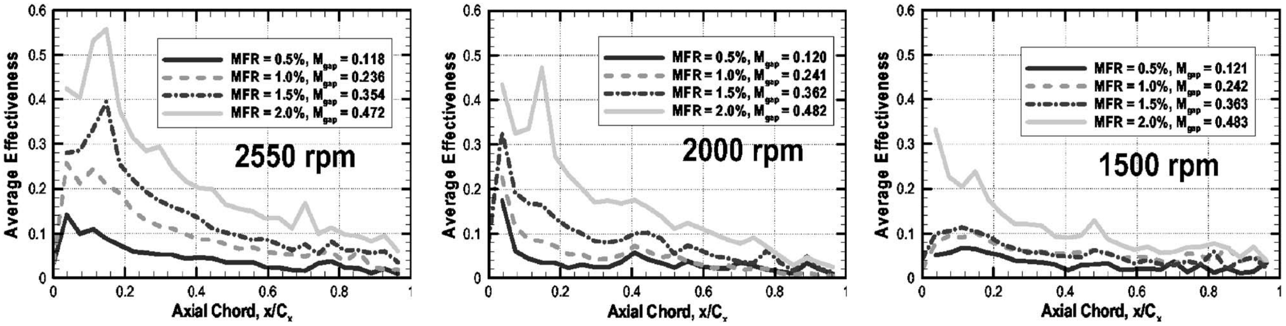

Fig. 16 Pitchwise averaged film cooling effectiveness distribution along axial chord for different turbine rotating speeds (mass flow ratio effect)

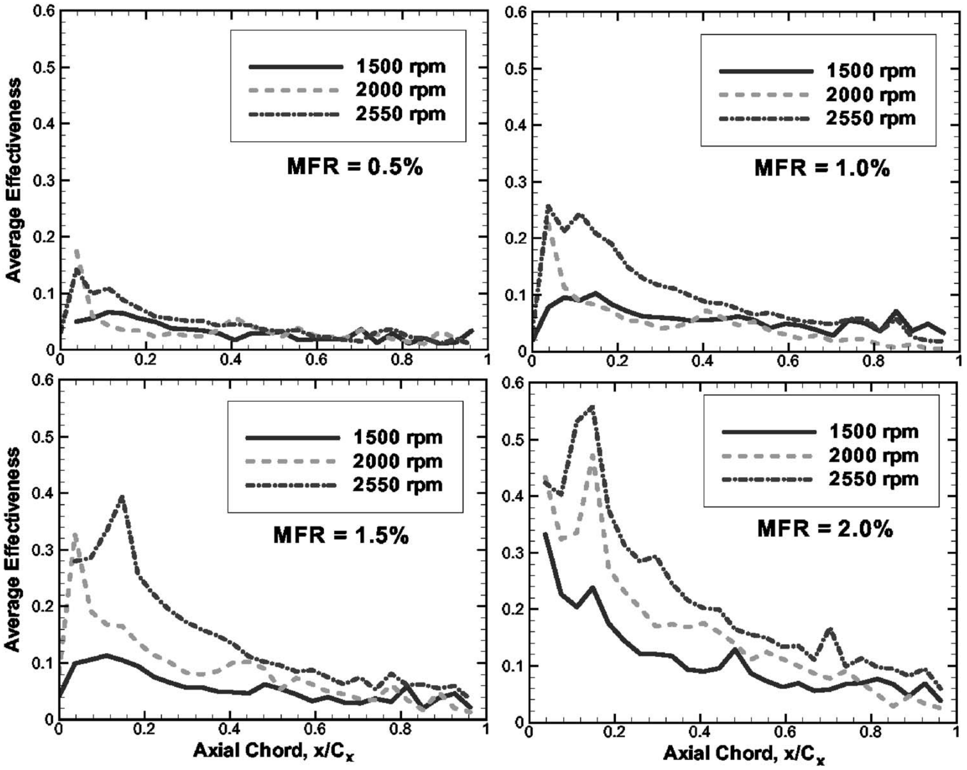

Fig. 17 Pitchwise averaged film cooling effectiveness distribution along axial chord for different mass flow ratios (turbine rotation speed effect)

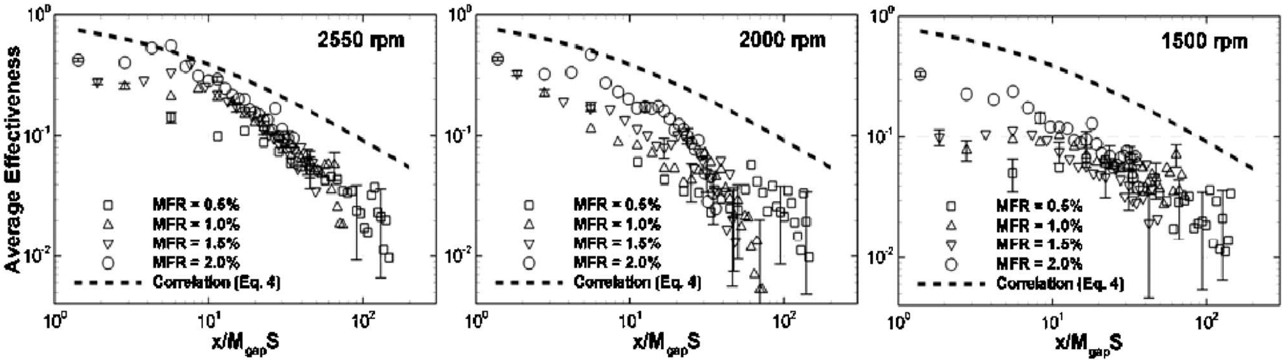

Fig. 18 Comparison of pitchwise average effectiveness with a correlation from Goldstein [48] for different rpm

correlation at $x/M_{\mathrm{gap}}S=10$ but decays rapidly due to the destructive action of the passage vortex on the coolant film. For lower rotating speeds than reference, more nonuniform pitchwise effectiveness distribution lowers the average effectiveness value with the data for 1500 rpm showing the largest deviation from the correlation.

## Conclusions

Experiments were performed for film cooling effectiveness obtained from purging of coolant through the wheelspace cavity on the first stage of a rotating platform of a three stage model turbine facility. Film cooling effectiveness results were obtained for four different coolant-to-mainstream mass flow ratios. Engine operation at reference and lower rotational speeds was investigated for all mass flow ratios. The main conclusions from this study are summarized below:

1. The new research turbine facility provides the basic features to extract information relevant to gas turbine design community. These features are: (a) stator-rotor unsteady interaction; (b) blade and platform rotation including the relative blade circulation and the exposure of the platform boundary layer to centrifugal and coriolis forces; and (c) the flow acceleration. Except for the last feature (c), none of the above features can be simulated in a cascade investigation;
2. Film cooling effectiveness due to coolant injection from the stator-rotor gap increases with increasing coolant-to-mainstream mass flow ratio;
3. Complete coverage of the passage platform cannot be obtained by using coolant injection from the stator-rotor gap. The passage vortex over the platform has an adverse impact on film adherence;
4. Film coolant traces become reoriented more toward the suction side for lower speeds than that observed for reference condition due to the stagnation region shift towards the pressure side;
5. Film cooling effectiveness decreases for lower rpm; and
6. The film cooling effectiveness on the blade platform decays much more rapidly than that observed in studies with film cooling on a flat stationary surface, primarily due to the presence of the passage vortex.

The present paper provides detailed data on film cooling on a rotating platform for the first time in open literature. By utilizing these results for film cooling, turbine researchers and designers will be better equipped with knowledge for film cooling under rotating conditions.

## Acknowledgment

This publication was prepared with the support of the U.S. Department of Energy, Office of Fossil Energy, National Energy Technology Laboratory. However, any opinions, findings, conclusions, or recommendations expressed herein are those of the authors and do not necessarily reflect the views of the DOE. Hee-Koo Moon from Solar Turbines, Inc. provided the concept of the stator-rotor gap geometry in this study.

## Nomenclature

$C$ = oxygen concentration
$C_x$ = axial chord length of the rotor blade (4.16 cm)
$D_h$ = rotor diameter at blade hub (cm)
$D_t$ = rotor diameter at blade tip (cm)
$i$ = incidence flow angle change from design point (3000 rpm) at the first stage rotor inlet
$I$ = pixel intensity for an image
$M_{\mathrm{gap}}$ = average blowing ratio $(=\rho_c V_c/\rho_m W_2)$
MFR = mass flow ratio (% of mainstream core flow)
LE = leading edge of the blade
M = Mach number
$P$ = local static pressure (Pa)
$P_{O_2}$ = partial pressure of oxygen
$r$ = degree of reaction $(=\Delta h''/(\Delta h'+\Delta h''))$
Ro = rotation number at first stage $(=U_2/W_2)$
$S$ = normal stator-rotor gap width (=2.3 mm)
$T_c$ = coolant temperature (°C)
$T_f$ = local film temperature (°C)
$T_m$ = mainstream temperature (°C)
$V_c$ = average velocity of coolant air from the stator-rotor gap (m/s)
$U$ = tangential average velocity (m/s)
$V$ = average absolute velocity of mainstream air(m/s)
$V_u$ = tangential component of absolute velocity (m/s)
$W$ = relative average velocity of mainstream air (m/s)
$x$ = axial distance from blade leading edge (cm)
$\alpha$ = absolute velocity flow angle
$\beta$ = relative velocity flow angle
$\Delta h'$ = static enthalpy difference in first stage stator
$\Delta h''$ = static enthalpy difference in first stage rotor
$\phi$ = first stage flow coefficient $(=V_{\mathrm{axial}}/U_3)$
$\lambda$ = first stage load coefficient $(=(U_2V_{u_2}+U_3V_{u_3})/U_3^2)$
$\eta$ = local film-cooling effectiveness
$\rho_c$ = density of coolant air $(\mathrm{kg/m^3})$
$\rho_m$ = density of mainstream air at first stage stator exit $(\mathrm{kg/m^3})=1.01\ \mathrm{kg/m^3}$

### Subscripts

1 = at first stage stator inlet
2 = at first stage stator exit (rotor inlet)
3 = at first stage rotor exit
air = mainstream air with air as coolant
mix = mainstream air with nitrogen as coolant
ref = reference image with no mainstream and coolant flow
blk = image without illumination (black)

### Superscript

$*$ = at lower rotating speeds than design point (3000 rpm)

## References

[1] Schobeiri, M. T., 1999, "Efficiency, Performance and Flow Measurement of Siemens-Westinghouse HP-Turbine Blades," Series 9600 and 5600, Final Report, Westinghouse.
[2] Schobeiri, M. T., Gilarranz, J. L., and Johansen, E. S., 2000, "Aerodynamic and Performance Studies of a Three Stage High Pressure Research Turbine with 3-D Blades, Design Points and Off-Design Experimental Investigations," Paper No. 2000-GT-484.
[3] Schobeiri, M. T., Suryanarayanan, A., Jermann, C., and Neuenschwander, T., 2004, "A Comparative Aerodynamic and Performance Study of a Three-Stage High Pressure Turbine With 3-D Bowed Blades and Cylindrical Blades," Paper No. GT-2004-53650.
[4] Lakshminarayana, B., 1996, *Fluid Dynamics and Heat Transfer of Turbomachinery*, Wiley, New York, NY.
[5] Schobeiri, M., 2005, *Turbomachinery Flow Physics and Dynamic Performance*, Springer-Verlag, New York, ISBN 3-540-22368-1.
[6] Langston, L. S., 1980, "Crossflows in Turbine Cascade Passage," ASME J. Eng. Power, **102**, pp. 866–874.
[7] Goldstein, R. J., and Spores, R. A., 1988, "Turbulent Transport on the Endwall in the Region Between Adjacent Turbine Blades," ASME J. Heat Transfer, **110**, pp. 862–869.
[8] Takeishi, K., Matsuura, M., Aoki, S., and Sato, T., 1990, "An Experimental Study of Heat Transfer and Film Cooling on Low Aspect Ratio Turbine Nozzles," ASME J. Turbomach., **112**, pp. 488–496.
[9] Denton, J. D., 1993, "Loss Mechanisms in Turbomachines," ASME J. Turbomach., **115**, pp. 621–656.
[10] Reid, K., Denton, J., Pullan, G., Curtis, E., and Longley, J., 2005, "The Interaction of Turbine Inter-platform Leakage Flow With the Mainstream Flow," ASME Paper No. GT2005-68151.

[11] Han, J. C., Dutta, S., and Ekkad, S. V., 2000, *Gas Turbine Heat Transfer and Cooling Technology*, Taylor & Francis, New York.

[12] Dring, R. P., Blair, M. F., and Hoslyn, H. D., 1980, “An Experimental Investigation of Film Cooling on a Turbine Rotor Blade,” ASME J. Eng. Power, **102**, pp. 81–87.

[13] Takeishi, M., Aoki, S., Sato, T., and Tsukagoshi, K., 1992, “Film Cooling on a Gas Turbine Rotor Blade,” ASME J. Turbomach., **114**, pp. 828–834.

[14] Abhari, R. S., and Epstein, A. H., 1994, “An Experimental Study of Film Cooling in a Rotating Transonic Turbine,” ASME J. Turbomach., **116**, pp. 63–70.

[15] Blair, M. F., 1994, “An Experimental Study of Heat Transfer in a Large-Scale Turbine Rotor Passage,” ASME J. Turbomach., **116**, pp. 1–13.

[16] Ahn, J., Schobeiri, M. T., Han, J. C., and Moon, H. K., 2004, “Film Cooling Effectiveness on the Leading Edge of a Rotating Turbine Blade,” Paper No. IMECE 2004-59852.

[17] Ahn, J., Schobeiri, M. T., Han, J. C., and Moon, H. K., 2005, “Film Cooling Effectiveness on the Leading Edge of a Rotating Film-Cooled Blade Using Pressure Sensitive Paint,” ASME Paper No. GT-2005-68344.

[18] Blair, M. F., 1974, “An Experimental Study of Heat Transfer and Film Cooling on Large-Scale Turbine Endwalls,” ASME J. Heat Transfer, pp. 524–529.

[19] Harasgama, S. P., and Burton, C. D., 1992, “Film Cooling Research on the Endwall of a Turbine Nozzle Guide Vane in a Short Duration Annular Cascade: Part 1—Experimental Technique and Results,” ASME J. Turbomach., **114**, pp. 734–740.

[20] Friedrichs, S., Hodson, H. P., and Dawes, W. N., 1996, “Distribution of Film-Cooling Effectiveness on a Turbine Endwall Measured Using Ammonia and Diazo Technique,” ASME J. Turbomach., **118**, pp. 613–621.

[21] Friedrichs, S., Hodson, H. P., and Dawes, W. N., 1997, “Aerodynamic Aspects of Endwall Film-Cooling,” ASME J. Turbomach., **119**, pp. 786–793.

[22] Chyu, M. K., 2001, “Heat Transfer Near Turbine Nozzle Endwall,” Ann. N.Y. Acad. Sci., **934**, pp. 27–36.

[23] Zhang, L. J., and Jaiswal, R. S., 2001, “Turbine Nozzle Endwall Film Cooling Study Using Pressure Sensitive Paint,” ASME J. Turbomach., **123**, pp. 730–738.

[24] Kost, F., and Nicklas, M., 2001, “Film-Cooled Turbine Endwall in a Transonic Flow Field: Part 1—Aerodynamic Measurements,” ASME J. Turbomach., **123**, pp. 709–719.

[25] Nicklas, M., 2001, “Film-Cooled Turbine Endwall in a Transonic Flow Field: Part 2—Heat Transfer and Film-Cooling Effectiveness,” ASME J. Turbomach., **123**, pp. 720–728.

[26] Mclean, C., Camci, C., and Glezer, B., 2001, “Mainstream Aerodynamic Effects Due to Wheelspace Coolant Injection in a High-Pressure Turbine Stage: Part I—Aerodynamic Measurements in the Stationary Frame,” ASME J. Turbomach., **123**(4), pp. 687–696.

[27] Mclean, C., Camci, C., and Glezer, B., 2001, “Mainstream Aerodynamic Effects Due to Wheelspace Coolant Injection in a High-Pressure Turbine Stage: Part 2—Aerodynamic Measurements in the Rotational Frame,” ASME J. Turbomach., **123**(4), pp. 697–703.

[28] Oke, R. A., Simon, T. W., Burd, S. W., and Wahlberg, R., 2000, “Measurements in a Turbine Cascade over a Contoured Endwall: Discrete Hole Injection of Bleed Flow,” ASME Paper No. 2000-GT-214.

[29] Oke, R. A., Simon, T. W., Shih, T., Zhu, B., Ling, Y. L., and Chyu, M., 2001, “Measurements Over a Film-Cooled Contoured Endwall With Various Injection Rates,” Paper No. 2001-GT-140.

[30] Oke, R. A., and Simon, T. W., 2002, “Film Cooling Experiments With Flow Introduced Upstream of a First Stage Nozzle Guide Vane Through Slots of Various Geometries,” ASME Paper No. GT-2002-30169.

[31] Knost, D. G., and Thole, K. A., 2004, “Adiabatic Effectiveness Measurements of Endwall Film-Cooling for a First Stage Vane,” ASME Paper No. GT-2004-53326.

[32] Zhang, L., and Moon, H. K., 2003, “Turbine Nozzle Endwall Inlet Film Cooling—The Effect of a Back-Facing Step,” ASME Paper No. GT-2003-38319.

[33] Piggush, J. D., and Simon, T. W., 2005, “Flow Measurements in a First Stage Nozzle Cascade Having Endwall Contouring, Leakage and Assembly Features,” ASME Paper No. GT-2005-68340.

[34] Cardwell, N. D., Sundaram, N., and Thole, K. A., 2005, “Effects of Mid-Passage Gap, Endwall Misalignment and Roughness on Endwall Film-Cooling,” ASME Paper No. GT-2005-68900.

[35] Barigozzi, G., Benzoni, G., Franchini, G., and Perdichizzi, A., 2005, “Fan-Shaped Hole Effects on the Aero-Thermal Performance of a Film Cooled Endwall,” ASME Paper No. GT-2005-68544.

[36] Wright, L. M., Gao, Z., Varvel, T. A., and Han, J. C., 2005, “Assessment of Steady State PSP, TSP and IR Measurement Techniques for Flat Plate Film Cooling,” ASME Paper No. HT-2005-72363.

[37] Gao, Z., Wright, L. M., and Han, J. C., 2005, “Assessment of Steady State PSP and Transient IR Measurement Techniques for Leading Edge Film Cooling,” ASME Paper No. IMECE-2005-80146.

[38] Ahn, J., Mhetras, S. P., and Han, J. C., 2004, “Film-Cooling Effectiveness on a Gas Turbine Blade Tip,” ASME Paper No. GT-2004-53249.

[39] Mhetras, S. M., Yang, H., Gao, Z., and Han, J. C., 2005, “Film Cooling Effectiveness on Squealer Rim Walls and Squealer Cavity Floor of a Gas Turbine Blade Tip Using Pressure Sensitive Paint,” ASME Paper No. GT-2005-68387.

[40] Schobeiri, M. T., 1989, “Optimum Trailing Edge Ejection for Cooled Gas Turbine Blades,” ASME J. Turbomach., **111**(4), pp. 510–514.

[41] Schobeiri, M. T., and Pappu, K., 1999, “Optimization of Trailing Edge Ejection Mixing Losses Downstream of Cooled Turbine Blades: A Theoretical and Experimental Study,” ASME J. Fluids Eng., **121**, pp. 118–125.

[42] McLachlan, B., and Bell, J., 1995, “Pressure-Sensitive Paint in Aerodynamic Testing,” Exp. Therm. Fluid Sci., **10**, pp. 470–485.

[43] Coleman, H. W., and Steele, W. G., 1989, *Experimentation and Uncertainty Analysis for Engineers*, Wiley, New York.

[44] Goldstein, R. J., 1971, “Film Cooling,” Adv. Heat Transfer, **7**, pp. 321–379.

**D. R. Sabatino**
Aerodynamics United Technologies Research Center,
411 Silver Lane, MS 129-73,
East Hartford, CT 06108

**C. R. Smith**
Department of Mechanical Engineering,
Lehigh University,
19 Memorial Drive West,
Bethlehem, PA 18015

# Boundary Layer Influence on the Unsteady Horseshoe Vortex Flow and Surface Heat Transfer

*The spatial-temporal flow field and associated surface heat transfer within the leading edge, end-wall region of a bluff body were examined using both particle image velocimetry and thermochromic liquid crystal temperature measurements. The horseshoe vortex system in the end-wall region is mechanistically linked to the upstream boundary layer unsteadiness. Hairpin vortex packets, associated with turbulent boundary layer bursting behavior, amalgamate with the horseshoe vortex resulting in unsteady strengthening and streamwise motion. The horseshoe vortex unsteadiness exhibits two different natural frequencies: one associated with the transient motion of the horseshoe vortex and the other with the transient surface heat transfer. Comparable unsteadiness occurs in the end-wall region of the more complex airfoil geometry of a linear turbine cascade. To directly compare the horseshoe vortex behavior around a turning airfoil to that of a simple bluff body, a length scale based on the maximum airfoil thickness is proposed.*

[DOI: 10.1115/1.2813001]

## Introduction

An end-wall juncture flow develops when an impinging boundary layer encounters a bluff body protruding from a surface with a developing boundary layer. The body-imposed adverse pressure gradient causes the boundary layer to separate and form a leading edge, or horseshoe, vortex system. The resulting aerodynamic losses and elevated heat transfer continue to drive research to minimize these effects (Han and Goldstein [1]; Zess and Thole [2]).

The most important flow structures in the horseshoe vortex (HV) system are represented in Fig. 1 (Praisner and Smith [3]; Ishii and Honami [4]; Agui and Andreopoulos [5]; Hunt et al. [6]). The figure shows that the most prominent feature on the symmetry plane is the large HV. The rotational sense of the HV is a result of the reorganization of the boundary layer vorticity into a coherent vortex structure. A secondary vortex (SV), generated by the viscous interaction between the HV and the near-wall fluid, is located just upstream of the HV and is significantly smaller. Farthest upstream from the bluff body is a tertiary vortex (TV) and, finally, the smallest vortex present is in the very near corner region.

Devenport and Simpson [7] were among the first to investigate the transient behavior of the HV. Probability density functions (PDFs) of the local velocity fluctuations near the HV indicated a bimodal distribution of the vortex streamwise position. The two different peaks suggested that the HV system might switch between two different stable modes. One mode indicates a large negative *u* velocity occurring directly beneath the HV, while the second mode suggests a near-zero streamwise velocity beneath the HV. The authors indicate that the near-zero mode is detected between 20% and 30% of the time and manually established the time between the change in modes from the velocity traces. Devenport and Simpson suggested that there might be a correlation between the energetic frequencies of the impinging turbulent boundary layer and the switching of the HV modes.

Agui and Andreopoulos [5] recorded the time-dependent surface pressure on the end-wall upstream of a cylinder in an impinging wind tunnel boundary layer. The dominant frequency of the pressure fluctuations was established by performing an autocorrelation on the pressure time traces. They compared the period of the HV activity to that of the bursting period within a typical turbulent boundary layer but did not find strong agreement. Agui and Andreopoulos hypothesized that the turbulent boundary layer plays an integral role in the periodic behavior of the HV, but vortex merging within the turbulent boundary layer upstream of the saddle point (see Fig. 1) may change the time scales measured near the HV.

Praisner and Smith [8] determined that the mode switching described by Devenport and Simpson [7] was due to vortex-induced surface fluid exchange. Praisner and Smith [8] observed that the ejection of the SV created a sharp increase in local surface heat transfer. Additionally, they determined that the unsteadiness of the HV was connected to the bursting frequency of the impinging turbulent boundary layer. Turbulent boundary "bursts" refer to events wherein near-wall fluid erupts or bursts from the surface quasiperiodically (Kline et al. [9]; Smith [10]). Adrian et al. [11] suggested that these events are a result of passing "packets" of hairpin-type vortices that are present within the boundary layer. The hairpin name refers to the resemblance of these vortices to an actual hairpin, as shown in Fig. 2 (Head and Bandyopadhyay [12]; Hairdari and Smith [13]).

The present study seeks to strengthen the understanding of the physical mechanisms that appear to connect the turbulent boundary layer with the HV system unsteadiness. Additionally, the study examines whether the mechanisms and scaling found to apply to a simple streamlined cylinder end-wall flow are equally valid when applied to a more representative linear turbine cascade.

## Experimental Arrangement

The experiments were conducted in a closed-circuit, free-surface water channel. The channel includes a 1.75:1 contraction and can achieve flow speeds of 0.01–0.4 m/s with ±2% spanwise uniformity and has a maximum turbulence intensity of 0.1%. Additional details are described by Sabatino [14]. A streamlined cylinder was used to create a HV system (Fig. 3). The cylinder had a diameter of 15.08 cm and a 5:1 trailing edge taper to eliminate shedding. The turbulent boundary layer was generated using a 3 mm threaded rod boundary layer trip placed 9 cm from the

---

Contributed by the International Gas Turbine Institute of ASME for publication in the Journal of Turbomachinery. Manuscript received June 19, 2007; final manuscript received August 24, 2007; published online November 6, 2008. Review conducted by David Wisler. Paper presented at the ASME Turbo Expo 2007: Land, Sea and Air (GT2007), Montreal, Quebec, Canada, May 14–17, 2007.

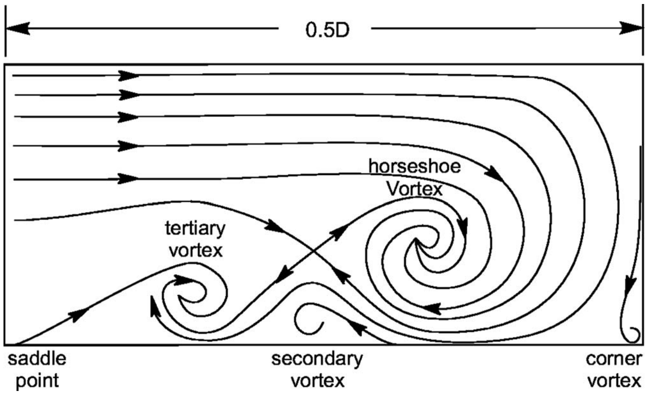

**Fig. 1 Schematic representation of typical time-mean symmetry plane streamlines for a horseshoe vortex system**

leading edge of the flat plate. The leading edge of the cylinder was 204 cm downstream of the leading edge of the plate.

The flow field upstream of the cylinder was recorded using a high-image-density digital particle image velocimetry (DPIV) system (Adrian [15]; Rockwell et al. [16]). The PIV and DPIV measurement uncertainty is $\pm 2\%$ and $\pm 5\%$, respectively (Praisner et al. [17]; Sabatino [14]). Surface heat transfer measurements were recorded using liquid crystal thermography. Figure 3 shows the experimental arrangement with the cylinder located on top of a liquid crystal (LC) test section. The test section consists of a thin (51 $\mu$m) stainless steel foil stretched across a sealed, air-filled cavity. The enlarged view, shown in Fig. 3, clarifies shows that the coating on the undersurface of the stainless steel foil is comprised of a layer of black paint (15 $\mu$m) and microencapsulated LCs (40 $\mu$m), which change color with temperature. The test section is manufactured from acrylic, allowing the nonflow surface of the stainless steel sheet to be viewed from below. Using a dc electrical current, the stainless steel creates a constant heat flux surface and the LCs are used to measure the surface temperature and ultimately provide essentially instantaneous surface heat transfer data with frequency response better than 30 Hz (Praisner [17]). The hue, or primary wavelength of reflected light, of the LCs is carefully calibrated to temperature across the entire LC coated surface. The resulting heat transfer distributions are ultimately represented as nondimensionalized local heat transfer coefficients in the form of the Stanton number. The Stanton number uncertainty varies between $\pm 3.7\%$ and $\pm 7.9\%$ as a function of surface temperature (Sabatino et al. [18]). Quantitative data were recorded using a 35mm film camera with a record length of 36 frames. Longer sequences were obtained using a digital camera, which allowed the extended observation of the spatial-temporal heat transfer patterns revealed by the LCs.

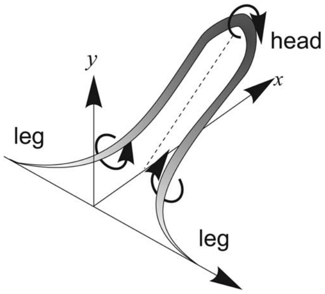

**Fig. 2 Idealized hairpin vortex model after Adrian et al. [11] and Haidari and Smith [13]**

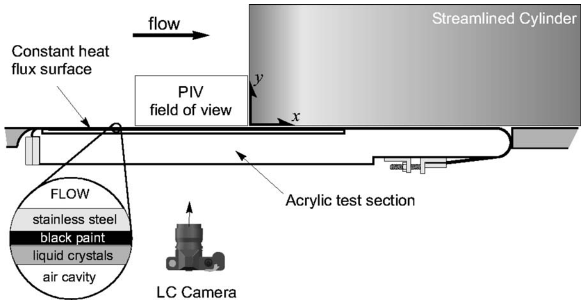

**Fig. 3 Plan view of LC test section with a streamlined cylinder**

**Table 1 Linear cascade geometry**

| | |
|---|---|
| Axial chord ($C$) | 10.06 cm |
| True chord | 10.78 cm |
| Leading edge diameter | 1.27 cm |
| Trailing edge diameter | 0.318 cm |
| Turning angle | 94 deg |

In addition to studies using a streamlined cylinder, the HV system behavior was also examined in conditions that more closely approximate turbomachinery applications. A linear turbine cascade, representative of a first stage high-pressure gas turbine, was also examined. The airfoils were manufactured from acrylic, and the details of their geometry are listed in Table 1. The cascade arrangement within the water channel is shown in Fig. 4.

## Results

**Streamlined Cylinder.** To investigate the relationship between the bursting events within a turbulent boundary layer and the unsteadiness of the HV, high-density film-based PIV was employed over a field of view of approximately one cylinder diameter upstream of the cylinder to capture both the HV system and the impinging boundary layer. The undisturbed boundary layer conditions were $\mathrm{Re}_\theta \cong 900$, $\mathrm{Re}_D = 1.9 \times 10^4$, and $\delta = 7.8$ cm with a heat flux of 6.9–7.9 kW/m$^2$. Heating was initiated 21 cm ($x/D = -1.4$) upstream of the leading edge of the cylinder. Figure 5 shows a typical temporal sequence, recorded at 5 frames/s, of the vorticity behavior upstream of the tapered cylinder. Vorticity contours of $-3.5$ s$^{-1}$ are shown to aid in identifying vortical structures of interest. The dashed lines shown in Figs. 5($a$) and 5($b$) indicate previous temporal locations of selected isovorticity contours, which help illustrate the temporal transport of the vorticity concentrations.

Figure 5($a$) indicates that the HV vortex is located at approximately $x/D = -0.14$, indicated by the strong concentration of nega-

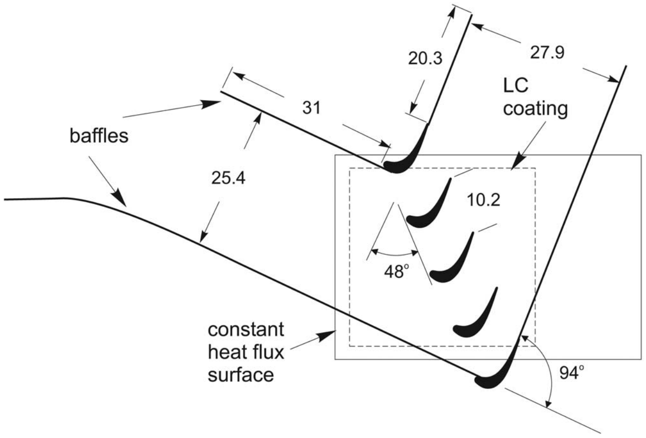

**Fig. 4 Plan view of linear cascade. All units are in cm.**

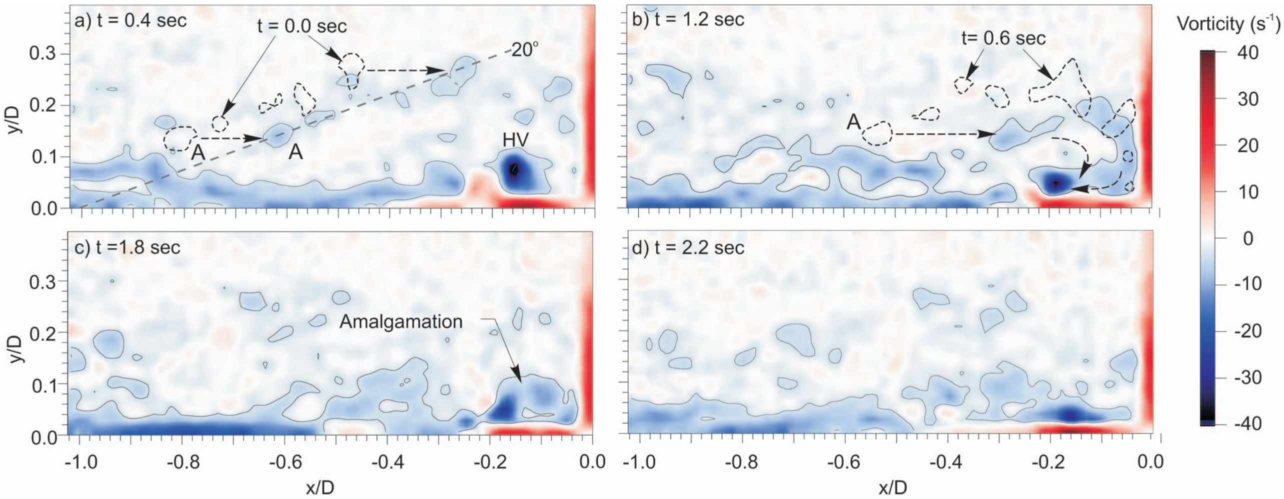

**Fig. 5** **Symmetry plane vorticity upstream of a streamlined cylinder ($q''=7.9$ kW/m$^2$). Isovorticity contours are shown for $\omega$ =3.5 s$^{-1}$.**

tive (blue) vorticity. A cluster of weakly negative vortical structures inclined to the surface is clearly visible for $t=0.4$ s (with their previous locations at $t=0.0$ s indicated by the dotted contours). As suggested by the findings of Smith [10] and Adrian et al. [11], these vortical structures are most likely the "heads" of hairpinlike structures that previously lifted from the surface and "ejected" into the impinging turbulent boundary layer as it approached the cylinder. These structures are inclined to the surface at an angle of approximately 20 deg, comparable to the observations of Adrian et al. [11], where they detected packets of hairpins within a turbulent boundary layer with their heads describing a line angled at 3–35 deg from the surface. Note that as these vortical structures advect downstream they remain in a roughly organized pattern until they impinge upon the cylinder surface. Figures 5(*b*) and 5(*c*) illustrate how the far-stream vorticity appears to impinge, amalgamate, and merge into the corner region. During this amalgamation process, this vorticity-bearing, higher-momentum fluid impinges on, and then moves down the cylinder surface, eventually turning upstream as it nears the end wall, and subsequently amalgamating with the HV vortex.

Note, in particular, the temporal behavior of the individual vortical structure, labeled A, as shown in Figs. 5(*a*) and 5(*b*). As this region of vorticity impinges upon the cylinder surface, Structure A moves just above the HV, as shown in Fig. 5(*b*). By $t=1.8$ s (Fig. 5(*c*)), the vortical structures that impinged on the cylinder have been carried down the cylinder face and back toward the HV. During this process, the vorticity comprising Structure A never reaches the cylinder but (as indicated by the arrow) is swept rapidly toward the end-wall surface and amalgamates with the HV due to its close proximity to the HV core.

The last image, Fig. 5(*d*), indicates a dramatic change in the HV due to the amalgamation with this impinging vorticity. Indeed, the subsequent results following Fig. 5(*d*) (not shown) indicate that following the amalgamation process, the HV moves both closer to the end-wall surface and upstream. The behavior documented in Fig. 5 is consistent with the behavior expected of a vortex of increased strength and proximity to the intersecting dual-wall surface, as characteristic of a junction flow (Doligalski et al. [19]). To better understand the spatial/temporal behavior of the HV, a two-dimensional probability distribution was generated of the $x$ and $y$ positions of the HV. The center of the vortex was assumed to be at the position of the peak negative vorticity. The position of the HV at any one coordinate is shown as a percentage of the total record (300 digital images) in Fig. 6. The symmetry plane behavior shown in Fig. 6(*a*) exhibits a bimodal distribution. Integrating over each region indicated that the smaller peak ($x/D=-0.125$) accounted for 20% of the HV motion. This corresponds well with the probability of the "secondary mode" discussed by Devenport and Simpson [7], as well as Praisner and Smith [8]. The behavior of the HV in a plane rotated 10 deg from the symmetry plane (Fig. 6(*b*)) indicates that the motion of the HV is considerably more restricted than on the symmetry plane. It is possible that the vortex stretching combined with the oblique angle to the structures within the impinging turbulent boundary layer may mitigate the HV bimodal behavior away from the symmetry plane.

To support the flow field observations, the heat transfer and flow field data were transformed into the frequency domain by means of an autocorrelation technique. The technique employed will be described using the instantaneous heat transfer as the example. Figure 7 shows a typical instantaneous surface heat transfer pattern around the streamlined cylinder. The pattern in Fig. 7 suggests that the highest heat transfer occurs immediately upstream of the cylinder (primary band) and is the result of cooler impinging far-field fluid, which washes down the face of the cylinder (the region of the corner vortex shown in Fig. 1).

Praisner and Smith [8] established that the secondary band of elevated heat transfer, farther upstream of the corner region, is the result of the periodic ejection of the SV, followed by the subse-

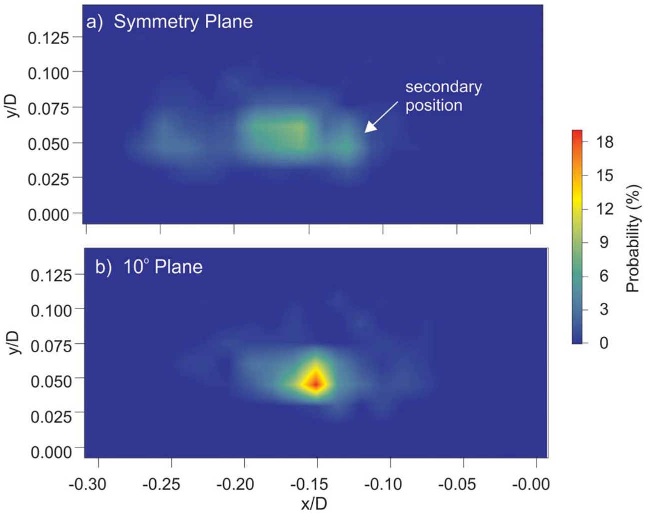

**Fig. 6** **PDFs for the HV position on the symmetry and 10 deg plane**

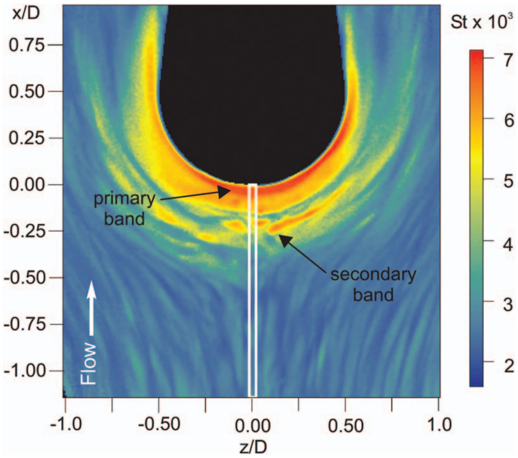

**Fig. 7 Instantaneous surface heat transfer upstream of a streamlined cylinder for $q''=6.9$ kW/m$^2$**

quent inrush of cooler far-field fluid. The periodicity of this ejection and inrush behavior, as well as its connection to the HV, is the focus of this examination. Figures 8(*a*) and 8(*b*) schematically illustrate the process by which quantitative temporal and spatial frequency information is established using a sequence of LC temperature patterns. The figure shows that a column of data on the symmetry plane upstream of the streamlined cylinder is extracted from each instantaneous image (i.e., the white outlined region in Fig. 7). The extracted columns of data for a sequence of images are then combined to create a spatial-temporal image of the Stanton number behavior on the symmetry plane. A two-dimensional autocorrelation is then performed on this temporal sequence over a spatial region of interest to establish the dominant period within the collective spatial-temporal pattern (Fig. 8(*b*)).

Figure 9(*a*) is a temporal sequence of 300 centerline hue images taken at 10 frames/s, which were extracted from a video sequence of the LC surface. No calibration was performed to convert the hue to temperature since only frequency information was of interest. Since hue is monotonic with temperature, the cooler surface temperatures are represented by blue and the warmer temperatures by red. These patterns are directly analogous to surface heat transfer. The outlined region was used to generate the subsequent autocorrelation, since this region lies directly below the HV and SV. The time scale is represented in wall units, which are based on the experimentally measured shear stress. A Clauser fit (Clauser [20]) of PIV velocity data was used to estimate the surface shear stress. The temporal resolution of the data presented in Fig. 9 is $3.34t^+$. Note that at $x/D=-0.25$ in Fig. 9(*a*), an undulating pattern of cooler (blue) temperatures appears, which is believed to be the effect of the periodic ejection of the SV.

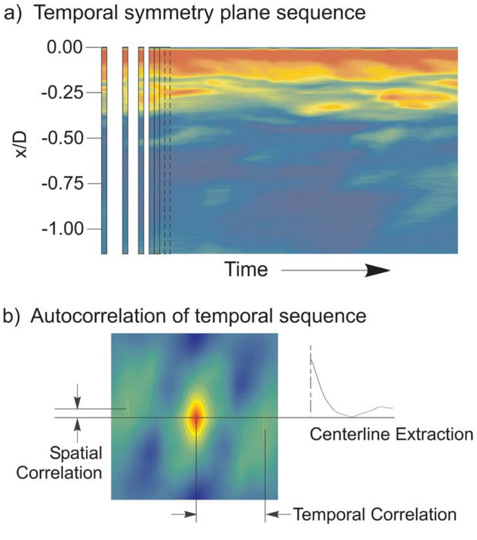

**Fig. 8 (*a*) Temporal record of symmetry plane surface heat transfer data. (*b*) Typical autocorrelation and interpretation of peak locations from temporal sequence.**

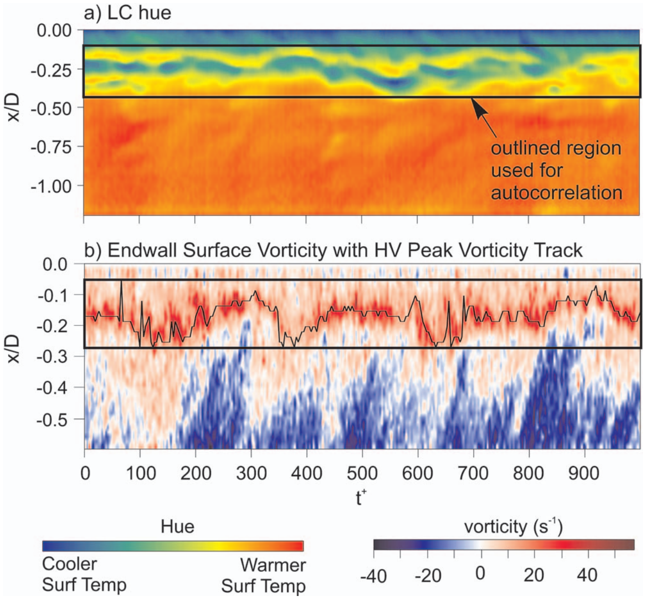

**Fig. 9 (*a*) End-wall surface heat transfer temporal behavior as captured by the LC hue. (*b*) End-wall surface vorticity and HV position.**

Vorticity on the end-wall surface, established from symmetry plane DPIV data, was extracted from 300 frames of DPIV data recorded at 10 frames/s using the same process described in Figs. 7 and 8. The complete temporal vorticity sequence is shown in Fig. 9(*b*); however, it was not recorded simultaneously with the data in Fig. 9(*a*). The region used for the autocorrelation of the end-wall surface vorticity is again outlined. Note that the line plot superimposed in Fig. 9(*b*) is the position of the HV as determined by the location of the peak negative vorticity, established from the same symmetry plane DPIV sequence. The figure shows a clear correlation between the HV position and the surface vorticity. It was determined that the temporal HV position provided much more distinct autocorrelation results and is subsequently used to reflect the periodicity of the HV. Figure 9(*b*) also shows a distinct pattern of incursion of negative vorticity (blue region) upstream of the HV that appears to correlate with the motion of the HV. This penetration of strongly negative vorticity toward the cylinder appears to precede the movement of the HV toward the cylinder. However, it is not clear if this surge in negative vorticity is a result of a weakening HV or a strengthening of the boundary layer associated with the approach of a hairpin packet.

Figure 10 shows the centerline extractions of the autocorrelations for both data sets presented in Fig. 9. Arrows mark the first peak in the autocorrelation that is greater than zero, which is representative of the dominant period. The data of Fig. 10 suggest two possible dominant frequencies of the HV system. The surface heat transfer (via LC hue) shows a peak between $150<t^+<200$, while the HV position data display a peak at $t^+=260$. These results indicate that the heat transfer unsteadiness reflects a markedly *higher* frequency than the motion of the HV. Note that the surface heat transfer patterns evident in Fig. 9(*a*) are presumed to be a result of the ejection of the SV into the far-field due to the interaction between the HV and the SV. Praisner and Smith [8] indi-

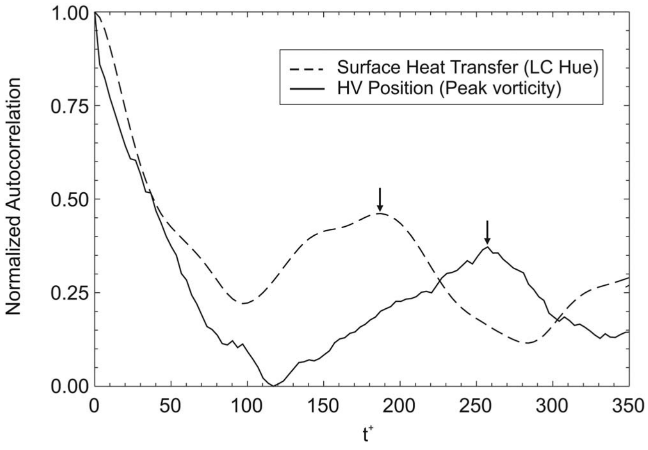

**Fig. 10 Normalized autocorrelations of surface heat transfer and HV position**

cated that the ejection of the SV was often preceded by the movement of the HV upstream and closer to the surface. Careful visual observation of the DPIV temporal vorticity field confirms that when the HV is strengthened and moves upstream (see Fig. 5), there may be *several* ejections of the SV vortex over one transient period of the HV. This increased SV vortex ejection frequency correlates with the higher surface heat transfer frequency shown in Fig. 10, supporting the hypothesis that the ejections cause the transient spikes in surface heat transfer.

To quantitatively compare these results to the bursting period of a turbulent boundary, the bursting frequency for the undisturbed base flow was experimentally established. Detecting turbulent boundary layer bursts is certainly difficult and the most effective method for detection is subject for debate. Different techniques have been developed (Blackwelder and Kaplan [21]; Lu and Smith [22]) but are quite sensitive to arbitrarily adjustable parameters. The present study applied the same autocorrelation technique used for the turbulent juncture flow to the impinging turbulent boundary layer using the surface vorticity as the indicator of the bursting or "active" events.

An autocorrelation of the surface vorticity at a single streamwise location was used to establish the dominant bursting frequency, employing the assumption that bursts are characterized by regions of significantly increased vorticity (Sabatino [14]). Using this approach, the dominant bursting period was determined to be $150 < t^+ < 250$, which is consistent with previous studies (Blackwelder and Haritonidis [23]; Lu and Smith [22]). Reexamining Fig. 10 indicates that both the surface heat transfer and HV position autocorrelation results are also consistent with the experimentally established bursting period for the impinging turbulent boundary layer.

We note that Praisner and Smith [8] established a period of $100t^+$ for the HV system behavior using techniques similar to the current study. However, the $t^+$ units are sensitive to the estimation of shear stress at the surface. Also, the longer time record in the current study is believed to allow for more accurate assessment of the HV motion.

**Linear Cascade.** The time-mean end-wall surface heat transfer behavior within a linear cascade was examined for similarities to the streamlined cylinder at comparable Reynolds numbers. Measurements were recorded for the flow conditions listed in Table 2. The surface shear velocity was experimentally estimated as described below.

Time-mean end-wall surface heat transfer for $\mathrm{Re}_C = 1.50 \times 10^4$, as established from 36 frames recorded at 5 frames/s, is shown in Fig. 11. Examining the heat transfer patterns upstream of Airfoil C, it is seen that the patterns are similar to those observed for the streamlined cylinder. There is a primary band of elevated heat transfer very near the leading edge of the airfoils, which is a result of the downwash and presence of a corner vortex. A secondary band of heat transfer is also present and most visible at the leading edge of Airfoil C. Also, the legs of the HV can be seen to form the passage vortex between the pressure and suction side of adjacent airfoils. Note that Airfoil C was used for the subsequent quantitative analysis of the HV behavior because of tip leakage flow that occurred around Airfoil B, which is evidenced by the notably smaller band of elevated heat transfer adjacent to the leading edge.

**Table 2 Linear cascade operating conditions**

| $U_\infty$ (m/s) | $\mathrm{Re}_C$ | $u_\tau$ (m/s)[a] | $q''$ (kW/m$^2$) |
|---|---|---|---|
| 0.122 | $1.50 \times 10^4$ | $5.97 \times 10^{-3}$ | 9.1 |
| 0.180 | $2.18 \times 10^4$ | $6.60 \times 10^{-3}$ | 9.1 |

[a] Estimated from the measured turbulent boundary layer streak spacing.

Figure 12(*a*) shows the time-averaged heat transfer along the symmetry plane at the leading edge of Airfoil C versus $x/C$, where $C$ is the airfoil chord. The symmetry plane Stanton number behavior for the tapered cylinder is also shown for comparison (plotted versus $x/D$). The peak Stanton number for the linear cascade is about $8 \times 10^{-3}$, which is approximately six times greater than that for the impinging turbulent boundary layer. This ratio is in agreement with that of Goldstein and Spores [24], who measured the end-wall mass transfer characteristics by means of a time-averaged napthalene sublimation technique. Additionally, Goldstein and Spores show a secondary peak located at approximately $x/C = -0.075$. This is similar to the current data, which indicate a secondary peak at $x/C = -0.1$ in Fig. 12(*a*).

Comparing the linear cascade to the streamlined cylinder, it is seen that the peak magnitude of the heat transfer is comparable. However, there is a significant difference between the nondimensional location of the secondary peak, which suggests that the

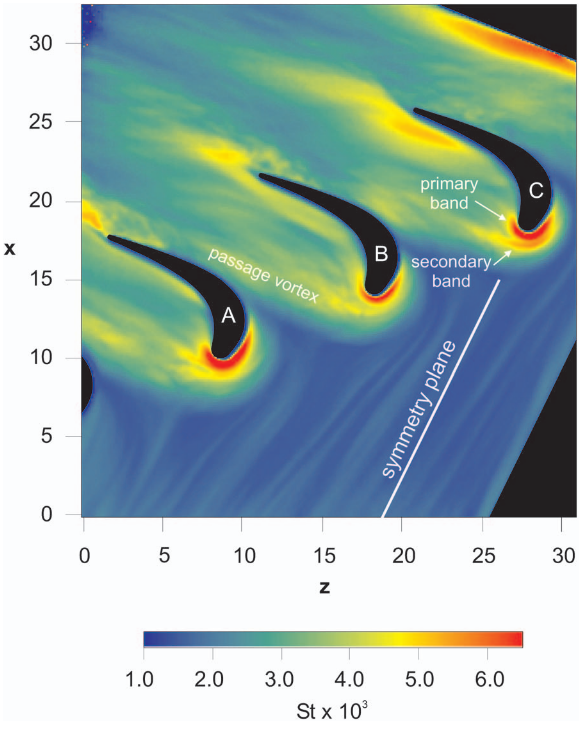

**Fig. 11 Time-mean end-wall heat transfer for $\mathrm{Re}_C = 1.50 \times 10^4$. All units are in cm.**

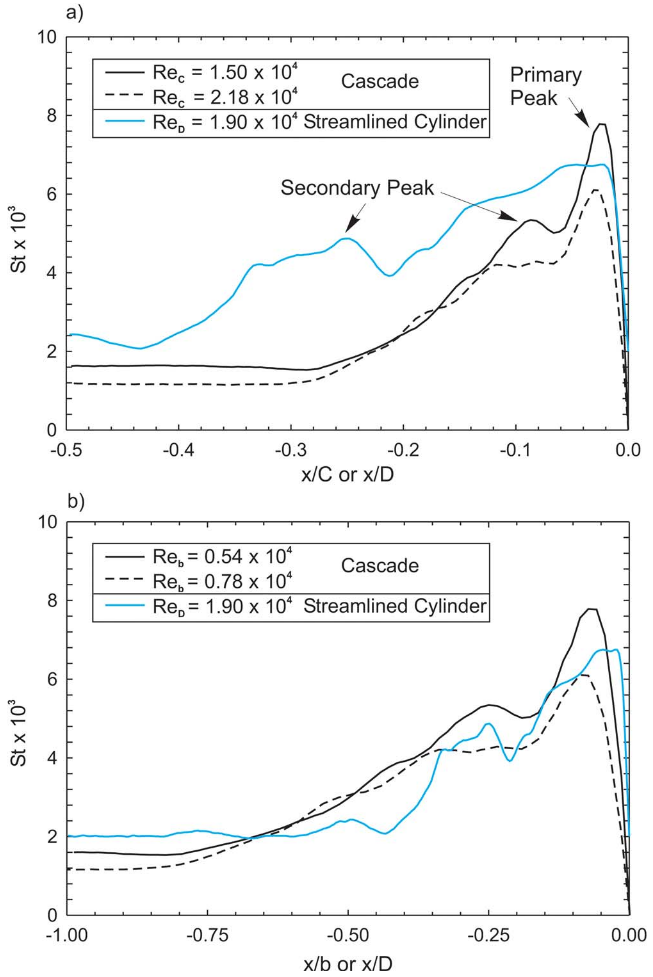

**Fig. 12 Time-mean end-wall surface heat transfer along the symmetry plane upstream of the linear cascade and streamlined cylinder. Streamlined cylinder data are plotted versus $x/D$. Turbine airfoil is plotted versus (*a*) axial chord and (*b*) maximum thickness $b$.**

axial chord is not of comparable length scale to the streamlined cylinder diameter. Therefore, several alternate length scales were investigated to determine a more appropriate length scaling including the leading edge diameter. However, the flow turning appears to create a HV system that is comparable to a HV upstream of a bluff body much larger than the leading edge diameter of the airfoil. This effect is illustrated by the diameter of the green patterns around the leading edge of the airfoils in Fig. 11.

It is hypothesized that a physical characteristic of the airfoil can be used to represent an "effective diameter" that would better account for the influence of the flow turning on the scale of the HV. The maximum thickness of the airfoil, $b$, was found to provide the best agreement of heat transfer peak locations between the airfoil and the streamlined cylinder. The maximum thickness is defined as the maximum normal distance between the true chord line and the suction surface (3.60 cm for these airfoils). Figure 12(*b*) shows the same symmetry plane surface heat transfer scaled using the maximum thickness. Note that the tapered cylinder is still plotted versus $x/D$. Using this alternative scaling, Fig. 12(*b*) illustrates that the magnitude and trend of the cylinder and linear cascade data are markedly similar.

Figure 12(*b*) also shows that the peak Stanton number diminishes and the secondary peak becomes less distinct with increasing Reynolds number. In general, the Stanton number decreases because the velocity term in the denominator is increasing. However, the lack of a secondary peak at high Reynolds numbers may be the result of the fixed temporal resolution of the data acquisition system. The secondary peak is believed to be due to transient ejections of the SV, which increase in frequency with increasing velocity. The fixed sampling frequency (5 frames/s) and record length (36 frames) of the current data likely mitigated the capture of the cumulative effects of these transient events at the higher velocity (i.e., Reynolds number).

When based on the maximum thickness, the Reynolds number for the airfoils is significantly lower than that for the streamlined cylinder (Fig. 12(*b*)). However, both Praisner [25] and Ballio et al. [26] found that the streamwise position of the HV system was weakly dependent on the Reynolds number. Praisner's results suggest that the difference in Reynolds number between the cascade and streamlined cylinder shown would shift the location of the secondary heat transfer peak by less than 10% or $0.03(x/b)$. Such a small shift does not impact the comparison or conclusions presented here.

A temporal sequence of instantaneous surface heat transfer for $\mathrm{Re}_C = 1.50 \times 10^4$ is shown in Fig. 13. At $t=0$ s, the heat transfer at the leading edge of Airfoil C is approximately five times greater than that for the impinging boundary layer. Between $t=2.65$ s. and 3.30 s, a prominent secondary band of heat transfer develops near the leading edge of Airfoil C, as indicated by the white arrows. The elevated band of heat transfer nearest the blade is due to the downwash events along the surface of the airfoil. The secondary band, which develops at $t=2.64$ s, is indicative of a significant increase in heat transfer due to the ejection of the SV and subsequent replacement by cooler far-field fluid, as described by Praisner and Smith [8] for a tapered cylinder juncture flow.

Besides the leading edge HV, the turbine cascade displays several additional features not present with the tapered cylinder flow. The leg of the HV, or passage vortex (labeled at $t=0$ s), generates a consistently elevated heat transfer region, which is approximately five times that of the turbulent boundary layer. However, the strong periodic nature of the HV at the leading edge of Airfoil C does not appear to strongly influence the temporal behavior of the passage vortex.

Also, note that at $t=1.32$ s, a region of high heat transfer develops along the trailing pressure side edge of Airfoil C (indicated by the white arrow). An examination of the complete 36 frames of data sequence suggests that the heat transfer within this trailing edge pressure region also behaves quasiperiodically. The time-mean results of Goldstein and Spores [24] also indicate an elevated region of heat transfer near the trailing pressure side region of their airfoil model. However, it is unclear how, or if, the corner vortices that are believed to occupy this region could be responsible for this transient behavior.

To properly quantify the HV system periodicity within the linear cascade requires the determination of appropriate turbulent boundary layer statistics to allow nondimensionalization of the results. However, the experimental arrangement made it difficult to accurately establish the wall shear stress via PIV, as was done for the streamlined cylinder.

Therefore, the shear velocity was inferred from the surface heat transfer data by measuring the low-speed streak spacing. Examining the instantaneous surface heat transfer patterns well upstream of the leading edge of the airfoils and assuming a typical streak spacing of $\lambda^+=100$ (Kline et al. [27]; Smith [10]), the wall shear velocity was estimated by direct measurement of the physical streak spacing. The average space between streaks was established from approximately five instantaneous heat transfer images using the autocorrelation technique described earlier. The shear velocity was then calculated from Eq. (1). Table 2 lists the estimated shear velocities for each operating condition.

$$\lambda^+ = \frac{z u_\tau}{\nu} \tag{1}$$

Symmetry plane autocorrelations, determined from the linear

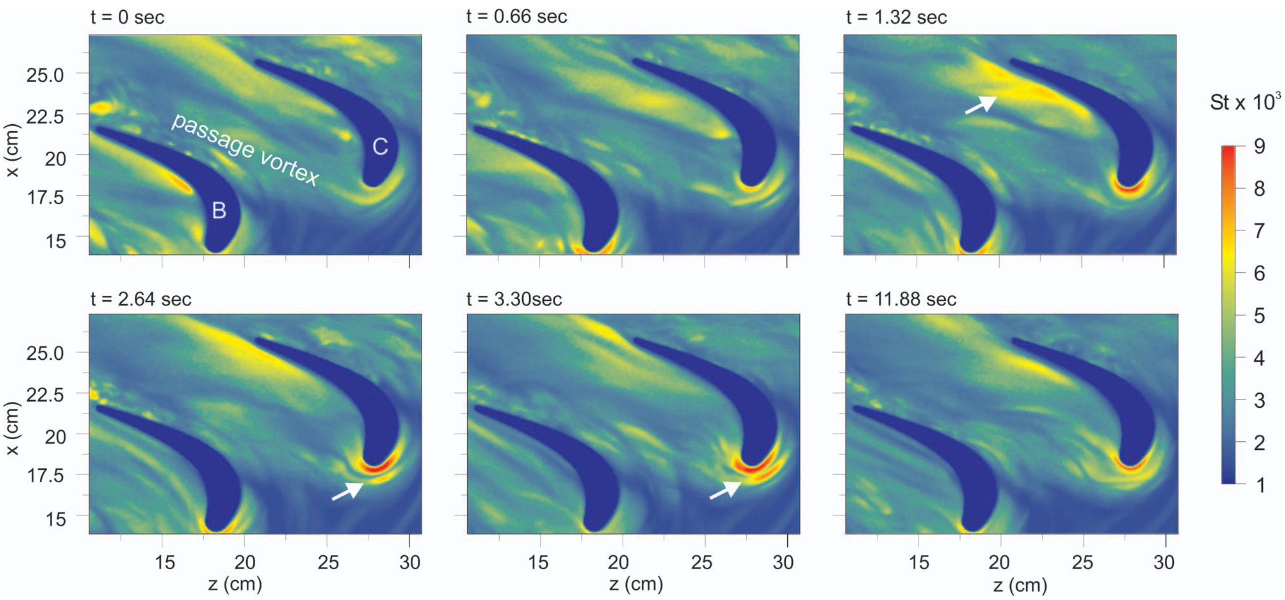

**Fig. 13 Temporal sequence of instantaneous surface heat transfer in a linear turbine cascade. $Re_C=1.50\times 10^4$.**

cascade surface heat transfer data, are shown in Fig. 14. Both cases suggest a correlation peak near $200t^+$. For $Re_C=2.18\times 10^4$, the peak is significantly more distributed than the lower speed case. This is because the temporal resolution of the LC data is reduced (in boundary layer units) with increasing Reynolds number. The temporal heat transfer behavior on the pressure side trailing edge of the airfoil was also examined for periodicity. However, the autocorrelations of the film-based surface heat transfer data proved inconclusive despite clear visual evidence of a quasi-periodicity.

## Conclusions

The data presented in this paper support the hypothesis that the temporal behavior of the HV system is driven by the temporal characteristics of the impinging turbulent boundary layer. Specifically, symmetry plane data suggest that the boundary layer influences the HV by means of “hairpin vortex packets,” which interact with the HV, causing it to strengthen and modify its streamwise position. This change in streamwise position has already been associated with SV ejections and increased surface heat transfer.

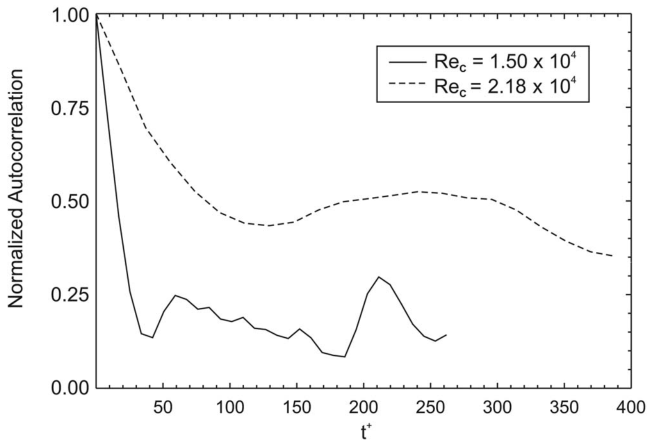

**Fig. 14 Normalized autocorrelations of end-wall surface heat transfer data along the linear cascade symmetry plane**

Although the transient HV behavior is not truly periodic, dominant natural frequencies can be established from HV flow field and surface heat transfer data. The dominant periods of the symmetry plane HV motion and surface temperature patterns were $260t^+$ and $200t^+$, respectively. The comparably determined turbulent boundary layer bursting period was between $150<t^+<250$, quantitatively supporting a link between the transient behavior within the impinging turbulent boundary layer and the transient HV behavior. This result suggests that modification, and possibly control, of the behavior of the end-wall HV system might be effectively achieved by modification of the flow structure and/or temporal behavior of the impinging turbulent boundary layer, specifically hairpin vortex packets.

An examination of the periodicity in the surface heat transfer patterns near the leading edge of a linear cascade airfoil also indicates a dominant period of $200t^+$, which is remarkably similar to that determined for the tapered cylinder experiments, despite the additional complexity of the flow geometry. The time-mean results indicate that an increase in heat transfer rate of up to 600% above the comparable level for the impinging turbulent boundary layer is experienced adjacent to the leading edge of the airfoils, principally due to the downwash along the face of the airfoil. The location of a secondary band of heat transfer, which is linked to the HV system unsteadiness, is determined to scale with the maximum thickness of the cascade airfoil. However, this length scale needs to be examined for a wider range of geometries to establish if it is generically applicable.

## Acknowledgment

The authors wish to thank the Air Force Office of Scientific Research for their support of this research.

## Nomenclature

$A$ = heat transfer area
$b$ = airfoil maximum thickness
$C$ = airfoil axial chord
$c_p$ = specific heat
$D$ = diameter of streamlined cylinder
$h$ = convective heat transfer coefficient, $q''/A(T_s-T_\infty)$
HV = horseshoe vortex
LC = liquid crystal

$q''$ = heat flux
Re = Reynolds number
St = Stanon number, $h/(\rho U_\infty c_p)$
SV = secondary vortex
TV = tertiary vortex
$t^+$ = nondimensional time, $t(u_\tau)^2/\nu$
$T_s$ = temperature at the wall
$T_\infty$ = free stream temperature
$U_\infty$ = free stream velocity
$u_\tau$ = wall shear velocity, $(\tau_w/\rho)^{1/2}$
$x$ = streamwise coordinate
$y$ = wall normal coordinate
$z$ = cross stream coordinate

**Greek Symbols**
$\delta$ = boundary layer thickness
$\lambda^+$ = nondimensional spacing, $zu_\tau/\nu$
$\rho$ = fluid density
$\theta$ = boundary layer momentum thickness
$\tau_w$ = wall shear
$\nu$ = kinematic viscosity
$\omega$ = vorticity

## References

[1] Han, S., and Goldstein, R. J., 2006, "Influence of Blade Leading Edge Geometry on Turbine Endwall Heat (Mass) Transfer," ASME J. Turbomach., **128**, pp. 798–813.

[2] Zess, G. A., and Thole, K. A., 2002, "Computational Design and Experimental Evaluation of Using a Leading Edge Fillet on a Gas Turbine Vane," ASME J. Turbomach., **124**, pp. 167–175.

[3] Praisner, T. J., and Smith, C. R., 2006, "The Dynamics of the Horseshoe Vortex and Associate Endwall Heat Transfer—Part II: Time-Mean Results," ASME J. Turbomach., **128**, pp. 755–762.

[4] Ishii, J., and Honami, S., 1986, "A Three-Dimensional Turbulent Detached Flow With a Horseshoe Vortex," ASME J. Eng. Gas Turbines Power, **108**, pp. 125–130.

[5] Agui, J. H., and Andreopoulos, J., 1992, "Experimental Investigation of a Three-Dimensional Boundary Layer Flow in the Vicinity of an Upright Wall Mounted Cylinder," ASME J. Fluids Eng., **114**, pp. 566–576.

[6] Hunt, J. C. R., Abell, C. J., Peterka, J. A., and Woo, H., 1978, "Kinematical Studies of the Flows Around Free or Surface-Mounted Obstacles; Applying Topology to Flow Visualization," J. Fluid Mech., **86**, pp. 179–200.

[7] Devenport, W. J., and Simpson, R. L., 1990, "Time-Dependent and Time-Averaged Turbulence Structure Near the Nose of a Wing-Body Junction," J. Fluid Mech., **210**, pp. 23–55.

[8] Praisner, T. J., and Smith, C. R., 2006, "The Dynamics of the Horseshoe Vortex and Associate Endwall Heat Transfer—Part I: Temporal Behavior," ASME J. Turbomach., **128**, pp. 747–754.

[9] Kline, S. J., Reynolds, W. C., Schraub, F. A., and Rundstadler, P. W., 1967, "The Structure of Turbulent Boundary Layers," J. Fluid Mech., **95**, pp. 741–773.

[10] Smith, C. R., 1996, "Coherent Flow Structures in Flat Wall Turbulent Boundary Layers: Facts, Mechanisms, Speculation," *Coherent Flow Structures in Open Channels*, P. J. Ashworth, J. L. Best, S. J. Bennett, and S. J. McLelland, eds., Wiley, New York, pp. 1–39.

[11] Adrian, R. J., Meinhart, C. D., and Tomkins, C. D., 1999, "Vortex Organization in the Outer Region of the Turbulent Boundary Layer," University of Illinois at Urbana-Champaign Theoretical and Applied Mechanics Report No. 924, UILU-ENG-99-6026.

[12] Head, M. R., and Bandyopadhyay, P., 1981, "New Aspects of Turbulent Boundary-Layer Structure," J. Fluid Mech., **107**, pp. 297–338.

[13] Hairdari, A. H., and Smith, C. R., 1994, "The Generation and Regeneration of Single Hairpin Vortices," J. Fluid Mech., **277**, pp. 135–162.

[14] Sabatino, D. R., 2000, "The Impact of Impinging Turbulence on Turbulent Juncture Flows: Boundary Layer, Grid Turbulence, and Periodic Wake Effects," Ph.D. thesis, Lehigh University, Bethlehem, PA.

[15] Adrian, R. J., 1991, "Particle-Imaging Techniques for Experimental Fluid Mechanics," Annual Review of Fluid Mechanics, Annu. Rev. Fluid Mech., **23**, pp. 261–304.

[16] Rockwell, D., Magness, C., Towfighi, J., Akin, O., and Corcoran, T., 1993, "High Image-Density Particle Image Velocimetry Using Laser Scanning Techniques," Exp. Fluids, **14**, pp. 181–192.

[17] Praisner, T. J., Sabatino D. R., and Smith, C. R., 2001, "Simultaneously Combined Liquid-Crystal Surface Heat Transfer and PIV Flow-Field Measurements," Exp. Fluids, **30**, pp. 1–10.

[18] Sabatino, D. R., Praisner, T. J., and Smith, C. R., 2001, "A High-Accuracy Calibration Technique for Thermochromic Liquid Crystal Temperature Measurement," Exp. Fluids, **28**, pp. 497–505.

[19] Doligalski, T. L., Smith, C. R., and Walker, J. D. A., 1994, "Vortex Interactions With Walls," Annu. Rev. Fluid Mech., **26**, pp. 573–616.

[20] Clauser, F. H., 1954, "Turbulent boundary layers in adverse pressure gradients," J. Aeronaut. Sci., **21**, pp. 91–108.

[21] Blackwelder, R. F., and Kaplan, R. E., 1976, "On the Wall Structure of the Turbulent Boundary Layer," J. Fluid Mech., **76**, pp. 89–112.

[22] Lu, L. J., and Smith, C. R., 1991, "Use of Flow Visualization Data to Examine Spatial-Temporal Velocity and Burst-Type Characteristics in a Turbulent Boundary Layer," J. Fluid Mech., **232**, pp. 303–340.

[23] Blackwelder, R. F., and Haritonidis, J. H., 1983, "Scaling of the Bursting Frequency in Turbulent Boundary Layers," J. Fluid Mech., **132**, pp. 87–103.

[24] Goldstein, R. J., and Spores, R. A., 1988, "Turbulent Transport on the Endwall in the Region Between Adjacent Turbine Blades," ASME J. Heat Transfer, **110**, pp. 862–869.

[25] Praisner, T. J., 1998, "Investigation of Turbulent Juncture Flow Endwall Heat Transfer and Fluid Flow," Ph.D. thesis, Lehigh University, Bethlehem, PA.

[26] Ballio, F., Bettoni, C., and Franzetti, S., 1998, "A Survey of Time-Averaged Characteristics of Laminar and Turbulent Horseshoe Vortices," ASME J. Fluids Eng., **120**, pp. 233–242.

[27] Kline, S. J., Reynolds, W. C., Schraub, F. A., and Rundstadler, P. W., 1967, "The Structure of Turbulent Boundary Layers," J. Fluid Mech., **95**, pp. 741–773.

# Gill Slot Trailing Edge Aerodynamics: Effects of Blowing Rate, Reynolds Number, and External Turbulence on Aerodynamic Losses and Pressure Distribution

**J. D. Johnson**
518 Combat Sustainment Squadron,
United States Air Force,
Hill AFB, UT 84056

**N. J. Fiala**
Energy and Environmental Research Center,
University of North Dakota,
Grand Forks, ND 58202

**F. E. Ames**
Mechanical Engineering Department,
University of North Dakota,
Grand Forks, ND 58202

*Gill slots (also called cutbacks) are a common method to cool the trailing edge of vanes and blades and to eject spent cooling air. Exit surveys detailing total pressure loss, turning angle, and secondary velocities have been acquired for a gill slot vane in a large-scale, low speed cascade facility. These measurements are compared with exit surveys of the base (solid) vane configuration. Exit surveys have been taken over a four to one range in chord Reynolds numbers (500,000, 1,000,000, and 2,000,000) based on exit conditions and for low (0.7%), grid (8.5%), and aerocombustor (13.5%) turbulence conditions with varying blowing rate (50%, 100%, 150%, and 200% design flows). Exit loss, angle, and secondary velocity measurements were acquired in the facility using a five-hole cone probe at two stations representing axial chord spacings of 0.25 and 0.50. Differences between losses with and without the gill slot for a given turbulence condition and Reynolds number are compared providing evidence of coolant ejection losses and losses due to the separation off the gill slot lip. Additionally, differences in the level of losses, distribution of losses, and secondary flow vectors are presented for the different turbulence conditions and at the different Reynolds numbers. The turbulence condition has been found to have only a small effect on the increase in losses due to the gill slot. However, decreasing Reynolds number has been found to produce an increasing increment in losses. The present paper, together with a companion paper (2007, "Gill Slot Trailing Edge Heat Transfer—Effects of Blowing Rate, Reynolds Number, and External Turbulence on Heat Transfer and Film Cooling Effectiveness," ASME Paper No. GT2007-27397), which documents gill slot heat transfer, is intended to provide designers with the heat transfer and aerodynamic loss information needed to compare competing trailing edge designs.* [DOI: 10.1115/1.2813002]

## Introduction

The trade-offs between heat transfer and aerodynamic losses are an important consideration in specifying a trailing edge cooling configuration. Consequently, this paper examines the losses associated with a gill slot configuration over a range in inlet turbulence conditions (0.7%, 8.5%, and 13.5%), chord exit Reynolds numbers (500,000, 1,000,000, and 2,000,000), and gill slot flow rates (50%, 100%, 150%, and 200% designs). This research builds on previous work where the exit losses associated with a solid vane profile were also measured. The base vane measurements provide a basis to assess the aerodynamic penalty associated with the present gill slot geometry. Similar to the base vane exit survey measurements, the gill slot vane exit measurements were acquired using a five-hole cone probe. This probe was traversed at two axial chord locations downstream from the vane trailing edge location. Measurements were taken over a four to one range in exit chord Reynolds numbers at very low, moderate, and high levels of inlet turbulence over a reasonable range in coolant flow rates. The exit survey measurements document important aerodynamic parameters such as local and mass-averaged total pressure loss and turning angle as well as local secondary velocities driven by the secondary flows along the endwall. This research compliments an associated paper on vane heat transfer for a gill slot vane [1]. Additionally, this work builds on the results previously documented for the base vane [2].

## Background

Denton [3] reviewed loss mechanisms in turbomachinery and indicated that turbine passage losses can originate from profile losses, endwall losses, and leakage losses. Denton suggested that endwall losses contribute significantly to the total loss. He also suggested that losses can be generated when turbulence causes mixing across inertial gradients. Glassman [4] suggested that the primary origin of profile losses is airfoil surface boundary layer growth and separation off the trailing edge. He indicated that trailing edge losses are typically proportional to trailing edge thickness and are affected by trailing edge shape. Moore et al. [5] found that up to 1/3 of the loss develops downstream of the trailing edge due to deformation work. Gregory-Smith and Cleak [6] investigated the influence of grid generated turbulence on exit losses. The grid turbulence increased profile losses by 7% yet overall losses were found to decrease by 12%. Ames and Plesniak [7] studied the influence of simulated aerocombustor turbulence on exit losses in an ambient cascade facility. They documented the

---

Contributed by the International Gas Turbine Institute of ASME for publication in the JOURNAL OF TURBOMACHINERY. Manuscript received June 20, 2007; final manuscript received September 12, 2007; published online November 6, 2008. Review conducted by David Wisler. Paper presented at the ASME Turbo Expo 2007: Land, Sea and Air (GT2007), Montreal, Quebec, Canada, May 14–17, 2007.

profile losses and suction surface boundary layer. In addition to vane boundary layer growth and trailing edge separation, they found "background" total pressure losses of up to 1.5% of the dynamic pressure. They attributed 1/3 to 1/2 of these losses to turbulent mixing and suggested that the remainder most likely originated from turbulent redistribution of endwall losses.

A significant fraction of turbine nozzle losses originate on the endwall due to boundary layer development, separation, and secondary flows. A noteworthy review of secondary flows in turbine passages was developed by Sieverding [8]. He presented the secondary flow models of Klein [9] and Langston et al. [10]. The model of Langston et al. [10] included suction and pressure side legs of the horseshoe vortex as well as the passage vortex. Sieverding [8] postulated that the corner vortex was the result of the interaction of the passage vortex with the suction surface. Marchal and Sieverding [11] found increased growth in secondary loses downstream from the maximum velocity. Burd and Simon [12] investigated secondary flows in a contoured endwall cascade and found a substantially reduced impact of secondary flows. Zess and Thole [13] investigated the effect of a leading edge fillet on secondary flows and also found that the fillet significantly reduced their impact. Ingram et al. [14] studied the influence of endwall profiling on secondary losses and, by reducing the cross-passage pressure gradient, they were able to decrease endwall losses by 24%.

The addition of a gill slot is expected to increase exit losses due to separation off the gill slot lip as well as the ejection of lower momentum coolant outflow into the gas path. Sieverding et al. [15] tested a cooled nozzle vane with trailing edge ejection (similar to the current gill slot) amounting to 3% of passage flow. They only found a minor impact of the coolant ejection on total pressure losses. Osnaghi et al. [16] investigated aerodynamic losses due to trailing edge discharge, a showerhead, and a combination of pressure and suction surface film cooling along with the trailing edge and showerhead. They investigated different coolant discharge rates and compared their results with a solid vane. The trailing edge flow discharged through a row of rectangular holes and comprised 38% of the flow at design. The design flow thermodynamic loss was 54% above the solid vane from all sources and 27% for the trailing edge discharge alone. The trailing edge discharge loss was found to be relatively insensitive to flow rate. Pappu and Schobeiri [17] investigated a range of trailing edge geometries with varied flow in order to optimize mixing losses. They concluded that mixing losses are minimized at a velocity ratio of 1, which is also in agreement with the theory of Schobeiri [18]. Kapteijn et al. [19] investigated a nozzle guide vane with a cutback (gill slot) and a covered trailing edge and found higher losses and higher turning for the cutback vane, especially in the supersonic range. They also found more rapid mixing for the cutback vane compared with the covered trailing edge for subsonic flow. Michelassi et al. [20] numerically investigated the previous two trailing edge configurations. They found that the trailing edge coolant discharge had only a small influence on measured and computed base pressures and wake shapes.

More recently, Uzol and Camci [21] investigated aerodynamic losses for a blade with pressure side cutbacks at 12.5% and 0% of chord upstream the trailing edge. They found that losses increased with coolant ejection flow rates up to 3% of the main flow but decreased for flow rates of 5% due to filling of the wake with high momentum fluid. They found that the 12.5% cutback produced lower losses than the 0% cutback. Telisinghe et al. [22] conducted a comparative study between a cutback and a conventional pressure side hole discharge scheme. They found that the cutback scheme has a higher discharge coefficient and did not suffer the "pinching" or "capping" effects of the conventional scheme. They noted that the cutback scheme produced a separated region. They reported little difference in the kinetic energy losses between the two geometries. Martini et al. [23] performed heat transfer experiments and made predictions for a cutback slot with internal rib arrays. Their heat transfer measurements and computational fluid dynamics (CFD) predictions evidenced a complex flow field with separation off the blunt cutback lib and jet grouping from flow exiting the rib arrays. They did not report exit losses. In the present paper, we compare exit survey measurements for a gill slot (similar to a cutback) cooled trailing edge with a solid vane profile. This present investigation uses an engine relevant gill slot configuration with an internal pin fin array. This vane configuration is tested over a four to one range in Reynolds number, at half, full, one and a half, and double design flow rates for low, grid, and aerocombustor turbulence conditions. Detailed exit surveys document the influence of these variables on total pressure loss, turning angle, and secondary flow distributions. Further, surface pressure distributions are also detailed as a function of gill slot flow rates.

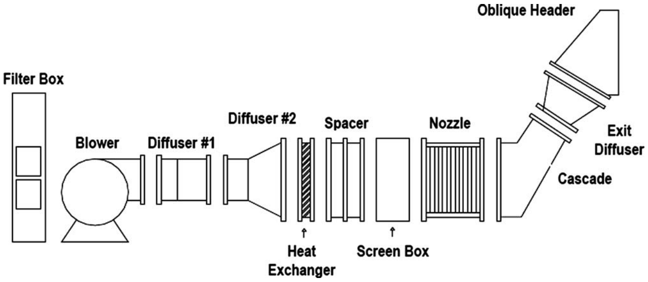

Fig. 1 Schematic of large-scale incompressible flow vane cascade wind tunnel

## Experimental Approach

The exit survey measurements documented in this paper were acquired in a wind tunnel facility designed for turbine vane and blade cascades. The wind tunnel facility, shown schematically in Fig. 1, consists of a filter box, a large fan, a two-section diffuser, a heat exchanger, a screen box, a nozzle, the cascade test section, a diffuser, and an oblique header. The filter box houses eight large high efficiency industrial filters with a rated capacity in excess of the design volumetric flow rate. The 45 kW fan has a static pressure rise of 5 kPa at a flow capacity of 6.6 $m^3/s$. The diffuser consists of two multivane diffusers used to recover pressure and spread out the flow. The diffusers exit into a heat exchanger with a makeup and recirculation system, which controls the tunnel air temperature. A short spool connects the heat exchanger with the screen box. The screen box helps reduce variations in the velocity distribution. The air is then directed into a 3.6 to 1 area ratio nozzle, which accelerates the flow into the cascade test section. The nozzle can be replaced by the simulated aerocombustor turbulence generator. The four vane cascade test section has the exit traversing mechanism attached to its exit, which in turn connects with a multivane diffuser designed to extend the Reynolds number range of the wind tunnel. Finally, an oblique header is attached to the exit diffuser to direct the air away from the ceiling.

**Turbulence Conditions.** The three turbulence conditions developed for aerodynamic testing were a low turbulence condition, a grid generated turbulence condition, and a simulated aerocombustor turbulence. The low turbulence condition, a result of the screen box and 3.6 to 1 area ratio nozzle, produced a turbulence level of 0.7%. The grid generated turbulence condition was produced by inserting a rectangular spool section, which contained a grid, in between the nozzle and cascade. The grid was a square bar square mesh design with 1.27 cm thick bars spaced at 6.35 cm. The grid was placed ten mesh lengths upstream from the vane leading edge plane and it produced a turbulence intensity of about 8.5% with an energy scale of about 3.5 cm. The combustor simulator, shown schematically in Fig. 2, was designed to have similar flow features to an annular combustor. The simulated combustor

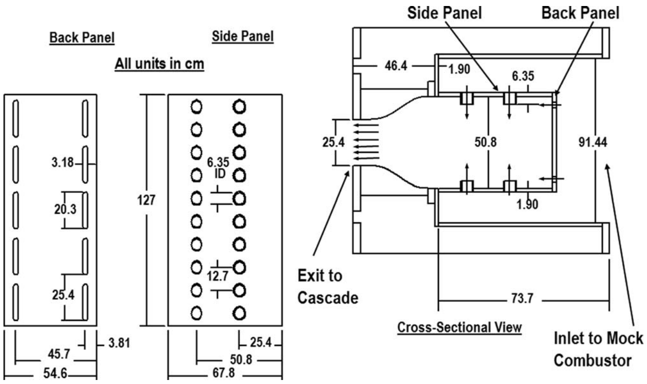

**Fig. 2 Schematic of aeroderivative combustor turbulence generator used in place of nozzle**

takes the place of the nozzle for the aerocombustor condition. The flow enters from behind the liner and is forced through the slots in the back panel and the plunged holes in the side panels. The back slots and the first row of holes work together, producing a recirculation zone. The second row of holes acts like dilution jets. This simulated combustor produces a turbulence intensity of about 13.5% with an energy scale of about 7 cm. The inlet conditions produced by the three inlet configurations for the three Reynolds numbers tested are referenced from Ref. [24] and presented in Table 1. Inlet boundary layer measurements, previously documented for the low and aerocombustor turbulence conditions, are presented in Ref. [2].

**Cascade Test Section.** The cascade test section was designed to produce a 2D representation of flow in a modern first stage vane relevant to a medium sized industrial gas turbine engine. The cascade shown in Fig. 3 is arranged in a four vane, three passage configuration with inlet bleeds designed along calculated streamlines. Tailboards are placed at the trailing edge of the top and bottom vanes to help control exit periodicity. A row of inlet static taps, 1/4 axial chord upstream from the vane leading edge plane, is used to monitor inlet uniformity. This plane is also the probe access point for the turbulence measurements. A row of exit static taps, 1/4 axial chord downstream of the vane trailing edge plane, is used to monitor exit periodicity and exit static pressure. The instrumented vane is located at the third position from the bottom because the passages surrounding Vane 3 are expected to have the cleanest flow. The leading edge plane of the cascade is 12.7 cm downstream from the cascade inlet, which has a span of 25.4 cm and a circumferential height of 127 cm.

**Pressure Vane and Base Line Pressure Distribution.** The cascade uses 11 times scale vanes with a true chord of 47.8 cm and an axial chord of 25.0 cm. The circumferential spacing is 38.39 cm. The vane leading edge diameter is 5.59 cm, while the trailing edge has a diameter of 0.98 cm. The gill slot vane is shown schematically in Fig. 4. The gill slot vane was cast in that same mold as the other cascade vanes but with the addition of an insert, which produced a nominal epoxy wall thickness of 0.84 cm. The pressure surface wall thickness varies from 0.84 cm at the entrance to the five-row aluminum pin fin array to 0.56 cm at the exit of the gill slot where the lip is rounded with a 0.56 cm radius. The gill slot channel height at the exit is 0.56 cm. The gill slot lip is located 5.15 cm from the vane trailing edge. The wall thickness generally stays constant on the suction side except that the wall has been machined to accept the 0.38 cm thick aluminum bottom plate of the pin fin array. From the exit of the gill slot to the trailing edge, the suction surface thickness tapers from 0.84 cm to 0.98 cm in an arc. The arc is tangent with both the inner suction surface at the exit of the gill slot and the pressure side trailing edge surface.

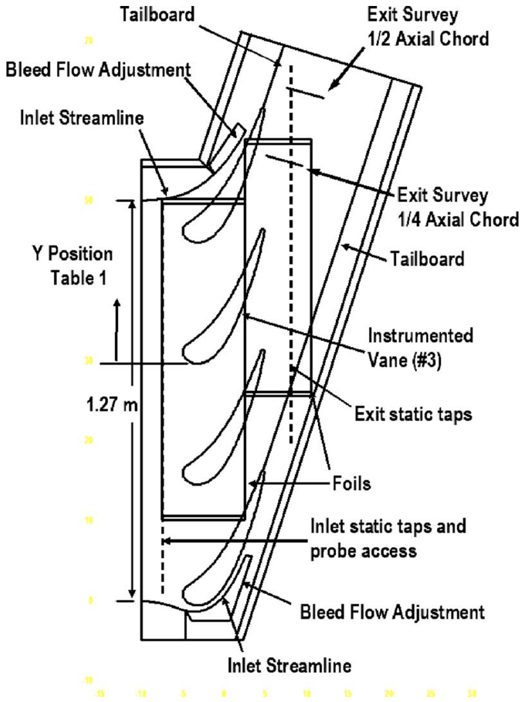

**Fig. 3 Schematic of four vane, 11 times scale cascade test section**

The gill slot aerodynamic vane was fabricated with 65 surface static pressure taps cast into its surface to determine the midspan pressure distribution. Their locations are shown in Fig. 4 using symbols. Additionally, one pressure tap is used to sense the feed tube pressure and one determines the coolant pressure upstream of the pin fin array. Flow enters the gill slot vane through the coolant

**Table 1 Characteristics of inlet turbulence for low, grid, and aerocombustor turbulence**

| | Reynolds | $T_u$ | $U$ (m/s) | $L_x$ (cm) | $L_u$ (cm) | $\varepsilon$ (m$^2$/s$^3$) |
|---|---|---|---|---|---|---|
| Low turbulence | 500,000 | 0.0069 | 4.96 | 8.12 | 127.0 | 0.00005 |
| | 1,000,000 | 0.0076 | 10.43 | 5.02 | 154.5 | 0.00035 |
| | 2,000,000 | 0.0060 | 18.71 | 3.58 | 15.5 | 0.0144 |
| Aeroderivative combustor | 500,000 | 0.1313 | 5.24 | 3.68 | 7.24 | 6.67 |
| | 1,000,000 | 0.1402 | 9.32 | 3.52 | 6.36 | 51.5 |
| | 2,000,000 | 0.1339 | 18.39 | 3.58 | 7.35 | 302.0 |
| Grid | 500,000 | 0.0821 | 4.77 | 2.00 | 3.27 | 2.70 |
| | 1,000,000 | 0.0861 | 10.19 | 2.04 | 3.35 | 29.8 |
| | 2,000,000 | 0.0884 | 19.27 | 2.35 | 3.53 | 206.8 |

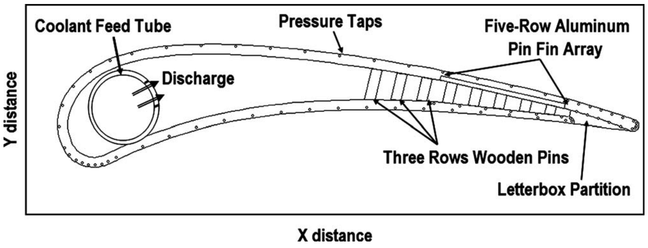

**Fig. 4 Schematic of vane cross section showing coolant feed tube, location of pressure taps, pin fin arrays, and gill slot geometry**

feed tube, which distributes the flow in the vane using 10–1.59 cm diameter holes. The coolant tube also has a constricting area from inlet to tip to keep the pressure distribution along the tube constant. Along the pressure surface in the region of the pin fin array, six of the pressure taps have been cast along the inner surface to provide row by row pressure drop through the pin fin array.

The vane profile was designed by Rolls–Royce to have a fully loaded pressure distribution, similar to a modern vane in a medium sized industrial gas turbine. The vane was specially designed for incompressible flow. Figure 5 compares the measured pressure distribution for the base vane with the calculated distribution. The local static to stagnation pressure difference is normalized by the inlet total to mean exit static pressure difference. This value is plotted as a function of surface arc with positive and negative surface distances relating to the suction and pressure surfaces, respectively. The comparison between the measured and predicted distributions suggests that the cascade aerodynamics is in reasonably close agreement of the conceptual 2D blade to blade flow. The low Mach number pressure distributions are also compared with the calculated distribution for the midspan of the compressible profile showing very similar loading profiles in Fig. 5.

**Exit Surveys.** Exit surveys of total pressure loss, angle, and velocity were acquired downstream of the third vane using a five-hole cone probe. The 60 deg included-angle cone probe was designed, fabricated, and calibrated for the present experiment. The 4.76 mm diameter probe was calibrated for both pitch and yaw over ±25 deg in each direction. The probe extended 9.5 cm from a 1.905 cm diameter holder with an offset conical end, which held the probe parallel to the endwall but within 4.76 mm of the surface. The 1.905 cm holder had two extensions allowing for traverses at 1/4 and 1/2 axial chords from the third vane's trailing edge in the direction of flow. The probe used two sets of miniature amplified pressure sensors to acquire the cone probe port pressures. Each set consisted of five sensors with ranges of ±5000 Pa and ±1250 Pa. Four sensors were connected between the middle port and one of the side ports, while the fifth was connected between the center port and the inlet total pressure port. The 5000 Pa range sensors were used for the 2,000,000 Reynolds number case, while the 1250 Pa sensors were used for the 1,000,000 and 500,000 Reynolds number cases. The connection between the pressure sensors and the cone probe was damped using in-line restrictors. The cone probe was positioned using a two-axis traversing system located at the exit of the cascade test section. The cascade exit makes a 72.3 deg angle from the cascade inlet plane. The resulting distance between the midpassages surrounding one vane is 11.67 cm. Each traverse acquired measurements at 675 locations with 25 locations in the circumferential direction and 27 positions normal to the endwall surface. At each location, the yaw and pitch angle, total pressure, and static pressure were determined from the measurements. Additionally, measurements were adjusted to correct for shear flow effects. The mass-averaged total pressure loss included an estimate for the boundary layer loss assuming Spaulding's law of the wall [25] profile.

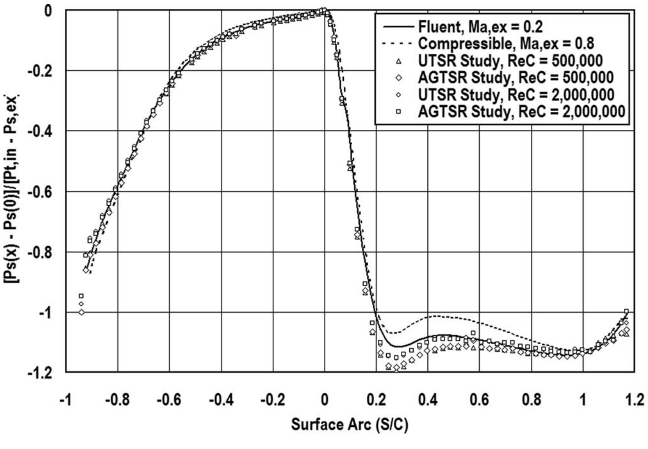

**Fig. 5 Measured solid vane pressure distribution compared with calculated pressure distributions for incompressible and compressible vanes** (FLUENT [27])

**Data Acquisition.** The cascade vane, inlet, and exit static pressures were all referenced to the inlet total pressure and were acquired using two Rosemount pressure transmitters with 0.1% accuracy. The Rosemount pressure transmitters were scaled to ranges of 250 Pa and 5000 Pa and were read in parallel taking the most sensitive reading within range. The two sensors were interfaced to the inlet total and static pressure sensors using a custom-made scanner. Each measurement was averaged over 20 readings. The five-element arrays of miniature pressure sensors, manufactured by Allsensors, were powered by a 5 V dc Acopian power supply and zeroed using a 1000 $\Omega$ potentiometer in parallel with each sensor. Each pressure was read from between 25 times and 75 times depending on the need for statistical resolution, which typically increased for higher turbulence level and lower Reynolds number. Both the pressure sensors and the type K thermocouples were read using an HP 3497A data acquisition unit with an integral voltmeter. The voltmeter has a sensitivity of 1 $\mu$V and each reading is integrated over one power line cycle. The type K thermocouples used to determine inlet and coolant temperatures were connected to the data acquisition unit through a passive constant temperature junction box, which was referenced to an ice bath.

**Data Uncertainties.** Uncertainty estimates for the total pressure loss coefficient $\Omega$, the turning angle $\beta$, and the normalized vane static pressure distribution were based on the root sum square method described by Moffat [26]. The uncertainties of these output variables are based on perturbing the raw variables by their uncertainties in the data reduction analysis. The uncertainty in the normalized vane static pressure due to uncertainties in pressure and position was estimated to be 0.02. Uncertainty in the local loss coefficient $\Omega$ was estimated to be as high as 0.008 for the aerocombustor low Reynolds number case and 0.006 for the low turbulence case. This uncertainty was largely due to the bias error in the pressure measurement at low Reynolds number, which was 0.005 of the dynamic pressure. Uncertainty in the relative bias error was estimated to be 0.0015 for the higher Reynolds numbers. Uncertainty in the local angle included bias error, unsteadiness error, and error in the setup angle. The maximum bias error was estimated to be 0.26 deg for the low Reynolds number. The maximum unsteadiness error was estimated at 0.25 deg and largely equal for all three Reynolds numbers for the aerocombustor turbulence condition. The maximum error in the setup angle was estimated to be only 0.20 deg as the angle of the probe could be referenced to the cascade using high resolution digital images. It should be noted that all surveys were taken with the same setup for the 1/4 axial chord positions and the same setup for the 1/2

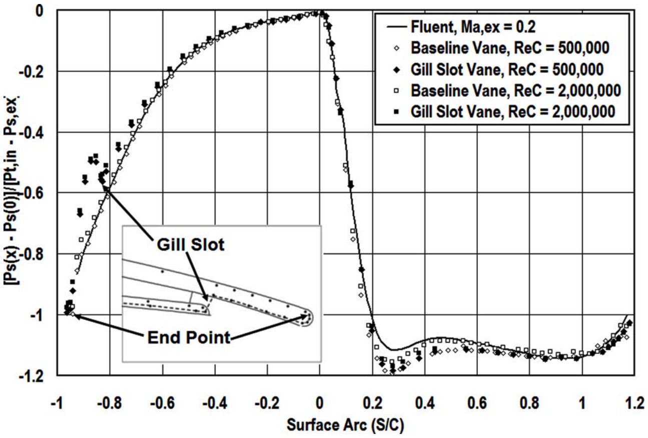

**Fig. 6 Comparison between measured gill slot vane at design flow rate, measured base line vane, and predicted (FLUENT [27]) base line vane pressure distributions**

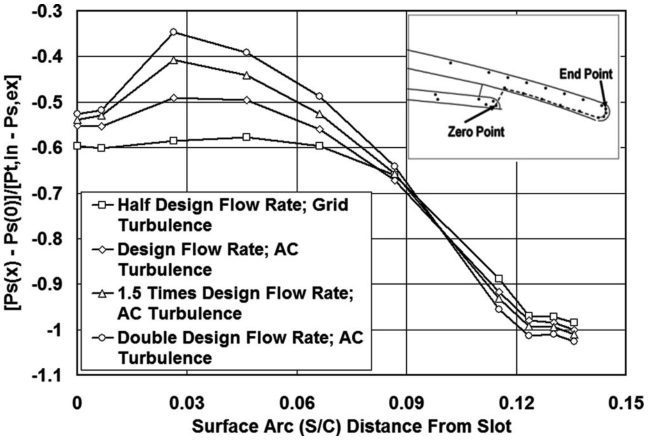

**Fig. 7 Trailing edge pressure distributions for the aerocombustor condition and 1,000,000 Reynolds numbers at four different mass flow rates**

axial chord positions. Uncertainties in the turbulence conditions can be found in Ref. [24]. Uncertainty estimates were all based on a 95% confidence interval.

## Experimental Results

The overall focus of this paper is to quantitatively document aerodynamic losses for the present gill slot configuration to enable the comparison with other trailing edge cooling configurations. The influence of discharge rate, Reynolds number, and turbulence condition on gill slot exit parameters will be examined, often in reference to base vane results. The effect of the gill slot on the mean surface pressure distribution will also be presented. Additionally, the correlation of local loss contours with secondary velocities will be shown across the full exit passage. Comparisons between the gill vane at various conditions and base vane results will be made for the cross-passage averaged loss and turning angle as a function of span. Finally, results will be presented in terms of the influence of the conditions on the incremental loss above the base vane values.

**Design Flow Rate.** Gill slot coolant flow rates have been presented in terms of half, full, 1 1/2 times, and 2 times the design flow rate. First stage vanes are fed from compressor discharge air, which bypasses the combustor. Consequently, the feed pressure available for the vane is related to the pressure drop across the combustor as well as the exit Mach number of the nozzle guide vane. A typical pressure drop credited to the combustor is 4–5%, while at an exit Mach number of 0.8, $P_{t_{\text{in}}}/P_{s_{\text{ex}}}$ is about 1.5. The present experiment had a ratio $(P_{t_{\text{in}}}-P_{s_{\text{co}}})/(P_{t_{\text{in}}}-P_{s_{\text{ex}}})$ of 0.55 at the gill slot. These ratios were used to estimate a pressure drop ratio for the experiment that was consistent with the ratio for a first stage vane in an engine. Consequently, the "design flow rate" pressure drop was set at approximately two-thirds of this available pressure drop assuming that one-third is typically lost across the coolant feed tube. Our design flow rate velocity was approximately 0.50 of $V_{\text{ex}}$ and approximately 0.66 of the external free-stream velocity at the gill slot. Design flow rate was determined to be between 2.5% and 2.6% of passage flow rate.

**Gill Slot Vane Pressure Distributions.** Gill slot vane pressure distributions are quite consistent with base vane distributions over the majority of the airfoil surface. However, as shown in Fig. 6, significant differences in the surface pressure distributions are found downstream of the gill slot exit lip. Figure 6 presents surface static pressure distributions normalized on $P_{t_{\text{in}}}-P_{s_{\text{ex}}}$ versus surface arc for the base vane and the gill slot vane at the design flow rate. The comparison between the pressure distributions are shown at Reynolds numbers of 500,000 and 2,000,000 along with the FLUENT [27] prediction. On the suction surface (positive surface arc), the base vane and gill slot vane pressure profiles are quite consistent. On the pressure surface (negative surface arc), the pressure profiles are similar but the pressure drop lags a little from the base vane until the gill slot lip. At the gill slot lip, there is a substantial departure from the base vane profile. The comparison clearly shows that the pressure distribution is significantly affected in the gill slot area. The flow in this region has an adverse pressure gradient, which is a function of flow rate. The dependence of gill exit pressure distribution on flow rate is shown in Fig. 7. Figure 7 compares pressure distributions downstream from the gill slot for flow rates of 1/2, 1, 1 1/2, and 2 times the design flow rate at a chord exit Reynolds number of 1,000,000 for the aerocombustor turbulence condition. The figure clearly demonstrates the dependence of pressure distribution on gill slot exit velocity showing increasingly strong adverse pressure gradients with increasing flow rate.

**Total Pressure Loss Contours and Secondary Velocities.** Full passage exit surveys were taken for the gill slot vane at low, grid, and aerocombustor turbulence conditions for Reynolds numbers of 500,000, 1,000,000, and 2,000,000. The coolant discharge flow was varied from 1/2 design to 2 times design flow rates and measurements were acquired at 1/4 and 1/2 axial chords downstream from the trailing edge of Vane 3. The test conditions, mass-averaged total pressure loss and turning angles, and the gill slot coolant discharge flow rates are summarized in Table 2. As a basis of comparison, results taken for the base vane at low, grid, and aerocombustor turbulence conditions for Reynolds numbers of 500,000, 1,000,000, and 2,000,000 are provided in Table 3.

Visualizations of total pressure loss contours ($\Omega$) and secondary velocity vectors are presented for the base vane and the gill slot vane at design flow rate in Figs. 8(*a*)–8(*f*) for the 1,000,000 Reynolds number conditions at 1/4 axial chord ($C_{\text{ax}}$). Figure 8(*a*) presents total pressure loss contours and secondary velocities for the base vane at the low turbulence condition showing the loss distribution. The wake is thin due to the laminar suction surface boundary layer and the core of the secondary losses is shown to have been convected off the surface of the endwall by the passage vortex. The contours also show significant total pressure losses near the corner vortex, which Sieverding [8] suggested is formed due to the interaction of the passage vortex with the suction surface. The characteristic overturning near the endwall is also apparent as expected due to the cross-passage pressure gradient. Qualitatively, the total pressure loss contours and the secondary velocities for the gill slot vane at the low turbulence condition shown in Fig. 8(*b*) are similar to the base vane visualization. The position of the loss core and the secondary velocities are quite

**Table 2 Summary table of gill slot losses and angles at full design flow**

| 1/4 $C_{ax}$ File | Aerocombustor | | | Low turbulence | | | Grid turbulence | | |
|---|---|---|---|---|---|---|---|---|---|
| | exsvglac53 | exsvglac13 | exsvglac23 | exsvgllt53 | exsvgllt13 | exsvgllt23 | exsvglgt53 | exsvglgt13 | exsvglgt23 |
| $\mathrm{Re}_{C_{ex}}$ | 505,107 | 998,691 | 2,006,273 | 502,785 | 1,002,688 | 2,001,287 | 499,192 | 997,661 | 1,987,008 |
| $T_{t_{in}}$ (K) | 288.2 | 293.5 | 296.4 | 290.8 | 289.9 | 295.4 | 288.2 | 294.4 | 294.7 |
| $P_{t_{in}}$ (Pa) | 99,406 | 100,015 | 100,767 | 99,990 | 100,530 | 102,326 | 99,852 | 99,712 | 101,448 |
| $V_{ex}$ (m/s) | 15.77 | 32.25 | 67.45 | 15.85 | 31.49 | 65.74 | 15.52 | 32.48 | 65.56 |
| $Ma_{ex}$ | 0.0463 | 0.0938 | 0.1947 | 0.0464 | 0.0922 | 0.1901 | 0.0456 | 0.0943 | 0.1898 |
| $\Omega$ (full) | 0.0764 | 0.0668 | 0.0632 | 0.0620 | 0.0485 | 0.0458 | 0.0670 | 0.0582 | 0.0547 |
| $\Omega$ (midline) | 0.0655 | 0.0576 | 0.0550 | 0.0655 | 0.0367 | 0.0327 | 0.0540 | 0.0454 | 0.0428 |
| $B$ (full) | 73.17 | 73.67 | 73.76 | 73.29 | 73.56 | 73.58 | 73.44 | 73.65 | 73.57 |
| $B$ (midline) | 72.96 | 73.47 | 73.65 | 73.14 | 73.97 | 74.06 | 73.48 | 73.73 | 73.91 |
| $M_{dot}$ (kg/s) | 0.0135 | 0.0272 | 0.0545 | 0.0134 | 0.0271 | 0.0541 | 0.0135 | 0.0270 | 0.0537 |
| $T_{orf}$ (K) | 288.5 | 305.1 | 286.7 | 290.3 | 292.0 | 290.8 | 289.7 | 287.1 | 290.4 |
| $\Delta P_{orf}$ (Pa) | 72.9 | 311.8 | 1,162.7 | 71.6 | 293.3 | 1,148.0 | 72.1 | 289.7 | 1136.3 |
| $P_{atm}$ (Pa) | 99,310.7 | 99,615.4 | 99,107.5 | 99,886.3 | 100,123.3 | 100,326.5 | 99,750.8 | 99,310.7 | 99,818.6 |

| 1/2 $C_{ax}$ File | Aerocombustor | | | Low turbulence | | | Grid turbulence | | |
|---|---|---|---|---|---|---|---|---|---|
| | exsvglac52 | exsvglac12 | exsvglac22 | exsvgllt52 | exsvgllt12 | exsvgllt22 | exsvglgt52 | exsvglgt12 | exsvglgt22 |
| $\mathrm{Re}_{C_{ex}}$ | 497,985 | 977,478 | 1,996,901 | 509,880 | 990,322 | 2,004,865 | 482,180 | 1,002,435 | 1,989,548 |
| $T_{t_{in}}$ (K) | 289.6 | 295.1 | 296.4 | 291.9 | 294.6 | 294.5 | 298.2 | 295.1 | 294.1 |
| $P_{t_{in}}$ (Pa) | 97,618 | 97,076 | 98,908 | 97,889 | 98,612 | 99,739 | 99,465 | 99,040 | 100,200 |
| $V_{ex}$ (m/s) | 15.97 | 32.83 | 68.45 | 16.54 | 32.64 | 67.32 | 15.98 | 33.01 | 66.25 |
| $Ma_{ex}$ | 0.0468 | 0.0953 | 0.1976 | 0.0483 | 0.0948 | 0.1950 | 0.0462 | 0.0958 | 0.1920 |
| $\Omega$ (full) | 0.0864 | 0.0795 | 0.0774 | 0.0722 | 0.0601 | 0.0578 | 0.0727 | 0.0693 | 0.0679 |
| $\Omega$ (midline) | 0.0701 | 0.0657 | 0.0669 | 0.0759 | 0.0417 | 0.0393 | 0.0519 | 0.0494 | 0.0513 |
| $B$ (full) | 73.35 | 73.91 | 74.09 | 73.36 | 73.84 | 73.84 | 73.25 | 73.80 | 73.87 |
| $B$ (midline) | 73.26 | 73.71 | 73.97 | 73.33 | 74.09 | 74.32 | 73.33 | 73.95 | 74.15 |
| $M_{dot}$ (kg/s) | 0.0138 | 0.0318 | 0.0543 | 0.0135 | 0.0267 | 0.0542 | 0.0135 | 0.0274 | 0.0545 |
| $T_{orf}$ (K) | 289.5 | 299.5 | 289.7 | 304.6 | 306.6 | 295.6 | 291.0 | 305.0 | 296.1 |
| $\Delta P_{orf}$ (Pa) | 77.9 | 427.4 | 1,188.6 | 77.6 | 305.4 | 1,196.3 | 73.6 | 319.7 | 1185.3 |
| $P_{atm}$ (Pa) | 97,516.1 | 97,075.9 | 97,245.2 | 97,787.0 | 98,193.3 | 98,057.9 | 98,882.5 | 98,230.2 | 98,531.9 |

| 1/4 $C_{ax}$ File | Aerocombustor | | | | Grid turb. | Low turb. |
|---|---|---|---|---|---|---|
| | exsvglac513 | exsvglac313 | exsvglac213 | exsvglac33 | exsvglgt513 | exsvgllt513 |
| $\mathrm{Re}_{C_{ex}}$ | 1,005,792 | 1,002,218 | 1,012,261 | 293,032 | 1,004,944 | 1,004,611 |
| $T_{t_{in}}$ (K) | 293.1 | 293.7 | 293.6 | 289.8 | 293.5 | 290.4 |
| $P_{t_{in}}$ (Pa) | 99,539 | 99,345 | 100,514 | 99,380 | 99,554 | 100,485 |
| $V_{ex}$ (m/s) | 32.55 | 32.61 | 32.53 | 9.23 | 32.60 | 31.66 |
| $Ma_{ex}$ | 0.0948 | 0.0948 | 0.0946 | 0.0270 | 0.0948 | 0.0926 |
| $\Omega$ (full) | 0.0664 | 0.0623 | 0.0535 | 0.0765 | 0.0539 | 0.0450 |
| $\Omega$ (midline) | 0.0570 | 0.0523 | 0.0427 | 0.0553 | 0.0395 | 0.0329 |
| $B$ (full) | 73.62 | 73.74 | 73.71 | 73.42 | 73.65 | 73.51 |
| $B$ (midline) | 73.36 | 73.57 | 73.56 | 73.02 | 73.75 | 73.91 |
| $M_{dot}$ (kg/s) | 0.0134 | 0.0429 | 0.0544 | 0.00809 | 0.0136 | 0.0135 |
| $T_{orf}$ (K) | 288.7 | 295.7 | 288.0 | 288.3 | 290.7 | 304.1 |
| $\Delta P_{orf}$ (Pa) | 71.8 | 746.2 | 1163.0 | 25.9 | 74.6 | |
| $p_{atm}$ (Pa) | 99,141.4 | 99,344.5 | 99,480.0 | 99,344.5 | 99,141.4 | 100,067.8 |

| 1/2 $C_{ax}$ File | 0.5× full flow Grid turb. exsvglgt512 | 0.5× full flow Low turb. exsvgllt512 |
|---|---|---|
| $\mathrm{Re}_{C_{ex}}$ | 1,017,012 | 1,009,935 |
| $T_{t_{in}}$ (K) | 290.4 | 294.0 |
| $P_{t_{in}}$ (Pa) | 99,950 | 97,685 |
| $V_{ex}$ (m/s) | 32.24 | 33.51 |
| $Ma_{ex}$ | 0.0943 | 0.0974 |
| $\Omega$ (full) | 0.0675 | 0.0576 |
| $\Omega$ (midline) | 0.0475 | 0.0376 |
| $B$ (full) | 73.79 | 73.88 |
| $B$ (midline) | 73.91 | 74.12 |
| $M_{dot}$ (kg/s) | 0.0136 | 0.0137 |
| $T_{orf}$ (K) | 290.5 | 305.4 |
| $\Delta P_{orf}$ (Pa) | | 79.7 |
| $P_{atm}$ (Pa) | 99,322.8 | 97,685.4 |

**Table 3 Summary table of base vane losses and angles**

| 1/4 $C_{ax}$ | Aerocombustor | | | Low turbulence | | | Grid turbulence | | |
|---|---|---|---|---|---|---|---|---|---|
| File | exsvac53 | exsvac13 | exsvac23 | exsvlt53 | exsvlt13 | exsvlt23 | exsvgt53 | exsvgt13 | exsvgt23 |
| $\mathrm{Re}_{C_{ex}}$ | 504,125 | 1,005,268 | 1,955,006 | 498,541 | 1,010,700 | 1,988,775 | 493,910 | 990,667 | 1,968,858 |
| $T_{t_{in}}$ (K) | 294.6 | 301.3 | 302.5 | 297.3 | 294.2 | 299.8 | 300.3 | 303.5 | 301.8 |
| $P_{t_{in}}$ (Pa) | 98,340 | 98,541 | 100,321 | 98,365 | 97,935 | 97,922 | 100,064 | 101,278 | 99,446 |
| $V_{ex}$ (m/s) | 16.55 | 34.53 | 68.46 | 16.63 | 33.48 | 70.43 | 16.48 | 33.52 | 69.34 |
| $Ma_{ex}$ | 0.0481 | 0.0992 | 0.1956 | 0.0481 | 0.0973 | 0.2021 | 0.0474 | 0.0959 | 0.1983 |
| Ω (full) | 0.0607 | 0.0564 | 0.0521 | 0.0444 | 0.0369 | 0.0356 | 0.0472 | 0.0453 | 0.0446 |
| Ω (midline) | 0.0494 | 0.0475 | 0.0429 | 0.0501 | 0.0251 | 0.0228 | 0.0326 | 0.0333 | 0.0311 |
| $B$ (full) | 72.91 | 73.50 | 73.47 | 73.30 | 73.32 | 73.38 | 73.30 | 73.58 | 73.38 |
| $B$ (midline) | 72.57 | 73.18 | 73.26 | 73.27 | 73.59 | 73.54 | 73.27 | 73.52 | 73.49 |

| 1/2 $C_{ax}$ | Aerocombustor | | | Low turbulence | | | Grid turbulence | | |
|---|---|---|---|---|---|---|---|---|---|
| File | exsvac52 | exsvac1 | exsvac22 | exsvlt5 | exsvlt1 | exsvlt2 | exsvgt52 | exsvgt12 | exsvgt22 |
| $\mathrm{Re}_{C_{ex}}$ | 511,810 | 999,290 | 1,960,947 | 511,475 | 978,582 | 2,006,766 | 507,293 | 992,146 | 1,988,973 |
| $T_{t_{in}}$ (K) | 293.4 | 300.0 | 302.3 | 296.6 | 300.6 | 300.9 | 293.3 | 300.5 | 299.1072 |
| $P_{t_{in}}$ (Pa) | 99,628 | 99,320 | 101,224 | 97,515 | 97,761 | 100,116 | 97,938 | 99,875 | 98,874.7 |
| $V_{ex}$ (m/s) | 16.46 | 33.79 | 67.94 | 17.14 | 33.73 | 69.87 | 16.59 | 33.45 | 69.37785 |
| $Ma_{ex}$ | 0.0479 | 0.0972 | 0.1942 | 0.0496 | 0.0970 | 0.2002 | 0.0483 | 0.0962 | 0.199329 |
| Ω (full) | 0.0706 | 0.0675 | 0.0653 | 0.0530 | 0.0442 | 0.0465 | 0.0593 | 0.0558 | 0.0552 |
| Ω (midline) | 0.0553 | 0.0522 | 0.0534 | 0.0583 | 0.0247 | 0.0271 | 0.0382 | 0.0370 | 0.0374 |
| $B$ (full) | 73.64 | 73.97 | 74.16 | 73.63 | 73.80 | 73.81 | 73.86 | 74.29 | 74.25 |
| $B$ (midline) | 73.29 | 73.67 | 74.02 | 73.60 | 74.09 | 73.99 | 73.85 | 74.20 | 74.37 |

consistent. However, one noticeable difference with the gill slot visualization is the thickness of the wake, which has significantly grown as compared with the base vane wake. The incremental increase in the mass-averaged total pressure loss at this condition is about 1.2%. Based on a simple assessment, about half of the incremental total pressure loss results from the coolant mass injection and, consequently, about half is the result of separation off the gill slot lip.

A visualization of the total pressure loss contours for the base vane at the grid turbulence condition is shown in Fig. 8(*c*). Compared with the base vane in Fig. 8(*a*), the loss contour is thick and appears less intense. The secondary velocities appear stronger near the endwall but less intense near the secondary loss core. The mass-averaged loss is about 0.8% higher for the grid turbulence at this Reynolds number compared with the low turbulence condition, largely due to a turbulent suction surface boundary layer. The gill slot vane total pressure loss contours presented in Fig. 8(*d*) at design flow are again qualitatively similar with the base vane for the grid turbulence condition. However, again a thickening of the wake is present and an intensification of the peak profile loss and core loss is apparent. The incremental increase in mass-averaged total pressure loss at this condition is about 1.3% higher than the base vane. Similar to the low turbulence condition, the coolant injection loss and gill slot lip separation loss contribute about equally to this incremental increase.

Total pressure loss contours and secondary velocities are displayed for the aerocombustor turbulence condition in Fig. 8(*e*). The character of these time averaged loss contours is much different than that of the loss contours of either the low turbulence or grid turbulence conditions. At these lower turbulence conditions, a very clear secondary loss contour is present. However, for the aerocombustor case, no discrete loss contour can be seen. The loss profile does show a region where the wake is thicker and the losses are greater, but this region is spread over a significant portion of the span. Overall, the aerocombustor case has midspan losses of 4.75%, which is nearly double the 2.51% total pressure loss of the low turbulence case. This increase in losses is due to the turbulent suction surface (1.41%), the inlet boundary layer difference (0.45%), and a loss due turbulent mixing (0.35%). The secondary velocities of the passage vortex are weaker but the overturning near the endwall is still quite strong. The total pressure loss contours and secondary velocities for aerocombustor condition for the gill slot vane are shown in Fig. 8(*f*). The wake resulting from the gill slot vane for the aerocombustor condition is even broader and more intense than the base vane for this 1/4 axial chord location. Qualitatively, the gill slot wake is quite similar to the base vane wake. Quantitatively, the mass-averaged total pressure loss for the gill slot vane is 6.68%, compared with a loss of 5.64% for the base vane. Similar to the base vane case, the total pressure losses near the corner vortex are quite significant.

**Character of Gill Slot Total Pressure Losses.** Losses generated by a gill slot trailing edge include coolant injection losses and losses due to separation off the gill slot lip. Since the pressure surface boundary layer is quite thin, flow off the pressure surface is close to two dimensional. Consequently, the incremental loss distribution due to the gill slot might be expected to be evenly distributed across the span. Figure 9 shows a comparison between the cross-passage averaged losses for the base vane and the gill slot vane for the low turbulence condition at a Reynolds number of 1,000,000. The profiles show the high losses near the endwall, an increased level of losses due to secondary loss core, and an incremental loss over most of the span. This same incremental loss is reasonably consistent over the span for the other two turbulence conditions.

**Turbulence Condition Effects.** The location of the secondary loss core is related to the strength of the secondary flows. The cross-passage pressure gradient sweeps low momentum fluid across the passage to the suction surface where the passage vortex in reaction to the surface swept the loss core up off the endwall. The secondary loss core is readily seen for the low and grid turbulence levels in Fig. 10 where cross-span averaged losses for the gill slot vane are plotted as a function of span for the three turbulence conditions. However, the character of the loss distribution for the aerocombustor turbulence is much different. Here, the loss is spread out across the span of the turbine passage with little indication of a specific location for secondary losses. The level of cross-passage averaged total pressure loss is higher everywhere for the aerocombustor case except in the area of the peak second-

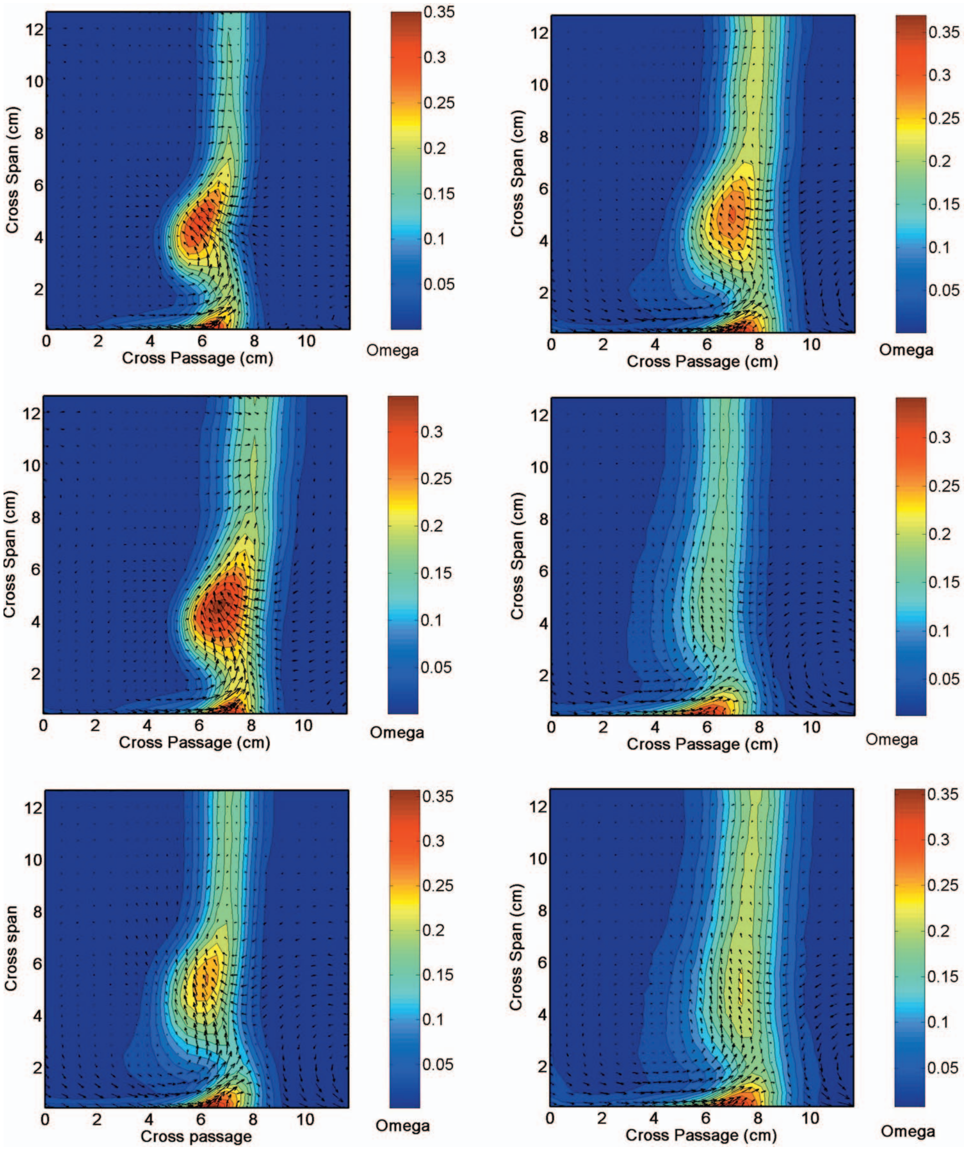

**Fig. 8** (*a*) Total pressure loss contours $\Omega$ with secondary velocity vectors, base vane, 1/4 $C_{ax}$, low turbulence, $Re_C=1,000,000$. (*b*) Total pressure loss contours $\Omega$ with secondary velocity vectors, gill slot vane, 1/4 $C_{ax}$, low turbulence, $Re_C=1,000,000$, design flow. (*c*) Total pressure loss contours $\Omega$ with secondary velocity vectors for the base vane, 1/4 $C_{ax}$, grid turbulence, $Re_C=1,000,000$. (*d*). Total pressure loss contours $\Omega$ with secondary velocity vectors, gill slot vane, 1/4 $C_{ax}$, grid turbulence, $Re_C=1,000,000$, design flow. (*e*) Total pressure loss contours $\Omega$ with secondary velocity vectors, base vane, 1/4 $C_{ax}$, aerocombustor turbulence, $Re_C=1,000,000$. (*f*). Total pressure loss contours $\Omega$ with secondary velocity vectors, gill slot vane, 1/4 $C_{ax}$, aerocombustor turbulence, $Re_C=1,000,000$, design flow.

ary loss. The increase in total pressure loss from the grid condition to the aerocombustor is about 0.86%. Loss mechanisms responsible for this increase include the turbulent mixing loss in the free stream, a thicker inlet boundary layer, and generally higher skin friction resulting from the higher turbulence. The incremental total pressure loss from the low turbulence to the grid turbulence is 0.97%. The turbulent suction surface boundary layer of the grid condition is expected to produce an incremental loss of at least this size.

The turbulent inlet conditions have a substantial influence on the turning angle distribution shown in Fig. 11. In this figure, cross-passage averaged turning angle $\beta$ for the three turbulence cases is plotted as a function of cross-span distance at an axial chord of 1/4 for a Reynolds number of 1,000,000 and for design flow. The character of the grid and aerocombustor turning angles is similar with strong overturning near the endwall due to the cross-passage pressure gradient. This overturning suggests that there is a reasonable level of low momentum fluid in this region. The low turbulence case has reduced overturning due to a thinner boundary layer implied by the lower near endwall losses as seen in Fig. 10. An underturning is present at the location of the peak secondary losses due to the secondary flows in that area. Finally, the turning angle recovers to a nearly constant value near midpassage. Qualitatively, the effects of turbulence conditions on loss and turning distributions shown in Figs. 10 and 11 are similar to the base vane results.

**Effects of Reynolds Number.** An earlier comparison of cross-span loss distributions for the base and gill slot vanes suggested that the gill slot causes an incremental increase in total pressure

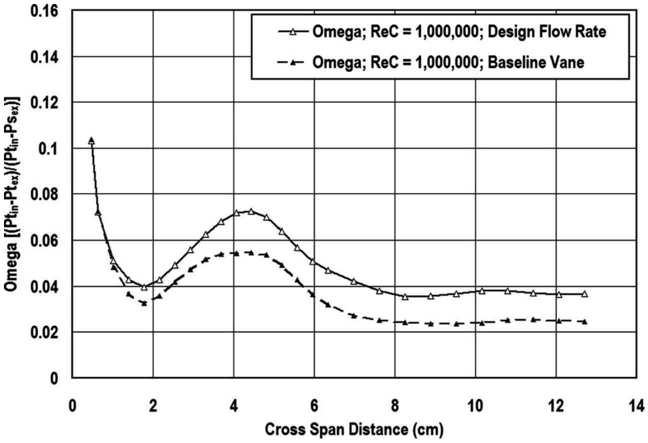

Fig. 9 Cross-passage averaged total pressure loss coefficient $\Omega$ for the gill slot vane and base vane, 1/4 $C_{ax}$, low turbulence, $Re_C$=1,000,000, design flow

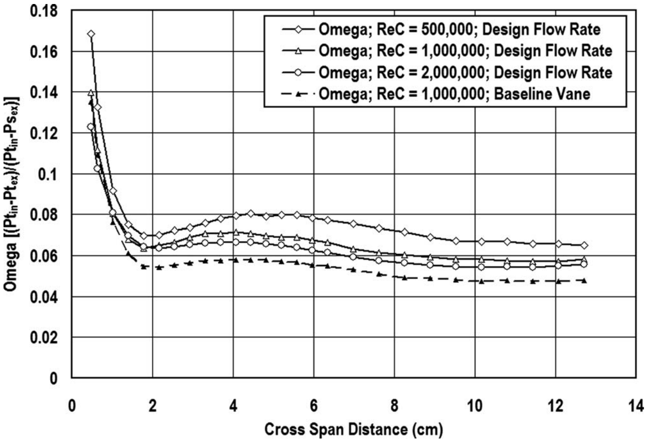

Fig. 12 Cross-passage averaged total pressure loss coefficient $\Omega$ for the gill slot vane, 1/4 $C_{ax}$, aerocombustor turbulence showing effect of Reynolds number

loss. Figure 12 presents cross-passage averaged losses versus span for the gill slot vane for the aerocombustor condition for the three Reynolds numbers and for the base vane at a Reynolds number of 1,000,000. The losses show a systematic increase with decreasing Reynolds number. The base vane results have a very similar trend. A comparison showing the incremental increase in losses for the three turbulence conditions between the gill slot and base vane is shown in Fig. 13 as a function of Reynolds numbers. The trends at all turbulence conditions are similar and show a decreasing gill slot loss with increasing Reynolds number.

The cross-passage averaged turning angle $\beta$ is shown as a function of span for the gill slot vane at the aerocombustor condition in Fig. 14. The base vane result is shown at a Reynolds number of 1,000,000 for comparison. Generally, the trends of the curves are very similar, showing a significant overturning near the endwall, an underturning in the region associated with secondary core losses, and nearly 2D behavior near midspan. The trend of the figure shows a modest increase in turning with Reynolds number. Generally, the results for all turbulence conditions show a very modest increase in turning with Reynolds number and a slight increase in turning for the gill slot vane compared to the base vane. This increased turning angle between the gill and base vane is less than 0.2 deg and is not considered significant.

**Effects of Gill Slot Flow Rate.** The influence of gill slot flow rate on total pressure losses and turning angle was investigated for the aerocombustor case. Cross-passage averaged total pressure losses are shown as a function of span for a range of coolant ejection flow rates in Fig. 15. These exit surveys were all taken at a Reynolds number of 1,000,000 and the base vane result is

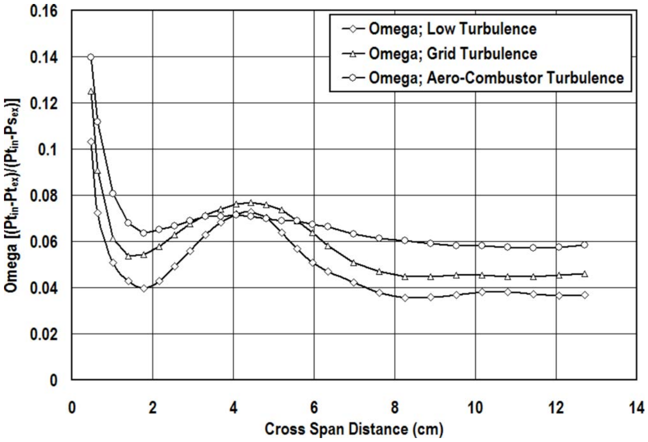

Fig. 10 Cross-passage averaged total pressure loss coefficient $\Omega$, gill slot vane, 1/4 $C_{ax}$, comparing turbulence conditions, $Re_C$=1,000,000 at design flow

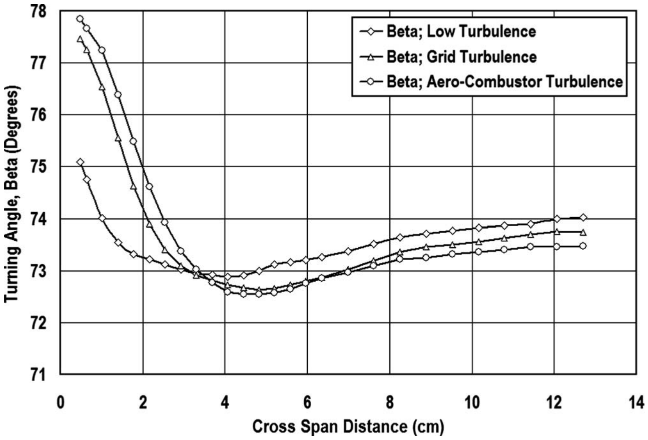

Fig. 11 Cross-passage averaged turning angle $\beta$ gill slot vane, 1/4 $C_{ax}$, comparing turbulence conditions, $Re_C$=1,000,000 at design flow

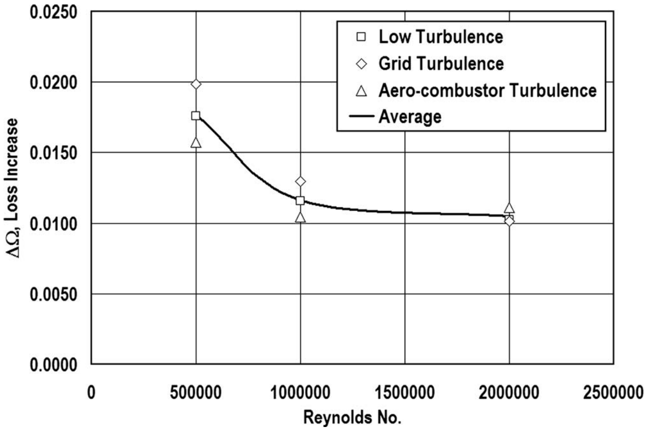

Fig. 13 Increase in mass-averaged total pressure loss coefficient $\Delta\Omega$ from base to gill slot vane versus Reynolds number, 1/4 $C_{ax}$, varying turbulence conditions

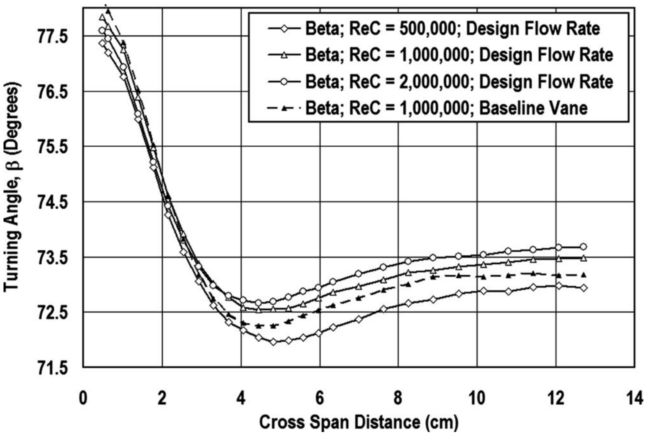

**Fig. 14 Cross-passage averaged turning angle $\beta$ for the gill slot vane at 1/4 axial chord, aerocombustor turbulence showing effect of Reynolds number**

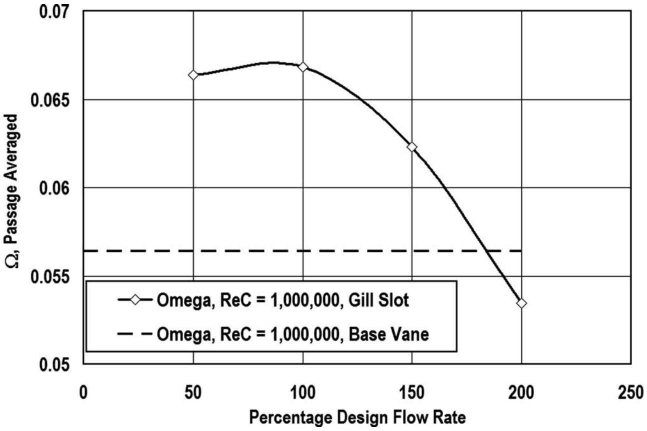

**Fig. 16 Mass-averaged total pressure loss coefficient $\Omega$ as a function of gill slot flow rate, 1/4 $C_{ax}$, aerocombustor turbulence, $Re_C$=1,000,000**

shown for comparison. Generally, the loss distribution is similar as a function of span and a clear variation as a function of the percent design flow rate can be seen. Largely, the differences in losses are seen to be incremental across the span. The passage averaged total pressure loss $\Omega$ is plotted as a function of percent design flow rate for the aerocombustor condition in Fig. 16. The base vane losses are shown as a line for comparison. The 50% and 100% design flow losses are about the same level, while losses decrease with increasing flow rate above the full design flow. This result is consistent with expectations as at 150% design flow, the exit momentum of the coolant flow is about the same as the free-stream flow at the gill slot exit. Consequently, at this flow rate, the losses are expected to be largely a function of gill slot separation losses. At 200% of the design flow rate, the velocity of the coolant ejection exceeds the local velocity of the free-stream energizing the local flow. Coolant ejection at 200% of design flow reduces the overall losses compared with the base vane. First stage vanes are expected to have available normalized coolant pressures similar to the design flow. However, downstream vanes and blades can have significantly higher effective coolant feed pressures.

Coolant feed rate appears to have a mild influence on the turning distribution. Figure 17 presents cross-passage averaged turning angle for the aerocombustor condition as a function of span for varying coolant discharge rates. At midspan turning angle is shown to increase slightly with discharge rate. However, near the endwall, the overturning is shown to decrease with increasing flow rate. At the higher coolant discharge rates, the high momentum coolant is believed to energize even the near endwall flow, reducing the impact of the cross-passage pressure gradient. The passage averaged turning angle shows a very small increase with increasing coolant flow and a slight increase over the base vane. Neither of these trends is significant compared with the experimental uncertainty in angle.

## Summary and Conclusions

Surface pressure distributions and full exit loss surveys have been acquired for a gill slot vane for low (0.7%), grid (8.5%), and aerocombustor (13.5%) turbulence conditions over a four to one range in chord exit Reynolds numbers (500,000, 1,000,000, and 2,000,000) with varying coolant discharge rates (50%, 100%, 150%, and 200% of design). These measurements have been compared with base vane measurements. Additionally, surface heat transfer and adiabatic effectiveness measurements downstream from the gill slot exit as well as total pressure drop and heat transfer for the converging pin array have been documented for this geometry in Ref. [1].

Surface pressure distributions are largely unaffected except downstream from the gill slot discharge. The pressure distribution downstream from the gill slot is shown to depend strongly on coolant flow rate.

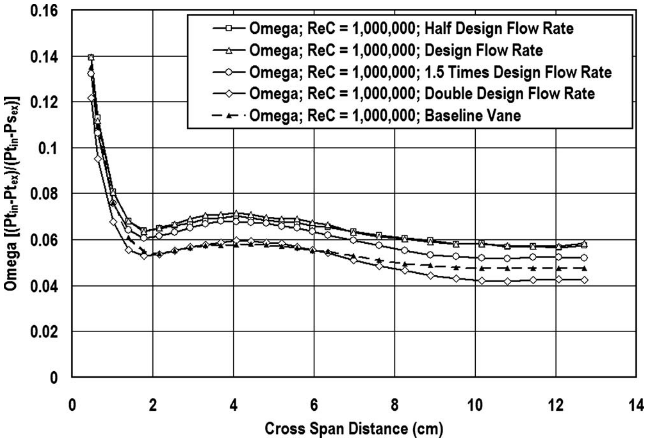

**Fig. 15 Cross-passage averaged total pressure loss coefficient $\Omega$, gill slot vane, 1/4 $C_{ax}$, aerocombustor turbulence showing effect of discharge flow rate, $Re_C$=1,000,000**

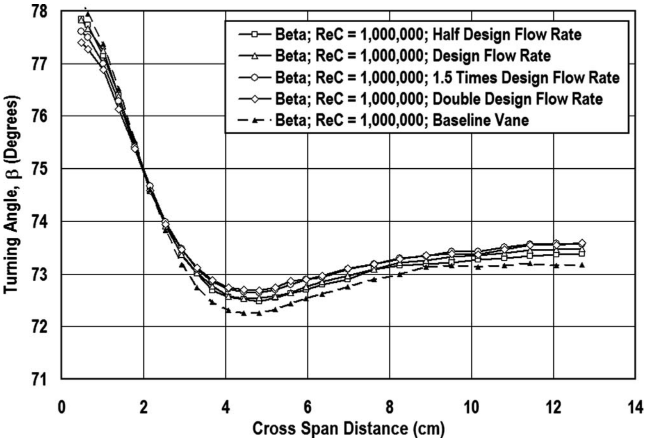

**Fig. 17 Cross-passage averaged turning angle $\beta$ for the gill slot vane at 1/4 axial chord, aerocombustor turbulence showing effect of discharge flow rate**

Generally, the gill slot vane produces a total pressure loss at design and near design flow rates that is measurably higher than the base vane. At design flow, this loss decreases with increasing Reynolds number. At flow rates greater than that of the design, losses decrease with increasing coolant injection rate.

Turning angle distribution is affected by both Reynolds number and discharge flow rate. However, while passage averaged turning angle shows mild increases with Reynolds number and discharge flow rate, neither of these trends is significant compared with experimental uncertainty.

## Acknowledgment

The authors gratefully acknowledge the support from the University Turbine System Research (UTSR) consortium, which is administrated by the South Carolina Institute for Energy Studies and largely funded through DOE's National Energy Technology Laboratory. The authors would also like to acknowledge the help of Rolls–Royce of Indianapolis for providing the vane geometry used in this study. Additionally, the facility used in this project was funded through a seed grant from the North Dakota EPSCoR program. In addition, the authors are indebted to the University of North Dakota for providing additional support and laboratory space.

## Nomenclature

beta = turning angle, ( °), also $\beta$
$C$ = vane true chord length (m)
$C_{\mathrm{ax}}$ = axial chord length (m)
$L_u$ = energy scale, $1.5|u'|^3/\varepsilon$ (m)
$L_x$ = longitudinal integral scale of $u'$ fluctuation (m)
$M_{\mathrm{dot}}$ = coolant mass flow rate (kg/s)
Omega = total pressure loss coefficient, $[\mathrm{Pt}_{\mathrm{in}}\text{-}\mathrm{Pt}_{\mathrm{ex}}]/[\mathrm{Pt}_{\mathrm{in}}\text{-}\mathrm{Ps}_{\mathrm{ex}}]$, also $\Omega$
$P$ = pressure (Pa)
$\mathrm{Re}_C$ = Reynolds number based on true chord and exit conditions
$S$ = vane surface arc length measured from stagnation point (m)
$T$ = temperature (K)
$T_u$ = turbulence level, $|u'|/U_\infty$
$U_\infty$ = free-stream velocity (m/s)
$V_{\mathrm{ex}}$ = cascade exit velocity (m/s)
$u', |u'|$ = streamwise component rms fluctuation velocity (m/s)

### Greek Letter Symbols

$\beta$ = turning angle (deg), also beta
$\varepsilon$ = turbulent dissipation rate (m$^2$/s$^3$)
$\Omega$ = total pressure loss coefficient, $[\mathrm{Pt}_{\mathrm{in}}-\mathrm{Pt}_{\mathrm{ex}}]/[\mathrm{Pt}_{\mathrm{in}}-\mathrm{Ps}_{\mathrm{ex}}]$, also omega

### Subscripts

co = conditions at the gill slot lip exit
ex = conditions at the nozzle exit plane
in = conditions at the nozzle inlet plane
orf = conditions at the orifice
$s$ = static condition
$t$ = total or stagnation condition
$\infty$ = evaluated in the free stream

## References

[1] Ames, F. E., Johnson, J. D., and Fiala, N. J., 2007, "Gill Slot Trailing Edge Heat Transfer—Effects of Blowing Rate, Reynolds Number, and External Turbulence on Heat Transfer and Film Cooling Effectiveness," ASME Paper No. GT2007-27397.
[2] Ames, F. E., Johnson, J. D., and Fiala, N. J., 2006, "The Influence of Aero-Derivative Combustor Turbulence and Reynolds Number on Vane Aerodynamic Losses, Secondary Flows, and Wake Growth," ASME Paper No. GT-2006-90168.
[3] Denton, J. D., 1993, "Loss Mechanisms in Turbomachines," ASME J. Turbomach., **115**, pp. 621–656.
[4] A. G. Glassman, ed., 1972–1975, *Turbine Design and Application*, National Aeronautics and Space Administration, Washington, DC, Vols. 1–3, NASA SP-290.
[5] Moore, J., Shaffer, D. M., and Moore, J. G., 1987, "Reynolds Stress and Dissipation Downstream of a Turbine Cascade," ASME J. Turbomach., **109**, pp. 258–267.
[6] Gregory-Smith, D. G., and Cleak, J. G. E., 1992, "Secondary Flow Measurements in a Turbine Cascade With High Inlet Turbulence," ASME J. Turbomach., **114**, pp. 173–183.
[7] Ames, F. E., and Plesniak, M. W., 1997, "The Influence of Large Scale, High Intensity Turbulence on Vane Aerodynamic Losses, Wake Growth, and Exit Turbulence Parameters," ASME J. Turbomach., **119**, pp. 182–192.
[8] Sieverding, C. H., 1985, "Recent Progress in the Understanding of Basic Aspects of Secondary Flow in Turbine Blade Passages," ASME J. Eng. Gas Turbines Power, **107**, pp. 248–257.
[9] Klein, A., 1966, "Investigation of the Entry Boundary Layer on the Secondary Flows in the Blading of Axial Turbines," BHRA T 1004.
[10] Langston, L. S., Nice, M. L., and Hooper, R. M., 1977, "Three-Dimensional Flow Within a Turbine Cascade Passage," ASME J. Eng. Power, **99**, pp. 21–28.
[11] Marchal, P., and Sieverding, C. H., 1977, "Secondary Flows Within Turbomachinery Bladings," *Secondary Flows in Turbomachines*, AGARD, The Hague, Netherlands.
[12] Burd, S. W., and Simon, T. W., 2000, "Flow Measurements in a Nozzle Guide Vane Passage With a Low Aspect Ratio and Endwall Contouring," ASME J. Turbomach., **122**, pp. 659–666.
[13] Zess, G. A., and Thole, K. A., 2001, "Computational Design and Experimental Evaluation of Using an Inlet Fillet on a Gas Turbine Vane," ASME Paper No. 2001-GT-404.
[14] Ingram, G., Gregory-Smith, D., Rose, M., Harvey, N., and Brennan, G., 2002, "The Effect of End-Wall Profiling on Secondary Flow and Low Development in a Turbine Cascade," ASME Paper No. GT2002-30339.
[15] Sieverding, C. H., Arts, T., and Denos, R., 1994, "Investigation of the Flow Field Downstream of a Turbine Trailing Edge Cooled Nozzle Guide Vane," ASME Paper No. 94-GT-209.
[16] Osnaghi, C., Perdichizzi, A., Savini, M., Harasgama, P., and Lutum, E., 1997, "The Influence of Film Cooling on the Aerodynamic Performance of a Turbine Nozzle Guide Vane," ASME Paper No. 97-GT-522.
[17] Pappu, K. R., and Schobeiri, M. T., 1997, "Optimization of Trailing Edge Ejection Mixing Losses A Theoretical and Experimental Study," ASME Paper No. 97-GT-523.
[18] Schobeiri, T., 1989, "Optimum Trailing Edge Ejection for Cooled Gas Turbine Blades," ASME J. Turbomach., **111**, pp. 510–514.
[19] Kapteijn, C., Amecke, J., and Michelassi, V., 1994, "Aerodynamic Performance of a Transonic Turbine Guide Vane with Trailing Edge Coolant Ejection: Part I—Experimental Approach," ASME Paper No. 94-GT-288.
[20] Michelassi, V., Martelli, F., and Amecke, J., 1994, "Aerodynamic Peformance of a Transonic Turbine Guide Vane With Trailing Edge Coolant Ejection: Part II—Numerical Approach," ASME Paper No. 94-GT-248.
[21] Uzol, O., and Camci, C., 2001, "Aerodynamic Loss Characteristics of a Turbine Blade with Trailing Edge Coolant Ejection: Part 2—External Aerodynamics, Total Pressure Losses, and Predictions," ASME J. Turbomach., **123**, pp. 249–257.
[22] Telisinghe, J. C., Ireland, P. T., Jones, T. V., Barrett, D., and Son, C., 2006, "Comparative Study Between a Cut-Back and Conventional Trailing Edge Film Cooling System," ASME Paper No. GT2006-91207.
[23] Martini, P., Schulz, A., and Wittig, S., 2003, "Experimental and Numerical Investigation of Trailing Edge Film Cooling by Circular Coolant Wall Jets Ejected From a Slot With Internal Rib Arrays," ASME Paper No. GT2003-38157.
[24] Ames, F. E., Barbot, P. A., and Wang, C., 2003, "Effects of Aeroderivative Combustor Turbulence on Endwall Heat Transfer Distributions Acquired in a Linear Vane Cascade," ASME J. Turbomach., **125**, pp. 210–220.
[25] White, F. M., 1991, *Viscous Fluid Flow*, 2nd ed., McGraw-Hill, New York.
[26] Moffat, R. J., 1988, "Describing the Uncertainties in Experimental Results," Exp. Therm. Fluid Sci., **1**, pp. 3–17.
[27] FLUENT 6.0, 2001, FLUENT 6.0 User's Guide, Fluent, Inc., Lebanon, NH.

# Endwall Boundary Layer Development in an Engine Representative Four-Stage Low Pressure Turbine Rig

**Maria Vera**[1]
Research Associate

**Elena de la Rosa Blanco**[2]
Senior Engineer

**Howard Hodson**

Whittle Laboratory,
University of Cambridge,
Cambridge CB3 0DY, UK

**Raul Vazquez**
Industria de Turbopropulsores,
Madrid 28830, Spain

*Research by de la Rosa Blanco et al. ("Influence of the State of the Inlet Endwall Boundary Layer on the Interaction Between the Pressure Surface Separation and the Endwall Flows," Proc. Inst. Mech. Eng., Part A,* ***217****, pp. 433–441) in a linear cascade of low pressure turbine (LPT) blades has shown that the position and strength of the vortices forming the endwall flows depend on the state of the inlet endwall boundary layer, i.e., whether it is laminar or turbulent. This determines, amongst other effects, the location where the inlet boundary layer rolls up into a passage vortex, the amount of fluid that is entrained into the passage vortex, and the interaction of the vortex with the pressure side separation bubble. As a consequence, the mass-averaged stagnation pressure loss and therefore the design of a LPT depend on the state of the inlet endwall boundary layer. Unfortunately, the state of the boundary layer along the hub and casing under realistic engine conditions is not known. The results presented in this paper are taken from hot-film measurements performed on the casing of the fourth stage of the nozzle guide vanes of the cold flow affordable near term low emission (ANTLE) LPT rig. These results are compared with those from a low speed linear cascade of similar LPT blades. In the four-stage LPT rig, a transitional boundary layer has been found on the platforms upstream of the leading edge of the blades. The boundary layer is more turbulent near the leading edge of the blade and for higher Reynolds numbers. Within the passage, for both the cold flow four-stage rig and the low speed linear cascade, the new inlet boundary layer formed behind the pressure leg of the horseshoe vortex is a transitional boundary layer. The transition process progresses from the pressure to the suction surface of the passage in the direction of the secondary flow.* [DOI: 10.1115/1.2952382]

## Introduction

In recent years, the provision of data related to the nature of the endwall boundary layer within the blade passage has become an important issue. One of the reasons for this is that the endwall flows depend on the state of the inlet endwall boundary layer. The first experiment that was related to this issue was conducted by Senoo [1]. He studied the boundary layer at the throat of a turbine-nozzle cascade. He found that, independent of the state of the inlet boundary layer, the boundary layer on the endwall was laminar upstream of the throat and became turbulent downstream of the throat. He stated that the reason for the laminar character of the boundary layer was the large favorable streamwise pressure gradient on that area of the endwall. However, Langston et al. [2] argued that it was caused by the formation of a new endwall boundary layer downstream of the pressure leg of the horseshoe vortex. This proposition was based on the results of hot wire measurements that were carried out in the endwall boundary layer of a linear turbine cascade. They found large regions of a very thin endwall boundary layer, although they could not establish its state.

Moore and Gregory-Smith [3] performed measurements of the intermittency close to the endwall by means of a hot wire. Harrison [4] and Ingram [5] performed hot-film experiments on the endwall boundary layer within the blade passage of a linear turbine cascade. Harrison [4] also compared his results with the shear stress information obtained from the oil dot measurements performed on the endwall of the same cascade. The main conclusion of the work of these authors is that the boundary layer on the endwall is far from being fully turbulent in that it presents large regions of laminar and transitional flows within the blade passage. Usually, endwall flows are considered to be fully turbulent in computational simulations. However, Moore and Gregory-Smith [3] used their results to impose a transitional flow in their computational simulations. They showed that the specification of transition on the endwall gave rise to more accurate computed predictions for the loss and the secondary flow field.

Holley et al. [6] made experimental measurements of the endwall skin friction coefficient on a low speed linear turbine cascade of high turning and low aspect ratio airfoils. They performed a detailed comparison between experimental measurements and computational fluid dynamics (CFD) predictions on the endwall in an attempt to explain the influence of the endwall shear stress on the losses. This comparison showed that mass-averaged total pressure loss and pitch-averaged skin friction coefficients followed similar trends along the passage. The latter was true for both measured and predicted quantities. However, the contribution of the endwall shear to the mass-averaged total pressure loss was not clear from their results. In addition, the CFD prediction of the absolute values was not accurate. It was concluded that measurements revealing the state of the boundary layer on the endwall are necessary in order to improve the accuracy of the CFD calculations.

In an engine, the general pattern of endwall flows will be affected by vortices and wakes from upstream blade rows. The pres-

---

[1] Present address: Institute for Aviation and the Environment, University of Cambridge, Cambridge CB2 1PX, UK.

[2] Present address: Aerodyne Research Inc., Billerica, MA 01821.

Contributed by the International Gas Turbine Institute of ASME for publication in the JOURNAL OF TURBOMACHINERY. Manuscript received November 20, 2007; final manuscript received November 29, 2007; published online November 6, 2008. Review conducted by David Wisler. Paper presented at the ASME Turbo Expo 2007: Land, Sea and Air (GT2007), Montreal, Quebec, Canada, May 14–17, 2007.

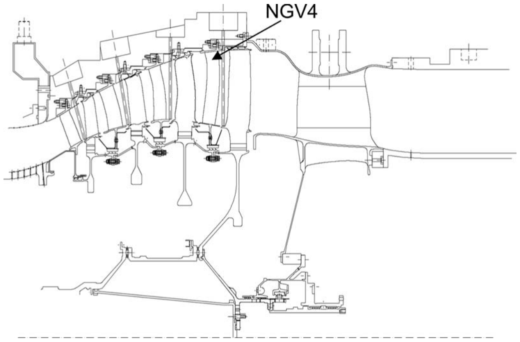

Fig. 1 General assembly of the fourth stage ANTLE LPT rig

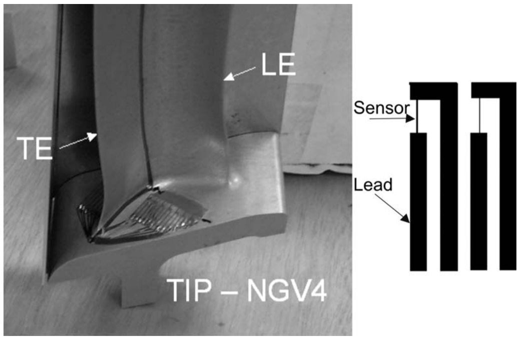

Fig. 2 Hot-film sensors on the tip passage of an NGV4 blade

ence of tip leakage and other leakage flows, like the ones from the interplatform gaps and from the cavity formed with the upstream blade row, will also influence the endwall flow structures. In addition, potential interactions and the presence of a radial pressure gradient will modify the structures of the endwall flows. Owing to the complexity of the flow around the endwalls and the nature of the experimental techniques employed, the discussion presented herein will be limited to the nature of the measured boundary layer in a cold flow four-stage LPT rig. A comparison between the measurements of the endwall boundary layer in the LPT rig and those on a linear LPT cascade is also presented.

## Experimental Apparatus

In this section, the facilities, the instrumentation of the blades, the data logging system, and the measurement technique are described together with the processing and representation of the data for both the low speed linear cascade and the cold flow four-stage rig.

The linear cascade tests were carried out in a low speed cascade wind tunnel. The linear cascade consisted of six high aspect ratio, high turning blades that are characteristic of a modern LPT. Studies on this blade have been previously presented by de la Rosa Blanco et al. in Ref. [7] and de la Rosa Blanco in Ref. [8].

Industria de Turbopropulsores (ITP) has been responsible for the design, manufacture, and assembly of the four-stage LPT of the affordable near term low emission (ANTLE) engine. The experiments were carried out in the altitude test facility at Rolls-Royce, Derby. The ANTLE LPT has been designed by following ITP's high through flow (HTF) design path, which intends to meet the new requirements for the removal of one stage of the LPT. The HTF designs are characterized by large flow parameters and conventional turnings, which imply a reduced annulus cross section. Details about the characteristics of the HTF blades can be found in Ref. [9]. A general assembly of the ANTLE LPT is shown in Fig. 1.

Hot-film sensors respond to the wall shear stress. The small degree of intrusiveness of these sensors and their simplicity of operation make hot-film anemometry a reliable measurement technique for the determination of the state of the boundary layer.

For the low speed linear cascade tests, the endwall was instrumented with small arrays cut from a SenFlex 93021 array of surface-mounted hot-film sensors. The results from the endwall flow visualization experiments presented in the next section were used to determine the location of the separation lines and the singular points and to define the direction of the streamlines.

For the four-stage LPT rig, specifically designed DANTEC multielement hot-film sensors were used. The sensors are 1 mm in length by 0.1 mm in width, and the sensor separation is 2.4 mm. Figure 2 shows the instrumentation on the casing shroud of an NGV4 blade. The sketch on the right hand side of the figure shows the geometry of the hot-film sensors. CFD predictions, not shown here, were used to define the direction of the streamlines and to determine the location of the sensors.

The temperature of the blades was measured by T-type foil thermocouples glued on the platforms of the blades. The temperature has to be measured at the same location as the sensors in order to obtain an accurate value of the anemometer's output voltage with no flow, $E_0$. This value is needed for the processing of the sensor output signals.

For both the low speed linear cascade and the cold flow four-stage rig tests, voltages were acquired with a PCI-MIO-16E-1 National Instruments Data Acquisition (NiDAQ) board. The ac signal is recorded at high gain and separately from the dc signal in order to obtain the maximum resolution of the ac signal. For the four-stage rig, the output signal from a once-per-revolution optical probe was connected to the NiDAQ. This signal activated the acquisition of the data. All the results presented for the four-stage rig were recorded simultaneously. The temperature was recorded with a Comark C8600 TEMPSCAN.

For the linear cascade tests, the measurements were carried out under steady inflow conditions. Therefore, no phase averaging was required and the results are then presented versus time. The data were logged at 25 kHz and the ac signal was recorded with the low-pass filter at 10 kHz.

For the four-stage rig tests, the time variable of the plots has been normalized by the wake passing period corresponding to Rotor 3. The data were logged at a frequency of 60 kHz. The ac signal was recorded with the low-pass filter set at 30 kHz. The blade passing frequency of the 90 blades of Rotor 3 was about 2950 Hz, which implies that approximately 20 sampled points per wake passing were recorded.

The methodology of the surface hot-film anemometry is a well-established technique and has been widely documented. In this paper, only the main issues are considered. More information can be found in Ref. [10]. These hot films were operated at constant temperature with an overheat ratio of 1.5. According to Hodson [10], meaningful information can be obtained from uncalibrated hot-film sensors assuming that

$$\tau_w \propto \left[\frac{E^2 - E_0^2}{E_0^2}\right]^3 \tag{1}$$

where $E$ is the instantaneous output voltage from the anemometer and $E_0$ is the bridge voltage under zero flow conditions. Using Eq. (1), a quantity proportional to the shear stress is obtained with the uncalibrated sensors.

At each measurement location, a number of points, $I$, per time trace are recorded. $N$ time traces are acquired for the ensemble averaged measurements. A total of 128 ensembles were recorded for the ac signal. The acquisition of each of these ensembles starts when indicated by the once-per-revolution signal.

The individual raw shear stress trace of a signal shows the evolution in time of the signal. The ensemble average of the quasi wall shear stress is given by Eq. (2). The ensemble average is calculated for a given time past a trigger pulse, $i$.

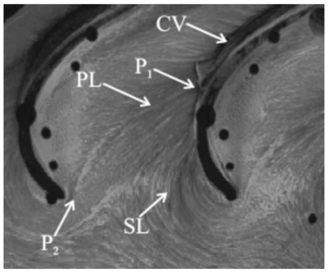

**Fig. 3 Flow visualization experiments on the endwall of the low speed linear cascade; Re=232,000**

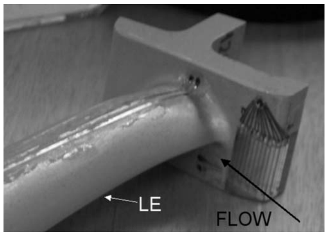

**Fig. 5 Hot-film sensors on the tip inlet platform of an NGV4 blade**

$$\langle x_i\rangle = \frac{1}{N}\sum_{n=1}^{N} x_{n,i}, \quad i=1,I \qquad (2)$$

The rms of the ensemble averaged signal is given by

$$\text{rms}_i = \sqrt{\frac{1}{(N-1)}\sum_{n=1}^{N} (x_{n,i}-\langle x_i\rangle)^2}, \quad i=1,I \qquad (3)$$

The nondimensional value of the rms is plotted as

$$\text{ND} \times \text{rms}_i = \frac{\text{rms}_i}{\text{rms}_{\text{max}}} \qquad (4)$$

where $\text{rms}_{\text{max}}$ is the maximum value of the rms.

## Results

In this section, the results corresponding to the low speed linear cascade will be presented first, followed by the ones from the cold flow four-stage rig.

**Low Speed Linear Cascade Tests.** Figure 3 shows the endwall flow visualization for the low speed linear cascade. The most relevant endwall flow features related to the wall measurements can be seen in this figure. The flow visualization shows the location of the saddle point associated with the formation of the horseshoe vortex ($P_2$). The pressure leg (PL) and the suction leg (SL) of the horseshoe vortex are also highlighted. The point at which the pressure side leg of the horseshoe vortex (PL) reaches the blade suction surface (SS) ($P_1$) under the influence of the pitchwise adverse pressure gradient is also shown, as well as the formation of the suction side corner vortex (CV).

Figure 4 shows a selection of raw shear stress traces on the endwall of the low speed linear cascade. For the case presented in the figure, the inlet endwall boundary layer is turbulent. The dots represent the location of all the hot films. For clarity reasons, only some traces are shown.

The solid lines in the figure represent the SL of the horseshoe vortex and the PL of the horseshoe vortex based on the flow visualization results presented above. The evolution of the flow is studied along a limiting streamline behind the PL of the horseshoe vortex. This is also shown in the figure (dashed line).

The flow in the region affected by the SL of the horseshoe vortex close to the blade SS has a transitional character, see Trace (a). Behind the separation line of the PL of the horseshoe vortex when moving from the blade pressure surface toward the SS of the adjacent blade along a limiting streamline (from (b) to (e)), the flow becomes more turbulent. The flow close to the blade pressure surface (b) is characterized by a quiet signal that resembles that of a laminar flow or early stages of transition and then develops into a more turbulent flow (e).

That there are large areas of laminar and transitional flow on the endwall within the blade was also shown by Harrison [4] and Ingram [5]. For the case presented here, the Reynolds number based on the axial chord and the exit velocity of the airfoil is 232,000. This value is lower than that used by Harrison [4], which was 780,000, or Ingram [5], which was 400,000.

**Cold Flow Four-Stage Rig Tests.** The design Reynolds number at the tip of the NGV4 is approximately 69,000 based on the axial chord and the exit velocity of the airfoil. Three groups of sensors were investigated. The first one is located on the inlet platform of the blade and the other two are located, respectively, near the suction and the pressure side of the blade. A period of time equivalent to six upstream rotor passing blades was sampled.

*Platform Boundary Layer*. Figure 5 shows the group of sensors on the inlet platform at the tip of a NGV4 blade. The sensors are located upstream of the position where the inlet endwall boundary layer is forced to roll up into the horseshoe vortex. The approxi-

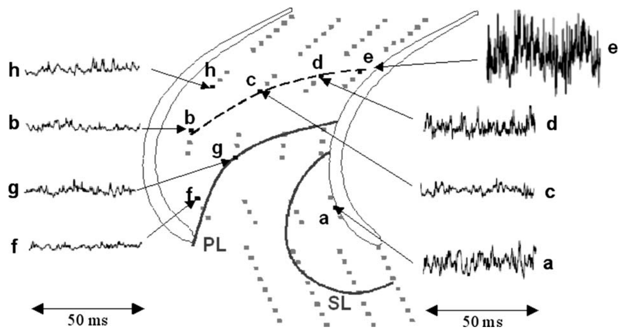

**Fig. 4 Raw shear stress traces on the endwall of the low speed linear cascade; Re=232,000**

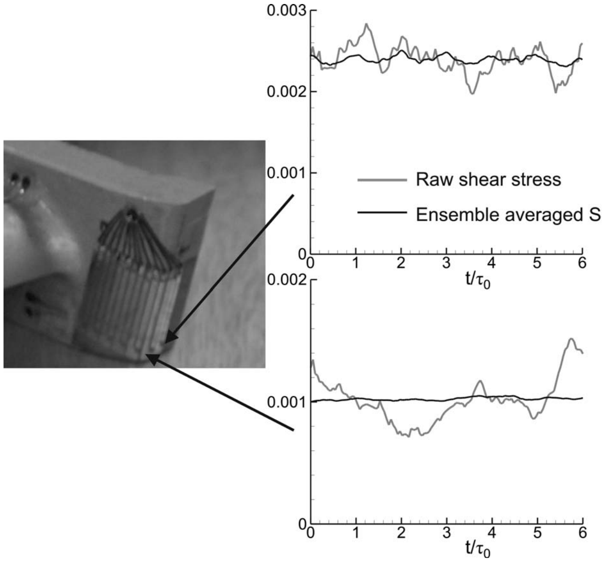

**Fig. 6 Raw (gray) and ensemble averaged (black) shear stress on the tip inlet platform of an NGV4 blade; Re=86,000**

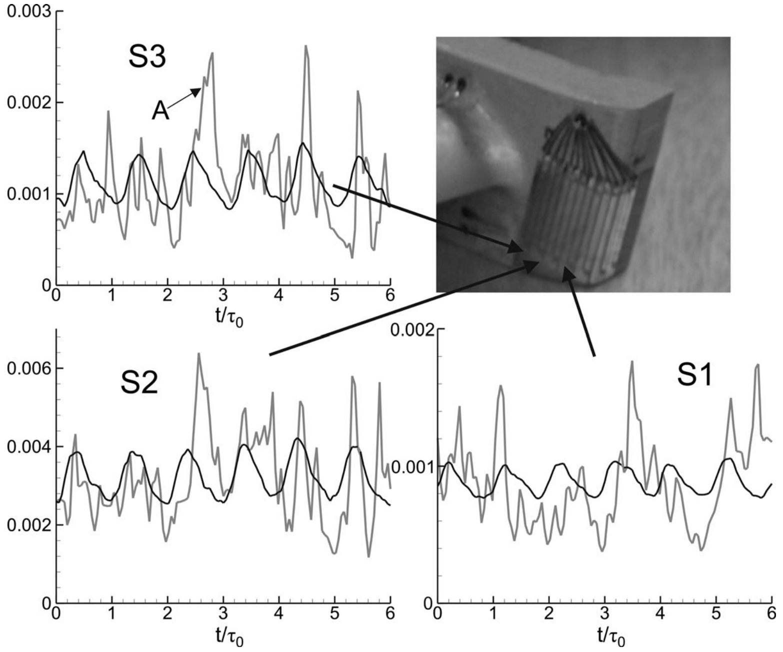

**Fig. 7 Raw (gray) and ensemble averaged (black) shear stress on the tip inlet platform of an NGV4 blade; Re=86,000**

mate direction of the inlet flow has been indicated in the picture.

Figure 6 shows the raw shear stress (gray) and the ensemble averaged shear stress (black) for the sensors that are within the cavity between Rotor 3 and NGV4. In this figure, the Reynolds number based on the axial chord at the tip and the exit velocity of the airfoil is about 86,000. The signal from these two sensors presents a peak to peak value of the ensemble mean, which is only a few percent of the mean value, indicating the low susceptibility of the flow within the cavity to the upstream blade row.

Figure 7 shows the raw shear stress (gray) and the ensemble averaged shear stress (black) for three of the sensors located on the platform for Re=86,000. The ensemble averaged shear stress highlights the periodicity of the signal locked to the blade passing frequency of the upstream rotor. The raw shear stress from sensor S1 does not present symmetric fluctuations around the ensemble averaged value. Instead, high-amplitude excursions of the raw shear stress from the ensemble averaged data are found. These patches are characteristic of a transitional boundary layer. By comparing the output from Sensors S1 and S3, it is seen that the long scale patches break down into lower amplitude higher frequency fluctuations indicating that transition progresses from the exit of the cavity, Sensor S1, to the proximity of the plane of the leading edges of the blade row, Sensor S3. However, large amplitude fluctuations are still found at Sensor S3 (see Label A) indicating that near the leading edge of the blade, the inlet boundary layer is not fully turbulent.

Figure 8 shows the nondimensional rms (gray) and the ensemble averaged shear stress (black) for the same case shown in Fig. 7. The scale on the $y$-axis is that corresponding to the nondimensional rms. It is seen that the random fluctuations are higher where there are peaks in the periodic fluctuations. This implies that the upstream blade row periodically modifies the inlet endwall boundary layer by promoting transitional events, which have a higher shear stress, that develop as they approach the leading edge of the blade. At this point, it is useful to remind the reader that the nondimensional rms is obtained dividing by the maximum value of rms. There is also a comparatively high level of nondimensional rms between the peaks of the periodic fluctuations, indicating that the boundary layer might also be transitional along this part of the blade passing period.

Figure 9 presents the raw and the ensemble averaged shear stress for the Sensors S1 and S3 at two different Reynolds numbers. For Sensor S1, apart from the level of the shear stress, the output does not change significantly when varying the Reynolds number. The most noticeable variation with Reynolds number is seen in Sensor S3, i.e., the sensor nearest to the leading edge of the blade. For this sensor, increasing the Reynolds number increases the presence of high frequency fluctuations around the ensemble averaged shear stress (see Label B). Even though Figs. 9(*c*) and 9(*d*) present a transitional boundary layer, the transition process has progressed more for the case of Fig. 9(*c*). The fact that the signal at Sensor S1 does not change significantly with Reynolds number suggests that the length of transition is shorter for the case of high Reynolds numbers. This latter inference can be drawn only if the streamlines on the inlet platform do not change with the Reynolds number.

Hodson and Dominy [11] presented the performance of a linear LPT cascade rotor hub over a range of Reynolds numbers and inlet boundary layer thickness amongst other parameters. These authors showed that the strength and position of the passage and other vortices forming the endwall flows depended on the inlet boundary layer. The thickening of a turbulent inlet endwall boundary layer leads to more fluid from the inlet endwall boundary layer getting entrained into the passage vortex. This modifies the position and the strength of this vortex [7]. The inlet boundary layer measured on the inlet platforms of NGV4 indicates the presence of a transitional boundary layer upstream of the leading edge of the blade. This transition develops as the flow approaches the plane of the leading edges of the blade row. The progression of the transition depends on the phase within the cycle of the blade passing period. This is because the upstream blade row periodically modifies the inlet endwall boundary layer by promoting transitional events that develop as they approach the leading edge of the blade. The findings about the state of the boundary layer could imply that the transitional events modify periodically the position and strength of the different vortices forming the endwall flows.

*Passage Boundary Layer*. In this section, the state of the boundary layer on the passage of the tip of the NGV4 will be presented. Two arrays of hot films were glued onto the passage near mid-

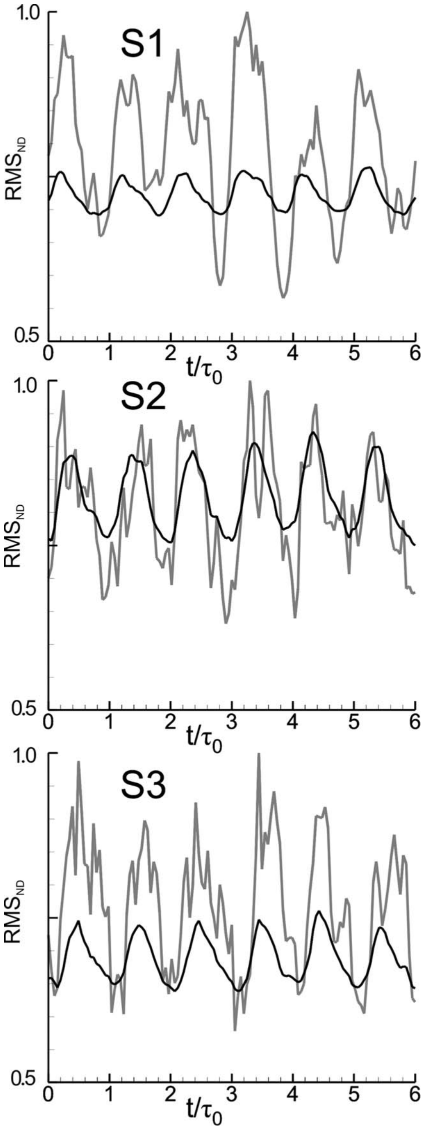

**Fig. 8 Nondimensional rms (gray) and ensemble averaged (black) shear stress on the tip inlet platform of an NGV4 blade; Re=86,000**

chord of the blade. One of the groups of sensors is located near the pressure side of the blade, see Fig. 2. A second group of sensors is located near the SS of blade.

*Pressure Side of the Passage*. Figure 10 shows the raw (gray) and the ensemble averaged shear stress (black) corresponding to the array of sensors located near the pressure side of blade for Re=69,000. The Sensor S4 is the nearest one to the pressure surface of the blade. Sensors S5–S7 are located increasingly further away from the blade surface toward midpassage along the pitchwise direction. The CFD results, not shown here, suggested that the group of Sensors S4–S7 is located behind the PL of horseshoe vortex.

Due to the pitchwise pressure gradient existing within the blade passage, the PL of the horseshoe vortex is driven toward the SS of the adjacent blade. While crossing the blade passage, it removes the inlet boundary layer from the endwall and, as a consequence, a new endwall boundary layer forms behind it. This new endwall boundary layer is driven by both the streamwise and the pitchwise pressure gradient.

Figure 10 shows that for the case of Sensor S4, a periodic increase in the raw shear stress is seen in every blade passing period. This is reflected in the ensemble average. In addition, some higher frequency fluctuations are seen in the raw signal. For Sensor S5, the amplitude of the ensemble average fluctuations is less than for Sensor S4. However, the raw shear stress of Sensor S5 contains more and larger amplitude excursions from the ensemble averaged shear stress (see Label C). This is indicative of a transitional boundary layer. By Sensor S6, the periodic component of the signal is even less evident. In addition, the signal starts to show more high frequency fluctuations around the ensemble averaged shear stress. By Sensor S7, this progression continues and longer phases of high frequency fluctuations can be seen around the ensemble averaged value (see Label D).

The results presented above suggest that the new endwall boundary layer evolves from a more laminar state at Sensor S4 to a more turbulent state by Sensor S7. These findings are in agreement with the low speed linear cascade results presented above, i.e., the flow is mainly laminar or transitional behind the PL of the horseshoe vortex and that transition progresses toward the suction side. Also, the periodic pattern becomes negligible as the flow migrates from near the pressure surface to midpassage, i.e., there is not a component of the upstream rotor blade passing frequency in the newly formed endwall boundary layer. This could be due to the presence of the PL of the horseshoe vortex, which, by removing the inlet endwall boundary layer and growing across the passage, shields the new endwall boundary layer from the effect of the upstream blade row. Based only on hot-film measurements on the wall, no conclusions can be drawn about the origin of the periodic oscillations on Sensor 4.

Figure 11 shows the raw and the ensemble averaged shear stress for the cases of higher and lower Reynolds numbers for Sensors S4 and S7. Even though some differences are visible in the signal of a given sensor when varying the Reynolds number, it seems as if the flow pattern does not change significantly. The similarities include the fact that the upstream rotor blade passing frequency is noticeable around Sensor S4 and that little or no trace of a periodic signal is seen at Sensor S7. In addition, for the two Reynolds numbers under consideration here, the boundary layer again evolves from a more laminar state at Sensor S4 to a more turbulent one at Sensor S7.

*Suction Side of the Passage*. Figure 12 shows the results corresponding to the array of Sensors located near the suction side of blade for the design Reynolds number. The Sensors are not visible in the figure; instead, the arrows indicate the location of the leads of the Sensors. In the signal from Sensor S8, there is little indication of a periodic effect coming from the upstream rotor. The raw shear stress from this Sensor again reveals a transitional pattern similar to that seen in Fig. 10 (Sensors S6 and S7) where the large nonsymmetric amplitude fluctuations with respect to the ensemble averaged data are present. By Sensor S9, the fluctuations in the raw signal are smaller and concentrated around the ensemble averaged value. This is evidence of the evolution of transition. This progression of the transition is evident in the signal from Sensor S10, where high frequency fluctuations around the ensemble averaged value can be distinguished. Sensor S10 is the one nearest to the SS of the blade. These results then agree with the findings from the low speed linear cascade tests presented in the above, which showed that in the region closer to the blade SS, the character of the boundary layer was turbulent or in the last stages of transition.

Figure 12 also shows that the ensemble averaged signal at Sensor S10 contains a periodic pattern similar to that found near the pressure side (Sensor S4). The difference between the signals from both Sensors being that Sensor S4 presents a laminarlike (early transition) pattern whereas Sensor S10 presents a nearly turbulent one.

Figure 13 shows the raw and the ensemble averaged shear stress for two different Reynolds numbers for Sensors S8 and S10. When increasing the Reynolds number, Sensor S8 does not present important differences from the case of the design Rey-

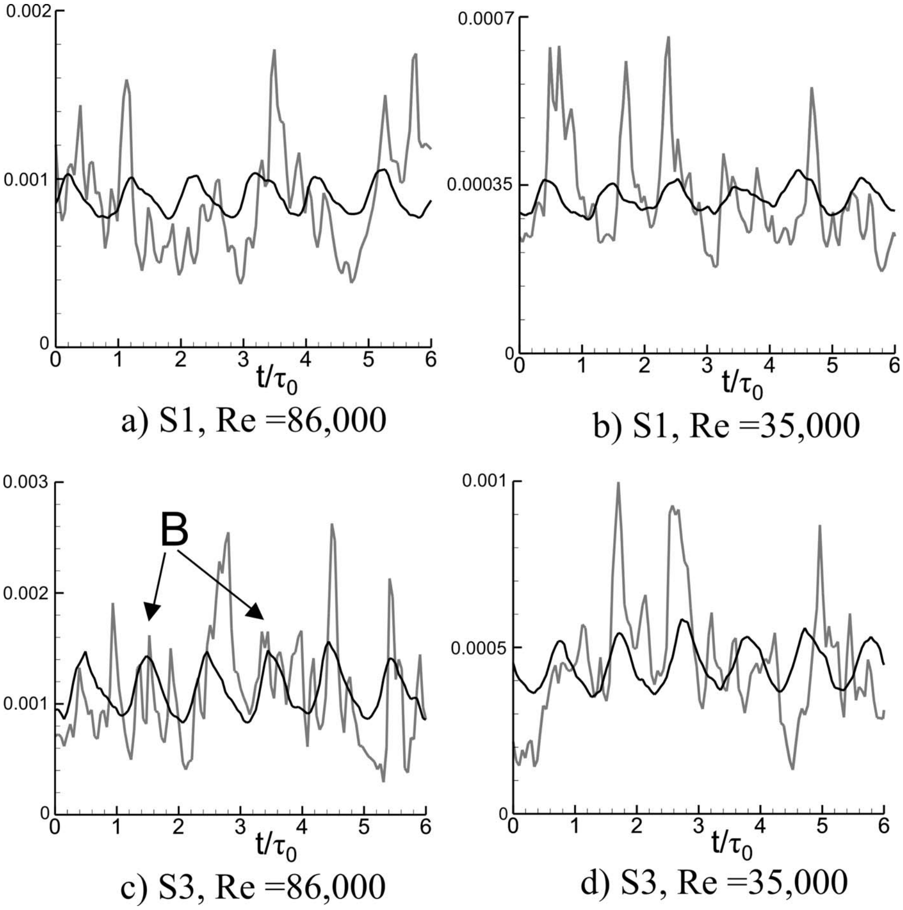

**Fig. 9 Raw (gray) and ensemble averaged (black) shear stress on selected sensors on the tip inlet platform of an NGV4 blade at different Reynolds numbers**

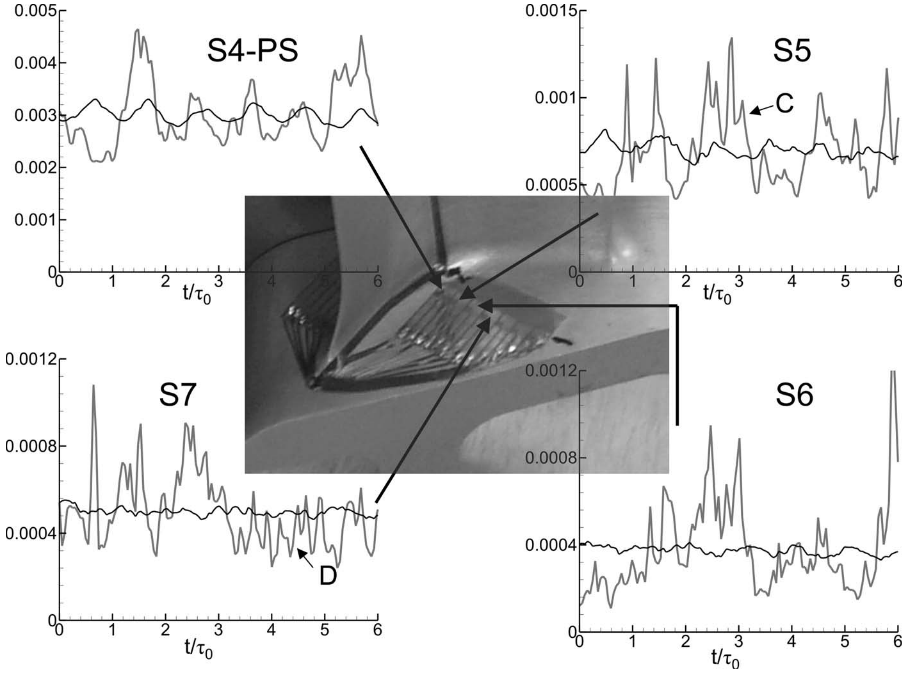

**Fig. 10 Raw (gray) and ensemble averaged (black) shear stress on the passage of the NGV4 tip; Pressure side; Re=69,000**

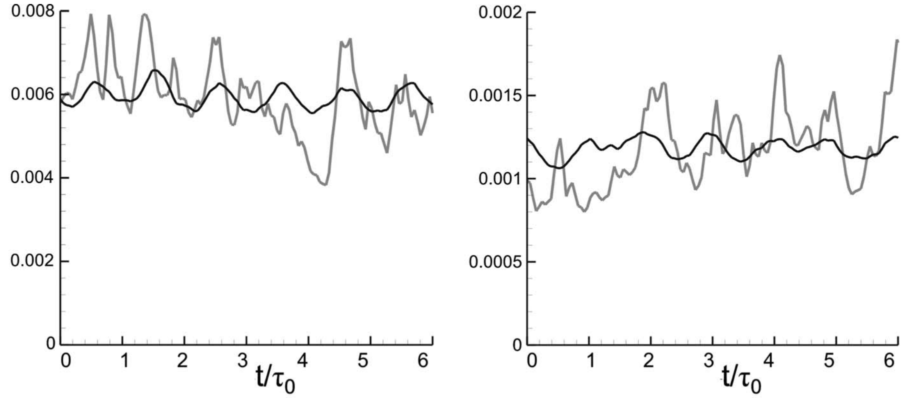

a) S4, Re =86,000 b) S4, Re =35,000

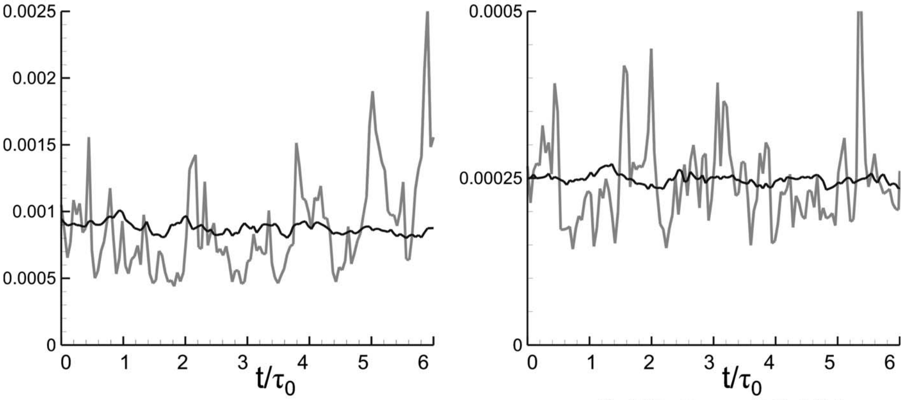

c) S7, Re =86,000 d) S7, Re =35,000

**Fig. 11 Raw (gray) and ensemble averaged (black) shear stress on selected sensors on the passage of the NGV4 tip at different Reynolds numbers; Pressure side**

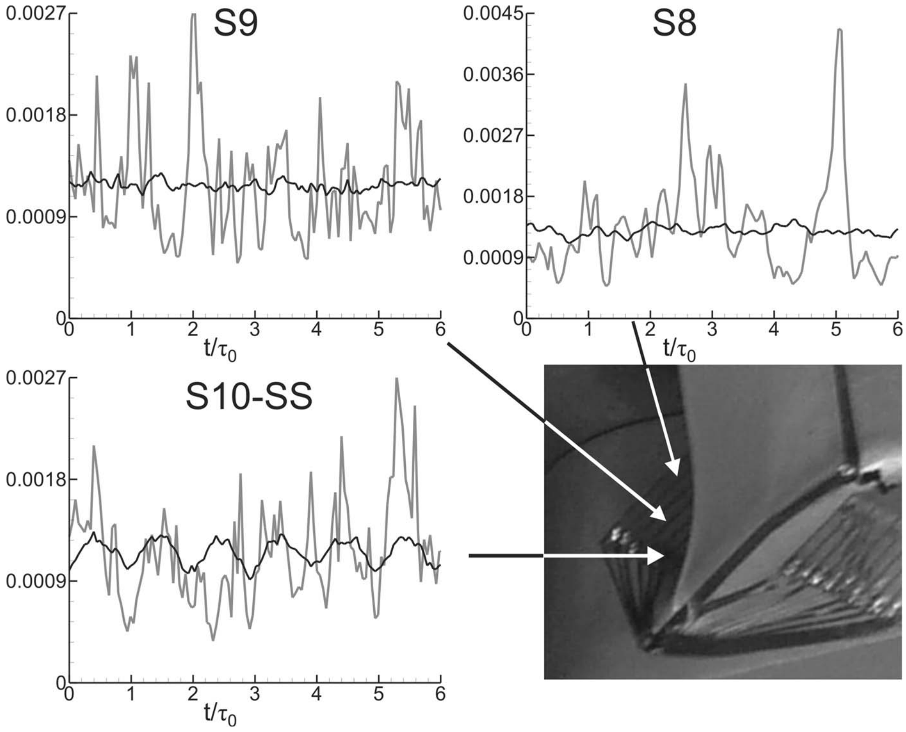

**Fig. 12 Raw (gray) and ensemble averaged (black) shear stress on the passage of the NGV4 tip; Suction side; Re=69,000**

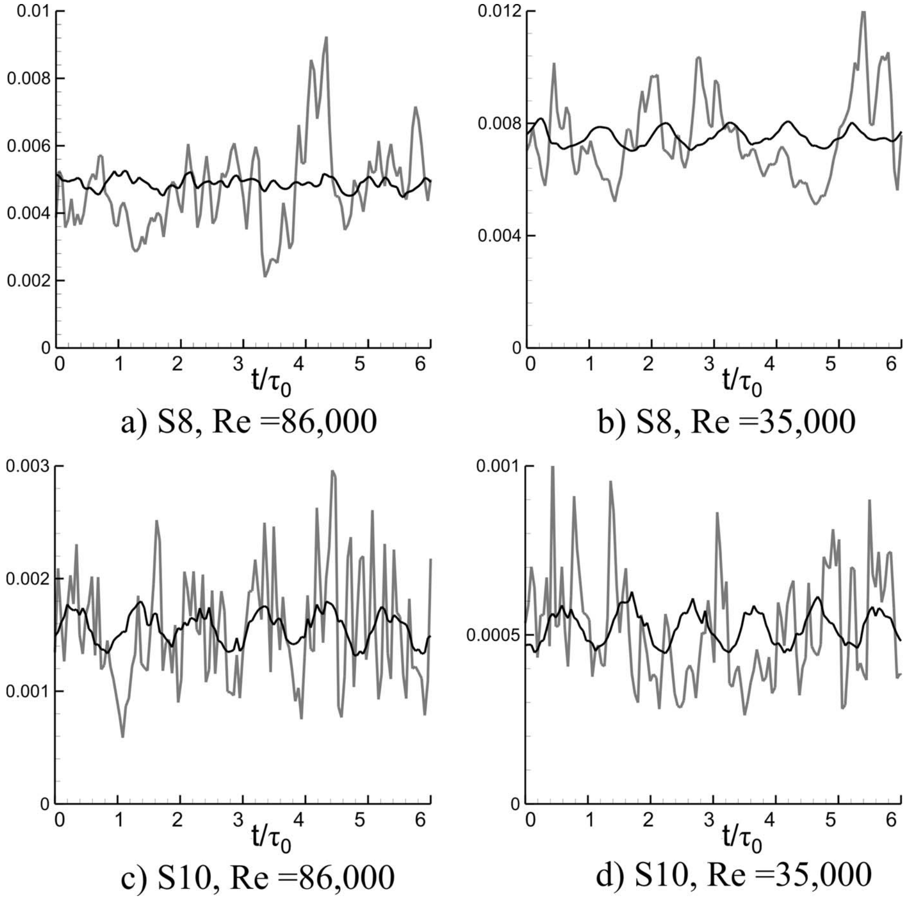

a) S8, Re =86,000

b) S8, Re =35,000

c) S10, Re =86,000

d) S10, Re =35,000

**Fig. 13 Raw (gray) and ensemble averaged (black) shear stress on selected sensors on the passage of the NGV4 tip at different Reynolds numbers; Suction side**

nolds number. However, Sensor S10 presents very high frequency fluctuations around the ensemble averaged shear stress indicating that the boundary layer is more turbulent.

When the Reynolds number is decreased, Sensors S8 and S10 show a decrease in the amount of high frequency fluctuations even though the transitional pattern does not vary noticeably in comparison to that found for the case of the Re=69,000. At the lowest Reynolds numbers, the blade passing frequency from the upstream rotor is visible on the Sensors across the passage, S8. The reason for this is not known.

For the four-stage cold flow rig, hot-film measurements were also carried out on the hub of selected nozzle guide vanes from the second stage of the rig. In the case of NGV2, and in accordance with what it is seen in the case of NGV4, a transitional boundary layer exists upstream of the leading edge of the blade. The boundary layer is more turbulent near the leading edge of the blade. Within the passage, the new inlet boundary layer formed behind the PL of the horseshoe vortex is also a transitional boundary layer. A transitional/turbulent boundary layer is seen near the exit plane of the passage and toward the suction side of the blade.

The results of this experimental work, both on a linear cascade and on the cold flow four-stage LPT rig, show that large regions of the endwall present a laminar and transitional boundary layer. Current CFD simulations assume fully turbulent endwall boundary layers. Based on these results and those from other authors, it is suggested that the computation of the endwall flows should employ a transition model in order to improve the prediction of LPT performance.

## Conclusions

This paper has presented the hot-film measurements performed on the casing of the fourth-stage NGV of the ANTLE LPT rig. Regarding the casing inlet platform, the outputs of the Sensors indicate the presence of a transitional boundary layer upstream of the leading edge of the blade. The boundary layer is more turbulent near the leading edge of the blade and for higher Reynolds numbers. A clear periodic pattern appears on the Sensors located on the inlet platform (outside the cavity).

Within the passage, the new inlet boundary layer formed behind the PL of the horseshoe is a transitional boundary layer. The transition process progresses from the pressure to the SS of the passage. The effect from the upstream rotor blades is only seen near the blade surfaces. The pattern of transition within the new endwall boundary layer was shown to be relatively insensitive to the Reynolds number.

Results from a linear cascade of LPT blades have also been presented. A comparison of these results with those from the four-stage turbine rig shows that the development of the endwall boundary layer within the passage is similar in the linear cascade and in the four-stage rig.

## Acknowledgment

The authors would like to thank Fred Bryant of the Whittle Laboratory for his work on the instrumentation of the blades. The authors would also like to thank ITP for the funding of the project and their permission to publish this paper.

## Nomenclature

$E$ = anemometer output voltage
$E_0$ = anemometer output voltage at no flow
LE = leading edge
ND = nondimensional
Re = Reynolds number
rms = root mean square
$t$ = time
TE = trailing edge
$\tau_0$ = blade passing period
$\tau_w$ = wall shear stress
$\langle \rangle$ = ensemble averaged quantity

## References

[1] Senoo, Y., 1958, "The Boundary Layer on the Endwall of a Turbine Nozzle Cascade," Trans. ASME, **80**, pp. 1711–1720.

[2] Langston, L. S., Nice, M. L., and Hooper, R. M., 1976, "Three-Dimensional Flow Within a Turbine Cascade Passage," ASME Paper No. 76-GT-50.

[3] Moore, H., and Gregory-Smith, D. G., 1996, "Transition Effects on Secondary Flows in a Turbine Cascade," ASME Paper No. 96-GT-100.

[4] Harrison, S., 1988, "The Influence of Blade Stacking on Turbine Losses," Ph.D. thesis, University of Cambridge, Cambridge, UK.

[5] Ingram, G. L., 2003, "Endwall Profiling for the Reduction of Secondary Flow in Turbines," Ph.D. thesis, University of Durham, Durham, UK.

[6] Holley, B. M., Becz, S., and Langston, L. S., 2006, "Measurement and Calculation of Turbine Cascade Endwall Pressure and Shear Stress," ASME J. Turbomach., **128**, pp. 232–239.

[7] de la Rosa Blanco, E., Hodson, H. P., Vazquez, R., and Torre, D., 2003, "Influence of the State of the Inlet Endwall Boundary Layer on the Interaction Between the Pressure Surface Separation and the Endwall Flows," Proc. Inst. Mech. Eng., Part A, **217**, pp. 433–441.

[8] de la Rosa Blanco, E., 2004, "Secondary Flows in Low Pressure Turbines," Ph.D. thesis, University of Cambridge, Cambridge, UK.

[9] Vazquez, R., Cadrecha, D., and Torre, D., 2003, "High Stage Loading Low Pressure Turbines. A New Proposal for an Efficiency Chart," ASME Paper No. GT2003-38374.

[10] Hodson, H. P., 1984, "Boundary Layer and Loss Measurements on the Rotor of an Axial-Flow Turbine," ASME J. Eng. Gas Turbines Power, **106**, pp. 391–399.

[11] Hodson, H. P., and Dominy, R. G., 1987, "The Off-Design Performance of a Low-Pressure Turbine Cascade," ASME J. Turbomach., **109**, pp. 201–209.

# Time Resolved Experimental Investigations of an Axial Compressor With Casing Treatment

**R. Emmrich**

**H. Hönen**

**R. Niehuis**[1]

Institute of Jet Propulsion and Turbomachinery,
RWTH Aachen University,
Templergraben 55,
D-52062 Aachen, Germany

*A casing treatment with axial and radial skewed slots ending in a plenum chamber has experimentally been investigated at a highly subsonic axial compressor stage. The aim was to investigate the physical phenomenon of this treatment family that is responsible for the stabilization of the blade passage flow and the drop in efficiency mostly observed. The experimentally gained performance results of this configuration showed an extension of the operating range by approximately 50%, while the efficiency for design conditions is reduced by 1.4%. Apart from this, operating points at part load conditions have been observed nearly without any loss in efficiency. The detailed flow analysis is performed by means of results from a 3D pneumatic probe with temperature sensor and a dynamic total pressure probe. The focus of the investigations is on the incidence flow to the compressor rotor, the tip clearance vortex flow in combination with the wall stall separation region and the blade stall due to suction side separation. The casing treatment configuration is investigated with a special interest in detecting those effects which have an impact on the stability and the compressor overall efficiency, including the interaction of the rotor and the stator flow fields.* [DOI: 10.1115/1.2813005]

*Keywords:* *casing treatment, axial compressor, unsteady flow, experimental investigation*

## Introduction

Demands on higher specific power in modern turbo compressors lead to reduced numbers of stages and airfoils per blade row resulting in a significant increase of the aerodynamic loading in single stages, which leads to a higher tendency of rotating stall or generally unstable compressor operation occurrence. In general, rotating stall is detected at the tip of the blades and therefore casing treatment has been an advantageous measure to improve the stable operating range of compressors. Various types have been reported since the early 1970s but mostly high stability is accompanied with high losses and therefore causes a reduction in compressor efficiency (Osborn et al. [1], Takata and Tsukuda [2], Greitzer et al. [3], Smith and Cumpsty [4], Fujita [5], and Azimian et al. [6]).

The experimental investigations in the past were mostly concerned with overall compressor performance data. Different casing treatment configurations were investigated and compared by means of the total pressure, total temperature, and total isentropic efficiency. Detailed experimental flow analyses are very rare, especially in recent years where the number of numerical simulations increases according to the computational speed (Crook et al. [7], Hall et al. [8], Yang et al. [9], Wilke and Kau [10], and Brignole et al. [11]). This overall trend makes it even more remarkable that very detailed measurement results published by Smith and Cumpsty [4] date back to the year 1984. The experimental investigations of axial skewed slots were performed at a low-speed compressor of 1.52 m tip diameter and a hub/tip ratio of 0.4. Measurements were performed with hot-wire anemometry, dynamic total pressure probes, and a rotating five-hole probe inside the rotor blade passage, gaining blade to blade results of the flow directly under the casing treatment. Smith and Cumpsty [4] explained the flow inside the slots and the extracting and injecting effect that influences the blade passage flow by means of their experimental results. The stabilizing effect they observed is the extraction of low momentum fluid from the tip clearance vortex at the blade pressure side. This influence of the wall stall region was already observed by Greitzer et al. [3]. By increasing the compressor load, the low momentum vortex moves upstream, blocking the main fluid close to the casing wall. At near surge conditions, the tip clearance vortex even moves in the circumferential direction, influencing the incidence angle to the neighboring blade. In transonic compressors, the tip clearance vortex plays an even more important role. At high pressures, the vortex core can loose its stability and breaks down shortly after passing the shock in the blade passage (Schlechtriem and Lötzerich [12]). A critical blockage of flow near the casing wall is formed by low energy fluid that causes massive flow instabilities in the rotor blade row (Wilke and Kau [10]). The casing treatment reduces the blockage of the wall stall separation region by extracting the low momentum fluid. In most treatment configurations, this fluid is injected again at the rotor inlet, using the pressure difference as the driving force for the extraction.

Another mechanism that is supposed to be responsible for the stabilizing effect of casing treatments is the blade stall phenomenon (Takata and Tsukuda [2]). While increasing the aerodynamic load of the rotor blades flow separation occurs on the suction side close to the leading edge. This phenomenon is stabilized by the tip clearance vortex but leads finally to surge of the whole compressor. The casing treatment suppresses this blade stall with a high speed injection at the leading edge of the blades that has a dynamic effect on the main flow resulting in an improvement of the flow conditions by means of the momentum interchange.

A third and last mechanism of stabilizing the blade passage flow with casing treatments is that of fluid injection at the inlet of

---

[1] Present address: University of the Federal Armed Forces, Munich—Werner-Heisenberg-Weg 39, D-85577 Neubiberg, Germany.

Contributed by the International Gas Turbine Institute of ASME for publication in the JOURNAL OF TURBOMACHINERY. Manuscript received June 22, 2007; final manuscript received August 18, 2007; published online November 10, 2008. Review conducted by David Wisler. Paper presented at the ASME Turbo Expo 2007: Land, Sea and Air (GT2007), Montreal, Quebec, Canada, May 14–17, 2007.

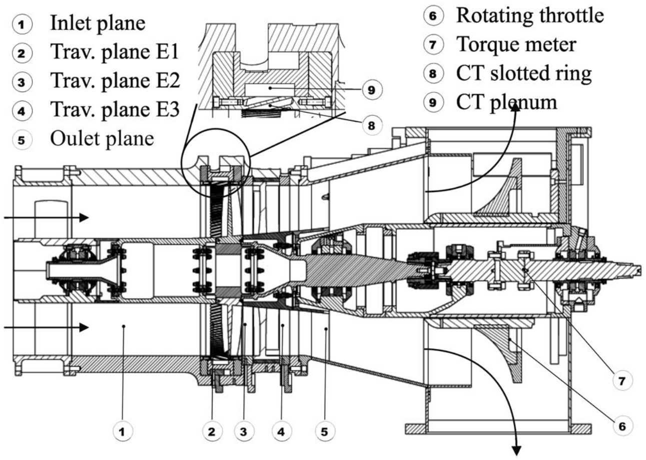

Fig. 1 Compressor test rig

**Table 1 Specification of the compressor stage**

| | | |
|---|---|---|
| Nominal rotational speed | 12,000 | rpm |
| Design pressure ratio | 1.187 | — |
| Design mass flow rate | 20 | kg/s |
| Design isentropic efficiency | 87.9 | % |
| Number of rotor blades | 16 | — |
| Number of stator vanes | 14 | — |
| Casing diameter | 421.6 | mm |
| Hub inlet diameter | 160 | mm |
| Maximum relative inlet tip Mach number | 0.88 | — |
| Cold rotor tip clearance | 0.45 | mm |
| Axial tip chord length | 42.5 | mm |
| Tip blade stagger angle | 54 | deg |
| Tip blade maximum thickness | 3.2 | mm |
| Exit plenum | 0.3 | $M^3$ |

the rotor blade row, in order to change the incidence angle and to lower blade tip loads close to the casing wall. This treatment is only effective when using a circulating flow passage that does not change the circumferential velocity component of the extracted fluid. This swirl is applied at the inlet to change the incidence angle to moderate values and to avoid the development of a blade stall separation. First investigations of this kind of casing treatment were performed on centrifugal compressors (Fischer [13] and Hunziker et al. [14]), but in recent years, it was approved for the application in an axial fan rotor as well (Hathaway [15]).

The casing treatment configuration investigated in this paper is similar to those investigated by several authors in the past, namely, Adams and Smith [16], Smith and Cumpsty [4], Fujita and Takata [5], Osborn et al. [1], and Guruprasad [17]. Most of these investigations have led to a significant performance map width enhancement and a reduced efficiency. Apart from these overall performance investigations, there are no publications known to the authors that have performed detailed time resolved traverse measurements. The experimental results presented in this paper shall provide these measurement data in order to understand the influence of the casing treatment configuration on the stage flow field.

## Compressor and Casing Treatment Design

A single stage axial compressor test rig at the Institute of Jet Propulsion and Turbomachinery of the RWTH Aachen University is used for experimental investigations of casing treatment configurations. Figure 1 presents the cross-sectional view of this compressor. The test facility is designed as an open loop with a 7 m long inlet duct, which provides an axial inlet velocity profile without any circumferential distortions. This inlet duct contains a calibrated short Venturi nozzle for the measurements of the compressor mass flow rate. Throttling the compressor is done by rotating an aerodynamic shaped ring that moves on a thread close to the exit casing. The inclination of the thread the ring turns on is designed to suit the requirements of an accurate throttle positioning while the stall point of the compressor is being measured. This device provides a homogeneous circumferential velocity distribution, which guarantees equal stall conditions in all blade passages.

The compressor shaft is split into two parts. A short intermediate shaft contains the torque meter and is combined by a gear coupling with the compressor rotor. In order to calculate the total torque of the rotor blades, the frictional losses of the three journal bearings are measured by means of temperature sensors and volume flow meters. The task of determining the overall compressor performance can be completed by total pressure and total temperature rakes located at two circumferential and five radial positions each in the inlet and outlet planes.

The geometric and aerodynamic design parameters for this highly subsonic test facility are listed in Table 1. The maximum relative inlet Mach number is 0.88 with a mass flow rate of 20 kg/s and a total pressure ratio of 1.187. The tip clearance height of the NACA 65 profiled rotor with 16 blades is about 1% of the axial tip chord length. The hub begins to be inclined at 4.8 deg just in front of the blade row while the casing is completely cylindrical. This hub inclination angle keeps constant in the stator row with 14 cantilevered vanes.

A cross-sectional view of the casing treatment ring is presented in the enlargement of Fig. 1. This treatment is set up by four parts: the slotted inner ring, one ring forming the plenum chamber, and two rings on the side that can be displaced to adjust the axial position of the treatment relative to the rotor blade. The complete treatment ring can be rotated in the circumferential direction in order to be able to perform traverse measurements in the inlet plane. The probe for these measurements needs to move through the treatment and therefore cannot indicate the flow field relative to the slots.

The design parameters of the casing treatment, presented in Table 2, primarily were taken from literature and adapted to suit the compressor stage design conditions (Osborne et al. [1], Fujita and Takata [5], Adams and Smith [16], Guruprasad [17], Zhao [18], and Prince [19]). The treatment contains 152 slots with a width of 4.0 mm each to gain a porosity of 65%. This slot width is about 30% higher than the maximum blade thickness of 3.2 mm. The slots are skewed axially by 15 deg against the machine axis and radially by 45 deg in the direction of rotor rotation. The radial height of the slots and the plenum height are 11 mm each. The slots and the plenum have an axial length of 42.5 mm. This value has been chosen from the axial blade tip chord length. In the axial direction, the treatment covers the blade by 38% axial chord. To determine the optimum configuration, this parameter was varied to 30% and 46% for design operating conditions. The results are presented in the compressor map of this paper.

**Table 2 Specification of the axial and radial skewed casing treatment with plenum chamber**

| | | |
|---|---|---|
| Number of slots | 152 | — |
| Nominal open area porosity | 65 | % |
| Slot width | 4.0 | mm |
| Axial length of slots | 42.5 | mm |
| Axial extend over rotor blade tip | 38 | % |
| Axial skew angle | 15 | deg |
| Radial skew angle | 45 | deg |
| Plenum radial depth | 11 | mm |
| Slot radial depth | 11 | mm |

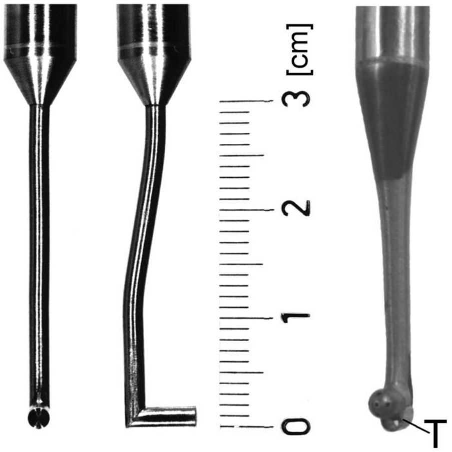

**Fig. 2 Transient total pressure probe (left) and five-hole pressure probe with temperature sensor (right)**

## Instrumentation

The performance measurement equipment, explained in the previous chapter, was selected to suit the high standards in overall efficiency for a single stage compressor. The reproducibility of the efficiency measurement has been approved by reassembling the casing and the casing inserted rings of the compressor test rig over ten times and is found to be smaller than the maximum deviation of ±0.2%.

A single fast response semiconductor pressure transducer (MSI Sensors, EPIH-111) is located at the casing and 25% of the axial tip chord length downstream of the blade leading edge. This sensor is used to detect the onset of stall. In addition, the occurrence of stall can be observed by a characteristic very loud noise as well. This acoustical detection of stall point conditions was also used for the casing treatment configuration. Casing wall static pressure taps are located at eight positions in the axial direction up to 80% chord length over the rotor blade for the solid casing configuration and will provide information about the location of flow separation close to the casing wall.

Traverse measurements were performed with a steady state 3D pneumatic probe with a temperature sensor (right hand side of Fig. 2). The probe with a head diameter of 3 mm was calibrated over a wide range of Mach numbers as well as yaw and pitch angles to cover the operating conditions of the compressor. The flow field of one stator passage was resolved by 320 points (20 in the radial direction, 16 in the circumferential direction) including a refinement close to the compressor casing walls.

The unsteady traverse measurements were performed with a single sensor dynamic total pressure probe (left hand side of Fig. 2). The head of this probe is 2 mm in diameter and equipped with

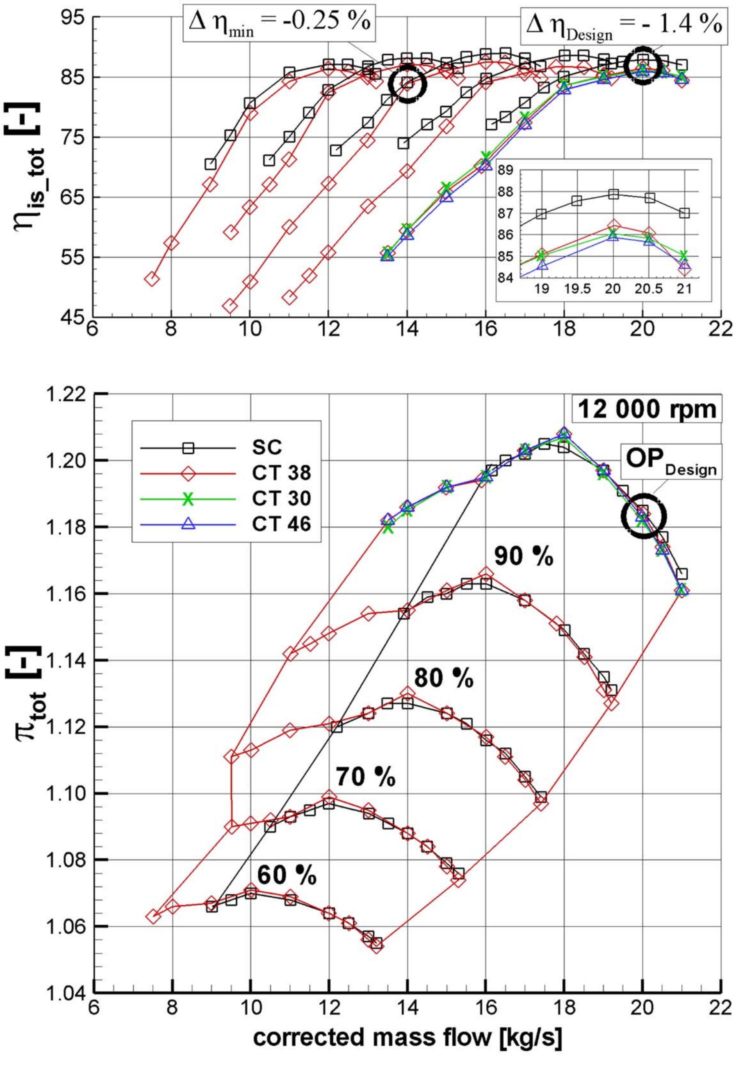

**Fig. 3 Compressor map**

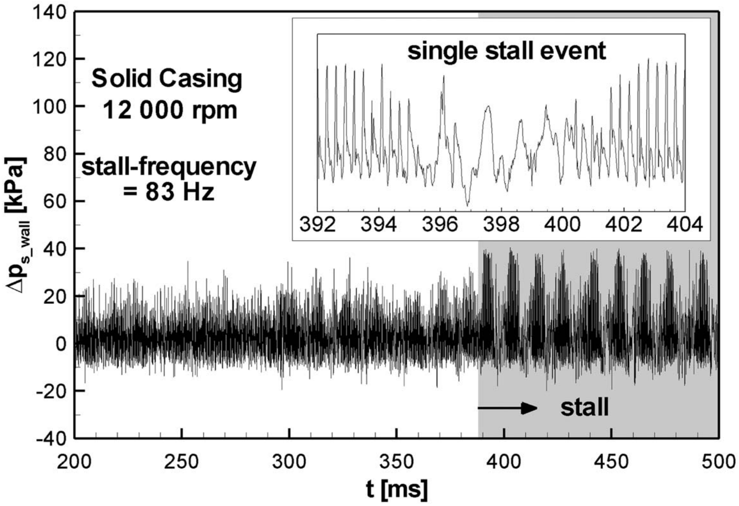

**Fig. 4 Unsteady wall pressure at stall event, 25% chord length from the blade leading edge**

an MSI Sensors EPIH-112 fast response semiconductor pressure transducer. It is supplied by constant current and calibrated by an independent variation of pressure and temperature. The approximation of the characteristics is realized by two-dimensional polynoms (Maass [20]). The orientation of the probe relative to the main velocity vector was taken from the time averaged flow direction that was investigated by the 3D pneumatic probe measurements. One rotor pitch is resolved by 64 time steps and recorded 128 times to gather information about the periodical, ensemble averaged (EA), and random (rms) fluctuations. The unsteady measurements were triggered once each rotor rotation with a shaft trigger signal.

## Experimental Results and Discussion

**Compressor Map and Performance Data.** The compressor map for the solid casing and the casing with treatment is presented in Fig. 3. The diagram shows the total pressure ratio and the isentropic compressor efficiency versus corrected mass flow rate from 60% to 100% nominal speed. In the case of the solid casing configuration, the total pressure ratio is 1.187 at a design mass flow rate of 20 kg/s and design speed of 12,000 rpm. The maximum total pressure ratio of 1.206 is obtained at a distance of approximately 30% from the stability line. Approaching the stability limit, this parameter decreases continuously caused by the development of regions with a high total pressure loss inside the compressor stage flow field. According to this, the isentropic compressor efficiency with a value of 87.9% at design point conditions decreases while moving closer to the stability line. A discontinuity can be observed at a mass flow rate of 18 kg/s corresponding to the observed maximum total pressure value.

The casing treatment configuration has been investigated for three axial positions relative to the blade leading edge at nominal speed conditions. Guruprasad [17] has performed similar measurements in a transonic compressor. He investigated the influence of the casing treatment for a variation range from 0%, 38%, and 62% to 100% overlapping area of the blade tip axial chord length. He found the maximum stabilizing effect at 38% with the minimum drop in efficiency. The enlargement in Fig. 3 shows only small differences in efficiency by varying the axial position further from 30% to 38% and 46% overlapping area. A slight advantage in the efficiency of 0.4% is observed for the position at 38% overlapping area. The total pressure ratio and the amount of map width enhancement have not changed substantially.

Therefore, the casing treatment configuration with 38% overlapping area was chosen for detailed measurement investigations. Compared to the solid casing configuration, the map width was enhanced by approximately 50%. Vibrations of the cantilevered stator row indicate vast instabilities at the speed lines of 60% and 70% nominal speed. These speed lines are limited by stator stall conditions and their mass flow range was only enhanced by approximately 20%. At the nominal speed line, the maximum total pressure ratio is obviously raised up to 1.208. The total pressure ratio decreases coming closer to the stability line, like already observed for the solid casing configuration. The maximum efficiency at design conditions is reduced by 1.4% with the casing treatment compared to the solid casing configuration. With decreasing mass flow rate, this difference decreases, leading even to an operating point with a minimum of −0.25% at 80% nominal speed. This operating point that can obviously be detected for each speed line corresponds to higher total pressure ratios of the casing treatment configuration.

A single fast response pressure transducer is located at the casing and 25% downstream of the blade leading edge in order to detect the occurrence of instabilities for the solid casing configuration. Figure 4 displays the time dependent static wall pressure for the compressor stall phenomenon at nominal speed. The stall frequency is calculated to be 83 Hz and is supposed to be the result of the very small-sized exit plenum of 0.3 $m^3$ between compressor and throttle. The enlargement in Fig. 4 Contains the pressure signal over one single stall event. At the beginning, the peaks in the signal represent the blade passing frequency of 3 335 Hz. After 3 ms, the first region with low pressure values occurs that can be regarded as a separation region covering one blade passage. During the following 5 ms, representing exactly one rotor revolution approximately, two of three blade passage flow fields are stalled, regenerating the following 2 ms and finally reflecting the beginning of the next cycle. This part span stall characteristic of the compressor is detected over the whole speed range while the stall frequency linearly decreases.

The static wall pressure from −85% up to 80% of the axial tip chord length of the rotor blades is presented in Fig. 5 for all operating points of the nominal speed line. The pressure rise begins at the blade leading edge without significant decrease in front of the stage. While throttling the compressor from design conditions, the pressure level constantly rises corresponding to a reduced mass flow down to 18.0 kg/s. Moving further toward the stability line, a flow separation indicated by a slope reduction of the pressure distribution starts between the first 10% and 30% axial chord length and is believed to be responsible for the onset of stall. The task of the time resolved investigations presented

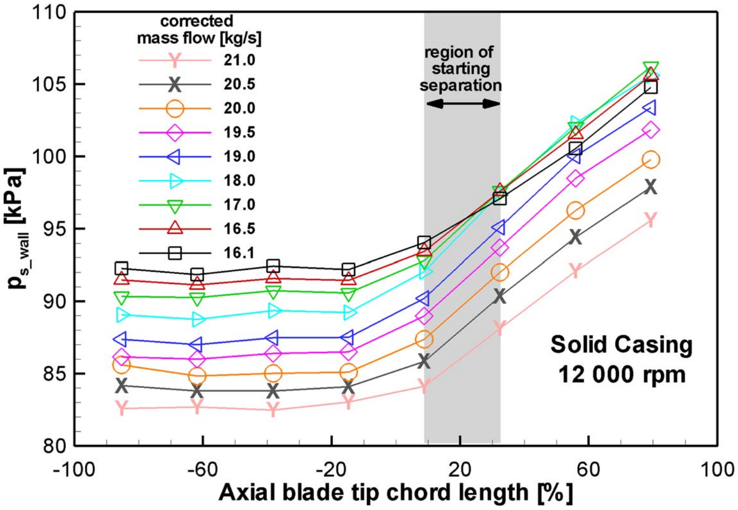

**Fig. 5 Static wall pressure rise over the relative axial blade tip chord length**

later in this paper is to obtain a clearer idea of where this flow separation takes place inside the rotor blade passage and which type of stall results from the separation.

**Time Averaged Traverse Measurements.** A detailed flow analysis is presented based on the time averaged and time resolved measurements with a five-hole probe and a fast response total pressure probe. The operating points at maximum efficiency and on the stall line are presented for 100% design speed. The changes in flow parameters of the solid casing and casing treatment configuration are discussed in the three measurement planes at the inlet of the rotor (E1), the outlet of the rotor (E2), and the outlet of the stator (E3). Each plot provides the flow parameter influences for both configurations. The two-dimensional plots of the time resolved measurements are orientated in the streamwise direction.

Figure 6 displays the circumferential averaged absolute flow angle alpha in Plane E1, that is, defined between the absolute circumferential and axial velocity components. The radial distribution of flow angle alpha is depicted for the maximum efficiency and the stall operating points, both with the solid casing and casing treatment configuration. For the design point conditions at maximum efficiency, only slight differences between the two configurations are observed. Due to the influence of the casing treatment, the flow angle alpha is reduced by approximately 2 deg.

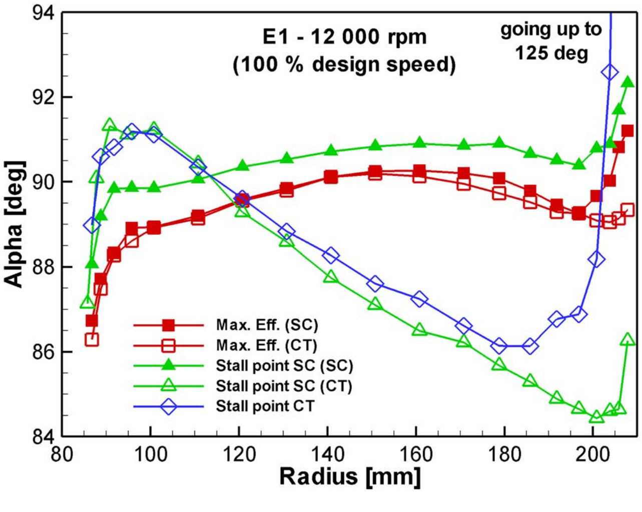

**Fig. 6 Circumferential averaged Absolute flow angle alpha in Plane E1**

At stall point conditions for the solid casing configuration, the flow angle alpha has increased by an average of 0.7 deg compared to the point at maximum efficiency. At the same operating point, the influence of the casing treatment becomes very obvious. The flow angle alpha has changed over the whole span by an average of −3 deg with maximum values of −6 deg close to the casing wall. At the hub, the angle has changed by +1.5 deg. A negative change of this angle is equivalent to a reduced incidence and therefore reduced load of the blade leading edge. In consequence of this, the blade tip load and the affection of a blade suction side separation in the first few percent of the rotor blade flow are reduced significantly. Note that the orientation of the treatment slots is opposite to the rotor rotating direction and can lead to higher incidence angles at the tip of the blade. At stall point conditions, the influence of the treatment on the inlet flow angle alpha is especially strong close to the casing where values of up to 125 deg are measured in the case of the casing treatment configuration. Apart from Fig. 6, the relative incidence angle defined between the blade stagger angle and the relative inlet flow angle has changed for this operating point by −4 deg compared to solid casing stall point conditions. From this result, we conclude that the positive swirl effect, which was found as the stabilizing reason of some other casing treatments (Hathaway [15]), cannot be detected as the dominating effect for the configuration under consideration of this paper.

Figure 7 displays the radial distribution of the circumferential averaged absolute flow angle alpha in Plane E2 for the maximum efficiency and the stall point with and without the casing treatment configuration. At design point conditions, no significant changes between the two configurations, can be observed. At the stall point with solid casing, the average flow angle alpha is reduced by 10 deg. This change of the incidence angle to the stator is based on the reduction of the axial velocity by throttling the compressor as well as compressibility effects. Apart from these different levels, the maximum changes in alpha occur close to the casing wall with values of up to −30 deg. The existence of a separation region close to the casing wall or at the blade suction side, with further slowing down low momentum fluid, is most likely the reason for this particular alpha distribution. While the blade passage flow is blocked, the flow velocity in undisturbed regions increases. This increase in axial velocity is followed by increasing values of flow angle alpha, which can be observed by comparing the two con-

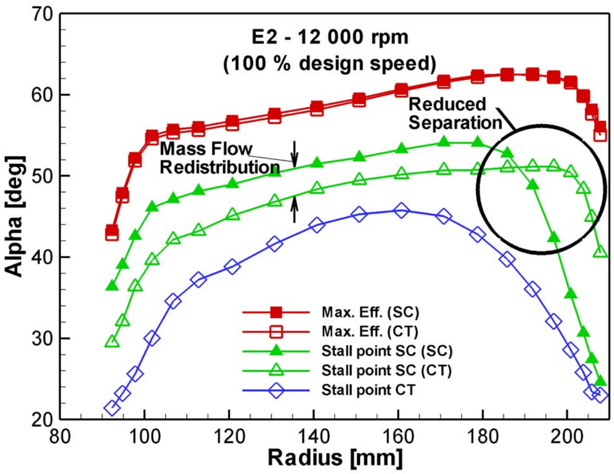

**Fig. 7 Circumferential averaged absolute flow angle alpha in Plane E2**

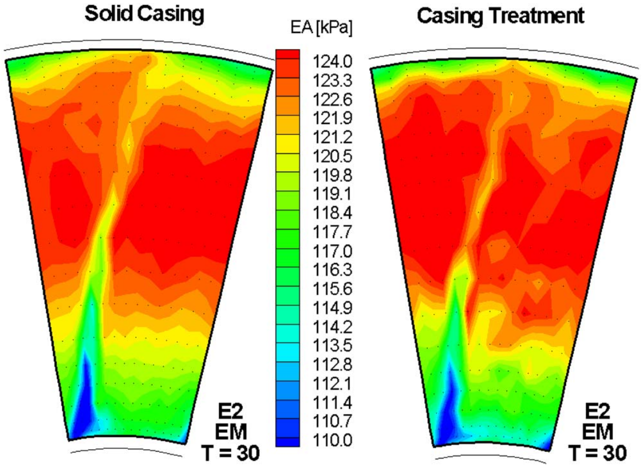

**Fig. 9 Snapshot of the EA total pressure distribution in the rotor exit Plane E2 at maximum efficiency**

figurations at stall point conditions. The average alpha values are the same in both cases, merely the distribution has changed. The observed separation region close to the casing wall is found to be stabilized with the casing treatment configuration. Reducing the mass flow further to the stall point of the casing treatment configuration, the alpha distribution changes again to the form of separated regions both at the hub and the casing wall. Although the blockage at the casing wall became larger compared to the stall point with the solid casing configuration, this flow situation is stable in terms of overall stage instabilities.

The radial distribution of circumferentially averaged total temperature in Plane E2 is presented in Fig. 8. The temperature for the solid casing configuration rises almost constantly from the hub to the casing wall. This distribution exhibits a slight progression while moving closer to the casing, detecting the influence of the tip clearance vortex and possible separation regions. The total temperature always tends to be higher for the casing treatment configuration close to the casing wall. This effect can be explained by understanding the blade passage flow close to the treatment as being extracted from and injected into the casing treatment system. This circulation principle is primarily based on changes of the velocity direction, which are subject to aerodynamic losses and lead finally to a rising temperature level inside the treatment.

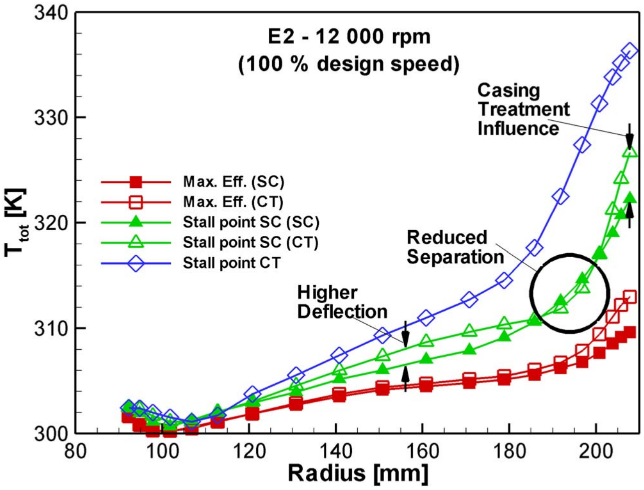

**Fig. 8 Circumferential averaged total temperature distribution in Plane E2**

So far, the measured data confirm this basic picture of the treatment system, but the question arises of how the temperature rise interacts with the positive effect in reducing separation regions.

At design point conditions the temperature with the casing treatment configuration is found to be an overall average of 0.6 K higher (Fig. 8). The influence slowly decreases from a difference of 4 K at the casing wall to 0 K midheight of the blade passage channel. At stall point conditions, the temperature is found to be an overall average of 1.6 K higher for the casing treatment configuration. The strong effect at the casing is slightly reduced and becomes even slightly lower in a small region than the temperature of the solid casing configuration. In the midheight of the blade passage channel, the temperature difference is positive again. At this operating point, superposed effects are observed. As already observed in Fig. 7, the separated flow region at the casing wall without casing treatment is reduced. With the casing treatment configuration, the temperature level in Fig. 8 is still higher than for the solid casing configuration but compares with operating conditions at maximum efficiency not as high as expected. As a first effect, the reduced flow separation close to the casing seems to reduce the temperature level as well. This effect becomes visible by lower temperatures than for the solid casing configuration. The second effect depends on the lower axial velocities at midheight of the blade passage that lead to a higher deflection and therefore to higher work that makes the temperature level raise. The temperature raise inside the treatment is the third effect that superposes the others close to the casing wall.

The temperature at the stall point with the casing treatment configuration increases close to the casing wall to a maximum value of 336 K ($\Delta T = 14$ K compared to solid casing). The temperature inside the treatment plenum is found to raise even higher up to 390 K and at the stall point with solid casing up to 354 K.

**Time Resolved Traverse Measurements.** Going into detail of the measured time resolved rotor exit flow field, the authors follow the aim to find changes induced by the casing treatment system and intend to understand the basic mechanisms of how the treatment influences the blade passage flow. In order to reach this aim, separated flow regions have to be located and distinguished between the two mechanisms of blade stall and wall stall separation. The following illustrations compare the two configurations for different operating points by means of the ensemble averaged EA and stochastic root mean square (rms) fluctuations of the total pressure distribution.

The most intensive change in the flow field of the rotor is close to the casing and the blade wake flow, where regions of flow separation can directly be observed. Figures 9 and 10 display

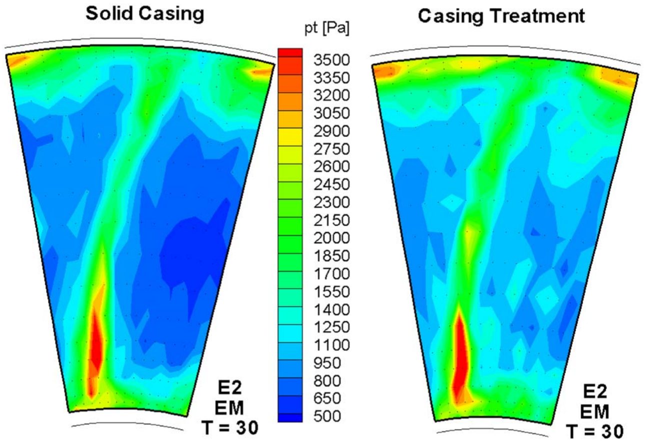

**Fig. 10 Snapshot of the RMS total pressure distribution in the rotor exit Plane E2 at maximum efficiency**

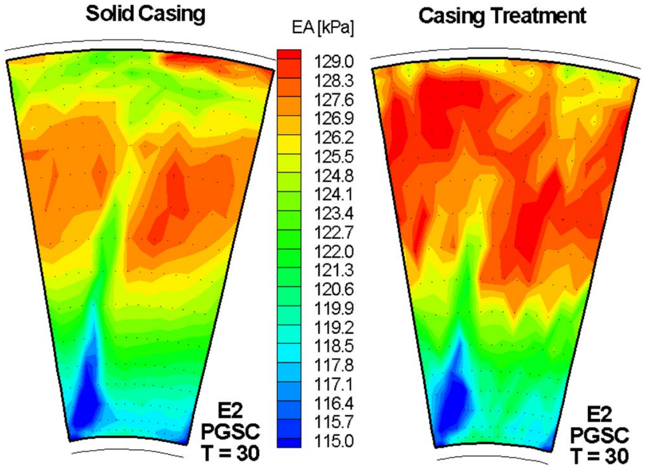

**Fig. 11 Snapshot of the EA total pressure distribution in the rotor exit Plane E2 at solid casing stall point**

snapshots of the periodic EA and stochastic rms distribution at design point conditions. The blade wake flow can easily be recognized as well as the tip clearance vortex close to the casing wall. At the hub corner of the blade, a region of very low EA and high rms values indicates a boundary layer separation for both configurations. The flow region influenced by the tip clearance vortex is slightly reduced in its radial extent in the case of the casing treatment configuration, but is increased in the circumferential direction. By means of the time resolved measurements over one blade pitch, the potential upstream influence of the stator vane can be observed, too. In the transient flow field with the casing treatment configuration, this influence is superposed by local changing EA levels over the whole blade passage channel. These spots of low total pressure values have obviously a strong periodic character and are found to be typical at all operating conditions with the casing treatment configuration. It is obvious that this effect is induced by the casing treatment system extracting or injecting fluid with the blade passing frequency at each slot position. The frequency of the pressure fluctuations downstream of the blade passage is therefore 9.5 times higher than the blade passing frequency.

The constant location of the measurement plane relative to the treatment slots is the reason for observing the fluctuations in the EA pressure distribution. It is assumed that the offset in the rms level of both configurations can be regarded as a result of the boundary layer development on the blade surface influenced by the above pressure fluctuations.

The time resolved flow field at stall point conditions is presented in Figs. 11 and 12 and gains information about the secondary flow separation regions. While overall trends can already be observed for the design operating point, the main influences on the blade passage flow field are even stronger developed at stall point conditions. Low total pressure values down to 15% of the blade span from the casing wall are detected for the solid casing configuration in Fig. 11, indicating the grown blockage effect of the tip clearance vortex. The stabilizing influence of the casing treatment system can be observed in high EA total pressure values close to the casing wall while local periodic high frequency low pressure spots indicate the previous discussed influence of the treatment slots. The total pressure ratio over the rotor blade row increases and therefore displays a better aerodynamic performance with the use of the casing treatment system.

The stochastic rms fluctuations in Fig. 12 visualize the flow phenomena in the exit of the rotor blade passage. Two counteracting influences are observed in this plot. The casing treatment mainly reduces the blockage region close to the casing wall but further down to the blade passage flow, the blade wake thickness is increased. This shifted influence induced by the casing treatment configuration has already been observed in the circumferential averaged alpha distribution in Fig. 7. The effects of reduced blade load at the tip and higher blade load in the passage both depend on the mass flow redistribution over the whole blade passage. Reducing a wall stall separation region, for example, by extracting the low momentum fluid into the casing treatment, will lead to higher velocities close to the casing wall and at the same time to reduced velocities over the rest of the passage. In the case of a reduction in blade stall separation close to the casing wall, the tip clearance vortex is secondarily being influenced by the reduced load in the tip region. The blockage reduction by changes in the tip clearance vortex and the blade stall separation will lead again to higher velocities close to the casing wall and at the same time to reduced velocities over the rest of the passage. This indicates that, from the actual point of view, one cannot distinguish between these two possible stabilizing effects.

By the interpretation of the casing treatment stall conditions presented on the right side of Fig. 13, an influence can be observed that tends the authors to believe more in a blade stall stabilizing effect. The question arises of how the flow field with the secondary flow distribution (rms) From Fig. 13, which seems to have a separated region over the whole circumference close to the casing, can remain stable when the solid casing configuration stalls with the distribution illustrated in Fig. 12. One possibility might be the stabilization of the blade stall separation region close to the blade tip leading edge. While the tip region flow is sup-

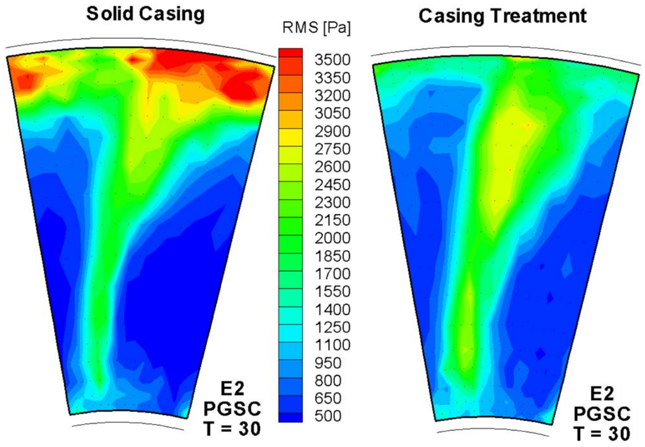

**Fig. 12 Snapshot of the RMS total pressure distribution in the rotor exit Plane E2 at solid casing stall point**

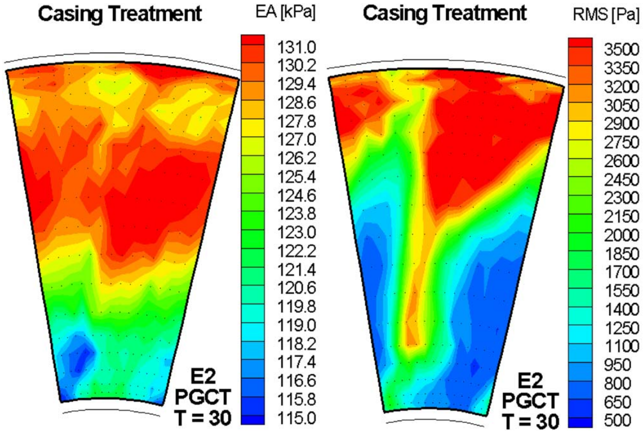

**Fig. 13 Snapshot of the EA and rms total pressure distribution in the rotor exit Plane E2 at casing treatment stall point**

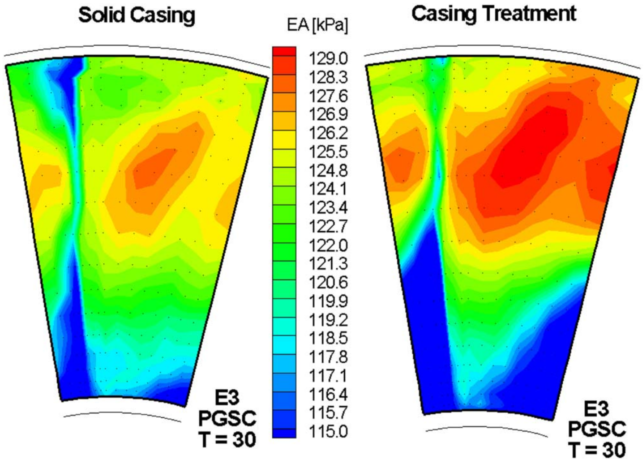

**Fig. 14 Snapshot of the EA total pressure distribution in the stator exit Plane E3 at solid casing stall point**

posed to be stable over the first 38% covered by the casing treatment, this region is thought to be of more importance than the wall stall effect.

**Influences on the Compressor Efficiency.** The overall isentropic compressor efficiency is decreased by the use of the casing treatment configuration over the entire nominal speed line. Temperature measurement results of the rotor exit plane indicate that the casing treatment increases the temperature level close to the casing wall and the stabilization effect leads to higher loads in the blade passage flow field that again increases the temperature because of higher blade loads (Fig. 8).

The design point conditions are supposed to be aerodynamically optimal that the casing treatment influence on the blade passage flow field should be as weak as possible. Since this is generally not the case, most casing treatment configurations observe decreasing efficiencies for the design operating point. At stall point conditions, the losses inside the treatment and the losses induced by the higher aerodynamic loading in total are compensated by the benefit obtained by reducing separation regions close to the casing wall. The positive effect of decreasing the temperature by reducing the separation regions, followed by an increasing pressure level, is the benefit, which causes the efficiency to rise. Deflection and friction effects inside the casing treatment are the governing forces, which will be decisive whether this benefit in total is higher than the losses.

In order to analyze the influence of the casing treatment on the overall compressor stage efficiency, the stator flow conditions have to be taken into account, too. The change of the stator inlet flow angle alpha illustrated in Fig. 7 indicates reduced loading close to the stabilized region at the casing wall and contrary to this a higher loading at the hub. These changes result in different aerodynamic flow conditions inside the stator flow field. In Fig. 14, a snapshot of the dynamic total pressure distribution at the outlet of the stator row is depicted that indicates a massive hub corner stall separation in the case of the casing treatment configuration. This region of flow separation leads again to high total pressure losses that cause a lower compressor efficiency. This observation indicates as well that a suitable design of a casing treatment configuration must be integrated into the whole compressor design process.

## Conclusions

The compressor under consideration has been experimentally investigated by means of overall performance and detailed time averaged and time resolved measurements. With the casing treatment configuration presented, the efficiency is reduced by 1.4% at design point conditions and the stall margin enhanced by approximately 50%. From measurements at the inlet of the rotor blade row, a positive swirl effect is detected that reduces the incidence angle and with this the aerodynamic load of the blade leading edge. This positive effect is found to be not influenced directly by the casing treatment system and is not strong enough in order to represent the main reason for the stabilizing effect of the present casing treatment configuration. The rotor exit flow angle changes over the whole span at stall point conditions, while influences close to the casing wall are observed that are due to the casing treatment stabilization effects. This phenomenon shifts the rotor blade aerodynamic load from the casing toward the main passage flow. The secondary flow field changes according to this shift in blade loading that is confirmed by time resolved dynamic total pressure measurements in the rotor exit plane. The change in aerodynamic load over the blade passage span can be traced back to a stabilization of wall stall or blade stall separation regions, but the authors did not see any inevitable reasons for one of the stall phenomena being primarily influenced by the casing treatment system.

The influence on the compressor efficiency is found to be mainly dependent on losses inside the treatment. Especially at design point conditions, where separation regions inside the blade passage flow field were not observed, the flow temperature distribution has increased close to the casing wall and according to this, the isentropic efficiency decreases. At stall point conditions, the casing treatment system not only increases the temperature level close to the casing wall. The stabilization effect also leads to higher loads in the blade passage flow field that again increases the temperature level. Taking the temperature reduction at the stabilized separation regions into account, there are three mechanisms that change the temperature level and influence the compressor efficiency at the rotor exit plane. The overall temperature level can mainly be influenced by the losses inside the treatment. Together with the interaction between the rotor and the stator flow field, which influence one another, these observations indicate that a suitable design of a casing treatment configuration must be integrated into the whole compressor design process.

Future detailed experimental investigations will be performed at part load operating conditions, which have been observed nearly without efficiency loss. The authors believe to find additional information about the discussed influences in order to be able to provide a database for future development of design tools for casing treatment configurations with a better performance.

## References

[1] Osborn, W. M., Lewis, G. L., and Heidelberg, L. J., 1971, "Effect of Several Porous Casing treatments on Stall Limit and on Overall Performance of an Axial-Flow Compressor Rotor," Report No. NASA TN D-6537.

[2] Takata, H., and Tsukuda, Y., 1977, "Stall Margin Improvement by Casing

Treatment—Its Mechanism and Effectiveness," ASME J. Eng. Power, **99**, pp. 121–133.

[3] Greitzer, E. M., Nikkanen, J. P., Haddad, D. E., Mazzawy, R. S., and Joslyn, H. D., 1979, "A Fundamental Criterion for the Application of Rotor Casing Treatment," ASME J. Fluids Eng., **101**, pp. 237–243.

[4] Smith, G. D. J., and Cumpsty, N. A., 1984, "Flow Phenomena in Compressor Casing Treatment," ASME J. Eng. Gas Turbines Power, **106**, pp. 532–541.

[5] Fujita, H., and Takata, H., 1984, "A Study on Configurations of Casing Treatment for Axial Flow Compressors," Bull. JSME, **27**(230), pp. 1675–1681, Paper No. 83-0079.

[6] Azimian, A. R., Elder, R. L., and McKenzie, A. B., 1989, "Application of Recess Vaned Casing Treatment to Axial Flow Fans," ASME Paper No. 89-GT-68.

[7] Crook, A. J., Greitzer, E. M., Tan, C. S., and Adamczyk, J. J., 1992, "Numerical Simulation of Compressor Endwall and Casing Treatment Flow Phenomena," ASME Paper No. 92-GT-300.

[8] Hall, E. J., Topp, D. A., Heidegger, N. J., McNulty, G. S., Weber, K. F., and Delaney, R. A., 1996, "Tasc 7—Endwall Treatment Inlet Flow Distortion Analysis Final Report," NASA Contractor Report No. 195468.

[9] Yang, H., Nuernberger, D., Nicke, E., and Weber, A., 2003, "Numerical Investigation of Casing Treatment Mechanisms With a Conservative Mixed-Cell Approach," ASME Paper No. GT2003-38483.

[10] Wilke, I., and Kau, H.-P., 2004, "A Numerical Investigation of the Flow Mechanisms in a High Pressure Compressor Front Stage With Axial Slots," ASME J. Turbomach., **126**, pp. 339–349.

[11] Brignole, G., Kau, H.-P., and Wilke, I., 2005, "Numerical Evaluation of Important Parameters Ruling the Effectiveness of Casing Treatments in Transonic Compressors," 17th Symposium on Airbreathing Engines, Munich, Germany, Paper No. ISABE-2005-1095.

[12] Schlechtriem, S., and Lötzerich, M., 1997, "Breakdown of Tip Leakage Vortices in Compressors at Flow Conditions Close to Stall," ASME Paper No. 97-GT-041.

[13] Fischer, F. B., 1988, "Application of Map Width Enhancement Devices to Turbocharger Compressor Stages," SAE Paper No. 880794.

[14] Hunziker, R., Dickmann, H.-P., and Emmrich, R., 2001, "Numerical and Experimental Investigation of a Centrifugal Compressor With an Inducer Casing Bleed System," Proc. Inst. Mech. Eng., Part A, **215**(A6), pp. 783–791.

[15] Hathaway, M. D., 2002, "Self-Recirculating Casing Treatment Concept for Enhanced Compressor Performance," NASA/TM-2002-211569.

[16] Adams, P. C., and Smith, G. D. J., 1987, "The Effect of Axial Slot Casing Treatment Geometry on the Stall Margin Improvement of a Low Speed Axial Flow Compressor," ISABE Paper No. 87-7036.

[17] Guruprasad, S. A., 1999, "Experimental Investigations on the Influence of Axial Extension and Location of Outer Casing Treatment on the Performance of an Axial Flow Compressor," Fourth International Symposium on Internal Flows, Dresden.

[18] Zhao, Q.-C., 1981, "Effect of Casing Treatment on Performance of a Three-Stage Low Pressure Compressor," ASME Paper No. 81-GT-159.

[19] Prince, D. C., 1974, "Study of Casing Treatment Stall Margin Improvement Phenomenon," NASA Paper No. CR-134552.

[20] Maass, M., 1995, "Kalibrierung von Halbleiter-Drucksonden," DLR-Mitteilung 95-03, Deutsche Forschungsanstalt für Luft- und Raumfahrt e. V., Köln.

# Film-Cooling on a Gas Turbine Blade Pressure Side or Suction Side With Compound Angle Shaped Holes

**Zhihong Gao**

**Diganta P. Narzary**

**Je-Chin Han**

Turbine Heat Transfer Laboratory,
Department of Mechanical Engineering,
Texas A&M University,
College Station, TX 77843-3123
e-mail: jc-han@tamu.edu

*The film-cooling effectiveness on the surface of a high pressure turbine blade is measured using the pressure sensitive paint technique. Compound angle laidback fan-shaped holes are used to cool the blade surface with four rows on the pressure side and two rows on the suction side. The coolant injects to one side of the blade, either pressure side or suction side. The presence of wake due to the upstream vanes is simulated by placing a periodic set of rods upstream of the test blade. The wake rods can be clocked by changing their stationary positions to simulate progressing wakes. The effect of wakes is recorded at four phase locations along the pitchwise direction. The freestream Reynolds number, based on the axial chord length and the exit velocity, is 750,000. The inlet and exit Mach numbers are 0.27 and 0.44, respectively, resulting in a pressure ratio of 1.14. Five average blowing ratios ranging from 0.4 to 1.5 are tested. Results reveal that the tip-leakage vortices and endwall vortices sweep the coolant on the suction side to the mid-span region. The compound angle laidback fan-shaped holes produce a good film coverage on the suction side except for the regions affected by the secondary vortices. Due to the concave surface, the coolant trace is short and the effectiveness level is low on the pressure surface. However, the pressure side acquires a relatively uniform film coverage with the multiple rows of cooling holes. The film-cooling effectiveness increases with the increasing average blowing ratio for either side of coolant ejection. The presence of stationary upstream wake results in lower film-cooling effectiveness on the blade surface. The compound angle shaped holes outperform the compound angle cylindrical holes by the elevated film-cooling effectiveness, particularly at higher blowing ratios.*

[DOI: 10.1115/1.2813012]

## Introduction

The ability of today's gas turbine engines to withstand increasingly higher turbine-inlet temperatures has been largely due to the advancement in cooling technology. One of the commonly used cooling techniques in modern high temperature gas turbine engines is film cooling. Among the variety of film cooling hole designs, four kinds of hole configurations are generally considered: cylindrical holes, laterally diffused (or fan-shaped) holes, forward-diffused (or laidback) holes, and laterally and forward-diffused (laidback fan-shaped) holes. The idea behind these so-called "shaped hole" is to expand the exit surface area to reduce the jet momentum and curb the jet lift-off.

Among the vast literatures related to the film cooling, majority of the recent work focuses on comparative assessment of two or more film cooling hole configurations. Goldstein et al. [1] showed the benefits of film cooling with shaped holes. Their study compared film-cooling effectiveness for straight round holes and axial shaped holes with lateral diffusion of 10 deg. The axis of both hole geometries were inclined at 35 deg from the test surface. They reported a significant increase in the film-cooling effectiveness immediately downstream of the shaped holes as well as increased lateral coolant coverage. They attributed this effect primarily on the reduced mean velocity of the coolant at the hole exit, causing the jet to stay closer to the surface. Thole et al. [2] carried out flow field measurements using Laser Doppler Velocimetry (LDV) at the exit of three different hole geometries. The hole geometries included a round hole, a hole with a laterally expanded exit, and a hole with a forward-laterally expanded exit, all oriented at an angle of 30 deg from the surface. Their findings showed that both shaped holes had less shear mixing of the injection jet with the mainstream and greater lateral spreading of the coolant compared to that of a round hole. Additionally, the forward-laterally shaped hole had relatively lower film effectiveness than the laterally expanded shaped hole due to excessive diffusion of the coolant and subsequent mainstream interaction. Gritsch et al. [3] studied the same cooling hole configurations and orientations as those in Ref. [2] with a density ratio of 1.85. Their film-cooling effectiveness measurements were confined to $x/d=10$ in order to focus in the near-field of the cooling hole. As compared to the cylindrical hole, both expanded holes showed significantly improved thermal protection of the surface downstream of the ejection location, particularly at high blowing ratios. Along similar lines, Yu et al. [4] studied film effectiveness and heat transfer distributions on a flat plate with a straight circular hole, 10 deg forward diffusion shaped hole, and another type of hole with an additional 10 deg lateral diffusion. In each case, the axis of the hole was inclined 30 deg relative to the mainstream direction. The last mentioned hole provided the highest film cooling performance as well as the overall heat transfer reduction.

All of the above studies were performed on a flat plate with axially oriented holes. Schmidt et al. [5] examined film-cooling performance of 60 deg compound angled holes on a flat plate surface, with and without a forward expanded shaped exit, and compared that with cylindrical holes aligned with the mainstream. The round and shaped exit holes with a compound angle had

---

Contributed by the International Gas Turbine Institute of ASME for publication in the JOURNAL OF TURBOMACHINERY. Manuscript received July 5, 2007; final manuscript received July 27, 2007; published online November 10, 2008. Review conducted by David Wisler. Paper presented at the 2007 ASME-JSME Thermal Engineering Conference and Summer Heat Transfer Conference Paper No. (HT2007), Vancouver, BC, Canada, July 8–12, 2007.

significantly greater effectiveness at larger momentum flux ratios. The compound angle holes with expanded exits had a much improved lateral distribution of coolant near the hole for all momentum flux ratios. Dittmar et al. [6], in a slight deviation, conducted measurements on a model of a suction side (SS) of an actual turbine guide vane inside a wind tunnel. Four different cooling hole configurations—a double row of cylindrical holes, a double row of discrete slots, a single row of straight fan-shaped holes, and a single row of compound angle fan-shaped holes—were chosen to study adiabatic film-cooling effectiveness and heat transfer coefficient. Both the shaped holes featured expansion only in the lateral direction. The streamwise injection angle was 45 deg for all cases with an additional lateral angle of 35 deg from the mainstream direction for compound shaped holes. According to their study, fan-shaped holes provided good effectiveness values at moderate and high blowing ratios unlike the cylindrical holes, which suffered from jet separation. In another study involving pressure side and SS models inside a wind tunnel, Chen et al. [7] investigated both axial and compound shaped holes with forward diffusion. The compound angle in their study was 45 deg. On the concave surface, improvement in laterally averaged effectiveness due to the addition of compound angle was found at a high blowing ratio of 2. On the convex surface, a significant improvement in effectiveness was seen at both low and high blowing ratios.

Hole shape studies in linear cascades are fewer in comparison to those in flat plate and model airfoils. Teng and Han [8] studied one row of film holes near the gill-hole portion of the SS. The hole geometries considered in their study were the same as those of Refs. [2,3], but with a slightly higher inclined angle of 45 deg. They reported that spanwise-averaged film effectiveness of shaped holes could be about two times higher than that of cylindrical holes. In addition, fan-shaped holes performed better than laidback fan-shaped holes. More recently, Mhetras et al. [9] observed the excellent coolant coverage offered by compound shaped holes near the tip region of the pressure side (PS). Their study showed that the shaped holes on the PS of the blade could be utilized in cooling the cutback region of the tip cavity floor.

The effect of unsteady wake on film cooling effectiveness and coolant jet temperature profiles on the SS of a turbine blade was investigated by Teng et al. [10] in a low speed cascade. A spoked-wheel mechanism was used to generate the upstream wakes. They found that an unsteady wake reduced the effectiveness magnitudes. A local heat transfer immediately downstream of the holes was found to increase by as much as 60% due to film injection. Ou et al. [11] simulated unsteady wake conditions using the same mechanism as that in Ref. [10] over a linear turbine blade cascade with film cooling. They tested no-wake case and wake Strouhal numbers of 0.1 and 0.3. Air and $CO_2$ were used to simulate the effect of density ratio. It was found that increasing wake passing frequency increased local Nusselt numbers for all blowing ratios, but this effect is reduced at higher blowing ratios. It was concluded that the additional increases in Nusselt numbers due to unsteady wake, blowing ratio, and density ratio were only secondary when compared to the dramatic increases in Nusselt numbers only due to film injection over the no-film-hole case. They concluded that heat transfer coefficients increased and film cooling effectiveness values decreased with an increase in unsteady wake strength. Further, Mehendale et al. [12], in the same test facility and for the same experimental conditions, found that an increase in wake Strouhal number led to a decrease in film effectiveness over most of the blade surface for both density ratio injections and at all blowing ratios. Du et al. [13] performed a similar experiment with the addition of trailing edge coolant ejection from the wake-producing bars. The addition of wake coolant had a relatively small effect on downstream blade heat transfer coefficient, but reduced leading edge film effectiveness below the wake case with no coolant ejection. Detailed heat transfer measurements on transonic film-cooled blades with and without Nozzle Guide Vane (NGV) shock waves and wakes were made by Rigby et al. [14]. It was found that there was a significant change of film-cooling behavior on the suction surface when simulated NGV unsteady effects were introduced. Heidmann et al. [15] studied the effect of wake passing on showerhead film-cooling performance in an annular cascade with an upstream rotating row of cylindrical rods. A high wake Strouhal number was found to decrease the effectiveness but it was also found to divert the coolant toward the PS resulting in a slightly better cooling on the PS.

Most experimental studies of the blade film cooling were focused on the midspan region only; the endwall effect and tip-leakage effect were not captured. By using the pressure sensitive paint (PSP) techniques, Mhetras and Han [16] obtained a detailed film cooling effectiveness distribution on a fully film-cooled blade surface. The test blade had three rows of cylindrical holes in the leading region with a radial angle of 30 deg. Compound angle cylindrical holes were used on the blade surface—four rows on the PS and two rows on the SS. During the film cooling test, all the holes on the PS, SS, and showerhead were open. They showed that the coolant on the SS was swept substantially to the midspan region because of the tip-leakage vortices and endwall vortices. The highest effectiveness was obtained at $M=0.9$ for the compound angle cylindrical holes. The upstream wake was also simulated by the stationary rods periodically placed upstream of the blade. Depending on the wake rod positions, the film cooling effectiveness degraded in different degrees. With the same film cooling design, Mhetras and Han [17] studied the coolant accumulation effect using the superposition method. Their results showed that the film cooling effectiveness on the SS was much higher than that on the PS, although PS had more rows of film cooling holes. The superposition from individual film cooling holes showed a good agreement with experimental data. Many other film cooling studies were documented in Han et al. [18]

The previous studies on the flat plates have shown that the shaped holes offer better film-cooling effectiveness than the cylindrical holes; the compound angle holes give higher effectiveness than axial holes. With the advancement of manufacturing techniques, shaped holes on the gas turbine blades become possible. The current study is focused on film cooling with compound angle laidback fan-shaped holes on a turbine blade PS or a SS. To control the blowing ratio distribution, the coolant is ejected from one side of the blade surface—either the PS or the SS. With the one-side coolant ejection, it is easier to examine the effect of film cooling hole configuration. Four rows of film cooling holes were distributed on the PS, while two rows were on the SS of the blade. The internal coolant supply passages were modeled similar to typical blade designs used in commercial gas turbines. Experiments were performed in a five-blade linear cascade with relatively high freestream Mach numbers. The upstream wake effect was simulated by placing stationary rod at different phase location upstream of the blade along the pitch direction. Five average blowing ratios from $M=0.4$ to $M=1.5$ were examined. The film cooling effectiveness was measured using the PSP technique.

## Experimental Setup

The measurements were conducted in a five-blade linear cascade facility, as shown in Fig. 1. The inlet cross section of the test section was 19.6 cm (width) × 12.7 cm (height), while the exit cross section was 12.9 cm (width) × 12.7 cm (height). The top plate, which acted as the shroud for the blades and the outer sidewalls of the test section, was machined out of 1.27 cm thick acrylic sheets for optical access. The mainstream air was supplied by a centrifugal compressor that could deliver a volume flow rate up to 6.2 $m^3/s$. A honeycomb mesh, 7.62 cm long with a cell size of 1.27 cm, was put 1.78 m upstream to the blade leading edge to make the flow uniform. Flow conditions in adjacent passages of the center blade were ensured to be identical by adjusting the trailing edge tailboards. The cascade inlet and exit velocities were set to be 96 m/s and 156 m/s, corresponding to inlet and exit Mach numbers of 0.27 and 0.44, respectively. The Reynolds num-

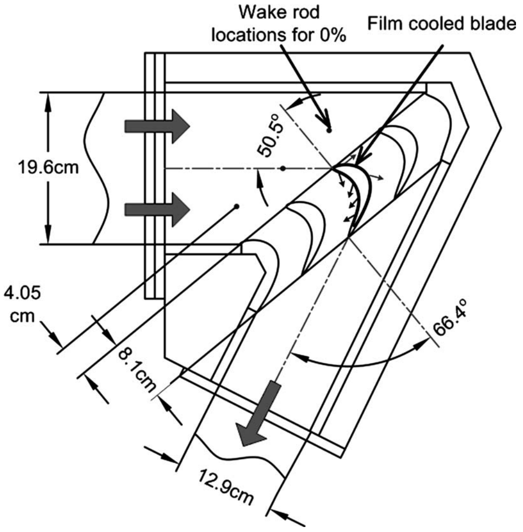

**Fig. 1 Schematic of the cascade with film-cooled blade**

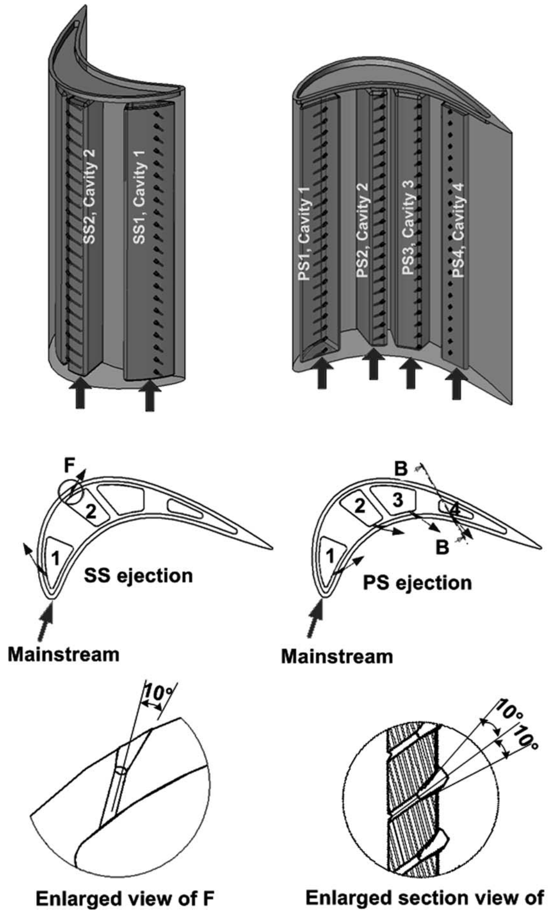

**Fig. 2 Film-cooled blades with compound angle laidback fan-shaped holes**

ber, based on the axial chord length and exit velocity, was 750,000. The overall pressure ratio ($P_t/P$) was 1.14 (where $P_t$ was the inlet total pressure and $P$ was the exit static pressure). Turbulence intensity was recorded 6.3 cm upstream of the middle blade using a hot-film probe. 1.75% turbulence intensity was measured in the center of channel. The boundary layer thickness, based on 99% of mainstream velocity, is about 25 mm. All the five blades in the cascade had a span of 12.64 cm and an axial chord length of 8.13 cm.

Figure 2 shows the film cooling hole configurations on the test blade with the internal coolant passage geometry. The test blade was made using stereolithography (SLA). The test blade had a squealer tip with a recess of 2.4% (2.84 mm) of blade span, while the two adjacent blades had a flat tip. The tip gap clearance for the test blade and the two adjacent guide blades was 1% of the blade span. The leading edge of the blade could be approximated as an arc with a radius of 2.4 mm. Compound angle laidback fan-shaped holes were distributed on the blade surface. Four rows were arranged on the PS at axial locations of 1.24 cm (PS1, 23 holes), 3.62 cm (PS2, 22 holes), 5.01 cm (PS3, 23 holes), and 6.1 cm (PS4, 22 holes). Two rows were provided on the SS at axial locations of 0.38 cm (SS1, 23 holes) and 3.56 cm (SS2, 22 holes). All these shaped holes were inclined 45 deg to the blade surface and held an angle of 45 deg to the axial direction. The shaped holes had a lateral diffusion angle of 10 deg from the hole centerline and a forward expansion angle of 10 deg to the blade surface. The hole diameter of metering part ($d$) was 0.65 mm and the total length of a hole was $9d$. The hole expansion started at $4.75d$, which resulted in an area ratio of 4.4 between the exit cross section and the inlet cross section. The holes were staggered; therefore, PS2, PS4, and SS2 had one hole less than PS1, PS3, and SS1. The spanwise spacing ($s$) of the holes was kept at $8.2d$. The coolant was supplied to the film holes via four cavities numbered from 1 to 4, as shown in Fig. 2. The cavity cross sections were modeled similar to the internal cooling passages in turbine blades with coolant injection through the bottom of the blade. The coolant flow rate in each cavity was monitored by a dedicated rotameter. The first cavity supplied coolant to row PS1 or row SS1; the secondary cavity supplied coolant to row PS2 holes or row SS2. The remaining two cavities supplied coolant to row PS3 and row PS4, respectively. During the test, coolant only ejected to one side of the blade surface (either PS or SS).

Metal rods were inserted upstream of the cascade inlet periodically to simulate stationary upstream wakes generated by the upstream vane. The size of the wake shed from the upstream vane is not only determined by the trailing edge thickness, but also the boundary layer displacement thickness near the vane trailing edge. A rod diameter of 4.8 mm was selected to simulate the relatively large wake, which is the upper bond case. Mhetras and Han [16] showed that a smaller diameter of rod reduced the wake rod effect. The rods were placed upstream of the blades at a distance equal to 50% of the axial chord. The rods were placed at four equally spaced intervals corresponding to the blade pitch, and their locations are shown in Fig. 3. The rod directly upstream of the leading edge was indicated as phase 0% and was 6.3 cm upstream of the leading edge in the flow direction. Rod locations for phase 25%, 50%, and 75% were progressively located along the blade pitch. The periodically placed upstream rods may be thought of as a progressing wake in a rotating turbine. Four sets of experiments were conducted to cover all phase locations. Two rods were placed with one in the PS passage of the test blade and

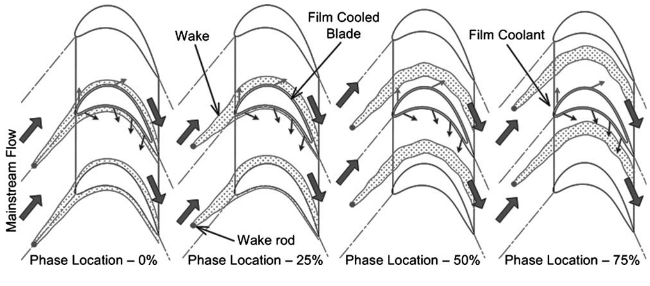

**Fig. 3 Wake rod phase locations and conceptual view of wake effect on the test blade**

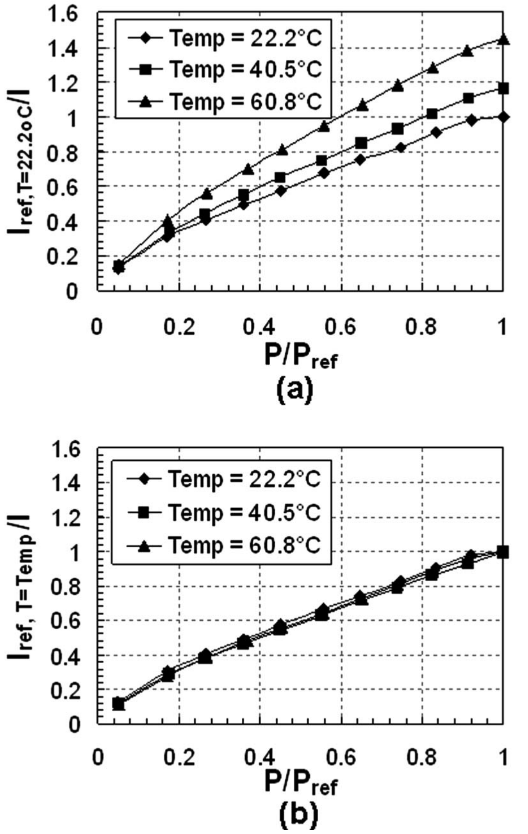

**Fig. 4 Calibration curve for PSP. (*a*) PSP calibration at single reference temperature. (*b*) PSP calibration at corresponding reference temperature.**

the other at the corresponding periodic location in the SS passage for phases 25%, 50%, and 75%, while a single rod was placed in front of the stagnation line of the test blade for phase 0%.

## Film-Cooling Effectiveness Measurement Theory and Data Analysis

Data for film-cooling effectiveness were obtained by using the PSP technique. PSP is a photoluminescent material that emits a longer wavelength of light when excited with a certain wavelength of light. The intensity of emission light is inversely proportional to the partial pressure of oxygen. This emission intensity was recorded using a 12 bit, scientific grade charge-coupled device (CCD) camera. The image intensity obtained from PSP by the camera during data acquisition was normalized with a reference image intensity ($I_{\text{ref}}$) taken under a no-flow condition. Background noise in the optical setup was removed by subtracting the intensities of the image obtained under no-flow conditions and without light excitation $I_{\text{blk}}$. The resulting intensity ratio can be converted to pressure ratio using a predetermined calibration curve and can be expressed as

$$\frac{I_{\text{ref}} - I_{\text{blk}}}{I - I_{\text{blk}}} = f\left(\frac{(P_{\text{O}_2})_{\text{air}}}{(P_{\text{O}_2})_{\text{ref}}}\right) = f(P_{\text{ratio}}) \tag{1}$$

where $I$ denotes the intensity obtained for each pixel and $f(P_{\text{ratio}})$ is the relationship between the intensity ratio and pressure ratio.

The calibration of the PSP system was performed using a vacuum chamber at several known pressures varying from 0 atm to 1.8 atm. The calibration curve is shown in Fig. 4. The same optical setup that was used during experiments was chosen for calibration. PSP is also sensitive to temperature, with higher temperatures resulting in lower emission intensity, as shown in Fig. 4(*a*). Hence, the paint was also calibrated at different temperatures. It was observed that if the emitted light intensity at a certain temperature was normalized with the reference image intensity taken at the same temperature, the temperature sensitivity can be minimized, as shown in Fig. 4(*b*). Hence, during experiments, the reference ($I_{\text{ref}}$) and black ($I_{\text{blk}}$) images were acquired immediately after stopping the mainstream flow so that the test blade surface temperature did not change appreciably. The coolant was heated to the same temperature as mainstream air (~35°C) before supplying through the holes.

To obtain film cooling effectiveness, air and nitrogen were used alternately as coolant. Nitrogen, which has nearly the same molecular weight as air, displaces the oxygen molecules on the surface, causing a change in the emitted light intensity from PSP. By noting the difference in partial pressure between the air and nitrogen injection cases, the film cooling effectiveness can be determined using the following equation:

$$\eta = \frac{C_{\text{mix}} - C_{\text{air}}}{C_{\text{N}_2} - C_{\text{air}}} = \frac{C_{\text{air}} - C_{\text{mix}}}{C_{\text{air}}} = \frac{(P_{\text{O}_2})_{\text{air}} - (P_{\text{O}_2})_{\text{mix}}}{(P_{\text{O}_2})_{\text{air}}} \tag{2}$$

where $C_{\text{air}}$, $C_{\text{mix}}$, and $C_{\text{N}_2}$ are the oxygen concentrations of mainstream air, air/nitrogen mixture, and nitrogen on the test surface, respectively. The definition of film effectiveness in Eq. (2) based on mass transfer analogy assumes a similar form as that of adiabatic film cooling effectiveness given in Eq. (3).

$$\eta = \frac{T_{\text{mix}} - T_m}{T_c - T_m} \tag{3}$$

The accuracy of the PSP technique for measuring film-cooling effectiveness has been compared by Wright et al. [19] on a flat plate with compound angled ejection holes using a steady-state infrared (IR) technique and a steady-state temperature sensitive paint (TSP) technique. Results were obtained for a range of blowing ratios and showed an agreement within 15% of each other. Larger uncertainties for heat transfer techniques such as IR and TSP methods were due to lateral heat conduction in the flat plate as corrections for heat conduction were not included in the presented results.

The center test blade under investigation was coated with PSP using an air brush. It was then excited using a strobe light fitted with a narrow bandpass interference filter (optical wavelength of 520 nm). A flexible dual fiber optic guide was used to get a uniform incident light distribution on the test surface. Upon excitation, the PSP coated surface emitted light with a wavelength larger than 600 nm. A 12 bit scientific grade CCD camera (Cooke Sensicam QE with CCD temperature maintained at −15°C using two-stage peltier cooler) was used to record images and was fitted with a 35 mm lens and a 600 nm long-pass filter. The filter mounted on the camera did not allow any reflected light from the illumination source to pass through.

A schematic of the optical component setup and camera positions is depicted in Fig. 5. Due to the blade curvature, images were captured from five camera positions—two on the PS and three on the SS. The camera and the strobe light were triggered simultaneously using a TTL signal from a function generator. A total of 200 tif images were captured and ensemble averaged to get the emission intensities. The spatial resolution of each image was 0.6 mm/pixel. A computer program was used to convert these pixel intensities into pressure using the calibration curve and then into film cooling effectiveness.

Uncertainty calculations were performed based on a confidence level of 95% and were based on the uncertainty analysis method of Coleman and Steele [20]. Lower effectiveness magnitudes had higher uncertainties. For an effectiveness magnitude of 0.3, the uncertainty was aroudn ±1%, while for an effectiveness magnitude of 0.05, the uncertainty was as high as ±8%. This uncertainty is the result of uncertainties in calibration (4%), image capture (1%), and blowing ratio (4%).

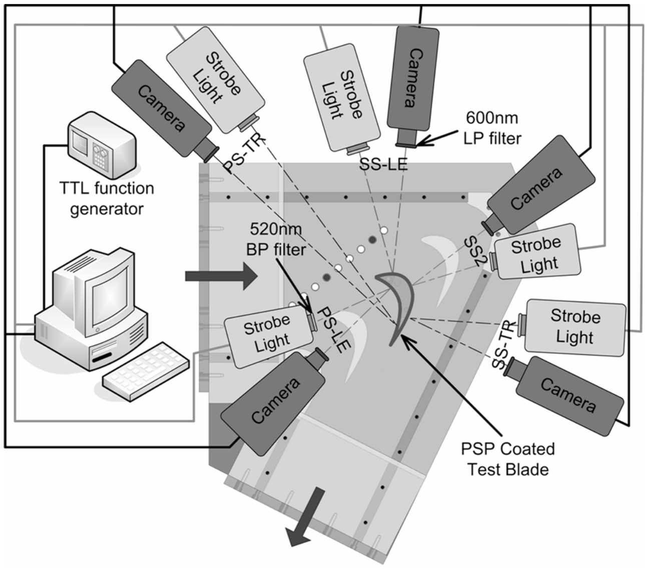

Fig. 5 Optical component setup

## Mach Number and Local Blowing Ratio Distribution on the Blade Surface

Figure 6 shows the Mach number distributions at three locations—50%, 75%, and 94%—of blade span without the presence of wake rods and film-cooling holes. These plots were obtained by measuring the static pressures at the respective locations using pressure taps instrumented on a separate blade. In addition, the inlet total pressure was measured using a Pitot tube placed 6.3 cm upstream of the center blade. Pressures were recorded with a 48-channel Scanivalve system coupled with the LABVIEW software. LABVIEW discarded all data that fell outside the initial mean ±1.5 standard deviation. It then recorded the mean value of the screened data. Every pressure measurement was repeated at least three times to reduce data uncertainty and verify data repeatability. The Mach number distributions on PS for all three span locations are more or less similar. There is gradual decrease in Mach number until $x/C_x \sim 0.6$, after which there is a sharp rise. On the SS, the Mach number distribution shows a steady increase until $x/C_x \sim 0.65$, beyond which it starts falling. The point of inflection on the SS corresponds to the throat region where the mainstream reaches its maximum velocity. The interaction of the mainstream and tip-leakage vortex can be clearly observed from this plot, with an appreciable reduction of Mach number for the 94% span case in the first half of the blade axial chord.

Figure 7 shows the Mach number distribution under the influence of stationary wakes at all phase locations and compares it with the case of no wake. Data are shown for the same three blade span locations. It is interesting to find that the midspan region is most affected by the upstream rods followed by 75% and 94% of span locations. This is indicative of the fact that the strong endwall vortices and tip leakage vortices override any small disturbance created by the wake rods. In the midspan region, the influence of endwall vortices is negligible; the effect of wake rods becomes apparent. In general, on the PS, the wake rods at phase 0% show the highest influence on the Mach number distribution followed by phase 75%. The other two wake phases show little or no effect. On the SS, phase 25% followed by phase 0% shows the highest influence in the midspan region. This agrees well with the conceptual wake paths depicted in Fig. 3. On the SS near the tip region (75% and 94% of the blade span), the wake effect is not substantial because the tip-leakage flow is predominant. The Mach numbers are about the same despite the presence of wake rods. It has to be noted that the pressure measurements were carried out on a separate blade without cooling holes. With the presence of film cooling, the boundary layer attached to the blade surface is disturbed. This is particularly true at higher blowing ratios.

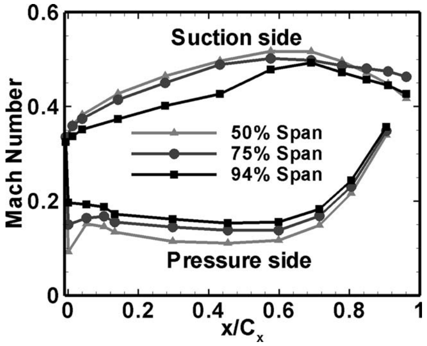

Fig. 6 Mach number distribution for the case of no wake

As mentioned earlier, the coolant ejected from only one side of the blade. Experiments were performed at five different average blowing ratios ($M$) of 0.4, 0.6, 0.9, 1.2, and 1.5. The average blowing ratio was defined as $M=\rho_c V_c/\rho_m V_m$, where $V_m$ is the mainstream velocity at the hole row location. In the present study, the density ratio was unity, so the blowing ratio was reduced to a velocity ratio. The mainstream velocity ($V_m$) at 50% of the blade span in the hole row location was taken in the $M$ calculation. By knowing the local mainstream velocity, the total coolant mass flow rate for a cavity was predetermined for a given blowing ratio and was set using a dedicated rotameter connected to the coolant cavity. The coolant velocity $V_c$ was calculated based on the coolant velocity in the metering section. The actual or local blowing ratio $M_{\text{local}}=\rho_{c,\text{local}}V_{c,\text{local}}/\rho_{m,\text{local}}V_{m,\text{local}}$ for the holes in a hole row can vary due to the pressure variation in the coolant cavity and on the outer surface of the blade. To check the coolant distribution, the local blowing ratio was examined. The discharge coefficients $C_D$, discussed by Gritsch et al. [21], were calculated. The static pressure on the blade surface was measured by the PSP. The total pressure inside a cavity was assumed constant along the spanwise direction for a given average blowing ratio. A constant discharge coefficient $C_D$ for all the holes in a loop was assumed

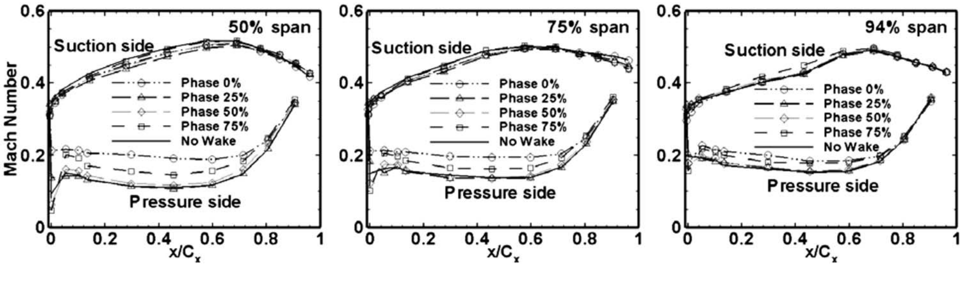

Fig. 7 Mach number distribution under the influence of upstream wake rods

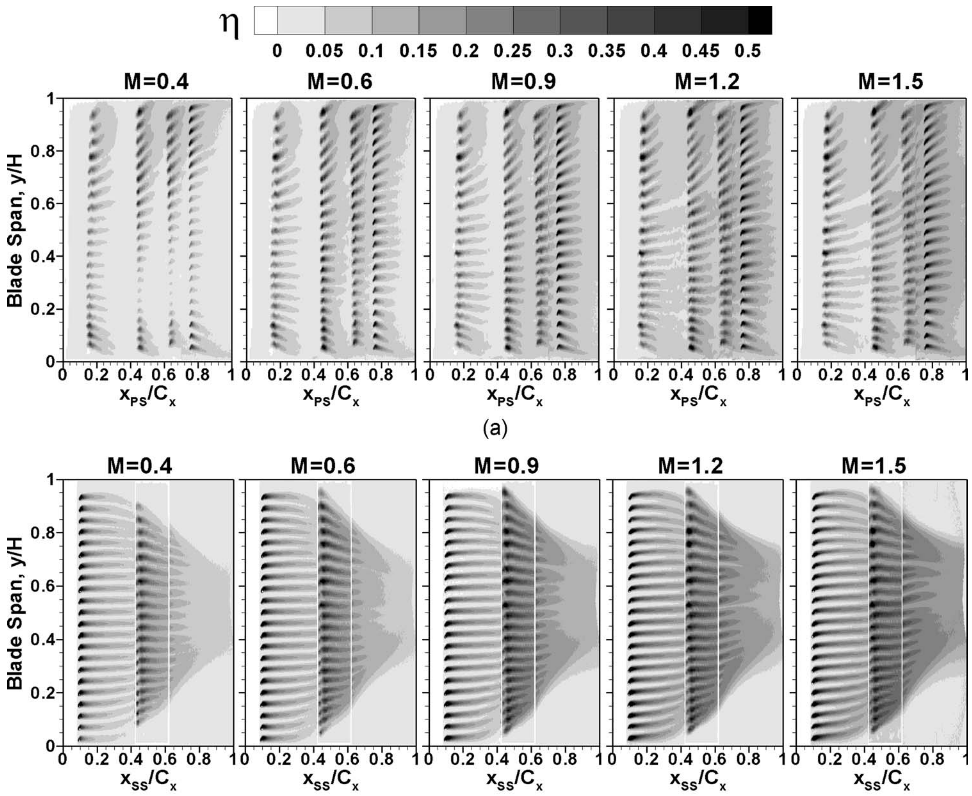

(a)

(b)

**Fig. 8 Film-cooling effectiveness distribution for varying blowing ratios for the case of no wake. (*a*) PS coolant ejection. (*b*) SS coolant ejection.**

for each average blowing ratio. By measuring the total mass flow rate supplied to a coolant loop and the pressures on the blade surface and inside the coolant cavity, the discharge coefficient $C_D$ for each loop and the coolant mass flow rate for each hole in the loop was calculated. $V_{m,\text{local}}$ in the definition of the local blowing ratio were calculated from the PSP data at corresponding locations. The results showed that the local blowing ratio for the holes in a cavity was close to the average blowing ratio. The coolant mass flow rate for holes in a cavity was found quite evenly distributed.

## Film-Cooling Effectiveness on the Blade Surface

The film-cooling effectiveness distributions on the blade surface were measured at different blowing ratios and wake rod phase positions using the PSP technique. As shown in Fig. 5, the camera was placed at two positions to capture the film-cooling effectiveness distribution on the pressure surface and at three positions to capture it on the suction surface. The effectiveness data obtained at each individual camera position were projected onto a radial plane passing through the axial chord of the blade and combined to form a complete picture for PS or SS. In the contour plots, the abscissa and the ordinate were normalized with the axial chord length and the blade height, respectively. During the film cooling effectiveness test, the coolant was ejected from only one side of the blade surface (either PS or SS).

Figure 8 shows the effectiveness distribution on the blade surface for the case of no wake. The average blowing ratios varied from 0.4 to 1.5. It can be seen that the film-cooling effectiveness increases with the increase of blowing ratio for either PS coolant ejection (PS ejection) or SS coolant ejection (SS ejection). Jet lift-off is not observed even for the highest blowing ratio $M = 1.5$. The lateral expansion provided to the cooling holes allows the coolant jets to expand 10 deg from their original direction (in the metering section), thus easing the coolant out with a much reduced mainstream-coolant interaction. Moreover, the 10 deg forward expansion helps the coolant sit back on the surface, thus avoiding jet penetration into the mainstream. Due to the expansion near the hole exit, the coolant jet velocity and momentum are reduced. Therefore, the coolant jets are more likely suppressed by the mainstream and stay close to the surface. This is more noticeable for the film-cooling effectiveness distribution on the SS. In similar flow conditions, cylindrical holes [17] produced thinner coolant traces, which is indicative of the higher mixing losses. The coolant traces on the SS are much longer than that on the pressure surface. The peak of effectiveness for the SS coolant ejection is also higher than the PS coolant ejection. The SS convex surface produces favorable pressure gradient and flow acceleration, making it easier for the coolant to stay on the surface. On the contrary, the concave surface on the PS more likely causes flow separation due to the adverse pressure gradient. Therefore, in general, the film coverage on the suction surface is better than that on the pressure surface, although there are more rows of cooling holes on the PS.

It can be seen in Fig. 8 that the coolant jet is deflected by the mainstream. Moreover, the detrimental effect of the secondary flow on film-cooling effectiveness distribution is also clearly observed near the endwall and blade tip. Starting at $x/C_x \sim 0.3$ on the SS, the spiraling motion of the passage vortex near the hub surface and the tip-leakage vortex draws the coolant toward the blade midspan. It is well known that the passage vortex drifts from the PS leading edge toward the SS trailing edge of the adjacent blade and climbs onto the suction surface with an upwash motion [22,23]. Together with the tip-leakage vortex, however, the passage vortex creates a downwash motion on the suction surface near the tip region. These vortices acting on the suction surface result in a well defined converged coolant trace toward the mid-

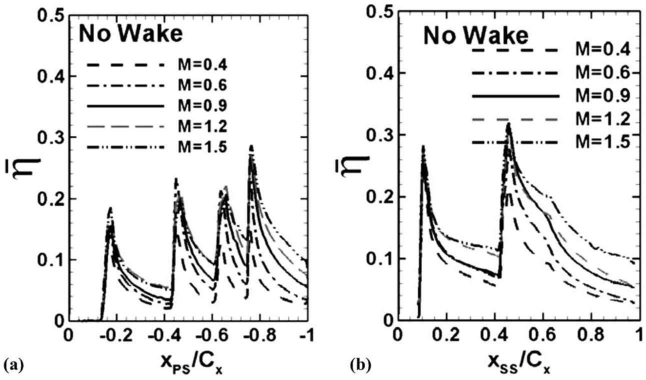

**Fig. 9 Spanwise-averaged film-cooling effectiveness for the case of no wake. (*a*) PS coolant ejection. (*b*) SS coolant ejection.**

span. On the PS, the corner vortices push the coolant to the hub region. This leads to downward coolant traces. However, the tip-leakage flow pushes the coolant to the blade tip. In the midspan region on the PS, the coolant basically follows the mainstream flow and is deflected to the axial direction. Mhetras et al. [17] also observed a similar effect on effectiveness distribution due to secondary vortices.

It can be seen clearly that the coolant from row SS1 extends to downstream of row SS2. This leads to an elevated effectiveness downstream of row SS2, particularly when blowing ratios are greater than 0.6. The accumulation effect from the upstream film cooling is also seen on the PS with an elevated film-cooling effectiveness in the downstream region.

The spanwise-averaged effectiveness versus normalized axial chord length for the case of no wake is presented in Fig. 9. The data inside the film-cooling holes were included in the averaged results. The sharp peaks in the plot correspond to the row locations. It should be noted that there might be shadow inside some holes due to view angle and lighting, so data inside those holes may be affected. The spanwise-averaged effectiveness increases with blowing ratios for either PS coolant ejection or SS coolant ejection. There is no optimal blowing ratio observed in the range considered. This result is consistent with earlier work [3,4] on flat plate studies and blowing ratio range of up to 1.75. Overall, the effectiveness levels on the SS are higher than that on the PS for a particular blowing ratio, as seen from the contour maps.

A one-to-one comparison of spanwise-averaged effectiveness distribution between the compound angle cylindrical hole blade [17] and the compound angle shaped hole blade is shown in Fig. 10 for the case of no wake. Results show a clear rise in effectiveness on the SS for the shaped holes. As the blowing ratio increases, the advantage of shaped holes becomes more evident. On the PS, at lower blowing ratios ($M=0.6$ and 0.9), the effectiveness for the cylindrical holes and the shaped holes is comparable. A blowing ratio of 0.9 offers the best film-cooling effectiveness for cylindrical holes. When the blowing ratio is further increased, the effectiveness from cylindrical holes starts dropping due to jet lift-off. At $M=1.5$, the very low effectiveness ($<6\%$) downstream of row PS1 and SS1 indicates the jet lift-off. While the shaped holes reduces the jet momentum at hole exit because of the expansion, the effectiveness keeps increasing at higher blowing ratios. When the blowing ratio on the PS is greater than 1, the shaped holes show much advantage over the cylindrical holes.

To understand the nature of influence exerted by the wake rods at each phase location, the effectiveness distribution for $M=0.9$ at four wake rod phases is presented in Fig. 11. Compared with the case of no wake, it can be seen that the wake produced by the rods reduces the film-cooling effectiveness. The mixing between the coolant and mainstream is enhanced by the wakes. The wake rod at phase 0% and phase 25% exhibits the more pronounced influence on film-cooling effectiveness. A conceptual view of the wake paths shown in Fig. 3 for phase 0% and phase 25% attest to this fact. Vortex shedding from the wake rods brings additional turbulence in the mainstream, resulting in more mixing of the mainstream with the coolant; thereby, the coolant trace is shortened. As seen from the plots, the wake rod effect can be so detrimental that the PS already lacks coolant coverage. The phase 0% shows more degradation of coolant trace on the PS. The downstream propaga-

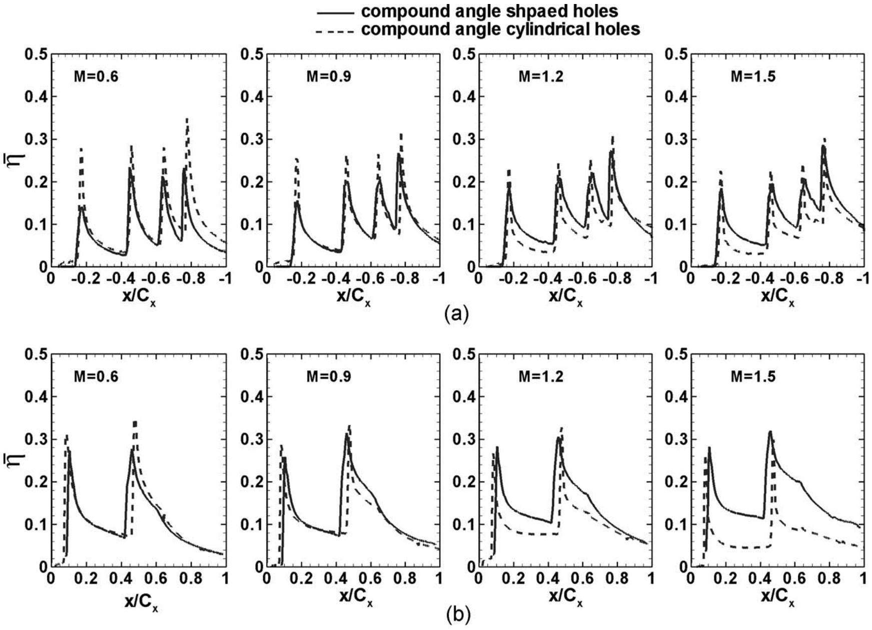

**Fig. 10 Comparison of spanwise-averaged film-cooling effectiveness for compound angle shaped holes (current study) and compound angle cylindrical holes [17]. (*a*) PS coolant ejection. (*b*) SS coolant ejection.**

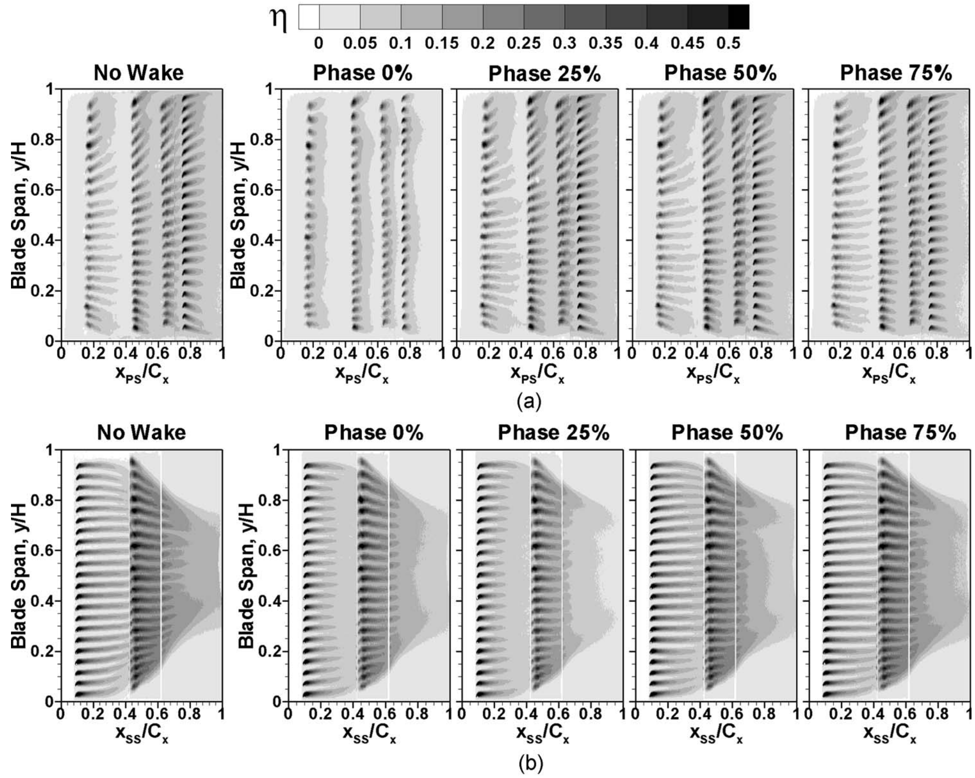

Fig. 11 Film-cooling effectiveness distribution for $M=0.9$ at varying wake rod phases. (*a*) PS coolant ejection. (*b*) SS coolant ejection.

tion of the wake is evident from the short coolant traces near the PS4 row. On the SS, it appears that the wake rod at phase 25% has a relatively higher impact. The wake propagation along the suction surface can be gauged by the coolant trace degradation near the trailing edge. It appears that the secondary vortices shield the coolant (SS2 row holes) to some extent from the incoming mainstream, as a result of which the coolant traces close to the tip and hub regions propagate downstream in comparison to those near the midspan region.

Figure 12 shows the effectiveness distribution on PS at phase 0% for varying blowing ratios. It can be seen that the effectiveness on PS is dramatically decreased at this phase location even at a blowing ratio of 1.5. The enhanced mainstream turbulence produced by the wakes mixes the coolant with mainstream immediately when the coolant is ejected from the holes. At phase 0%, the pressure surface is barely protected by the film cooling.

Figure 13 shows the effectiveness distribution on the SS at phase 25% for varying blowing ratios. It can be seen that the effectiveness on the suction surface increases with the increase of blowing ratios. However, the effectiveness enhancement is not significant from $M=1.2$ to $M=1.5$. For the SS coolant ejection, the coolant trace on the surface is much shortened compared to the case of no wake. The effect of secondary vortices is predominant in the tip and hub regions. The wake effect is more pronounced in the midspan region.

The blowing ratio effect and the wake rod effect on the spanwise-averaged film-cooling effectiveness are presented in

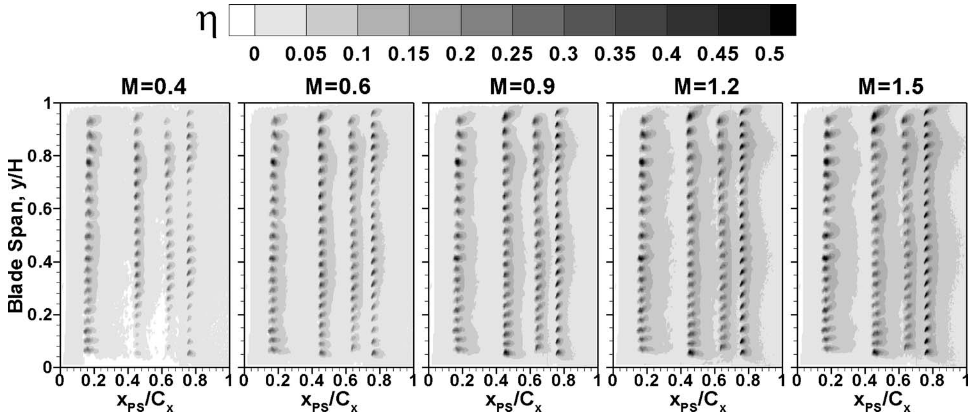

Fig. 12 Film-cooling effectiveness distribution for the PS coolant ejection at wake rod phase 0%

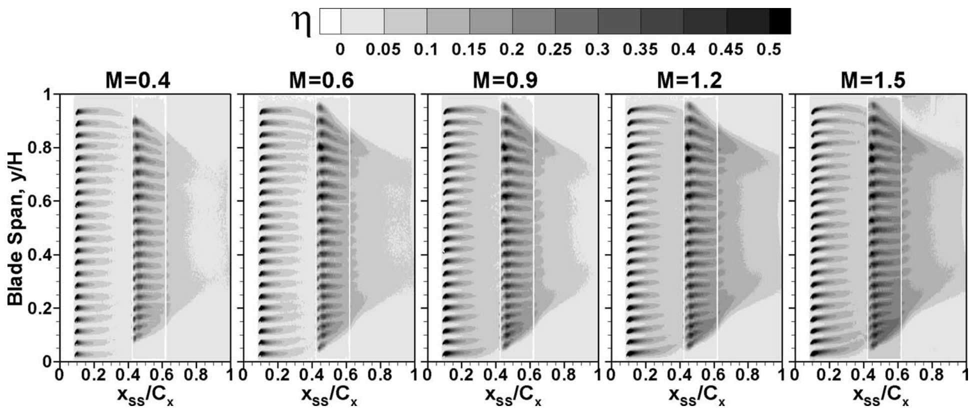

**Fig. 13 Film-cooling effectiveness distribution for the SS coolant ejection at wake rod phase 25%**

Figs. 14 and 15, respectively. It can be seen from Fig. 14 that the effectiveness increases when the blowing ratio increases for both the PS coolant ejection and the SS coolant ejection at all the wake rod phase positions. The effectiveness trend pretty much follows that of the no-wake case. Figure 15 shows that, for a given blowing ratio, the lowest effectiveness occurs at phase 0% for the pressure surface and at phase 25% for the suction surface.

## Conclusions

Experimental tests were performed on a high pressure turbine rotor blade with fan-shaped, laidback compound angled holes. The shaped holes were featured with a 10 deg expansion in the lateral direction and an additional 10 deg in the forward direction. The coolant was ejected from either PS film-cooling holes or SS film-cooling holes. The effect of blowing ratios and the presence of stationary, upstream wakes were examined. Some of the main highlights from the current study are presented below.

(1) Film-cooling effectiveness from the compound angle shaped holes increases with blowing ratio on either surface of the blade. There is no optimal blowing ratio observed in the range of study ($M=0.4-1.5$).
(2) The compound angle laidback fan-shaped holes provide uniform and wide coolant coverage over a large portion of the SS blade surface.
(3) Compared with compound angle cylindrical holes, the compound angle shaped holes show higher effectiveness values on either PS or SS, particularly at higher blowing ratios.

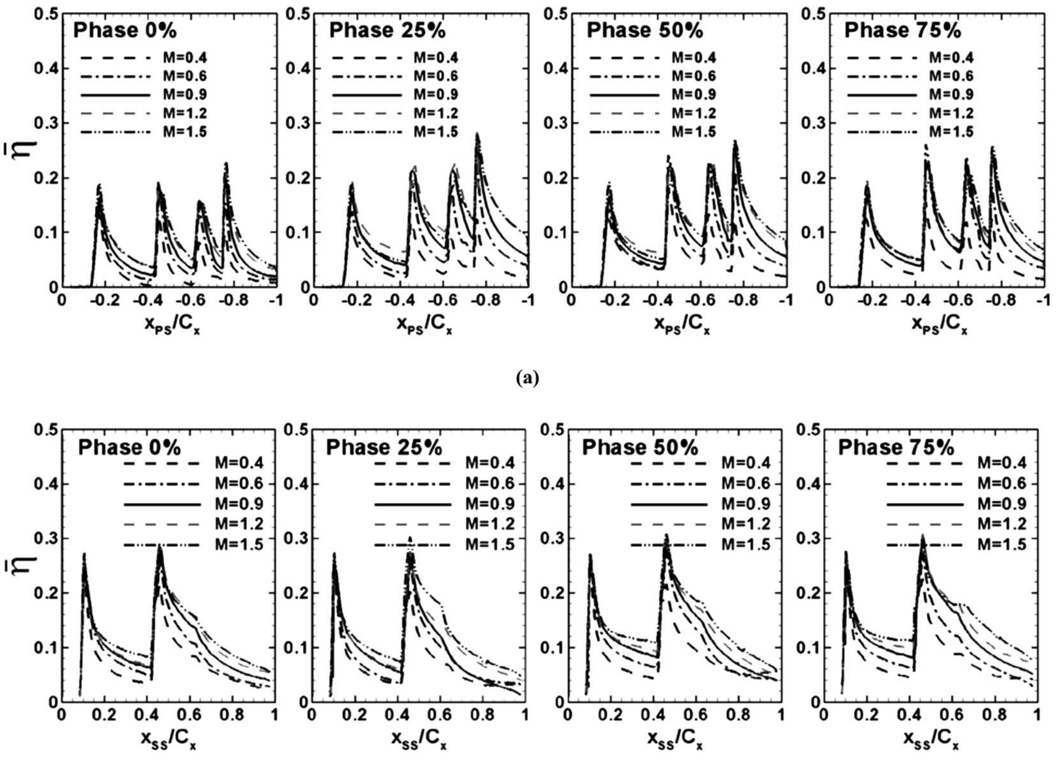

(a)

(b)

**Fig. 14 Spanwise-averaged film-cooling effectiveness (effect of blowing ratio). (*a*) PS coolant ejection. (*b*) SS coolant ejection.**

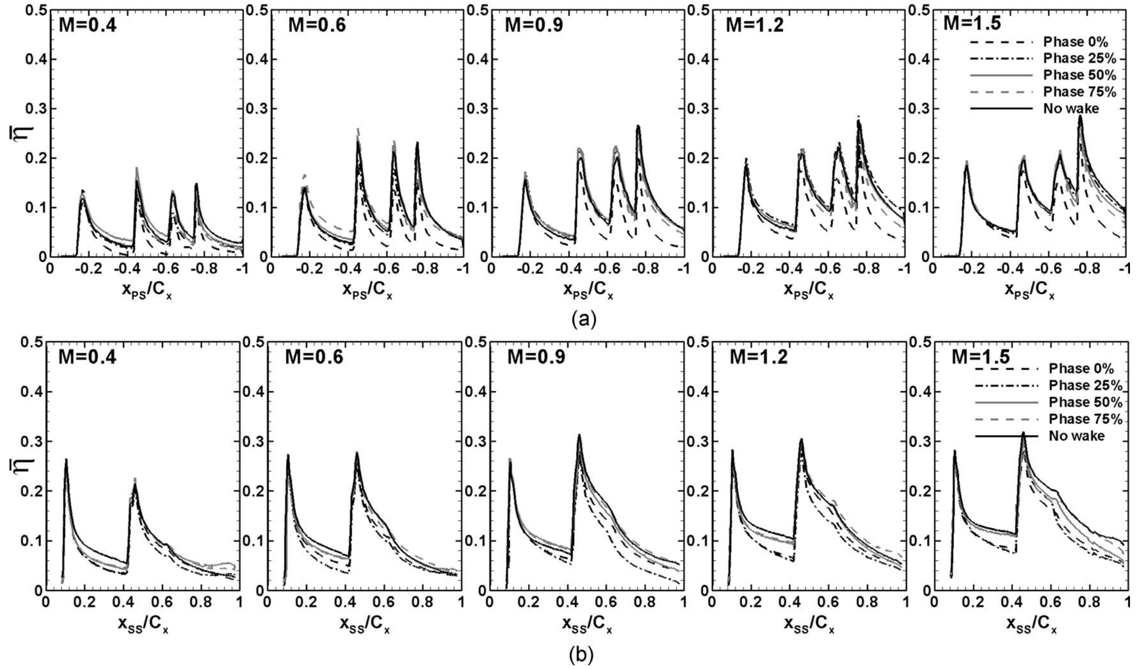

**Fig. 15 Spanwise-averaged film-cooling effectiveness (effect of wake rod phase). (*a*) PS coolant ejection. (*b*) SS coolant ejection.**

(4) An upstream wake can have severe detrimental effect on film coverage depending on the wake rod phase positions. Wake rods at phase 0% and phase 25% significantly decrease the film-cooling effectiveness magnitudes. Wakes from phase 50% and phase 75% do not attach to the blade surfaces and hence do not impact the film-cooling effectiveness as much.

(5) The tip-leakage vortices and endwall vortices are predominant at near tip and near hub regions. The upstream wake effect on SS is more observable in the midspan region.

(6) The PSP technique enables us to clearly visualize the impact of the passage vortex, corner vortex, and tip-leakage vortex on the coolant film trace distribution over the blade surface.

## Acknowledgment

This work was funded through the Marcus Easterling Endowment Fund.

## Nomenclature

$C$ = oxygen concentration
$C_x$ = axial chord length (cm)
$d$ = film-cooling hole diameter (mm)
$H$ = blade height (cm)
$M$ = average blowing ratio ($=\rho_c V_c/\rho_m V_m$)
$P_t$ = total pressure upstream of the blades (Pa)
$P_{O_2}$ = partial pressure of oxygen (Pa)
$s$ = spanwise spacing of film-cooling holes (mm)
$T_c$ = coolant temperature (°C)
$T_f$ = local film temperature (°C)
$T_m$ = mainstream temperature (°C)
$V_c$ = average coolant velocity from film-cooling holes (m/s)
$V_m$ = average mainstream velocity at hole row location (m/s)
$x$ = axial distance from blade leading edge (cm)
$y$ = spanwise distance measured from hub (cm)
$\eta$ = local film-cooling effectiveness
$\bar{\eta}$ = spanwise-averaged film-cooling effectiveness
$\rho_c$ = density of coolant (kg/m$^3$)
$\rho_m$ = density of mainstream (kg/m$^3$)

### Subscripts

air = mainstream air with air as coolant
mix = mainstream air with nitrogen as coolant
ref = reference image with no mainstream and coolant flow
blk = image without illumination (black)

## References

[1] Goldstein, R. J., Eckert, E. R. G., and Burggraf, F., 1974, "Effects of Hole Geometry and Density on Three-Dimensional Film Cooling," Int. J. Heat Mass Transfer, **17**, pp. 595–607.

[2] Thole, K., Gritsch, M., Schulz, A., and Wittig, S., 1996, "Flowfield Measurements for Film Cooling Holes With Expanded Exits," ASME Paper No. 96-GT-174.

[3] Gritsch, M., Schulz, A., and Wittig, S., 1997, "Adiabatic Wall Effectiveness Measurements of Film-Cooling Holes With Expanded Exits," ASME Paper No. 97-GT-164.

[4] Yu, Y., Yen, C.-H., Shih, T. I.-P., Chyu, M. K., and Gogineni, S., 1999, "Film Cooling Effectiveness and Heat Transfer Coefficient Distributions Around Diffusion Shaped Holes," ASME Paper No. 99-GT-34.

[5] Schmidt, D. L., Sen, B., and Bogard, D. G., 1994, "Film Cooling With Compound Angle Holes: Adiabatic Effectiveness," ASME Paper No. 94-GT-312.

[6] Dittmar, J., Schulz, A., and Wittig, S., 2002, "Assessment of Various Film Cooling Configurations Including Shaped and Compound Angle Holes Based on Large Scale Experiments," ASME Paper No. GT-2002-30176.

[7] Chen, P. H., Hung, M. S., and Ding, P. P., 2001, "Film Cooling Performance on Curved Walls With Compound Angle Hole Configuration," Ann. N.Y. Acad. Sci., **934**, pp. 353–360.

[8] Teng, S., and Han, J. C., 2001, "Effect of Film-Hole Shape on Turbine-Blade Film-Cooling Performance," J. Thermophys. Heat Transfer, **15**(3), pp. 257–265.

[9] Mhetras, S., Narzary, D., Gao, Z., and Han, J. C., 2006, "Effect of a Cutback Squealer and Cavity Depth on Film-Cooling Effectiveness on a Gas Turbine Blade Tip," AIAA Paper No. AIAA-2006-3404.

[10] Teng, S., Sohn, D. K., and Han, J. C., 2000, "Unsteady Wake Effect on Film Temperature and Effectiveness Distributions for a Gas Turbine Blade," ASME J. Turbomach., **122**, pp. 340–347.

[11] Ou, S., Han, J. C., Mehendale, A. G., and Lee, C. P., 1994, "Unsteady Wake Over a Linear Turbine Blade Cascade With Air and $CO_2$ Film Injection: Part I—Effect on Heat Transfer Coefficients," ASME J. Turbomach., **116**, pp. 721–729.

[12] Mehendale, A. B., Han, J. C., Ou, S., and Lee, C. P., 1994, "Unsteady Wake

Over a Linear Turbine Blade Cascade With Air and $CO_2$ Film Injection: Part II—Effect on Film Effectiveness and Heat Transfer Distributions," ASME J. Turbomach., **116**, pp. 730–737.

[13] Du, H., Ekkad, S. V., and Han, J. C., 1999, "Effect of Unsteady Wake With Trailing Edge Ejection on Film Cooling Performance for a Gas Turbine Blade," ASME J. Turbomach., **121**, pp. 448–455.

[14] Rigby, M. J., Johnson, A. B., and Oldfield, M. L. G., 1990, "Gas Turbine Rotor Blade Film Cooling With and Without Simulated NGV Shock Waves and Wakes," ASME Paper No. 90-GT-78.

[15] Heidmann, J. D., Lucci, B. L., and Reshotko, E., 2001, "An Experimental Study of the Effect of Wake Passing on Turbine Blade Film Cooling," ASME J. Turbomach., **123**, pp. 214–221.

[16] Mhetras, S., and Han, J. C., 2006, "Effect of Unsteady Wake on Full Coverage Film-Cooling Effectiveness for a Gas Turbine Blade," AIAA Paper No. AIAA-2006-3404.

[17] Mhetras, S., and Han, J. C., 2006, "Effect of Superposition on Spanwise Film-Cooling Effectiveness Distribution on a Gas Turbine Blade," ASME Paper No. IMECE 2006-18084.

[18] Han, J. C., Dutta, S., and Ekkad, S. V., 2001, *Gas Turbine Heat Transfer and Cooling Technology*, Taylor & Francis, New York.

[19] Wright, L. M., Gao, Z., Varvel, T. A., and Han, J. C., 2005, "Assessment of Steady State PSP, TSP and IR Measurement Techniques for Flat Plate Film Cooling," ASME Paper No. HT-2005-72363.

[20] Coleman, H. W., and Steele, W. G., 1989, *Experimentation and Uncertainty Analysis for Engineers*, Wiley, New York, Chaps. 3 and 4.

[21] Gritsch, M., Schulz, A., and Wittig, S., 1997, "Discharge Coefficient Measurements of Film-Cooling Holes With Expanded Exits," ASME Paper No. 97-GT-165.

[22] Langston, L. S., 1980, "Crossflows in a Turbine Cascade Passage," ASME J. Eng. Power, **102**, pp. 866–874.

[23] Wang, H., Olson, S. J., Goldstein, R. J., and Eckert, E. R. G., 1997, "Flow Visualization in a Linear Turbine Cascade of High Performance Turbine Blades." ASME J. Turbomach., **119**, pp. 36–42.

# Effect of End Wall Contouring on Performance of Ultra-Low Aspect Ratio Transonic Turbine Inlet Guide Vanes

**Toyotaka Sonoda**
Honda R&D Co.,
Aircraft Engine R&D Center,
1-4-1 Chuo, Wako-shi,
Saitama 351-0193, Japan

**Martina Hasenjäger**
Honda Research Institute Europe GmbH,
Carl-Legien-Strasse 30,
D-63073 Offenbach/Main, Germany
e-mail: martina.hasenjaeger@honda-ri.de

**Toshiyuki Arima**
Honda R&D Co.,
Fundamental Technology Research Center,
1-4-1 Chuo, Wako-shi,
Saitama 351-0193, Japan

**Bernhard Sendhoff**
Honda Research Institute Europe GmbH,
Carl-Legien-Strasse 30,
D-63073 Offenbach/Main, Germany
e-mail: bs@honda-ri.de

*In our previous work on ultralow-aspect ratio transonic turbine inlet guide vanes (IGVs) for a small turbofan engine (Hasenjäger et al., 2005, "Three Dimensional Aerodynamic Optimization for an Ultra-Low Aspect Ratio Transonic Turbine Stator Blade," ASME Paper No. GT2005-68680), we used numerical stochastic design optimization to propose the new design concept of an extremely aft-loaded airfoil to improve the difficult-to-control aerodynamic loss. At the same time, it is well known that end wall contouring is an effective method for reducing the secondary flow loss. In the literature, both "axisymmetric" and "nonaxisymmetric" end wall geometries have been suggested. Almost all of these geometric variations have been based on the expertise of the turbine designer. In our current work, we employed a stochastic optimization method—the evolution strategy—to optimize and analyze the effect of the axisymmetric end wall contouring on the IGV's performance. In the optimization, the design of the end wall contour was divided into three different approaches: (1) only hub contour, (2) only tip contour, and (3) hub and tip contour, together with the possibility to observe the correlation between hub/tip changes with regard to their joint influence on the pressure loss. Furthermore, three-dimensional flow mechanisms, related to a secondary flow near the end wall region in the low-aspect ratio transonic turbine IGV, was investigated, based on the above optimization results. A design concept and secondary flow characteristics for the low-aspect ratio full annular transonic turbine IGV is discussed in this paper.*
[DOI: 10.1115/1.2813015]

## Introduction

In order to meet increasing technical demands on small gas turbine engines, we investigate the use of low-aspect-ratio (AR) blades for which the influence of secondary flow losses on the turbine stage efficiency is very large, especially for the high-pressure turbine (HPT). A lot of literature that is concerned with the secondary flow mechanisms has been published so far. Some models for the spatial secondary flow have been obtained from flow visualization, e.g., Klein [1], Langston et al. [2,3], Sieverding and Van den Bosch [4], Sonoda [5], and Wang et al. [6]. These models are almost all based on low speed and especially on linear cascades. As an example, Fig. 1 shows the author's result obtained with low speed for a linear cascade, i.e., a high-AR turbine cascade. It is well known that the transverse (circumferential) static pressure gradient from pressure surface (PS) to suction surface (SS) plays an important role. The basic behavior of the vortex motion in Fig. 1 agrees with the previously reported results. Furthermore, according to the total pressure measurement downstream of the trailing edge (TE), the losses related to the horseshoe vortices: $H_p$ and $H_s$ are smaller than the loss related to the vortex IV. However, from an engineering point of view the following question must be raised: Is the secondary flow model obtained from the linear cascade (high aspect ratio) still applicable to an annular low-AR high speed cascade, especially for an ultralow-AR annular transonic turbine inlet guide vane (IGV) cascade?

Regarding the secondary flow control technique, airfoil lean and/or bowed stacking has been used especially in a low-pressure turbine for large-midsize engines. Another important method for secondary flow reduction is end wall contouring. There are two contouring types: with and without axis symmetry. In this research, we focus on the axisymmetric contouring because it is relatively simple and leads to a lower manufacturing cost than the nonaxisymmetric type.

Deich et al. [7] reported an optimal contraction ratio as a function of the AR. Ewen et al. [8] incorporated a tip contouring in the stator of a single-stage research turbine. They pointed out the importance of improved rotor inlet flow conditions. Morris and Hoare [9] showed a large reduction in the total pressure loss in the half span adjacent to the flat wall and no change around the contouring side in their plain cascade. Kopper et al. [10] tested a linear cascade of turbine vanes with and without end wall contouring. The aerodynamic loading was reduced around the frontal part of the vane, and the point of minimum pressure was moved closer to the TE. The adverse pressure gradient from the point of minimum pressure to the TE was reduced for the flat wall, but was increased for the end wall contouring. The mass averaged data showed that the contouring reduced the overall loss by 17% compared to the parallel walls. The most significant loss reduction occurred at the planar wall.

Regarding the end wall contouring of the low speed annular cascade, Boletis [11] showed that the transverse pressure gradient was significantly decreased at the frontal part, while the radial pressure gradient imposed by the blade design was counteracted by the creation of a low static pressure region at the tip end wall suction side corner. Also, the importance of the radial gradient was reported. The AR of the vane was 0.6.

Regarding the end wall contouring of the transonic annular and/or supersonic cascade, Haas [12] showed that the contoured stators had higher loss near the tip contouring side and lower loss

---

Contributed by the International Gas Turbine Institute of ASME for publication in the Journal of Turbomachinery. Manuscript received July 23, 2007; final manuscript received August 20, 2007; published online November 10, 2008. Review conducted by David Wisler. Paper presented at the ASME Turbo Expo 2007: Land, Sea and Air (GT2007), Montreal, QB, Canada, May 14–17, 2007.

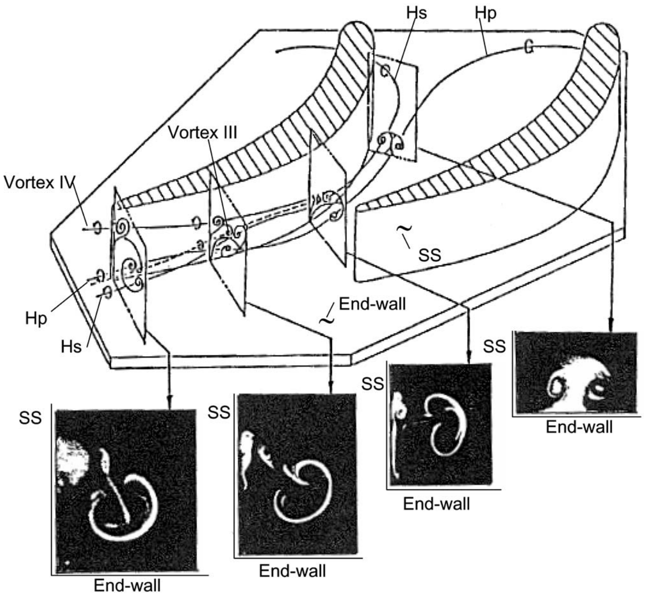

**Fig. 1 Secondary flow model for a low speed and high-AR turbine blade (obtained from Sonoda [5])**

near the hub than the cylindrical stator. He also pointed out the increase of the mass flow rate for the contoured stator because of differences in the physical throat areas. Moustapha and Williamson [13] reported on the effect of the tip end wall contouring for annular transonic and/or supersonic cascades. They showed improvement of the loss at the hub region, while the loss was increased at the contoured tip side. They also noticed a significant underturning region near the hub side.

As we mentioned already, the aerodynamic characteristics of end wall contouring for subsonic speed has been thoroughly investigated. However, much less work has concentrated on transonic end wall contouring, and the corresponding secondary flow mechanisms remain unclear.

Therefore, the main objective of this research is to investigate the effect of three types of end wall contouring: (1) only hub contour, (2) only tip contour, and (3) hub and tip contour on the aerodynamic performance of the ultralow-AR transonic turbine IGV. Furthermore, we investigate the secondary flow mechanisms, particularly whether there is a difference between the secondary flow model obtained from the low speed and from the linear cascade conditions.

**Ultralow-Aspect-Ratio Transonic Turbine Inlet Guide Vanes.** Figure 2 shows the meridional passage of the ultralow-aspect-ratio transonic turbine IGVs. The vane used in the present investigation is an IGV in a single-stage HPT for a small turbofan engine that has been installed in a small business jet. The corrected mass flow rate is relatively low at 0.84 kg/s, and the exit Mach number and flow angle are 1.04 and 72.8 deg at midspan height, respectively. The Reynolds number Re based on the actual (true) chord at midspan height is 3,500,000. The number of blades (NB) was set at 8 in order to avoid the first resonance with a downstream rotor within the operating range, keeping the vane solidity constant. This leads to an "ultralow-AR vane" of 0.21 (ratio of exit passage height to actual chord at hub), and the passage contraction ratio is 0.52. These parameters correspond to the optimized contraction line proposed by Deich et al. [7]. Constrained by manufacturing costs, e.g., due to necessary cooling, the blade geometry is defined by only two cross sections, the hub and the tip section. Linear interpolation between these two sections is used to define the remaining blade geometry. The stator blade is circumferentially leaned by 14 deg in order to suppress the development of a secondary flow near the hub end wall. The blade axial solidity is constant along the span, and it is 0.76. Zweifel's loading coefficient Zw is 0.80. The axial coordinate $X=0$ roughly corresponds to the TE of the ultralow-AR vane and $X=+0.13$ refers to the leading edge (LE) location downstream of the rotor blade, called Station 2. In the following, we will refer to this blade and passage as the base line vane and base line passage, respectively, particularly when we compare it to the optimization results.

## Design Optimization With Evolutionary Algorithms

Evolutionary algorithms [14] are a class of stochastic optimization algorithms whose use in design optimization problems is well established by now [15]. These algorithms are inspired by principles of evolutionary biology and make use of a population of individuals—each individual representing a specific design—to search the design space for the optimum solution. Typical operators applied during evolutionary optimization are selection to direct the search to promising regions of the search space, recombination to combine promising features of known solutions, and mutation to introduce some random changes of the solutions.

In our approach to aerodynamic design optimization, we use a special variant of evolutionary algorithms, namely, an evolution strategy (ES) with covariance matrix adaptation (CMA) [16]. The basic idea of CMA-ES is to make maximum use of the information contained in the search history for a self-adaptation of the search direction that is defined in terms of the covariance matrix of a normal distribution from which new tentative solutions or individuals are drawn. Thereby, the population size is decoupled from the dimension of the search space.

Especially the latter feature is indispensable in aerodynamic design optimization, which, in general, is characterized by a fundamental conflict: On the one hand, the design space easily becomes relatively high dimensional. As a consequence, a large

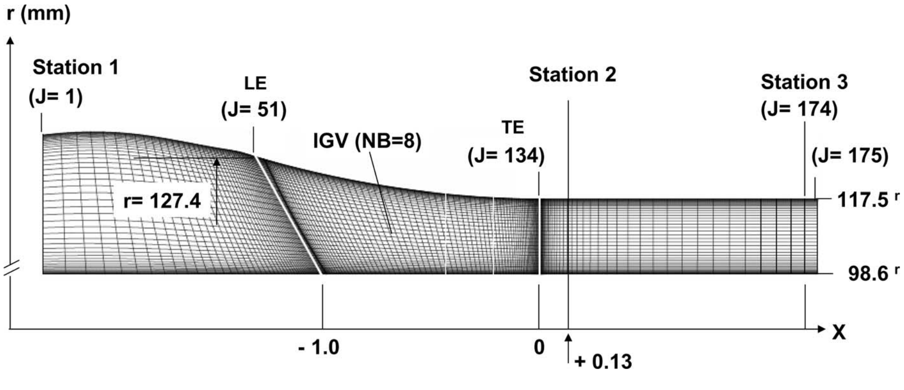

**Fig. 2 Meridional passage of an ultralow-AR IGV**

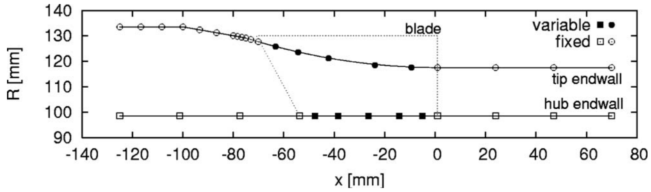

**Fig. 3 Passage modeling**

number of different designs have to be evaluated during optimization. On the other hand, however, the evaluations typically involve computational fluid dynamics (CFD) based flow analyses and are thus highly challenging tasks with respect to the necessary computational resources as well as with respect to the time requirements. As a result, only a limited number of evaluations can be afforded.

**Geometrical Models.** A crucial point in design optimization is the parametric model of the geometry that will be optimized since this determines the design space, i.e., the set of all possible designs and the topology of the design or quality space. There are a number of requirements for the parametric model:

- flexibility: the model must be flexible enough to represent a wide variety of different designs
- compactness: the number of parameters describing the model must be low enough to allow for reasonable convergence times of the optimization algorithm
- locality: variations of a single model parameter should result in only local variations of the model and should not affect the global model shape

A good choice to fulfil these requirements is to use nonuniform rational *B*-spline (NURBS) models [17] to represent geometrical models in design optimization. In general, NURBS models are defined by (i) a set of control points, (ii) a weight for each control point, and (iii) a single knot vector in the case of NURBS curves or two knot vectors in the case of NURBS surfaces, one for each parameter. Usually not all of these parameters are subject to optimization. We should note that the NURBS representation only fulfils the flexibility condition if the number of control points is sufficiently large.

**Passage Model.** The passage model consists of two open nonuniform *B*-spline curves, one curve modeling the hub end wall and the other curve modeling the tip end wall (Fig. 3). As parameters in the optimization, we considered a subset of the control points of the *B*-spline curves and allowed them to vary in both the radial and the axial coordinate. Note that allowing the axial control point position to vary is not redundant but introduces a flexibility into the model that is worthwhile in terms of possible performance gains.

The hub end wall is defined by 13 control points shown as squares in Fig. 3. Only 5 of these 13 control points are used as design variables in the optimization. Variation of the control point position is possible in both the $x$ coordinate of the control point as well as in the $y$ coordinate. This gives us ten variable parameters to model the hub passage contour. The tip end wall is defined by 21 control points shown as circles in Fig. 3. Only the five control points shown as filled circles in Fig. 3 are variable. Again, variation of the control point position during optimization is possible in both the $x$ coordinate of the control point as well as in the $y$ coordinate. So, we have ten variable parameters to model the casing passage contour. In both end wall models, the knot vectors of the nonuniform *B*-spline curves are fixed and not subject to optimization.

**Objective Function in the Optimization.** The performance measure $f$ of a specific passage design is given by the single objective of minimizing the mass averaged pressure loss $\omega$ of the stator. Additionally, we use range constraints on (i) the $\beta_2$ outflow angle and (ii) the mass flow rate. The outflow angle is constrained to lie in the range of $\delta\beta_2$ around the design value $\beta_{2\text{design}}$. In the same way, the mass flow rate is constrained to lie in the range of $\delta\dot{m}$ around the design value $\dot{m}_{\text{design}}$. The constraints are included in the objective function in the form of a weighted sum of penalty terms. Thus, the objective function for the optimization is given by

$$f = \omega + \sum_{i=1}^{2} w_i t_l^2 \rightarrow \min \tag{1}$$

with

$$t_1 = \max(0, |\beta_{2,\text{design}} - \beta_2| - \delta\beta_2)$$

$$t_2 = \max(0, |\dot{m}_{\text{design}} - \dot{m}| - \delta\dot{m})$$

We used the following design values, tolerances, and weights in the fitness function:

$$\beta_{2,\text{design}} = 72.0 \text{ deg}$$

$$\delta\beta_2 = 0.5 \text{ deg}$$

$$w_1 = 10^{19}$$

$$\dot{m}_{\text{design}} = 0.84 \text{ kg s}^{-1}$$

$$\delta\dot{m} = 0.017 \text{ kg s}^{-1}$$

$$w_2 = 10^5$$

Here, the averaged pressure loss $\omega$ is estimated far downstream at outlet Station 3 for considering mixing losses. The mass flow rate $\dot{m}$ and the outflow angle $\beta_2$ are estimated at outlet Station 2, just downstream of the TE (see Fig. 2 for the location of the outlet stations). The design outflow angle $\beta_2$ of 72.0 deg used in the optimization is slightly different from that in the actual turbine aerodynamic design of 72.8 deg. The reason will be explained in the section on the reliability of 3D Navier–Stokes solver. The geometrical model of the base line passage that was used to initialize the optimization lies within the feasible region of the design space. According to Eq. (1), only violated constraints contribute to the objective function. The weights $w_1$ and $w_2$ on the constraints are constant during optimization and are chosen such that the contribution of a violated constraint by far outweighs the contribution of the objective $\omega$ in order to quickly drive the search back into the feasible region.

**Flow Solver.** For the simulation of the fluid dynamic properties of the passage designs, we used the parallelized 3D in-house Navier-Stokes flow solver HSTAR3D (see Ref. [18]), with Wilcox's $k$-$\omega$ two equation model [19]. Prior to optimization, we performed CFD calculations of the base line geometry to determine the necessary grid size for a high resolution of the boundary layer development. The computational grid consisted of $175(J) \times 52(K) \times 64(L) = 58{,}2400$ cells. The average $y^+$ of the first grid point from the wall is about 1.5 for all calculations. The computation time for one flow analysis with this grid depends on the passage geometry. It takes roughly 1 h on two AMD Opteron 2 GHz dual processors.

**Optimization Algorithm.** A flowchart of our optimization environment is given in Fig. 4. The basic setup is governed by two parallelization levels. On the first level, the evolutionary operators are used to generate the offspring population, i.e., the new blade designs. In our algorithm, we do not use a recombination procedure. Instead, changes are induced during mutation by adding normally distributed random numbers to the design parameters that are subject to optimization. As noted before, the covariance matrix

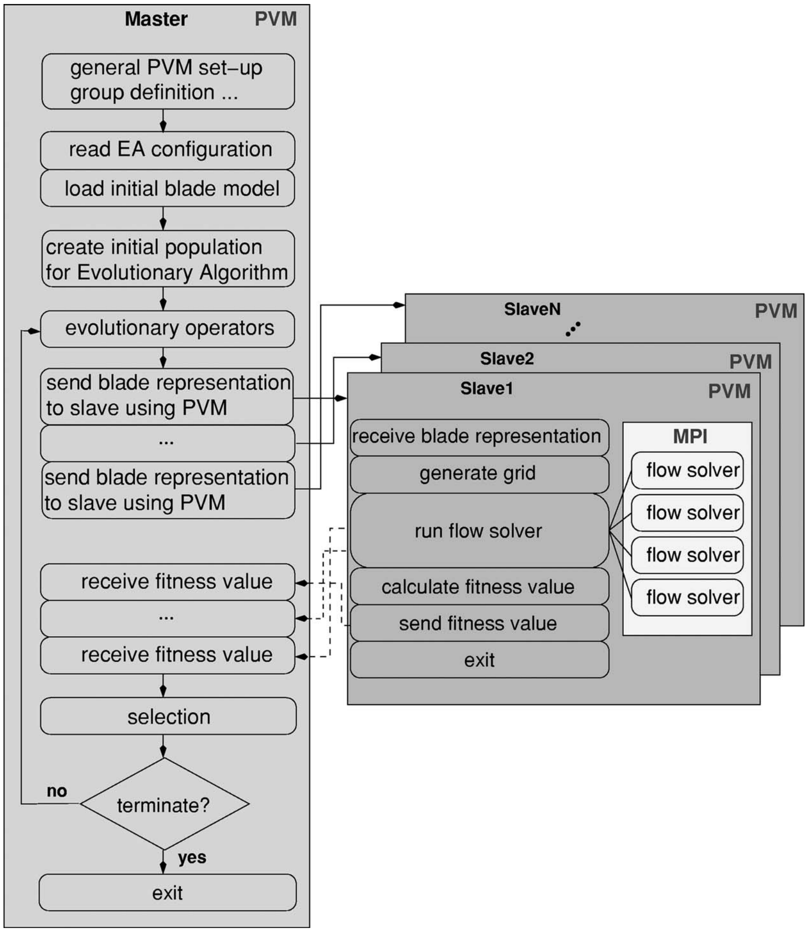

Fig. 4 Flowchart of optimization environment

of the normal distribution is adapted to the local topology of the search space. The λ offspring individuals—here, λ denotes the offspring population size—are evaluated in parallel by sending each blade representation to separate slave processes using the parallel virtual machine (PVM) library [20]. The slave processes generate the computational grid and run the flow solver using an additional set of four processes, which are distributed using message passing interface (MPI) [21]. This constitutes the second level of parallelization. The slave processes calculate the objective function (Eq. (1)) and send the resulting quality value back to the master process. The master collects the quality values for all λ individuals or blade designs. Next, the best $\mu$ designs are selected from these λ individuals to become the parent population of the next generation. In evolutionary algorithms, this type of "deterministic" selection method is written as the $(\mu,\lambda)$ selection. The evolutionary cycle proceeds with the creation of the next offspring generation as long as the stop criteria are not met. Ideally, stop criteria should depend on the expected performance gain and should stop the optimization when this value falls below a certain threshold. In reality, the optimization is often stopped because of time constraints.

For the results presented in this paper, a $(\mu,\lambda)$ CMA-ES with $\mu=1$ parent individual and $\lambda=10$ offspring individuals was used. The optimization was initialized with a geometry similar to the base line passage. All offspring individuals were evaluated in parallel. For this, we used a 40 processor computing cluster: ten parallel processes were running in the first level of parallelization and each of these spawned four processes in the second level of parallelization.

## Results and Discussions

**Reliability of 3D Navier-Stokes Flow Solver.** It is very important to estimate the reliability of the 3D flow solver used in this turbine end wall optimization in advance. So far, the flow solver has been successfully used for compressor and turbine blades. For example, the 3D flow solver with a low Reynolds $k$-$\varepsilon$ turbulence model proposed by Chien [22] has been successfully applied to the compressor blade of NASA Rotor67 and 37 [18].

A 2D version of the flow solver with the same turbulence model has also been applied successfully to a transonic turbine cascade [23]. In this research and in our previous work [24], the Wilcox's $k$-$\omega$ model [19] has been used for the 3D transonic turbine blade for an easier determination of the length from the wall. However, a precise validation with the new model has not been done yet. The reason is that it is very expensive and time consuming to prepare the validation data for the 3D transonic annular turbine cascade. Therefore, we estimate the reliability as far as possible based on data obtained from a transonic turbine stage rig shown in Fig. 5. We should note that the following data were not measured for the purpose of validation and that errors are inherent.

The comparison of EXP and CFD was carried out, focusing on the oil flow visualization and the loss and the exit flow angle distributions at the nominal IGV exit plane: Station 2, i.e., 7 mm downstream of the TE (corresponding to 0.13 axial chord downstream of the TE). The test facility was designed for full size testing of the HPT, and the test was carried out under the "cold" condition at the design corrected mass flow rate. Therefore, the axial gap between the base line IGV and the rotor was newly

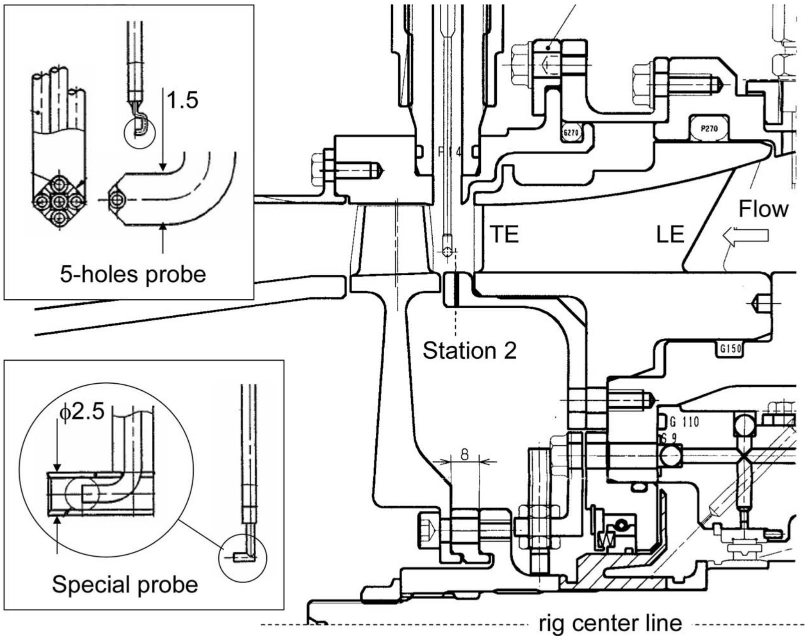

**Fig. 5 Experimental apparatus for IGV wake traverse measurement at Station 2, using a transonic turbine stage rig**

extended to be able to do the traverse measurement radially and circumferentially. However, there are no static pressure taps on the IGV surface because this rig has been used for the estimation of the stage performance, as already mentioned above.

The traverse was performed using two types of probes. One is a special probe that is not sensitive for the flow angle variation, as shown in Fig. 5. This was mainly used for total pressure measurement. The other one is a five-hole probe for the flow angle measurement, also shown in Fig. 5. Regarding the total pressure measurement, the circumferential increment is 2 deg to the 1 pitch (45 deg: NB=8), and about 1 pitch measure was done. The radial positions were seven sections, so the total number of measure points is 161 points ($23\times 7$).

In this research, the total pressure loss coefficient is not defined in terms of the exit dynamic head as the denominator, but in terms of the inlet total pressure. There are two reasons for this: firstly, a large circumferential variation (not negligibly small) of the static pressure value was observed on the outer casing downstream of the IGV-TE (at Station 2) (not shown here). This may be due to a narrow gap between the IGV and a rotor. The second reason is that as far as CFD results are concerned, there is no linear distribution at Station 2 (not shown here). Therefore, we decided to use the inlet total pressure, instead of the exit dynamic head, in order to achieve a high accuracy on the data processing.

For the flow angle measurement using the five-hole probe, the radial flow component was neglected. The traverse measurement was done with the same circumferential increment as the total pressure measurement, but the radial measurement positions were reduced from seven to five sections. The flow direction was manually determined by adjusting the pressure difference of the right hole and the left hole to be zero in the free wake region. The measurement accuracy for the total pressure loss is considered to be accurate to within $\pm 0.002$ in the areas of relatively low total pressure loss, while the flow angle accuracy is about $\pm 0.5$ deg.

Firstly, the oil flow visualization was carried out for the base line vane, experimentally and numerically, as shown in Fig. 6, in order to understand the overall image of the secondary flow pattern for the transonic IGV. In the experiment, this picture corre-

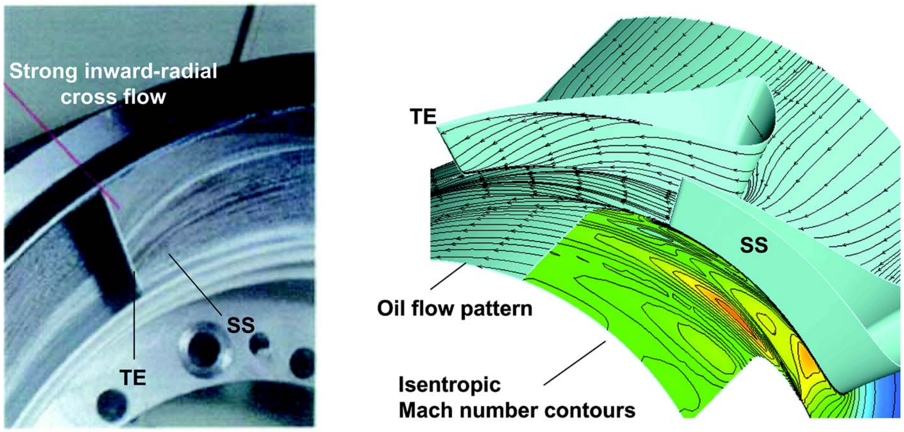

(a) EXP (NB=10)

(b) CFD (NB= 8)

**Fig. 6 Comparison of vane surface oil flow visualization for (*a*) EXP and (*b*) CFD**

sponds to NB=10, but the tendency is almost the same as for the base line case with NB=8. There is a strong inward-radial flow near the rear part of the SS, and there is no interaction between the shock, emanating from the TE of the adjacent vane, and the SS boundary layer. It seems that the inward-radial flow pattern for the ultralow-aspect IGV is much stronger than the one for a high-AR IGV. The tendency of the oil flow pattern in CFD is almost the same as in the experiment. The end wall isentropic Mach number contours in Fig. 6(*b*) clearly show the complexity of the flow pattern. This will be discussed in the section on flow mechanism in ultra-low AR IGV.

Figure 7 (top and bottom) shows the circumferential-mass-averaged spanwise distribution of the total pressure loss and the exit flow angle, respectively. In general, a good qualitative agreement between EXP and CFD is obtained for both loss and flow angle distribution. However, the pattern of the flow angle distribution near the hub region is different from the established knowledge on the secondary flow. We observe a tendency of underturning of the exit flow angle near the hub wall. Moustapha and Williamson [13] obtained similar results for the annular cascade. They found experimentally in their annular cascade testing an overturning tendency near the hub wall in the subsonic exit Mach number. However, in the transonic and supersonic exit Mach number regions, a tendency to underturn is predominant. Unfortunately, there is no clear explanation of the reason. We will discuss this in more detail in the section on flow mechanism in ultralow-AR IGV.

Regarding the spanwise exit flow angle distribution in Fig. 7 (bottom), there is a tendency of the underestimation of about 1.0 deg at the midspan height. Therefore, in the optimization used in this paper, the design exit flow angle was set to 72 deg, instead of to 72.8 deg.

Figure 8 shows the experimental and numerical comparison of the total pressure loss contour at Station 2. As already mentioned above, there are only seven radial measurement sections for the total pressure loss, which is not sufficient for an accurate comparison between EXP and CFD. However, it seems worthwhile to highlight the unusual flow characteristics around the left of the PS circumferential area near the hub and tip wall in the experiment where the losses are never low in such an ultralow-AR transonic turbine IGV.

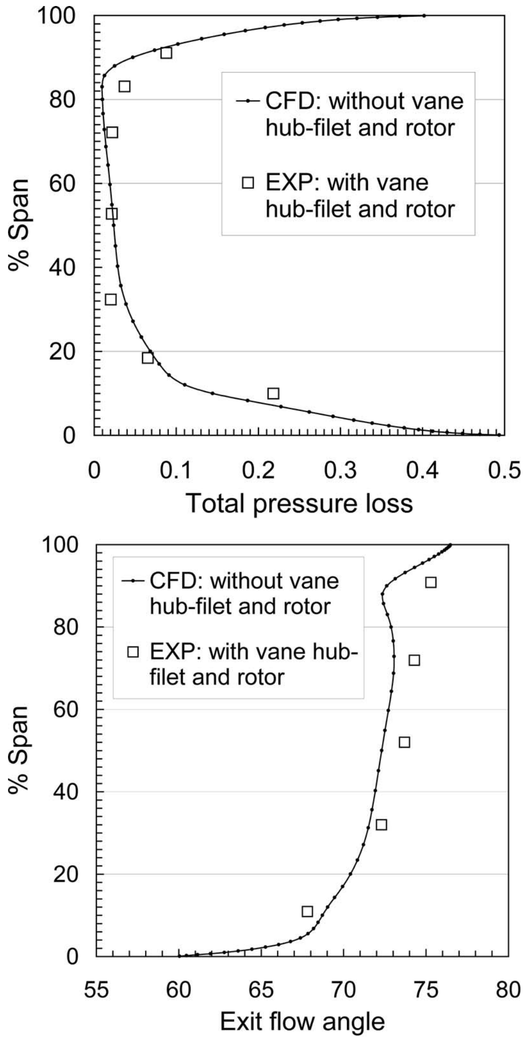

**Fig. 7 Comparison of loss (top) and exit flow angle (bottom) at Station 2 for EXP and CFD**

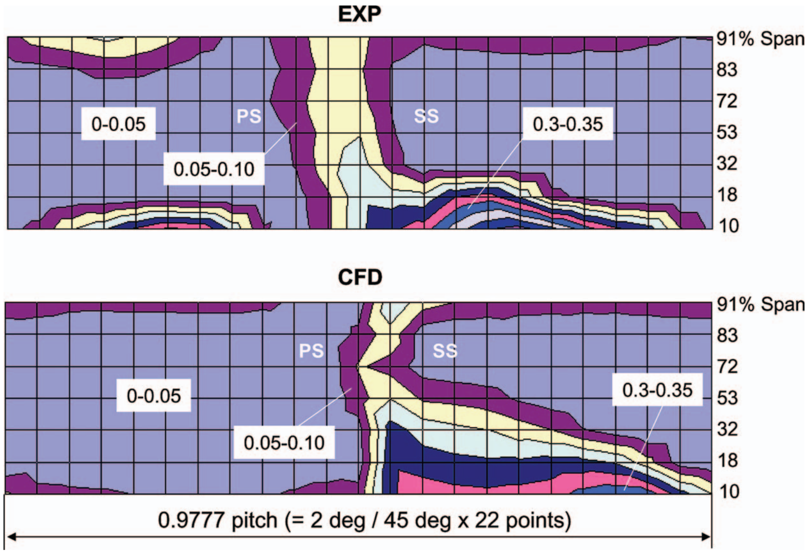

**Fig. 8 Comparison of total pressure loss at Station 2 for EXP (top) and CFD (bottom); 0.05 increment**

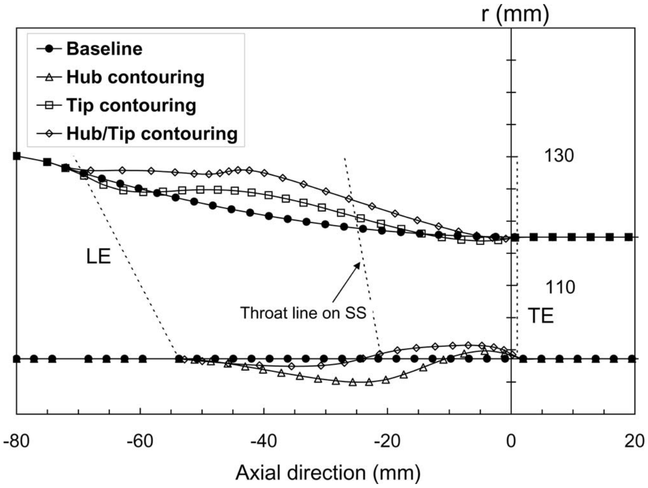

**Fig. 9 Base line and optimized three passages**

Comparing the wake pattern in the EXP and CFD in more detail, the wake mixing process in CFD around the wake-free region at 72% of span height is not established. At the same time, a qualitative agreement is obtained for the tip region only. A possible reason for the different quality for the hub and tip regions may be the effect of the blade filet in the EXP and the CFD. In both CFD and EXP, there is no filet on the tip end wall (under the same condition). On the contrary for the hub end wall, we only observe a filet in EXP, but not in CFD (not the same condition). The mechanism behind the unusually high loss region found around the PS in the experiment will be explained in more detail using the CFD results in the section on flow mechanism in ultralow-AR IGV.

**Effect of End Wall Contouring.** Figure 9 shows the passage geometries obtained from the optimization for the three cases, i.e., "hub contouring," "tip contouring," and "hub and tip contouring." The base line is also shown in the figure (black circles). In the case of hub contouring, the hub radius gradually decreases from the LE to the minimum, which is reached around the middle axial hub chord; from there, the radius gradually increases toward the TE. Furthermore, we observe an unusual hump (overshoot) of the hub line around the TE. In the case of the tip end wall contouring, a unique tip line (*S* type) is obtained. In the case of the combined hub and tip optimization, the frontal part of the passage diverges; i.e., the passage width increases and the flow is decelerated. Indeed, this is a common characteristic for all three optimization cases. The passages diverge around the frontal part and converge; i.e., the passage width decreases and the flow is accelerated around the rear part.

Figure 10 shows the isentropic Mach number distribution on the IGV surface for the three cases and the base line. Compared to the base line (Fig. 10(*a*)) in the hub contouring case (Fig. 10(*b*)), the circumferential pressure gradient, frequently called the "driving force of the secondary flow," is significantly reduced especially around the middle axial chord part and remarkably at the

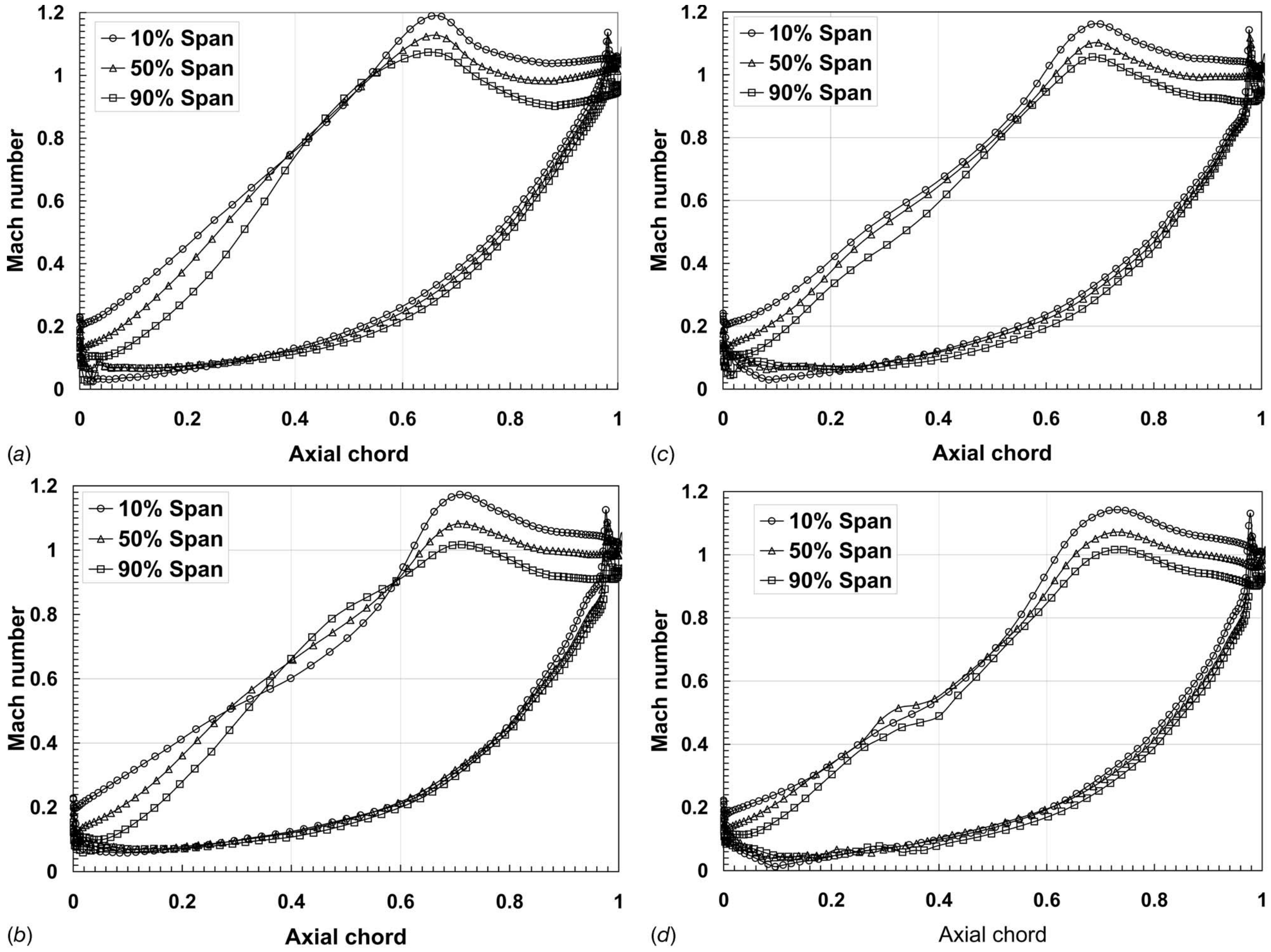

**Fig. 10 Comparison of blade surface Mach number distribution for base line and three optimized passages. (*a*) base line, (*b*) hub contouring, (*c*) tip contouring, and (*d*) hub and tip contouring.**

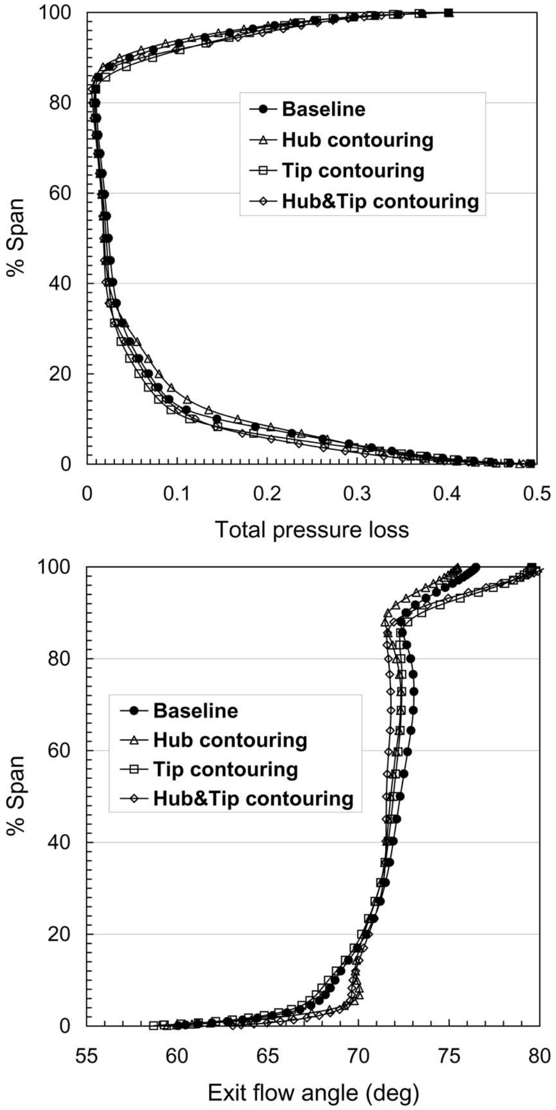

**Fig. 11 Spanwise distribution of loss (top) and exit flow angle (bottom) for base line and three optimized passages**

hub region (10% span). This leads to a reverse pressure gradient ($P_s$, tip $<P_s$, hub) around 40%–59% axial chord, which results in a reduction of the secondary flow, because the circumferential and spanwise (radial) driving forces are weaker. However, while the aerodynamic loading in the aft part is circumferentially and radially increased, the gain obtained at the middle part may disappear. This general tendency is also observed for the remaining two cases (the tip contouring and the combination of hub and tip contouring). In the case of tip contouring (Fig. 10(*c*)), there is no intersecting distribution on the SS, which is observed for the hub contouring (see Fig. 10(*b*)). In the case of the hub and tip contouring (Fig. 10(*d*)), the highest circumferential loading is observed around 80% axial chord position. Figure 11 (top) and Table 1 show the circumferential-mass averaged spanwise loss distribution and the overall mass averaged values for the three end wall contouring cases and the base line, respectively. Comparing the hub contouring with the base line, the loss between about 5% and 36% span height is worse, but for the other spanwise positions, it is improved. As a result, the overall loss reduction is 7% at Station 2 and 4% at the downstream position (Station 3), as shown in Table 1.

As already mentioned the loss at Station 2 does not include the mixing loss, but the loss at Station 3 includes both the mixing loss and the friction loss due to a large exit swirl angle (about 72 deg) from Station 2 (just downstream of IGV to Station 3) (far downstream). Here, we can see that the largest reduction rate of the loss, including the mixing and the friction losses, is achieved at Station 3 by the hub and tip contouring because all four cases have almost the same exit swirl angle and the same mass flow rate between Stations 2 and 3.

In the case of the tip end wall contouring, the minimal loss value is reached between 10% and 30% span height. Regarding the exit flow angle distribution in Fig. 11 (bottom), the underturning tendency near the hub end wall region, observed in the base line, is changed in the case of the hub contouring and the hub and tip contouring where we notice a tendency of overturning. This will be discussed in the section of flow mechanism in ultralow-AR IGV.

In summary, the optimized geometries show a lower loss than the base line. The reduction rate is 4% for the hub contouring, 5% for the tip contouring, and 10% for the combination at Station 3. Remember that we define the loss in terms of the inlet total pressure and not in terms of the exit dynamic head.

**Flow Mechanism in UltraLow-Aspect-Ratio Inlet Guide Vane.** Figure 12 shows the loss contours for the three optimized geometries and for the base line at Station 2. This does not correspond to an actual physical plane, but to the grid point used in CFD because this simplifies the discussion of the end wall region. Regarding the high loss region around the left side of PS, observed in the experiment (see Fig. 8, top), the CFD shows a similar loss region indexed as No. 1 in Fig. 12(*a*). Also, CFD seems to simulate the near tip region No. 2 well. Apart from the high loss region Nos. 1 and 2, there are two more high loss regions termed Nos. 3 and 4 near the hub end wall located at the SS. In the hub contouring (see Fig. 12(*b*)), the losses at Nos. 1 and 4 are reduced, but remarkably increased at No. 3. This is the reason why the loss around the 5% and 36% span is increased (see Fig. 11, top). In the case of the tip contouring (see Fig. 12(*c*)), the loss at No. 3 is dramatically decreased, but increased at Nos. 1 and 4. This is the reason why the minimal loss region is positioned at around 10%–30% span height for the tip contouring. For the combined contouring (see Fig. 12(*d*)), the loss at No. 3 is again increased, but not more than for the hub contouring. Also, the loss levels at Nos. 1 and 4 are minimal. This is one reason why the hub and tip contouring shows the maximal loss reduction.

**Table 1 Performance comparison for base line and three optimized passage**

| | Total pressure loss (%) | | Exit flow angle | | |
|---|---|---|---|---|---|
| Optimization cases | Station 2 | Station 3 | Station 2 | Station 3 | Corrected mass flow at Station 2 |
| Base line | 5.92 (1.00) | 10.61 (1.00) | 71.8 | 71.7 | 0.84 (kg/s) |
| 1. Hub contouring | 5.53 (0.93) | 10.22 (0.96) | 71.5 | 71.6 | 0.85 |
| 2. Tip contouring | 5.38 (0.90) | 10.13 (0.95) | 71.5 | 71.6 | 0.85 |
| 3. Hub and tip contouring | 5.00 (0.84) | 9.57 (0.90) | 71.5 | 71.7 | 0.85 |

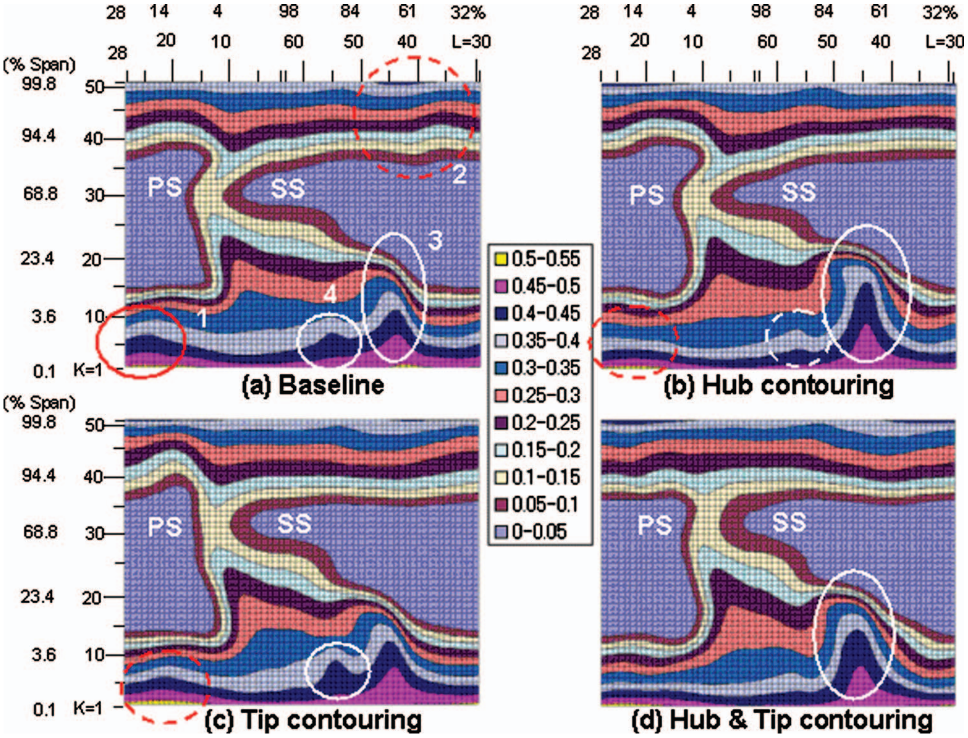

**Fig. 12** Total pressure loss contour for base line and three optimized passages at Station 2

The underturning around the hub region can be mainly observed for the base line and the tip end wall contouring and is much less pronounced for the hub contouring and the hub and tip combination (see Fig. 11, bottom). The reason is that the flow angle is strongly influenced by the high loss region No. 4. Figure 13 shows the total pressure contours and the exit flow angle contours for the base line and the hub and tip contouring. In the case of the base line, there is a large underturning region corresponding to the high loss at No. 4. On the contrary, overturning is observed at around the high loss at No. 1. In the case of the hub and tip contouring, the underturning is decreased by the reduced loss at No. 4. Also, the overturning is decreased by the reduced loss at No. 1. Tentatively, we can conclude that there is a concentrated vortex around the high loss region No. 4 and the rotational direc-

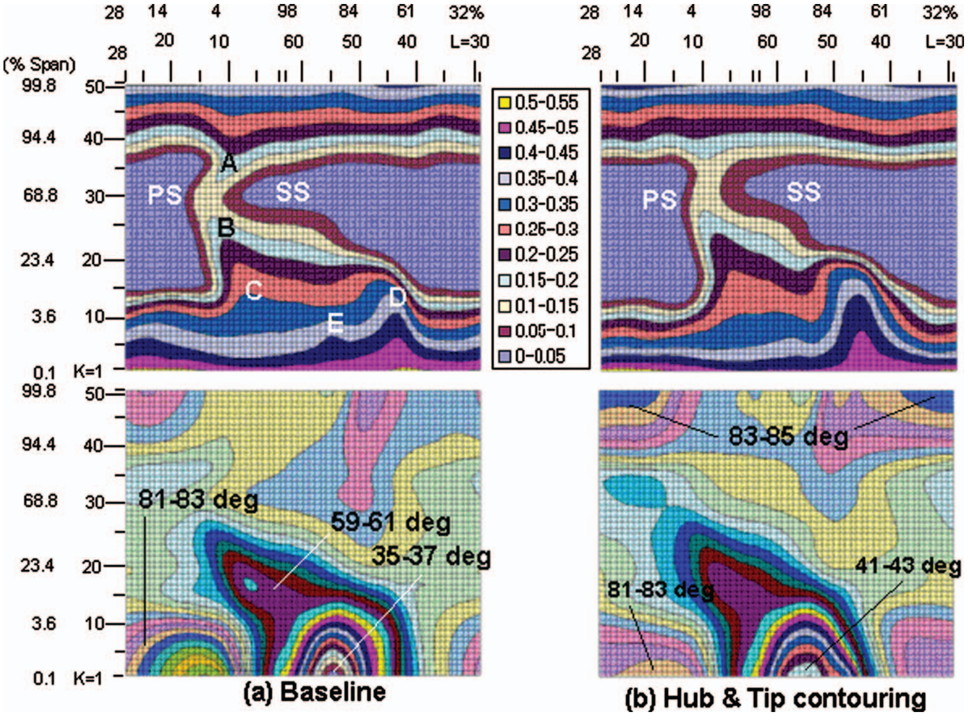

**Fig. 13** Comparison of loss and exit flow angle for (*a*) base line and (*b*) hub and tip contouring

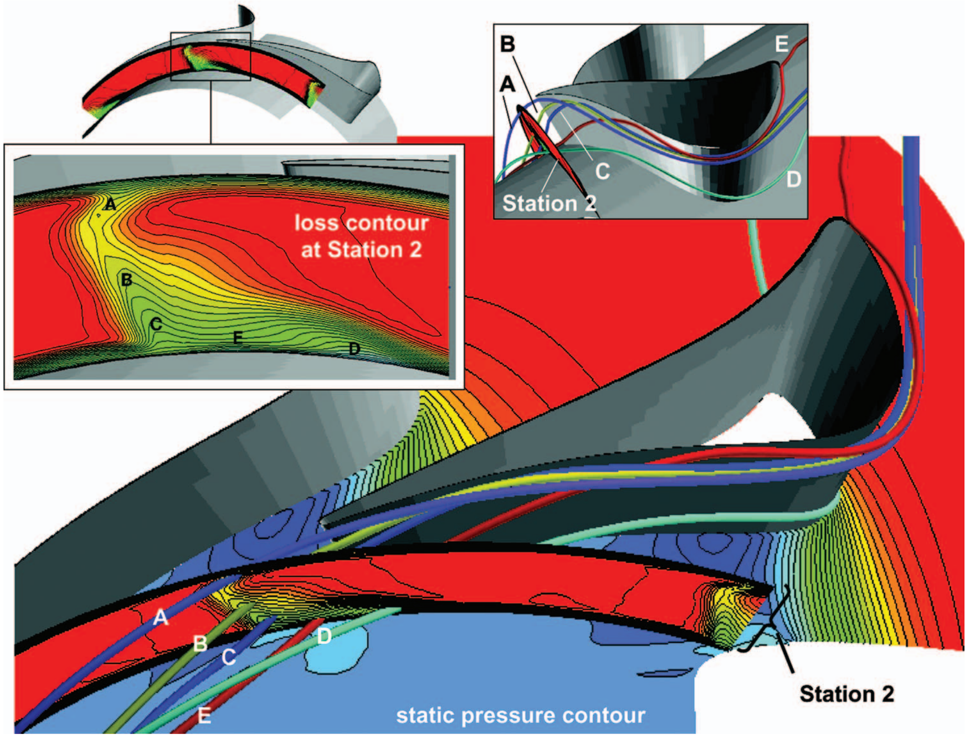

Fig. 14 Relation of high loss region and streamline for base line

tion is opposite to the $H_p$ (see Fig. 1). However, the question remains: What are the reasons behind the high losses at Nos. 3 and 4? Therefore, a particle trace visualization was carried out. The particle was released at points A, B, C, D, and E, as shown in Fig. 13, top-left.

Figure 14 shows the results. It is very surprising that the fluid particles released at A, B, and C all come from the tip end wall, showing a spiral movement. The movement of the particles started at E seems to be independent of the A, B, C group. A particle released at D comes from the hub end wall, showing a lift-up around the middle axial chord.

Figure 15 is similar to Fig. 14, but the viewpoint is from the top in order to estimate the exit flow angle. The high loss region at E mainly causes the underturning observed near the hub region in the experiment (see Fig. 7, bottom). Also, regarding the high isentropic Mach number region downstream of the TE as shown in Fig. 6, right, there is no corresponding part in Fig. 15 (see the wall static pressure contours). Therefore, the static pressure field adja-

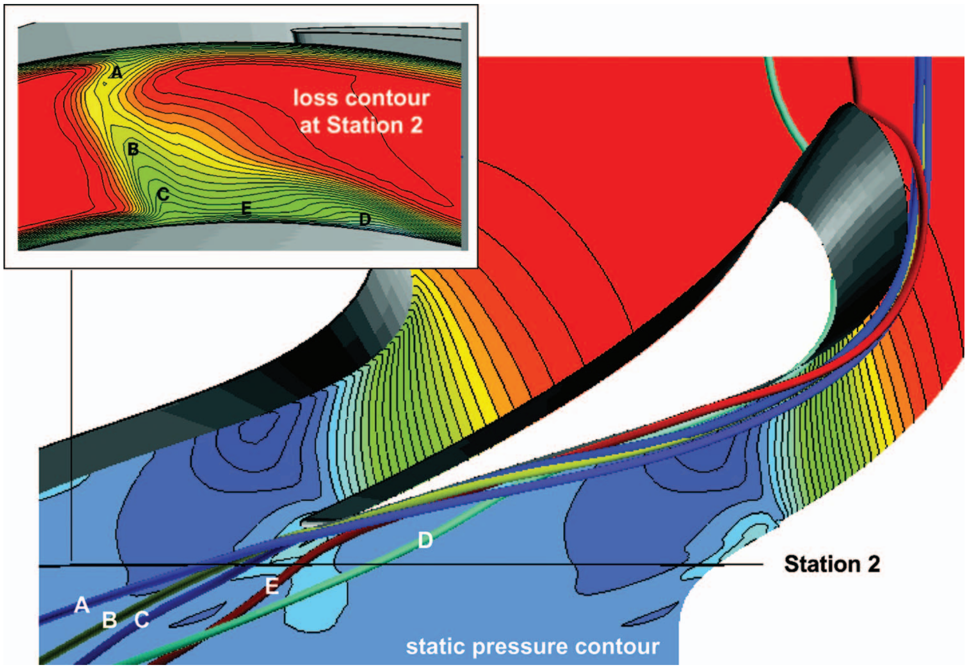

Fig. 15 Relation of high loss region and flow angle for base line

cent to the wall where the oil flow and the Mach number were estimated in Fig. 6 should be different from the wall static pressure due to the complex flow field, as shown in Figs. 12 and 13. A related stage testing for an optimized end wall contouring is currently being planned.

## Conclusions

In this study, we employed a numerical, stochastic optimization method, namely, the ES, to investigate the effect of the end wall contouring for an ultralow-AR transonic turbine IGV in a small size HPT. The target was to investigate the effect of the end wall contouring on the aerodynamic performance and to investigate the secondary flow mechanism in order to find out whether it differs from the model obtained from the low speed and linear cascade conditions. From an aerodynamic point of view, the following conclusions can be drawn.

- The hub contouring, the tip contouring, and the hub and tip contouring all reduce the mass averaged overall loss by 4%, 5%, and 10%, respectively, as compared to the base line. Remember that we define the loss in terms of the inlet total pressure and not in terms of the exit dynamic head.
- Each contouring significantly influences the flow mechanism related to the secondary flow near the hub end wall where we observe areas of high losses and a large variation of the exit flow angle already in the base line experiments.
- The useful design concept is an aft-loaded pattern because the spanwise (radial) static pressure gradient within blade to blade is more dominant than the circumferential static pressure gradient.
- The flow mechanism in the small size full annular ultralow-AR transonic turbine IGV is different from the secondary flow model obtained from the low speed linear cascade.
- Further investigation is needed to completely clarify the secondary flow mechanism for a small size ultralow-AR transonic annular turbine cascade.

## Acknowledgment

The authors are grateful to Gensuke Hoshino and Kouji Murata from the Honda R&D, who performed the test series.

## Nomenclature

$\dot{m}$ = mass flow rate at Station 2
$\dot{m}_{\text{design}}$ = design mass flow rate at Station 2
$P_t$ = total pressure
$P_s$ = static pressure
$r$ = radius
Re = Reynolds number, based on true (actual) chord and midheight exit flow conditions
$w_i$ = weight in fitness function
$X$ = coordinate related to the stator passage
$y^+$ = normal distance from the wall
Zw = Zweifel loading coefficient
$\beta_2$ = exit flow angle at Station 2
$\beta_{2,\text{design}}$ = design value of the exit flow angle at Station 2
$\delta\beta_2$ = tolerance in the exit flow angle at Station 2
$\delta\dot{m}$ = tolerance in the mass flow rate at Station 2
$\omega$ = total pressure loss coefficient $(=(\mathrm{Pt}_1\text{-}\mathrm{Pt}_2)/\mathrm{Pt}_1)$

### Abbreviations

EXP = experiment
$H_p$ = pressure side leg of horseshoe vortex
$H_s$ = suction side leg of horseshoe vortex

### Subscripts

1 = upstream position
2 = just downstream stator TE or rotor LE position
3 = far downstream of stator
ax = axial

## References

[1] Klein, A., 1966, "Investigation of the Entry Boundary Layer on the Secondary Flows in the Blading of Axial Turbines," BHRA T1004.
[2] Langston, L. S., Nice, M. L., and Hooper, R. M., 1977, "Three-Dimensional Flow Within a Turbine Cascade Passage," ASME J. Eng. Power, **99**, pp. 21–28.
[3] Langston, L. S., 1980, "Crossflows in a Turbine Cascade Passage," ASME J. Eng. Power, **102**(4), pp. 866–874.
[4] Sieverding, C. H., and Van den Bosch, P., 1983, "The Use of Coloured Smoke to Visualize Secondary Flows in a Turbine-Blade Cascade," J. Fluid Mech., **134**, pp. 85–89.
[5] Sonoda, T., 1985, "Experimental Investigation on Spatial Development of Streamwise Vortices in a Turbine Inlet Guide Vane Cascade," ASME Paper No. 85-GT-20.
[6] Wang, H. P., Olson, S. J., Goldstein, R. J., and Eckert, E. R. G., 1997, "Flow Visualization in a Linear Turbine Cascade of High Performance Turbine Blades," ASME J. Turbomach., **119**, pp. 1–8.
[7] Deich, M. E., Zaryankin, A. E., Fillipov, G. A., and Zatsepin, M. F., 1960, "Method of Increasing the Efficiency of Turbine Stages With Short Blades," Translation No. 2816, Associated Electrical Industries Ltd., Manchester, England.
[8] Ewen, J. S., Huber, F. W., and Mitchell, J. P., 1973, "Investigation of the Aerodynamic Performance of a Small Axial Turbine," ASME Paper No. 73-GT-3.
[9] Morris, A. W. H., and Hoare, R. G., 1975, "Secondary Loss Measurements in a Cascade of Turbine Blades With Meridional Wall Profiling," ASME Paper No. 75-WA/GT-13.
[10] Kopper, F. C., Milano, R., and Vanco, M., 1981, "Experimental Investigation of Endwall Profiling in a Turbine Vane Cascade," AIAA J., **19**(8), pp. 1033–1040.
[11] Boletis, E., 1985, "Effects of Tip Endwall Contouring on the Three-Dimensional Flow Field in an Annular Turbine Nozzle Guide Vane: Part 1—Experimental Investigation," ASME J. Eng. Gas Turbines Power, **107**, pp. 983–990.
[12] Haas, J. E., 1982, "Analytical and Experimental Investigation of Stator Endwall Contouring in a Small Axial-Flow Turbine. 1—Stator Performance," NASA Report No. TP-2023.
[13] Moustapha, S. H., and Williamson, R. G., 1985, "Investigation of the Effect of Two Endwall Contours on the Performance of an Annular Nozzle Cascade," AIAA Paper No. 85–1218.
[14] 2000, *Evolutionary Computation 1: Basic Algorithms and Operators*, T. Baeck, D. B. Fogel, and T. Michalewicz, eds., Institute of Physics, University of Reading, Berkshire.
[15] Osyczka, A., 2002, *Evolutionary Algorithms for Single and Multicriteria Design Optimization*, Physica, Heidelberg.
[16] Hansen, N., and Ostermeier, A., 2001, "Completely Derandomized Self-Adaptation in Evolution Strategies," Evol. Comput., **9**(2), pp. 159–195.
[17] Farin, G., 1997, *Curves and Surfaces for Computer-Aided Geometric Design*, 4th ed., Academic, San Diego.
[18] Arima, T., Sonoda, T., Shirotori, M., Tamura, A., and Kikuchi, K., 1999, "A Numerical Investigation of Transonic Axial Compressor Rotor Flow Using a Low-Reynolds-Number k-$\varepsilon$ Turbulence Model," ASME J. Turbomach., **121**, pp. 44–58.
[19] Wilcox, D. C., 1988, "Reassessment of the Scale-Determining Equation for Advanced Turbulence Models," AIAA J. **26**, pp. 1299–1310.
[20] Geist, A., Beguelin, A., Dongarra, J., Jiang, W., Mancheck, R., and Sunderam, V., 1994, *PVM: Parallel Virtual Machine: A Users' Guide and Tutorial for Network Parallel Computing*, MIT, Cambridge, MA.
[21] MPI: A message-passing interface standard, http://www-unix.mcs.anl.gov/mpi/
[22] Chien, J. Y., 1982, "Predictions of Channel and Boundary Layers With a Low-Reynolds-Number Two Equation Model of Turbulence," AIAA J., **20**, pp. 33–38.
[23] Sonoda, T., Arima, T., Olhofer, M., Sendhoff, B., Kost, F., and Giess, P.-A., 2006, "A Study of Advanced High Loaded Transonic Turbine Airfoils," ASME J. Turbomach., **128**, pp. 650–657.
[24] Hasenjäger, M., Sendhoff, B., Sonoda, T., and Arima, T., 2005, "Three Dimensional Aerodynamic Optimization for an Ultra-Low Aspect Ratio Transonic Turbine Stator Blade," ASME Paper No. GT2005–68680.

# Experimental and Numerical Impingement Heat Transfer in an Airfoil Leading-Edge Cooling Channel With Cross-Flow

**M. E. Taslim**

**D. Bethka**

Mechanical and Industrial Engineering
Department,
Northeastern University,
Boston, MA 02115

*To enhance the internal heat transfer around the airfoil leading-edge area, a combination of rib-roughened cooling channels, film cooling, and impingement cooling is often employed. Experimental data for impingement on various leading-edge geometries are reported by these and other investigators. The effects of strong cross-flows on the leading—edge impingement heat transfer, however, have not been studied to that extent. This investigation dealt with impingement on the leading edge of an airfoil in the presence of cross-flows beyond the cross-flow created by the upstream jets (spent air). Measurements of heat transfer coefficients on the airfoil nose area as well as the pressure and suction side areas are reported. The tests were run for a range of axial to jet mass flow rates* ($M_{axial}/M_{jet}$) *ranging from 1.14 to 6.4 and jet Reynolds numbers ranging from 8000 to 48,000. Comparisons are also made between the experimental results of impingement with and without the presence of cross-flow and between representative numerical and measured heat transfer results. It was concluded that (a) the presence of the external cross-flow reduces the impinging jet effectiveness both on the nose and sidewalls; (b) even for an axial to jet mass flow ratio as high as 5, the convective heat transfer coefficient produced by the axial channel flow was less than that of the impinging jet without the presence of the external cross-flow; and (c) the agreement between the numerical and experimental results was reasonable with an average difference ranging from* $-8\%$ *to* $-20\%$. [DOI: 10.1115/1.2950058]

## Introduction

Various methods have been developed over the years to keep the turbine airfoils' temperatures below critical levels consistent with the required life for each component. Parallel with advances in airfoil material properties, advances in airfoil cooling schemes have also been remarkable. A main objective in turbine airfoil cooling design is to achieve maximum heat removal from the airfoil metal while minimizing the required coolant flow rate. One such method is to route coolant air through serpentine passages within the airfoil and convectively remove heat from the airfoil. The coolant is then ejected either at the tip of the airfoil, through the cooling slots along the trailing edge, or the film holes on the airfoil surface at critical locations. To further enhance the heat transfer, the cooling channel walls are often roughened with ribs. Extensive research has been conducted on various aspects of the rib-roughened channels and it is concluded that geometric parameters such as passage aspect ratio (AR), rib height to passage hydraulic diameter or blockage ratio ($e/D_h$), rib angle of attack ($\alpha$), the manner in which the ribs are positioned relative to one another (in-line, staggered, crisscross, etc.), rib pitch-to-height ratio ($P/e$), and rib shape (round versus sharp corners, fillets, rib aspect ratio ($AR_{rib}$), and skewness towards the flow direction) have pronounced effects on both local and overall heat transfer coefficients. The interested reader is referred to the work of investigators such as Burggraf [1], Chandra and Han [2], El-Husayni et al. [3], Han [4], Han et al. [5–7], Metzger et al. [8–10], Taslim and Spring [11,12], Taslim et al. [13–15], Webb et al. [16], and Zhang et al. [17].

Airfoil leading-edge surface, being exposed to very high gas temperatures, is often a life-limiting region and requires more complex cooling schemes especially in modern gas turbines with elevated turbine inlet temperatures. A combination of convective and film cooling is used in conventional designs to maintain the leading-edge metal temperature at levels consistent with airfoil design life. The cooling flow usually enters the leading-edge channel from one end of the airfoil and flows radially to the other side. In some recent designs, however, the coolant enters the leading-edge cooling channel from the adjacent cooling channel through a series of cross over holes on the partition wall between the two channels. In the latter case, the crossover jets impinge on the leading-edge wall and exit through the showerhead film holes and/or gill film holes on the pressure and suction sides. Depending on the number of leading-edge film holes, these jets may form a cross-flow in the leading-edge cavity and move toward the end of the cooling channel. A survey of many existing gas turbine airfoil geometries show that, for analytical as well as experimental analyses, such cavities can be simplified by simulating the shape as a four-sided polygon with one curved side that simulates the leading-edge curvature, a rectangle with one curved side (often the smaller side), or a trapezoid, the smaller base of which is replaced with a curved wall. The available data in open literature are mostly for the jet impingement on flat surfaces that are smooth or rib-roughened and a few cases of impingement on concave but smooth surfaces. These studies include the work of Chupp et al. [18], Metzger et al. [19], Kercher and Tabakoff [20], Florschuetz et al. [21–23], Metzger and Bunker [24], Bunker and Metzger [25], Van Treuren et al. [26], Chang et al. [27], Huang et al. [28], and Akella and Han [29]. However, as dictated by the external shape of an airfoil leading edge, the test section in this investiga-

---

Contributed by the International Gas Turbine Institute of ASME for publication in the Journal of Turbomachinery. Manuscript received June 12, 2007; final manuscript received September 26, 2007; published online November 26, 2008. Review conducted by Karen A. Thole. Paper presented at the ASME Turbo Expo 2007: Land, Sea and Air (GT2007), Montreal, QC, Canada, May 14–17, 2007.

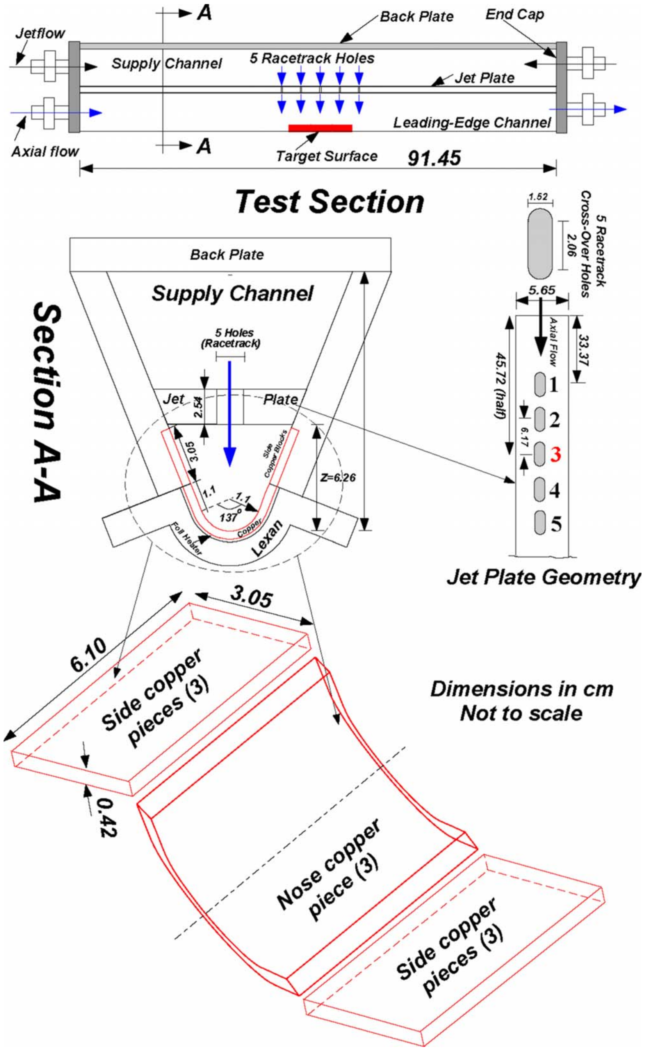

Fig. 1 Schematic of the test apparatus

tion was a symmetric channel with a circular nose, two tapered sidewalls, and a flat fourth wall on which the crossover jets were positioned. Experimental results for this setup with circular as well as racetrack-shaped crossover holes and for a variety of target surface geometries with and without the presence of showerhead and gill film holes have already been reported by Taslim et al. [30–34]. The present study, however, deals with the impingement of jets issued from racetrack-shaped crossover holes on a concave target surface, simulating the airfoil leading-edge cooling cavity, in the presence of a strong cross-flow. This flow arrangement also simulates the impingement in some trailing-edge cooling cavities with supplemental cooling air (refresher air) that is introduced from the airfoil root. The crossover jets interact with the externally induced cross-flow, impinge on the concave surface, and, along with the cross-flow, exit from the end of the cooling cavity.

## Test Sections

Figure 1 shows schematically the rig layout and its cross-sectional area, the target surface, and the crossover hole geometry. A conventional technique of heated walls in conjunction with thermocouples was used to measure the heat transfer coefficient. The test wall, where all measurements were taken, consisted of nine removable machined copper pieces, which were heated by foil heaters attached on the back of the pieces. By proper adjustment of the Ohmic power to the foil heater immediately underneath the copper pieces, the desirable surface temperature was obtained. The test rig was 91.5 cm long. The circular wall simulating the leading-edge nose with an inner radius of 1.1 cm and an arc angle of 137 deg was made of acrylic plastic with a 9.9 cm long recess in the middle to house the nine copper pieces. A flange on each side of the leading-edge piece facilitated the connection of the sidewalls to this piece and proper connection of the cross-flow inlet and exit lines. The circular recess along the inner radius with a depth of 3.2 mm and a length of 18.5 cm allowed the copper pieces to be fitted into the Lexan® shell. A removable 2.54 cm thick jet plate corresponding to a $Z/d_{\text{jet}}$ value of 2.8 was made of acrylic plastic to produce the impinging jets. Five racetrack-shaped holes with a cross section shown in Fig. 1 were drilled at a distance of 6.17 cm from each other (center to center) on the jet plate. The jet plate was attached and sealed to the side channel walls to simulate the partition wall between the leading edge and its adjacent cooling cavity in an airfoil. The crossover holes were centered with respect to both the length and width of the jet plate. The jet plate was positioned such that a jet impinged at the center of each copper piece. The removable copper pieces, installed in the acrylic nose piece, provided the ability to change the impingement surface geometries in the test rig. Custom-made thin etched-foil heaters with a thickness of about 0.2 mm were glued around the outer surface of each copper piece to provide the necessary heat flux. For each geometry, three identical copper pieces, separated by a 1 mm thick rubber insulator, were mounted next to each other. Heat transfer coefficients were measured on the middle piece while the other two pieces acted as guard heaters to minimize the heat losses to the adjacent walls. The test section wall temperature was adjusted to a desirable level by varying the Ohmic power to these heaters. Six thermocouples were embedded in each of the three middle copper pieces with their beads close to the exposed surface. Three thermocouples were embedded in each guard copper piece. The average of the six thermocouple readings in the middle copper pieces, which, if different, only differed by a fraction of a degree, was used as the surface temperature in the data reduction software for the average heat transfer coefficient. A nominal surface temperature of 45°C was selected so that with a jet temperature of about 20°C, a reasonable 25°C temperature difference existed between the wall surface and air. ac power was supplied to individual heaters through an existing power panel with individual Variacs for each heater. Typical amperage and voltage levels for each heater varied from 0.23 to 0.4 A and 20 V to 45 V, respectively. Air properties were evaluated at jet temperature.

The trapezoidal supply channel was formed by the exterior walls of the side channels, the jet plate, and a 1.27 cm thick aluminum backplate, as shown in Fig. 1. The end caps were fixed such that it was possible to control the flow and pressure in each channel, thus simulating many variations that may occur in actual airfoil environments. Static pressure taps and thermocouples in each channel measured the pressure and temperature at different locations. The test sections were covered on all sides, by 5 cm thick glass wool insulation to minimize heat losses to the environment. A contact micromanometer with an accuracy of 0.025 mm of water column as well as a series of oil and mercury manometers measured the pressures and pressure differences between the static pressure taps mounted on both sides of the roughened section for each geometry. For all cases, two critical venturimeters were used to measure the jet and axial flow rates separately. Data were gathered for a range of jet Reynolds number up to 48,000 and were compared with those numerically calculated. Fig. 1 Schematic of the test apparatus

## Computational Models

Taking advantage of symmetry, the computational models were constructed for half of the entire test section in the spanwise direction with a symmetric plane cutting through the test section centerline along the axial flow direction. The domain included the leading-edge channel, its adjacent supply channel that provided

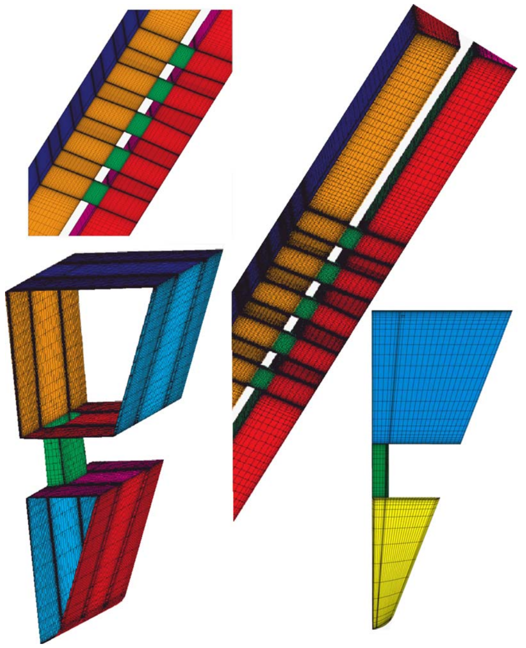

Fig. 2 Typical mesh arrangement around the computational domain periphery

the jet flow, and the crossover racetrack-shaped holes. Figure 2 shows the meshed domain and details of the mesh distribution around a crossover hole. The computational fluiddynamics (CFD) analysis was performed using STAR-CD solver by Adapco, Inc., a pressure-correction based, multi block, multigrid, unstructured/adaptive solver. Best results were generated using the $\nu 2f$ turbulence model. Other available turbulence models in this commercial code did not produce results that were in any better agreement with the measured results. Mesh density in the wall region was varied such that the average $y^+$ for the first layer of cells varied between 20 and 100 for all cases. Mesh independence was achieved at about 1 M cells for a typical model. Cells in all models were entirely hexagonal, a preferred choice for CFD analyses, and were varied in size bigeometrically from the boundaries to the center of the computational domain in order to have finer mesh close to the boundaries.

## Results and Discussion

A total of 60 tests were run in this investigation. All tests had several common features. There were always five impinging jets issuing from the jet plate. The middle jet (third) always impinged on the copper leading-edge test piece in the middle of the test section and the reported heat transfer results are always for that middle copper test pieces (a leading-edge piece and two side pieces). The main data reduction equations were

$$h = [(vi/A_{\mathrm{HT}}) - q_{\mathrm{loss}}]/(T_s - T_{\mathrm{jet}}) \tag{1}$$

$$\mathrm{Nu}_{\mathrm{jet}} = hd_{\mathrm{jet}}/k \tag{2}$$

$$\mathrm{Re}_{\mathrm{jet}} = (4M_{\mathrm{jet,middle}}/P_{\mathrm{hole}}\mu) \tag{3}$$

$$\mathrm{Re}_{\mathrm{axial}} = (4M_{\mathrm{axial}}/P\mu) \tag{4}$$

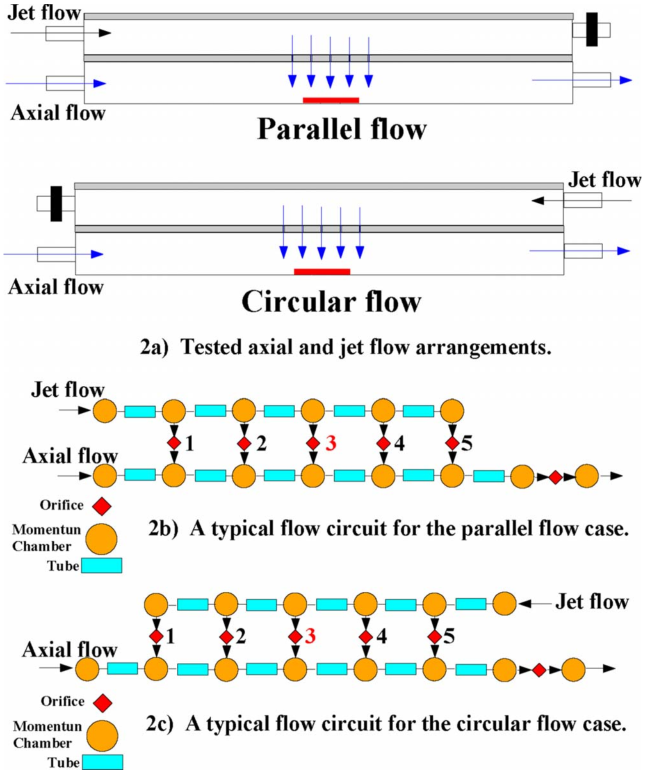

2a) Tested axial and jet flow arrangements.

2b) A typical flow circuit for the parallel flow case.

2c) A typical flow circuit for the circular flow case.

Fig. 3 Flow arrangements and circuits for flow analyses

The jet temperature was measured at the entrance of the third crossover hole. Heat losses from the middle copper pieces to the ambient by conduction and convection (about 0.02%) as well as the heat losses by radiation to the unheated walls (about 0.8%) were taken into consideration when the impingement heat transfer coefficient was calculated. The second and fourth jets impinged on the adjacent copper pieces that acted as guard heaters. The remaining two jets impinged on the acrylic leading-edge wall to simulate the flow field in a typical leading-edge cooling channel. Two jet flow arrangements to the supply channel, as shown in Fig. 3(*a*), where the jet air either entered from the same end as that of the axial flow or opposite to that of the axial flow, were tested. These flow arrangements are called "parallel" or "circular," respectively. The jet Reynolds number is based on the mass flow rate through the middle crossover hole. Depending on the jet to axial mass flow rate, the share of the middle crossover hole from the total mass flow varies from 20% to 40%, as shown in Fig. 4. To determine the air mass flow rate variation across the crossover

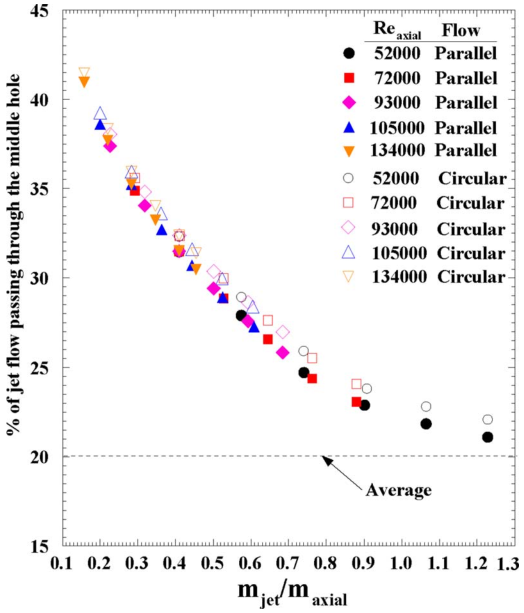

Fig. 4 Percentage of the total jet flow passing through the middle crossover hole

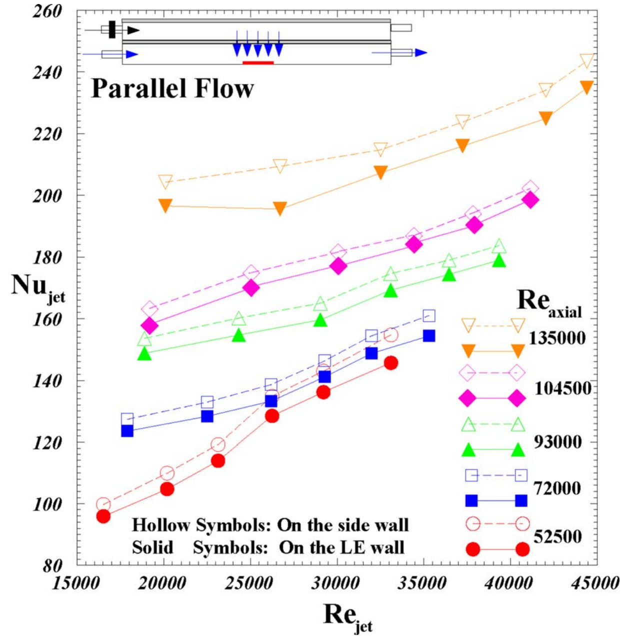

**Fig. 5 Nusselt number variation with jet Reynolds number for the parallel flow arrangement**

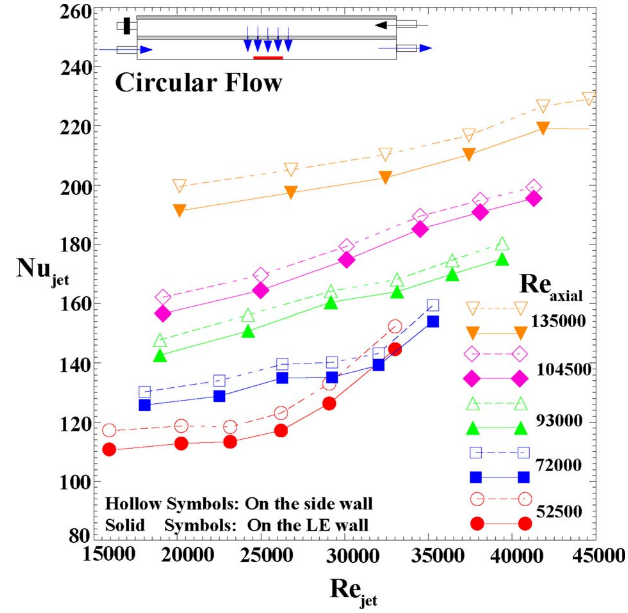

**Fig. 6 Nusselt number variation with jet Reynolds number for the circular flow arrangement**

holes, a one-dimensional flow circuit of each test setup consisting of appropriate orifices with the discharge coefficients determined from the NASA report of Rohde et al. [35], tubes, momentum, and pressure chambers, shown in Fig. 3(*c*), was built and analyzed. Appropriate discharge coefficients for the orifices were calculated from correlations for sharp-corner holes. The results, shown in Fig. 4, reveal that the air mass flow rate through the middle (third) crossover hole for both parallel and circular flow cases approaches the average value of 20% as the jet mass flow rate becomes dominant. Our previous work on impingement with no external crossflow [33,34] also showed that the middle hole mass flow rate was within 1% of the average mass flow rate for each crossover hole. For those cases that the axial mass flow rate is dominant (small $M_{\text{jet}}/M_{\text{axial}}$ ratios), it creates a reverse flow across the first and, in some cases, across the second crossover hole thus increasing the mass flow through the middle hole and even more through the fourth and fifth holes. This behavior was confirmed qualitatively by our CFD analyses to be discussed later. Figure 4 also shows that middle jet mass flow rates for the parallel cases (solid symbols) are slightly (1–1.5%) less than those of corresponding circular cases. The reason for this slight difference is that the flow analysis results showed a smaller reverse flow through the first and second holes in the parallel flow cases. This small reduction in axial flow entrainment into the feed channel caused the slight flow reduction in the middle crossover hole. Experimental uncertainty in heat transfer coefficient, following the method of Kline and McClintock [36], was determined to be 6%. For clarity, we will discuss the results of parallel and circular flows separately and then compare them.

Figure 5 shows the heat transfer results for the parallel flow cases on the nose and sidewall of the leading-edge channel at five axial flow Reynolds numbers. Several observations are made. The heat transfer coefficients on the sidewalls are consistently higher than those on the leading-edge nose. This behavior, which is the opposite of what is observed for the impingement with no external cross-flow, was expected due to the presence of the external axial flow in this study. The leading-edge axial flow not only has a strong convective effect on the sidewalls but it diverts the impinging jets away from the nose and towards the sidewalls thus further increases the sidewalls, heat transfer coefficient. As the axial flow Reynolds number (mass flow rate) increases, the slopes of the heat transfer coefficient trends reduce indicating that, as the axial flow becomes dominant, impinging jets, especially at lower jet Reynolds numbers, have less and less effects on the heat transfer coefficients.

Figure 6 shows the heat transfer results for the circular flow cases on the nose and sidewall of the leading-edge channel at five axial flow Reynolds numbers. The general behaviors of the heat transfer results are similar to that of the parallel flow, i.e., the heat transfer coefficients on the sidewalls are consistently higher than those on the leading-edge nose and as the axial flow increases, the slopes of the heat transfer coefficient trends reduce. The same reasoning applies to this flow arrangement since the only difference between the two sets of results is a slight increase or decrease in the heat transfer coefficients depending on the jet and axial flow Reynolds numbers.

Figure 7 compares the heat transfer results of this study with

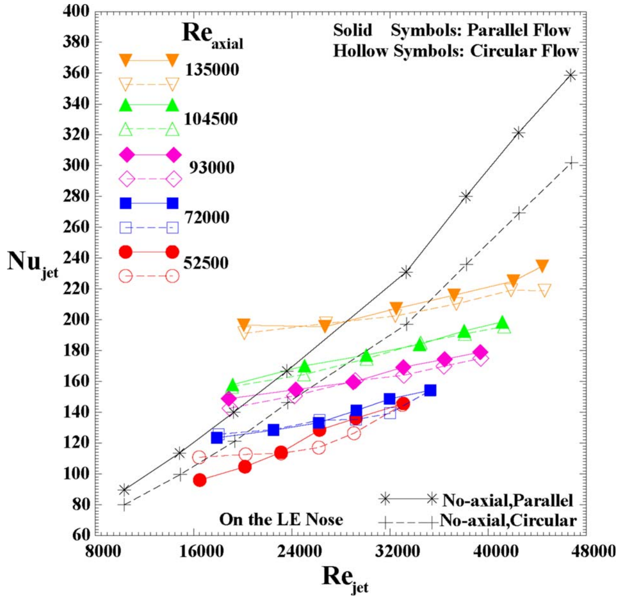

**Fig. 7 Comparison between the heat transfer results with and without the presence of external cross-flow and nose surface**

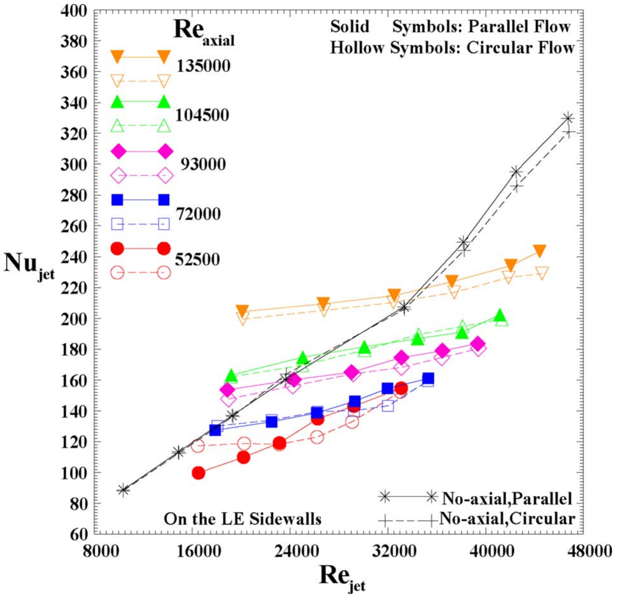

**Fig. 8 Comparison between the heat transfer results with and without the presence of external cross-flow and sidewalls**

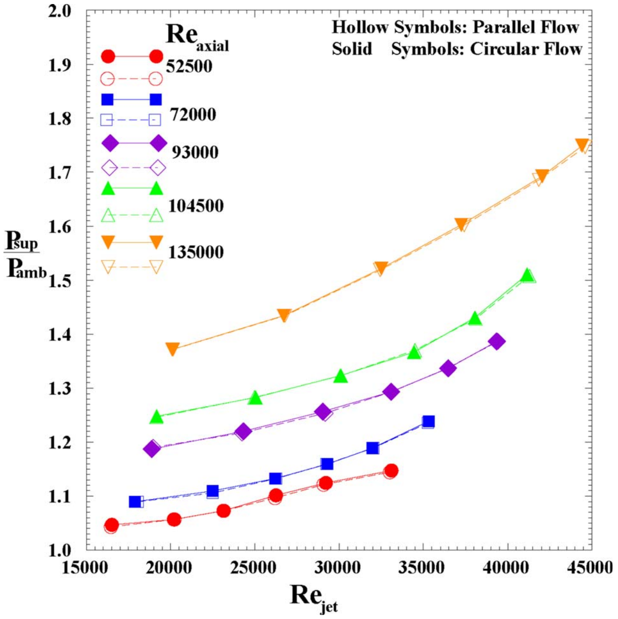

**Fig. 9 Supply channel pressure variation**

those of jet impingement in the same geometry with no external leading-edge axial flow. For better clarity and at the same time comparing the parallel and circular flow results of otherwise identical conditions, Fig. 7 represents the heat transfer results on the nose area of the leading-edge channel while Fig. 8 shows the sidewall results. In both figures, impingement without any external axial flow curves has much higher slopes compared to those corresponding to impingement in the presence of a strong cross-flow for which as $M_{\text{jet}}/M_{\text{axial}}$ decreases, slopes of the curves decrease until they reach a close to zero slope indicating that a strong axial flow washes away the impinging jets as the numerical results shown in Figs. 10 and 11 confirm that. It is seen that the general effect of the cross-flow is a reduction heat transfer coefficients both on the nose and sidewalls. Those limited data points corresponding to the case of impingement in the presence of axial flow that are higher in magnitude than those for the cases of impingement without any external cross-flow are at the lower end on the jet Reynolds numbers and at the highest end of the axial flow Reynolds numbers. In other words, only a very strong axial cooling flow could have the heat transfer effects of an impinging cooling flow with a mass flow rate less than one-fifth of that (see Fig. 4).

Figure 9 represents the pressure ratio variation with the jet Reynolds number for all axial flow conditions. This pressure ratio represents the supply channel pressure normalized with the ambient pressure to which the leading-edge channel is dumped. The supply channel pressure that, for most cases, acted like a plenum was measured at the middle crossover hole location. For the same reason, no pressure difference was measured between the supply and leading-edge channels. As expected, the supply channel pressure increased with both jet flow and axial flow rates. The difference in pressure ratio for the parallel and circular flows was insignificant.

**Numerical Results.** Velocity vectors for parallel and circular flows of otherwise identical conditions are shown in Figs. 10 and 11. These vector plots are on the symmetry planes that pass through the centers of the supply and leading-edge channels as well as the crossover holes. It is seen that the general flow fields around the impingement target surfaces are very similar and as our flow circuit analysis showed, the first two crossover holes do not receive their share of the jet flow due to the strong resistance from the axial flow in the leading-edge channel. The impingement effects of the middle jet are reduced by the presence of the cross-flow and only the fourth and fifth jets have effectively penetrated into the axial channel flow. CFD results of heat transfer coefficients on the active target surface (copper pieces) are shown in Fig. 12. CFD models with constant heat flux boundary conditions were run on a unix workstation. A typical case took about 5000 iterations and about 10–20 h to converge. The high values on the first set of guard heaters are due to the start of thermal boundary layer at that location. On the middle pieces, however, a fairly uniform heat transfer coefficient is seen on both nose and

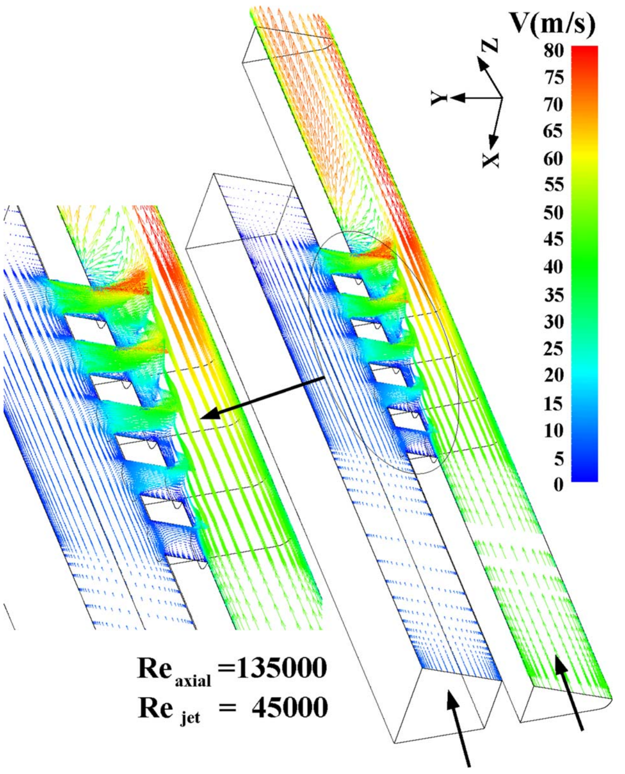

**Fig. 10 CFD results of parallel flow velocity field on the symmetry plane**

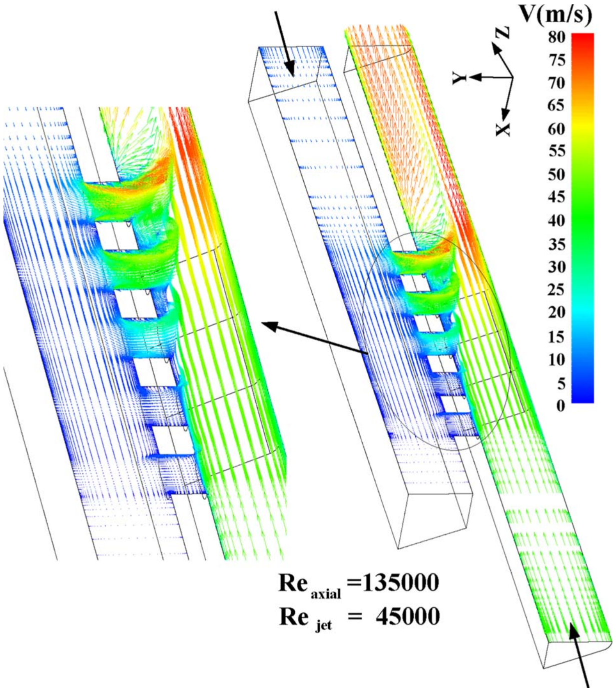

**Fig. 11 CFD results of circular flow velocity field on the symmetry plane**

sidewalls.

Figure 13 compares the measured and numerically calculated heat transfer results on both the nose and sidewalls for a typical circular flow arrangement. Given the fairly complex flow domain, the agreement between the test and CFD results is good. The CFD results both on the nose and sidewalls, falling consistently below the measured values, show a difference ranging from $-8\%$ to $-20\%$. These results, as was mentioned above, were obtained using the $\nu 2f$ turbulence model. Other available turbulence models including the $k$-$\varepsilon$ model produced results that were about 20% less than those of the $\nu 2f$ model.

## Conclusions

Leading-edge impingement heat transfer coefficients in the presence of an external cross-flow were measured for two jets versus axial flow arrangements. Heat transfer results on the leading-edge nose and on the sidewalls were measured and reported separately. Representative CFD results were also presented. The major conclusions of this study were as follows.

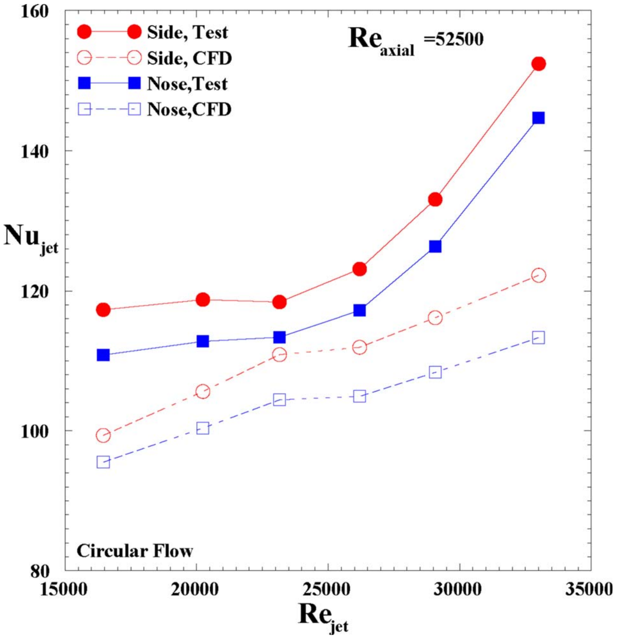

**Fig. 13 Comparison between the experimental and numerical heat transfer results**

(a) The presence of the external cross-flow reduced the impinging jet effectiveness both on the nose and sidewalls.
(b) Even for an axial to jet mass flow ratio as high as 5, the convective heat transfer coefficient produced by the axial channel flow was less than that of the impinging jet without the presence of the external cross-flow.
(c) The agreement between the numerical and experimental results was reasonable with an average difference ranging from $-8\%$ to $-20\%$.

## Nomenclature

$A_{HT}$ = heat transfer area

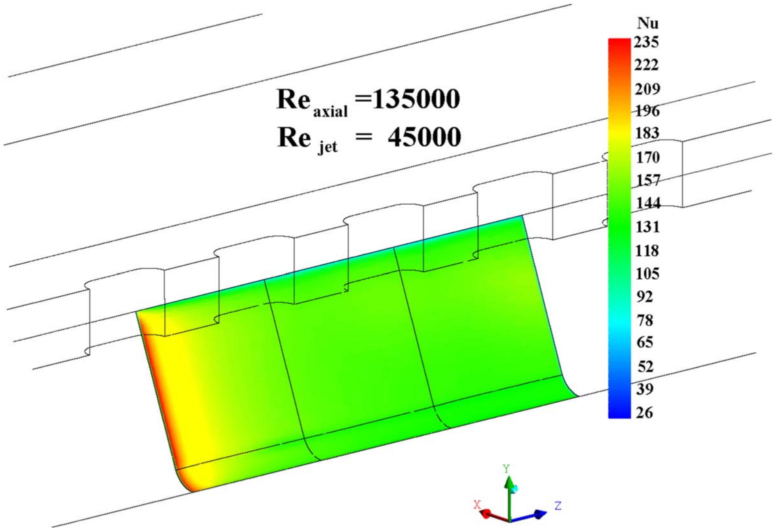

**Fig. 12 Typical CFD results of heat transfer coefficient on the target surface**

$d_{\text{jet}}$ = racetrack crossover hole hydraulic diameter (2.229 cm)
$D_h$ = leading-edge channel hydraulic diameter (4.684 cm)
$h$ = average heat transfer coefficient on the leading edge or sidewalls, $[(vi/A_{\text{HT}})-q_{\text{loss}}]/(T_s-T_{\text{jet}})$
$i$ = current through the foil heater on the middle copper piece
$k$ = air thermal conductivity
$M_{\text{axial}}$ = axial mass flow rate entering the leading-edge channel
$M_{\text{jet}}$ = total jet mass flow rate entering the supply channel
$M_{\text{jet,middle}}$ = middle jet mass flow impinging on the leading-edge channel walls
$\text{Nu}_{\text{jet}}$ = average Nusselt number based on the crossover hole hydraulic diameter, $hd_{\text{jet}}/k$
$P$ = leading-edge channel perimeter
$P_{\text{hole}}$ = each crossover hole perimeter
$P_{\text{sup}}$ = supply channel pressure
$P_{\text{amb}}$ = ambient pressure
$q_{\text{loss}}$ = heat losses from the middle brass piece to the ambient by conduction and convection as well as the heat losses by radiation to the unheated walls
$R_{\text{nose}}$ = channel radius at the leading edge
$\text{Re}_{\text{axial}}$ = axial flow Reynolds number based on the leading-edge channel diameter $(4M_{\text{axial}}/P\mu)$
$\text{Re}_{\text{jet}}$ = jet Reynolds number based on the middle jet mass flow rate and hydraulic diameter $(4M_{\text{jet,middle}}/P_{\text{hole}}\mu)$
$T_{\text{jet}}$ = air jet temperature
$T_s$ = surface temperature
$Z$ = jet place distance to the target surface (Fig. 1)
$v$ = voltage drop across the foil heater on the middle copper pieces
$\mu$ = air dynamic viscosity at jet temperature
$\rho$ = air density at jet temperature and pressure

## References

[1] Burggraf, F., 1970, "Experimental Heat Transfer and Pressure Drop With Two Dimensional Turbulence Promoters Applied to Two Opposite Walls of a Square Tube," *Augmentation of Convective Heat and Mass Transfer*, A. E. Bergles and R. L. Webb, eds., ASME, New York, pp. 70–79.
[2] Chandra, P. R., and Han, J. C., 1989, "Pressure Drop and Mass Transfer in Two-Pass Ribbed Channels," J. Thermophysics, **3**(3), pp. 315–319.
[3] El-Husayni, H. A., Taslim, M. E., and Kercher, D. M., 1994, "An Experimental Investigation of Heat Transfer Coefficients in a Spanwise Rotating Channel With Two Opposite Rib-Roughened Walls," ASME J. Turbomach., **113**, pp. 75–82.
[4] Han, J. C., 1984, "Heat Transfer and Friction in Channels With Two Opposite Rib-Roughened Walls," ASME J. Heat Transfer, **106**(4), pp. 774–781.
[5] Han, J. C., Glicksman, L. R., and Rohsenow, W. M., 1978, "An Investigation of Heat Transfer and Friction for Rib Roughened Surfaces," Int. J. Heat Mass Transfer, **21**, pp. 1143–1156.
[6] Han, J. C., Park, J. S., and Lei, C. K., 1985, "Heat Transfer Enhancement in Channels With Turbulence Promoters," ASME J. Eng. Gas Turbines Power, **107**(1), pp. 628–635.
[7] Han, J. C., Zhang, Y. M., and Lee, C. P., 1992, "Influence of Surface Heat Flux Ratio on Heat Transfer Augmentation in Square Channels With Parallel, Crossed, and V-shaped Angled Ribs," ASME J. Turbomach., **114**, pp. 872–880.
[8] Metzger, D. E., Vedula, R. P., and Breen, D. D., 1987, "The Effect of Rib Angle and Length on Convection Heat Transfer in Rib-Roughened Triangular Ducts," *Proceedings of the ASME-JSME Thermal Engineering Joint Conference*, Vol. 3, pp. 327–333.
[9] Metzger, D. E, Chyu, M. K., and Bunker, R. S., 1988, "The Contribution of On-Rib Heat Transfer Coefficients to Total Heat Transfer From Rib-Roughened Surfaces," *Transport Phenomena in Rotating Machinery*, J. H. Kim, ed., Hemisphere, Washington, DC.
[10] Metzger, D. E., Fan, C. S., and Yu, Y., 1990, "Effects of Rib Angle and Orientation on Local Heat Transfer in Square Channels With Angled Roughness Ribs," *Compact Heat Exchangers: A Festschrift for A. L. London*, Hemisphere, Washington, DC, pp. 151–167.
[11] Taslim, M. E., and Spring, S. D., 1988, "An Experimental Investigation of Heat Transfer Coefficients and Friction Factors in Passages of Different Aspect Ratios Roughened With 45° Turbulators," *Proceedings of National Heat Conference*, Houston, TX.
[12] Taslim, M. E., and Spring, S. D., 1988, "Experimental Heat Transfer and Friction Factors in Turbulated Cooling Passages of Different Aspect Ratios, Where Turbulators are Staggered," Paper No. AIAA-88-3014.
[13] Taslim, M. E., Bondi, L. A., and Kercher, D. M., 1991, "An Experimental Investigation of Heat Transfer in an Orthogonally Rotating Channel Roughened 45 Degree Criss-Cross Ribs on Two Opposite Walls," ASME J. Turbomach., **113**, pp. 346–353.
[14] Taslim, M. E., and Spring, S. D., 1991, "An Experimental Investigation Into the Effects Turbulator Profile and Spacing Have on Heat Transfer Coefficients and Friction Factors in Small Cooled Turbine Airfoils," Paper No. AIAA-91-2033.
[15] Taslim, M. E., Rahman, A., and Spring, S. D., 1991, "An Experimental Investigation of Heat Transfer Coefficients in a Spanwise Rotating Channel With Two Opposite Rib-Roughened Walls," ASME J. Turbomach., **113**, pp. 75–82.
[16] Webb, R. L., Eckert, E. R. G., and Goldstein, R. J., 1971, "Heat Transfer and Friction in Tubes With Repeated-Rib-Roughness," Int. J. Heat Mass Transfer, **14**, pp. 601–617.
[17] Zhang, Y. M., Gu, W. Z., and Han, J. C., 1994, "Heat Transfer and Friction in Rectangular Channels With Ribbed or Ribbed-Grooved Walls," ASME J. Heat Transfer, **116**(1), pp. 58–65.
[18] Chupp, R. E., Helms, H. E., McFadden, P. W., and Brown, T. R., 1969, "Evaluation of Internal Heat Transfer Coefficients for Impingement Cooled Turbine Blades," J. Aircr., **6**(1), pp. 203–208.
[19] Metzger, D. E., Yamashita, T., and Jenkins, C. W., 1969, "Impingement Cooling of Concave Surfaces With Lines of Circular Air Jets," ASME J. Eng. Power, **93**(3), pp. 149–155.
[20] Kercher, D. M., and Tabakoff, W., 1970, "Heat Transfer by a Square Array of Round Air Jets Impinging Perpendicular to a Flat Surface Including the Effect of Spent Air," ASME J. Eng. Power, **92**(1), pp. 73–82.
[21] Florschuetz, L. W., Berry, R. A., and Metzger, D. E., 1980, "Periodic Streamwise Variation of Heat Transfer Coefficients for Inline and Staggered of Circular Jets With Crossflow of Spent Air," ASME J. Heat Transfer, **102**(1), pp. 132–137.
[22] Florschuetz, L. W., Truman, C. R., and Metzger, D. E., 1981, "Streamwise Flow and Heat Transfer Distribution for Jet Impingement With Crossflow," ASME J. Heat Transfer, **103**(2), pp. 337–342.
[23] Florschuetz, L. W., Metzger, D. E., Su, C. C., Isoda, Y., and Tseng, H. H., 1984, "Heat Transfer Characteristics for Jet Arrays Impingement With Initial Crossflow," ASME J. Heat Transfer, **106**(1), pp. 34–41.
[24] Metzger, D. E., and Bunker, R. S., 1990, "Local Heat Transfer in Internally Cooled Turbine Air-Foil Leading Edge Regions: Part I—Impingement Cooling Without Film Coolant Extraction," ASME J. Turbomach., **112**(3), pp. 451–458.
[25] Bunker, R. S., and Metzger, D. E., 1990, "Local Heat Transfer in Internally Cooled Turbine Air-Foil Leading Edge Regions: Part II—Impingement Cooling With Film Coolant Extraction," ASME J. Turbomach., **112**(3), pp. 459–466.
[26] Van Treuren, K. W., Wang, Z., Ireland, P. T., and Jones, T. V., 1994, "Detailed Measurements of Local Heat Transfer Coefficient and Adiabatic Wall Temperature Beneath an Array of Impinging Jets," ASME J. Turbomach., **116**(2), pp. 269–374.
[27] Chang, H., Zhang, D., and Huang, T., 1997, "Impingement Heat Transfer From Rib Roughened Surface Within Arrays of Circular Jet: The Effect of the Relative Position of the Jet Hole to the Ribs," Paper No. 97-GT-331.
[28] Huang, Y., Ekkad, S. V., and Han, J. C., 1998, "Detailed Heat Transfer Distributions Under an Array of Orthogonal Impinging Jets," J. Thermophys. Heat Transfer, **12**(1), pp. 73–79.
[29] Akella, K. V., and Han, J. C., 1999, "Impingement Cooling in Rotating Two-Pass Rectangular Channels With Ribbed Walls," J. Thermophys. Heat Transfer, **13**(3), pp. 364–371.
[30] Taslim, M. E., Pan, Y., and Spring, S. D., 2001, "An Experimental Study of Impingement on Roughened Airfoil Leading-Walls With Film Holes," ASME J. Turbomach., **123**(4), pp. 766–773.
[31] Taslim, M. E., and Setayeshgar, L., 2001, "Experimental Leading-Edge Impingement Cooling Through Racetrack Crossover Holes," Paper No. 2001-GT-0153.
[32] Taslim, M. E., Setayeshgar, L., and Spring, S. D., 2001, "An Experimental Evaluation of Advanced Leading Edge Impingement Cooling Concepts," ASME J. Turbomach., **123**(2), pp. 147–153.
[33] Taslim, M. E., Bakhtari, K., and Liu, H., 2003, "Experimental and Numerical Investigation of Impingement on a Rib-Roughened Leading-Wall," ASME J. Turbomach., **125**, pp. 682–691.
[34] Taslim, M. E., and Khanicheh, A., 2006, "Experimental and Numerical Study of Impingement on an Airfoil Leading-Edge With and Without Showerhead and Gill Film Holes," ASME J. Turbomach., **128**(2), pp. 310–320.
[35] Rohde, J. E., Richards, H. T., and Metger, G. W., 1969, "Discharge Coefficients for Thick Plate Orifices With Approach Flow Perpendicular and Inclined to the Orifice Axis," NASA Report No. TN-5467.
[36] Kline, S. J., and McClintock, F. A., 1953, "Describing Uncertainty in Single-Sample Experiments," Mech. Eng. (Am. Soc. Mech. Eng.), **75**, pp. 3–8.